Morphology-Dependent Black Hole Mass Scaling Relations

Nandini Sahu

Presented in fulfillment of the requirements
of the degree of Doctor of Philosophy

December 2021

School of Science, Computing and Engineering Technologies
Swinburne University of Technology

Abstract

Since the consensus that a massive black hole (BH) resides at the centre of almost every galaxy (local quiescent as well as the distant active galaxies), astronomers have tried to determine the correlations between BH mass ($M_{\rm BH}$) and host galaxy properties, as evidence of the BH-galaxy *co-evolution*. This thesis expands on the previous efforts to discover these relations, using the largest-yet sample of 127 galaxies, doubling the sample in Savorgnan et al. (2016), with reliable directly-measured $M_{\rm BH}$ and host galaxy properties obtained using state-of-the-art image analysis techniques.

I used the software Isofit and Cmodel to create galaxy models capturing the galaxy's surface brightness, ellipticity, position angle, and structural irregularities, especially prevalent in multi-component galaxies, quantified using the higher-order Fourier coefficients, at each isophote. This information and additional research on each galaxy to identify its components (e.g., the presence of disk, bar, and nuclear components identified from kinematic surveys, literature, and Hubble Space Telescope images) were taken into account while disassembling the total galaxy light into its components, using special functions to capture the luminosity associated with each galaxy component. This analysis provided detailed galaxy morphology, including accurate bulge stellar mass ($M_{*,\rm sph}$), and other bulge structural properties captured by the Sérsic model parameters: Sérsic index (shape parameter, $n_{\rm sph}$), effective half-light radius ($R_{\rm e,sph}$), and surface brightness (*aka* projected luminosity density) $\mu_{\rm e,sph}$ at this radius. I additionally deprojected the Sérsic model of the bulge to obtain the internal stellar density, $\rho(r)$, profile and associated parameters.

In this thesis I investigated an array of morphology-dependent correlations of $M_{\rm BH}$ with host galaxy's total stellar mass ($M_{*,\rm gal}$), central stellar velocity dispersion (σ), and various spheroid properties, e.g., $M_{*,\rm sph}$, central light concentration (inferred by $n_{\rm sph}$), spheroid scale radii (including $R_{\rm e,sph}$), projected density at various spheroid radii (including densities $\mu_{0,\rm sph}$ and $\mu_{\rm e,sph}$ at the centre and $R_{\rm e,sph}$, respectively), and internal (deprojected) density $\rho_{\rm sph}$ at various spheroid radii (including the density $\rho_{\rm soi,sph}$ at the sphere-of-influence of the central BH). Importantly, I explored the role of galaxy morphology in these BH-galaxy correlations by analyzing the behaviour of various morphological classes. For example, early-type galaxies (ETGs: E, ES, S0) versus late-type galaxies (LTGs: S),

galaxies with and without a rotating stellar disk, barred versus non-barred galaxies, active and quiescent galaxies (in terms of an AGN), and Sérsic (normal/low-mass, evolve through gas-rich processes) versus core-Sérsic (massive, evolve through dry-mergers) galaxies.

Consequently, this investigation has discovered significantly modified black hole mass scaling relations with consistent morphology-dependent substructures. ETGs without a disk (E, slow rotators), ETGs with a disk (ES/S0, fast-rotators), and LTGs (spiral galaxies) define distinct relations in the $M_{\rm BH}$–spheroid (mass, size, and density) diagrams. An $M_{\rm BH}$–$M_{*,\rm gal}$ relation exists where ETGs and LTGs define different relations. The $M_{\rm BH}$–σ relation has an upturn at the high-$M_{\rm BH}$ end due to the core-Sérsic galaxies, whereas Sérsic galaxies define the shallower part of the relation. The $M_{\rm BH}$–$\rho_{\rm soi,sph}$ diagram shows a similar but independent division due to core-Sérsic and Sérsic galaxies; however, further investigation shows a role of the Sérsic index in this division suggesting a possible BH-spheroid plane $M_{\rm BH}$–$\rho_{\rm soi,sph}$–$n_{\rm sph}$, to be explored in the future. These new morphology-dependent scaling relations significantly improve our understanding of BH-galaxy correlations and challenge the notion of a single fundamental BH-galaxy relation, identified in the past, based on intrinsic scatter inherent in the various scaling relations. If defaulting to the smallest scatter as the basis for identifying the fundamental relation, then such an approach currently suggests different fundamental relations depending on galaxy type.

The current BH scaling relations depend on galaxy morphology, where a galaxy's morphology is linked with its formation and evolutionary paths. Thus, these relations can form tests for modern simulations and theories of black hole-galaxy co-evolution. Our various morphology-dependent BH scaling relations accurately predict $M_{\rm BH}$ in other galaxies and provide alternatives to do the same. Additionally, the relations pose ramifications for many areas of astronomy, including the virial-mass f-factor required in the reverberation mapping technique and offer morphology-aware BH mass functions, improved estimates of BH merger time scale, and the BH merger rate (i.e., the number of merging BH binaries per unit volume, redshift, and binary mass) required for estimating detectable amplitude and frequency of the stochastic gravitational waves. Thus, these scaling relations can improve predictions for detecting long-wavelength gravitational waves (generated during massive BH mergers) by the pulsar timing arrays and the upcoming space interferometers.

Dedicated to my father, Mr. Munna Lal Sahu, who himself couldn't get an opportunity to go to school, but worked extremely hard to make me capable of achieving the highest degree in my favourite field of science.

Acknowledgements

Many people have inspired me and paved my path during my student life, leading me here. My parents and elder siblings are the constants who always ensured to provide me with all the resources to study and choose my career. Since I was a little girl, I aspired to become an astronaut after my father told me about Indian origin astronaut Dr. Kalpana Chawla. I realized my passion for mathematics and science after my brother-cum-teacher Mr. Shakti Kumar started giving me challenging problems while preparing for a secondary school scholarship. This passion was boosted when I got an opportunity to learn science and maths from my secondary school teachers Mr. Rakesh Pratap Mishra and Mr. Kamal Kumar Singh, at Jawahar Navodaya Vidyalaya Faizabad, and my senior year teachers Mr. Gaurav Yadav and Mr. Shantipada Panda, discussions with whom made physics fun for me. During my integrated master's degree, my short-term internship at IIST, which hosts brilliant female astrophysicists like Dr. Sarita Vig, Dr. Reshmi Lekshmi, and Dr. Anandmayee Tej, pumped me with inspirations to study astrophysics. And, further, working with my master's supervisor, Dr. Prasun Dutta, motivated me to pursue an academic career in astrophysics. I am truly grateful to these people and many co-passengers of my life's journey until now who influenced me in such a way that I landed here in Melbourne, Australia, to achieve my doctorate in astrophysics.

My Ph.D. experience has been fantastic at CAS, which hosts an inclusive and encouraging environment, and so many brilliant, hard-working researchers, simply looking at the people around me doing their own job so devotedly, always motivated me to do my best. I am sincerely grateful to have Prof. Alister Graham as my Ph.D. supervisor, whose guidance for my thesis has resulted in what I believe is a significant contribution to the field. I am incredibly thankful to him for his patience and time to help me improve my academic writing and always entertain my silly questions. A big thanks to my co-supervisor, Dr. Benjamin Davis, for his supervision and patience in listening to my arbitrary ideas, many of which were unfounded, but some of them became a part of my thesis. Thanks to Dr. Michelle Cluver, who has been a great mentor, and Dr. Edward (Ned) Taylor for always encouraging me.

I additionally thank my thesis examiners Prof. Richard McDermid and Dr. Dieu Nyugen, for reading my thesis with great interest and providing valuable comments and suggestions for future work. Due to the COVID-19 pandemic, I got relocated to Brisbane in March 2020. I am very grateful to the astrophysics group at the University of Queensland (UQ), especially Prof. Tamara Davis and Dr. Sarah Sweet, for providing me a great office space for a whole year. Thanks to Hayley Valiantis for arranging this and for all the other help during my stay at UQ.

I am also thankful to my Ph.D. siblings and friends Poojan, Gurvarinder, Rahul, Arianna, and Hasti, who were always supportive, occasionally got me out of stuck-in-work mode with cupcakes and coffee, and made my time at CAS very enjoyable. A huge thanks to my dear friend Bharti for her continued interest in my work, life events, and support during the low times of the pandemic. Finally, a huge thank you to the moon and back Harshit, who has been my inspiration for the last four years and has been extremely supportive and motivating for me.

Declaration

The work presented in this thesis has been carried out in the Centre for Astrophysics & Supercomputing at Swinburne University of Technology between November 2017 and August 2021. This thesis contains no material that has been accepted for the award of any other degree or diploma. To the best of my knowledge, this thesis contains no material previously published or written by another author, except where due reference is made in the text of the thesis. The content of the chapters listed below has appeared in refereed journals.

- Chapter 2 has been published as **Nandini Sahu**, Alister W. Graham, Benjamin L. Davis, "**Black Hole Mass Scaling Relations for Early-type Galaxies. I. $M_{\rm BH}$–$M_{*,\rm sph}$ and $M_{\rm BH}$–$M_{*,\rm gal}$**", 2019a Astrophysical Journal, 876, 155.
- Chapter 3 has been published as **Nandini Sahu**, Alister W. Graham, Benjamin L. Davis, "**Revealing Hidden Substructures in the $M_{\rm BH}$–σ Diagram, and Refining the Bend in the L–σ Relation**", 2019b Astrophysical Journal, 887, 10.
- Chapter 4 has been published as **Nandini Sahu**, Alister W. Graham, Benjamin L. Davis, "**Defining the (black hole)-spheroid connection with the discovery of morphology-dependent substructures in the $M_{\rm BH}$–$\rm n_{sph}$ and $M_{\rm BH}$–$\rm R_{e,sph}$ diagrams: new tests for advanced theories and realistic simulations**", 2020 Astrophysical Journal, 903, 97.

The content of following chapter is accepted to appear in a refereed journal.

- Chapter 5 is to be submitted as **Nandini Sahu**, Alister W. Graham, Benjamin L. Davis,"**The (Black Hole Mass)-(Spheroid Stellar Density) Relations: $M_{\rm BH}$–μ (and $M_{\rm BH}$–Σ) and $M_{\rm BH}$–ρ**", 2021 Astrophysical Journal.

My contribution to these papers includes performing all the required analysis, presentation, interpretation of the results, and writing the manuscripts, accounting for 80% of the final manuscripts. Critical discussions on science and interpretation of results with Prof. Alister Graham was very helpful in accomplishing this work. I acknowledge that comments and feedback on the written manuscripts from the co-authors Prof. Alister Graham and Dr Benjamin Davis significantly improved the quality of these papers, accounting for about 15% and 5% of the final manuscripts.

I warrant that I have obtained, where necessary, permission from the copyright owners to use any third party copyright material reproduced in the thesis, or to use any of my own published work in which the copyright is held by another party. The Astrophysical Journal is a part of American Astronomical Society (AAS) journals. AAS grants the named authors right to include a Preprint or Accepted Manuscript (after the embargo period) in the online version of the thesis or dissertation, provided it is done in accordance with their policies on sharing Preprints or Accepted Manuscripts[1]. This thesis uses the accepted versions of the published papers. The published sources have been acknowledged above, along with a link to the published versions, as per AAS policy.

Nandini Sahu
Melbourne, Victoria, Australia
December 2021

[1] See the journal's website for more details.

Contents

List of Figures

List of Tables

1

Black Holes and their Host Galaxies

In the early 1600s, Galileo Galilei used his telescope to reveal that our home nebula, the Milky Way galaxy, consists of a vast number of stars in addition to the ones visible to the naked eye. The term nebula was generally used for extended cloudy objects seen in the night sky. The astronomer Thomas Wright hypothesised in 1750 that, similar to the solar system, the Milky Way is a rotating body comprised of numerous gravitationally bound stars. Building on this, in 1755, philosopher Immanuel Kant speculated that the extended interstellar cloudy objects seen in our night sky are not a part of the Milky Way, but they are separate nebulae, popularly called as *Island Universes*, beyond the Milky Way. Of all the bright objects visible with the naked eye in the night sky, most are the stars belonging to our home galaxy, except for the neighbouring[1] galaxies Andromeda (Messier or M 31), Triangulum (M 33), and the Milky Way's satellite galaxies, the Large Magellanic Cloud (LMC) and Small Magellanic Cloud (SMC). Many such nebulae (i.e., galaxies) which were closest to Earth were identified in the catalogue of Charles Messier (1781), William Herschel (1786, 1789, 1802), and later, John Herschel (1864). Owing to improvements in instrumentation, the hypothesis of independent *Island Universes* outside the Milky Way was supported by subsequent photographic and spectrographic observations (Rosse, 1850; Slipher, 1913; Curtis, 1913, 1917; Opik, 1922; Hubble, 1929), inaugurating the field of extragalactic astronomy.

Extragalactic astronomy includes the study of all the galaxies outside the Milky Way

[1] These galaxies are one of the many members of our Local (galaxy) Group (Hubble, 1936).

up to the first galaxies[2], estimated to have formed less than a billion years after the Big Bang, and various phenomena or objects they host, including the exotic object such as a *black hole*. Black holes (BHs) are incredibly dense regions of space-time with extreme gravity such that even the light with its unbeatable speed cannot escape from it; hence, such objects are invisible on their own. The presence of such objects was first hypothesized by philosopher John Michell (1784), who called them "black stars". However, the firm mathematical prediction of BHs originated from Einstein's theory of general relatively (Einstein, 1916; Schwarzschild, 1916; Droste, 1917; Eddington, 1924; Lemaître, 1933).

Continuously improving technology, better telescopes, and better observations have enabled significant developments in galaxy formation and evolution physics. Notably, the observational study of BHs has advanced tremendously, beginning with the detection of the first star-like galaxy (3C 273) with an active central BH, billions of light-years away from us (Schmidt, 1965) to now directly imaging the BHs (Event Horizon Telescope Collaboration et al., 2019). Now, almost all the galaxies are assumed to host a massive BH, active or not, at their centres (Lynden-Bell & Rees, 1971), where the BH feeds on the local content of the galaxy. Inevitably, the host galaxy controls the growth of BH through feeding and mergers, and the other way around, the central BH can affect the properties of the host galaxy via feedback (Silk & Rees, 1998; Fabian, 1999), suggesting a "Co-evolution" between the BH and the host galaxy.

This thesis investigates the case of (black hole)-(host galaxy) co-evolution by observing the correlations between BH mass and various host galaxy properties using an up-to-date sample of accurately measured BH masses and galaxy properties. The literature holds numerous investigations on the correlations between BH mass and the mass of spheroid, which immediately surrounds the BH in most galaxies and is one of the many other possible components present in a galaxy. Extracting the spheroid mass from the rest of the galaxy is a challenging task, and it requires one to identify and account for various structures present in the galaxy. We use unprecedented techniques and large field-of-view images, primarily taken by the Spitzer Space Telescope, to extract the bulge properties, including its mass, and expanded on previous efforts to establish various BH scaling relations.

The following Section 1.1 presents a historical recap of notable efforts on classifying

[2] A recent observational evidence can be seen in Oesch et al. (2016).

galaxies based on their apparent structure, which formed the basis of current galactic formation evolution studies and introduced some recent advances in the morphological scheme, which will also play a vital role in the understanding of the latest observed black hole-galaxy correlations. Section 1.2 provides a brief historical account of essential studies on BHs, from the very first recorded speculation of the existence of something like a BH to the belief that BHs may be present in almost every galaxy (Section 1.2). Section 1.3 reviews some of the numerous past efforts in establishing the black hole-spheroid relations, and Section 1.4 highlights the direct application of BH scaling relations for other closely related studies. Section 1.5 highlights the objectives of this work which are present in the following chapters.

1.1 Galaxy Structure and Morphology

Galaxies are observed in different shapes and have various structures formed over time, depending on the kinematics of their progenitor gas/dust cloud and the environment. Hence, the galaxy structure, encoded in *galaxy morphology*, observed at a time, holds information about the evolutionary track followed in the past. Since the realization of other galaxies outside our galaxy in the late 1800s and early 1900s, astronomers have tried to classify galaxies based on their apparent structures to understand their evolution. Around that time, the perceived idea about the galaxy evolution was that in the early Universe, the proto-galactic clouds collapsed into simple spheroidal or elliptical galaxies, which went on being oblate due to rotation, generated prominent two-dimensional (2D) disks surrounding their spheroid, and external gravitational torques from the nearby passing galaxies (flybys) pulled on a galaxy's material forming the curved spiral arms due to rotation. This galaxy evolution sequence was based on the hypothesis of the solar system formation by Laplace (1796), which was modified by Aitken (1906) to include spiral arms in spiral galaxies, first seen by William Parsons (Rosse, 1850). This theorised evolutionary sequence led Aitkens, Jeans and Hubble to the notion of early- and late-type galaxies, a theory they dropped by the mid-1920s but the early- and late-type galaxy terminology remained.

The tuning fork sequence

One of the famously referred classification schemes is the Jeans-Hubble tuning fork diagram (Hubble, 1926; Jeans, 1928; Hubble, 1936) representing the above galaxy evolution sequence (Aitken, 1906), which also subsumed some ideas suggested by other theoretical and observational works[3] (e.g. Curtis, 1918; Jeans, 1919b,a; Reynolds, 1920, 1925; Lundmark, 1925). The tuning fork diagram begins with almost pure spheroidal elliptical (E0-E4) galaxies, then oblate ellipticals (e.g., E5-E7) represented on the handle of the tuning fork, followed by the lenticulars (S0) forming the junction between oblate ellipticals and spirals galaxies. Spirals were divided by the two prongs of the tuning fork depending on the presence of a bar (e.g., Sa, Sb, Sc for non-barred and SBa, SBb, SBc for barred spirals), where the bar in a spiral galaxy was first recognized by Knox-Shaw (1915) and Curtis (1918). The number associated with the letter E (or elliptical sub-type) indicates the apparent ellipticity without the decimal (or ten times the ellipticity[4] value). This sequence between ellipticals to spirals was simply based on the apparent bulge-to-disk dominance. The spiral sub-types (a, b, c) were based on the relative dominance of the bulge, the winding angle, and the resolution of spiral arms. The galaxies that were thought to be formed first were called early-type galaxies (ETGs: elliptical and lenticular), and the ones with complicated structures that were thought to form later were called the late-type galaxies (LTGs: spirals). Now it is agreed upon that the so-called ETGs and LTGs do not follow such a temporal evolution sequence. However, we still adhere to the early- and late-type galaxy terminology to refer to the two categories of galaxies.

Modified tuning fork sequence

de Vaucouleurs (1959a,b) and, subsequently, Sandage (1961), revised and expanded the tuning fork classification scheme with the addition of barred (B)/weak-barred (AB), lenticular galaxies, Sd-type (Shapley & Paraskevopoulos, 1940) for spiral galaxies with smaller central bulges and open/irregular/knotty spiral arms (than the Sc-type), Sm-type for LMC-like galaxies with a single asymmetric arm, Irr for SMC-like irregular galaxies, and

[3]See a short review in Sandage (2004) and a detailed review in Graham (2019a).

[4]Ellipticity is calculated as $(1 - R_{min}/R_{maj})$, where R_{maj} and R_{min} are the semi-major and semi-minor axes of the galaxy image.

importantly, they added a third dimension based on whether the spiral arms for LTGs originated from the nucleus/bulge (s), or a ring (r), or mixed (rs), e.g., used in de Vaucouleurs et al. (1991). These modifications complicated the tuning fork diagram, as accounting for every small galaxy structure in the morphology diagram is not very simple. Some other studies converted the tuning fork to Trident (van den Bergh, 1976) and Comb (Cappellari et al., 2011). The trident's handle represented elliptical galaxies as in the tuning fork, and the three arms of trident represented Spiral galaxies with normal spiral arms (Sa-Sb-Sc), weak spiral arms (Aa-Ab-Ac), and no spiral arm (S0a-S0b-S0c). This diagram was further modified to a Comb scheme, which aligned the handle (E0-E7) with the S0 arm.

The structural variation of LTGs, i.e., varying winding angle of spiral arms, presence and absence of a bar which has been generally associated with spiral galaxies, were very well captured by the Jeans-Hubble tuning fork diagram and its modifications. However, all these diagrams failed to represent the structural diversity of ETGs, especially the presence of intermediate-scale disks in the oblate ellipticals revealed by kinematic studies. Also, in general, the presence of large-scale disks were often missed in the previously classified E5-7 galaxies, as were bars in the previously classified S0 galaxies with photometric observations. Now, these ETG forms have been incorporated in a simple 2D morphology grid (Graham, 2019a).

Morphology Grid

Graham (2019a) presented a detailed structural classification of ETGs as well as LTGs in their morphology grid, shown in Figure 1.1. Here, ETGs include (spheroidal) elliptical galaxies, lenticular galaxies having large scale rotating stellar disks surrounding the bulge, and the ellicular (ES) galaxies having intermediate scale disks within their bulges, first identified by Liller (1966), placed between the first two classes. The term "ellicular" was coined by portmanteau of the words elliptical and lenticular in Graham et al. (2016a). This is because the presence of ellicular galaxies suggests a disk evolution sequence connecting elliptical and lenticular ETGs. LTGs include spiral galaxies, from Sa with very tightly bound spiral arms to Sd with loosely bound spiral arms and, further, (bulge-less) Sm-type galaxies with asymmetric/single spiral arms. The irregular (Irr) galaxies were not shown in this scheme, as they are unsettled systems that may later adopt one of the morphologies

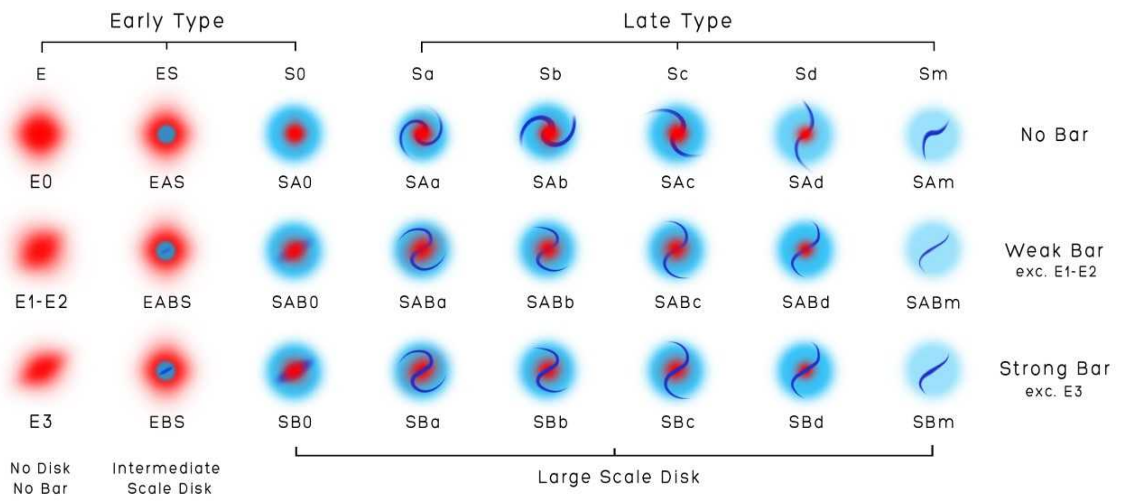

Figure 1.1 A new galaxy morphology diagram incorporating the structural diversity of ETGs as well as the LTGs (Graham, 2019a). The first column representing elliptical galaxies of this two-dimensional morphology grid is excluded from the classification, suggesting the absence (A: top row) or the presence of a weak (AB: middle row) or a strong (B: bottom row) bar component, as mentioned at the right side of the image.

included in the grid (Graham, 2019a). The horizontal axis of the grid, from left to the right, shows a sequence of bulge versus disk dominance. The vertical axis is based on presence of a strong bar (B), weak bar (AB), and no bar (A), from bottom to top, where the first column of (pure spheroidal) Elliptical galaxies are excluded from this designation.

In addition to bulge, disk, bar, and spiral arms (in LTGs), a galaxy can have other components, e.g., bar-lens, peanut-shell shaped bulges, ansae, bar-ring, which are all associated with the bar. Some of these features can be seen in the barred-galaxy images presented in Knapen (2005). In addition, there may be an outer ring, nuclear disk, nuclear bar[5], nuclear star cluster, etc. A bar is hosted in the galactic disk, it is an elongated structure spanning across the galactic centre, and its length relative to the bulge diameter can vary for different galaxies. The galactic bar is generally observed to be comprised of old stars, whose orbits get elongated because of large scale disk instabilities (Safronov, 1960; Toomre, 1964; Hohl, 1971; Combes & Elmegreen, 1993). A bar also has internal instabilities which cause it to buckle within and above the disk plane, generating a peanut-shell-shaped or "X"-type structure easily observed in edge-on barred galaxies (Combes et al.,

[5] An interesting observation of a bar within a bar can be seen in (Knapen & Beckman, 1994).

1990; Ciambur & Graham, 2016; Ciambur et al., 2017; Saha et al., 2018; Ciambur et al., 2021).

In a face-on galaxy, this peanut-shell-shaped structure looks like an oval-shaped structure elongated along the bar, this oval structure surrounding the bar is called a bar-lens, and it is also referred to as a pseudo-bulge structure by some studies (Athanassoula et al., 2015; Buta et al., 2010, they included such components in their galaxy classification). Some barred-lenticular galaxies have a perpendicular handle-type of structure at the ends of the bar, which is called ansae. In many barred-spiral galaxies, the spiral arms begin at the end of the bar, and sometimes it can be a complete closed circle, called a bar-ring, which is generally at an intermediate-scale. A ring is generally speculated to have formed with recent/new star formation. It can be seen at inner (intermediate-scale) regions holding the bar (bar-ring) and can also be seen independently at the nuclear or outer galactic regions.

The presence of a bar, ring, or spiral arms in a galaxy is an indicator of slow and isolated evolution through internal processes and/or possible contributions from the long-term interaction with the galaxy's surrounding, known as the secular evolutionary path of a galaxy (see a review on secular evolution by Knapen, 2010; Sellwood, 2014). In contrast, the featureless spheroidal elliptical galaxies are results of mergers, i.e., hierarchical evolution (Cole et al., 2000). Thus, merely knowing a galaxy's current morphology tells us a lot about the galaxy's past activities and surroundings. It can be complex to incorporate all the nuances of a galaxy's structure in a morphological type. However, it is essential to recognise these features, and take into account their contribution to the total galaxy luminosity, so that one can accurately extract the bulge luminosity required to establish the exact correlation between black hole mass and the bulge mass, which is one of the main objectives of this thesis. The above classification scheme (Figure 1.1) incorporates all fundamental categories of various galaxy forms, which will assist in forming a framework for the detailed analysis of black hole–bulge property diagrams obtained in this work.

1.2 Black Holes

It is astonishing that the prediction of the existence of black holes dates back to 1783 by John Michell (1784), "one of the most inventive astronomers of the eighteenth century" as Schaffer (1979) addressed him. Using the concept of escape velocity based on then dominant Newton's laws of gravitation, Michell speculated[6] that "black stars" (now identified as black holes[7]) are objects with extreme gravity such that even their light can not escape them; hence, they are invisible. He also suggested that the mass of such unsightable objects can be constrained using the motion of satellite stars moving under the influence of the black star's gravity.

1.2.1 Prediction of singularity and black hole

In 1916, Albert Einstein (1916) published his general theory of relativity, and Karl Schwarzschild (1916) presented a solution of Einstein's field equations, known as the *Schwarzschild metric* for a non-rotating uncharged spherically symmetric body of very high mass. His metric included a physical parameter r_s, known as the *Schwarzschild radius*, in the terms $(1 - \mathrm{r_s}/\mathrm{r})$ and $1/(1 - \mathrm{r_s}/\mathrm{r})$, which suggested infinite curvature and density, i.e., *singularity*, at radii $\mathrm{r} = 0$ and $\mathrm{r} = \mathrm{r_s}$. Interestingly, subsequent studies (e.g., Eddington, 1924; Lemaître, 1933) suggested that the singularity occurs only at the centre, not at the Schwarzschild radius. A physical realization of these solutions would be a black hole. However, the concept of singularity was debated and not accepted by many, including Einstein.

Subsequent analytical studies on stellar evolution[8] supported the existence of a central singularity. Many astronomers (e.g., Frenkel, 1928; Stoner, 1929; Anderson, 1929; Stoner, 1930; Chandrasekhar, 1931) suggested the formation of a white dwarf, a dense remnant core left behind after the collapse of a low or intermediate mass star ($\lesssim 8\,\mathrm{M}_\odot$) at the end of its life. Based on the electron degeneracy pressure model, they derived a maximum mass

[6]Michell used the term "dark stars" for now known black holes perhaps because he used the escape velocity of an object from the surface of the Sun as a reference to speculate the escape velocity from a dense black star.

[7]The term black hole for "gravitationally completely collapsed object" advocated by astronomer John Wheeler (1968) was suggested by someone from Wheeler's audience in a conference in 1967.

[8]See a review in Kippenhahn & Weigert (1990)

limit, now known as the Chandrasekhar limit ($\sim 1.4\,\mathrm{M_\odot}$), for white dwarfs. This suggested that a white dwarf with a mass of more than $\sim 1.4\,\mathrm{M_\odot}$ is unstable, and the electron degeneracy pressure at its core is not enough to counter its gravitational collapse into a planetary nebula or a Type Ia Supernova. Whereas the cores of higher mass progenitor stars ($\gtrsim 8\,\mathrm{M_\odot}$) could collapse into a denser neutron star supported by neutron degeneracy pressure (Landau, 1932; Oppenheimer & Volkoff, 1939). Where a neutron star heavier than $2-3\,\mathrm{M_\odot}$ is unstable and ultimately collapses[9] into the singularity, i.e., a black hole with a mass of the order of the solar mass (Landau, 1932; Chandrasekhar, 1932; Baade & Zwicky, 1934; Chandrasekhar, 1935; Oppenheimer & Snyder, 1939).

About three decades after Schwarzschild's claim on the presence of a singularity sphere, David Finkelstein (1958) along with Charles W. Misner, while exploring topological defects in the gravitational metric, modified the Schwarzschild metric. Their modification as well removed the coordinate singularity at the Schwarzschild sphere ($\mathrm{r} = \mathrm{r_s}$) and concentrated the singularity at the centre (also described in Kruskal, 1960). Importantly, Finkelstein (1958) presented a physical realization of this spherical surface as "a perfect unidirectional membrane: causal influences can cross it but only in one direction", which is now known as a black hole's "event horizon", coined by (Rindler, 1956). Thus, the Schwarzschild radius represented the event horizon of a non-rotating black hole with a singularity at its centre. Further, Kerr (1963) presented a metric for a spinning black hole (also see Newman & Janis, 1965), denoting a more realistic black hole that gained some angular momentum through the accretion disk or during its formation via the collapse of a star. This is now modified and called as the *Kerr-Newman metric* (Newman & Adamo, 2014). Finkelstein (1958) and other such studies around that time encouraged many theoretical and analytical developments on the existence of black holes and their event horizon (Penrose, 1965, 1969; Vishveshwara, 1970; Hawking & Penrose, 1970).

1.2.2 Observational hints on the existence of black holes

By 1950, observational astronomers had already identified (unusual) spectral emission lines and high energy jets from the centre of many active galaxies (Fath, 1909; Slipher, 1917;

[9] Ivanenko & Kurdgelaidze (1965) suggested that the collapsing core from a neutron star to singularity also goes through a hypothetical state of quark stars.

Curtis, 1918; Mayall, 1934; Humason, 1932; Mayall, 1939; Seyfert, 1943). Soviet physicist Viktor Ambartsumian was the first to introduce the active galactic nucleus (AGN), which he presented in the 1958 Solvay Conference on Physics. Ambartsumian suggested that active nuclei of galaxies undergo enormous explosions expelling out large amounts of mass from the galaxy, and for this to happen, the galactic nuclei must have a considerable mass of some unknown nature (as stated by Israelian, 1997, in the obituary of American Astronomical Society).

Radio observations accelerated the study of AGNs (e.g., the radio observations of nearby galactic nuclei in Bolton et al., 1949; Baade & Minkowski, 1954). Astronomers discovered some very bright star-like objects with spectra different from the stars. They were called quasi-stellar radio sources (quasars) or quasi-stellar objects denoted with the acronym QSO. With the help of the Parkes Radio Telescope and using lunar occultation, astronomers made a breakthrough measurement of the redshift (distance) to quasar 3C 273 (Schmidt, 1963; Hazard et al., 1963; Oke, 1963; Schmidt, 1965). This revelation suggested that 3C 273 and other such objects (e.g., 3C 48 Greenstein & Matthews, 1963) are the extremely luminous centres, i.e., AGNs of galaxies which are billions of light-years away from us. This followed multiple studies suggesting that these bright nuclei were a result of the enormous amount of energy released when the local galactic matter fell into the gravitational potential well of a central compact massive object, which could be a massive black hole of mass in the range of 10^5 to $10^8\,\mathrm{M}_\odot$ (e.g., Hoyle & Fowler, 1963; Salpeter, 1964; Zel'dovich, 1964).

Apart from AGNs, Jocelyn Bell-Burnell made another discovery in 1968 that boosted the belief in the existence of stellar-mass black holes, 30 years after the prediction of the eventual collapse of stars into white dwarfs, or neutron stars, or black holes. She detected periodic bursts of radio signals from a pulsating radio source (pulsar), which are essentially highly magnetized rotating neutron stars (or white dwarfs), reported in (PSR B1919+21 Hewish et al., 1968).

Indicating an evolutionary link between quasars and local (inactive) galaxies, some studies (e.g., Burbidge et al., 1963) argued that quasars are the early forms of galaxies with a violent nucleus; they evolve with time and end up as low-luminosity galaxies (e.g., Seyfert, 1943) observed in the local (late) universe. Subsequently, Sandage (1965) reported the abundance of radio-quiet quasars in addition to radio-loud quasars, in a way, advising the perception of a compact massive object at the centres of all kinds of galaxies, active or inactive. Further, Lynden-Bell (1969) argued that the emissions from the nuclei of local (generally radio-quiet) galaxies are powered by the collapsed mass of (old) quasars at their centre, i.e., black holes. Lynden-Bell (1969) advocated that given the abundance of active quasars in the early universe and lifetime energy output of quasars (see also Lynden-Bell & Rees, 1971), the black holes (active or dead quasars) should be expected at the centres of all galaxies. As such, he suggested that nuclei of oldest galaxies ("true dead quasars") may have a mass of $10^{10-11}\,\mathrm{M}_\odot$ while normal Milky Way-like galaxies may have a black hole of mass $10^{7-8}\,\mathrm{M}_\odot$ at their centre.

The current consensus of the presence of massive black holes at the centres of all the galaxies is built on multiple pioneering studies in the second part of the 20th century[10]. See a detailed review on various aspects of AGNs and the perception of black hole's at galactic nuclei in Shields (1999). Thanks to technological developments, astronomy has taken a giant leap to directly imaging the invisible black holes (Event Horizon Telescope Collaboration et al., 2019). Astronomers are now directly measuring the black hole masses, investigating their evolution, and detecting the long-awaited gravitational waves (GWs, proposed and predicted by Poincaré, 1906; Einstein, 1916, 1918) generated during binary neutron star or (stellar-mass) black hole mergers (Abbott et al., 2016a, the first reported detection of BH-BH merger GW150914). However, the long-wavelength (milliHertz to nano Hertz) gravitational waves generated by merging massive black holes are yet to be detected.

1.2.3 Black hole mass

Mass is one of the most studied properties of a black hole, which also has a spin and charge (Newman & Janis, 1965; Newman & Adamo, 2014). Observations suggest that black holes might exist in a continuum of masses, starting with the stellar-mass black holes (a few $M_\odot$ to $\sim 100\,M_\odot$; Belczynski et al., 2010), Intermediate-Mass Black Holes (IMBH; Miller, 2003; Baumgardt & Makino, 2004; Mapelli, 2016), and super-massive black holes (SMBHs, $10^5\,M_\odot - 10^{10}\,M_\odot$; Lynden-Bell, 1969; Wolfe & Burbidge, 1970; Lynden-Bell &

[10] Genzel (2021) also presents a short recap on proving the existence of black holes and their detection.

Rees, 1971; Natarajan & Treister, 2009; Inayoshi & Haiman, 2016).

There may be several thousand to millions of stellar-mass black holes in a galaxy (Hailey & Others, 2018; Elbert et al., 2018), speculatively, hundreds to thousands of IMBHs, but only one SMBH residing at the galactic centre, unless if it is an ongoing merger which can host more than one SMBH. The direct measurements of stellar-mass black holes are now counted in dozens; there are about 140 of SMBHs (listed with their sources in Chapter 3); whereas only a few IMBHs are confidently detected. For example: at the high IMBH end, stellar dynamical modelling revealed a $\sim 10^5 \mathrm{M}_\odot$ black hole at the centre of the nearby dwarf lenticular galaxy NGG 404 (3.1 Mpc; Nguyen et al., 2017), which was recently refined by also combining molecular gas kinematics information (Davis et al., 2020); less than a $\sim 10^6 \mathrm{M}_\odot$ black hole in NGC 5102 (3.2 Mpc) and NGC 5206 (3.5 Mpc; Nguyen et al., 2018, 2019); and a $\sim 10^3 \mathrm{M}_\odot$ black hole in NGC 205 (0.82 Mpc; Nguyen et al., 2019). At the low IMBH end, the LIGO-VIRGO collaboration (Abbott et al., 2020) recently reported the detection of gravitational wave event GW190521 produced by a merger of two stellar-mass black holes resulting in a $142\,\mathrm{M}_\odot$ IMBH.

Moreover, in the past, multiple studies have already predicted potential IMBH candidates at the centres of dwarf/low-mass galaxies, off the centres, young star clusters and, possibly, in a small fraction of (old) globular clusters[11] (Colbert & Mushotzky, 1999; Farrell et al., 2009; Soria et al., 2010; Seth et al., 2010; Secrest et al., 2012; Valencia-S et al., 2012; Baldassare et al., 2015; Pasham et al., 2015; Webb et al., 2017; Mezcua, 2017; Kızıltan et al., 2017; Chilingarian et al., 2018; Graham & Soria, 2018; Graham et al., 2018; Baumgardt et al., 2020; Greene et al., 2020; Davis & Graham, 2021). These predictions shall be confirmed as the technology improves to detect stellar orbits near the IMBH's sphere-of-influence.

Commonly used direct black hole mass measurement methods use high-resolution observations of kinematics of stars, gas, or maser sources within the sphere-of-influence of a black hole, where the black hole's gravity influences their motion, to constrain the black hole mass. The primary methods are:

[11] As the globular clusters are the oldest tightly bound collection of a large number of stars, they are expected to have black holes, specifically IMBHs, at their centres formed through the runaway collision of main-sequence stars (Miller & Hamilton, 2002; Baumgardt & Makino, 2004; Maccarone et al., 2007). However, some kinematic evidence suggest that IMBHs may not be very common at the centres of globular clusters (e.g., Baumgardt, 2017; Baumgardt et al., 2019).

1. **Proper motion of individual stars:** This method involves observing the proper motion, i.e. tracking the stellar orbit, of individual stars around a black hole. Two decades of observation of our galactic centre, and the high-resolution requirements for individual stellar orbits fulfilled by the *Keck* telescope (speckle images using speckle holography) combined with adaptive optics, has enabled the most accurate measurement of the black hole mass $M_{\rm BH} = (4.02 \pm 0.20) \times 10^6 M_\odot$ of Sagittarius A*, the central black hole of our galaxy (Boehle et al., 2016), which is at a distance of 7.86 ± 0.18 kpc from us. However, due to resolution limitations, this method has not been used for other distant galaxies yet.

2. **Stellar and gas dynamics:** The most used method to directly measure the black hole mass is by observing the collective motion of stars within the sphere-of-influence of a black hole. The stellar dynamical modelling involves matching the observation of the surface brightness profiles and the line-of-sight velocity distribution of stars near the black hole with the superposition of individual stellar orbits taken from a library of stellar orbits. Where, these stellar orbits are obtained using sophisticated algorithms (e.g., see van der Marel et al., 1998; Cretton et al., 1999; Thomas et al., 2004) based on Schwarzschild modelling (Schwarzschild, 1979) or, less computationally intensive, Jeans Anisotropic Modelling (JAM, Cappellari, 2008). Similarly, gas dynamical modelling is done by matching the observed velocity map (or rotation curve) of emission-line gas at the galactic core with the constructed circular motion of the gas (and dust) clumps moving under the gravitational field of stars in the equatorial plane (van der Marel & van den Bosch, 1998). Measurements from stellar dynamical modelling[12] are more reliable as the stars are influenced by a black hole's gravity only, while gases are prone to non-gravitational forces as well, for example, a supernova explosion, the black hole outflows, and local turbulences.

3. **Megamasers:** A black hole mass measurement of similar quality is obtained from megamaser kinematics. Megamasers[13] are extragalactic naturally stimulated and amplified microwave emissions which are about 100 million times brighter than the

[12] See a review on the stellar and gas dynamical measurement of black hole mass in Ferrarese & Ford (2005).

[13] See Lo (2005) for a review on megamasers.

Galactic masers (Gordon et al., 1955). Galaxies with their nucleus obscured by a large column of molecular gas clouds containing any of the hydroxyl, water, formaldehyde, or methine molecules, form a natural astrophysical maser. These molecules absorb the continuum radiation coming from the accretion disk of the black hole and re-emit in microwave (radio) frequencies, amplified through population inversion. By capturing these Doppler-shifted maser emissions, one can derive the kinematics of the megamaser sources, i.e. the gas clouds accelerated by the central black hole and further constrain the black hole mass. As these emissions are in radio frequencies, a very high angular resolution can be attained with very long baseline interferometry (VLBI[14]) techniques (Clark & Kellermann, 1968), which lead to accurate measurements.

4. **Direct imaging:** In addition to the above methods, using the VLBI technique, the Event Horizon Telescope Collaboration et al. (2019) has made possible the *Direct Imaging* and, ergo, the mass measurement of the black hole at the centre of M87[15]. The EHT collaboration used a worldwide network of radio telescopes generating a virtual radio telescope with an effective aperture diameter as Earth. This provided sufficient angular resolution ($\sim 25\,$micro arcsecond) to resolve the event-horizon of the SMBH hosted by M87 (and Sagittarius A*) and measure the central black hole mass.

Overall, there are about 145 directly measured black hole masses available in literature (all listed in Chapter 2) based on the above primary and most reliable methods. Most of the masses are based on stellar-dynamical modelling. Some black hole masses are measured via more than one method producing consistent values (e.g., NGC 4258, NGC 404, etc.), ensuring that these direct measurements are reliable.

[14]VLBI technique involves correlating the signals from a source received at multiple radio telescopes, separated by hundreds to thousands of kilometres, at different times to effectively construct a virtual telescope with a big aperture producing a high-resolution image of the source (Jennison, 1958).

[15]Event Horizon Telescope Collaboration et al. (2019) suggested that the black hole at the centre of M87 follows Kerr-metric and provides evidence for the connection between AGN and SMBHs.

1.2.4 Black holes at the centre of galaxies

SMBHs, due to their strong gravitational pull, accrete material from the local part of the galaxy and form a disk of hot gases and dust around them, known as an accretion disk (Thorne, 1974). Materials spiralling around the black hole have so much friction in between them that they release an enormous amount of energy (Bardeen & Wagoner, 1969) in a wide range of electromagnetic wavelength bands, especially X-rays, making the active centre of a galaxy super luminous. AGN is just another name for the central black hole with a bright accretion disk in active galaxies, whereas so-called "quiescent" galaxies also host a central black hole, but their accretion rate and radiative efficiency are low; hence, their accretion disk is not as luminous (Peterson, 2014).

There are many theories[16] for how SMBHs form and end up residing at the center of a galaxy. Some studies suggest that the formation of these SMBHs started with low BH mass seeds, formed from the remnants of the first generation of massive stars (Volonteri et al., 2008; Nguyen et al., 2018). Some other studies favor IMBH seeds, either formed by runaway collision of a group of massive old stars in a dense star cluster (or globular cluster) at/near the center of a galaxy or direct merger of stellar-mass black holes (Miller, 2003; Miller & Colbert, 2004; van der Marel, 2004; Baumgardt & Makino, 2004). Further, the IMBH grows into an SMBH through the continuous accretion of mass from the host galaxy (e.g., Boekholt & Others, 2018) and/or grows through the collisional evolution of their host galaxy (e.g., Mayer & Others, 2007).

Another theory advocates the presence of massive black hole seeds in the early Universe (Kawasaki et al., 2012). This suggests that they were formed just after the Big Bang by the gravitational collapse of big/dense gas clouds, formed by the collection of gases moving at supersonic speeds through dark matter clumps, into a region of infinite density (e.g., Hirano & Others, 2017), which further kept on accreting and became super-massive, meanwhile galaxies built upon them forming the stellar bulge, disk, and other components.

Whether the central black hole formed first or the galaxy (spheroid) formed first, the growth of the two seems connected. This is because the massive black holes live and accrete on the central galactic material, and in return, the black holes are also believed to control

[16] For the formation scenarios of black holes see Celotti et al. (1999) and references therein.

host galaxy properties via their powerful gas outflows, forming a feedback mechanism (Rees, 1984; Fabian & Canizares, 1988; Blandford, 1999; Ciotti & Ostriker, 2001; Di Matteo et al., 2005). How this black hole feedback works, given the difference in the physical size of a black hole and its host galaxy/spheroid, is still puzzling (Ruszkowski et al., 2019). The correlations observed between black hole mass and host galaxy properties form evidence of black hole-galaxy interplay, i.e., the "co-evolution" and can help establish the physics behind black hole feedback. This thesis mainly focuses on observing black hole mass-galaxy correlations based on the most reliable measurements of black hole mass and host galaxy properties. The following sections review various efforts of the astronomical community to look for the correlation between black hole mass and host galaxy properties, especially with the spheroid mass and the stellar velocity dispersion.

1.3 History of the Black Hole Scaling Relations

1.3.1 (Black hole mass)-(host spheroid)

The efforts to uncover the fundamental relations between black hole mass and host bulge properties date back to 1988, based on just a few massive galaxies with their central black hole masses measured reliably. Dressler & Richstone (1988) used stellar dynamical modelling to suggest the presence of SMBHs at the centres of the two neighbouring galaxies M31 (NGC 224) and M32 (NGC 221), and predicted an upper limit of $10^9\,M_\odot$ for the central SMBH mass of the galaxies with the largest spheroids, based on the ratio of central black hole mass ($M_{\rm BH}$) and spheroid stellar mass ($M_{\rm sph}$ or $M_{\rm bulge}$) in the two galaxies, posing the idea of a relation between $M_{\rm BH}$ and $M_{\rm sph}$. Further, Dressler (1989) directly, and Yee (1992) indirectly, suggested a linear relationship between the black hole mass and bulge mass of a galaxy. Subsequently, Kormendy & Richstone (1995), as well, reported a linear distribution of $M_{\rm BH}$ against $M_{\rm bulge}$, using only six galaxies.

Linear relation

Observations after the Hubble Space Telescope (HST) launch in 1990 started to append the sample of local galaxies with high-quality photometric images, and stellar spectra resolved enough to constrain the central black hole masses directly. Using the HST data of

32 galaxies, Magorrian et al. (1998) performed a linear[17] $M_{\rm BH}$–$M_{\rm bulge}$ fit to their sample. However, they also noted that the most massive (cored) galaxies might have a steeper $M_{\rm BH}$–$M_{\rm bulge}$ relation than the relatively low-mass (power-law) galaxies. Although, admittedly, it was a premature speculation, given only a handful of power-law galaxies relative to that of cored galaxies in their sample (Magorrian et al., 1998, their figure 8).

Building on above local (redshift $z \sim 0$) galaxy sample with directly measured black hole masses, many studies continued to report a near-linear $M_{\rm BH}$–$M_{\rm bulge}$ (or bulge luminosity: $L_{\rm bulge}$) relation for nearly two decades (e.g., Ho, 1999; Häring & Rix, 2004; Ferrarese & Ford, 2005; Graham, 2007b; Gültekin et al., 2009b; Sani & Others, 2011; Kormendy et al., 2011; Kormendy & Ho, 2013). However, the later studies (Gültekin et al., 2009b; Sani & Others, 2011; Kormendy & Ho, 2013) excluded low-mass bulges/galaxies from their sample, calling them "pseudo-bulges" (e.g., Kormendy et al., 2011, their figure 1), which preserved their idea of a linear relation between $M_{\rm BH}$ and $M_{\rm bulge}$.

Broken relation

On the other hand, during the same period, some studies reported steeper $M_{\rm BH}$–$M_{\rm bulge}$ relations (e.g. Laor, 1998; Wandel, 1999; Salucci & Others, 2000; Laor, 2001), which was mainly because of the addition of low-mass galaxies in their sample. For example: Salucci & Others (2000) suggested that LTGs (spirals) follow a steeper relation between $M_{\rm BH}$ and $M_{\rm bulge}$ than the massive elliptical galaxies, and further, Laor (2001) reported a non-linear ($M_{\rm BH} \propto M_{\rm bulge}^{1.53\pm0.14}$) relation using a sample of 40 quasars.

After updating the distances and black hole mass measures for a sample of 30 galaxies from (Häring & Rix, 2004), Graham (2012) observed a break in the $M_{\rm BH}$–L_{bulge} diagram, i.e., different relations for galaxies with Sérsic or core-Sérsic spheroids. Graham (2012) observed a near-linear $M_{\rm BH} - L_{bulge}$ relation for the (massive) core-Sérsic galaxies (which were all ETGs), and a "super-quadratic"[18] relation for the (low-mass) Sérsic galaxies (most of which were late-type i.e. spiral galaxies).

Core-Sérsic galaxies are the massive ones that have undergone major dry (gas-poor) mergers, and therefore, have a deficit of light at their spheroid cores. This depletion of

[17] Here and throughout the thesis, linear or non-linear relation refers to a power-law slope (e.g., for a $\log M_{\rm BH}$–$\log M_{\rm bulge}$ relation) of one or more than one.
[18] Here, "super-quadratic" describes a power-law slope between 2 and 3.

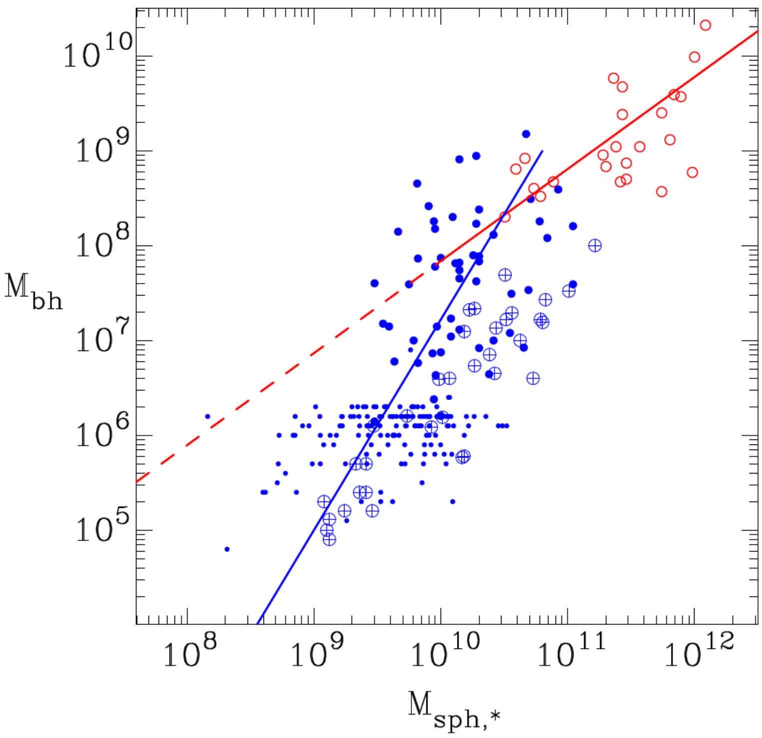

Figure 1.2 The black hole mass versus spheroid mass relations, as defined by Sérsic (marked with blue) and core-Sérsic (marked with red) galaxies, taken from Graham & Scott (2013, 2015). Tiny blue dots represent the low-mass AGNs from Jiang & Others (2011), many of which may have so-called pseudo-bulges, and some high-mass AGNs are marked with blue crosshairs.

light happens because the massive BHs from the two merging galaxies scour out the stars from the centre of the remnant/merged galaxy through the transfer of their orbital angular momentum to the surrounding stars (Begelman et al., 1980). Such galaxies with a (partially) depleted core were discovered by King & Minkowski (1966, 1972) and are referred to as core-Sérsic or cored galaxies, described using a core-Sérsic function[19] (Graham & Others, 2003), due to their flattened core relative to the inward extrapolation of their bulge's outer Sérsic (Sérsic, 1963) light profile. Whereas, the galaxies which grow over time via accretion or gas-rich mergers are likely to have bulges with Sérsic light profiles and, thus, are called Sérsic galaxies.

[19]The core-Sérsic function is a combination of a shallow (inner) power law, describing the deficit core, followed by a normal Sérsic function.

Pseudo-bulges following the broken relation

Graham & Scott (2013) and Scott et al. (2013), using a bigger sample of 72 galaxies, confirmed the broken (or bent) M_{BH}–L_{sph} relation of (Graham, 2012), where, the core-Sérsic and Sérsic galaxies defined a linear and a super-quadratic power-law, respectively. Further, Graham & Scott (2015) showed that the alleged pseudo-bulges (Gadotti & Kauffmann, 2009; Kormendy et al., 2011), which were essentially small bulges of low-mass galaxies, also followed the non-linear (Sérsic relation) part of the bent M_{BH}–M_{sph} relation, see Figure 1.2.

Assuming the black hole–galaxy co-evolution along the M_{BH}–M_{sph} relations, a steeper (than linear) arm of the relation suggested that the fractional growth of M_{BH} is greater than the fractional growth of the host M_{sph} in Sérsic galaxies, which evolved through gas-abundant processes. Whereas, almost linear M_{BH}–M_{sph} relation for core-Sérsic galaxies reflected their hierarchical growth through major dry mergers (Graham & Scott, 2015). This scenario was consistent with many concurrent observational studies on relating AGN accretion rate with host star formation rate (Diamond-Stanic & Rieke, 2012; Seymour et al., 2012; LaMassa & Others, 2013; Drouart et al., 2014), theoretical/analytical studies, and simulations (Cirasuolo et al., 2005; Fontanot et al., 2006; Hopkins & Quataert, 2010; Dubois et al., 2012; Khandai et al., 2012; Bonoli et al., 2014; Neistein & Netzer, 2014).

Thus, the broken M_{BH}–M_{sph} relation offered important ramifications for other analytical studies and simulations based on the previously seen linear relations (e.g. Fabian, 1999; Wyithe & Loeb, 2003; Marconi et al., 2004; Springel et al., 2005; Begelman & Nath, 2005; Croton et al., 2006; Di Matteo et al., 2008; Natarajan & Volonteri, 2012). Importantly, this bent relation also solved the discrepancies observed (e.g., reported in Gadotti & Kauffmann, 2009) between the black hole mass estimated using the linear M_{BH}–M_{sph} relation and then known relation between M_{BH} and stellar velocity dispersion σ.

The possibility of a M_{BH}–total galaxy mass correlation

Literature on the black hole scaling relations is piled up with papers on the M_{BH}–M_{sph} (or L_{sph}) relations with increasing sample size and updated M_{BH} and M_{sph} measurements. This reflects a firm consensus for the existence of a stronger relation between central black hole mass and the immediately surrounding spheroid mass than other global galaxy properties or components. However, this correlation would not explain the black hole–galaxy link for a bulge-less galaxy. Interestingly, Läsker et al. (2014), using a sample of 35 galaxies comprised of primarily ETG and four LTGs, claimed that M_{BH} can have an equally strong correlation with the total galaxy luminosity as it does with the bulge luminosity. In addition, the detection of several bulge-less (disk dominant) galaxies with central black holes (e.g., Reines et al., 2011; Secrest et al., 2012; Schramm et al., 2013; Simmons et al., 2013; Satyapal et al., 2014), also supports the possibility of a correlation between M_{BH} and the total galaxy mass (M_{gal}) and, possibly, a M_{BH}–disk mass relation as well.

Red and blue sequence

Recently, based on a sample of 47 ETGs and 19 LTGs, Savorgnan et al. (2016, their figures 1 and 2) recovered a M_{BH}–L_{gal} correlation equally good as that of the M_{BH}–M_{sph} relation; however, only for ETGs, not for LTGs. This revelation partially supported the claim in Läsker et al. (2014, which did not have significant sample of LTGs).

Notably, (Savorgnan & Graham, 2016b) performed a multi-component photometric decomposition of total galaxy light to obtain accurate stellar bulge masses for their galaxies. On separating their sample into core-Sérsic and Sérsic galaxies, they do not find significantly different relations for core-Sérsic and Sérsic galaxies, conflicting with Graham & Scott (2013) in terms of the morphological-dependence of the break in the M_{BH}–M_{sph} relation. Instead of core-Sérsic and Sérsic galaxies, they found their ETGs and LTGs defining distinct M_{BH}–M_{sph} trends, where ETG followed a shallow relation (slope=1.04) and the distribution of LTGs suggested a steeper relation (slope between 2-3). However, the relation for LTGs was not very well constrained given the smaller number of LTGs in their sample (Savorgnan et al., 2016, their figure 5). They referred to the two trends for ETGs and LTGs as the "red sequence" and a "blue sequence", respectively; nonetheless, the colour information was not provided in their M_{BH}–M_{sph} diagram.

This left some objectives for future studies with a bigger sample, precise spheroid mass, and correct morphology to interrogate the morphological reason behind the possible break in the M_{BH}–M_{sph} diagram and quantify the scaling relation. Another vital aspect that remained unclear was whether a $M_{\rm BH}$–$M_{\rm gal}$ relation exists for all galaxy types (ETG and LTGs), or if there is a morphological dependence similar to the $M_{\rm BH}$–$M_{\rm sph}$ diagram. If established, the $M_{\rm BH}$–$M_{\rm gal}$ relation can enable a much easier way to predict black hole mass, especially for distant unresolved galaxies, than the $M_{\rm BH}$–$M_{\rm sph}$ relation, where one has to disassemble the bulge mass from the rest of the galaxy mass, which is prone to systematic errors.

1.3.2 Black hole mass–stellar velocity dispersion

The virial theorem (Clausius, 1870) establishes $\mathrm{M} \propto \mathrm{R} * \mathrm{V}^2_{\rm rms}/\mathrm{G}$ for a self-gravitating system of objects and has many applications in astrophysics. For galaxies, $\mathrm{V}_{\rm rms}$ is the observed root-mean-square velocity (*aka* the second moment of velocity), which is in general a combination of two velocity components the stellar velocity dispersion (σ) and the rotational velocity (V_{rot}) given by $\sqrt{(}\sigma^2 + V^2_{rot}/sin^2 i)$ (Busarello et al., 1992; Ferrarese & Merritt, 2000), where V_{rot} is the line-of-sight mean stellar rotational velocity and i is the inclination angle of a galaxy. M represents the mass enclosed within an aperture size of R, and G is Newton's gravitational constant. In galactic bulges, the velocity dispersion of stars dominates their kinematics, whereas, in galaxies with a rotating stellar disk, V_{rms} measured within a larger aperture size may be dominated by the rotational component.

The virial theorem has been the basis of many pioneering works, including Jeans scale-length (Jeans, 1902), the discovery of the existence of dark matter (Zwicky, 1933), and the derivation of the Chandrashekhar limit (Chandrasekhar, 1931). Importantly, it linked the stellar velocity dispersion and the mass enclosed in the galactic bulges. This, in combination with the observed correlations between black hole mass and host bulge stellar mass, was a hint for a possible correlation between the central black hole mass and the velocity dispersion of stars in its host bulge/galaxy.

The first $M_{\rm BH}$–σ relations and a discrepancy between them

The very first $M_{\rm BH}$–σ relations established by Ferrarese & Merritt (2000) and Gebhardt et al. (2000) suggested that it can be the fundamental relation between a black hole and its host galaxy, based on the reported minimal intrinsic scatter, consistent with zero. However, the slopes found in the two studies were different, which were conforming with two different black hole–galaxy feedback models. Ferrarese & Merritt (2000) reported $M_{\rm BH} \propto \sigma^{4.80\pm0.50}$, supporting the prediction ($M_{\rm BH} \propto \sigma^5$) of the energy-balancing feedback model by Silk & Rees (1998). Whereas, Gebhardt et al. (2000) obtained $M_{\rm BH} \propto \sigma^{3.75\pm0.30}$, which agreed with the prediction ($M_{\rm BH} \propto \sigma^4$) by the feedback model of Fabian (1999) based upon momentum conservation. This raised the important question: which one of the two relations should be preferred?

The role of regressions performed

Merritt & Ferrarese (2001) explored four different regressions to investigate the above issue of different $M_{\rm BH}$–σ slopes, based on a similar sample. They performed the regressions, namely, Ordinary Least Square (OLS), General Least Square (GLS), Orthogonal Distance Regression (ODR), and Regression with bivariate errors and intrinsic scatter (BRS). Where the first two consider measurement errors only in the dependent variable ($M_{\rm BH}$), while ODR and BRS treat the measurement errors in both the variables equally. They concluded that different $M_{\rm BH}$–σ relations were obtained because of the use of different symmetrical and non-symmetrical regressions by Ferrarese & Merritt (2000) and Gebhardt et al. (2000), respectively. This highlighted the discrepancies in scaling relations based on the regression used.

Gebhardt et al. (2000) had found a shallower slope due to the asymmetric linear regression routine they used, which ignored the measurement errors in the velocity dispersion. Additionally, their relation was biased by the low-velocity dispersion used for the Milky Way (Merritt & Ferrarese, 2001). An observer, who assumes the $M_{\rm BH}$ as the dependent variable and σ as the independent variable, would prefer to apply an asymmetric regression which minimizes the scatter in the $M_{\rm BH}$–direction. However, a theorist will instead prefer a symmetric regression to provide equal treatment to both the variables, because whether the central black hole originates first or the host galaxy (and its properties) is another "chicken or egg" kind of question (see Novak et al., 2006, for guidelines on the use of regressions). Whereas, the reason behind obtaining almost zero intrinsic scatter in both studies (Ferrarese & Merritt, 2000; Gebhardt et al., 2000) could be precisely measured σ values and partly the small sample size.

ODR and BRS regressions were implemented in the FITEXY routine by Press et al.

(1992) and in the Bivariate Correlated Errors and Intrinsic Scatter (BCES) routine by Akritas & Bershady (1996), respectively. These are two famously-used regression routines used for establishing scaling relations. BCES allows for the intrinsic scatter in both the fitted quantities, while FITEXY does not. Tremaine et al. (2002) later modified the FITEXY routine from Press et al. (1992) allowing for intrinsic scatter in the vertical-direction. Although, Press et al. (1992) and later Tremaine et al. (2002) called FITEXY (and its modified) routine to be symmetric, but actually it is not[20], and it requires averaging the inclination and slopes of the forward (FITEXY($M_{\rm BH}|\sigma$)) and inverse (FITEXY($\sigma|M_{\rm BH}$)) regressions to obtain the symmetric (bisector) regression line as explained in Novak et al. (2006). This concept of symmetric regression is similar to the BCES routine which provides the BCES($Y|X$) line, BCES($X|Y$) line, and the regression line which symmetrically bisects the two, i.e., the BCES(Bisector).

Graham & Li (2009) tried three types of symmetrical regressions on their data: BCES (Bisector), modified FITEXY(Bisector) (bisecting the line obtained from forward and inverse FITEXY regression), and an IDL routine (Kelly, 2007) based on a Bayesian estimator. They found that all three revealed very similar results on using the same uncertainties in velocity dispersion. This also suggested that, while comparing or using scaling relations from different studies, one should note the (symmetric or non-symmetric) regression applied and the uncertainties used.

Substructure in the $M_{\rm BH}$–σ diagram

Interestingly, (Graham, 2007a; Hu, 2008) observed that the barred galaxies are offset from the non-barred galaxies in the $M_{\rm BH}$–σ diagram. Hu (2008) added that the offset barred galaxies in their sample also host pseudo-bulges which are known to have small $M_{\rm BH}$. Graham (2008a) suggested that the offset could be either because of a low $M_{\rm BH}$ in pseudo-bulges or the high velocity dispersions in barred galaxies. Therefore, the inclusion of barred galaxies in a single regression to obtain the $M_{\rm BH}$–σ relation could produce a steeper relation with larger scatter (Graham & Others, 2011; Graham & Scott, 2013). Further, Hartmann et al. (2014), using their simulation, suggested that the presence of a bar in a galaxy may cause an increased velocity dispersion in galactic bulges, independent

[20] It has been tested in (Davis et al., 2018a, 2019a) by comparing the best-fit lines with two other routines.

of classical or pseudo-bulges. This suggested that different regressions should be performed for barred and non-barred galaxies in the $M_{\rm BH}$–σ diagram.

Using a sample of 64 galaxies with reliable $M_{\rm BH}$ measurements, Graham & Others (2011) found $M_{\rm BH} \propto \sigma^{5.13\pm0.34}$ with a total rms scatter in the $\log M_{\rm BH}$-direction ($\Delta_{\rm rms|BH}$) of 0.43 dex. This relation was obtained assuming $M_{\rm BH}$ as the dependent variable (i.e., from an observer's view), by minimising the offset between the data and the fitted line in the $M_{\rm BH}$–direction using the BCES($BH|\sigma$) routine. Additionally, they pointed out a potential sample selection bias in the $M_{\rm BH}$–σ relation, arising because of the lack of measured black hole masses below $10^6 M_\odot$ due to technological limitations to resolve the sphere-of-influence of low-mass black holes. To obtain a relation unbiased by this issue, following Lynden-Bell et al. (1988, see their figure 10) they performed an inverse regression BCES($\sigma|M_{\rm BH}$), assuming they had a nearly complete range of σ values, which produced a relatively steeper $M_{\rm BH} \propto \sigma^{5.95\pm0.44}$ relation. They noticed that the barred galaxies were below the non-barred galaxies, offset by ~ 0.3 dex in the vertical direction, and the slope became shallower (5.40) and the scatter ($\Delta_{\rm rms|BH} = 0.41$ dex) reduced on excluding the barred galaxies from the regression.

Graham & Scott (2013) extended the sample size to 72 galaxies and found $M_{\rm BH} \propto \sigma^{6.08\pm0.31}$ using the inverse regression. For their 51 non-barred galaxies, they obtained $M_{\rm BH} \propto \sigma^{5.53\pm0.34}$, and for 21 barred galaxies, $M_{\rm BH} \propto \sigma^{5.29\pm1.47}$ with an offset of $\sim$ 0.5 dex between the two lines in the $\log M_{\rm BH}$-direction. This supported the suspicion of a substructure due to barred galaxies in the $M_{\rm BH}$–σ diagram.

Is there a bend in the $M_{\rm BH}$–σ relation?

Shortly after, McConnell & Ma (2013), with their total sample of 72 galaxies including barred galaxies, reported $M_{\rm BH} \propto \sigma^{5.64}$ using forward regression. While, as noted by Graham (2013), inverse regression would have provided a much steeper slope, suggesting a steeper bisector (symmetrical) regression line, the reason being the inclusion of barred galaxies.

Importantly, in the $M_{\rm BH}$–σ diagram of McConnell & Ma (2013), at the high-$M_{\rm BH}$ end, some galaxies with massive $M_{\rm BH}$ were observed to be offset (upturn) from the best-fit relations towards the high-$M_{\rm BH}$ side. These galaxies were, presumably, the massive core-Sérsic galaxies, which are often the Brightest Cluster Galaxies (BCGs), gone through multiple dry mergers. This upturn is understandable from the theories which suggest that during major mergers, BCGs grow their galaxy mass and black hole mass while they cannot keep a comparable growth rate for their stellar velocity dispersion (Burkert & Silk, 2001; Ciotti & van Albada, 2001; King, 2010; Oser et al., 2012; King & Nealon, 2019). Volonteri & Ciotti (2013), based on their analytical and semi-analytical models, found that BCGs are offset in the $M_{\rm BH}$–σ relation, possibly because they undergo multiple gas-poor (dry) mergers resulting in over massive black holes relative to the $M_{\rm BH}$–σ line with only mildly increased velocity dispersions.

Stretching the sample of Graham & Scott (2013) to 89 galaxies with directly measured black holes masses, Savorgnan & Graham (2015) provided an inverse regression relation $M_{\rm BH} \propto \sigma^{6.34\pm0.80}$ with a total rms scatter of $\Delta_{rms} = 0.57\,$dex in the $\log M_{\rm BH}$-direction, for their 57 non-barred galaxies, noting that barred galaxies are offset from non-barred ones. Interestingly, their work suggested that most massive galaxies, which host the most massive black holes and reside at the high-mass end of the $M_{\rm BH}$–σ relation, are not particularly the galaxies that have undergone the highest number of (dissipation-less) dry mergers, questioning the above speculations about BCGs or cored galaxies.

Further, Savorgnan & Graham (2015) claimed that Sérsic and core-Sérsic galaxies broadly follow the same $M_{\rm BH}$–σ relation, likewise for the slow- and fast-rotating galaxies. Similarly, just by visual inspection of their scaling diagrams (figure 2 and 4 from Savorgnan & Graham, 2015) the barred galaxies do not look offset from the non-barred ones. Thus, whether or not there is a statistically significant substructure in the $M_{\rm BH}$–σ diagram due to barred versus non-barred galaxies and Sérsic versus core-Sérsic galaxies, or perhaps some other morphological classification, remains questionable, mainly because of a small number of core-Sérsic or barred galaxies in the then available sample of galaxies with $M_{\rm BH}$ measurements.

Shankar et al. (2016) observed an offset in the σ–M_{gal} diagram between the sample of ETG with dynamically (directly) measured black hole masses and a large sample of active galaxies from the Sloan Digital Sky Survey (SDSS) data release-7, for whom the sphere-of-influence is not resolved yet; thus they do not have a dynamically measured black hole mass. Based on this offset, Shankar et al. (2016) suggested that the black hole scaling relations established using the galaxy sample with direct $M_{\rm BH}$ measurements (e.g., the ETG sample from Savorgnan et al., 2016) are selection biased. This selection bias has not been addressed since. The updated relation based on the current expanded sample of galaxies with directly measured $M_{\rm BH}$ shall provide some clues to assess the validity of this bias.

1.3.3 Luminosity versus stellar velocity dispersion

The first studies to investigate the correlation between galaxy luminosity,L, (or total absolute magnitude, $\mathfrak{M} = -2.5\log(L)$) and the velocity dispersion of stars dates back to Minkowski (1962). He observed a positive L–σ correlation and advocated the same. However, he could not obtain a very good fit to his sample consisting of 14 galaxies, partly because he plotted σ against $\mathfrak{M}$ (Minkowski, 1962, their figure 1), instead of $\log\sigma$–$\mathfrak{M}$. A decade later, Faber & Jackson (1976) provided the first well-established scaling relation $\mathrm{L_B} \propto \sigma^4$, famously known as the "Faber-Jackson relation" for ETGs, using their measurements for the velocity dispersion for 25 ETGs.

Curved or bent L–σ relation

The Faber-Jackson relation was followed by numerous studies, which reported different power-laws in the L–σ diagram with an increasing number of reliable measurements of velocity dispersion for bright and faint (i.e., high- and low-mass) galaxies and luminosities (L_λ) in different wavelength bands (λ). Schechter (1980) reported $L_B \propto \sigma^{5.4\pm1.0}$ using a sample of 32 galaxies, comprised majorly of the bright elliptical galaxies. Malumuth & Kirshner (1981) found that Brightest Cluster Member (BCM) galaxies do not follow the relation ($L_V \propto \sigma^{3.8\pm0.6}$) they found for the (relatively low-luminosity) elliptical galaxies in their sample. Instead, the BCM galaxies had higher velocity dispersions than predicted by the relation for their low-mass elliptical galaxies. This suggested that a steeper L–σ relation may fit better for massive galaxies.

At the same time, Tonry (1981) reported a relationship with a slightly shallower slope, $L_B \propto \sigma^{3.2\pm0.2}$ upon including faint elliptical galaxies in the single regression, which also included bright elliptical galaxies. They suggested that a bent or curved L–σ relation describes the distribution of ETGs better (see also Binney, 1982; Farouki et al., 1983).

Supporting the above claims, other studies revealed a power-law slope of ≈ 2 for dwarf elliptical galaxies, emphasizing on a bend in the L–σ relation with the bend-point at $\mathfrak{M}_B \approx -20.5$ mag in the Vega magnitude system (Davies et al., 1983; Held et al., 1992; de Rijcke et al., 2005; Matković & Guzmán, 2005).

Using a large sample of 143 ETGs, Matković & Guzmán (2005) confirmed the shallow relation $L \propto \sigma^{2.01\pm0.36}$ for faint ETGs and a steeper relation for luminous (massive) galaxies ($\mathfrak{M}_R < -22.17$ mag), with the transition/bend-point at $\mathfrak{M}_R \approx -22.17$ mag. Their R-band bend-point was approximately consistent with the B-band bend-point $\mathfrak{M}_B = -20.5$ mag (recovered in recent studies, Kourkchi et al., 2012; Graham & Soria, 2018).

The bend at high-mass end

This bend in the $\mathfrak{M}_\mathrm{B}$–σ diagram at $\mathfrak{M}_B = -20.5$ mag, complemented the bend seen in the $\mathfrak{M}_\mathrm{B}$ versus central surface brightness (μ_0, also known as the central projected luminosity density) relation found in Graham & Guzmán (2003, their figure 9), such that the most luminous cored (core-Sérsic) galaxies depart from the positive $\mathfrak{M}_\mathrm{B}$–μ_0 relation defined by relatively less luminous (Sérsic) galaxies. This departure (or opposite trend) was seen because the formation of the light depleted core, which is which is larger/more significant for more massive/luminous galaxies (Graham, 2004; Dullo & Graham, 2014), in the core-Sérsic galaxies, results in a negative trend between $\mathfrak{M}_\mathrm{B}$ and μ_0.

Using V-band magnitudes and central stellar velocity dispersion values from HyperLeda (Paturel et al., 2003) for a large sample of about 200 galaxies, Lauer et al. (2007) supported the bend in the L–σ relation, with the point of bend at $\mathfrak{M}_V \approx -21$ mag (Vega). They reported $L \propto \sigma^{6.5\pm1.3}$ for galaxies with a depleted core plus BCGs (which are generally cored), and $L \propto \sigma^{2.6\pm0.3}$ for the (relatively less-luminous) core-less galaxies. Lauer et al. (2007) used a three-parameter model, (Nuker law, Lauer et al., 1995) to fit the light profile of their galaxies. They called their core-less galaxies the power-law galaxies, as they thought that the light profile of these galaxies could be described using a single (steep) power-law, whereas the light profile of cored galaxies required two power laws joined at the core radius. Later, Dullo & Graham (2012, 2013) showed that the Nuker model disagreed with the presence/absence of a core as determined by the core-Sérsic model 18% of the time, i.e., nearly 1 in 5 galaxies. The core-less or power-law galaxies are now referred to as Sérsic galaxies because they have Sérsic bulge profiles (with optional components) and galaxies with a depleted core are called core-Sérsic galaxies. Thus, Lauer's fit parameters for the L–σ relation for Sérsic and core-Sérsic galaxies may have been biased due to inaccurate classification of about 18% galaxies.

Subsequently, using the elliptical galaxy sample from Lauer et al. (2007) with some modifications, Kormendy & Bender (2013) found $L_V \propto \sigma^4$ for the core-less (Sérsic) elliptical galaxies and $L_V \propto \sigma^8$ for the cored (core-Sérsic) elliptical galaxies. For which they mentioned to use the symmetric least squares regression routine from Tremaine et al. (2002). However, for the data used by Kormendy & Bender (2013), the symmetric application of the modified FITEXY regression routine gives $L_V \propto \sigma^{4.39 \pm 0.61}$ for the core-Sérsic elliptical galaxies, and $L_V \propto \sigma^{2.98 \pm 0.31}$ for the Sérsic elliptical galaxies. It is possible that they may have used the inverse application of the routine from Tremaine et al. (2002), i.e., FITEXY($\sigma|L$) producing a steeper L–σ slope.

The abundance of investigations on the L–σ relations point towards a broken or maybe a curved relation. However, given a colour-magnitude relation followed by Sérsic galaxies, it is essential to know whether or not this bend is universal and how the slopes of the two arms change with colour. Another associated question is whether the break in the L–σ relation is due to the core-Sérsic versus Sérsic galaxies or the elliptical (slow-rotators) galaxies versus ellicular plus lenticular (fast rotators) galaxies, suggested as another interpretation of the bend seen in (Graham & Soria, 2018).

1.3.4 Black hole mass versus the spheroid mass distribution

Finding out the most fundamental relation between black hole mass and the host spheroid/galaxy is one of the primary goals of various black hole scaling relations studies. Graham et al. (2001a) suggested that possibly the central black hole mass may have a better correlation with how the mass is distributed, especially at the central spheroid regions, than the bulk of the spheroid stellar mass.

Trujillo et al. (2001) defined a concentration index for a component (spheroid or galaxy) with a Sérsic surface brightness profile (Sérsic, 1963, 1968a). The Sérsic profile,

$$\mathrm{I(R)} = \mathrm{I_e} \exp\left[-\mathrm{b_n}\left\{\left(\frac{\mathrm{R}}{\mathrm{R_e}}\right)^{1/\mathrm{n}} - 1\right\}\right], \tag{1.1}$$

is characterised by three parameters, Sérsic index or profile shape parameter (n), half-light radius $\mathrm{R_e}$, and the surface brightness μ_e ($= -2.5 \log \mathrm{I_e}$) at $\mathrm{R_e}$. Sérsic index traces the central concentration of the light within the spheroid (Trujillo et al., 2001; Graham et al., 2001b), suggesting that Sérsic index itself can be directly used to infer the central light concentration of a bulge (or galaxy).

Many studies in the past have investigated the M_BH–n relation based on then-available sample Graham et al. (2003); Graham & Driver (2007a); Vika et al. (2012); Beifiori et al. (2012); Savorgnan et al. (2013); Savorgnan (2016). Notably, Graham & Driver (2007a) advocated a curved M_BH–n relation, steeper at low-n end and almost saturated at the high-n end, putting an upper limit of $\sim 10^{10}\mathrm{M}_\odot$ on M_BH. However, subsequent studies could not recover a curved relation. Savorgnan (2016) hinted at the presence of a red and blue sequence in the M_BH–n diagram as well; however, they could not obtain a very tight fit.

Graham & Driver (2007a) also predicted a correlation between black hole mass and the central surface brightness, μ_0, also known as the central projected luminosity or central column density of the host spheroid. Additionally, they emphasized the possibility of an even stronger relation between black holes mass and the (de-projected) internal mass density. The possibility of morphology-dependent substructures in the M_BH–(central light concentration or n) diagram along with the possible correlations of M_BH with the effective size, the surface brightness (or projected mass density), and the internal mass density of the host bulge (and galaxy), which have not been explored enough in the past, require a thorough investigation using the updated and larger black hole sample now available.

1.4 Applications of Black Hole Scaling Relations

The study of black hole scaling relation is essential on its own to quantify the relative growth of galaxy properties and black hole mass, which can directly assist related studies and other areas of astronomy, some of which are as follows. The (black hole)–(galaxy) correlations hold crucial insights for various studies on their interplay, e.g., the regulation of material (gas/dust) in the galaxy through AGN feedback, the link between BH growth and star formation rate in the host galaxy, where the star formation is linked with the availability of gas and, further, the galaxy morphology (Marconi et al., 2008; Volonteri & Ciotti, 2013; Heckman & Best, 2014; Calvi et al., 2018; King, 2019).

Importantly, the scaling relations of BH mass with the host galaxy properties are directly used to predict the BH masses in other galaxies, where the BH's sphere-of-influence cannot be resolved due to technological limitations, but the host galaxy properties are relatively easier to measure. Additionally, these relations are used to calibrate the secondary BH mass measurement methods, e.g., constraining the virial f-factors for the reverberation mapping method (e.g., Onken et al., 2004; Graham & Others, 2011; Bennert et al., 2011; Bentz & Katz, 2015; Yu et al., 2019). The current sample of galaxies with dynamically measured BHs resides in the local Universe ($z \sim 0$); therefore, the BH–galaxy correlations established for $z \sim 0$ can work as a benchmark for studies attempting to determine the evolution of these relations for high redshifts (e.g., Bennert et al., 2011; Hiner, 2012; Sexton et al., 2019).

Further, these BH scaling relations are used to calculate the black hole mass function of the Universe (e.g., Driver, 2006; Driver et al., 2007), SMBH merger time scale (e.g., Biava et al., 2019), and constrain the SMBH merger rates (e.g., Chen et al., 2019). These can further be used to constrain the ground-based detection of the (stochastic) long-wavelength gravitational waves generated by merging SMBH binaries, which are actively being searched for by the Parkes Pulsar Timing Array (PPTA, Shannon et al., 2015; Hobbs & Dai, 2017), the European Pulsar Timing Array (EPTA, Stappers & Kramer, 2011), and the North American Nanohertz Observatory for Gravitational Waves (NANOGrav, Siemens, 2019). Furthermore, these scaling relations can also be used to predict the space-based detection of stochastic as well as individual long-wavelength gravitational waves by the Laser Interferometer Space Antenna (LISA, Danzmann, 2017).

1.5 Aim of the Thesis

When I started my PhD in November 2017, we had a total sample of 127 local galaxies with directly measured black hole masses available in the literature. This sample is comprised of 84 ETGs and 43 LTGs (spiral galaxies). The majority (81%) of our galaxy images are in 3.6μm-band taken by the Spitzer Space Telescope, and the remaining galaxy images are taken from the archive of HST, SDSS, and Two Micron All Sky Survey (2MASS). We perform state-of-art two-dimensional modelling and multi-component decomposition of total galaxy light, disassembling it into its components. This process enables us to obtain accurate stellar masses and structural parameters of the bulge, disk, other galaxy components, and the total galaxy stellar mass. Of 84 ETGs, the image analysis for 40 galaxies are taken from (Savorgnan & Graham, 2016b), I analysed the remaining 44 ETGs, which are presented in (Sahu et al., 2019a, Chapter 2 here), and 43 LTGs were analysed by (Davis et al., 2019a).

We now have a total combined data set of 127 galaxies with reliable black hole masses and host galaxy properties carefully measured with copious attention given to every galaxy. Almost doubling the sample of such galaxies used in Savorgnan et al. (2016), this thesis aims to investigate the following:

- Whether the correlation between black hole mass and the host spheroid mass is linear or non-linear? Is it dependent on galaxy morphology? If it has morphology-dependent divisions, whether it is because of core-Sérsic versus Sérsic galaxies or ETG versus LTG, or some other classification?

- Does the black hole mass correlate with total galaxy stellar mass? Furthermore, is it dependent on galaxy morphology?

- Obtaining the correlation between black hole mass and the host central stellar velocity dispersion and investigating possible substructures due to Sérsic versus core-Sérsic, barred versus non-barred, ETGs versus LTGs, and AGN versus non-AGN host classifications.

- Establishing the near infra-red luminosity–velocity dispersion relation and investigating the presence of a bend or curve. Further, examining the selection bias observed in the stellar velocity dispersion versus galaxy stellar mass diagram (Shankar et al., 2016).

- Investigating the correlation between black hole mass and other bulge properties, e.g., size, and the distribution of mass inferred by, e.g., central mass concentration (Sérsic index), central surface brightness or the projected mass density, and internal stellar mass density, at central and extended spheroid radii. Furthermore, analysing the possible dependence on morphology and comparing it with other scaling relations.

- Which relation is the fundamental line or curve between the black hole and host galaxy, and which ones are secondary? Is there a fundamental plane?

Chapter 2 presents a detailed description of our imaging data-set, our primary data reduction process, galaxy modelling, and the multi-component decomposition technique, which enabled us to disassemble the bulge mass from the total galaxy mass and identify the morphology of our galaxies, required to answer the questions posed above. The multi-component decomposition profiles of 44 early-type galaxies that I worked on are provided in **Appendix A**. The decomposition profile for the remaining 40 ETGs and 43 LTGs are available in Savorgnan & Graham (2016b) and Davis et al. (2019a), respectively. Importantly, **Chapter 2** presents the correlations we found between BH mass and both the bulge stellar mass and the galaxy mass for ETGs, and further combining the work on LTGs from (Davis et al., 2018a, 2019a), this chapter details our investigation for the dependence of these BH scaling relations on the host galaxy morphology.

By 2019, the number of local galaxies with directly measured black hole mass grew to 145. **Chapter 3** uses this appended sample to update the correlation between black hole mass and central stellar velocity dispersion. This chapter presents a detailed investigation for possible morphology dependent substructures in the $M_{\rm BH}$–σ diagram and provides a comparison with the noted findings in the past. Here, we also establish the $3.6\,\mu$m L–σ relation, and re-analysed the V-band L–σ relation by performing a symmetric regression on the V-band data from Lauer et al. (2007) with updated core-Sérsic versus Sérsic classifications (when available). In this chapter, we re-analyse the basis of a selection bias proposed in Shankar et al. (2016), by comparing their σ–$M_{*,\rm gal}$ curve for active galaxies with our updated σ–$M_{*,\mathrm{gal}}$ relations.

Chapter 4 expands on possible correlations between black hole mass and central light concentration of the bulge, which is very well inferred by the Sérsic index of the bulge light profile. Here, we also investigate the correlations between black hole mass and bulge (effective) sizes, e.g., (half (50%)-, 10%-, and 90%- light radii). **Chapter 4** also presents the M_{sph}–n and M_{sph}–size relations compares it with the proposed curved mass-size relations (Graham, 2019b). We investigate for possible dependence on morphology in all these diagrams. Additionally, we test internal consistency between our M_{BH}–n, M_{sph}–size, and M_{BH}–M_{sph} relations.

Chapter 5 probes the scaling relations between black hole mass and the surface brightness (also known as the projected luminosity density) and projected stellar mass density at the centre and various inner and outer spheroid radii. Importantly, we performed de-projection of the (2D) spheroid surface brightness profiles to obtain their (three-dimensional) internal stellar mass density, which is the true measure of density rather than the directly observed, projected density. Here, we present our detailed investigation for the correlations between black hole mass and internal density at various spheroid radii, including the black hole's sphere-of-influence and their significant implications. This chapter also addresses the fundamental black hole relation and the possibility of a fundamental plane.

Chapter 6 summarises the investigations performed in science Chapters (2, 3, 4, and 5), lists the main conclusions, improvements/ramifications for the applications (mentioned in Section 1.4), and the future scope of this work.

2

Black Hole Mass Scaling Relations for Early-Type Galaxies. I. M_{BH}–$M_{*,sph}$ and M_{BH}–$M_{*,gal}$

Analyzing a sample of 84 early-type galaxies with directly-measured super-massive black hole masses-and nearly doubling the sample size of such galaxies with multi-component decompositions—a symmetric linear regression on the reduced (merger-free) sample of 76 galaxies reveals $M_{BH} \propto M_{*,sph}^{1.27\pm0.07}$ with a total scatter of $\Delta_{rms} = 0.52$ dex in the $\log(M_{BH})$ direction. However, and importantly, we discover that the ES/S0-type galaxies with disks are offset from the E-type galaxies by more than a factor of ten in their $M_{BH}/M_{*,sph}$ ratio, with ramifications for formation theories, simulations, and some virial factor measurements used to convert AGN virial masses into M_{BH}. Separately, each population follows a steeper relation with slopes of 1.86 ± 0.20 and 1.90 ± 0.20, respectively. The offset mass ratio is mainly due to the exclusion of the disk mass, with the two populations offset by only a factor of two in their $M_{BH}/M_{*,gal}$ ratio in the M_{BH}–$M_{*,gal}$ diagram where $M_{BH} \propto M_{*,gal}^{1.8\pm0.2}$ and $\Delta_{rms} = 0.6 \pm 0.1$ dex depending on the sample. For $M_{BH} \gtrsim 10^7 M_\odot$, we detect no significant bend nor offset in either the M_{BH}–$M_{*,sph}$ or M_{BH}–$M_{*,gal}$ relations due to barred versus non-barred, or core-Sérsic versus Sérsic, early-type galaxies. The total ensemble of 43 late-type galaxies (from Davis et al., 2019a), which invariably are Sérsic galaxies, follow M_{BH}–$M_{*,sph}$ and M_{BH}–$M_{*,gal}$ relations with slopes equal to 2.16 ± 0.32 and 3.05 ± 0.70, respectively. Finally, we provide some useful conversion coefficients, υ, accounting for the different stellar mass-to-light ratios used in the literature, and we report

the discovery of a local, compact massive spheroid in NGC 5252.

2.1 Introduction

There is growing evidence suggesting that black holes exist in a continuum of masses, from stellar mass black holes (a few $M_\odot$ to $\approx 100\,M_\odot$; Belczynski et al., 2010; Abbott et al., 2016a) to super-massive black holes ($10^5\,M_\odot - 10^{10}\,M_\odot$; Lynden-Bell, 1969; Wolfe & Burbidge, 1970; Lynden-Bell & Rees, 1971; Natarajan & Treister, 2009; Inayoshi & Haiman, 2016). In between these two mass ranges lie the intermediate-mass black holes (Miller, 2003; Mapelli, 2016; Mezcua, 2017; Graham et al., 2018, and references therein). A galaxy may contain several thousand (Hailey & Others, 2018) to millions (Elbert et al., 2018) of stellar mass black holes, but typically only one central Super-Massive Black Hole (SMBH) for which there are many theories (Miller, 2003; Mayer & Others, 2007; Hirano & Others, 2017; Morganti, 2017).

In order to obtain insight for these theories, for the last three decades, astronomers have been investigating the underlying relations between SMBHs and various properties of the host galaxies (see the review in Graham, 2016, and references therein). Based on Dressler (1989), and various black hole formation scenarios and feedback models, most astronomers have come to envision a fundamental scaling relation existing between the mass of an SMBH and that of the spheroidal stellar component of the host galaxy.

Building on some of the previous estimates of black hole masses, Dressler & Richstone (1988) predicted an upper limit of $10^9\,M_\odot$ for the central SMBH mass of the galaxies with the largest spheroids. Their prediction was based on the central black hole mass (M_{BH}) and spheroid stellar mass (M_{sph} or M_{bulge}) ratios in the two neighboring galaxies M31 and M32. Dressler (1989) directly, and Yee (1992) indirectly, suggested a linear relationship between the black hole mass and bulge mass of a galaxy. Kormendy & Richstone (1995) and Magorrian et al. (1998) subsequently observed a linear relation between M_{BH} and M_{bulge}.

Using larger samples of galaxies and updated black hole masses, most astronomers continued to report a near-linear M_{BH}–M_{bulge} relation for nearly two decades (e.g. Ho, 1999; Ferrarese & Ford, 2005; Graham, 2007b; Gültekin et al., 2009b; Sani & Others, 2011). However, during the same period, some astronomers (Laor, 1998; Wandel, 1999) found a steeper relation due to the addition of low-mass galaxies in their datasets. Salucci & Others (2000) reported that spiral galaxies have a steeper $M_{BH} - M_{bulge}$ slope than massive elliptical galaxies. Further, Laor (2001) reported $M_{BH} \propto M_{bulge}^{1.53\pm0.14}$ from his work on an updated sample of 40 quasars.

Graham (2012) observed two different slopes in the M_{BH}–L_{bulge} diagram for galaxies with Sérsic or core-Sérsic spheroids (Graham & Others, 2003). He found a near-linear $M_{BH} - L_{bulge}$ relation for the massive core-Sérsic galaxies (all of which were early-type galaxies), and a "super-quadratic"[1] relation for the low-mass Sérsic galaxies (most of which were late-type galaxies). Further, Graham & Scott (2013) and Scott et al. (2013), with their work on a bigger sample of galaxies, recovered this bent relation and Graham & Scott (2015) showed that the so-called pseudobulges (Gadotti & Kauffmann, 2009; Kormendy et al., 2011) also complied with the non-linear (super-quadratic) arm of the bent relation. The bent relation strongly suggested the need to re-visit various theories and implications based on the previously assumed linear relation. For example, if there is evolution along the M_{BH}–M_{sph} relation, then the steeper relation reveals that the fractional growth of a black hole's mass is faster than that of low-mass spheroids (Sérsic galaxies), consistent with many other works (e.g. Diamond-Stanic & Rieke, 2012; Seymour et al., 2012; LaMassa & Others, 2013; Drouart et al., 2014).

These M_{BH} scaling relations will help us understand the rate at which the black hole mass grows relative to the star formation rate in the host galaxy, which further aids formation and evolution theories of black holes and the galaxies which encase them (e.g. Shankar et al., 2009). It also provides insight into the understanding of AGN feedback models between an SMBH and its host galaxy (e.g. Hopkins et al., 2006). In the past, some simulations have reported steeper (at the low-mass end) and bent M_{BH}–$M_{*,sph}$ relations (Cirasuolo et al., 2005; Fontanot et al., 2006; Dubois et al., 2012; Khandai et al., 2012; Bonoli et al., 2014; Neistein & Netzer, 2014; Anglés-Alcázar et al., 2017), which partly supports our findings.

Gadotti & Kauffmann (2009) reported discrepancies between the black hole mass esti-

[1] The phrase "super-quadratic" was used to describe a power-law with a slope greater than 2 but not as steep as 3.

mated from the $M_{\rm BH}$–σ relation and the single linear M_{BH}–$M_{*,sph}$ relation for all type of (elliptical, lenticular and spiral) galaxies. There are in fact many influential works which have based their predictions on a single linear M_{BH}–$M_{*,sph}$ relation, for all type of galaxies (Fabian, 1999; Wyithe & Loeb, 2003; Marconi et al., 2004; Springel et al., 2005; Begelman & Nath, 2005; Croton et al., 2006; Di Matteo et al., 2008; Natarajan & Volonteri, 2012). This can affect the inferred science; hence, we recommend that these simulations be revisited using the new scaling relations.

Numerous investigations of the M_{BH}–M_{sph} relation were based on the belief that there is a large possibility of black hole mass correlating better with its host bulge stellar mass, rather than with its host galaxy (or total) stellar mass, reflected by the smaller scatter in the M_{BH}–M_{sph} relation. However, Läsker et al. (2014)[2] with their (early-type galaxy)-dominated sample of 35 galaxies claimed that black hole mass correlates with total galaxy luminosity equally well as it does with the bulge luminosity. Additionally, there have been several detections of bulge-less galaxies which harbor massive black holes at their center (e.g. Reines et al., 2011; Secrest et al., 2012; Schramm et al., 2013; Simmons et al., 2013; Satyapal et al., 2014). This suggests the possibility of the black hole mass correlating directly with the galaxy mass (M_{gal}), whether this be the stellar, baryonic, or total mass (Ferrarese, 2002; Baes et al., 2003; Sabra et al., 2015; Davis et al., 2018a).

The recent work by Savorgnan et al. (2016) used a larger sample of 66 galaxies—consisting of 47 early-type galaxies (ETGs) and 19 late-type galaxies (LTGs)—and reported that black hole mass correlates equally well with bulge luminosity and total galaxy luminosity only for ETGs, not for LTGs (see their Figures 1 and 2). They also suggested a different idea for the bend in the M_{BH}–M_{sph} relation that was not detected by Läsker et al. (2014). For the core-Sérsic and Sérsic galaxies in Savorgnan et al. (2016), they found $M_{BH} \propto M_{*,sph}^{1.19\pm0.23}$ and $M_{BH} \propto M_{*,sph}^{1.48\pm0.20}$, respectively. These slopes for the two populations have overlapping uncertainties (within the 1σ level) and unlike in Scott et al. (2013), which estimated the bulge masses using a morphologically-dependent bulge-to-total ratio for 75 late-type and early-type galaxies, there was no clear bend. Furthermore, Savorgnan et al. (2016) found different trends for their early-type and late-type galaxies, which they referred to as a "red sequence" and a "blue sequence", respectively, although

[2]Läsker et al. (2014) had only 4 late-type galaxies in their sample

color information was not shown in that diagram.

Our work on the hitherto largest dataset of 84 early-type galaxies, with directly-measured black hole masses, builds on Savorgnan & Graham (2016b) and nearly doubles their number of ETGs with multi-component decompositions. ETGs consist of ellipticals (E), ellicularsᶾ (ES), and lenticulars (S0), where the latter two types have disks. Ellicular and lenticular galaxies often contain bars, bar-lenses, inner disks, rings, and ansae in addition to the bulge and disk. ETGs are often misclassified, as many catalogs, e.g., Third Reference Catalogue of Bright Galaxies (RC3), de Vaucouleurs et al. (1991), failed to identify disks from a visual inspection of the images. For our set of ETGs, we perform multi-component decompositions to identify disks, and bars, and separate the bulge luminosity from the total galaxy luminosity. We intend to refine how the black hole mass correlates with its host spheroid stellar mass, and determine how it correlates with the host galaxy stellar mass. We investigate whether or not the core-Sérsic and Sérsic galaxies cause the bend in M_{BH}–M_{sph} relation. Also, we combine our work on ETGs with the study of LTGs by Davis et al. (2019a, 2018a) to further explore the reason behind the bend in the M_{BH}–M_{sph} relation. We additionally explore the possibility of different M_{BH}–M_{sph} relations depending on the ETG sub-morphology, i.e., for galaxies with and without a disk, and galaxies with and without a bar. In all the cases, we also investigate the prospect of a better or equally likely correlation of black hole mass with total galaxy stellar mass.

In the following Sections, we describe our imaging dataset and primary data reduction techniques. Section 2.3 illustrates the galaxy modeling and multi-component decomposition of the galaxy light. This section also presents a detailed discussion of the stellar mass-to-light ratios that we applied to the luminosity to determine the stellar masses. We compare the masses of the galaxies calculated using different (color-dependent) stellar mass-to-light ratios, and we provide a conversion coefficient which can be applied to bring them into agreement with alternate prescriptions for the mass-to-light ratio. In Section 2.4, we present the black hole scaling relations for our ETG sample, along with an extensive discussion of the nature of the M_{BH}–$M_{*,sph}$ and M_{BH}–$M_{*,gal}$ relations for various cases: Sérsic and core-Sérsic galaxies; galaxies with and without a disk; galaxies with and

[3]ETGs with intermediate stellar disks (Liller, 1966; Graham et al., 2016a)

without a bar; and ETGs versus LTGs. Finally, in Section 2.5, we summarize our work and present the main implications. Henceforth, we will be using the terms spheroid and bulge of a galaxy interchangeably.

2.2 Imaging Data

We have compiled an exhaustive sample of all 84 ETGs currently with a directly measured SMBH mass. We use the black hole masses measured from direct methods, i.e., modeling of stellar and gas dynamics. Gas-dynamical modeling is fundamentally simpler, as gases being viscous, easily settle down and rotate in a circular disk-like structure, while stellar dynamical modeling is complex and computationally expensive (Walsh et al., 2013). Although both have their pros and cons, we prefer to use the black hole masses measured from stellar dynamics, as stars are influenced only by gravitational forces, while gas dynamics are more prone to non-gravitational forces. In order to know more about the above primary methods of black hole mass measurement, readers are directed to the review by Ferrarese & Ford (2005).

Out of a total of 84 ETGs, we obtain SMBH masses, distances, and light profile component parameters for 40 galaxies from Savorgnan & Graham (2016b). For NGC 1271 and NGC 1277, we directly used the SMBH masses, and the bulge and total galaxy stellar masses, from the work on their H- and V- band Hubble Space Telescope (HST) Images retrieved and reduced by Graham et al. (2016a) and Graham et al. (2016b), respectively. The remaining 42 galaxies were modeled by us, which also includes seven galaxies (A3565 BCG, NGC 524, NGC 2787, NGC 1374, NGC 4026, NGC 5845, and NGC 7052) from the dataset of Savorgnan & Graham (2016b) that we remodeled. About 80% of the galaxy images used in this work are Spitzer Space Telescope (SST) 3.6 μm images, taken with the Infra-Red Array Camera (IRAC). The remaining few images are Sloan Digital Sky Survey (SDSS, York et al., 2000) r'-band images and Two Micron All Sky Survey (2MASS, Jarrett et al., 2003) K_s-band images.

2.2.1 Image Sources

IRAC 3.6 μm images (IRAC1) are unaffected by dust absorption, have large fields-of-view, and are sufficiently spatially resolved to enable us to visually identify the primary galaxy components, thereby increasing the accuracy of disassembling galaxy images. Hence, for our analysis, we preferred to use IRAC 3.6 μm images. However, for some galaxies whose Spitzer images are not available, we used images from the SDSS archive and 2MASS catalog.

The 42 galaxy images (including seven remodeled) that we modeled were comprised of 33 images in the 3.6 μm band, out of which five images are downloaded from the Spitzer Survey of Stellar Structure in Galaxies (S^4G: Sheth et al., 2010; Muñoz-Mateos et al., 2013; Querejeta et al., 2015) pipeline-1, and 28 images are obtained from the Spitzer Heritage Archive (SHA: Levine et al., 2009; Wu et al., 2010; Capak et al., 2013). Of the remaining 9 galaxies, six K_s-band images are obtained from 2MASS (Jarrett et al., 2003) and three r'-band images are from the SDSS Data Release-8 (Aihara et al., 2011).

Images from the S^4G pipeline-1 (P1)[4] are science-ready, calibrated images formed by mosaicking individual Basic Calibrated Data (BCD) frames. The S^4G survey is limited to galaxies with a maximum distance of 40 Mpc, brighter than a B-band apparent magnitude of 15.5 mag, and a size limit $D_{25} > 1'$ (Sheth et al., 2010). Hence, we obtained 3.6 μm images of galaxies not fitting this criteria from SHA, which are level-2, post-Basic Calibrated Data (pBCD)[5] images. The pBCD images are a mosaicked form of level-1 corrected Basic Calibrated Data (cBCD) frames. Level-1 cBCD frames have already undergone dark current subtraction, flat-field correction, various instrument artifact corrections, and flux calibration.

The r'-band images of three galaxies (NGC 6086, NGC 307, NGC 4486B) from the SDSS catalog are also basic corrected and calibrated. Although optical-band images suffer from dust extinction, we justify our choice of SDSS images, as they have a large field-of-view and sufficient resolution to help us identify galaxy components. For the remaining six galaxies (A1836 BCG, MRK 1216, NGC 1550, NGC 4751, NGC 5328, NGC 5516,),

[4]`http://irsa.ipac.caltech.edu/data/SPITZER/S4G/docs/pipelines_readme.html`
[5]`https://irsa.ipac.caltech.edu/data/SPITZER/docs/dataanalysistools/cookbook/6/`

Table 2.1. Photometric Parameters

Image Source	Zero-Point (mag[a])	Pixel Scale ($''$)	Υ_* $M_\odot/L_\odot$	$MAG_\odot$ mag
S4G	21.097[b]	0.75	0.6[f]	6.02
SHA	21.581[c]	0.6	0.6[f]	6.02
2MASS	Image specific[d]	1	0.7[g]	5.08
SDSS	22.5[e]	0.4	2.8[h]	4.65

Note. — Columns: (1) Image Source. (2) Photo-metric zero-points of images in AB magnitude. (3) Pixel size of images. (4) Stellar mass-to-light ratios used to convert measured luminosities into stellar masses. (5) Absolute magnitude of sun in AB magnitude system.

[a]AB magnitude system.

[b]Salo et al. (2015, their Equation-13).

[c]Muñoz-Mateos et al. (2016, their Equation-1).

[d]Zero-points specified in image headers were converted from Vega magnitude to AB magnitude using equation (5) from Blanton et al. (2005).

[e] Blanton et al. (2005, their Equation-4).

[f]Taken from Meidt et al. (2014) for 3.6 μm band.

[g]Using $\Upsilon_*^{3.6}$ in the equation $\Upsilon_*^{3.6\mu m} = 0.92\times\Upsilon_*^{K_s} - 0.05$ from Oh et al. (2008).

[h]Calibrated using $\Upsilon_*^{r'} = \Upsilon_*^{K_s} \times L_{K_s}/L_{r'}$ with $\Upsilon_*^{K_s} = 0.7$.

we used flux calibrated[6] K_s-band images from the 2MASS catalog.

About 95% of the images in our total galaxy sample of 84 are in either the 3.6 μm (roughly L-band) or the 2.17 μm (K_s-band), which helps us obtain a more reliable distribution and measurement of luminosity and stellar mass, due in part to a stable stellar mass-to-light ratio in these bands (described in Section 2.3.3). Table 2.1 lists the flux calibration zero points, image pixel scale, stellar mass-to-light ratios used in this work, and solar absolute magnitude in different image pass-bands.

2.2.2 Image Reduction and Analysis

All the images obtained from the various telescope pipelines described above have already undergone dark current subtraction, flat fielding, bad pixel and cosmic ray correction, sky-

[6]`https://www.ipac.caltech.edu/2mass/releases/allsky/doc/sec4_1.html`, `https://www.ipac.caltech.edu/2mass/releases/allsky/doc/sec4_2.html`

subtraction (except for S^4G and 2MASS images), and flux calibration. The automated routines in the telescope pipelines either over or under-estimated the sky-background intensity, which we observed for most of our galaxies. Hence, we started our image analysis by measuring the sky-background intensities, then generating the image masks and calculating the telescope's point spread function.

Sky Backgrounds

Sky-background level subtraction is one of the crucial steps to measure a galaxy's luminosity accurately. As our target galaxy images are extended over a large number of pixels in the CCD images that we are using, an error in sky background intensity subtraction will lead to a systematic error in the surface brightness profile, especially at the larger radii and result in an erroneous measurement of the galaxy component at large radii, and in turn the inner components and the galaxy luminosity. The wide-field images that we obtained from the SHA and SDSS pipelines have already undergone sky subtraction, but as we analyzed the intensity distribution of the images, we found that the peak of the sky-background level was offset from zero for almost all of the images. Hence, it was necessary to calculate the correction in order to tune the sky level of these images to zero.

To calculate the sky-background intensity level, we follow a similar procedure as explained in Almoznino et al. (1993). The intensity distribution of the sky-background photons incident on a CCD image ideally follows a Poisson distribution when the only source of systematic error is random emission from the radiating object, in this case, the "sky-background". However, many other systematic errors are introduced in a CCD image when it undergoes telescope pipelining. In that case, a Gaussian distribution (normal distribution) can be a better approximation for the intensity distribution of the "sky-background". We constructed the intensity function (pixel number of given intensity versus intensity histogram) of the entire image frame (not just a few portions of the sky that appear free of sources) and fit a Gaussian to the portion of the histogram dominated by the sky (the peak at lower-intensity values), as shown in Figure 2.1. Intensity values of the pixels occupied by other radiating sources, including our target galaxy, produce the long tail towards higher intensities. The Gaussian fit gives us an optimally accurate mean sky value and the standard deviation (rms error) in any one pixel.

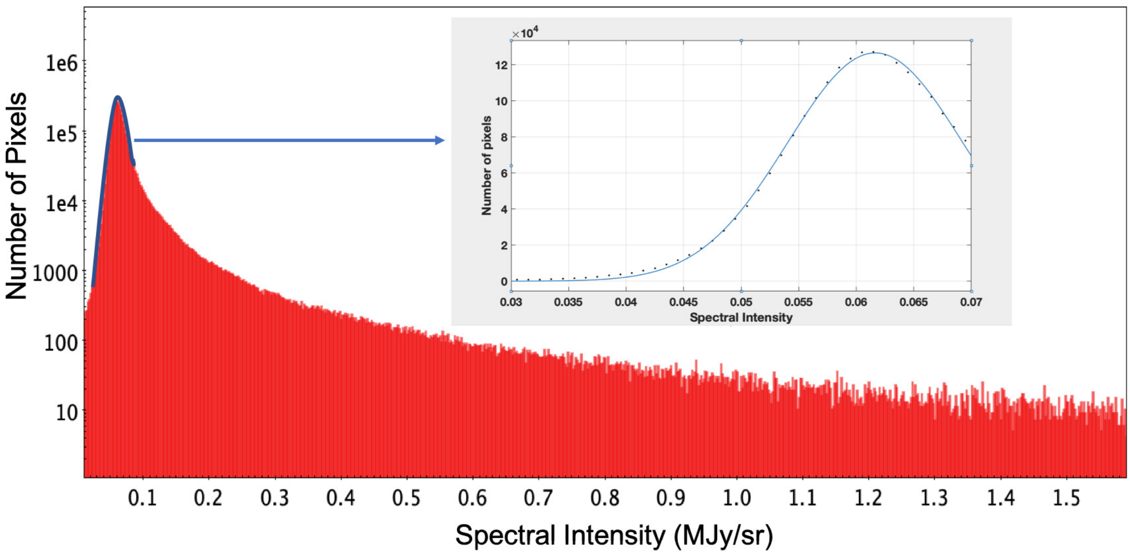

Figure 2.1 Gaussian fit to the sky-background intensity of the "level-2 corrected", 3.6 μm -band image of NGC 1600 from SHA, which has already undergone sky subtraction, but the sky level peaking at a non-zero value indicates that it still requires adjustment. The red distribution shows the faint (sky-dominated) end of the intensity histogram (number of pixels at each intensity value) from the CCD image of NGC 1600. The inset plot shows a Gaussian fit (blue curve) to the sky values in the range of 0.03 to 0.07 MJy/sr, peaking at 0.062 MJy/sr. The intensity distribution following the peak includes the intensity of our target galaxy and other radiating sources (added with the sky value).

Masking

Images for our galaxy sample have large fields-of-view. Apart from our target galaxy, these images also contain other radiating sources around and overlapping with the target galaxy. Major contaminating sources are background quasars and foreground stars that overlap the pixel area occupied by the galaxy of interest. Hence, for an accurate measurement of the galaxy luminosity, we eliminate the contribution of these contaminating sources by generating a mask file. A mask is either a .fits or .pl file marking (with their pixel coordinates and pixel size) the areas and sources to be discarded during the analysis.

We used the task MSKREGIONS in the Image Reduction and Analysis Facility (IRAF) software to read a list of user-specified regions to be masked in our image. The task then generates a mask file (.pl or .fits file) using our galaxy image as a reference for the size of the mask file. The list of contaminating objects and subsequent masks are generated in two parts by us:

1. SOURCE EXTRACTOR (Bertin & Arnouts, 1996): It uses a threshold background value to automatically identify all the objects present in an image and makes a catalog of them, designating each object by its physical coordinates in the image. We can identify and remove our target galaxy from this list (knowing its physical coordinates) and generate a mask file using this catalog using the task MSKREGIONS.

2. MANUAL MASKING: SOURCE-EXTRACTOR cannot identify the background and foreground objects overlapping with the pixel area of our target galaxy. However, it is important to mask them in order to avoid biasing the image decomposition; therefore, we need to mask them manually. We carefully find the overlapping sources by observing our galaxy at different brightness (contrast) levels. For this purpose, we use the astronomical imaging and data visualization application SAOIMAGE DS9. We generate the second mask file of contaminating objects with the MSKREGION task.

We combine the above two mask files using the IMARITH task in IRAF and further use the final mask as a reference for avoiding the contaminated pixels during extraction and modeling of the target galaxy light. Extra care was taken to manually mask dust in the three SDSS r'-band images.

PSF determination

The spatial resolution of an image is limited by the telescope's aperture size, the wavelength of observation, the pixel size of its instrument, and the atmospheric blurring for ground-based observations. A distant star is a point source, whose light profile is ideally described by a delta function, but due to the collective resolution limitations, it is imaged as an extended object, and its light profile becomes a function with a non-zero width. Hence, the Full Width at Half Maximum (FWHM) of the light profile of a star in an image is a measure of the total *seeing effect*, which is quantified by the Point Spread Function (PSF) of the telescope.

The image of an object obtained by a telescope can be mathematically described as a convolution of its actual profile with the telescope's PSF. Hence, in order to measure the parameters of the actual light (or surface brightness) profile of a galaxy and its components, we need our fitting functions to be convolved with the telescope's PSF.

Moffat (1969) describes how the wings of the seeing profile (PSF) of a telescope is represented better by a Moffat function rather than a Gaussian function. A "Moffat function" has the mathematical form

$$I(R) = I_0 \left(1 + \left(\frac{R}{\alpha}\right)^2\right)^{-\beta}, \tag{2.1}$$

where α is the width parameter and β controls the spread in the wings of the seeing profile (see Figure 3 in Moffat, 1969). The parameters α and β are related to the FWHM of the profile through the equation FWHM $= 2\alpha\sqrt{2^{\frac{1}{\beta}} - 1}$. The value of α and β increases with poor seeing (e.g., higher atmospheric turbulence) and gradually, the profile that they describe approaches a Gaussian. We used the IRAF task IMEXAMINE to determine the PSF of our images. The IMEXAMINE task fits the radial profile of selected stars with a Moffat function and provides the required parameters: FWHM and β.

2.3 Modeling and decomposing the galaxy light

The luminosity of a galaxy is modeled by fitting quasi-elliptical isophotes[7] at each radius along the semi-major axis (R_{maj}). Ciambur (2016), in his introduction section, and Savorgnan & Graham (2016b), in their Section 4.1, employ both 1D (one-dimensional) and 2D (two-dimensional) modeling and provide a critical comparison of the two techniques. Savorgnan & Graham (2016b) had more success modeling the galaxies as a set of 1D profiles; hence we also prefer to use 1D profile modeling, which takes into account the radial variation in all of the isophotal parameters such as ellipticity (ϵ), position angle (PA), and the irregularity in an isophote's shape across the whole 2π azimuthal range as quantified using Fourier harmonic coefficients. Therefore, 1D modeling should not be confused with the light profile obtained only from a one-dimensional cut of a galaxy image.

Early-type galaxies are commonly ill-considered to be featureless (no sub-components) and are expected to have regular elliptical isophotes, a scenario which is only valid for purely elliptical galaxies. Early-type galaxies can be morphologically sub-classified as ellipticals (E) consisting of an extended spheroid, elliculars (ES) consisting of an extended spheroid with an intermediate-scale disk (e.g., Graham et al., 2016a), and lenticulars (S0) comprised of a spheroid and an extended large-scale disk. Apart from these standard components, ETGs may also contain nuclear disks, inner rings, bars, bar-lenses (Sandage, 1961; Laurikainen et al., 2009; Saha et al., 2018), outer rings, and ansae (Saha et al., 2018; Martinez-Valpuesta et al., 2007), which can cause non-elliptical or irregular isophotes in a galaxy.

2.3.1 One-dimensional Representation of the Galaxy Light

We use the new IRAF tasks Isofit and Cmodel (Ciambur, 2015) to extract the 1D light profile and associated parameter profiles (e.g., ellipticity, PA, etc.), and create a 2D model of each galaxy. Isofit and Cmodel are upgraded versions of the IRAF tasks Ellipse and Bmodel (Jedrzejewski, 1987a,b), respectively.

In order to extract a galaxy light profile, Isofit reads a 2D image of a galaxy, the associated mask file, and fits quasi-elliptical isophotes at each radius of the galaxy, starting

[7] A curve which connects the points of equal brightness

from its photometric center to its apparent edge, thus including every part of the galaxy. Further, ISOFIT uniformly samples each isophote across the whole azimuthal range, using a natural angular coordinate for ellipses, known as the "Eccentric Anomaly" (ψ, for more details see Section 3 of Ciambur, 2015), and provides average intensity and associated parameters of the isophotes as a function of semi-major axis radii. The isophotal intensity can be expressed in terms of the average intensity $\langle I_{ell} \rangle$ and Fourier perturbations such that

$$I(\psi) = \langle I_{ell} \rangle + \sum_n \left[A_n sin(n\psi) + B_n cos(n\psi) \right] \tag{2.2}$$

where, A_n and B_n are nth order Fourier harmonic coefficients.

As explained by Ciambur (2015), while fitting each isophote, ISOFIT calculates A_n and B_n, these Fourier coefficients when added together, account for the irregular isophotal shapes and give a near-perfect fit. Ciambur (2015) also mentions that the value of A_n and B_n decreases with increasing order (n); therefore, we calculate a sufficient number of even harmonic coefficients, up to a maximum of $n = 10$. Apart from the $n = 3$ harmonic, odd-ordered Fourier harmonic coefficients ($n = 5, 7, 9$,etc.) appear to provide almost no refinement in an isophote's shape; thus we can obtain a very good light profile and galaxy model, without them. Also, for the light profile along the major axis ($\psi = 0$), the sine terms are zero; hence we corrected our major-axis intensity values only for the cosine perturbations (B_n).

The original ELLIPSE task is limited to only work well for face-on galaxies with almost purely elliptical isophotes (with few or no additional components), as it does not properly utilize the higher-order harmonics to fit and quantify irregularities in the isophotal shapes. Figure 2.2 provides a comparison of models obtained for NGC 4762 using the ELLIPSE and ISOFIT tasks.

Various isophotal parameters (ϵ, PA, A_n and B_n) obtained from the ISOFIT task, are sufficient to generate an excellent 2D model of a galaxy using the CMODEL task. The galaxy model can be further subtracted from the galaxy image to obtain a residual image, which is useful to study various foreground and background sources overlapping with the galaxy pixels. The quality of the residual image depends on how accurately the isophotal model emulates the galaxy. The quality of the model generated using the ISOFIT and

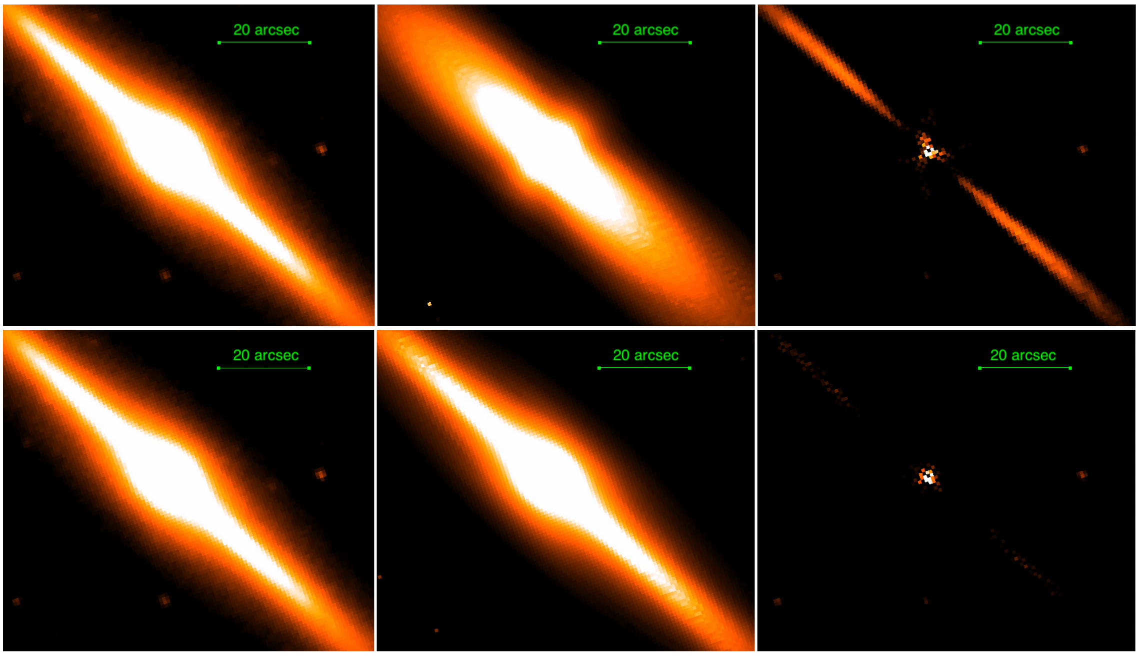

Figure 2.2 Comparison of models and residual images for NGC 4762. First row of images are the galaxy image, model, and the residual image generated using the Ellipse and Bmodel tasks in IRAF. The second-row of images are the galaxy image, model, and the residual image generated using the Isofit and Cmodel tasks (Ciambur, 2015).

CMODEL tasks can be appreciated in Figure 2.2.

It is evident in Figure 2.2 that the ELLIPSE task could not construct a very good fit to the irregular isophotes of NGC 4762 due to the high inclination of the galaxy and its (peanut shell)-shaped bulge associated with the bar (as seen in the light profile, Figure 2.3). The ELLIPSE task fails to properly model the galaxy light along the disk, leaving behind the bright stripes in the residual image.

2.3.2 Disassembling the Galaxy Image

The isophotal table, obtained from ISOFIT, is used by the software PROFILER (Ciambur, 2016) to plot and fit the 1D radial surface brightness profile of a galaxy, with respect to both its semi-major axis radius (R_{maj}) and the equivalent axis (R_{eq}). R_{eq} is the geometric mean of R_{maj} and R_{min}. It is the radius of an imaginary circular isophote equivalent in area to the elliptical isophote with major- and minor-axis radius R_{maj} and R_{min}, conserving the total surface brightness of the elliptical isophote. This gives $R_{eq} = \sqrt{R_{maj}R_{min}} = R_{maj}\sqrt{1-\epsilon}$, where ϵ is the ellipticity of the isophote. Along with the surface brightness profile, PROFILER also plots the radial profiles of the isophote's ellipticity, position angle, and some of the higher-order Fourier harmonic coefficients (B4, B6, B8).

To decompose the galaxy light into its components, we use a wide variety of parametric analytical functions available in PROFILER. For example, Sérsic (1963) and Core-Sérsic (Graham & Others, 2003) functions for galactic bulges; exponential, truncated/anti-truncated exponential, and inclined-disk models for various types and orientations of disks; Ferrers (1877) function for bars; Sérsic for bar-lenses/pseudobulges, Gaussian for rings, and ansae (centered at the ring/anase radius); and PSFs for nuclear point sources. Table 2.2 presents the mathematical formulae for the radial surface brightness profiles of these functions and the corresponding expressions to determine the apparent magnitudes from the fit parameters. More details about the surface brightness profiles of the various fitting functions can be found in Section 3 of Ciambur (2016).

Table 2.2. Fitting Functions

Function	Radial Surface Brightness[a] $\mu(R)$ (mag arcsec^{-2})	Apparent Magnitude[b] m (mag)	Profile Parameters
Sérsic[c]	$\mu_e + (2.5 * b_n / \ln 10)\,[(R/R_e)^{1/n} - 1]$	$\mu_e - 5\log R_e - 2.5\log[2\pi n \left(\exp b_n/(b_n)^{2n}\right)\Gamma(2n)]$	μ_e, n, R_e
Core-Sérsic[d]	$\mu' - 2.5\gamma/\alpha(\log[1 + (R_b/R)^{\alpha}]) + 2.5/ln(10)[b_n\left((R^{\alpha} + R_b^{\alpha})/R_e^{\alpha}\right)^{1/n\alpha}]$	$\mu_b - 2.5\log 2\pi[R_b^2/2.\gamma + ne^{(b_n(R_b/R_e)^{1/n})}(\Gamma(2n) - \gamma(2n,(R_b/R_e)^{1/n}))]$	$\mu', R_b, R_e, n, \alpha, \gamma$
Exponential[e]	$\mu_0 + (2.5/ln(10))(R/h)$	$\mu_0 - 2.5\log[2\pi h^2]$	μ_0, h
Truncated[f] disk	$\mu_0 + (2.5/ln(10))(R/h_1)$ (for $R \leq R_b$) $\mu_b + (2.5/ln(10))((R - R_b)/h_2)$ (for $R > R_b$)	$\mu_0 - 2.5\log 2\pi[h_1^2 + e^{-R_b/h_1}(h_2 - h_1)(h_2 + h_1 + R_b)]$	μ_0, h_1, h_2, R_b
Inclined disk[g]	$\mu_0 - 2.5\log[(R/h_r)K_1(R/h_r)]$	Integrated Numerically	μ_0, h_r
Ferrer[h]	$\mu_0 - 2.5\alpha\log[1 - (R/R_{out})^{2-\beta}]$	$\mu_0 - 2.5\log[\pi R_{out}^2 * hyp2F1(-\alpha, 2/(2-\beta), (4-\beta)/(2-\beta), 1)]$	$\mu_0, R_{out}, \alpha, \beta$
Gaussian[i]	$\mu_r + (2.5/ln(10))((R - R_r)^2/2\sigma^2)$	$\mu_r - 2.5\log 2\pi[\sigma^2 e^{-R_r^2/2\sigma^2} + \sigma R_r\sqrt{\pi/2}(1 + erf(R_r/\sigma\sqrt{2}))]$	μ_r, R_r, σ

[a] The radial surface brightness profile was obtained from the intensity profile, using $\mu(R) = -2.5\log(I(R))+$ zero-point (see Table 2.1).

[b] $m = -2.5\log(L)$, where luminosity (L)$= \int 2\pi R\, I(R) dR$, $I(R)$ is the radial intensity profile.

[c] From Ciotti (1991) and Graham & Driver (2005), the quantity b_n is calculated by solving $\Gamma(2n) = 2\gamma(2n, b_n)$.

[d] Equation 5 from Graham & Others (2003), μ' and μ_b are related through Equation 6 from Graham & Others (2003). The expression for the apparent magnitude is deduced under the approximation, $\alpha \to \infty$ (Equation A20 from Trujillo et al., 2004).

[e] Equation 14 from Graham & Driver (2005), for n=1.

[f] Equation 10 from Ciambur (2016).

[g] Equation 12 from Ciambur (2016) along the major axis, and $K_1(R/h_r)$ is the modified Bessel function of the second kind.

[h] From Ferrers (1877); $hyp2F1$ in the apparent magnitude expression represents the hyper-geometric function.

[i] The parameter μ_r is the peak value of the Gaussian surface brightness profile at the "peak radius" r, and σ is the width of the Gaussian.

We disassemble the galaxy light into its components by fitting various features present in the galaxy light profile, using the functions mentioned in Table 2.2. To help identify the components that are present in a galaxy, we visually inspect the galaxy image at various contrast levels using DS9, and we also inspect various features present in the ellipticity, position angle, $B4$, and $B6$ profiles (if required), which is beneficial in discerning galaxy components. Apart from that, we went through the literature, reviewing previous structural and kinematical studies of our galaxies, which gave us clues about the components present, their relative intensity (or surface brightness) levels, and their radial extents (sizes). In order to distinguish the components, like an inner disk, inner ring, nuclear star cluster, and most importantly, to identify the deficit of light at the center of a galaxy (core-Sérsic), we consulted previous works with highly resolved Hubble Space Telescope images (e.g., Dullo & Graham, 2014).

Having obtained a fit for the light profile—based on real physical structure/components—for the major-axis, we map it to the equivalent-axis (R_{eq}), ensuring the central (R=0) surface brightness of each component remains roughly constant. The equivalent-axis parameters for each component of a galaxy are required so that PROFILER can use the circular symmetry of the equivalent-axis to integrate the surface brightness profiles and calculate the apparent magnitudes for all the components and the whole galaxy itself.

Figure 2.3 shows the multi-component fit to the surface brightness profile of NGC 4762, for both the major- and equivalent-axes. It is a barred-lenticular galaxy with a small bulge, an (oval-shaped) bar-lens, a bar, ansae, and a truncated disk. Laurikainen et al. (2005, 2007, 2011) observed that many S0 galaxies contain bars and "ovals" (also known as "lenses" or "bar-lenses"), with the inner regions of vertically-heated bars appearing as boxy/(peanut shell)-shaped structures referred to by some as pseudobulges (see Combes & Sanders, 1981; Athanassoula, 2002, 2005). The bumps in the light profile of NGC 4762, as well as the ellipticity, B_4, and B_6 profiles at $R_{maj} \approx 30''$ and $R_{maj} \approx 80''$ correspond to the perturbation of the isophotes due to the bar-lens/pseudobulge and the bar, respectively. As shown in the simulations by Saha et al. (2018, their Figure 7), the adjacent bump ($R_{maj} \approx 80''$) and dip ($R_{maj} \approx 120''$) in the B_6 profile suggest the presence of an ansae at $R_{maj} \approx 100''$, at the end of the bar.

We also note that the decomposition results from Saha et al. (2018, e.g., their Figure

Table 2.3. Model parameters for the NGC 4762 light profile

Component	Function	Major-axis parameters	Equivalent-axis parameters
Bulge	Sérsic	$\mu_e = 17.89, n = 2.36, R_e = 4.39$	$\mu_e = 17.09, n = 1.85, R_e = 2.24$
Barlens	Sérsic	$\mu_e = 18.98, n = 0.28, R_e = 28.81$	$\mu_e = 18.89, n = 0.31, R_e = 14.4$
Bar	Ferrers	$\mu_0 = 19.72, R_{out} = 94.56, \alpha = 1.65, \beta = 0.01$	$\mu_0 = 19.72, R_{out} = 40.66, \alpha = 3.81, \beta = 0.01$
Ansae	Gaussian	$\mu_r = 20.74, R_r = 96.45, FWHM = 21.30$	$\mu_r = 20.77, R_r = 37.06, FWHM = 15.89$
Disk	Truncated Exponential	$\mu_0 = 20.48, R_b = 155.07, h1 = 82.62, h2 = 10.23$	$\mu_0 = 20.48, R_b = 79.36, h1 = 40.92, h2 = 4.72$

Note. — Scale size parameters ($R_e, R_{out}, R_r, h1$, and $h2$) are in units of arcseconds, and surface brightnesses (μ_e, μ_0, and μ_r) pertains to the 3.6 μm-band (AB mag). FWHM of the Gaussian can be related to its standard deviation (σ) by, $FWHM = 2\sigma\sqrt{2\ln 2}$. Equivalent-axis is also known as the "geometric mean" axis, given by the square root of the product of major- and minor-axis.

11; see also NGC 4026 and NGC 4371 in our Appendix A) support the truncated disk model[8] in NGC 4762. Also, according to Kormendy & Bender (2012), the warped disk at the outer edge is possibly due to some ongoing tidal encounter. Table 2.3 lists the fit parameters for the components in NGC 4762. Light profile fits for all other galaxies can be found in the Appendix A.

2.3.3 Stellar Mass Calculation

We calculate the absolute magnitudes for all the galaxies, and their spheroids, using their apparent magnitudes measured using Profiler, and the distances in Table 2.4. These absolute magnitudes, after applying the small corrective term for cosmological dimming[9] (Tolman, 1930) are used to calculate the corresponding intrinsic luminosities. The intrinsic luminosity is derived in terms of the solar luminosity in each band (see Table 2.1), and these luminosity values are then converted into stellar masses by multiplying them with the stellar mass-to-light ratio (Υ_*) for each band.

Stellar mass-to-light ratios depend on many factors, such as the Initial Mass Function (IMF) of stars in a galaxy, star formation history, metallicity, age, and they can be biased due to attenuation from dust in a galaxy. The interdependence of these factors and their effect on the stellar mass-to-light ratio is not very well known. Therefore, the mass-to-light ratio dependence on these properties has large uncertainties associated with it.

[8] A truncated disk model has a change in slope beyond the truncation radius

[9] A magnitude of $10\log(1 + z)$ is subtracted to account for the dimming of the observed magnitudes due to the expansion of the Universe, where z is redshift based on the galaxy distance. Red-shift was calculated assuming the latest cosmological parameters $H_0 = 67.4$, $\Omega_m = 0.315$, $\Omega_{vacuum} = 0.685$ (Planck Collaboration et al., 2020).

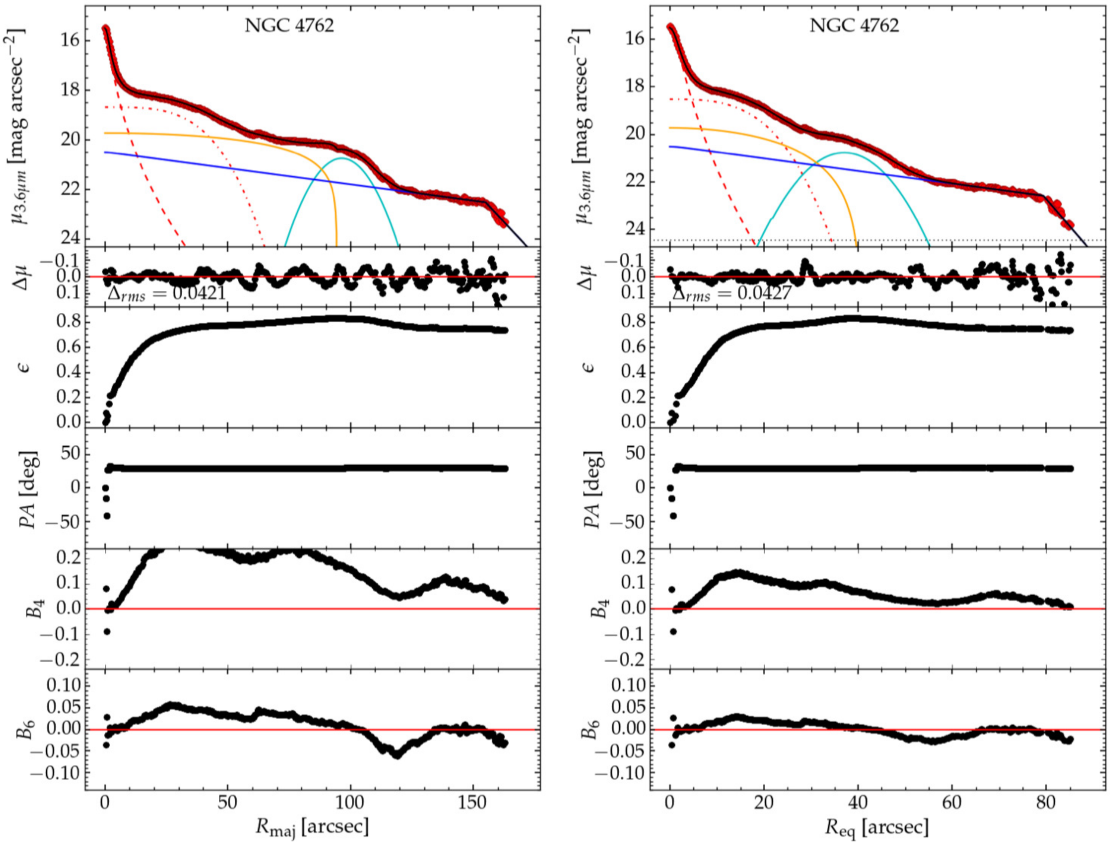

Figure 2.3 3.6 μm surface brightness profile of NGC 4762, plotted and fit using PROFILER. The left panel shows the profile along the major-axis with Δ_{rms} = 0.0421 mag arcsec^{-2}, and the right panel shows the profile along the equivalent-axis with Δ_{rms} = 0.0427 mag arcsec^{-2}. Physical sizes can be derived using a scale of 11 pc/$''$ based on a distance of 22.6 Mpc. NGC 4762 is a barred lenticular galaxy with its multi-component fit comprised of a Sérsic function for the bulge (- - -), a low index Sérsic function for the bar-lens/pseudobulge (-·-·-), a Ferrers function for the bar (—), a Gaussian for the ansae (—), and a truncated exponential model for the extended warped disk (—).

Meidt et al. (2014) suggest a constant, optimal, stellar mass-to-light ratio of $\Upsilon_* = 0.6$ for the 3.6 μm band, based on the Chabrier (2003) IMF, which is consistent with the age-metallicity relation and can be used for both old, metal-rich and young, metal-poor stellar populations. The emission at 3.6 μm and 2.2 μm is largely unaffected by the luminosity bias due to young stars, and also it undergoes minimal dust extinction (Querejeta et al., 2015), enabling us a somewhat stable mass-to-light ratio. Using $\Upsilon_*^{3.6\mu m} = 0.6$ in the following equation from Oh et al. (2008):

$$\Upsilon_*^{3.6\mu m} = 0.92 \times \Upsilon_*^{K_s} - 0.05, \tag{2.3}$$

which relates the stellar mass-to-light ratio at 3.6 μm and that of the K_s-band, we obtained a constant stellar mass-to-light ratio of $\Upsilon_*^{K_s} = 0.7$ for the K_s-band images. The latest relation: $\Upsilon_*^{3.6\mu m} = 1.03 \times \Upsilon_*^{K_s} - 0.16$ (J.Schombert, private communication), which is based on a larger $K_s - 3.6\,\mu$m dataset, also revealed a consistent value for $\Upsilon_*^{K_s}$.

For our three r'-band data, we used an average stellar mass-to-light ratio of $\Upsilon_*^{r'} \equiv M_*/L_{r'} = 2.8$ to obtain the corresponding stellar masses. $\Upsilon_*^{r'}$ was calibrated using

$$\frac{M_*}{L_{r'}} = \left(\frac{L_{K_s}}{L_{r'}}\right)\left(\frac{M_*}{L_{K_s}}\right), \tag{2.4}$$

ensuring that the galaxy stellar masses are consistent with the masses obtained using K_s-band magnitudes (obtained from 2MASS imaging of these galaxies), and a stellar mass-to-light ratio of $\Upsilon_*^{K_s} = 0.7$. We present the spheroid and total galaxy stellar masses for our galaxies in Table 2.4.

2.3.4 Comparison of Stellar Masses

Here we compare the galaxy stellar masses measured using the 3.6 μm-band images (calculated as described above) with the galaxy stellar masses calculated using (already available) K_s, i', and r'-band magnitudes and three different formula for the corresponding stellar mass-to-light ratios. The comparison and the best fit lines are shown in Figure 2.4, where the horizontal-axis designates the (3.6 μm-band)-derived masses, labeled $\log(M_{*,Gal_{3.6\mu m}}/M_\odot)$, and the vertical-axis depicts the masses based on the K_s, i' and r'

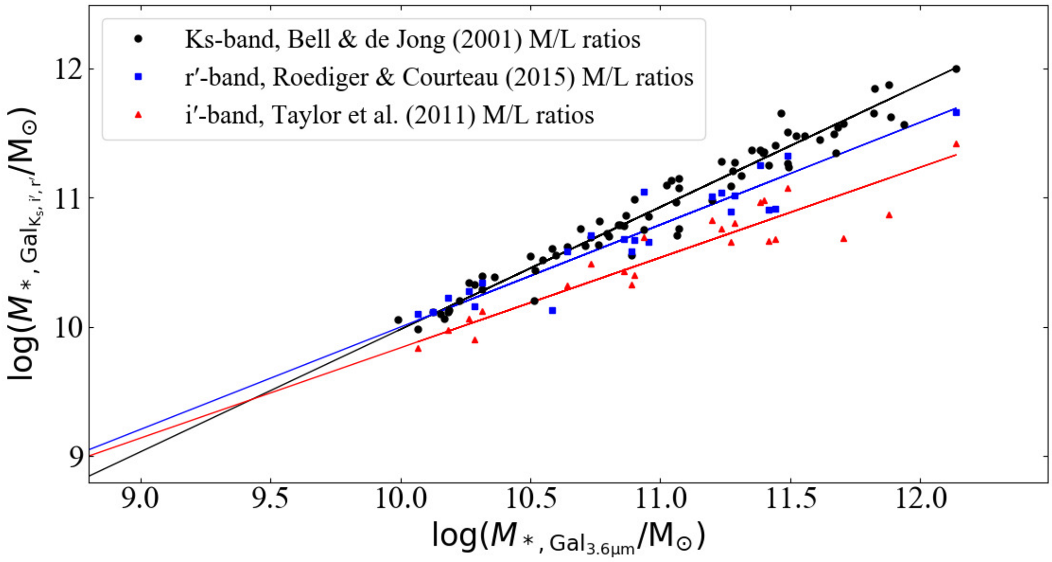

Figure 2.4 Comparison of the galaxy stellar masses for our sample. The masses on the horizontal axis are calculated from 3.6 μm imaging with $\Upsilon_*^{3.6\,\mu m} = 0.6$, while the ($K_s$-, r'-, and i'- band)-derived masses are shown on the vertical axis. The **black** dots represent the total galaxy stellar masses of 71 galaxies based on improved K_s-band magnitudes and ($B - K_s$ color-dependent) K_s-band stellar mass-to-light ratios from Bell & de Jong (2001). Blue squares show the total galaxy stellar masses of 23 galaxies obtained using r'-band magnitudes and $g' - r'$ color-dependent mass-to-light ratios from Roediger & Courteau (2015), and the red triangles mark the total galaxy stellar masses of the same 23 galaxies calculated using i'-band magnitudes and $g' - i'$ color-dependent mass-to-light ratios from Taylor et al. (2011). Black, blue, and red lines are the least-square regression lines defining a relation between these masses.

band magnitudes, labeled $\log(M_{*,Gal_{K_s,i',r'}}/M_\odot)$.

The black dots in Figure 2.4 show the masses of 71 galaxies calculated here using K_s-band magnitudes and ($B - K_s$ color-dependent) K_s-band stellar mass-to-light ratios from Bell & de Jong (2001, their Table 1), placed with respect to our (3.6 μm-band) stellar masses. The K_s and B-band magnitudes were obtained from the 2MASS catalog (Jarrett et al., 2003) and the Third Reference Catalogue (RC3) of Bright Galaxies (de Vaucouleurs et al., 1991), respectively. The K_s-band magnitudes obtained from the 2MASS data reduction pipelines are usually underestimated (Schombert & Smith, 2012), therefore we used Equation 1 from Scott et al. (2013) to correct for this. The size of this correction was < 0.35 mag. The K_s-band stellar mass-to-light ratios were brought to a Chabrier IMF, from the scaled/diet Salpeter IMF used by Bell & de Jong (2001), by subtracting

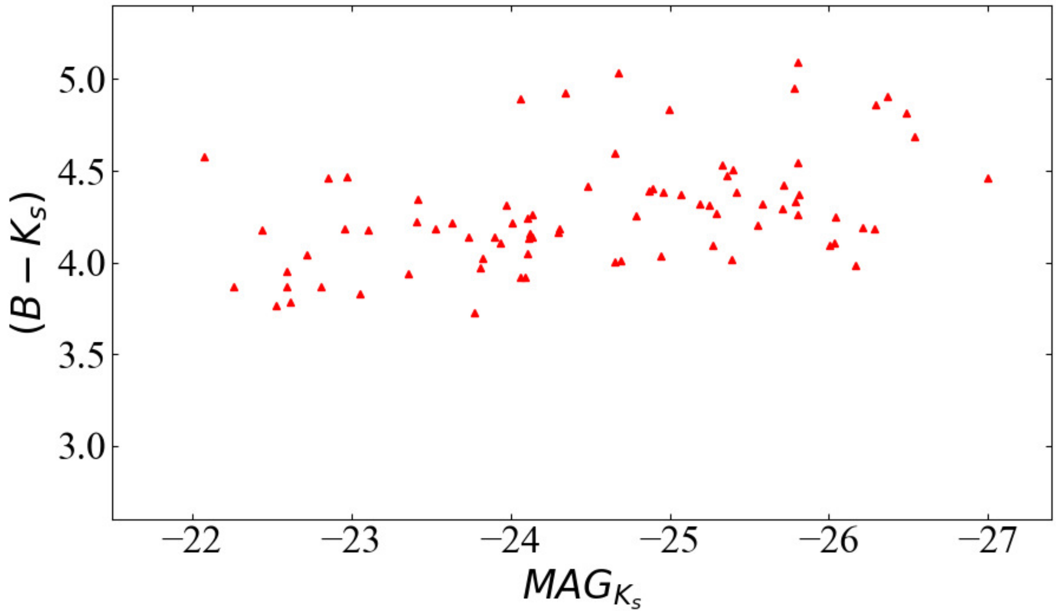

Figure 2.5 $(B - K_s)$-color versus K_s-band absolute magnitude (in Vega system) diagram for 82 ETGs. Most of our sample resides along the relatively flat arm (for $MAG_{K_s} < -22$ mag) of the color-magnitude diagram presented by Graham & Soria (2018).

an IMF dependent constant of 0.093 dex (Taylor et al., 2011; Mitchell et al., 2013). In Figure 2.5, we also present the $(B - K_s)$-color versus the K_s-band magnitude for our sample, which is consistent with the color-magnitude diagram presented by Graham & Soria (2018, their Figure 11), implying that our galaxies belong to the red-sequence, which flattens ($B - K_s \approx 4$) at bright magnitudes ($MAG_{K_s} < -22$ mag).

The red triangles in Figure 2.4 are the masses of 23 galaxies calculated using i'-band magnitudes and ($g' - i'$ color-dependent) i'-band stellar mass-to-light ratios (based on a Chabrier IMF) from Taylor et al. (2011, their Equation 7).

The blue squares represent the masses of 23 galaxies calculated using r'-band magnitudes and ($g' - r'$ color-dependent) r'-band stellar mass-to-light ratios from Roediger & Courteau (2015), which are based on the Stellar Population Synthesis (SPS) model by Conroy et al. (2009). The apparent galaxy magnitudes in the g', r', and i'-bands were obtained from the SDSS data release 6 (Adelman-McCarthy et al., 2008).

The black, blue, and red lines in Figure 2.4 represent the least-squares fits to the three corresponding types of data points. We found that there is almost a linear one-to-one relationship between the (K_s-band)-derived masses (black line) and our (3.6 μm)-derived masses. The galaxy stellar masses based on r'- and i'-band magnitudes (blue line and red line, respectively) are systematically offset. Although the offset is small, it systematically increases at higher galaxy masses. Such an offset has been noticed in a few other studies (e.g. Taylor et al., 2011; Graham et al., 2018). The systematic offset between the above three lines can be attributed mainly to the initial mass functions, star formation rates, and the stellar evolutionary histories assumed to derive the mass-to-light ratios, and possibly some systematic uncertainties introduced in the apparent magnitudes by various telescope pipeline processes.

Figure 2.4 mainly serves to depict that the use of different stellar mass-to-light ratio prescriptions for luminosities (magnitudes) obtained in different bands can produce different stellar masses for a galaxy and its components (see Kannappan & Gawiser, 2007, for a detailed comparison of masses calculated using different methods). In passing, we note that we will explore if this may be a factor contributing to the offset observed by (Shankar et al., 2016) between galaxies with directly measured black hole masses and the population at large.

Differences in estimated stellar mass will lead to different estimates of a galaxy's black hole mass when using the black hole mass scaling relations presented here and elsewhere. Hence, in our forth-coming equations for the M_{BH}–$M_{*,sph}$ and M_{BH}–$M_{*,gal}$ relations, we are including a conversion or correcting coefficient, υ (lower case upsilon), for the stellar masses (see Davis et al., 2019a). This stellar mass correcting coefficient accounts for the difference in stellar mass of a galaxy due to either the difference in the stellar mass-to-light ratio (Υ_*) used for the same passband, or due to a different passband magnitude as well as a different mass-to-light ratio applied to it. If Υ_*^{IRAC1} is a user-preferred Spitzer 3.6 μm-band stellar mass-to-light ratio, the correction coefficient $\upsilon_{*,IRAC1}$ is given by,

$$\upsilon_{*,IRAC1} = \frac{\Upsilon_*^{IRAC1}}{0.6}, \tag{2.5}$$

where 0.6 is the stellar mass-to-light ratio for the IRAC1 (3.6 μm) passband used in this work, adopted from Meidt et al. (2014).

The correcting coefficient (υ), for the masses (M_{*,K_s}, $M_{*,r'}$, $M_{*,i'}$) derived using the

K_s-, i'-, and r'-band magnitudes with the three stellar mass-to-light ratio trends shown in Figure 2.4, can be expressed as follows:

$$\log \upsilon_{*,K_s} = -0.06 \log \left(\frac{M_{*,K_s}}{10^{10} M_\odot} \right) - 0.06, \tag{2.6}$$

$$\log \upsilon_{*,r'} = -0.26 \log \left(\frac{M_{*,r'}}{10^{10} M_\odot} \right) + 0.03, \tag{2.7}$$

$$\log \upsilon_{*,i'} = -0.43 \log \left(\frac{M_{*,i'}}{10^{10} M_\odot} \right) - 0.21. \tag{2.8}$$

These equations are obtained by calculating the offset of the three lines shown in Figure 2.4 from our (3.6 μm)-derived galaxy masses calculated in Section 2.3.3.

2.3.5 Error Analysis

Our spheroid and galaxy stellar masses depend on three main independent quantities, which are: the stellar mass-to-light ratio (Υ_*); distance (D); and the apparent magnitude (m). We have estimated the error in the above three quantities and added them in quadrature.

Our galaxy sample, dominated by near-infrared imaging, enables us to apply a relatively stable stellar mass-to-light ratio adopted from Meidt et al. (2014) and Querejeta et al. (2015). Meidt et al. (2014) recommend the use of a more liberal 15% uncertainty on the 3.6 μm stellar mass-to-light ratio, accounting for an atypical evolutionary history or non-stellar emissions (which are dominant in red colors). As $\Upsilon_*^{r'}$ for our r'-band images are calibrated against 2MASS imaging and $\Upsilon_*^{K_s}$, and $\Upsilon_*^{K_s}$ in turn is derived from $\Upsilon_*^{3.6\mu m}$, as described in Section 2.3.3, we assign a constant uncertainty of 15% to the stellar mass-to-light ratios for all the galaxies.

For most of the 42 galaxies (Table 2.4) that we modeled, we obtained the error in their distances from the publication which presented their directly measured SMBH mass. For the rest of the galaxies (including the galaxies from Savorgnan & Graham (2016b)), we are using a constant error of 7% in their distances, which is a typical percentage error in the ($Virgo+GA+Shapley$)-corrected Hubble flow distances, obtained from NASA/IPAC Extragalactic Database.

Some of the sources of error in the apparent magnitudes are imprecise sky subtraction; error in the telescope's PSF size measurement; and error in the decomposition of the galaxy light. The decomposition error can include an error due to neglecting a component of the galaxy; misinterpreting a component's size or position; error in the calibrated zero-point magnitude; misinterpreting nuclear components or being unable to resolve it; etc. It is nearly impossible to quantify all these errors.

If we assume that we have used an accurate method to measure the sky level and the telescope's PSF, and trust various telescope pipelines (where we downloaded our images) for their zero-point flux calibration, then our main source of error in magnitude will be the error in the galaxy light decomposition process. Although, Profiler provides the formal random error for each fit parameter of the various components of a galaxy, which is the rms error obtained by least square minimization between data and the fitting function, it is very small. To better quantify the uncertainty in the decomposition, we have followed the (light profile fit-quality) grading scheme described by Savorgnan & Graham (2016b, in their section-4.2.1), except that we have assigned a symmetric error of 0.2 mag, 0.6 mag, and 0.8 mag to the spheroidal component of our grade-1, grade-2, and grade-3 galaxies, respectively.

As we are dealing with the stellar masses in log, we calculate these errors in log (dex). An error of δm mag in apparent magnitude, a δD error in distance, and a $\delta\Upsilon_*$ error in the stellar mass-to-light ratio, added in quadrature, give us the error in the stellar mass (in dex), as

$$\delta \log M = \sqrt{\left(\frac{\delta m}{2.5}\right)^2 + \left(2\frac{\delta D}{D\ln(10)}\right)^2 + \left(\frac{\delta\Upsilon_*}{\Upsilon_*\ln(10)}\right)^2}. \tag{2.9}$$

We assign a constant error of 0.12 dex to the galaxy masses, which is equivalent to the total quadrature error (calculated using Equation 2.9) assigned to the spheroid masses of our grade-1 galaxies, which are mostly single component galaxies.

Table 2.4. Galaxy Sample

Galaxy (1)	Type (2)	Core (3)	Distance (Mpc) (4)	$\log(M_{BH}/M_{\odot})$ (5)	MAG_{sph} (mag) (6)	MAG_{gal} (mag) (7)	$\log(M_{*,sph}/M_{\odot})$ (8)	$\log(M_{*,gal}/M_{\odot})$ (9)
A1836 BCG[a]	E1-2	yes	158.00±11.06	9.59±0.06[5a,G]	-24.56±0.20	-24.56±0.20	11.70±0.12	11.70±0.12
A3565 BCG	E1	no	40.70 ±2.90[4a]	9.04±0.09[5a,G]	-23.22±0.6	-23.26±0.20	11.47± 0.26	11.49±0.12
NGC 0307[b]	SAB0	no	52.80±3.70	8.34±0.13[5c,S]	-20.31±0.80	-21.14±0.20	10.43±0.33	10.76±0.12
NGC 0404	S0	no	3.06±0.37	4.85±0.13[5d,S]	-14.43±0.60	-17.33±0.20	7.96±0.27	9.12±0.12
NGC 0524	SA0(rs)	yes	23.30±1.63	8.92±0.10[5e,S]	-20.97±0.60	-22.21±0.20	10.57±0.26	11.07±0.12
NGC 1194	S0	no	53.20±3.70	7.81±0.04[5f,M]	-21.31±0.80	-21.87±0.20	10.71±0.33	10.94±0.12
NGC 1275	E	no	72.9±5.10[4a]	8.90±0.20[5g,G]	-24.14±0.60	-24.23±0.20	11.84±0.26	11.88±0.12
NGC 1374	S0	no?	19.20±1.34	8.76±0.05[5h,S]	-20.09±0.60	-20.83±0.20	10.22±0.26	10.52±0.12
NGC 1407	E	yes	28.05±3.37	9.65±0.08[5h,S]	-23.19±0.60	-23.34±0.02	11.46±0.27	11.52±0.12
NGC 1550[a]	E1	yes	51.57±3.61	9.57±0.06[5h,S]	-23.14±0.20	-23.14±0.20	11.13±0.12	11.13±0.12
NGC 1600	E3	yes	64.00±4.48	10.23±0.05[5i,S]	-24.09±0.20	-24.09±0.20	11.82±0.12	11.82±0.12
NGC 2787	SB0(r)	no	7.30±0.51	7.60±0.06[5j,G]	-17.35±0.60	-19.51±0.20	9.13± 0.26	9.99±0.12
NGC 3665	S0	no	34.70±2.43	8.76±0.10[5k,G]	-22.12±0.60	-22.74±0.20	11.03±0.26	11.28±0.12
NGC 3923	E4	yes	20.88±2.70	9.45±0.13[5l,S]	-23.02±0.20	-23.02±0.20	11.40±0.15	11.40±0.12
NGC 4026	SB0	no	13.20±0.92	8.26±0.11[5m,S]	-19.82±0.80	-20.44±0.20	10.11±0.33	10.36±0.12
NGC 4339	S0	no	16.00±1.33	7.63±0.33[5n,S]	-18.72±0.60	-19.96±0.20	9.67±0.26	10.17±0.12
NGC 4342	ES/S0	no	23.00±1.00	8.65±0.18[5o,S]	-19.38±0.60	-20.20±0.20	9.94±0.25	10.26±0.12
NGC 4350	EBS	no	16.80±1.18	8.86±0.41[5p,SG]	-20.22±0.60	-20.90±0.20	10.28±0.26	10.55±0.12
NGC 4371	SB(r)0	no	16.90±1.48	6.84±0.08[5l,S]	-19.27±0.60	-21.03±0.20	9.89±0.26	10.60±0.12
NGC 4429	SB(r)0	no	16.50±1.60	8.18±0.09[5q,G]	-20.69±0.60	-21.79±0.20	10.46± 0.26	10.90±0.12
NGC 4434	S0	no	22.40±1.57	7.84±0.17[5n,S]	-19.32±0.60	-20.00±0.20	9.91±0.26	10.18±0.12
NGC 4486B[b]	E1	no	15.30±0.32	8.76±0.24[5r,S]	-17.90±0.80	-17.90±0.20	9.46± 0.33	9.46±0.12
NGC 4526	S0	no	16.90±1.69	8.67±0.04[5s,G]	-21.27±0.60	-22.14±0.20	10.70± 0.26	11.04±0.12
NGC 4552	E	no	14.90±0.95	8.67±0.05[5t,S]	-21.75±0.60	-21.92±0.20	10.88± 0.25	10.95±0.12
NGC 4578	S0(r)	no	16.30±1.14	7.28±0.35[5n,S]	-18.97±0.60	-20.10±0.20	9.77± 0.26	10.23±0.12
NGC 4649	E2	yes	16.40±1.10	9.67±0.10[5u,S]	-23.14±0.20	-23.14±0.20	11.44± 0.12	11.44±0.12
NGC 4742	S0	no	15.50±1.15	7.15±0.18[5v,S]	-19.21±0.60	-19.92±0.20	9.87± 0.26	10.15±0.12
NGC 4751[a]	S0	yes?	26.92±1.88	9.15±0.05[5h,S]	-21.53±0.60	-22.11±0.20	10.49± 0.26	10.72±0.12
NGC 4762	SB0	no	22.60±3.39	7.36±0.15[5n,S]	-19.45±0.60	-22.19±0.20	9.97± 0.28	11.06±0.12
NGC 5018	S0	no	40.55±4.87	8.02±0.09[5l,S]	-21.97±0.60	-22.91±0.20	10.98± 0.27	11.35±0.12
NGC 5252	S0	no	96.80±6.78	9.00±0.40[5w,G]	-21.67±0.60	-23.00±0.20	10.85± 0.26	11.38±0.12
NGC 5328[a]	E1	yes	64.10±4.49	9.67±0.15[5h,S]	-24.03±0.20	-24.03±0.20	11.49± 0.12	11.49±0.12
NGC 5419	E2-3	yes	56.20±3.93	9.86±0.14[5x,S]	-23.15±0.20	-23.15±0.20	11.44± 0.12	11.44±0.12
NGC 5516[a]	E1-2	yes?	58.44±4.09	9.52±0.06[5h,S]	-23.91±0.20	-23.91±0.20	11.44± 0.12	11.44±0.12
NGC 5813	S0	yes	31.30±2.60	8.83±0.06[5y,S]	-21.68±0.60	-22.62±0.20	10.86± 0.26	11.23±0.12
NGC 5845	ES	no	25.20±1.76	8.41±0.22[5z,S]	-19.83±0.60	-20.32±0.20	10.12± 0.26	10.32±0.12
NGC 6086[b]	E	yes	138.00±9.66	9.57±0.16[5aa,S]	-23.03±0.60	-23.03±0.20	11.52± 0.26	11.52±0.12
NGC 6861	ES	no	27.30±4.49	9.30±0.08[5h,S]	-21.88±0.60	-22.10±0.20	10.94±0.29	11.02±0.12
NGC 7052	E4	yes	66.40±4.65[4a]	8.57±0.23[5ab,G]	-23.19±0.20	-23.19±0.20	11.46±0.12	11.46±0.12
NGC 7332	SB0(pec)	no	24.89±2.49	7.11±0.20[5ac,S]	-20.08±0.80	-21.63±0.20	10.22±0.34	10.84±0.12
NGC 7457	S0	no	14.00±0.98	7.00±0.30[5ad,S]	-18.04±0.60	-20.00±0.20	9.40±0.26	10.19±0.12

Note. — Columns: (1) Galaxy name. (2) Morphology, based on our decompositions. (3) Presence of partially depleted core. (4) Distance, primarily from the corresponding paper presenting the measured SMBH mass (M_{BH}). For some galaxies which did not have any error associated with these, we assigned an error of 7% (see Section 2.3.5). (5) Directly measured super-massive black hole mass, reference, and method used (S: Stellar dynamics, G: Gas dynamics, M: H_2O Megamaser). The error in M_{BH}, obtained from the corresponding papers, was added in quadrature with the distance error. (6) Spheroid absolute magnitude at 3.6 μm, unless otherwise noted in Column 1 (AB mag system). (7) Total galaxy absolute magnitude at 3.6 μm, unless otherwise noted in Column 1 (AB mag system). (8) Spheroidal mass measured in this work, see Section 2.3.3. (9) Galaxy mass measured in this work.
References: 4a=NED (Virgo + GA + Shapley)-corrected Hubble flow distances; 5a=Dalla Bontà et al. (2009); 5b=Walsh et al. (2017); 5c=Erwin et al. (2018); 5d=Nguyen et al. (2017); 5e=Krajnović et al. (2009); 5f =Kuo et al. (2011); 5g=Scharwächter et al. (2013); 5h=Rusli et al. (2013b); 5i=Thomas et al. (2016); 5j=Sarzi et al. (2001); 5k=Onishi et al. (2017); 5l=Saglia et al. (2016); 5m=Gültekin et al. (2009a); 5n=Krajnović et al. (2018); 5o=Cretton & van den Bosch (1999); 5p=Pignatelli et al. (2001); 5q=Davis et al. (2018b); 5r=Kormendy et al. (1996); 5s=Gould (2013); 5t=Hu (2008); 5u=Shen & Gebhardt (2010); 5v=Tremaine et al. (2002); 5w=Capetti et al. (2005); 5x=Mazzalay et al. (2016); 5y=Hu (2008); 5z=Gebhardt et al. (2003); 5aa=McConnell et al. (2011); 5ab=van der Marel & van den Bosch (1998); 5ac=Batcheldor et al. (2013); 5ad=Schulze & Gebhardt (2011).

[a] 2MASS K_s-band galaxy images

[b] SDSS r'-band galaxy images

2.4 Results and discussion

We performed a Bivariate Correlated Errors and Intrinsic Scatter (BCES) regression (Akritas & Bershady, 1996) between the SMBH masses and both the spheroid masses and the total galaxy masses of our sample. BCES is simply an extension of Ordinary Least Squares (OLS) estimator permitting dependent measurement errors in both the variables. We use the bisector line obtained by the BCES[10] regression; this line symmetrically bisects the regression lines obtained using BCES(X|Y)[11] and BCES(Y|X)[12]. The bisector regression line offers equal treatment to the measurement errors in both the coordinates, and allows for intrinsic scatter. In addition to the BCES routine, we also used the modified FITEXY routine (Press et al., 1992; Tremaine et al., 2002) to perform a regression on our data for the M_{BH}–$M_{*,sph}$ and M_{BH}–$M_{*,sph}$ relations. We found results highly consistent with that of the BCES regression, within the 1σ bounds.

In our analysis, we have excluded eight galaxies (MRK 1216, NGC 404, NGC 1277, NGC 1316, NGC 2787, NGC 4342, NGC 4486B, and NGC 5128), which leaves us with a reduced dataset of 76 ETGs. In all our plots hereafter, these galaxies are shown by a black star (except for MRK 1216). We excluded MRK 1216 from our regression analysis because we did not obtain a suitably resolved and deep image to determine the spheroidal component of this galaxy.

NGC 1316 (Fornax-A) and NGC 5128 (Cen A) are galaxy mergers in progress. According to Kormendy & Ho (2013), these two galaxies have much higher bulge masses compared to their central supermassive black hole masses, which can make them stand out in the black hole mass scaling relations.

NGC 404 has the lowest SMBH mass in our sample. Nguyen et al. (2017) provide a measured black hole mass of $7^{+1.5}_{-2.0} \times 10^4 M_\odot$, using Jeans Anisotropic Modeling (JAM) of stellar orbits, along with a 3σ upper limit of $1.5 \times 10^5 M_\odot$ in M_{BH}. Although, NGC 404 does not appear to be an outlier in our dataset, as it follows the regression lines at the low-mass end, we still exclude it as it would anchor the low-mass end of the relationship

[10] To perform the BCES regression, we used the PYTHON script (available at `https://github.com/rsnemmen/BCES`) written by Nemmen et al. (2012), we modified it to calculate the intrinsic scatter (Equation 1 from Graham & Driver, 2007a).

[11] Minimizes scatter in the X-direction.

[12] Minimizes scatter in the Y-direction.

and we do not want our regression lines to be biased by any individual galaxy.

We also exclude NGC 4342 and NGC 4486B because they have been tidally stripped due to the gravitational pull of their nearby massive companion galaxies, NGC 4365 (Blom et al., 2014) and NGC 4486 (Batcheldor et al., 2010), respectively. NGC 4342 and NGC 4486B are left with a significantly reduced galaxy mass and can be seen clearly offset in our M_{BH}–$M_{*,sph}$ and M_{BH}–$M_{*,gal}$ diagrams (towards the low-mass side of the $M_{*,sph}$ and $M_{*,gal}$ coordinate axes). NGC 221 (M32) is another, similar, well known offset galaxy due to the tidal stripping from the massive companion galaxy M31 (e.g., Graham, 2002). Such compact elliptical galaxies are relatively rare among the general population and are recommended to be excluded from M_{BH}–$M_{*,gal}$ scaling relations (see Graham & Soria, 2018).

NGC 1277 (peculiar morphology) and NGC 2787 are two disk galaxies which are potential outliers at the high- and low-mass end of our relations, respectively. They have a torquing effect on our regression lines, especially for the sub-category of galaxies with a disk (ES/S0). We have therefore excluded these galaxies from our regressions to avoid biasing the slope of our scaling relations. Furthermore, the stellar mass for NGC 1277 is measured from V-band imaging (Graham et al., 2016b) and a stellar mass-to-light ratio based on an unusual bottom heavy IMF (Martín-Navarro et al., 2015). According to Courteau et al. (2014, their Figure 8), stellar mass-to-light ratios based on a bottom heavy IMF can be a factor $\sim$6 higher than stellar mass-to-light ratios based on the Chabrier IMF that we have adopted, which is likely to be the principal reason for NGC 1277 outstanding at the high-mass end of our relations.

The above galaxies remain excluded in all the regressions presented in this paper. In Figures 2.6-2.11, we identify an additional five galaxies with a peculiar morphology, to investigate if they might be outliers, but they are included in the regressions.

In our search for the underlying relation between super-massive black hole mass and host galaxy property, we explored various possibilities for the scaling relations by dividing the galaxy sample into different categories. Specifically: Sérsic and core-Sérsic galaxies; galaxies with and without a disk; and galaxies with and without a bar. We will analyze and discuss the scaling relations for these categories in the following sections.

2.4.1 Sérsic and Core-Sérsic Galaxies

Core-Sérsic galaxies are massive ETGs with a central supermassive black hole that likely formed from the merging of the central black holes of two or more galaxies (Begelman et al., 1980; Graham, 2004; Merritt, 2006). They occupy the high-mass end of the black hole mass scaling relations. The discovery of the bent M_{BH}–L_{sph} ($M_{*,sph}$) relation for Sérsic and core-Sérsic galaxies was based on a mixed sample of elliptical, lenticular, and spiral galaxies (Graham, 2012; Graham & Scott, 2013; Scott et al., 2013). In our work, we investigated the nature of the above relation based on a larger sample of only early-type galaxies.

We categorized Sérsic and core-Sérsic galaxies based on their central light profiles, as determined from previous studies of high-resolution images (Ferrarese et al., 2006a; Richings et al., 2011; Dullo & Graham, 2014). Figure 2.6 presents two regressions performed on the two categories (Sérsic and core-Sérsic) for the SMBH mass versus both the spheroid stellar mass (left panel) and the total galaxy stellar mass (right panel) relations.

The BCES bisector regression of our 45 Sérsic and 31 core-Sérsic galaxies revealed $M_{BH} \propto M_{*,sph}^{1.30\pm0.14}$ and $M_{BH} \propto M_{*,sph}^{1.38\pm0.21}$, respectively. For the black hole mass versus total galaxy mass diagram we obtained $M_{BH} \propto M_{*,gal}^{1.61\pm0.18}$ and $M_{BH} \propto M_{*,gal}^{1.47\pm0.18}$ for Sérsic and core-Sérsic galaxies, respectively. For both the M_{BH}–M_{sph} and M_{BH}–M_{gal} relations, the slopes and intercepts of the regression lines for the Sérsic (blue line) and core-Sérsic (red line) ETGs are consistent within the 1σ confidence interval. Slopes and intercepts for the BCES bisector, as well as BCES($Y|X$) and BCES($X|Y$), regression lines for the Sérsic and core-Sérsic galaxies, for both the M_{BH}–M_{sph} and M_{BH}–M_{gal} relations, can be found in Table 2.5.

Our findings are unlike the relations $M_{BH} \propto M_{*,sph}^{(2.22\pm0.58)}$ and $M_{BH} \propto M_{*,sph}^{(0.94\pm0.14)}$ obtained by Scott et al. (2013) for their Sérsic and core-Sérsic galaxies, respectively. It appears that they may have found the break in the M_{BH}–$M_{*,sph}$ relation due to the inclusion of spiral galaxies, which steepened the M_{BH}–M_{sph} relation for for their Sérsic galaxies (see Section 2.4.4).

The consistency of the regression lines for the Sérsic and core-Sérsic ETGs suggest that all the early-type galaxies (whether Sérsic or core-Sérsic) may follow single log-linear

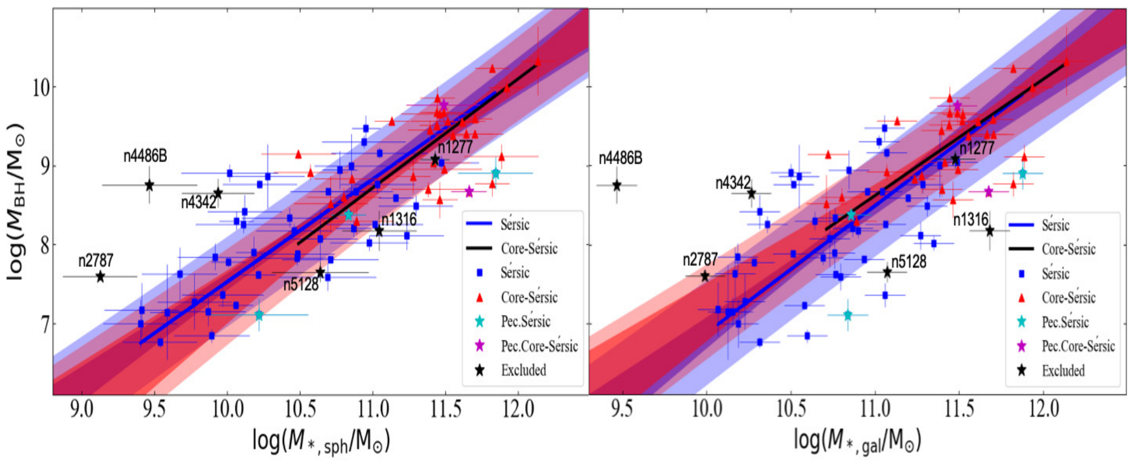

Figure 2.6 Black hole mass versus spheroid stellar mass (left) and total galaxy stellar mass (right). Over-plotted are Sérsic galaxies (blue squares) and core-Sérsic galaxies (red triangles). The blue and **black** lines represent the corresponding bisector regression lines of Sérsic and core-Sérsic galaxies, and the dark blue and dark red bands display the $\pm 1\sigma$ uncertainty on the slope and intercept of the lines. The light blue and light red regions show the $\pm 1\sigma$ rms scatter of the data about the blue and **black** regression lines for Sérsic and core-Sérsic galaxies, respectively. Peculiar Sérsic (three cyan stars) and peculiar core-Sérsic (two magenta stars) galaxies are depicted with a different symbol but they were included in the regressions. The six **black** stars are galaxies excluded from the regression: NGC 1316 and NGC 5128 are mergers; NGC 4486B and NGC 4342 are stripped galaxies; and NGC 1277 and NGC 2787 are potential outliers at the extremities of the spheroid mass range which may bias the regression line. Their relative position remains the same from Figures 2.6 to 2.10. We do not show the remaining two excluded galaxies: NGC 404 lies at low mass end of the diagrams (see Figure 2.11) and for MRK 1216, we could not properly measure its spheroid and total galaxy stellar masses due to the lack of a good image. It is evident that both populations overlie with each other, leading us to the conclusion that there is no "bend" in the M_{BH}–$M_{*,sph}$ nor M_{BH}–$M_{*,gal}$ relations for ETGs with $M_{BH} \gtrsim 10^7\, M_\odot$ due to Sérsic or core-Sérsic galaxies (see also Savorgnan et al., 2016).

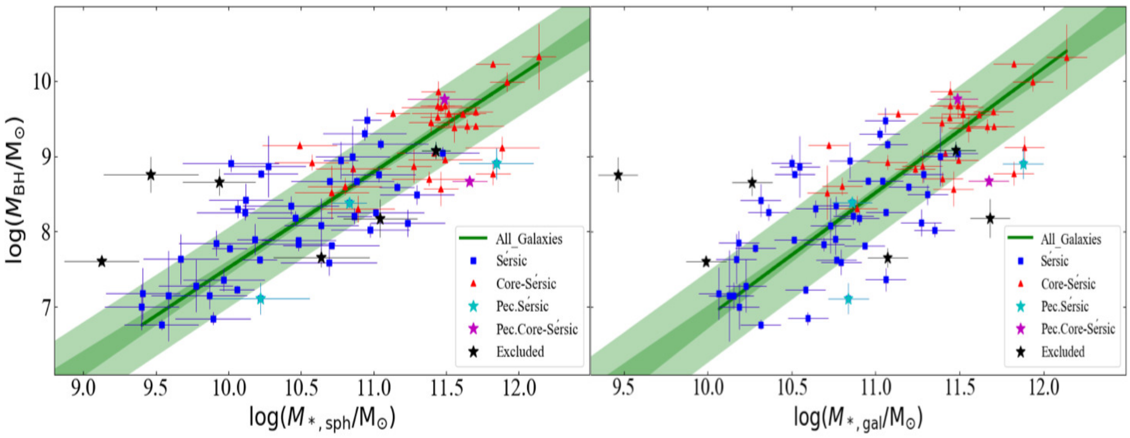

Figure 2.7 Similar to Figure 2.6. The green lines represent the single bisector regression lines for the sample of (84-8=) 76 ETGs with $M_{BH} \gtrsim 10^7\,M_\odot$. Both diagrams depict Sérsic and core-Sérsic ETGs following a unique relation in both the M_{BH}–$M_{*,sph}$ and M_{BH}–$M_{*,gal}$ diagrams. Such that, $M_{BH} \propto M_{*,sph}^{1.27\pm0.07}$ and $M_{BH} \propto M_{*,gal}^{1.65\pm0.11}$ with an rms scatter of 0.52 dex and 0.58 dex (in the log M_{BH} direction), respectively.

relations in the M_{BH}–$M_{*,sph}$ and M_{BH}–$M_{*,gal}$ diagrams. Fitting single BCES bisector regression lines, for the M_{BH}–$M_{*,sph}$ and M_{BH}–$M_{*,gal}$ relations over our total (reduced) sample of 76 ETGs (Figure 2.7), revealed two tight relations, which can be expressed as,

$$\log(M_{BH}/M_\odot) = (1.27 \pm 0.07) \log\left(\frac{M_{*,sph}}{\upsilon(5 \times 10^{10}\,M_\odot)}\right) + (8.41 \pm 0.06), \qquad (2.10)$$

and

$$\log(M_{BH}/M_\odot) = (1.65 \pm 0.11) \log\left(\frac{M_{*,gal}}{\upsilon(5 \times 10^{10}\,M_\odot)}\right) + (8.02 \pm 0.08), \qquad (2.11)$$

with total rms scatters, in $\log(M_{BH})$, of 0.52 dex and 0.58 dex, respectively.

The dark green line in both panels of Figure 2.7 represents the BCES bisector regression line for our sample of 76 ETGs, which is surrounded by a dark green shade showing the $\pm1\sigma$ uncertainty in the slope and the intercept of the line. The light green shade represents the $\pm1\sigma$ rms scatter of the data about the regression line.

The similarity in the scatter about both relations (Equations 2.10 and 2.11) suggests that the black hole mass correlates nearly as well with galaxy stellar mass (or luminosity) as it does with spheroid stellar mass (or luminosity) for ETGs. This partly supports the claim of Läsker et al. (2014), albeit qualified by the restriction to ETGs, as was noted by Savorgnan et al. (2016). Hence, with knowledge of the galaxy stellar mass, it would appear (at this stage of the analysis) that one can use the M_{BH}–$M_{*,gal}$ relation to estimate the black hole mass of an ETG nearly as accurately as if estimated using the M_{BH}–$M_{*,sph}$ relation. Additionally, it should be remembered that a poor bulge/disk decomposition may introduce an error of noticeably more than 0.1 dex to the bulge stellar mass, and thus the M_{BH}–$M_{*,gal}$ relation may in many instances be preferable.

For our total galaxy stellar masses, we used a constant uncertainty of 0.12 dex (see Section 2.3.3) in all the regressions. However, we also derived the M_{BH}–$M_{*,gal}$ relation using a range of different uncertainties (0.10 dex, 0.12 dex, 0.15 dex, 0.20 dex) on log $M_{*,gal}$, and found that the slope and intercept of equation 2.11 remained within the $\pm 1\sigma$ bound.

Our scaling relations are based on the use of a different constant stellar mass-to-light ratio for each passband (see Table 2.1 and Section 2.3.3). However, we checked the robustness of our M_{BH}–$M_{*,sph}$ and M_{BH}–$M_{*,gal}$ relations, using the color-dependent stellar mass-to-light ratios to calculate galaxy and spheroid stellar masses for our galaxies. As explained in Section 2.3.4, we calculated $B-K_s$ color-dependent K_s-band stellar mass-to-light ratios ($\Upsilon_*^{K_s}$) for all our galaxies, using the equation $\log\left(\Upsilon_*^{K_s}\right) = 0.2119 \times (B - K_s) - 0.9586$ from Bell & de Jong (2001). Further, we used this $\Upsilon_*^{K_s}$ in the formulae from Oh et al. (2008), (Equation 2.3) to obtain color-dependent $\Upsilon_*^{3.6\mu m}$. For the remaining two[13] SDSS r'-band images we used $\Upsilon_*^{r'} = 2.8$, calibrated against 2MASS imaging as described in Section 2.3.3. The use of color-dependent stellar mass-to-light ratios for the spheroid and galaxy stellar masses of our sample resulted in $M_{BH} \propto M_{*,sph}^{1.20\pm0.07}$ and $M_{BH} \propto M_{*,gal}^{1.52\pm0.10}$. These relations are consistent within the $\pm 1\sigma$ bound of our previous relations (Equations 2.10 and 2.11), obtained using the masses based on the constant stellar mass-to-light ratios described in Section 2.3.3.

2.4.2 Galaxies With a Disk (ES/S0) and Without a Disk (E)

We divided our ETG sample into those with an intermediate or extended disk (ES- and S0-type) and those without a disk (E-type), and performed separate BCES bisector re-

[13]NGC 4486B, which is excluded from our regressions, is one of the three galaxies for which we used SDSS r'-band images.

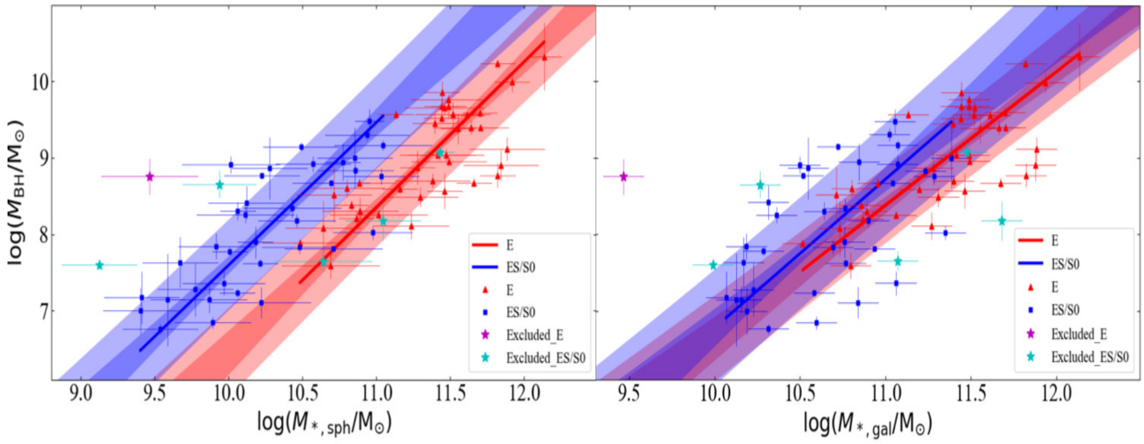

Figure 2.8 Similar to Figure 2.6, but now showing ETGs with (ES/S0) and without (E) a disk. In the M_{BH}–$M_{*,sph}$ diagram, the blue regression line for galaxies with a disk (blue squares) is offset from the red regression line for galaxies without a disk (red triangles) by more than an order of magnitude. This offset reveals two different scaling relations (Equation 2.12 and 2.13) for the two sub-morphological types (ES/S0 and E) with rms scatters in the log(M_{BH}) direction of 0.57 dex and 0.50 dex, respectively. In the M_{BH}–$M_{*,gal}$ diagram, both the regression lines (Equation 2.14 and 2.15) are consistent with each other, suggesting a single relation (Equation 2.11) for galaxies with and without a disk.

gressions on each category. Figure 2.8 reveals separate relations for galaxies with a disk and galaxies without a disk in the M_{BH}–$M_{*,sph}$ diagram. The two relations are:

$$\log(M_{BH}/M_\odot) = (1.86 \pm 0.20) \log\left(\frac{M_{*,sph}}{\upsilon(5 \times 10^{10} M_\odot)}\right) + (8.90 \pm 0.13), \qquad (2.12)$$

for 36 galaxies with a disk, and

$$\log(M_{BH}/M_\odot) = (1.90 \pm 0.20) \log\left(\frac{M_{*,sph}}{\upsilon(5 \times 10^{10} M_\odot)}\right) + (7.78 \pm 0.15), \qquad (2.13)$$

for 40 galaxies without a disk, with an rms scatter of 0.57 dex and 0.50 dex, respectively. While the slopes are consistent, the intercepts, are different by 1.12 dex (more than an order of magnitude). Therefore, to estimate the black hole mass using the spheroid stellar mass of an ETG, it is beneficial to know if the galaxy has a disk (ES/S0) or not (E).

In the M_{BH}–$M_{*,gal}$ diagram (Figure 2.8, right panel), the slopes of the regression lines for galaxies with (Equation 2.14) and without (Equation 2.15) a disk are again consistent.

However, the intercepts of each relation now only differ by a factor of 2, rather than 13 (i.e, 1.12 dex), in black hole mass. While the 1σ uncertainty on these two intercepts does not quite overlap, we derive a single M_{BH}–$M_{*,gal}$ relation for ES/S0 and E-type galaxies. Given that one may not know if their ETG of interest contains a disk, to estimate black hole mass using the total galaxy stellar mass, one may prefer the relation obtained by performing the single regression (Equation 2.11) on the whole ETGs sample. The bisector regression line for the 36 ETGs with a disk is

$$\log(M_{BH}/M_{\odot}) = (1.94 \pm 0.21) \log\left(\frac{M_{*,gal}}{\upsilon(5 \times 10^{10} M_{\odot})}\right) + (8.14 \pm 0.12), \qquad (2.14)$$

with an rms scatter of 0.71 dex, and for the 40 galaxies without a disk we obtained

$$\log(M_{BH}/M_{\odot}) = (1.74 \pm 0.16) \log\left(\frac{M_{*,gal}}{\upsilon(5 \times 10^{10} M_{\odot})}\right) + (7.85 \pm 0.12), \qquad (2.15)$$

with an rms scatter of 0.48 dex.

The above results agree with the fact that most *elliptical* galaxies primarily consist of an extended spheroid; hence their total galaxy mass is nearly equal to their spheroid mass. Thus, in both the M_{BH}–$M_{*,sph}$ and M_{BH}–$M_{*,gal}$ diagrams, elliptical galaxies reside at the same place, usually at the high-mass end. The ellicular (ES) and lenticular (S0) galaxies have their total galaxy stellar mass distributed in their spheroid, disk, and sometimes other components. Therefore, their spheroid stellar mass can be significantly less than the galaxy stellar mass, and in the M_{BH}–$M_{*,sph}$ diagram they reside at the low-mass (left) side creating an offset from the galaxies without a disk. We also performed BCES$(Y|X)$ and BCES$(X|Y)$ regressions for the above cases and the best fit parameters can be found in Table 2.5.

2.4.3 Barred and Non-barred Galaxies

The $M_{BH} - \sigma$ relation is often reported to be the most fundamental relationship between the super-massive black hole mass and any galaxy property, where σ is the velocity dispersion of the host galaxy's spheroid (Ferrarese & Merritt, 2000; Gebhardt et al., 2000). However, previous studies have found that barred galaxies are offset towards higher σ

values in the $M_{BH} - \sigma$ diagram (Graham, 2007a, 2008b; Graham & Others, 2011). This offset can be accounted for in one of two ways: either the velocity dispersion of barred galaxies is systematically higher than non-barred galaxies (Hartmann et al., 2014), or their central super-massive black hole mass is under-estimated.

In an attempt to solve this problem, we performed separate regressions for the barred and non-barred galaxies in the M_{BH}–$M_{*,sph}$ and M_{BH}–$M_{*,gal}$ diagrams (see Figure 2.9). Our reduced sample of 76 ETGs consists of 15 barred galaxies (red squares) and 61 non-barred galaxies (blue triangles). The slope of the M_{BH}–$M_{*,gal}$ relation for barred and non-barred ETGs are consistent with each other. However, with only 15 barred ETGs in our sample, the uncertainty on the slope of the M_{BH}–$M_{*,sph}$ relation for the barred galaxies is large (see Table 2.5) and makes it problematic to determine at what mass to compare the intercepts. From a visual inspection of Figure 2.9, we feel that it would be premature to draw any firm conclusion until more barred ETGs are in the sample.

The parameters of the BCES bisector, along with BCES($Y|X$) and BCES($Y|X$), regression lines for our dataset of 15 barred and 61 non-barred ETGs can be found in Table 2.5.

In Figure 2.10, we have again shown the single ETG regression line for both the M_{BH}–$M_{*,sph}$ and the M_{BH}–$M_{*,gal}$ relations (as in Figure 2.7), but here we identify the barred (blue squares) and non-barred (red triangles) galaxies with different symbols. The barred galaxies are not offset in the M_{BH}–$M_{*,gal}$ diagram, and there is no clear evidence for an offset to lower black hole masses in the M_{BH}–$M_{*,sph}$ diagram, implying that the barred galaxies likely have a higher velocity dispersion relative to the non-barred galaxies thereby creating the offset in the $M_{BH} - \sigma$ diagram.

2.4.4 Early-type Galaxies and Late-type Galaxies

We have combined our ETG data with the recent work on the largest sample of late-type galaxies (LTGs, i.e. spirals) by Davis et al. (2019a). We found that the regression lines followed by these two populations, ETGs and LTGs[14], in the M_{BH}–$M_{*,sph}$ and M_{BH}–$M_{*,gal}$ diagrams are not consistent with each other (see Figure-2.11).

In the black hole mass versus spheroid mass diagram, the regression line for the reduced

[14] We have taken the BCES bisector regression line from Davis et al. (2018a)

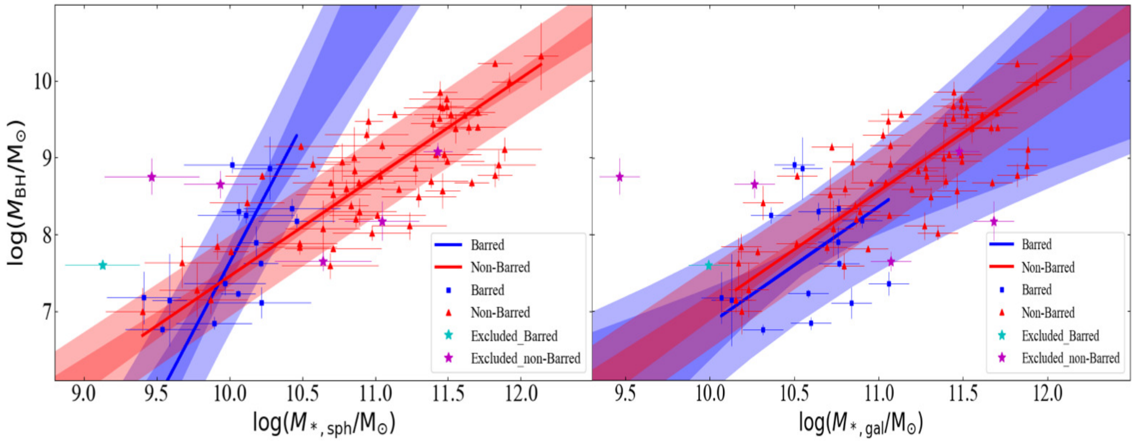

Figure 2.9 Similar to Figure 2.6, but now showing galaxies with a bar (15 blue squares) and without a bar (61 red triangles). Upon performing separate regressions for barred (blue line) and non-barred (red line) galaxies, we found that the slopes of the two lines in the M_{BH}–$M_{*,gal}$ diagram are consistent (see Table 2.5), suggesting a single slope for barred and non-barred ETGs (see Figure 2.10). However, we require a larger dataset of barred galaxies to draw a firm conclusion on whether or not barred galaxies create an offset in the M_{BH}–$M_{*,sph}$ relation.

sample of 40 LTGs from Davis et al. (2019a, accepted) can be expressed as,

$$\log(M_{BH}/M_\odot) = (2.16 \pm 0.32) \log\left(\frac{M_{*,sph}}{\upsilon(5 \times 10^{10} M_\odot)}\right) + (8.58 \pm 0.22), \tag{2.16}$$

which has a slope approximately twice as steep as that of the ETGs: $M_{BH} \propto M_{*,sph}^{1.27 \pm 0.07}$ (Equation 2.10). Similarly, in the black hole mass versus galaxy stellar mass diagram, LTGs define the relation

$$\log(M_{BH}/M_\odot) = (3.05 \pm 0.70) \log\left(\frac{M_{*,gal}}{\upsilon(5 \times 10^{10} M_\odot)}\right) + (6.93 \pm 0.14), \tag{2.17}$$

while the ETGs follow the proportionality $M_{BH} \propto M_{*,gal}^{1.65 \pm 0.11}$ (Equation 2.11).

This shallow and steep relation is roughly consistent with the bend observed by Savorgnan et al. (2016), where they found a near-linear relation, $M_{BH} \propto M_{*,sph}^{1.04 \pm 0.10}$, for their reduced[15] sample of 45 ETGs, with an rms scatter of 0.51 dex in the black hole mass, and $M_{BH} \propto M_{*,sph}^{2-3}$ for their 17 LTGs. They refer to the two correlations as an *early-type*

[15]Savorgnan et al. (2016) excluded 2 ETGs and 2 LTGs from their total sample.

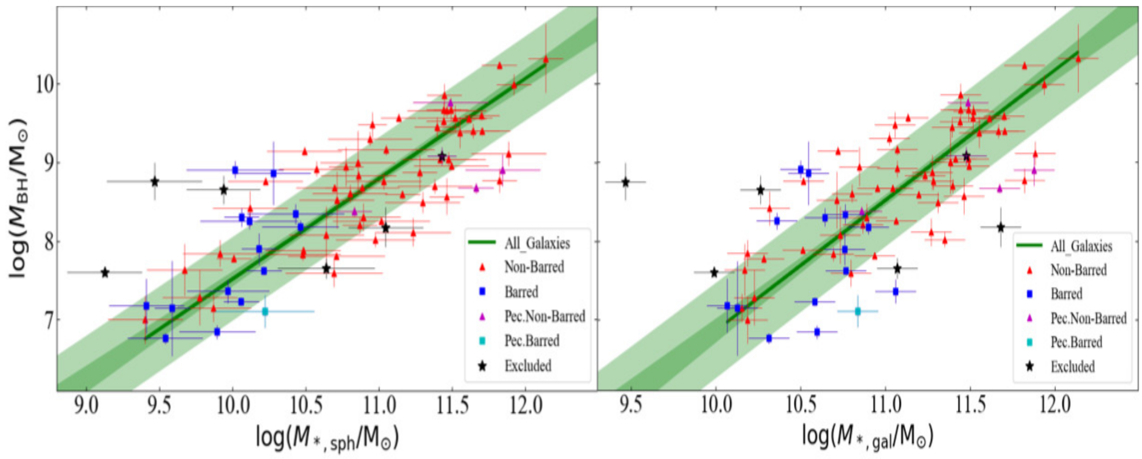

Figure 2.10 Similar to Figure 2.7, but showing which galaxies are barred.

sequence (or *red-type sequence*) and a *late-type sequence* (or *blue-type sequence*). Parameters for our BCES($Y|X$) and BCES($X|Y$) regression lines for LTGs and ETGs can be found in Table 2.5.

From our work, we infer that the previous papers found a bent M_{BH}–$M_{*,sph}$ relation due to Sérsic and core-Sérsic galaxies (e.g. Scott et al., 2013) because most of the Sérsic galaxies in their sample were LTGs and most of the core-Sérsic galaxies were ETGs. The bend in their relation was supposedly due to the different formation processes (dry merging versus gaseous growth), as traced by the difference in the central surface brightness profile of the galaxies. However, we find that the bend is due to the two broad morphological classes of galaxies: ETGs (consisting of ellipticals E, ellicular ES, and lenticulars S0) and LTGs (consisting of spirals Sp), supporting the finding in Savorgnan et al. (2016), which was also later shown by van den Bosch (2016, see his Figure 2).

The situation is, however, a little more complicated than presented above. As explained in Graham & Soria (2018), the color-magnitude relation for ETGs had confounded the situation when working with B-band magnitudes. This results in the fainter Sérsic ETGs following a steep B-band M_{BH}–$L_{B,sph}$ relation (and a shallow L_B–σ relation). Additionally, we have established that the bulges of ETGs follow a steep M_{BH}–$M_{*,sph}$ relation if one has a sample consisting of pure E-type or a sample of ES and S0 type. Section 2.4.2 reveals a slope of around 1.9 ± 0.2 for both of these populations, which is not overly dissimilar to the slope of 2.16 ± 0.32 for bulges in spiral galaxies.

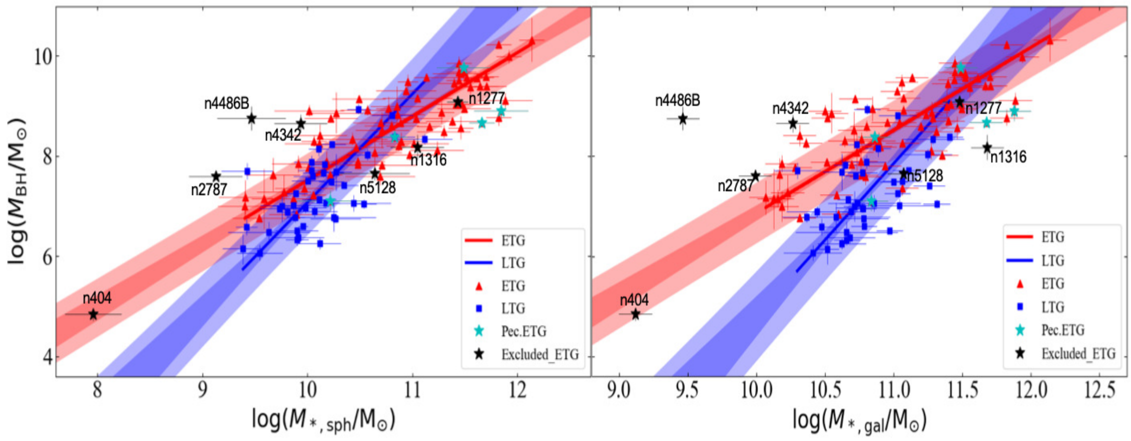

Figure 2.11 M_{BH}–$M_{*,sph}$ and M_{BH}–$M_{*,gal}$ relations for ETGs (red triangles) and LTGs (blue squares). Data for the late-type galaxies is taken from Davis et al. (2019a). In both panels, the red and blue lines represent the bisector regression lines for ETGs and LTGs, respectively. In the M_{BH}–$M_{*,sph}$ diagram, $M_{BH} \propto M_{*,sph}^{1.27\pm0.07}$ for ETGs and $M_{BH} \propto M_{*,Sph}^{2.17\pm0.32}$ for LTGs. In the M_{BH}–$M_{*,gal}$ diagram, $M_{BH} \propto M_{*,gal}^{1.65\pm0.11}$ for ETGs and $M_{BH} \propto M_{*,Gal}^{3.05\pm0.70}$ for LTGs. Although, the ETG NGC 404 ($\log M_{BH}/M\odot = 4.84$) is excluded from the regressions, it follows the regression lines for ETGs. NGC 4486B, which has the second lowest galaxy stellar mass in our sample is a stripped compact elliptical galaxy.

Importantly, we find that the $(M_{BH}/M_{*,sph})$–$M_{*,sph}$ and $(M_{BH}/M_{*,gal})$–$M_{*,gal}$ relations (see Figure 2.12) are qualitatively and quantitatively consistent with our M_{BH}–$M_{*,sph}$ and M_{BH}–$M_{*,gal}$ relations for the sub-populations of ETGs (ES/S0 and E) and LTGs (Sp), within 1σ bound. Parameters for these regression lines can be found in Table 2.5. Figure 2.12 also depicts how the $M_{BH}/M_{*,sph}$ and $M_{BH}/M_{*,gal}$ ratios do not have a constant value as was implied by our M_{BH}–$M_{*,sph}$ and M_{BH}–$M_{*,gal}$ relations.

2.4.5 NGC 5252: A Compact Massive Spheroid

In addition to the above scaling relations, we have discovered a compact massive spheroid in NGC 5252 ($z \approx 0.02$), with a stellar mass of $M_{*,sph} = 7.1^{+5.8}_{-3.2} \times 10^{10} M_\odot$ and a half light radius ($R_{e,sph}$) of just 0.672 kpc, adding to the sample of 21 identified by Graham et al. (2015).

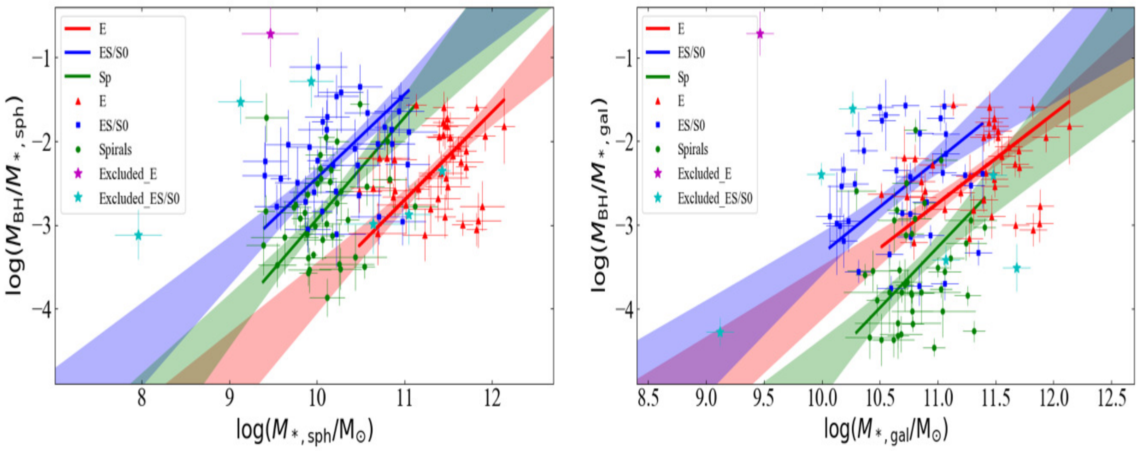

Figure 2.12 $(M_{BH}/M_{*,sph})$–$M_{*,sph}$ and $(M_{BH}/M_{*,gal})$–$M_{*,gal}$ relations for ETGs with a disk (blue squares), ETGs without a disk (red triangles), and LTGs (green circles). In both the panels, blue, red, and green lines represent the bisector regression lines for the three sub-populations of ES/S0-, E-, and Sp-type galaxies, respectively. Dark bands around the lines shows the $\pm 1\sigma$ uncertainty in the corresponding slopes and intercepts. In the $(M_{BH}/M_{*,sph})$–$M_{*,sph}$ diagram, the regression line for ETGs with a disk is offset from the regression line for ETGs without a disk by 1.28 ± 0.17 dex in their $(M_{BH}/M_{*,sph})$ ratios, which is consistent with the offset observed in the M_{BH}–$M_{*,sph}$ diagram within the 1σ bound. In the $M_{BH}/M_{*,gal}$–$M_{*,gal}$ diagram, spiral galaxies follow steeper relation than ETGs, analogous to the right panel of Figure 2.11.

Table 2.5. Linear Regressions

Regression (1)	Minimization (2)	α (3)	β (4)	ϵ (dex) (5)	Δ_{rms} (dex) (6)	r' (7)	$\log p$ (8)	r_s (9)	$\log p_s$ (10)
76 Early-Type Galaxies									
$\boldsymbol{\log(M_{BH}/M_\odot) = \alpha \log(M_{*,sph}/[\upsilon(5 \times 10^{10}\ M_\odot)]) + \beta}$									
BCES($Bisector$)	*Symmetric*	1.27 ± 0.07	8.41 ± 0.06	0.41	0.52				
BCES($M_{BH}\|M_{*,sph}$)	M_{BH}	1.12 ± 0.08	8.43 ± 0.06	0.40	0.49	0.82	−18.96	0.80	−17.20
BCES($M_{*,sph}\|M_{BH}$)	$M_{*,sph}$	1.45 ± 0.09	8.38 ± 0.07	0.45	0.57				
$\boldsymbol{\log(M_{BH}/M_\odot) = \alpha \log(M_{*,gal}/[\upsilon(5 \times 10^{10}\ M_\odot)]) + \beta}$									
BCES($Bisector$)	*Symmetric*	1.65 ± 0.11	8.02 ± 0.08	0.53	0.58				
BCES($M_{BH}\|M_{*,gal}$)	M_{BH}	1.33 ± 0.12	8.13 ± 0.08	0.51	0.55	0.76	−15.12	0.76	−14.71
BCES($M_{*,gal}\|M_{BH}$)	$M_{*,gal}$	2.10 ± 0.18	7.86 ± 0.11	0.63	0.69				
Sérsic and Core-Sérsic Galaxies									
45 Sérsic Galaxies: $\boldsymbol{\log(M_{BH}/M_\odot) = \alpha \log(M_{*,sph}/[\upsilon(5 \times 10^{10}\ M_\odot)]) + \beta}$									
BCES($Bisector$)	*Symmetric*	1.30 ± 0.14	8.43 ± 0.10	0.42	0.55				
BCES($M_{BH}\|M_{*,sph}$)	M_{BH}	1.05 ± 0.14	8.37 ± 0.09	0.40	0.50	0.71	−7.34	0.71	−7.23
BCES($M_{*,sph}\|M_{BH}$)	$M_{*,sph}$	1.63 ± 0.23	8.52 ± 0.13	0.49	0.66				
31 Core-Sérsic Galaxies: $\boldsymbol{\log(M_{BH}/M_\odot) = \alpha \log(M_{*,sph}/[\upsilon(5 \times 10^{10}\ M_\odot)]) + \beta}$									
BCES($Bisector$)	*Symmetric*	1.38 ± 0.21	8.30 ± 0.20	0.43	0.50				
BCES($M_{BH}\|M_{*,sph}$)	M_{BH}	0.92 ± 0.27	8.62 ± 0.20	0.39	0.43	0.56	−2.96	0.47	−2.11
BCES($M_{*,sph}\|M_{BH}$)	$M_{*,sph}$	2.20 ± 0.55	7.72 ± 0.47	0.58	0.72				
45 Sérsic Galaxies: $\boldsymbol{\log(M_{BH}/M_\odot) = \alpha \log(M_{*,gal}/[\upsilon(5 \times 10^{10}\ M_\odot)]) + \beta}$									
BCES($Bisector$)	*Symmetric*	1.61 ± 0.18	8.00 ± 0.09	0.59	0.63				
BCES($M_{BH}\|M_{*,gal}$)	M_{BH}	1.05 ± 0.17	8.04 ± 0.09	0.54	0.57	0.58	−4.62	0.58	−4.52
BCES($M_{*,gal}\|M_{BH}$)	$M_{*,gal}$	2.71 ± 0.55	7.93 ± 0.14	0.86	0.92				
31 Core-Sérsic Galaxies: $\boldsymbol{\log(M_{BH}/M_\odot) = \alpha \log(M_{*,gal}/[\upsilon(5 \times 10^{10}\ M_\odot)]) + \beta}$									
BCES($Bisector$)	*Symmetric*	1.47 ± 0.18	8.17 ± 0.17	0.43	0.46				
BCES($M_{BH}\|M_{*,gal}$)	M_{BH}	0.96 ± 0.24	8.56 ± 0.18	0.39	0.42	0.58	−3.22	0.48	−2.21
BCES($M_{*,gal}\|M_{BH}$)	$M_{*,gal}$	2.44 ± 0.64	7.45 ± 0.55	0.62	0.68				

Table 2.5 (cont'd)

Regression (1)	Minimization (2)	α (3)	β (4)	ϵ (dex) (5)	Δ_{rms} (dex) (6)	r' (7)	$\log p$ (8)	r_s (9)	$\log p_s$ (10)
Galaxies with a Disk (ES/S0) and Galaxies without a Disk (E)									
36 Galaxies with a Disk (ES/S0): $\log(M_{\rm BH}/{\rm M}_\odot) = \alpha\log(M_{*,\rm sph}/[\upsilon(5\times10^{10}\ {\rm M}_\odot)]) + \beta$									
BCES($Bisector$)	$Symmetric$	1.86 ± 0.20	8.90 ± 0.13	0.28	0.57				
BCES($M_{\rm BH}\|M_{*,\rm sph}$)	$M_{\rm BH}$	1.70 ± 0.22	8.83 ± 0.14	0.29	0.54	0.77	-7.39	0.77	-7.49
BCES($M_{*,\rm sph}\|M_{\rm BH}$)	$M_{*,\rm sph}$	2.05 ± 0.26	8.98 ± 0.15	0.29	0.62				
40 Galaxies without a Disk (E): $\log(M_{\rm BH}/{\rm M}_\odot) = \alpha\log(M_{*,\rm sph}/[\upsilon(5\times10^{10}\ {\rm M}_\odot)]) + \beta$									
BCES($Bisector$)	$Symmetric$	1.90 ± 0.20	7.78 ± 0.15	0.36	0.50				
BCES($M_{\rm BH}\|M_{*,\rm sph}$)	$M_{\rm BH}$	1.68 ± 0.24	7.92 ± 0.15	0.34	0.46	0.75	-7.63	0.70	-6.32
BCES($M_{*,\rm sph}\|M_{\rm BH}$)	$M_{*,\rm sph}$	2.16 ± 0.26	7.60 ± 0.21	0.39	0.56				
36 Galaxies with a Disk (ES/S0): $\log(M_{\rm BH}/{\rm M}_\odot) = \alpha\log(M_{*,\rm gal}/[\upsilon(5\times10^{10}\ {\rm M}_\odot)]) + \beta$									
BCES($Bisector$)	$Symmetric$	1.94 ± 0.21	8.14 ± 0.12	0.67	0.71				
BCES($M_{\rm BH}\|M_{*,\rm gal}$)	$M_{\rm BH}$	1.26 ± 0.25	8.12 ± 0.11	0.62	0.64	0.57	-3.52	0.56	-3.47
BCES($M_{*,\rm gal}\|M_{\rm BH}$)	$M_{*,\rm gal}$	3.47 ± 0.76	8.16 ± 0.18	1.01	1.08				
40 Galaxies without a Disk (E): $\log(M_{\rm BH}/{\rm M}_\odot) = \alpha\log(M_{*,\rm gal}/[\upsilon(5\times10^{10}\ {\rm M}_\odot)]) + \beta$									
BCES($Bisector$)	$Symmetric$	1.74 ± 0.16	7.85 ± 0.12	0.42	0.48				
BCES($M_{\rm BH}\|M_{*,\rm gal}$)	$M_{\rm BH}$	1.38 ± 0.18	8.10 ± 0.12	0.40	0.45	0.74	-7.28	0.70	-6.27
BCES($M_{*,\rm gal}\|M_{\rm BH}$)	$M_{*,\rm gal}$	2.27 ± 0.29	7.50 ± 0.24	0.51	0.58				
Galaxies with and without a Bar									
15 Galaxies with a Bar: $\log(M_{\rm BH}/{\rm M}_\odot) = \alpha\log(M_{*,\rm sph}/[\upsilon(5\times10^{10}\ {\rm M}_\odot)]) + \beta$									
BCES($Bisector$)	$Symmetric$	3.59 ± 1.79	10.14 ± 1.15	0.34	0.86				
BCES($M_{\rm BH}\|M_{*,\rm sph}$)	$M_{\rm BH}$	3.58 ± 2.40	10.13 ± 1.55	0.33	0.86	0.60	-1.76	0.56	-1.53
BCES($M_{*,\rm sph}\|M_{\rm BH}$)	$M_{*,\rm sph}$	3.61 ± 1.37	10.15 ± 0.90	0.34	0.86				
61 Galaxies without a Bar: $\log(M_{\rm BH}/{\rm M}_\odot) = \alpha\log(M_{*,\rm sph}/[\upsilon(5\times10^{10}\ {\rm M}_\odot)]) + \beta$									
BCES($Bisector$)	$Symmetric$	1.29 ± 0.09	8.36 ± 0.07	0.41	0.51				
BCES($M_{\rm BH}\|M_{*,\rm sph}$)	$M_{\rm BH}$	1.10 ± 0.10	8.42 ± 0.07	0.39	0.47	0.78	-13.14	0.73	-10.78
BCES($M_{*,\rm sph}\|M_{\rm BH}$)	$M_{*,\rm sph}$	1.52 ± 0.13	8.28 ± 0.10	0.46	0.58				
15 Galaxies with a Bar: $\log(M_{\rm BH}/{\rm M}_\odot) = \alpha\log(M_{*,\rm gal}/[\upsilon(5\times10^{10}\ {\rm M}_\odot)]) + \beta$									
BCES($Bisector$)	$Symmetric$	1.52 ± 0.59	7.90 ± 0.22	0.73	0.73				
						0.18	-0.29	0.14	-0.20

Table 2.5 (cont'd)

Regression	Minimization	α	β	ϵ (dex)	Δ_{rms} (dex)	r'	$\log p$	r_s	$\log p_s$
(1)	(2)	(3)	(4)	(5)	(6)	(7)	(8)	(9)	(10)
BCES$(M_{\rm BH}\|M_{*,\rm gal})$	$M_{\rm BH}$	0.53 ± 0.56	7.79 ± 0.18	0.67	0.67				
BCES$(M_{*,\rm gal}\|M_{\rm BH})$	$M_{*,\rm gal}$	13.19 ± 16.19	9.19 ± 1.56	3.41	3.51				
61 Galaxies without a Bar: $\log{(M_{\rm BH}/{\rm M}_{\odot})} = \alpha \log{(M_{*,\rm gal}/[\upsilon(5 \times 10^{10}\ {\rm M}_{\odot})])} + \beta$									
BCES(*Bisector*)	*Symmetric*	1.52 ± 0.10	8.10 ± 0.08	0.46	0.50				
BCES$(M_{\rm BH}\|M_{*,\rm gal})$	$M_{\rm BH}$	1.23 ± 0.12	8.23 ± 0.08	0.44	0.48	0.78	−12.65	0.74	−11.05
BCES$(M_{*,\rm gal}\|M_{\rm BH})$	$M_{*,\rm gal}$	1.90 ± 0.16	7.93 ± 0.11	0.54 0.59					
40 Late-Type Galaxies									
$\log{(M_{\rm BH}/{\rm M}_{\odot})} = \alpha \log{(M_{*,\rm sph}/[\upsilon(5 \times 10^{10}\ {\rm M}_{\odot})])} + \beta$									
BCES(*Bisector*)	*Symmetric*	2.16 ± 0.32	8.58 ± 0.22	0.48	0.64				
BCES$(M_{\rm BH}\|M_{*,\rm sph})$	$M_{\rm BH}$	1.70 ± 0.35	8.30 ± 0.22	0.46	0.56	0.66	−5.35	0.62	−4.62
BCES$(M_{*,\rm sph}\|M_{\rm BH})$	$M_{*,\rm sph}$	2.90 ± 0.55	9.03 ± 0.39	0.59	0.82				
$\log{(M_{\rm BH}/{\rm M}_{\odot})} = \alpha \log{(M_{*,\rm gal}/[\upsilon(5 \times 10^{10}\ {\rm M}_{\odot})])} + \beta$									
BCES(*Bisector*)	*Symmetric*	3.05 ± 0.70	6.93 ± 0.14	0.70	0.79				
BCES$(M_{\rm BH}\|M_{*,\rm gal})$	$M_{\rm BH}$	2.04 ± 0.72	7.04 ± 0.14	0.61	0.66	0.47	−2.70	0.53	−3.34
BCES$(M_{*,\rm gal}\|M_{\rm BH})$	$M_{*,\rm gal}$	5.60 ± 1.57	6.66 ± 0.22	1.11	1.31				
ETGs with a disk (ES/S0), ETGs without a disk (E) and LTGs (Sp)									
36 Galaxies with a Disk (ES/S0): $\log{(M_{\rm BH}/M_{*,\rm sph})} = \alpha \log{(M_{*,\rm sph}/[\upsilon(5 \times 10^{10}\ {\rm M}_{\odot})])} + \beta$									
BCES(*Bisector*)	*Symmetric*	1.00 ± 0.14	-1.74 ± 0.12	0.46	0.60	0.25	−0.84	0.31	−1.17
40 Galaxies without a Disk (E): $\log{(M_{\rm BH}/M_{*,\rm sph})} = \alpha \log{(M_{*,\rm sph}/[\upsilon(5 \times 10^{10}\ {\rm M}_{\odot})])} + \beta$									
BCES(*Bisector*)	*Symmetric*	1.05 ± 0.11	-3.02 ± 0.12	0.45	0.53	0.23	−0.82	0.21	−0.69
40 Late-Type Galaxies (Sp): $\log{(M_{\rm BH}/M_{*,\rm sph})} = \alpha \log{(M_{*,\rm sph}/[\upsilon(5 \times 10^{10}\ {\rm M}_{\odot})])} + \beta$									
BCES(*Bisector*)	*Symmetric*	1.22 ± 0.21	-2.08 ± 0.16	0.56	0.65	0.18	−0.56	0.18	−0.59
36 Galaxies with a Disk (ES/S0): $\log{(M_{\rm BH}/M_{*,\rm gal})} = \alpha \log{(M_{*,\rm gal}/[\upsilon(5 \times 10^{10}\ {\rm M}_{\odot})])} + \beta$									
BCES(*Bisector*)	*Symmetric*	1.12 ± 0.17	-2.56 ± 0.12	0.72	0.74	0.10	−0.25	0.12	−0.30
40 Galaxies without a Disk (E): $\log{(M_{\rm BH}/M_{*,\rm gal})} = \alpha \log{(M_{*,\rm gal}/[\upsilon(5 \times 10^{10}\ {\rm M}_{\odot})])} + \beta$									
BCES(*Bisector*)	*Symmetric*	1.07 ± 0.08	-3.06 ± 0.10	0.50	0.54	0.23	−0.83	0.21	−0.72
40 Late-Type Galaxies (Sp): $\log{(M_{\rm BH}/M_{*,\rm gal})} = \alpha \log{(M_{*,\rm gal}/[\upsilon(5 \times 10^{10}\ {\rm M}_{\odot})])} + \beta$									
BCES(*Bisector*)	*Symmetric*	1.45 ± 0.66	-3.70 ± 0.14	0.67	0.70	0.12	−0.32	0.18	−0.56

Note. — The data and linear regression for late-type galaxies is taken from Davis et al. (2019a). Columns: (1) Regression performed. (2) The coordinate direction in which the offsets from the regression line is minimized. (3) Slope of the regression line. (4) Intercept of the regression line. (5) Intrinsic scatter in the $M_{\rm BH}$ direction (using Equation 1 from Graham & Driver, 2007a). (6) Root mean square scatter in the $M_{\rm BH}$ direction. (7) Pearson correlation coefficient. (8) The Pearson correlation probability value. (9) Spearman rank-order correlation coefficient. (10) The Spearman rank-order correlation probability value.

2.5 Conclusions and Implications

Our work, based on the largest sample of ETGs with directly-measured SMBH masses, establishes a robust relation between the black hole mass and both the spheroid and galaxy stellar mass. While the color-magnitude relation for ETGs results in a steep M_{BH}–$L_{*,sph}$ relation in the optical bands for $MAG_{K_s} > -22$ mag, i.e., $B - K_s \leq 4.0$ (Graham & Soria, 2018), the slopes at the low- and high-luminosity end of the M_{BH}–$L_{*,sph}$ relation based on infrared magnitudes are equal to each other. That is, the M_{BH}–$M_{*,sph}$ relation for ETGs appears to be defined by a single log-linear relation. This helps to clarify debate over the existence of a steeper (at the low-mass end) and "bent" M_{BH}–$M_{*,sph}$ relation for ETGs.

Using our image reduction, profile extraction, and multi-component decomposition techniques, we carefully measured the spheroid and galaxy stellar luminosities and masses. We applied the BCES bisector regression to our dataset, providing a symmetric treatment to both the M_{BH} and $M_{*,sph}$ or $M_{*,gal}$ data (we additionally report the scaling relations obtained from other asymmetric regressions in Table 2.5).

We checked the consistency of our M_{BH}–$M_{*,sph}$ and M_{BH}–$M_{*,gal}$ scaling relations using stellar masses based on color-dependent stellar mass-to-light ratios and found it to be in agreement with our scaling relations based on the constant stellar mass-to-light ratios. This may in part be because our ETGs have fairly constant, red, colors (Figure 2.5). Our key results can be summarized as follows:

- Having performed separate regressions using 45 Sérsic and 31 core-Sérsic galaxies, we found that, for ETGs, there is no significant bend in either the M_{BH}–$M_{*,sph}$ or M_{BH}–$M_{*,gal}$ diagram due to Sérsic and core-Sérsic galaxies (Figure-2.6).

- ETGs follow a steep $M_{BH} \propto M_{*,sph}^{1.27\pm0.07}$ relation, with total rms scatter of 0.52 dex in the $\log M_{BH}$. The slope of this relation is non-linear at the 3σ bound, leading us to the conclusion that a steeper than linear M_{BH}–$M_{*,sph}$ relation exists for ETGs. This also implies that the $M_{BH}/M_{*,sph}$ ratio is not a constant but varies along the relation.

- The SMBH mass of ETGs follow an even steeper relation with the host *galaxy* stellar mass: $M_{BH} \propto M_{*,gal}^{1.65\pm0.11}$ with an rms scatter (in the $\log M_{BH}$ direction) of 0.58 dex. The slope of this relation is non-linear at the 5.9σ level. The similarity in the rms scatter of this relation with that of M_{BH}–$M_{*,sph}$ relation suggests that black hole mass correlates almost equally well with galaxy mass (luminosity) as it does with spheroid mass (luminosity) for ETGs (Figure 2.7). Hence, for the cases where bulge/disk decomposition is difficult, the M_{BH}–$M_{*,gal}$ relation can be used to estimate the black hole mass of an ETG using the total galaxy stellar mass. However, as noted below, this approach is not preferred if one knows whether or not the ETG under study contains a disk.

- We discovered separate relations for ETGs with an intermediate-scale or extended disk (ES or S0) and ETGs without a disk (E), having slopes 1.86±0.20 and 1.90±0.20

in the M_{BH}–$M_{*,sph}$ diagram, with an rms scatter in the $\log M_{BH}$ direction of 0.57 dex and 0.50 dex, respectively. Crucially, galaxies with a disk are offset from galaxies without a disk (Figure 2.8) by more than an order of magnitude (1.12 dex) in their $M_{BH}/M_{*,sph}$ ratio. This is likely due to the exclusion of the disk light, rather than an issue with the black hole mass. To better estimate the black hole mass of an ETG, one should use the corresponding M_{BH}–$M_{*,sph}$ relation depending on whether the ETG has a disk or not.

- For the M_{BH}–$M_{*,gal}$ relation, the intercepts of the two regression lines (for galaxies with and without a disk) differ only by a factor of 2. Hence, the relation obtained by a single regression (Equation 2.11) may still prove to be preferable for estimating the black hole mass when uncertain about the presence of a disk in an ETG, or for those without a careful multi-component decomposition.

- We found that the regression line for the barred galaxies (which reside at the lower-mass end of our diagrams) are largely consistent with the regression line for the non-barred galaxies in both the M_{BH}–$M_{*,sph}$ and M_{BH}–$M_{*,gal}$ diagrams (Figures 2.9 and 2.10). However, with only 15 barred galaxies, we restrict our conclusion to noting that the barred galaxies do not appear to have lower SMBH masses than the non-barred galaxies in either the M_{BH}–$M_{*,sph}$ diagram or the M_{BH}–$M_{*,gal}$ diagram.

- Combining the 76 ETGs studied here, with the 40 LTGs from Davis et al. (2019a), we observe a difference in the slope of the regression lines for ETGs and LTGs (Figure 2.11) in both the M_{BH}–$M_{*,sph}$ and M_{BH}–M_{*gal} diagrams. The LTGs define steeper relations, such that $M_{BH} \propto M_{*,sph}^{2.17\pm0.32}$ and $M_{BH} \propto M_{*,gal}^{3.05\pm0.70}$. These slopes for the LTGs are almost double that of the ETGs. This agrees with the change noticed by Savorgnan et al. (2016) in the M_{BH}–$M_{*,sph}$ diagram.

- We also found that the behaviour of three sub-populations of galaxies (E, ES/S0 and, Sp) in the $(M_{BH}/M_{*,sph})$–$M_{*,sph}$ and $(M_{BH}/M_{*,gal})$–$M_{*,gal}$ diagrams agree with the corresponding M_{BH}–$M_{*,sph}$ and M_{BH}–$M_{*,gal}$ relations (see Figures 2.8, 2.11 and 2.12), supporting the obvious implication of our non-linear M_{BH} vs $M_{*,sph}$ and $M_{*,gal}$ scaling relations, specifically that the $M_{BH}/M_{*,sph}$ and $M_{BH}/M_{*,sph}$ ratios are not constant.

The existence of substructure within the M_{BH}–$M_{*,sph}$ diagram, due to sub-populations of ETGs with and without disks, and spiral galaxy bulges, means that past efforts to calibrate the virial f-factor using the M_{BH}–$M_{*,sph}$ diagram—used for converting virial masses of active galactic nuclei into black hole masses (e.g., Bentz & Manne-Nicholas, 2018)— will benefit from revisiting. Calibration of the offset between the ensemble of virial masses for AGN and the ensemble of directly measured black hole mass should be performed separately using the significantly different, non-linear, M_{BH}–$M_{*,sph}$ relations for ETGs and LTGs, while taking into account the presence or absence of a disk in the ETGs. A similar situation exists with the M_{BH}–σ diagram, due to the offset sub-populations of galaxies with and without bars (Graham & Others, 2011). In Sahu et al. (2019, in preparation) we will present an analysis of the M_{BH}–σ relation based on the various sub-samples of the ETG population used in this paper. We will also do this using our combined sample of 120 ETGs and LTGs.

Extending our search for the most fundamental black hole mass scaling relation, we will explore the correlation of black hole mass with the spheroid's Sérsic index[16] (n) and half light radius (R_e). We already have these two parameters from our homogeneous bulge/disk decomposition of ETGs and LTGs (Davis et al., 2019a) . We intend to check for the existence of a fundamental plane rather than a line. However, care needs to be taken given that the L–R_e relation is curved (e.g. Graham & Worley, 2008, Graham 2019, submitted).

The black hole mass scaling relations presented in this work, based on a local ($z \approx 0$) sample of ETGs, can be used to estimate the black hole masses in other galaxies which do not have their SMBH's gravitational sphere-of-influence spatially resolved.

These scaling relations can be further used to derive the black hole mass function from the galaxy luminosity function, for the first time separating the galaxy population according to their morphological type. We plan to calculate the SMBH mass function by applying the black hole mass scaling relations for ETGs and LTGs to the updated spheroid and galaxy luminosity functions from GAMA data (Driver et al., 2009) for which the morphological types are known and bulge/disk decompositions have been performed.

[16]The Sérsic index is a measure of the radial concentration of stellar mass.

The SMBH mass function, accompanied with knowledge of the galaxy/SMBH merger rate, can be used to constrain the ground-based detection rate of long-wavelength gravitational waves, which are actively being searched for by the Parkes Pulsar Timing Array (PPTA, Shannon et al., 2015; Hobbs & Dai, 2017), the European Pulsar Timing Array (EPTA, Stappers & Kramer, 2011), and the North American Nanohertz Observatory for Gravitational Waves (NANOGrav, Siemens, 2019). Using the forth-coming SMBH mass function, we intend to improve the predictions for the detection of the gravitational waves from PTA and make new predictions for detection from the recently inaugurated MeerKAT telescope (Jonas, 2007). The revised black hole scaling relations can also be used to predict the detection of gravitational waves from future space-based detectors. For example, Mapelli & Others (2012) investigate the detection of gravitational waves produced from the merger of SMBHs with stellar mass BHs and neutron stars in the central nuclear star clusters of galaxies (Hartmann, 2011).

2.6 Acknowledgements

We thank Edward (Ned) Taylor for his helpful comments on calibrating the stellar mass-to-light ratios for r'-band images and conversion of IMFs. This research was conducted by the Australian Research Council Centre of Excellence for Gravitational Wave Discovery (OzGrav), through project number CE170100004. AWG was supported under the Australian Research Councils funding scheme DP17012923. This work has made use of the NASA/IPAC Infrared Science Archive and the NASA/IPAC Extragalactic Database (NED). This research has also made use of the Two Micron All Sky Survey and Sloan Digital Sky Survey database. We also acknowledge the use of the HyperLeda database `http://leda.univ-lyon1.fr`.

3

Revealing Hidden Substructures in the M_{BH}–σ Diagram, and Refining the Bend in the L–σ Relation

Using 145 early- and late-type galaxies (ETGs and LTGs) with directly-measured supermassive black hole masses, M_{BH}, we build upon our previous discoveries that: (i) LTGs, most of which have been alleged to contain a pseudobulge, follow the relation $M_{BH} \propto M_{*,sph}^{2.16\pm0.32}$; and (ii) the ETG relation $M_{BH} \propto M_{*,sph}^{1.27\pm0.07}$ is an artifact of ETGs with/without disks following parallel $M_{BH} \propto M_{*,sph}^{1.9\pm0.2}$ relations which are offset by an order of magnitude in the M_{BH}-direction. Here, we searched for substructure in the M_{BH}–(central velocity dispersion, σ) diagram using our recently published, multi-component, galaxy decompositions; investigating divisions based on the presence of a depleted stellar core (major dry-merger), a disk (minor wet/dry-merger, gas accretion), or a bar (evolved unstable disk). The Sérsic and core-Sérsic galaxies define two distinct relations: $M_{BH} \propto \sigma^{5.75\pm0.34}$ and $M_{BH} \propto \sigma^{8.64\pm1.10}$, with $\Delta_{rms|BH} = 0.55$ and 0.46 dex, respectively. We also report on the consistency with the slopes and bends in the galaxy luminosity (L)–σ relation due to Sérsic and core-Sérsic ETGs, and LTGs which all have Sérsic light-profiles. Two distinct relations (superficially) reappear in the M_{BH}–σ diagram upon separating galaxies with/without a disk (primarily for the ETG sample), while we find no significant offset between barred and non-barred galaxies, nor between galaxies with/without active galactic nuclei. We also address selection biases suggested to affect the scaling relations for

dynamically-measured M_{BH} samples. Our new, (morphological type)-dependent, M_{BH}–σ relations precisely estimate M_{BH} in other galaxies, hold implications for galaxy/black hole co-evolution and feedback theories, simulations, and calibration of virial f-factors for reverberation-mapping.

3.1 Introduction

The first observational works on the correlation between central black hole mass (M_{BH}) and the stellar velocity dispersion (σ) of a galaxy (Ferrarese & Merritt, 2000; Gebhardt et al., 2000) revealed a relation with little or no intrinsic scatter, suggesting that the M_{BH}–σ relation could be the most fundamental of the black hole scaling relations. However, surprisingly, the slopes reported by the two studies were not in agreement and supported two competing feedback models between the super-massive black holes (SMBHs) and their host galaxies. Ferrarese & Merritt (2000) found $M_{BH} \propto \sigma^{4.80\pm0.50}$, which supported the prediction $M_{BH} \propto \sigma^5$ based on the energy-balancing feedback model of Silk & Rees (1998). Gebhardt et al. (2000) reported $M_{BH} \propto \sigma^{3.75\pm0.30}$, supporting the feedback model of Fabian (1999) based upon momentum conservation, which predicted $M_{BH} \propto \sigma^4$.

Merritt & Ferrarese (2001) later revealed that Gebhardt et al. (2000) had found a shallower slope due to the asymmetric linear regression routine that Gebhardt et al. (2000) employed[1], plus Gebhardt et al.'s relation was biased by the low-velocity dispersion which they had used for the Milky Way. Gebhardt et al. (2000) had effectively solved the "Observer's Question" while Ferrarese & Merritt (2000) had effectively answered the "Theorist's Question," as was later posed by Novak et al. (2006). The reason behind obtaining almost zero intrinsic scatter in the M_{BH}–σ relation was possibly the small sample size, or perhaps Ferrarese & Merritt (2000) had a "gold standard" of reliable black hole masses with well-resolved spheres-of-influence (Ferrarese & Ford, 2005). Subsequent works on larger galaxy samples have found a non-zero intrinsic scatter.

With an increase in the number of barred galaxies with directly measured SMBH masses, some studies (Graham, 2007a, 2008b,a; Hu, 2008) found that barred galaxies have a tendency to be offset, from the M_{BH}–σ relation, towards higher σ or lower M_{BH}, sug-

[1]Tremaine et al. (2002) also used an asymmetric linear regression, ignoring the intrinsic scatter in the velocity dispersion direction (see Novak et al., 2006; Graham, 2016, his section titled "slippery slopes").

gesting that the inclusion of barred galaxies may produce a steeper relation with larger scatter as warned by (Graham & Others, 2011) and (Graham & Scott, 2013). Hu (2008) claimed that the offset galaxies in their sample had "pseudo-bulges"[2] with low-mass black holes, while according to Graham (2008a), the offset could be either because of a low black hole mass in pseudo-bulges or the elevated velocity dispersions in barred galaxies. Supporting the latter possibility, the simulation by Hartmann et al. (2014) suggested that bars may cause increased velocity dispersion in galactic bulges whether they are classical or pseudo-bulges (see also Brown et al., 2013). Interestingly, the recent observational work by Sahu et al. (2019a) found that barred galaxies are not offset in the black hole mass versus galaxy stellar mass ($M_{*,gal}$) diagram, nor in the black hole mass versus spheroid/bulge stellar mass ($M_{*,sph}$) diagram, eliminating under-massive black holes as the reason behind the apparent offset in the M_{BH}–σ diagram and strengthening the prospect of barred galaxies having an increased velocity dispersion. However, as the number of barred galaxies in Sahu et al. (2019a) is still quite small, this interpretation may require further confirmation.

In addition to the reported substructure in the M_{BH}–σ diagram due to barred galaxies, some studies (e.g., McConnell & Ma, 2013; Bogdán et al., 2018, see their figure 5) have noticed that massive galaxies are offset towards the high-M_{BH} side of their M_{BH}–σ relation. These galaxies are mostly brightest cluster galaxies (BCGs) or central cluster galaxies (CCGs) which are considered to be a product of multiple dry mergers. Galaxies which have undergone dry mergers can have a deficit of light at their centers because the binary SMBHs formed from the two merging galaxies can scour out the stars from the center of the merged galaxy through the transfer of their orbital angular momentum (Begelman et al., 1980; Merritt & Milosavljević, 2005). Such galaxies with a (partially) depleted core were discovered by King & Minkowski (1966, 1972) and are referred to as core-Sérsic (Graham & Others, 2003) galaxies due to their flattened core relative to the inward extrapolation of their bulge's outer Sérsic (Sérsic, 1963) light profile. Galaxies which grow over time via gas-rich processes are likely to have bulges with Sérsic light-profiles.

Contrary to McConnell & Ma (2013), the recent work by Savorgnan & Graham (2015)

[2]Pseudo-bulges are difficult to identify (Graham, 2014), and Graham (2019a) explains why diagrams using Sérsic indices and "effective" half-light parameters cannot be used to identify pseudo-bulges. Moreover, the range of diagnostics used to classify pseudo-bulges need to be subjectively applied (Kormendy & Kennicutt Robert C., 2004), making it extremely problematic to distinguish pseudo-bulges from classical bulges. Furthermore, many galaxies contain both (Erwin et al., 2015).

found that Sérsic and core-Sérsic galaxies broadly follow the same M_{BH}–σ relation, and so was the case with slow and fast rotating galaxies in their sample. Thus, still, debates over the substructures in the M_{BH}–σ diagram due to barred and non-barred galaxies, Sérsic and core-Sérsic galaxies, and fast and slow rotating galaxies (galaxies with and without a rotating disk) persist.

Using the hitherto largest sample of 145 galaxies, comprised of all early-type galaxies (ETGs) and late-type galaxies (LTGs) with directly measured SMBH masses, our work investigates the underlying relationship between black hole mass and central velocity dispersion for various sub-classes of the host galaxy. We classify these galaxies into Sérsic, core-Sérsic, barred, non-barred, and galaxies with and without a disk, based on our detailed multi-component decompositions (coupled with kinematical information) presented in Davis et al. (2019a) and Sahu et al. (2019a), and also into galaxies with and without an Active Galactic Nucleus (AGN) identified using the catalog of Véron-Cetty & Véron (2010).

We endeavor here to build upon our recent revelation that ETGs superficially follow the relation $M_{BH} \propto M_{*,sph}^{1.27\pm0.07}$ (Sahu et al., 2019a, their Equation 10). We showed in Sahu et al. (2019a, see their Figure 8) that this single relation for ETGs is misleading because ETGs with and without a disk define two separate (parallel) $M_{BH} \propto M_{*,sph}^{1.9\pm0.2}$ relations which are offset by more than an order of magnitude (1.12 dex) in the M_{BH}-direction. This paradigm shifting discovery provided further impetus for us to re-examine old and search for new substructure in the M_{BH}-σ diagram.

In order to provide a consistency check between the various scaling relations, this paper also establishes the galaxy luminosity (L)–σ relation for our ETG sample observed at $3.6\,\mu$m, and for an updated V-band data-set of ETGs (Lauer et al., 2007). We find a bend in the ETG L–σ relation from both data-sets, which has been observed in other bands (e.g., Matković & Guzmán, 2005; de Rijcke et al., 2005; Graham & Soria, 2018). Additionally, we explore the behavior of LTGs (spirals) with directly measured black hole masses in the L–σ diagram. We mate these L–σ relations with the M_{BH}–L and M_{BH}–σ relations to investigate the consistency between the scaling relations.

Section 3.2 describes our data-set. In Section 3.3, we briefly discuss the method of linear regression that we have used to establish our scaling relations, and the galaxy exclusions applied, along with the reasons for this. We further present the new M_{BH}–σ relations that we have found for the various categories based on the morphological classes mentioned above. This is accompanied by discussions on the behavior of the M_{BH}–σ relation for each category.

In Section 3.4, we check on the internal consistency between our M_{BH}–σ relations and the latest M_{BH}–$M_{*,gal}$ (and M_{BH}–$M_{*,sph}$) relations, while Section 3.5 presents the bent L–σ relations, based on different wavelength bands. Section 3.6 addresses a much-discussed selection bias regarding the spatial-resolution of the gravitational sphere-of-influence of the black holes, and investigates the previously observed offset between galaxies with a dynamically measured black hole mass and galaxies without a dynamically measured black hole mass in the L–σ, or rather σ–$M_{*,gal}$, diagram (Shankar et al., 2016). This is followed by the main conclusions of our work summarized in Section 3.7 and a brief discussion on the implications of the new scaling relations.

3.2 Data

We have identified 145 galaxies with directly measured super-massive black hole masses obtained from stellar dynamics, gas dynamics, kinematics of megamasers, proper motion, or recent direct imaging technique. This sample is comprised of 96 early-type and 49 late-type galaxies. Data for 84 ETGs came from Sahu et al. (2019a) and Savorgnan et al. (2016). These 84 ETGs have been used in Sahu et al. (2019a) to establish the M_{BH}–$M_{*,sph}$ and M_{BH}–$M_{*,gal}$ relations for ETGs, based on the bulge and total galaxy stellar masses measured using state-of-the-art two dimensional (2D) isophotal modelling [3,4] and multi-component decompositions of predominantly near infra-red (NIR) images.

For the remaining 12 ETGs, data for two galaxies came from Nowak et al. (2007) and

[3]Davis et al. (2019a) and Sahu et al. (2019a) use ISOFIT (Ciambur, 2015) to generate a 2D model of each galaxy, and further use PROFILER (Ciambur, 2016) to effectively realign the semi-major axis of each isophote. This 1D surface brightness profile effectively encapsulates all of the key information about the galaxy structure and flux, including ellipticity gradients, position angle twists, and deviations from elliptical-shaped isophotes up to the 12th order Fourier harmonic coefficients. This major axis surface brightness profile is used for multi-component decomposition of the galaxy light. It should not be confused with a simple surface brightness profile obtained from a 1D cut of a galaxy image.

[4]Ciambur (2016) provide a critical comparision between 1D and 2D decomposition techniques, concluding that multi-component galaxies may be easily modelled in 2D but gradients in the ellipticity, position angle, and structural perturbations are better captured in 1D. Furthermore, Savorgnan & Graham (2016b) tried both 1D and 2D decompositions, and had more success using the 1D multi-component decomposition techniques.

Gültekin et al. (2014), who measured M_{BH} using stellar dynamics. Another galaxy is taken from Huré et al. (2011) with M_{BH} measured using water masers, while the data for the remaining nine ETGs is taken from recent papers. Out of these nine, two ETGs are from Nguyen et al. (2018) and six ETGs come from Thater et al. (2019), where M_{BH} is measured using stellar dynamics. Data for the last ETG is taken from Boizelle et al. (2019) who measured M_{BH} using gas dynamics.

Data for 44 of the 49 LTGs (spiral galaxies) is taken from Davis et al. (2018a) and Davis et al. (2019a), where they also present the M_{BH}–$M_{*,sph}$, M_{BH}–$M_{*,disk}$, and M_{BH}–$M_{*,gal}$ relations for spiral galaxies based on predominantly NIR imaging and multi-component decompositions. Out of the remaining five LTGs, four are taken from Combes et al. (2019), and one from Nguyen et al. (2020), where the central SMBH masses have been measured using gas dynamics.

Our galaxy sample is listed in Table 3.1, which includes information on the galaxy type, distance, updated morphology, presence of a bar, disk, depleted stellar core, AGN, M_{BH}, and the central stellar velocity dispersion. The morphologies reflect the presence, or not, of an intermediate or large-scale disk, and also bar, with types designated by the morphological galaxy classification grid given by Graham (2019a).

The velocity dispersion has been measured in many ways in literature, for example: luminosity-weighted line-of-sight stellar velocity dispersion within one effective radius ($R_{e,sph}$) of the spheroid $\sigma_{e,sph}$ (e.g., Gebhardt et al., 2000); luminosity-weighted line-of-sight stellar rotation and velocity dispersion (added in quadrature) within one effective radius of either the spheroid ($R_{e,sph}$) or the whole galaxy ($R_{e,gal}$) (Gültekin et al., 2009b); or velocity dispersions within an aperture of radius equal to one-eighth [5] of $R_{e,sph}$, $\sigma_{e/8}$ (e.g., Ferrarese & Merritt, 2000).

It should be noted that the effective radius of the spheroid and the effective radius of the whole galaxy are, in general, different quantities. Velocity dispersions measured using an aperture size equal to the effective radius of a galaxy is highly prone to contamination from the kinematics of the stellar disk in those galaxies with a (large-scale or intermediate-scale) disk. Whereas, studies (e.g., Gültekin et al., 2009a) which use the luminosity-weighted

[5]The velocity dispersion measurements available in Sloan Digital Sky Survey (SDSS) database use this aperture size.

average of both the stellar rotation and the velocity dispersion certainly represent a biased velocity dispersion. The use of the effective radius of the spheroid (bulge) as a scale of aperture size is also precarious as the measured velocity dispersion may also have contributions from the disk. Moreover, $R_{e,sph}$ does not have any physical significance, see Graham (2019b) for a detailed study on $R_{e,sph}$. The introduction of radii containing 50% of the light reflects an arbitrary and physically meaningless percentage. The use of a different percentage, x, results in R_e/R_x ratios that systematically change with luminosity, and in turn σ_e/σ_x changes. There is nothing physically meaningful with σ_e, and M_{BH}–σ_x relations are a function of the arbitrary percentage x.

Bennert et al. (2015, their Figure 1) compare velocity dispersions based on different aperture sizes ($R_{e,sph}, R_{e,sph}/8, R_{e,gal}$) and conclude that different methods may produce velocity dispersion values different by up to 40%. However, for most of their sample, the agreement between σ_{SDSS} (aperture size $R_{e,sph}/8$) and their $\sigma_{e,sph}$ (aperture size $R_{e,sph}$) values is much better than 40%. The radial variation of aperture velocity dispersions are a weak function of radius for ETGs, e.g., $\sigma_R = \sigma_e \times (R/R_e)^{-0.04}$ (Jorgensen et al., 1995), and $\sigma_R = \sigma_e \times (R/R_e)^{-0.066}$ (Cappellari et al., 2006). These empirical relations explain the reasonable agreement between σ based on different apertures, however this might be true only for simple ETGs. Whereas for multi-component (barred-ETG, spiral) galaxies, σ measurements are more complicated and large aperture sizes can introduce significant errors.

Given the inconsistency in the use of aperture size and contamination due to both disk rotation and velocity dispersion when using a large aperture size, we use the central velocity dispersion. Moreover, such data exists. The central velocity dispersions for the majority of our galaxies are taken from the HyperLeda database[6] (Paturel et al., 2003), as of October 2019. Galaxies for which we obtained velocity dispersions from other sources are indicated in Table 3.1. Velocity dispersions obtained from the HyperLeda database are homogenized for a uniform aperture size of $0.595\,\mathrm{h}^{-1}$ kpc.

A source of error in the measured central velocity dispersions is broad line region (BLR) emission from AGNs and the movement of stars within the central black hole's sphere-of-influence. However, as our central velocity dispersions are based on an aperture

[6] `http://leda.univ-lyon1.fr/leda/param/vdis.html`

size a few hundred times the typical radial extent of the sphere-of-influence, which is a few parsecs, the contamination in the luminosity-weighted velocity dispersion will be minimal.

In the past, velocity dispersion observations have been obtained using long-slit spectroscopy. Nowadays, we can get better measurements using integral field spectrographs equipped with Integral Field Units (IFUs), where a spatially resolved 2D spectrum gives an accurate measurement of the stellar velocity dispersion of a galaxy. However, this measurement is not available for most of our galaxy sample; hence, we proceed with the central velocity dispersion measurements available on HyperLeda.

For the majority of galaxies in our sample, the uncertainty in the velocity dispersion reported by HyperLeda is $\lesssim 10\%$. Given that seeing and slit orientation can influence the measured velocity dispersion, we use a constant uncertainty of 10%, whereas, for M_{BH}, we use the errors provided by the references, listed in Table 3.1. In addition, we check the robustness of our M_{BH}–σ relations by using a 5% to 15% uncertainty on σ.

Table 3.1. Galaxy Sample

Galaxy	Type	Distance (Mpc)	Morph	Bar	Disk	Core	AGN	$\log(M_{BH}/M_{\odot})$ (dex)	Source	$\log(\sigma/\mathrm{km\,s^{-1}})$ (dex)
(1)	(2)	(3)	(4)	(5)	(6)	(7)	(8)	(9)	(10)	(11)
IC 1459	ETG	28.4	E	no	no	yes	yes	9.38 ± 0.20[S]	SG(2016)	2.47
NGC 0821	ETG	23.4	E	no	no	no	no	7.59 ± 0.17[S]	SG(2016)	2.30
NGC 1023	ETG	11.1	S0-bar	yes	yes	no	no	7.62 ± 0.05[S]	SG(2016)	2.29
NGC 1316	ETG	18.6	SAB0 (merger)	yes	yes	no	no	8.18 ± 0.26[S]	SG(2016)	2.35
NGC 1332	ETG	22.3	ES	no	yes	no	no	9.16 ± 0.07[S]	SG(2016)	2.47
NGC 1399	ETG	19.4	E	no	no	yes	no	8.67 ± 0.06[S]	SG(2016)	2.52
NGC 2549	ETG	12.3	S0	yes	yes	no	no	7.15 ± 0.60[S]	SG(2016)	2.15
NGC 2778	ETG	22.3	S0	yes	yes	no	no	7.18 ± 0.34[S]	SG(2016)	2.19
NGC 3091	ETG	51.2	E	no	no	yes	no	9.56 ± 0.04[S]	SG(2016)	2.49
NGC 3115	ETG	9.4	S0	no	yes	no	no	8.94 ± 0.25[S]	SG(2016)	2.42
NGC 3245	ETG	20.3	S0	yes	yes	no	no	8.30 ± 0.12[G]	SG(2016)	2.32
NGC 3377	ETG	10.9	E	no	no	no	no	7.89 ± 0.04[S]	SG(2016)	2.13
NGC 3379 (M 105)	ETG	10.3	E	no	no	yes	no	8.60 ± 0.12[S]	SG(2016)	2.31
NGC 3384[a]	ETG	11.3	S0	yes	yes	no	no	7.23 ± 0.05[S]	SG(2016)	2.16
NGC 3414	ETG	24.5	E	no	no	no	no	8.38 ± 0.06[S]	SG(2016)	2.38
NGC 3489[a]	ETG	11.7	S0	yes	yes	no	no	6.76 ± 0.07[S]	SG(2016)	2.02
NGC 3585	ETG	19.5	E	no	no	no	no	8.49 ± 0.13[S]	SG(2016)	2.33
NGC 3607	ETG	22.2	E	no	no	no	yes	8.11 ± 0.18[S]	SG(2016)	2.35
NGC 3608	ETG	22.3	E	no	no	yes	no	8.30 ± 0.18[S]	SG(2016)	2.29
NGC 3842	ETG	98.4	E	no	no	yes	no	9.99 ± 0.13[S]	SG(2016)	2.49
NGC 3998	ETG	13.7	S0	yes	yes	no	yes	8.91 ± 0.11[S]	SG(2016)	2.42
NGC 4261	ETG	30.8	E	no	no	yes	yes	8.70 ± 0.09[S]	SG(2016)	2.47
NGC 4291	ETG	25.5	E	no	no	yes	no	8.52 ± 0.36[S]	SG(2016)	2.47
NGC 4374 (M 84)	ETG	17.9	E	no	no	yes	yes	8.95 ± 0.05[S]	SG(2016)	2.44
NGC 4459	ETG	15.7	S0	no	yes	no	no	7.83 ± 0.09[G]	SG(2016)	2.24
NGC 4472 (M 49)	ETG	17.1	E	no	no	yes	yes	9.40 ± 0.05[S]	SG(2016)	2.45
NGC 4473	ETG	15.3	E	no	no	no	no	8.08 ± 0.36[S]	SG(2016)	2.25
NGC 4486 (M 87)	ETG	16.8	E	no	no	yes	yes	9.81±0.05[DI][b]	SG(2016)	2.51
NGC 4564	ETG	14.6	S0	no	yes	no	no	7.78 ± 0.06[S]	SG(2016)	2.19
NGC 4596	ETG	17.0	S0	yes	yes	no	no	7.90 ± 0.20[G]	SG(2016)	2.15
NGC 4621 (M 59)	ETG	17.8	E	no	no	no	no	8.59 ± 0.05[S]	SG(2016)	2.36
NGC 4697	ETG	11.4	E	no	no	no	no	8.26 ± 0.05[S]	SG(2016)	2.22
NGC 4889	ETG	103.2	E	no	no	yes	no	10.32 ± 0.44[S]	SG(2016)	2.59
NGC 5077	ETG	41.2	E	no	no	yes	yes	8.87 ± 0.22[G]	SG(2016)	2.40
NGC 5128	ETG	3.8	S0 (merger)	no	yes	no	no	7.65±0.13[SG]	SG(2016)	2.01
NGC 5576	ETG	24.8	E	no	no	no	no	8.20 ± 0.10[S]	SG(2016)	2.26
NGC 5846	ETG	24.2	E	no	no	yes	no	9.04 ± 0.05[S]	SG(2016)	2.38
NGC 6251	ETG	104.6	E	no	no	yes	yes	8.77 ± 0.16[G]	SG(2016)	2.49
NGC 7619	ETG	51.5	E	no	no	yes	no	9.40 ± 0.09[S]	SG(2016)	2.50
NGC 7768	ETG	112.8	E	no	no	yes	no	9.11 ± 0.15[S]	SG(2016)	2.46
NGC 1271	ETG	80.0	ES	no	yes	no	no	9.48 ± 0.16[S]	GCS(2016)	2.44 [11a]
NGC 1277	ETG	72.5	ES	no	yes	no	no	9.08 ± 0.12[S]	G+7(2016)	2.48 [11b]
A1836 BCG	ETG	158.0	E	no	no	yes	no	9.59 ± 0.06[G]	SGD(2019)	2.49 [11c]
A3565 BCG (IC 4296)	ETG	40.7	E	no	no	no	yes	9.04 ± 0.09[G]	SGD(2019)	2.52
Mrk 1216	ETG	94.0	S0	no	yes	no	yes	9.69 ± 0.16[S]	SGD(2019)	2.51
NGC 0307	ETG	52.8	SAB0	yes	yes	no	no	8.34 ± 0.13[S]	SGD(2019)	2.43

Table 3.1 (cont'd)

Galaxy (1)	Type (2)	Distance (Mpc) (3)	Morph (4)	Bar (5)	Disk (6)	Core (7)	AGN (8)	$\log(M_{BH}/M_{\odot})$ (dex) (9)	Source (10)	$\log(\sigma/\mathrm{km\,s^{-1}})$ (dex) (11)
NGC 0404	ETG	3.1	S0	no	yes	no	no	4.85 ± 0.13[S]	SGD(2019)	1.54
NGC 0524	ETG	23.3	SA0(rs)	no	yes	yes	no	8.92 ± 0.10[S]	SGD(2019)	2.37
NGC 1194	ETG	53.2	S0 (merger?)	no	yes	no	yes	7.81 ± 0.04[M]	SGD(2019)	2.17 [11d]
NGC 1275	ETG	72.9	E	no	no	no	yes	8.90 ± 0.20[G]	SGD(2019)	2.39
NGC 1374	ETG	19.2	S0	no	yes	no	no	8.76 ± 0.05[S]	SGD(2019)	2.25
NGC 1407	ETG	28.0	E	no	no	yes	no	9.65 ± 0.08[S]	SGD(2019)	2.42
NGC 1550	ETG	51.6	E	no	no	yes	no	9.57 ± 0.06[S]	SGD(2019)	2.48
NGC 1600	ETG	64.0	E	no	no	yes	no	10.23 ± 0.05[S]	SGD(2019)	2.52
NGC 2787[a]	ETG	7.3	SB0(r)	yes	yes	no	yes	7.60 ± 0.06[G]	SGD(2019)	2.28
NGC 3665	ETG	34.7	S0	no	yes	no	no	8.76 ± 0.10[G]	SGD(2019)	2.33
NGC 3923	ETG	20.9	E	no	no	yes	no	9.45 ± 0.13[S]	SGD(2019)	2.39
NGC 4026	ETG	13.2	SB0	yes	yes	no	no	8.26 ± 0.11[S]	SGD(2019)	2.24
NGC 4339	ETG	16.0	S0	no	yes	no	no	7.63 ± 0.33[S]	SGD(2019)	2.05
NGC 4342	ETG	23.0	ES	no	yes	no	no	8.65 ± 0.18[S]	SGD(2019)	2.38
NGC 4350	ETG	16.8	EBS	yes	yes	no	no	8.86 ± 0.41[SG]	SGD(2019)	2.26
NGC 4371[a]	ETG	16.9	SB(r)0	yes	yes	no	no	6.85 ± 0.08[S]	SGD(2019)	2.11
NGC 4429	ETG	16.5	SB(r)0	yes	yes	no	no	8.18 ± 0.09[G]	SGD(2019)	2.24
NGC 4434	ETG	22.4	S0	no	yes	no	no	7.85 ± 0.17[S]	SGD(2019)	2.07
NGC 4486B	ETG	15.3	E	no	no	no	no	8.76 ± 0.24[S]	SGD(2019)	2.22
NGC 4526	ETG	16.9	S0	no	yes	no	no	8.67 ± 0.05[G]	SGD(2019)	2.35
NGC 4552	ETG	14.9	E	no	no	no	yes	8.67 ± 0.05[S]	SGD(2019)	2.40
NGC 4578	ETG	16.3	S0(r)	no	yes	no	no	7.28 ± 0.35[S]	SGD(2019)	2.05
NGC 4649	ETG	16.4	E	no	no	yes	no	9.67 ± 0.10[S]	SGD(2019)	2.52
NGC 4742	ETG	15.5	S0	no	yes	no	no	7.15 ± 0.18[S]	SGD(2019)	2.01
NGC 4751	ETG	26.9	S0	no	yes	yes	no	9.15 ± 0.05[S]	SGD(2019)	2.54
NGC 4762	ETG	22.6	SB0	yes	yes	no	no	7.36 ± 0.15[S]	SGD(2019)	2.15
NGC 5018	ETG	40.6	S0 (merger)	no	yes	no	no	8.02 ± 0.09[S]	SGD(2019)	2.33
NGC 5252	ETG	96.8	S0	no	yes	no	yes	9.00 ± 0.40[G]	SGD(2019)	2.27
NGC 5328	ETG	64.1	E	no	no	yes	no	9.67 ± 0.15[S]	SGD(2019)	2.50
NGC 5419	ETG	56.2	E	no	no	yes	no	9.86 ± 0.14[S]	SGD(2019)	2.54
NGC 5516	ETG	58.4	E	no	no	yes	no	9.52 ± 0.06[S]	SGD(2019)	2.49
NGC 5813	ETG	31.3	S0	no	yes	yes	no	8.83 ± 0.06[S]	SGD(2019)	2.37
NGC 5845	ETG	25.2	ES	no	yes	no	no	8.41 ± 0.22[S]	SGD(2019)	2.36
NGC 6086	ETG	138.0	E	no	no	yes	no	9.57 ± 0.17[S]	SGD(2019)	2.51
NGC 6861	ETG	27.3	ES	no	yes	no	no	9.30 ± 0.08[S]	SGD(2019)	2.59
NGC 7052	ETG	66.4	E	no	no	yes	no	8.57 ± 0.23[G]	SGD(2019)	2.45
NGC 7332	ETG	24.9	SB0	yes	yes	no	no	7.11 ± 0.20[S]	SGD(2019)	2.11
NGC 7457	ETG	14.0	S0	no	yes	no	no	7.00 ± 0.30[S]	SGD(2019)	1.83
NGC 4486A	ETG	13.9	E	no	no	no	no	7.10 ± 0.32[S]	No+7(2007)	2.12
NGC 5102	ETG	3.2	S0	no	yes	no	no	5.94 ± 0.38[S]	Ngu+10(2018)	1.79
NGC 5206	ETG	3.5	dE/dS0	no	no?	no	no	5.67 ± 0.36[S]	Ngu+10(2018)	1.62
NGC 0584	ETG	19.1	S0	no	yes	yes	no	8.11 ± 0.18[S]	Th+6(2019)	2.33 [11e]
NGC 2784	ETG	9.6	S0	no	yes	no	no	8.00 ± 0.31[S]	Th+6(2019)	2.39 [11e]
NGC 3640	ETG	26.3	E	no	no	yes	no	7.89 ± 0.34[S]	Th+6(2019)	2.24 [11e]
NGC 4281	ETG	24.4	S0	no	yes	no	no	8.73 ± 0.08[S]	Th+6(2019)	2.50 [11e]
NGC 4570	ETG	17.1	S0	no	yes	no	no	7.83 ± 0.14[S]	Th+6(2019)	2.32 [11e]

Table 3.1 (cont'd)

Galaxy (1)	Type (2)	Distance (Mpc) (3)	Morph (4)	Bar (5)	Disk (6)	Core (7)	AGN (8)	$\log(M_{BH}/M_\odot)$ (dex) (9)	Source (10)	$\log(\sigma/\mathrm{km\,s^{-1}})$ (dex) (11)
NGC 7049	ETG	29.9	S0	no	yes	no	no	8.51 ± 0.12[S]	Th+6(2019)	2.42 [11e]
NGC 3258	ETG	31.3	E	no	no	yes	no	9.35 ± 0.05[G]	Bo+7(2019)	2.41
IC 1481	ETG	89.9	E? (merger)	...	...	...	...	7.15 ± 0.13[S]	Hu+4(2011)	...
NGC 3706	ETG	46	S0	no	yes	yes	no	8.78 ± 0.06[S]	Gu+6(2014)	2.41
Circinus[a]	LTG	4.2	SABb	no	yes	no	yes	6.25 ± 0.11[M]	DGC(2019)	2.17
Cygnus A	LTG	258.8	S	no	yes	no	yes	9.44 ± 0.13[G]	DGC(2019)	2.43 [11f]
ESO558-G009[a]	LTG	115.4	Sbc	no	yes	no	no	7.26 ± 0.04[M]	DGC(2019)	2.23 [11g]
IC 2560[a]	LTG	31.0	SBb	yes	yes	no	yes	6.49 ± 0.20[M]	DGC(2019)	2.14
J0437+2456[a]	LTG	72.8	SB	yes	yes	no	no	6.51 ± 0.05[M]	DGC(2019)	2.04 [11g]
Milky Way[a]	LTG	7.9	SBbc	yes	yes	no	no	6.60 ± 0.02[P]	DGC(2019)	2.02 [11f]
Mrk 1029[a]	LTG	136.9	S	no	yes	no	no	6.33 ± 0.12[M]	DGC(2019)	2.12 [11g]
NGC 0224	LTG	0.8	SBb	yes	yes	no	no	8.15 ± 0.16[S]	DGC(2019)	2.19
NGC 0253[a]	LTG	3.5	SABc	yes	yes	no	no	7.00 ± 0.30[G]	DGC(2019)	1.98
NGC 1068[a]	LTG	10.1	SBb	yes	yes	no	yes	6.75 ± 0.08[M]	DGC(2019)	2.21
NGC 1097[a]	LTG	24.9	SBb	yes	yes	no	yes	8.38 ± 0.04[G]	DGC(2019)	2.29 [11h]
NGC 1300[a]	LTG	14.5	SBbc	yes	yes	no	no	7.71 ± 0.16[G]	DGC(2019)	2.34
NGC 1320[a]	LTG	37.7	Sa	no	yes	no	no	6.78 ± 0.29[M]	DGC(2019)	2.04
NGC 1398	LTG	24.8	SBab	yes	yes	no	no	8.03 ± 0.11[S]	DGC(2019)	2.29
NGC 2273[a]	LTG	31.6	SBa	yes	yes	no	no	6.97 ± 0.09[M]	DGC(2019)	2.15
NGC 2748[a]	LTG	18.2	Sbc	no	yes	no	no	7.54 ± 0.21[G]	DGC(2019)	1.98
NGC 2960[a]	LTG	71.1	Sa (merger)	no	yes	no	no	7.06 ± 0.17[M]	DGC(2019)	2.22 [11i]
NGC 2974	LTG	21.5	SB	yes	yes	no	yes	8.23 ± 0.07[S]	DGC(2019)	2.37
NGC 3031	LTG	3.5	SABab	no	yes	no	no	7.83 ± 0.09[G]	DGC(2019)	2.18
NGC 3079[a]	LTG	16.5	SBcd	yes	yes	no	yes	6.38 ± 0.12[M]	DGC(2019)	2.24
NGC 3227[a]	LTG	21.1	SABa	yes	yes	no	yes	7.88 ± 0.14[SG]	DGC(2019)	2.10
NGC 3368[a]	LTG	10.7	SABa	yes	yes	no	no	6.89 ± 0.09[SG]	DGC(2019)	2.07
NGC 3393[a]	LTG	55.8	SBa	yes	yes	no	yes	7.49 ± 0.05[M]	DGC(2019)	2.30
NGC 3627[a]	LTG	10.6	SBb	yes	yes	no	yes	6.95 ± 0.05[S]	DGC(2019)	2.10
NGC 4151	LTG	19.0	SABa	yes	yes	no	yes	7.68 ± 0.37[SG]	DGC(2019)	1.96
NGC 4258	LTG	7.6	SABb	yes	yes	no	yes	7.60 ± 0.01[M]	DGC(2019)	2.12
NGC 4303[a]	LTG	12.3	SBbc	yes	yes	no	yes	6.58 ± 0.17[G]	DGC(2019)	1.98
NGC 4388[a]	LTG	17.8	SBcd	yes	yes	no	yes	6.90 ± 0.11[M]	DGC(2019)	2.00
NGC 4395	LTG	4.8	SBm	yes	yes	no	yes	5.64 ± 0.17[G]	DGC(2019)	1.42
NGC 4501[a]	LTG	11.2	Sb	no	yes	no	yes	7.13 ± 0.08[S]	DGC(2019)	2.22
NGC 4594	LTG	9.6	Sa	no	yes	no	yes	8.81 ± 0.03[S]	DGC(2019)	2.35
NGC 4699[a]	LTG	23.7	SABb	yes	yes	no	no	8.34 ± 0.10[S]	DGC(2019)	2.28
NGC 4736[a]	LTG	4.4	SABab	no	yes	no	yes	6.78 ± 0.10[S]	DGC(2019)	2.03
NGC 4826[a]	LTG	5.6	Sab	no	yes	no	yes	6.07 ± 0.15[S]	DGC(2019)	1.99
NGC 4945[a]	LTG	3.7	SABc	no	yes	no	yes	6.15 ± 0.30[M]	DGC(2019)	2.07
NGC 5055[a]	LTG	8.9	Sbc	no	yes	no	no	8.94 ± 0.10[G]	DGC(2019)	2.00
NGC 5495[a]	LTG	101.1	SBc	yes	yes	no	no	7.04 ± 0.08[M]	DGC(2019)	2.22 [11g]
NGC 5765b[a]	LTG	133.9	SABb	yes	yes	no	no	7.72 ± 0.05[M]	DGC(2019)	2.21 [11g]
NGC 6264[a]	LTG	153.9	SBb	yes	yes	no	yes	7.51 ± 0.06[M]	DGC(2019)	2.20 [11f]
NGC 6323[a]	LTG	116.9	SBab	yes	yes	no	no	7.02 ± 0.14[M]	DGC(2019)	2.20 [11f]
NGC 6926[a]	LTG	86.6	SBc	yes	yes	no	yes	7.74 ± 0.50[M]	DGC(2019)	...
NGC 7582[a]	LTG	19.9	SBab	yes	yes	no	yes	7.67 ± 0.09[G]	DGC(2019)	2.07

Table 3.1 (cont'd)

Galaxy (1)	Type (2)	Distance (Mpc) (3)	Morph (4)	Bar (5)	Disk (6)	Core (7)	AGN (8)	$\log(M_{BH}/M_{\odot})$ (dex) (9)	Source (10)	$\log(\sigma/\mathrm{km\,s^{-1}})$ (dex) (11)
UGC 3789[a]	LTG	49.6	SABa	yes	yes	no	no	7.06 ± 0.05[M]	DGC(2019)	2.03 [11f]
UGC 6093[a]	LTG	152.8	SBbc	yes	yes	no	no	7.41 ± 0.03[M]	DGC(2019)	2.19 [11f]
NGC 0613[a]	LTG	17.2	SB(rs)bc	yes	yes	no	no	7.57 ± 0.15[G]	Co+14(2019)	2.09
NGC 1365[a]	LTG	17.8	SB(s)b	yes	yes	no	yes	6.60 ± 0.30[G]	Co+14(2019)	2.15
NGC 1566[a]	LTG	7.2	SAB(s)bc	yes	yes	no	yes	6.83 ± 0.30[G]	Co+14(2019)	1.99
NGC 1672[a]	LTG	11.4	SB(s)b	yes	yes	no	yes	7.70 ± 0.10[G]	Co+14(2019)	2.04
NGC 3504	LTG	13.6	SABab	yes	yes	no	yes	7.01 ± 0.07[G]	Ngu+10(2019)	2.08

Note. — Column: (1) Galaxy name. (2) Galaxy type: early-type or late-type. (3) Distance to the galaxy. (4) Galaxy Morphology. (5) Presence of bar. (6) Presence of a rotating intermediate-scale (ES) or large-scale (S0/Sp) disk. (7) Presence of a depleted stellar core. (8) Presence of active galactic nucleus. (9) Directly measured black hole mass along with measurement method indicated by [P]= proper motion, [S]= stellar-dynamical modeling, [G]= gas dynamical modeling, [SG]= stellar and gas dynamical modeling, [M]= megamaser kinematics, and [DI]= direct imaging. (10) Catalog references, where the information for column (2) to column (9) comes from SG(2016)= Savorgnan et al. (2016), GCS(2016)= Graham et al. (2016a), G+7(2016)= Graham et al. (2016b), SGD(2019)= Sahu et al. (2019a), No+7(2007)= (Nowak et al., 2007), Ngu+10(2018)= Nguyen et al. (2018), Th+6(2019)= Thater et al. (2019), Bo+7(2019)= Boizelle et al. (2019), Hu+4(2011)= Huré et al. (2011), Gu+6(2014)= Gültekin et al. (2014), DGC(2019)= Davis et al. (2019a), Co+14(2019)= Combes et al. (2019), and Ngu+10(2019)=Nguyen et al. (2020). (11) Central velocity dispersion of galaxies mostly archived in Hyperleda (Paturel et al., 2003) unless otherwise specified: [11a]= Walsh et al. (2015); [11b]= Graham et al. (2016b), [11c]= Dalla Bontà et al. (2009); [11d]=Greene et al. (2010); [11e]=Thater et al. (2019); [11f]=Kormendy & Ho (2013); [11g]= Greene et al. (2016), [11h]= van den Bosch (2016); [11i]= Saglia et al. (2016). Bulge and galaxy stellar masses can also be found in Savorgnan & Graham (2016b); Davis et al. (2019a); and Sahu et al. (2019a).

[a]Alleged to host a pseudo-bulge according to Kormendy & Ho (2013), Saglia et al. (2016), and the references mentioned in Table 1 of Davis et al. (2017). NGC 0613, NGC 1365, NGC 1566, and NGC 1672 are claimed to have pseudo-bulges by Combes et al. (2019).

[b]Latest black hole mass measurement from the Event Horizon Telescope Collaboration through direct imaging (Event Horizon Telescope Collaboration et al., 2019).

3.3 M_{BH}–σ Relations

In this work, we use both the BCES[7] (Akritas & Bershady, 1996) routine and the bisector line from the modified FITEXY (Press et al., 1992) routine (MPFITEXY, Tremaine et al., 2002; Novak et al., 2006; Bedregal et al., 2006; Williams et al., 2010; Markwardt, 2012) to establish the M–σ relations. Both the BCES and MPFITEXY regression routines take into account the measurement errors in the X and Y coordinates and allow for intrinsic scatter in the data.

The BCES routine directly provides the forward regression BCES($Y|X$) line, the inverse regression BCES($X|Y$) line, and the regression line which symmetrically bisects the two, i.e., BCES(Bisector)[8]. However, to obtain a symmetrical treatment (MPFITEXY(bisector)) of the data with the MPFITEXY routine requires averaging the inclination of the best-fit lines obtained from the forward (MPFITEXY($Y|X$)) and inverse (MPFITEXY($X|Y$)) regressions as explained in Novak et al. (2006).

[7]The BCES routine was used via the PYTHON module written by Rodrigo Nemmen (Nemmen et al., 2012), which is available at `https://github.com/rsnemmen/BCES`.

[8]BCES($Y|X$) minimizes the offsets in the Y-direction, and BCES($X|Y$) minimizes, the offsets in the X-direction.

We prefer the symmetric (bisector) regressions obtained from both the routines because we do not know whether the central SMBH mass fundamentally governs the central velocity dispersion of a galaxy or vice-versa, or indirectly through a third parameter. A symmetrical regression is also preferable for theoretical grounds, see Novak et al. (2006).

In our plots, we show the BCES(Bisector) regression line. These are also presented in Table 3.2. In addition, asymmetric (BCES($Y|X$) and BCES($X|Y$)) regression parameters are also provided in the Appendix B (Table B.1). We do not provide the MPFITEXY parameters for our relations as these were found to always be consistent with the parameters obtained from the BCES routine within the $\pm 1\sigma$ confidence limits.

3.3.1 Galaxy Exclusions

We identify and exclude the following eight galaxies which may bias the M_{BH}–σ relation: NGC 404; NGC 5102; NGC 5206; NGC 7457; IC 1481; NGC 4395; NGC 5055; and NGC 6926; where the last three galaxies are LTGs.

NGC 404 is the only galaxy anchoring the intermediate black hole mass end ($\lesssim 10^5 M_\odot$) of the relation, as such it may bias the best-fit line. Additionally, as we will see, NGC 404, NGC 5102, and NGC 5206, for whom we obtained black hole masses from the same group (Nguyen et al., 2017, 2018), all seem to lie above the M_{BH}–σ relation defined by the remaining galaxies. As we have only a four galaxies (NGC 404, NGC 5102, NGC 5206, and NGC 4395) with $M_{BH} \lesssim 10^6 M_\odot$ (as can be seen in Figure 3.1 and further in the left-hand panel of Figure 3.2), we do not include them in our primary regressions. As noted above, this also helps us detect possible departures at the low-mass end.

NGC 7457 has an unusually low-velocity dispersion, possibly because of a counter-rotating core (Molaeinezhad et al., 2019), which makes it fall beyond the $\pm 2\sigma$ scatter bounds of our single regression relation. Similarly, NGC 4395 and NGC 5055 have lower velocity-dispersion values than expected from the M_{BH}–σ relation defined by the bulk of the sample, which makes them stand out from the, soon to be seen, best-fit lines. These three (NGC 7457, NGC 4395, and NGC 5055) outlying galaxies significantly affect our best-fit lines; hence we exclude them from our regressions in order to obtain more stable relations reflective of the majority of the population.

For IC 1481 and NGC 6926, we do not have a reliable measurement of their central velocity dispersion. We have also provided regression parameters including all excluded galaxies (except IC 1481 and NGC 6926) in Table B.2 of the Appendix B to show how much these few galaxies bias our best-fit lines. Overall, we exclude a total of 8 galaxies, which leaves us with a reduced sample of 137 galaxies.

In our reduced sample, five galaxies (NGC 1316, NGC 2960, NGC 5128, NGC 5018, and NGC 1194) are mergers identified by Kormendy & Ho (2013, their section 6.4), Saglia et al. (2016), and Sahu et al. (2019a, see the light profile of NGC 1194 and references). A merger designation refers to the stage when a galaxy is yet to reach a relaxed (stable) post merger configuration. Kormendy & Ho (2013) suggest excluding mergers from the black hole scaling relations as they may bias the results. However, given the small number of mergers in our sample, and given that they are not (significant) outliers in the M_{BH}–σ relations, we include them.

Additionally, NGC 4342 (Blom et al., 2014) and NGC 4486B (Batcheldor et al., 2010) are tidally stripped of their stellar mass by the gravitational pull of their massive companion galaxies NGC 4365 and NGC 4486 (M87), respectively. However, stripping of the outer stellar mass should not considerably affect the central stellar velocity dispersions, hence we also include these galaxies in our M_{BH}–σ relations. These seven (mergers and stripped) galaxies are displayed with a different color (yellow star) in our Figure 3.1, to show that these galaxies are neither significant outliers nor do they bias the relation. Excluding these mergers and stripped galaxies changes the slope and intercept of the best-fit-lines on an average by 1% and 0.1%, respectively, which is insignificant compared to the error bars on the slopes and intercepts.

In what follows, we divided our reduced sample of 137 galaxies into various categories, for example, early-type and late-type galaxies, Sérsic and core-Sérsic galaxies, galaxies with and without a disk, galaxies with and without a bar, and galaxies with and without an AGN. The following subsections describe the scaling relations obtained for these sub-morphological classes.

3.3.2 Early-type Galaxies and Late-type Galaxies

After excluding the eight galaxies mentioned in Section 3.3.1, our reduced sample is comprised of 91 ETGs and 46 LTGs[9]. The BCES(Bisector) regression line for the ETGs can be expressed as,

$$\log(M_{BH}/M_{\odot}) = (5.71 \pm 0.33) \log\left(\frac{\sigma}{200\,\mathrm{km\,s^{-1}}}\right) + (8.32 \pm 0.05), \tag{3.1}$$

with a total rms scatter of $\Delta_{rms|BH} = 0.44$ dex in the $\log M_{BH}$-direction. The relation followed by the LTGs can be formulated as,

$$\log(M_{BH}/M_{\odot}) = (5.82 \pm 0.75) \log\left(\frac{\sigma}{200\,\mathrm{km\,s^{-1}}}\right) + (8.17 \pm 0.14), \tag{3.2}$$

with $\Delta_{rms|BH} = 0.63$ dex. The slopes and intercepts of both lines (see Figure 3.1) are consistent within the $\pm 1\sigma$ confidence limits, suggesting a single M_{BH} versus σ relation for both ETGs and LTGs is adequate. Therefore, we perform a single regression on the total sample of 137 galaxies, which is represented in Figure 3.2. The BCES(Bisector) best-fit line obtained from the single regression can be written as

$$\log(M_{BH}/M_{\odot}) = (6.10 \pm 0.28) \log\left(\frac{\sigma}{200\,\mathrm{km\,s^{-1}}}\right) + (8.27 \pm 0.04), \tag{3.3}$$

with $\Delta_{rms|BH} = 0.53$ dex. However, as we will see in the following subsection, it is deceptive to think that one line is sufficient to understand the connection between supermassive black holes and the stellar velocity dispersion of the host galaxies.

Although we assigned a 10% uncertainty to the measured velocity dispersions, as discussed in Section 3.2, we find consistent results for our regressions when using either 5% or 15% uncertainties on σ, or using the uncertainties provided in HyperLeda and the other corresponding sources (Column 11 of Table 3.1). In addition to the BCES(Bisector) regression line parameters, the slopes and intercepts of the best-fit lines from the BCES($M_{BH}|\sigma$) and BCES($\sigma|M_{BH}$) regressions, along with the scatter, Pearson correlation coefficient, and Spearman rank-order correlation coefficients are presented in Table B.1 in the Appendix

[9] As noted in Section 3.3.1, results including the six of these eight galaxies with velocity dispersions can be found in the Appendix B.

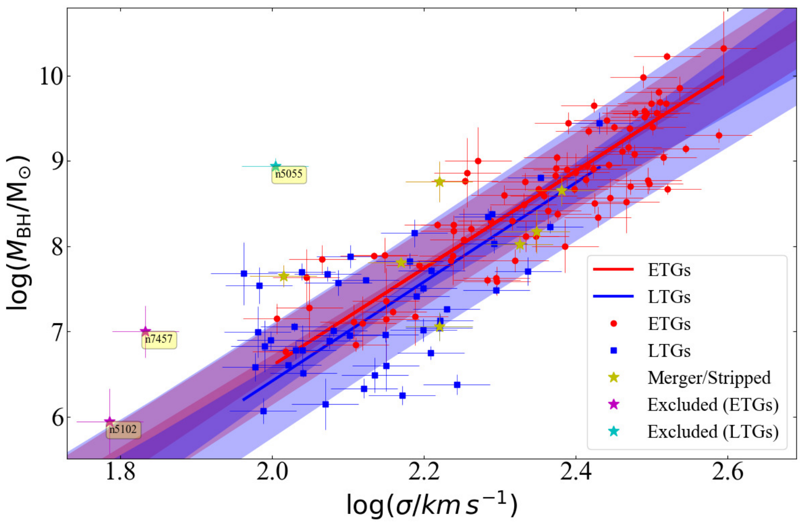

Figure 3.1 Black hole mass versus central velocity dispersion relation followed by 91 ETGs (red circles) and 46 LTGs (blue squares). Dark red and blue lines are the BCES(BISECTOR) best-fit lines for ETGs and LTGs. The red and blue bands around these lines represent the $\pm 1\sigma$ uncertainty limits in their slopes and the intercepts. Furthermore, the light red and light blue shaded regions depict the $\pm 1\sigma$ scatter in the ETG and LTG samples, respectively. The yellow stars represent either merger or stripped galaxies. Labeled data-points represent galaxies excluded from the regressions, as noted in the inset legend. The best-fit lines for the two sub-populations are consistent (Equations 3.1 and 3.2) with each other, suggesting a single M_{BH}–σ relation as shown in Figure 3.2.

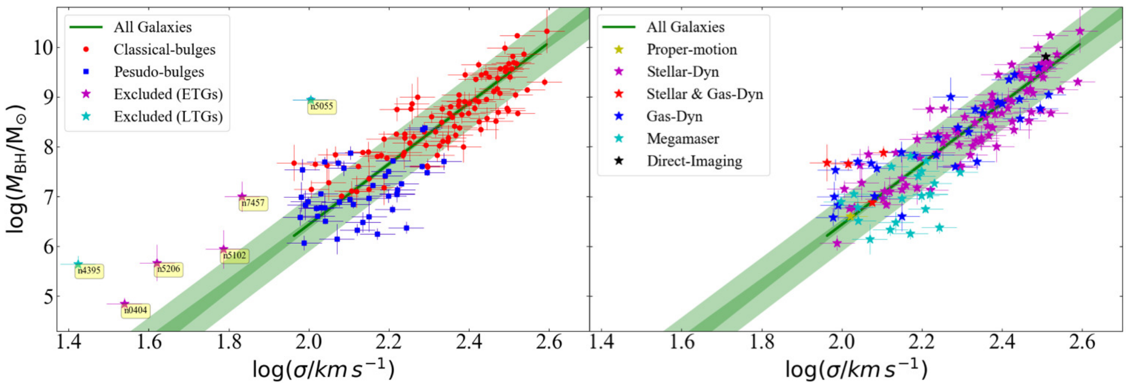

Figure 3.2 Black hole mass versus central velocity dispersion relation obtained from a single regression on the sample of 137 ETGs and LTGs. The dark green line is the best-fit BCES(BISECTOR) regression line (Equation 3.3). The dark green band around the dark green line shows the $\pm 1\sigma$ uncertainty in the slope and intercept of the best-fit line. The light green shaded region represents the $\pm 1\sigma$ scatter in the data. This explanation of the dark and light-shaded regions around the best-fit line applies to all the subsequent figures in this paper. Labeled data-points in the left-hand panel represent all the excluded galaxies except for IC 1481 and NGC 6926, which cannot be included as they have no reliable σ measurements (see Section 3.3.1). The blue squares in the left-hand panel represent the galaxies which are alleged to contain pseudobulges by Kormendy & Ho (2013), Saglia et al. (2016), and the references mentioned in Table 1 of Davis et al. (2017). This plot suggests that pseudobulges do follow the M_{BH}–σ relation similar to classical bulges. Moreover, these pseudobulges are distributed above and below the best-fit line, albeit they are spread over a short range of M_{BH} and σ. Right-hand panel shows the same plot but each galaxy is color coded according to the method used to measure its black hole mass.

B.

In the left hand panel of Figure 3.2, we show the galaxies NGC 404, NGC 5102, NGC 5206, and NGC 4395 which are excluded from our regressions because they are the only data points in the low-mass ($M_{BH} \lesssim 10^6 M_\odot$) range. The first three galaxies are taken from Nguyen et al. (2017, 2018). These galaxies depart from the line defined by galaxies with $M_{BH} \gtrsim 10^6 M_\odot$, perhaps revealing here a bend in the M_{BH}–σ relation not detected by Nguyen et al. (2017, 2018). Including these galaxies in the regression produces a shallower slope of 5.39 ± 0.34 (cf. 6.10 ± 0.28 from Equation 3.3), suggesting these four galaxies may have a significant effect on our best-fit line for the full sample, which is why we decided to exclude them from our regressions.

In the left-hand panel of Figure 3.2, we have additionally highlighted galaxies alleged to have pseudo-bulges by Kormendy & Ho (2013), Saglia et al. (2016), and a few additional studies mentioned in Davis et al. (2017, their Table 1). These pseudo-bulges appear to follow the M_{BH}–σ relation (see Figure 3.2); they are distributed about the best-fit (green) line, though with slightly more scatter than that of galaxies hosting classical bulges. However, given the difficulties in assigning a bulge type (see Footnote 2), it is premature to draw conclusions about the co-evolution or not of black holes in pseudo-bulges.

In a recent work, van den Bosch (2016) fit a single M_{BH}–σ line to all the morphological types of galaxies, and reported $M_{BH} \propto \sigma^{5.35\pm0.23}$, which is shallower than our relation (Equation 3.3). We suspect that their best-fit line may be influenced by the inclusion of a few low-mass dwarf galaxies, the use of upper limits on M_{BH} for many galaxies, and 24 reverberation-mapped black hole mass estimates (pre-calibrated to a prior M_{BH}–σ relation with a slope of 5.31 ± 0.33 from Woo et al., 2013b).

3.3.3 Sérsic and Core-Sérsic Galaxies

Out of the 91 ETGs in our reduced sample, 35 are core-Sérsic, i.e., galaxies which have a deficit of stars at their center relative to the outer Sérsic profile (Graham & Others, 2003), while the remaining 56 ETGs, and all 46 LTGs, are Sérsic galaxies. Core-Sérsic or Sérsic classifications for each of our galaxies are borrowed from their parent works, i.e., Savorgnan et al. (2016), Davis et al. (2019a), and Sahu et al. (2019a), as mentioned in Table 3.1 (Column 10).

We first performed separate regressions for the Sérsic and core-Sérsic ETGs, then on the combined sample of 137 galaxies. The M_{BH}–σ plots for these two divisions are shown in Figure 3.3 and Figure 3.4, respectively.

Sérsic and core-Sérsic categorization reveals two different relations followed by the two sub-populations. The symmetric best-fit line followed by the early-type Sérsic galaxies can be expressed as

$$\log(M_{BH}/M_{\odot}) = (4.95 \pm 0.38) \log\left(\frac{\sigma}{200\,\mathrm{km\,s^{-1}}}\right) + (8.28 \pm 0.06), \tag{3.4}$$

with $\Delta_{rms|BH} = 0.42$ dex, represented by the dark blue line in Figure 3.3. The total Sérsic

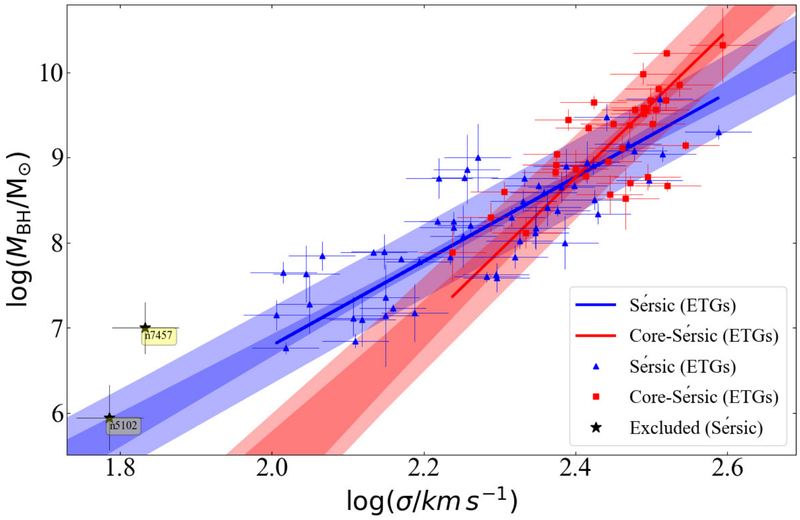

Figure 3.3 Black hole mass versus central velocity dispersion relation for Sérsic (blue triangles) and core-Sérsic (red squares) ETGs. These two sub-populations follow two distinct relations (Equations 3.4 and 3.6), suggesting a broken M_{BH}–σ relation.

population, consisting of 102 early- and late-type Sérsic galaxies, produces the relation

$$\log(M_{BH}/M_\odot) = (5.75 \pm 0.34) \log\left(\frac{\sigma}{200\,\mathrm{km\,s^{-1}}}\right) + (8.24 \pm 0.05), \tag{3.5}$$

represented by the dark blue line in Figure 3.4, with $\Delta_{rms|BH} = 0.55$ dex. The best-fit lines obtained for only early-type Sérsic galaxies and for all the Sérsic galaxies are marginally consistent with each other within the $\pm 1\sigma$ bound of their slopes and intercepts.

However, the core-Sérsic galaxies follow a much steeper M_{BH}–σ relation, with $\Delta_{rms|BH} = 0.46$ dex, as is shown by the dark red lines in both Figures 3.3 and 3.4, which can be expressed as

$$\log(M_{BH}/M_\odot) = (8.64 \pm 1.10) \log\left(\frac{\sigma}{200\,\mathrm{km\,s^{-1}}}\right) + (7.91 \pm 0.20). \tag{3.6}$$

The slope of this line is inconsistent with that of the Sérsic galaxies. The difference in their slopes reveals that Sérsic and core-Sérsic galaxies follow two distinct relations, potentially linked to the evolutionary paths followed by these two type of galaxies, i.e., evolution via major dry-mergers versus gas-rich mergers and accretion events. Additionally, core-Sérsic galaxies follow a steeper relation, that is, their σ values do not appear to saturate or

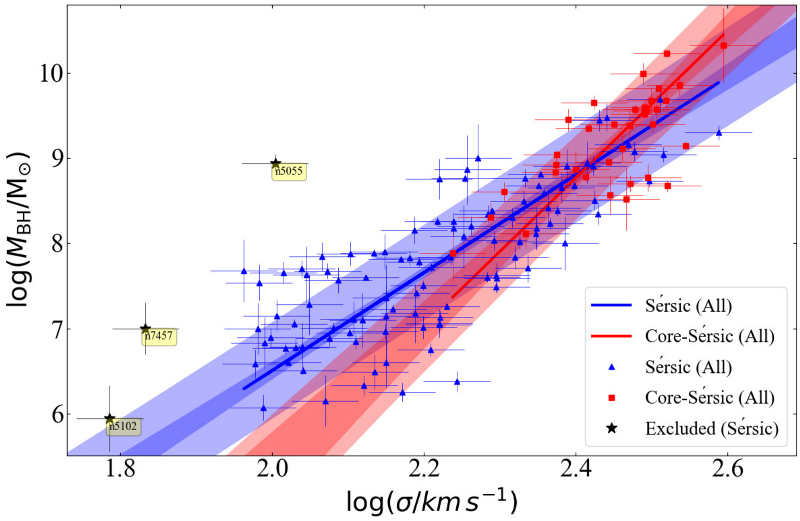

Figure 3.4 Similar to Figure 3.3, but including all early- and late-type Sérsic galaxies in the same category (blue triangles) while all core-Sérsic galaxies (red squares) are early-type galaxies. Upon including the LTGs (spirals) which are all Sérsic galaxies, we still find two different M_{BH}–σ relations followed by the Sérsic and core-Sérsic galaxies (Equations 3.5 and 3.6).

asymptote at the high black hole mass end.

Core-Sérsic galaxies are old, gas-poor, massive galaxies, many of which are BCGs which have undergone multiple major (equal mass) dissipation-less dry-mergers. During a dry-merger, their central SMBHs inspiral, expelling out stars from the center, thereby creating a deficit of light at the core of the resulting galaxy. The stellar mass deficit, relative to the central black hole mass, may be a measure of the number of dry mergers a galaxy has undergone (Merritt & Milosavljević, 2005; Savorgnan & Graham, 2015), with the radial size of the depleted core known to be correlated with the black hole mass (Dullo & Graham, 2014; Thomas et al., 2016; Mehrgan et al., 2019).

The steeper M_{BH}–σ relation for core-Sérsic galaxies reveals that dry mergers do not increase the velocity dispersion, relative to the increased black hole mass, at the pace followed by Sérsic galaxies (built through either gas-rich mergers or accretion of gas from their surroundings). This has also been suggested by some theoretical studies (e.g., Ciotti & van Albada, 2001; Oser et al., 2012; Shankar et al., 2013; Hilz et al., 2013). Furthermore, Volonteri & Ciotti (2013) used their analytical and semi-analytical models to show that simulated BCGs are offset from the M_{BH}–σ relation defined by non-BCGs because they

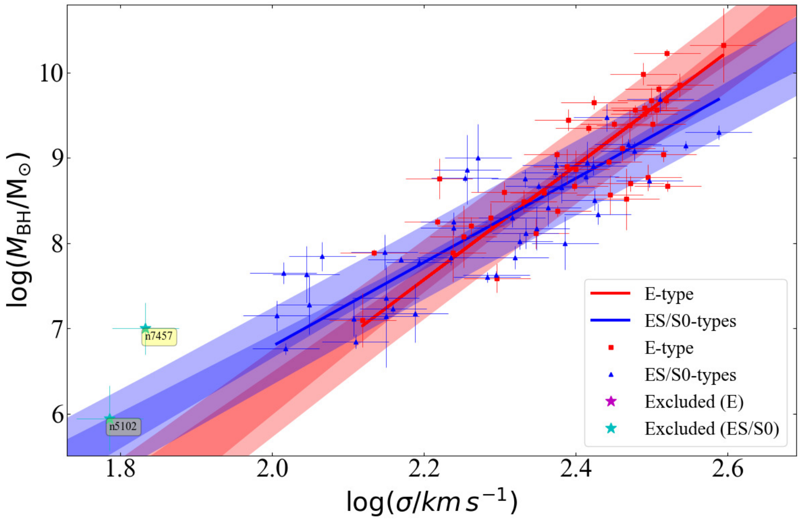

Figure 3.5 Black hole mass versus central velocity dispersion relations for ETGs with a disk (ES/S0-types) and ETGs without a disk (E-type). We find two slightly different relations for galaxies with and without a disk, which is similar (but less pronounced) to the separation in the M_{BH}–σ diagram due to Sérsic and core-Sérsic galaxies (see Figure 3.3). This is not surprising as most of the elliptical galaxies in our sample are core-Sérsic galaxies and most of the ETGs with a disk (ES/S0-types) are Sérsic galaxies, hence the difference is caused by core-Sérsic and Sérsic galaxies.

undergo multiple gas-poor (dry) mergers resulting in over-massive black holes with only mildly increased velocity dispersion.

3.3.4 Galaxies With a Disk (ES/S0/Sp) and Without a Disk (E)

ETGs include elliptical (E), ellicular (ES), and lenticular (S0) galaxies. Elliptical galaxies are pressure-supported, spheroid-dominated galaxies with minimal rotation. Ellicular galaxies host an intermediate-scale (rotating) stellar disk within their spheroids (Liller, 1966; Graham et al., 2016a), while lenticular galaxies have a large-scale disk extending beyond their bulges (see Graham, 2019a, for a detailed morphological classification grid). LTGs are spiral (Sp) galaxies with a bulge, a large-scale disk, and spiral arms. The LTGs in our sample are predominantly early-type spirals (Sa–Sb).

Our reduced sample of 137 galaxies is comprised of 44 elliptical galaxies which do not have a rotating disk, plus 93 galaxies with a disk, which includes 47 ES or S0-types (ETGs) and 46 spirals (LTGs).

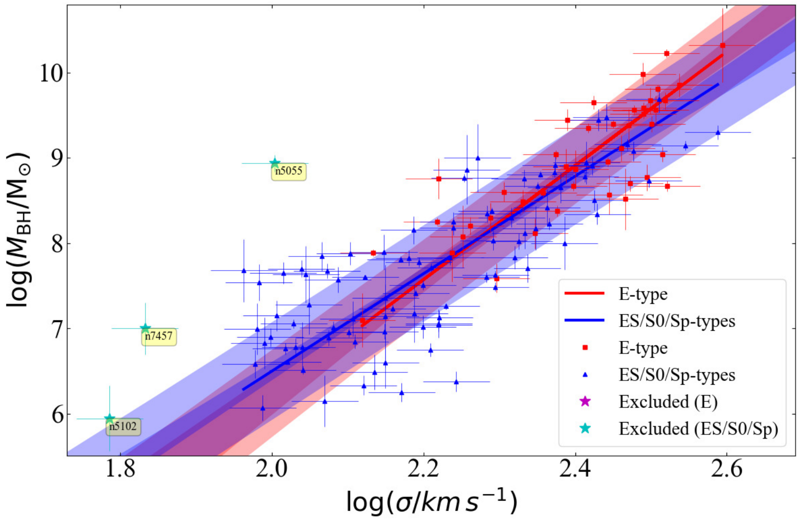

Figure 3.6 Similar to Figure 3.5, but now including spiral (Sp) galaxies—all of which have an extended rotating disk—along with the ellicular (ES) and lenticular (S0) galaxies in the category of galaxies with a disk, while elliptical (E) galaxies without a disk are all ETGs. Here, we again find two slightly different relations in the M_{BH}–σ diagram, but not as pronounced as between Sérsic and core-Sérsic galaxies. See Table 3.2 for full equations of the two lines.

We first performed separate regressions on the ETGs with (ES/S0) and without (E) a disk, as shown in Figure 3.5 where the blue and red lines correspond to $M_{BH} \propto \sigma^{4.93\pm0.39}$ and $M_{BH} \propto \sigma^{6.69\pm0.59}$, respectively. Then we performed regressions on all types of galaxies with a disk (ES/S0/Sp), and without a disk (E-types), as represented in Figure 3.6 where the blue line defines $M_{BH} \propto \sigma^{5.72\pm0.34}$ and the red line is the same as that in Figure 3.5, i.e., $M_{BH} \propto \sigma^{6.69\pm0.59}$. Full equations of the best-fit lines can be found in our Table 3.2.

Not surprisingly, we find that galaxies with and without a disk seem to follow two slightly different relations in both cases (ETG-only, ETG+LTG). This is more apparent for the ETG sample (Figure 3.5) than for the total sample (Figure 3.6) because upon including spiral galaxies with ETGs with a disk (ES/S0), the apparent difference in slopes of the blue and red lines reduces.

This difference in the M_{BH}–σ relations due to galaxies with and without a disk is likely because most of the elliptical galaxies in our sample are (massive) core-Sérsic galaxies and almost all the galaxies with a rotating disk are Sérsic galaxies. The extent of the difference between the M_{BH}–σ relation for core-Sérsic and Sérsic galaxies is greater than that of the relations followed by the galaxies with and without a disk. This suggests that the two distinct relations in the M_{BH}–σ diagram are predominantly caused by core-Sérsic versus Sérsic galaxies. It should be noted that core-Sérsic galaxies can also have disks (e.g. Dullo & Graham, 2013, 2014; Dullo, 2014), for example the lenticular galaxies NGC 524, NGC 584, NGC 3706, NGC 4751, and NGC 5813 in our sample have depleted stellar cores.

We speculate that Savorgnan & Graham (2015) failed to detect different M_{BH}–σ relations for core-Sérsic and Sérsic galaxies, or slow and fast rotators[10], because of their smaller sample size. However, some of their core-Sérsic galaxies can be spotted to be offset from their single M_{BH}–σ relation at the high-mass end.

3.3.5 Barred and Non-barred Galaxies

In the past, some observational studies (Graham, 2007a; Hu, 2008; Graham, 2008b,a) and simulations (Brown et al., 2013; Hartmann et al., 2014) have revealed that barred galaxies are offset towards the higher σ side in the M_{BH}–σ diagram. Based on that offset, these studies suggest that barred galaxies should be separated from non-barred galaxies in order to obtain M_{BH}–σ relations for barred and non-barred galaxies.

To investigate the above offset using our larger data-set, accompanied with our revised classifications based upon multi-component decompositions, we also divided our sample into barred and non-barred galaxies, and performed separate regressions on both populations. This was first done for barred and non-barred ETGs, then using the total (reduced) sample of 137 galaxies, as shown in Figures 3.7 and 3.8, respectively. Our ETG sample consists of 17 barred and 74 non-barred galaxies, while the full sample comprises 50 barred and 87 non-barred galaxies.

Surprisingly, we do not find any offset between barred and non-barred galaxies, in either case, i.e., only ETGs and the ETG + LTG sample. The best-fit line for the 17 barred ETGs is

$$\log(M_{BH}/M_{\odot}) = (5.98 \pm 0.80) \log\left(\frac{\sigma}{200\,\mathrm{km\,s^{-1}}}\right) + (8.19 \pm 0.14), \tag{3.7}$$

with $\Delta_{rms|BH} = 0.41$ dex. However, we require a larger sample of barred ETGs for a robust

[10]Note: ES galaxies are both fast rotators and slow rotators (e.g., Bellstedt et al., 2017).

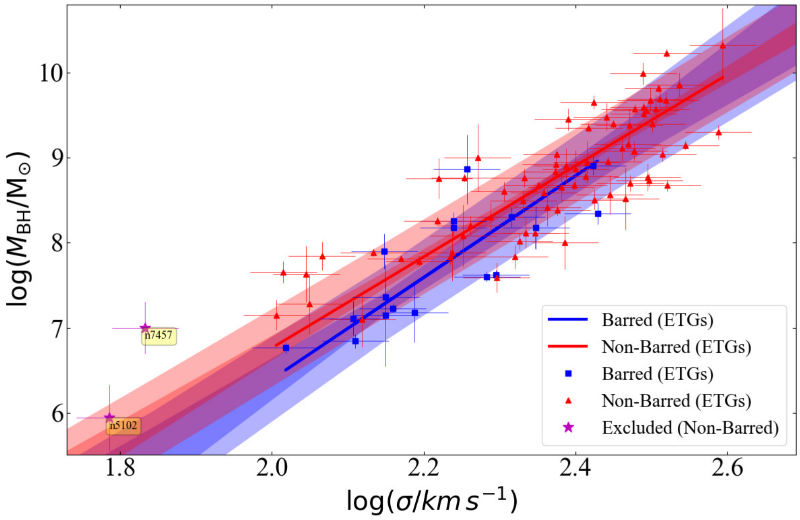

Figure 3.7 Black hole mass versus central velocity dispersion relation for barred and non-barred ETGs. Although we only have a small sample of 17 barred ETGs, the consistency of the two regression lines (blue and red lines) suggests no offset between barred (Equation 3.7) and non-barred (Equation 3.8) ETGs in the M_{BH}–σ diagram.

relation. The 74 non-barred ETGs define the following relation, with $\Delta_{rms|BH} = 0.43$,

$$\log(M_{BH}/M_{\odot}) = (5.35 \pm 0.39) \log\left(\frac{\sigma}{200\,\mathrm{km\,s^{-1}}}\right) + (8.37 \pm 0.06). \tag{3.8}$$

The 50 barred ETG + LTG population defines the line,

$$\log(M_{BH}/M_{\odot}) = (5.30 \pm 0.54) \log\left(\frac{\sigma}{200\,\mathrm{km\,s^{-1}}}\right) + (8.14 \pm 0.10), \tag{3.9}$$

with $\Delta_{rms|BH} = 0.53$ dex. The 87 non-barred galaxies define the relation

$$\log(M_{BH}/M_{\odot}) = (6.16 \pm 0.42) \log\left(\frac{\sigma}{200\,\mathrm{km\,s^{-1}}}\right) + (8.28 \pm 0.06), \tag{3.10}$$

with $\Delta_{rms|BH} = 0.51$ dex. The best-fit lines for the barred and non-barred galaxies are consistent within the $\pm 1\sigma$ bounds of their slopes and intercepts, suggesting no significant offset between barred and non-barred galaxies.

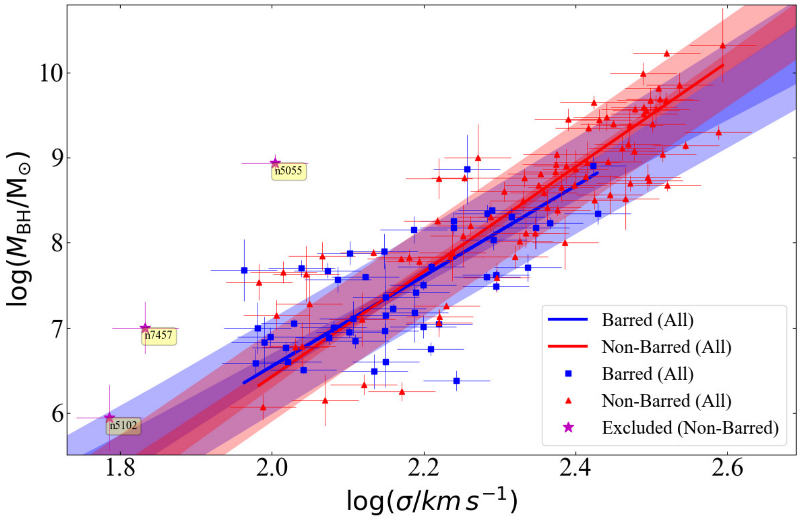

Figure 3.8 Similar to Figure 3.7, but including barred and non-barred late-type galaxies as well. The regression lines obtained for the 50 barred (blue line, Equation 3.9) and 87 non-barred (red line, Equation 3.10) galaxies are overlapping and consistent with each other, implying no-offset between barred and non-barred galaxies.

Investigating Previous Offsets

To find the reason behind the offset observed by Graham & Scott (2013), we have compared their regression lines with ours obtained using the latest M_{BH}, σ, and updated bar-morphologies. Their sample of 72 galaxies was comprised of 21 barred and 51 non-barred galaxies, according to the morphological classifications they adopted, which were obtained from the NASA/IPAC Extragalactic Database (NED). All of their galaxies are present in our current sample, and in order to make a comparison, we use only the galaxies present in the data-set of Graham & Scott (2013).

Interestingly, out of those common 72 galaxies, we have classified 27 as barred, and 45 as non-barred. The barred and non-barred classifications for our current sample are based on the morphologies obtained from the multi-component decompositions of these galaxies presented in our recent works (Savorgnan & Graham, 2016b; Davis et al., 2019a; Sahu et al., 2019a). We notice that in the data-set of Graham & Scott (2013), seven barred galaxies (NGC 224, NGC 2974, NGC 3245, NGC 3998, NGC 4026, NGC 4388, and NGC 6264) were misclassified as non-barred due to the presence of weak bars not detected in optical images (Eskridge et al., 2000)[11]. Also, one non-barred galaxy (NGC 4945) in their sample appears to have been misclassified as barred, with Davis et al. (2019a) reporting only a nuclear bar too weak to include in their modelling.

The green and yellow lines in Figure 3.9 are the BCES symmetric best-fit lines from Graham & Scott (2013) for the barred and non-barred galaxies, respectively. These two lines are offset by ~ 0.5 dex at the median velocity dispersion of $200\,\mathrm{km\,s^{-1}}$. The blue and red BCES bisector lines for the 72 reclassified barred and non-barred galaxies from our current data-set, are offset by only 0.16 dex. Moreover, on using the total (reduced) sample of 137 galaxies comprising 50 barred and 87 non-barred galaxies, as is represented in Figure 3.8, the offset reduces to 0.14 dex (see Equations 3.9 and 3.10).

We find that there are two main reasons why Graham & Scott (2013) found an offset. First, they largely classified their galaxies as barred or non-barred based on the morphologies provided by NED, which are mainly from the RC3 catalog (de Vaucouleurs et al., 1991) and in many cases it failed to identify bars and some other galaxy structures as well. The second reason is that their sample of 72 galaxies lacked (a sufficiently large sample of) barred galaxies residing above their regression line (the green line in Figure 3.9). Another reason for the difference might have been the updated black hole masses and velocity dispersions. For example, the updated (Greene & Ho, 2006) velocity dispersion for the barred spiral galaxy NGC 4151 is $91.8 \pm 9.9\,\mathrm{km\,s^{-1}}$, which is notably different from the old value of $156 \pm 7.8\,\mathrm{km\,s^{-1}}$ reported in HyperLeda. However, we have found that, collectively, the updated velocity dispersions do not seem to have a significant effect on the offset between the regression lines for the barred and non-barred galaxies, because the latest σ values are not particularly different for most of the galaxies.

Strong versus Weak or Faint Bars

We also investigated if weak/faint barred galaxies are biasing our barred M_{BH}–σ relation (Equation 3.9). There was a possibility that perhaps most of the weak/faint barred galaxies fall above the best-fit relation (blue line in Figure 3.8) for the barred galaxies in our current sample, and thereby reduce the offset between the best-fit relation for barred and non-

[11]Eskridge et al. (2000) claim that bars are more detectable in NIR band than optical. However, see Buta et al. (2010, and references therein) which suggest that bar-fraction is similar in the two wavelengths.

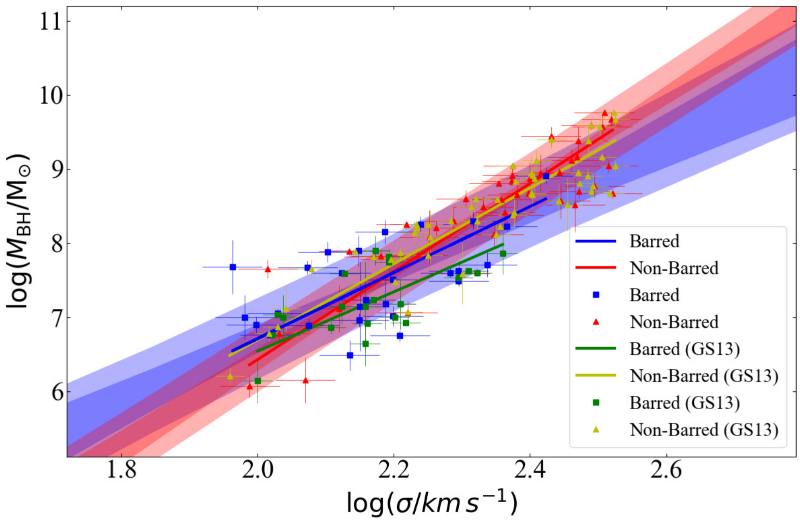

Figure 3.9 Comparison of our M_{BH}–σ relations for barred and non-barred galaxies with the relations reported in Graham & Scott (2013, GS13). Their galaxy sample is a sub-set of our current sample, thus, for a comparison, we use our latest data for the galaxies in their sample, applied with our new bar morphologies (blue and red points). The barred and non-barred data points (i.e., the green squares and yellow triangles, respectively) of Graham & Scott (2013) represent the M_{BH}, σ, and bar classifications they used. Using the same galaxy sample as that of Graham & Scott (2013), we do not find any significant offset between barred and non-barred galaxies.

barred galaxies.

For this investigation, we used the bar-to-total (galaxy) luminosity (L_{bar}/L_{tot}) ratio to categorize our barred galaxies into strong and weak/faint categories. However, as we were not sure of where to make the cut, we performed this test twice, first making the division at $L_{bar}/L_{tot} = 0.05$, then at $L_{bar}/L_{tot} = 0.1$. Figure 3.10 shows the barred galaxies color coded as black strong-barred ($L_{bar}/L_{tot} \geq 0.1$), yellow faint-barred ($L_{bar}/L_{tot} \leq 0.05$), and green with intermediate bar strength ($0.05 < L_{bar}/L_{tot} < 0.1$). For 14 barred-galaxies, 9 of which are from (Savorgnan & Graham, 2016b), 4 are from Combes et al. (2019), and one is from Nguyen et al. (2020), we do not have the luminosity of the bar. Hence, we categorized them on the basis of their multi-component decomposition profile, the morphological bar classification provided by the literature, and a visual inspection of their images which was also performed for all the other barred galaxies. Overall, our total sample of 50 barred galaxies consists of 27 strong, 10 weak/faint, and 13 intermediate-strength barred galaxies.

For the first test, i.e., for the division at $L_{bar}/L_{tot} = 0.05$, all the strong (and intermediate) barred galaxies are distributed almost uniformly about the best-fit (blue) line for the barred galaxies, and many of the faint barred galaxies are below the best-fit line (see Figure 3.10). This suggests that galaxies with faint-bars do not minimize the offset between barred and non-barred galaxies. As for the second cut at $L_{bar}/L_{tot} = 0.1$, we can see in Figure 3.10, that most of the intermediate and faint barred galaxies are below the best-fit line for barred-galaxies, again indicating that weak/faint- barred, or even intermediate-barred galaxies, do not take part in reducing the offset between barred and non-barred galaxies. Strongly-barred galaxies are distributed above and below the best-fit line for barred galaxies.

3.3.6 Galaxies with and without an AGN

Our reduced sample of 137 galaxies includes 41 galaxies hosting an AGN. We identified the AGN hosts using the 13th edition of the catalog of quasars and active nuclei presented by Véron-Cetty & Véron (2010). Interestingly, these AGN hosts are spread almost uniformly about the best-fit bisector regression line (for the sample of 137 galaxies) for the range of M_{BH} and σ that we have, indicating that galaxies with and without an AGN follow a single relation.

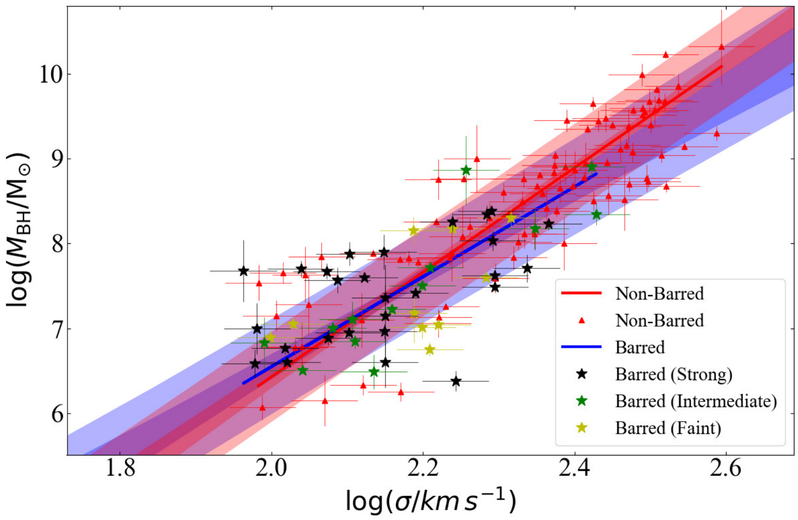

Figure 3.10 Similar to Figure 3.8, but now categorizing our barred galaxies into strong, intermediate, and faint barred galaxies.

Also, upon performing separate regressions on AGN hosts and galaxies without AGN, we obtain almost overlapping regression lines for the two categories, such that their slopes and intercept are consistent with each other within the $\pm 1\sigma$ confidence bounds (Figure 3.11). The regression parameters for the best-fit lines for galaxies with and without AGNs are given in Table 3.2. A galaxy hosting an AGN can be Sérsic or core-Sérsic, as can a galaxy without an AGN; hence, regardless of whether a galaxy hosts an AGN or not, the M_{BH}–σ relations defined by Sérsic and core-Sérsic galaxies remain applicable, and should be used depending on the presence or absence of a core (deficit of star light, not due to dust obscuration).

3.4 Internal consistency between the M_{BH}–$M_{*,gal}$, M_{BH}–$M_{*,sph}$, and M_{BH}–σ relations

Recent studies by Sahu et al. (2019a) and Davis et al. (2019a) established robust M_{BH}–$M_{*,gal}$ and M_{BH}–$M_{*,sph}$ correlations for ETGs and LTGs, using a (reduced) sample of 76 ETGs and 40 LTGs, respectively. As elaborated above in Section 3.3, we also observe a strong correlation between black hole mass and the central stellar velocity dispersion, along with the discovery of two distinct relations in the M_{BH}–σ diagram due to Sérsic

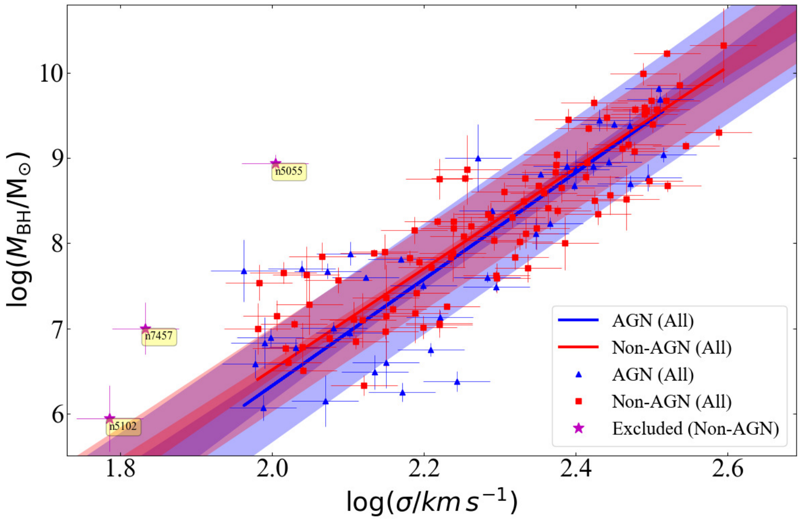

Figure 3.11 Black hole mass versus velocity dispersion followed by galaxies hosting an AGN and galaxies without an AGN.

Table 3.2. Linear Regressions [$\log(M_{\rm BH}/{\rm M}_\odot) = \alpha \log(\sigma/200) + \beta$]

Category (1)	Number (2)	α (3)	β (dex) (4)	ϵ (dex) (5)	$\Delta_{rms\|BH}$ (dex) (6)	r (7)	r_s (8)
Early-Type Galaxies	91	5.71 ± 0.33	8.32 ± 0.05	0.32	0.44	0.86	0.85
Late-Type Galaxies	46	5.82 ± 0.75	8.17 ± 0.14	0.57	0.63	0.59	0.49
All Galaxies	137	6.10 ± 0.28	8.27 ± 0.04	0.43	0.53	0.86	0.87
Sérsic Galaxies	102	5.75 ± 0.34	8.24 ± 0.05	0.46	0.55	0.78	0.78
Core-Sérsic Galaxies	35	8.64 ± 1.10	7.91 ± 0.20	0.25	0.46	0.73	0.65
Galaxies with a disk (ES, S0, Sp-types)	93	5.72 ± 0.34	8.22 ± 0.06	0.47	0.56	0.79	0.78
Galaxies without a disk (E-type)	44	6.69 ± 0.59	8.25 ± 0.10	0.30	0.43	0.82	0.80
Barred Galaxies	50	5.30 ± 0.54	8.14 ± 0.10	0.45	0.53	0.65	0.61
Non-Barred Galaxies	87	6.16 ± 0.42	8.28 ± 0.06	0.40	0.51	0.86	0.86
AGN host Galaxies	41	6.26 ± 0.49	8.21 ± 0.09	0.55	0.63	0.83	0.79
Galaxies without AGN	96	5.92 ± 0.31	8.30 ± 0.05	0.37	0.48	0.87	0.88

Note. — Columns: (1) Subclass of galaxies. (2) Number of galaxies in a subclass. (3) Slope of the line obtained from the BCES(Bisector) regression. (4) Intercept of the line obtained from the BCES(Bisector) regression. (5) Intrinsic scatter in the log $M_{\rm BH}$-direction (using Equation 1 from Graham & Driver, 2007a). (6) Total root mean square (rms) scatter in the log $M_{\rm BH}$ direction. (7) Pearson correlation coefficient. (8) Spearman rank-order correlation coefficient.

and core-Sérsic galaxies.

The M_{BH}–$M_{*,gal}$ (and M_{BH}–$M_{*,sph}$) relations combined with our M_{BH}–σ relations can predict the $M_{*,gal}$–σ and $M_{*,sph}$–σ relations. They should be compared with the observed $M_{*,gal}$–σ and $M_{*,sph}$–σ relations to check for internal consistency of our relations. The ETGs and LTGs of Sahu et al. (2019a) and Davis et al. (2019a), respectively, constitute 85% of the sample used in this work to obtain the M_{BH}–σ relations, hence their M_{BH}–$M_{*,gal}$ and M_{BH}–$M_{*,sph}$ relations are appropriate for internal consistency checks. To derive the $M_{*,gal}$–σ and $M_{*,sph}$–σ relations, we used the galaxy and spheroid stellar masses measured in Davis et al. (2018a), Davis et al. (2019a) and Sahu et al. (2019a).

Sérsic and core-Sérsic ETGs have been found to follow the same M_{BH}–$M_{*,gal}$ and M_{BH}–$M_{*,sph}$ relations in Sahu et al. (2019a), such that $M_{BH} \propto M_{*,gal}^{1.65\pm0.11}$ and $M_{BH} \propto M_{*,sph}^{1.27\pm0.07}$ for all ETGs, i.e., when combining those with a disk and those without a disk. Whereas, the LTGs in Davis et al. (2019a), all of which are Sérsic galaxies, define the relations $M_{BH} \propto M_{*,gal}^{3.05\pm0.70}$ and $M_{BH} \propto M_{*,sph}^{2.16\pm0.32}$, with slopes almost twice that of the (single regression) slopes for ETGs in Sahu et al. (2019a, see their Figure 11). However, separating the ETGs into those with and without a disk reveals that they follow two different M_{BH}–$M_{*,sph}$ relations with slopes of approximately 1.9 ± 0.2 but with intercepts offset by more than a factor of 10 in the M_{BH}-direction (Sahu et al., 2019a, their Figure 8). While in the M_{BH}–$M_{*,gal}$ diagram, the two relations for ETGs with and without a disk agree with each other much more closely, suggesting that the M_{BH}–$M_{*,gal}$ relation obtained from the single regression is a reasonable approximation for ETGs with and without a disk. In the M_{BH}–σ diagram, Sérsic and core-Sérsic galaxies in our total (ETG+LTG) sample define two distinct relations, see Equations 3.5 and 3.6, respectively.

Theoretically, to check on the consistency between all of these M_{BH}–$M_{*,sph}$, M_{BH}–σ, and $M_{*,sph}$–σ relations for ETGs, we should use the two distinct M_{BH}–$M_{*,sph}$ relations for ETGs with and without a disk with the two M_{BH}–σ relations for core-Sérsic and Sérsic ETGs (Section 3.3.3), to predict different $M_{*,sph}$–σ relations for core-Sérsic ETGs with and without a disk and Sérsic ETGs with and without a disk. However, if we separate the core-Sérsic (or Sérsic) ETGs into galaxies with and without a disk, each sub-population will be too small to derive a robust $M_{*,sph}$–σ relation for comparison with the predicted relation. Hence, for the current consistency checks, we have used the following single regression relation for ETGs: $M_{BH} \propto M_{*,sph}^{1.27\pm0.07}$.

Using $M_{BH} \propto \sigma^{8.64\pm1.10}$ (Equation 3.6) for our core-Sérsic galaxies, all of which are ETGs, and the M_{BH}–$M_{*,gal}$ (and M_{BH}–$M_{*,sph}$) relations for the ETGs from Sahu et al. (2019a), we expect the relations $M_{*,gal} \propto \sigma^{5.24\pm0.75}$ and $M_{*,sph} \propto \sigma^{6.80\pm0.94}$ for core-Sérsic galaxies. These two relations are found to be consistent with the directly derived relations $M_{*,gal} \propto \sigma^{6.07\pm1.04}$ and $M_{*,sph} \propto \sigma^{6.41\pm1.31}$, obtained for our core-Sérsic galaxies using the BCES(BISECTOR) regression.

Using the single relation for all (ETG+LTG) Sérsic galaxies, $M_{BH} \propto \sigma^{5.75\pm0.34}$ (Equation 3.5), and the M_{BH}–$M_{*,gal}$ (and M_{BH}–$M_{*,sph}$) relations for the ETGs from Sahu et al. (2019a), Sérsic ETGs are expected to follow $M_{*,gal} \propto \sigma^{3.48\pm0.31}$ and $M_{*,sph} \propto \sigma^{4.52\pm0.36}$. These are consistent with the directly-derived relations $M_{*,gal} \propto \sigma^{2.90\pm0.36}$ and $M_{*,sph} \propto \sigma^{3.85\pm0.46}$ using the BCES(BISECTOR) regression.

Similarly, for Sérsic LTGs, using our Equation 3.5 and the M_{BH}–$M_{*,gal}$ (and M_{BH}–$M_{*,sph}$) relations for LTGs from Davis et al. (2019a), we predict the relations $M_{*,gal} \propto \sigma^{1.88\pm0.45}$ and $M_{*,sph} \propto \sigma^{2.66\pm0.42}$, which are consistent with the directly-derived relations $M_{*,gal} \propto \sigma^{2.00\pm0.38}$ and $M_{*,sph} \propto \sigma^{2.96\pm0.55}$. In the same way, the relations for all the other subcategories, as described in the above subsections, have been found to be internally consistent. In the following sections, we turn our attention to matters of external consistency.

3.5 The L–σ diagram

For half a century, astronomers have been studying the correlation between the total luminosity of a galaxy and the velocity dispersion of the stars in it (Minkowski, 1962). However, with the increase in the number of reliable measurements at high and low luminosities, various studies found different relations when using different samples (Faber & Jackson, 1976; Schechter, 1980; Malumuth & Kirshner, 1981; Tonry, 1981; Binney, 1982; Farouki et al., 1983; Davies et al., 1983; Held et al., 1992; de Rijcke et al., 2005; Matković & Guzmán, 2005; Lauer et al., 2007), which collectively suggested a broken or curved L–σ relation (see Graham, 2016; Graham & Soria, 2018, for a brief overview of previous studies). Here, we re-investigate the bend or curve in the L–σ diagram.

3.5.1 V-band Data-set

Using elliptical galaxies from the V-band data-set of Lauer et al. (2007), with several modifications, Kormendy & Bender (2013) reported a steep $L_V \propto \sigma^8$ relation for the core (core-Sérsic) elliptical galaxies, and $L_V \propto \sigma^4$ for the core-less (Sérsic) elliptical galaxies. Although they specifically mention the use of a symmetric least squares regression routine from Tremaine et al. (2002, modified FITEXY), the slopes they report seem to be obtained from an asymmetric regression, i.e., a least squares minimization of the offsets in the σ-direction over V-band absolute magnitude ($\mathfrak{M}_V$) which produces a steep L_V–σ slope[12]. The modified FITEXY routine from (Tremaine et al., 2002) does not directly provide a symmetric regression line: one first needs to obtain the forward $(Y|X)$ and inverse $(X|Y)$ regression lines using this routine, and then find the bisector line. For the data used by Kormendy & Bender (2013), we report here that the symmetric application of the modified FITEXY regression routine gives $L_V \propto \sigma^{4.39\pm0.61}$ for the core-Sérsic elliptical galaxies, and $L_V \propto \sigma^{2.98\pm0.31}$ for the Sérsic elliptical galaxies.

We have used all of the 178 ETGs (for which σ is available) from Lauer et al. (2007) to revisit the V-band $\mathfrak{M}_V$–σ relations[13], except for the stripped M32-type[14] compact elliptical galaxies which can bias the relation (Graham & Soria, 2018, see their Figure 11). We updated the core designation for the galaxies NGC 4458, NGC 4473, NGC 4478, and NGC 4482 according to Kormendy et al. (2009, their Table 1), and the core designation of NGC 524, NGC 821, NGC 1374, NGC 3607, and NGC 5576 according to our Table 3.1. We also changed the designation of NGC 4552 from core-Sérsic to Sérsic following Bonfini et al. (2018), who claimed that the apparent core detected in this galaxy is because of the dust rings obstructing the light from the galactic center.

We used a constant 10% error on the velocity dispersion, and a 0.2 mag uncertainty on the absolute magnitude, i.e., a 20% error in the luminosity. Before performing the regression on the updated data-set, we checked to see if any single galaxies might bias the underlying relation defined by the bulk of the sample. This led us to exclude the Sérsic

[12] $\mathfrak{M} = -2.5\log(L)$

[13] Kormendy & Bender (2013) pruned the data sample from Lauer et al. (2007) by excluding many dwarf ETGs which define the low-mass slope, and by excluding some lenticular galaxies while including other lenticular galaxies which had been misclassified as elliptical galaxies (see Graham 2019b).

[14] These M32-type compact elliptical galaxies are M32, VCC 1192 (NGC 4467), VCC 1199, VCC 1297 (NGC 4486B), VCC 1440 (IC 798), VCC 1545 (IC 3509), and VCC 1627.

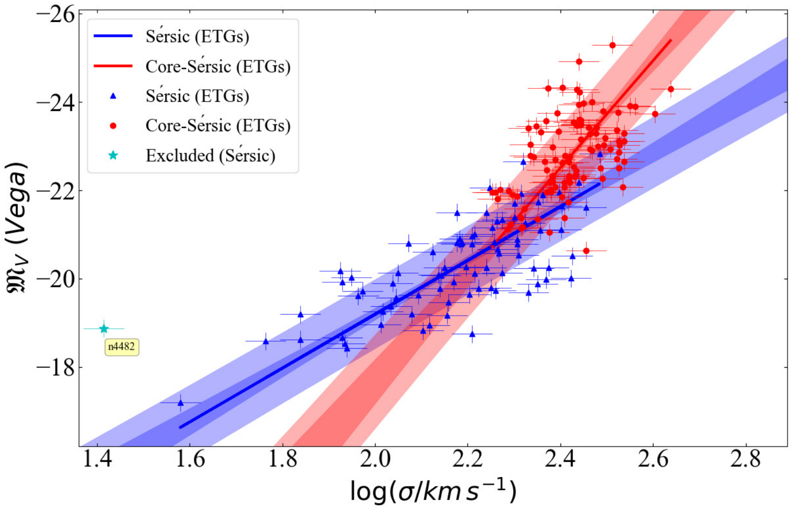

Figure 3.12 V-band absolute magnitude versus velocity dispersion diagram for Sérsic and core-Sérsic ETGs taken from the sample of Lauer et al. (2007). The BCES(BISECTOR) regression provides the relations $L_V \propto \sigma^{2.44\pm0.18}$ (Equation 3.12) and $L_V \propto \sigma^{4.86\pm0.54}$ (Equation 3.11) for Sérsic and core-Sérsic ETGs, respectively. This diagram suggests a broken L–σ relation with the bend point at $\mathfrak{M}_V \approx -20.7$ mag (Vega).

galaxy NGC 4482 from our regressions as it appears to have an underestimated velocity dispersion (Figure 3.12).

Figure 3.12 shows the V-band magnitude versus the velocity dispersion relation for Sérsic and core-Sérsic ETGs from the updated sample of Lauer et al. (2007). We obtain the bend-point at $\mathfrak{M}_V = -20.7$ mag (Vega), with 97 core-Sérsic ETGs defining the relation

$$\log(L_V) = (4.86 \pm 0.54) \log\left(\frac{\sigma}{200\,\mathrm{km\,s^{-1}}}\right) + (8.52 \pm 0.07), \tag{3.11}$$

with $\Delta_{rms|L_V} = 0.37$ dex in the $\log L_V$-direction, and 80 Sérsic ETGs defining a shallower relation given by,

$$\log(L_V) = (2.44 \pm 0.18) \log\left(\frac{\sigma}{200\,\mathrm{km\,s^{-1}}}\right) + (8.41 \pm 0.04), \tag{3.12}$$

with $\Delta_{rms|L_V} = 0.31$ dex, obtained using the BCES(BISECTOR) regression[15].

[15] Including NGC 4482 changes the Sérsic slope to 2.18 ± 0.25, revealing that this single galaxy has a significant leverage on the slope of Sérsic population, hence it is better to exclude NGC 4482.

3.5.2 3.6 μm Data-set

To probe the behavior of Sérsic and core-Sérsic ETGs in the L–σ diagram using near-infrared 3.6 μm-derived luminosities, we obtained the 3.6 μm absolute magnitudes ($\mathfrak{M}_{3.6\mu m}$) for 73 ETGs from Sahu et al. (2019a). This sample of 73 ETGs with 3.6 μm absolute magnitudes, has two galaxies (NGC 404, NGC 7457) common to our excluded sample (Section 3.3.1) and five galaxies (NGC 404, NGC 1316, NGC 2787, NGC 4342 and NGC 5128) common to the exclusions applied in Sahu et al. (2019a, their Section 4). Hence, to maintain a consistency we exclude those galaxies in the $L_{3.6\mu m}$–σ as well, which leaves us with a reduced 3.6 μm data-set of 67 ETGs. Checking for considerable outliers, we found that the core-Sérsic ETG NGC 4291 (shown in Figure 3.13 by a magenta-colored star), is a more than 2σ outlier, and significantly biases (changes the slope for) the best-fit line for core-Sérsic galaxies, hence we exclude NGC 4291 from the regression. The reduced 3.6 μm ETG sample is comprised of 42 Sérsic and 24 core-Sérsic ETGs.

Using our 3.6 μm data for ETGs, we recover the bend in the L–σ relation (Figure 3.13). Our core-Sérsic galaxies follow the relation

$$\log(L_{3.6\mu\mathrm{m}}) = (5.16 \pm 0.53) \log\left(\frac{\sigma}{200\,\mathrm{km\,s^{-1}}}\right) + (8.56 \pm 0.08), \tag{3.13}$$

with $\Delta_{rms|L_{3.6\mu\mathrm{m}}} = 0.19$ dex (in the $\log L_{3.6\mu\mathrm{m}}$-direction) and Sérsic galaxies follow the shallower relation,

$$\log(L_{3.6\mu\mathrm{m}}) = (2.97 \pm 0.43) \log\left(\frac{\sigma}{200\,\mathrm{km\,s^{-1}}}\right) + (8.72 \pm 0.07), \tag{3.14}$$

with $\Delta_{rms|L_{3.6\mu\mathrm{m}}} = 0.36$ dex[16].

The different exponent of the relations $L_B \propto \sigma^2$ (Graham & Soria, 2018), $L_V \propto \sigma^{2.5}$ (Figure 3.12, Equation 3.12), and $L_{3.6\,\mu\mathrm{m}} \propto \sigma^3$ (Figure 3.13, Equation 3.14) followed by Sérsic ETGs in different wavelength bands is consistent with the fact that they also follow a color-magnitude relation. Core-Sérsic ETGs, on the other hand, have roughly a constant color, suggesting similar slopes of the L–σ relation for all wavelength bands. The observed L–σ relations for core-Sérsic ETGs in different bands, i.e., $L_B \propto \sigma^{4-6}$ (Graham & Soria,

[16]Including NGC 4291 in the regression changes the slope for the core-Sérsic galaxies to 5.94 ± 1.00, proving that this one single outlier does affect the relation and hence it should remain excluded.

2018), $L_V \propto \sigma^{4.9}$ (Figure 3.12, Equation 3.11), and $L_{3.6\,\mu\mathrm{m}} \propto \sigma^{5.2}$ (Figure 3.13, Equation 3.13), are consistent as expected.

In the 3.6 μm magnitude ($\mathfrak{M}_{3.6\,\mu\mathrm{m}}$) versus velocity dispersion diagram, we observe the bend-point at $\mathfrak{M}_{3.6\,\mu\mathrm{m}} \approx -22.3$ mag in the AB magnitude system, which is $\mathfrak{M}_{3.6\,\mu\mathrm{m}} \approx -25.1$ mag in the Vega magnitude system. Assuming a $B - 3.6\,\mu$m color of ~ 5 (based on $B - K \approx 4$ and $K - 3.6\,\mu\mathrm{m} \approx 1$), it seems to be consistent with the bend-point reported by previous studies at $\mathfrak{M}_B \approx -20.5$ mag (Graham & Soria, 2018), $\mathfrak{M}_V \approx -21$ mag (Lauer et al., 2007), and $\mathfrak{M}_R \approx -22.17$ mag (Matković & Guzmán, 2005).

In Sahu et al. (2019a), we found that Sérsic and core-Sérsic ETGs follow the same $M_{BH} \propto M_{*,gal}^{1.65\pm0.11}$ relation. The relations $M_{BH} \propto \sigma^{4.95\pm0.38}$ for Sérsic ETGs (Equation 3.4) and $M_{BH} \propto \sigma^{8.64\pm1.10}$ for core-Sérsic galaxies (Equation 3.6), all of which are ETGs, combined with the above M_{BH}–$M_{*,gal}$ relation from Sahu et al. (2019a) predict $M_{*,gal} \propto \sigma^{3.00\pm0.30}$ and $M_{*,gal} \propto \sigma^{5.24\pm0.75}$ for Sérsic and core-Sérsic ETGs, respectively. These two expected relations are consistent with what we have obtained (Equations 3.14 and 3.13, respectively) given that a constant stellar mass-to-light ratio of 0.6 ± 0.1 (Meidt et al., 2014) was used for 3.6 μm data in Sahu et al. (2019a).

We have also plotted and performed regressions on our 26 LTGs (with 3.6 μm data from Davis et al. (2018a)) in the $L_{3.6\mu\mathrm{m}}$–σ diagram, as shown in Figure 3.14. This sample of 26 LTGs, includes only one galaxy (NGC 5055) common to exclusions applied for our M_{BH}–σ relations (described in Section 3.3.1). In addition to NGC 5055, we also exclude NGC 1300 as it is a considerable (more than 2σ) outlier which can bias the relation for LTGs, as can be seen in Figure 3.14 with a cyan-colored star.

The reduced 3.6 μm sample of 24 LTGs define the relation

$$\log(L_{3.6\mu\mathrm{m}}) = (2.10 \pm 0.41) \log\left(\frac{\sigma}{200\,\mathrm{km\,s^{-1}}}\right) + (8.90 \pm 0.09), \tag{3.15}$$

with $\Delta_{rms|L_{3.6\mu\mathrm{m}}} = 0.20$ dex[17], consistent with the expected $M_{*,gal} \propto \sigma^{1.88\pm0.45}$ relation, derived from the relations $M_{BH} \propto M_{*,gal}^{3.05\pm0.70}$ (Davis et al., 2019a) and $M_{BH} \propto \sigma^{5.75\pm0.34}$ (Equation 3.2). The slope of the L–σ relation that we derived for the LTGs, is also consistent with the B-band slope of 2.13 reported by Graham et al. (2018, see their Figure

[17] Including NGC 1300 in the regression changes the slope to 1.88 ± 0.48.

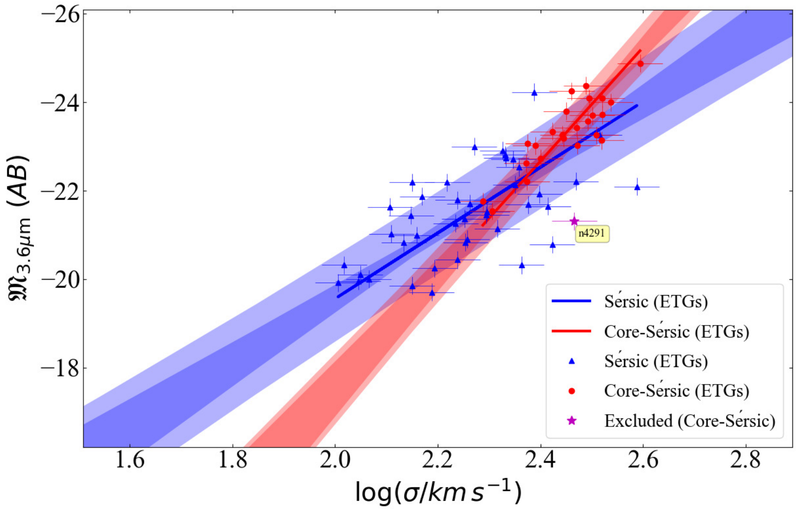

Figure 3.13 3.6 μm absolute magnitude versus velocity dispersion for the Sérsic and core-Sérsic ETGs in our sample. We find the bend in the relation at $\mathfrak{M}_{3.6\mu m} \approx -22.3$ mag (AB) with Sérsic and core-Sérsic galaxies following the best-fit lines $L_{3.6\mu m} \propto \sigma^{2.97\pm0.43}$ (Equation 3.14) and $L_{3.6\mu m} \propto \sigma^{5.16\pm0.53}$ (Equation 3.13), respectively. The color-magnitude relation for Sérsic ETGs explains the different slope of $\sim 2.44 \pm 0.18$ in Figure 3.12 for the L_V–σ relation.

7).

The parameters obtained from the asymmetric regression routines (BCES($Y|X$) and BCES($X|Y$)), for all the L–σ relations discussed above, are presented in Table B.3 in the Appendix B.

3.6 Some Musings on Selection biases

The lack of directly measured low-mass SMBHs, due to the technological limitations to resolve their spheres-of-influence, poses a possible selection bias on the black hole mass scaling relations. In the past, several studies have discussed the consequences of, and possible solutions to, this sample selection bias (e.g., Batcheldor, 2010; Graham & Others, 2011; Shankar et al., 2016).

Batcheldor (2010) obtained an artificial M_{BH}–σ relation using simulated random M_{BH} and σ data, selected through the constraint of a best available resolution limit of $0\farcs1$ attainable from the *Hubble Space Telescope (HST)*, for a maximum distance of 100 Mpc. The fake data produced the relation $\log(M_{BH}/M_\odot) = (4.0\pm0.3)\log\left(\sigma/200\,\mathrm{km\,s^{-1}}\right) + (8.3\pm$

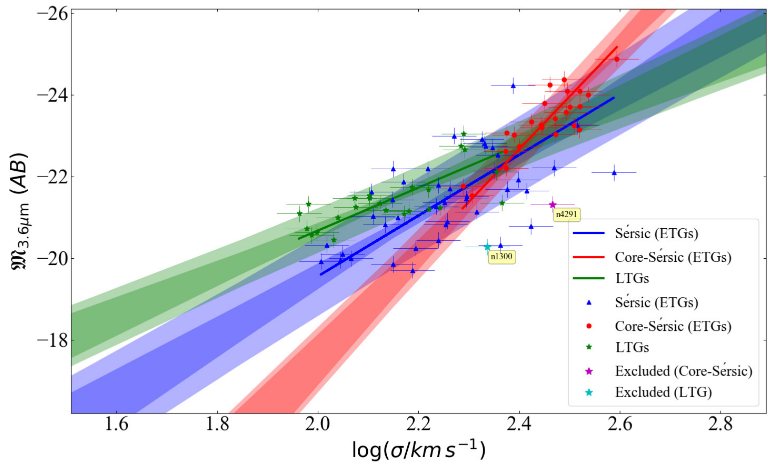

Figure 3.14 Similar to Figure 3.13 but including LTGs (spirals). All the spirals in our sample are Sérsic galaxies, and they also seem to define a tight correlation in the L–σ diagram (Equation 3.15).

0.2), which was nearly consistent with the then observed M_{BH}–σ relation of Gültekin et al. (2009a). Batcheldor (2010) highlighted a crucial point for assessing the credibility of the observed black hole scaling relations. However, his relation with a slope of around 4 is lower than the steeper M_{BH}–σ relations based on larger samples of dynamically measured M_{BH} data (Graham & Others, 2011; McConnell & Ma, 2013; Graham & Scott, 2013; Savorgnan & Graham, 2015; Sabra et al., 2015).

Shankar et al. (2016) claim that galaxies which host a directly measured central SMBH have a higher velocity dispersion in comparison to other galaxies of similar stellar mass but without a direct SMBH measurement. Their claim is based on the offset they observed in the velocity dispersion versus galaxy stellar mass diagram (σ–M_{STAR}, their Figure-1), between several samples of local ETGs with dynamically measured SMBH masses and a larger data-set of galaxies from Data Release-7 of the Sloan Digital Sky Survey (SDSS, York et al., 2000; Abazajian et al., 2009). This is restated in Shankar et al. (2019) with a slight change in their galaxy stellar masses based on the SDSS data they used.

Shankar et al. (2016) suggest that the offset they obtain is a consequence of a sample selection effect in which galaxies with low-mass BHs are excluded because it is not possible to resolve their spheres-of-influence due to technological limitations. They performed the

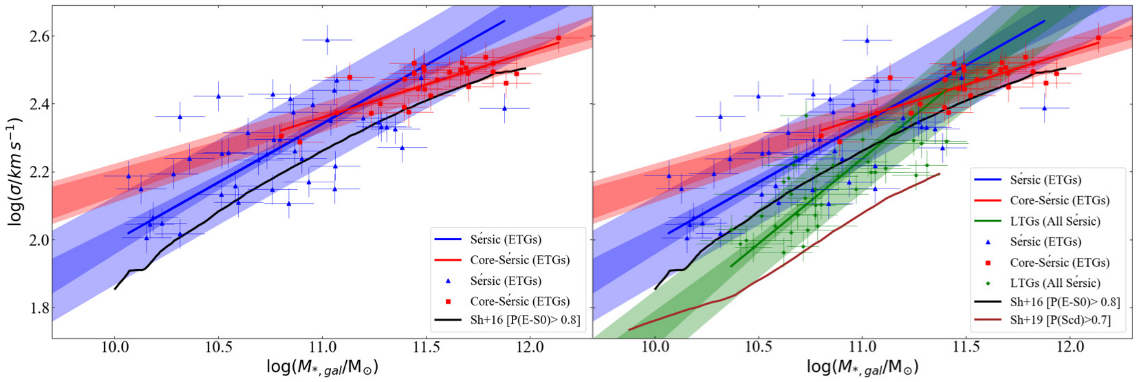

Figure 3.15 Velocity dispersion versus total galaxy stellar mass for Sérsic and core-Sérsic ETGs (left panel), and including LTGs, which are all Sérsic galaxies, in a separate panel for clarity. The mean σ–$M_{*,gal}$ distribution for (i) SDSS early-type galaxies from Shankar et al. (2016, their Figure 1) (black curve) and (ii) late spiral galaxies (P(Scd)>0.7) from Shankar et al. (2019, their Figure 1) (brown curve) are shown. The brown curve resides below the relation defined by our LTG sample which are predominantly early (Sa-Sb) spirals. The black curve may reside below the relation defined by our ETG sample because of contamination by early spirals.

comparison with the data from four different observational studies and provided a unified conclusion that galaxies hosting a directly-measured SMBH are offset in the σ–$M_{*,gal}$ relation, such that they have a higher σ relative to other similar mass galaxies. However, this is not completely true for all the data-sets they used and all of the galaxy stellar mass range in their plots. In their Figure-1, a significant number of data points from Savorgnan et al. (2016) overlap with the grey $\pm 1\sigma$ dispersion bands around the mean curve of the SDSS data, especially in the high-mass range $11 \lesssim \log(M_{*,gal}/M_{\odot}) \lesssim 12$. This can similarly be observed in Figure 1 of Shankar et al. (2019).

Interestingly, as described in Section 3.4, we have shown that Sérsic and core-Sérsic ETGs follow two distinct $M_{*,gal}$–σ relations, consistent with Sérsic and core-Sérsic ETGs following two different M_{BH}–σ relations (Section 3.3.3), but a single M_{BH}–$M_{*,gal}$ relation (Sahu et al., 2019a). Thus, we have two different relations in the σ–$M_{*,gal}$ diagram for Sérsic and core-Sérsic ETGs as shown in the left panel of Figure 3.15. The mean (black) curve from Shankar et al. (2016) lays within the $\pm 1\sigma$ scatter of the two relations followed by our Sérsic and core-Sérsic ETGs with directly-measured black hole masses, but outside of the more relevant darker (red and blue) bands denoting the $\pm 1\sigma$ uncertainty on the

σ–$M_{*,gal}$ relations for ETGs with directly-measured black hole masses.

Upon inclusion of our LTGs (in the right panel of Figure 3.15), all of which are Sérsic galaxies, along with the (core-Sérsic and Sérsic) ETGs, we find that at the low-mass range, $10 \lesssim \log(M_{*,gal}/M_{\odot}) \lesssim 11$, their (black) curve resides between the two relations followed by our Sérsic ETGs (blue line) and LTGs (green line) which are primarily early-type (Sa-Sc) spiral galaxies. This suggests that their galaxy sample of ETGs may contain LTGs which could (partly) cause the offset.

In Shankar et al. (2016), the criteria for selecting only ETGs out of the exhaustive SDSS data-set was based upon having a probability of greater than 0.8 for a galaxy being an E- or S0-type ($P(E-S0) \geq 0.8$). From the probabilities of galaxy types made available by Meert et al. (2015), we have calculated a $\sim$10% contamination by spiral galaxies (LTGs) in the Shankar et al.'s ETG sample. Their best-fit σ–$M_{*,gal}$ relation's position in-between the relation followed by our Sérsic ETGs and LTGs (right panel of Figure 3.15), coupled with their ETG selection criteria based on probability, supports the suspicion that some of the offset may be due to spiral galaxy contamination in their SDSS ETG sample.

In the right-hand panel of Figure 3.15, we also include the brown curve for late spiral galaxies ($P(Scd) \geq 0.7$) from Shankar et al. (2019, see the left panel in their Figure 1), which lies below the relation defined by our predominantly early spiral galaxies (Sa-Sb), simply referred to as LTGs in this paper. The various curves in Figure 3.15 represent the major morphological types. Their layering suggests that the apparent offset between galaxies with and without a directly measured black hole mass, as observed by Shankar et al. (2016, 2019), could simply be a reflection of the difference in the dominant morphological type in each sample. However, this is not conclusive and further investigation is required as their may yet be a selection bias or a discrepancy in the way that velocity dispersions are measured.

3.7 Conclusions and Implications

Using the reduced sample of 137 galaxies with updated black hole masses and central stellar velocity dispersions, our work reveals sub-structure in the M_{BH}–σ diagram due to galaxies with and without a core. Our previous galaxy decompositions (Savorgnan &

Graham, 2016b; Davis et al., 2019a; Sahu et al., 2019a) have enabled us to accurately identify various structural components, such as intermediate or extended disks, bars, and partially-depleted stellar cores. This allowed us to search for substructures in the M_{BH}–σ diagram, based on galaxy morphology, and also enabled us to clarify the situation regarding offset barred galaxies found in previous observational studies.

We performed and reported both symmetric BCES(BISECTOR) and asymmetric BCES($Y|X$) and BCES($X|Y$) regressions. The best-fit line obtained from the symmetric BCES(BISECTOR) regression is preferred because we are looking for a fundamental relation between two quantities (Feigelson & Babu, 1992; Novak et al., 2006). For all our relations, we also obtained a symmetric (bisector) regression line using the MPFITEXY (modified FITEXY) routine, which are consistent with the corresponding BCES(BISECTOR) best-fit lines within the $\pm 1\sigma$ limits of the slopes and intercepts.

Our main results can be summarized as follows:

- The consistency between the best-fit lines for ETGs and LTGs in the M_{BH} versus σ diagram (Figure 3.1), suggests that ETGs and LTGs follow the same $M_{BH} \propto \sigma^{6.10\pm0.28}$ relation with a total scatter of $\Delta_{rms|BH} = 0.53$ dex, obtained using a single regression (Equation 3.3). However, this result depends on the galaxy sample and is somewhat misleading or limited. It is a fusion of substructures caused by (massive) core-Sérsic and (low-mass) Sérsic galaxies following two different M_{BH}–σ relations.

- Core-Sérsic galaxies define the relation $M_{BH} \propto \sigma^{8.64\pm1.10}$ (Equation 3.6) and Sérsic galaxies define the relation $M_{BH} \propto \sigma^{5.75\pm0.34}$ (Equation 3.5), with $\Delta_{rms|BH} = 0.46$ dex and $\Delta_{rms|BH} = 0.55$ dex, respectively. The inconsistency between the slopes of these two relations suggests two distinct relations in the M_{BH}–σ diagram. The two lines intersect at $\sigma \approx 255\,\mathrm{km\,s^{-1}}$ in Figure 3.4 .

- We also detect a substructure in the M_{BH}–σ diagram upon dividing our sample into galaxies with and without a stellar disk (Figures 3.5 and 3.6). However, this is likely because most of the elliptical ETGs are massive core-Sérsic galaxies, while most of the galaxies with a disk (ES, S0, and Sp-types) are Sérsic galaxies.

- We do not find any offset between the slope or intercept of the best-fit lines for barred and non-barred galaxies (Figures 3.7 and 3.8). We reveal that some previous studies noticed an offset in the intercepts between the M_{BH}–σ relations for barred and non-barred galaxies partly because they relied on incomplete bar morphologies for several galaxies which failed to identify weak bars. Our previous image analysis improved upon this situation, and in our current larger sample we also have new galaxies with bars. Given that bars are known to elevate the velocity dispersion (Hartmann et al., 2014), this result begs further investigation, possibly folding in disc inclination, bar orientation to our line-of-sight, and rotational velocity.

- Galaxies with and without an AGN follow consistent relations in the M_{BH}–σ diagram (Figure 3.11). Hence, the M_{BH}–σ relations defined by Sérsic and core-Sérsic galaxies should be valid for a galaxy irrespective of whether or not its nucleus is active.

- Analyzing the L–σ relation, based on V-band data from Lauer et al. (2007), our $3.6\,\mu$m data from Spitzer, and previously reported L–σ relations using B- and R-bands, we investigated the L–σ relation (Figures 3.12 and 3.13). We found that the relation between the luminosity of a galaxy and its central stellar velocity dispersion is bent due to core-Sérsic and Sérsic galaxies, analogous and consistent with the bend found in the M_{BH}–σ relation and the L–μ_0 relation (Graham & Guzmán, 2003). Core-Sérsic galaxies follow the relation $L_V \propto \sigma^{4.86\pm0.54}$ and $L_{3.6\,\mu\mathrm{m}} \propto \sigma^{5.16\pm0.53}$ (Equations 3.11 and 3.13), whereas Sérsic galaxies follow the relation $L_V \propto \sigma^{2.44\pm0.18}$ and $L_{3.6\,\mu\mathrm{m}} \propto \sigma^{2.97\pm0.43}$ (Equations 3.12 and 3.14). The bend-point is consistent in the B-, V-, and $3.6\,\mu$m bands, corresponding to a stellar mass of $\approx 11\,M_\odot$.

- The LTGs in our sample follow the relation $L_{3.6\,\mu\mathrm{m}} \propto \sigma^{2.10\pm0.41}$ (Equation 3.15), and the $L_{3.6\,\mu\mathrm{m}}$–σ relations for Sérsic ETGs, core-Sérsic ETGs, and LTGs are internally consistent with our M_{BH}–σ relations, and the M_{BH}–$M_{*,gal}$ relations from (Sahu et al., 2019a).

Our M_{BH}–σ (and M_{BH}–$M_{*,gal}$, and M_{BH}–$M_{*,sph}$) relations hold insights for theoretical studies into the co-evolution of black holes with their host galaxy properties (e.g., Volonteri & Ciotti, 2013; Heckman & Best, 2014), AGN feedback (Marconi et al., 2008), and the connection between black hole growth and star formation rates which have been found to depend on galaxy morphology (Calvi et al., 2018). Black hole mass scaling relations are also used to determine virial f-factors, for calculating AGN (black hole) masses (e.g., Onken et al., 2004; Graham & Others, 2011; Bennert et al., 2011; Bentz & Katz, 2015; Yu et al., 2019). Our M_{BH}–σ relation due to Sérsic and core-Sérsic galaxies can be used to improve the virial f-factor based upon the galaxy core-type.

The new black hole mass scaling relations can be used to estimate the black hole masses of other galaxies using their easily measured properties, i.e., their galaxy stellar mass, spheroid/bulge stellar mass, or stellar velocity dispersion. These scaling relations, based on high resolution images of local ($z \sim 0$) galaxies, provide a benchmark for studies attempting to determine the evolution of the M_{BH}–σ (or M_{BH}–$M_{*,gal}$ and M_{BH}–$M_{*,sph}$) relations (Woo et al., 2006; Salviander et al., 2007; Bennert et al., 2011; Sexton et al., 2019). Moreover, given the different scaling relations based on the galaxy sub-morphologies, care should be taken in regard to the galaxy types present in one's sample. For distant galaxies where it is difficult to perform multi-component decompositions to obtain bulge masses and extract detailed morphologies, M_{BH}–$M_{*,gal}$ relations can be used provided ETG or LTG classifications are known because ETGs and LTGs follow two different M_{BH}–$M_{*,gal}$ relations (Sahu et al., 2019a). Similarly, as it might be difficult to detect the (depleted) core in distant galaxies, the single regression M_{BH}–σ relation presented in this paper (Equation 3.3) can be used. However, if one is primarily sampling massive distant galaxies, with $\sigma \gtrsim 255\mathrm{kms}^{-1}$, it would be preferable to compare that data with the core-Sérsic M_{BH}–σ relation, or risk inferring a false evolution if using the shallower relation.

Our scaling relations can be used to estimate black hole masses for a large data-set of galaxies to obtain the black hole mass function in the local Universe (McLure & Dunlop, 2004; Shankar et al., 2004; Graham & Others, 2007). This can be used to improve the predictions of the amplitude and frequency of ground-based detections of long-wavelength gravitational waves, produced by merging SMBHs, using pulsar timing arrays (Shannon et al., 2015; Hobbs & Dai, 2017) and also MeerKAT (Jonas, 2007). Furthermore, these scaling relations can also be used to constrain the space-based detection of long-wavelength gravitational waves by the Laser Interferometer Space Antenna (LISA, Danzmann, 2017), and beyond LISA (bLISA, Baker et al., 2019).

3.8 Acknowledgements

We thank the anonymous referee whose comments helped to increase the clarity of this paper. This research was conducted with the Australian Research Council Centre of Excellence for Gravitational Wave Discovery (OzGrav), through project number CE170100004. AWG was supported under the Australian Research Council's funding scheme DP17012923. We also acknowledge the use of the HyperLeda database `http://leda.univ-lyon1.fr`.

4

Defining The (Black Hole)-Spheroid Connection with the Discovery of Morphology-dependent Substructure in the $M_{\rm BH}$–$\rm n_{sph}$ and $M_{\rm BH}$–$\rm R_{e,sph}$ Diagrams: New Tests for Advanced Theories and Realistic Simulations

For 123 local galaxies with directly-measured black hole masses ($M_{\rm BH}$), we provide the host spheroid's Sérsic index ($\rm n_{sph}$), effective half-light radius ($\rm R_{e,sph}$), and effective surface brightness (μ_e), obtained from careful multi-component decompositions, and we use these to derive the morphology-dependent $M_{\rm BH}$–$\rm n_{sph}$ and $M_{\rm BH}$–$\rm R_{e,sph}$ relations. We additionally present the morphology-dependent $M_{*,\rm sph}$–$\rm n_{sph}$ and $M_{*,\rm sph}$–$\rm R_{e,sph}$ relations. We explored differences due to: early-type galaxies (ETGs) versus late-type galaxies (LTGs); Sérsic versus core-Sérsic galaxies; barred versus non-barred galaxies; and galaxies with and without a stellar disk. We detect two different $M_{\rm BH}$–$\rm n_{sph}$ relations due to ETGs and LTGs with power-law slopes 3.95 ± 0.34 and 2.85 ± 0.31. We additionally quantified the correlation between $M_{\rm BH}$ and the spheroid's central concentration index, which varies monotonically with the Sérsic index. Furthermore, we observe a single, near-linear $M_{*,\rm sph}$–$\rm R_{e,sph}^{1.08\pm0.04}$ relation for ETGs and LTGs, which encompasses both classical and alleged pseudobulges. In contrast, ETGs and LTGs define two distinct $M_{\rm BH}$–$\rm R_{e,sph}$ relations

with $\Delta_{\mathrm{rms|BH}} \sim 0.60$ dex (cf. $\sim$0.51 dex for the M_{BH}–σ relation and $\sim$0.58 dex for the M_{BH}–$M_{*,\mathrm{sph}}$ relation), and the ETGs alone define two steeper M_{BH}–$\mathrm{R}_{\mathrm{e,sph}}$ relations, offset by $\sim$1 dex in the $\log M_{\mathrm{BH}}$-direction, depending on whether they have a disk or not and explaining their similar offset in the M_{BH}–$M_{*,\mathrm{sph}}$ diagram. This trend holds using 10%, 50%, or 90% radii. These relations offer pivotal checks for simulations trying to reproduce realistic galaxies, and for theoretical studies investigating the dependency of black hole mass on basic spheroid properties.

4.1 Introduction

It is widely known that the mass of the black hole (BH) residing at the centre of most galaxies is correlated with both the host spheroid's stellar mass ($M_{*,\mathrm{sph}}$) and its central stellar velocity dispersion (σ). At the same time, bulgeless galaxies, for example, NGC 2478, NGC 4395, and NGC 6926, have also been observed to house massive BHs (e.g. Secrest et al., 2013; Simmons et al., 2013; den Brok et al., 2015; Davis et al., 2019a, and references therein), and one of the tightest scaling relations is between black hole mass (M_{BH}) and the winding/pitch angle of the spiral arms in spiral galaxies (Seigar et al., 2008; Berrier et al., 2013; Davis et al., 2017). Additional correlations exist between M_{BH} and disk stellar mass (Davis et al., 2018a), disk rotation, and dark matter halo mass (Ferrarese, 2002; Baes et al., 2003; Volonteri et al., 2011; Davis et al., 2019b). Collectively, this goes beyond the notion of a single primary (causal) relation for all galaxies plus secondary (indirect/consequential) relations, and reveals a greater level of complexity. Indeed, the markedly different M_{BH}–$M_{*,\mathrm{gal}}$ and M_{BH}–$M_{*,\mathrm{sph}}$ relations for early-type galaxies (ETGs, comprised of E-, ES[1]-, and S0-types) and late-type galaxies (LTGs), i.e. spiral galaxies (Davis et al., 2018a, 2019a; Sahu et al., 2019a), undoubtedly reflects the different physical processes, gas supply history, net angular momentum, involved in building these systems.

The review of the BH scaling relations by Graham (2016) highlighted the need to achieve internal consistency among the various scaling relations, in particular between the M_{BH}–σ, M_{BH}–$M_{*,\mathrm{sph}}$, and σ–$M_{*,\mathrm{sph}}$ relations. This followed Graham (2012) who reported on a near-linear and super-quadratic M_{BH}–$M_{*,\mathrm{sph}}$ relation, respectively, for spheroids with

[1]ES-type represents ellicular galaxies which have an intermediate-scale stellar disk confined to within their spheroid (Liller, 1966; Graham, 2019a).

a Sérsic or core-Sérsic[2] light profile (see also Graham & Scott (2013) and Scott et al. (2013)). Savorgnan et al. (2016) subsequently discovered an improved division due to ETGs and LTGs (none of which have core-Sérsic bulge profiles) in the M_{BH}–$M_{*,\mathrm{sph}}$ diagram, and in the M_{BH}–($\mathrm{L_{gal}}$, galaxy luminosity) diagram. This was also later reported by van den Bosch (2016). Savorgnan et al. (2016) coined the notion of a red and blue sequence when two tracks, due to ETGs and LTGs, are evident in a BH mass scaling diagram (see also Terrazas et al., 2016; Dullo et al., 2020a). Sahu et al. (2019a) additionally found that the M_{BH}–$M_{*,\mathrm{sph}}$ relation for ETGs with a disk (ES and S0) and ETGs without a disk (E-type) is roughly quadratic, while the two relations are offset by more than an order of magnitude in the M_{BH}-direction. This has since been found in a recent simulation by Marshall et al. (2020). Clearly, it is not simply the amount of stellar mass that matters, but also how it was accumulated and is now distributed. In this vein, we explore the relationship that the BH mass has with the size and shape (centrally concentrated or diffused) of the surrounding bulge/spheroid— terms that we use interchangeably—and as a function of the morphology of the host galaxy.

The above mentioned developments represent a key advance in our understanding of the coevolution of galaxies and black holes. It built upon works such as Wandel (1999), Laor (2001), and Graham (2012) and voided the notion (Dressler, 1989; Kormendy & Richstone, 1995; Magorrian et al., 1998) that the black hole mass simply co-evolved linearly with the spheroid mass. The recognition of a more nuanced situation is perhaps not surprising given the variety of accretion/merger histories, and resulting structures among galaxies. For example, core-Sérsic galaxies, thought to be built from the dry merger of galaxies with pre-existing black holes (Begelman, 1984), appear to follow a steeper relation in the M_{BH}–σ diagram (Sahu et al., 2019b), see also Terrazas et al. (2016, their Figure 3a) and Bogdán et al. (2018, their Figure 5).

Based on the low intrinsic scatter about the M_{BH}–σ relation (Ferrarese & Merritt, 2000; Gebhardt et al., 2000), some studies have concluded that it is the most fundamental relation between black hole mass and galaxy (e.g. van den Bosch, 2016; de Nicola et al., 2019). However, it may be a premature conclusion without considering the correlations

[2]Core-Sérsic galaxies have a deficit of light at their centre; hence, their central (bulge) light profile is described using a shallow power-law followed by a Sérsic (1963) function beyond the core (Graham & Others, 2003). This population was first discussed by King & Minkowski (1966, 1972).

between BH mass and other basic galaxy properties, or allowing for the morphology-dependence and thus (formation physics)-dependence of galaxies. Moreover, it overlooks that the M_{BH}–pitch angle (ϕ) relation has the least total scatter at 0.43 dex (Davis et al., 2017) compared to 0.51 dex in the latest $M_{\rm BH}$–σ diagram (Sahu et al., 2019b).

Establishing if a, and which, single relation is the most fundamental, i.e., the primary relation, and how it depends upon morphology is important for understanding the co-evolution of galaxies and BHs. The secondary scaling relations — not to be confused with the morphology dependent substructure which reveals an additional parameter/factor modulating the co-joined growth of galaxies and BHs[3] — are, however, also important. They can still be used, for example, to predict BH masses or to check on the accuracy of computer simulations e.g., CLUES (Yepes et al., 2009), Magneticum (Dolag, 2015), Bolshoi (Klypin et al., 2011), EAGLE (Schaye et al., 2015), Illustris (Vogelsberger et al., 2014), IllustrisTNG (Pillepich et al., 2018), FIRE (Hopkins et al., 2018), and SIMBA (Davé et al., 2019), which are trying to produce realistic galaxies[4]. These empirical relations help to decipher the physics behind the effect of the central supermassive black hole on the host spheroid or galaxy properties and vice versa. How such black hole feedback drives galaxy evolution is the challenge yet to be fully answered (Choi et al., 2018; Ruszkowski et al., 2019; Terrazas et al., 2020; Martín-Navarro et al., 2020).

Here, we will expand upon the previous efforts in establishing the $M_{\rm BH}$–$n_{\rm sph}$ relation (e.g., Graham et al., 2003; Graham & Driver, 2007a; Vika et al., 2012; Beifiori et al., 2012; Savorgnan et al., 2013; Savorgnan, 2016), the $M_{*,\rm sph}$–$n_{\rm sph}$ relation (e.g., Andredakis et al., 1995; Jerjen et al., 2000; Graham & Guzmán, 2003; Ferrarese et al., 2006b; Savorgnan, 2016), the $M_{*,\rm sph}$–$R_{\rm e,sph}$ relation (e.g., Sérsic, 1968a; Graham & Worley, 2008; Lange et al., 2015), and the $M_{\rm BH}$–$R_{\rm e,sph}$ relation (e.g., de Nicola et al., 2019) using our extensive sample of 83 ETGs and 40 LTGs with careful (individual, not automated) multi-component decompositions. Importantly, we explore potential substructures due to galaxy sub-morphologies, i.e., Sérsic versus core-Sérsic galaxies, barred versus non-barred galax-

[3]We could re-frame these results by constructing a simplified 'fundamental plane', i.e., a 3-parameter equation involving $M_{\rm BH}$, σ (or M_*) and morphological type (even if just a binary parameter). This would effectively unite the morphology-dependent $M_{\rm BH}$–σ ($M_{\rm BH}$–M_*) relations and reduce the scatter about the two-parameter relations which ignore the morphological type. We will pursue this in future work.

[4]Simulations lacking primary information about the spheroid can still be tested against the non-linear, morphology-dependent, $M_{\rm BH}$–$M_{*,\rm gal}$ relations (Davis et al., 2018a; Sahu et al., 2019a).

ies, galaxies with a disk versus galaxies without a disk, and ETGs versus LTGs. We also investigate the relation between $M_{\rm BH}$ and the central concentration index (Graham et al., 2001a), which is known to vary monotonically with the Sérsic index (Trujillo et al., 2001; Graham et al., 2001b).

As with the $M_{\rm BH}$–$M_{*,\rm sph}$ relation, the $M_{\rm BH}$–$\rm n_{sph}$ and $M_{\rm BH}$–$\rm R_{e,sph}$ relations can be applied to large surveys of galaxies (Casura et al., 2019) — if their bulge Sérsic parameters are reliable — to estimate their black hole masses and further construct the black hole mass function (BHMF). The BHMF holds interesting information for cosmologists, e.g., to estimate the mass density of the Universe contained in BHs (e.g. Fukugita & Peebles, 2004; Graham & Driver, 2007b), to map the growth of BHs and constrain theoretical models of BH evolution (e.g. Kelly & Merloni, 2012). In addition, the latest BHMF, along with the galaxy merger rate (Chen et al., 2019; Volonteri et al., 2020), will help improve the prediction for the amplitude and time until detection of the long-wavelength gravitation wave background — as generated from merging supermassive black holes — using pulsar timing arrays (Siemens et al., 2013; Shannon et al., 2015; Sesana et al., 2016) and using the upcoming Laser Interferometer Space Antenna (LISA, Danzmann, 2017; Baker et al., 2019).

Section 4.2 details the galaxy sample and parameters which we used for our investigation, and the regression routines applied to obtain the correlations. Various correlations we observed, including their dependencies on galaxy morphology, are described in the subsections of Section 4.3. In sub-section 4.3.1, we present the scaling relations observed between the spheroid stellar mass and spheroid Sérsic index. Sub-section 4.3.2 presents the expected correlation between black hole mass and the bulge Sérsic index by combing the correlation observed between spheroid stellar mass and spheroid Sérsic index with our latest correlation between black hole mass and spheroid stellar mass. It then presents the observed correlations between black hole mass and the bulge Sérsic index based on our data-set. We also show the relationship between the Sérsic index and the central light concentration, and we present the correlation observed between the black hole mass and the central concentration index. In sub-section 4.3.3, we present the correlations observed between the spheroid stellar mass and the effective spheroid half-light radius. Here, we also explore the correlations of the spheroid stellar mass with the spheroid radii containing

10% and 90% of the light of the spheroid. Sub-section 4.3.4 provides the expected correlations these radii might have with the black hole mass, before presenting the observed correlations between the black hole mass and the spheroid effective half-light radius, along with the correlations between the black hole mass and the spheroid radii containing 10% and 90% of spheroid's light. These subsections additionally provide a discussion and some explanation for the correlations that we find. Finally, Section 4.4 presents a summary of our main results.

4.2 Data

The Sérsic (1963, 1968a) function is nowadays used to describe the light profiles of elliptical galaxies (E) and, when present, the spheroidal component of galaxies with a disk (ES/S0/Sp). A review of the Sérsic function, and its many associated expressions, can be found in Graham & Driver (2005). Briefly, the intensity of a Sérsic light profile can be expressed as a function of the projected galactic radius (R), such that

$$\mathrm{I(R)} = \mathrm{I_e} \exp\left[-\mathrm{b_n}\left\{\left(\frac{\mathrm{R}}{\mathrm{R_e}}\right)^{1/\mathrm{n}} - 1\right\}\right], \tag{4.1}$$

where I_e, R_e, and n are profile parameters. The term I_e is the effective intensity at the effective radius R_e, which bounds 50% of the total light in the associated 2D image. Graham (2019b) provides a detailed review of this popular radius and addresses the misconceptions about its physical significance. The surface brightness at this effective radius (μ_e) is related to I_e through $\mu_e \equiv -2.5 \log(I_e)$.

The Sérsic index n (also known as the shape parameter), describes the curvature of the light profile, such that a Sérsic light profile with a higher Sérsic index is steeper at the centre and has a shallower distribution at larger radius, whereas, a profile with a smaller Sérsic index is shallower at the centre followed by a steeper drop at outer radii (see Figure 2 in Graham, 2019b). Thus, the Sérsic index traces the central concentration of the light within the spheroid (Trujillo et al., 2001; Graham et al., 2001b, their Figure 2); and also the inner gradient of the gravitational potential[5] (Terzić & Graham, 2005, their Figures 2 and 3). The value of the term b_n in Equation 4.1 depends solely on n, and is obtained by

[5]This holds when dark matter is negligible, and there is no significant stellar mass-to-light ratio gradient.

solving $\Gamma(2\mathrm{n}) = 2\gamma(2\mathrm{n}, \mathrm{b_n})$, where Γ denotes the gamma function and γ is the incomplete gamma function. It can also be approximated by $\mathrm{b_n} \approx 1.9992\,\mathrm{n} - 0.3271$ for $0.5 < n < 10$ (Capaccioli, 1989).

In this work, we have used a sample of 123 galaxies with directly-measured black hole masses, for whom the Sérsic model parameters ($\mathrm{n}, \mathrm{R_e}, \mathrm{and}\, \mu_\mathrm{e}$) describing their spheroid's surface brightness distribution were obtained by a careful multi-component decomposition of the galaxy's light. These parameters are collectively taken from Savorgnan & Graham (2016b), Davis et al. (2019a), and Sahu et al. (2019a). These studies performed a 2-dimensional (2D) isophotal analysis, first extracting a 2D luminosity model using Isofit and Cmodel (Ciambur, 2015) to capture the radial gradients in the ellipticity, position angle, and Fourier harmonic coefficients describing the isophote's deviations from a pure ellipse, and then performing a multi-component decomposition using the isophotal-averaged 1D surface-brightness profile along the major and geometric-mean[6] axis of the galaxies. For this purpose, they used the software Profiler (Ciambur, 2016), which is inbuilt with many functions for specific galaxy components, including the Sérsic function for galactic bulges/spheroids. The major and geometric-mean axis were modelled independently (see Section 3 in Sahu et al., 2019a, for more details).

Table C.1 in our Appendix C lists both the major-axis bulge parameters ($\mathrm{n_{maj}}$, $\mathrm{R_{e,maj}}$, $\mu_\mathrm{e,maj}$), and the equivalent-axis bulge parameters ($\mathrm{n_{eq}}$, $\mathrm{R_{e,eq}}$, $\mu_\mathrm{e,eq}$), plus the morphologies, and the bulge masses ($M_{*,\mathrm{sph}}$) taken from Savorgnan & Graham (2016b), Davis et al. (2019a), and Sahu et al. (2019a), along with the distances and the directly-measured black hole masses of the galaxies. To show the consistency between the structural decomposition of the major- and equivalent-axis surface brightness profiles, we have plotted $\mu_\mathrm{e,sph,maj}$ versus $\mu_\mathrm{e,sph,eq}$ in Figure 4.1. The 1σ scatter in this diagram is $0.58\,\mathrm{mag\,arcsec^{-2}}$ which corresponds to a 1σ scatter in $\mathrm{R_e}$ of $\approx$30% given that the Sérsic model's surface brightness profile has slopes of $\sim$1.8 to $\sim$2.1 (for n = 1 to 10) at $\mathrm{R} = \mathrm{R_e}$, where $\mathrm{d}\mu(\mathrm{R})/\mathrm{dR}|_\mathrm{R_e} = 2.5\mathrm{b_n}/(\ln(10)\,\mathrm{n}\,\mathrm{R_e}) \approx [2.17 - 0.36/\mathrm{n}]/\mathrm{Re}$. Table C.1 also provides the radial concentration

[6]The geometric-mean axis, which is also known as the "equivalent axis", is the radius of the circularized form of the elliptical isophote with major axis radius $\mathrm{R_{maj}}$ and minor axis radius $\mathrm{R_{min}}$, which conserves the same amount of flux. This results in the equivalent axis radius (R_eq) being the geometric mean of $\mathrm{R_{maj}}$ and $\mathrm{R_{min}}$ ($\mathrm{R_{eq}} = \sqrt{\mathrm{R_{maj}} * \mathrm{R_{min}}}$), which is also represented as $\mathrm{R_{geom}}$ (for more details see the appendix section in Ciambur, 2015).

index (C: see Section 4.3) and the physical (arcsec to kpc) size scale of the galaxies[7]. The morphologies of these galaxies are based on the multi-component decompositions found in Savorgnan & Graham (2016b), Davis et al. (2019a), and Sahu et al. (2019a).

The black hole masses used here have been obtained from various sources in the literature. Their original sources are listed in Savorgnan et al. (2016) and Sahu et al. (2019a) for the ETGs, and in Davis et al. (2019a) for the LTGs. These black hole masses have been directly-measured using either the stellar dynamical modelling, gas dynamical modelling, megamaser kinematics, proper motions (Sgr A^*), or the latest direct imaging methods (M87*). As the distances to the galaxies have been revised over time, the BH masses have also been updated to keep pace with this, and thereby provide a consistent analysis with the arcsecond-to-kpc and apparent-to-absolute magnitude conversions.

Our total sample is comprised of 123 galaxies, of which 83 are ETGs, and 40 are LTGs. We have used the Bivariate Correlated Errors and Intrinsic Scatter (BCES) regression (Akritas & Bershady, 1996) to obtain the symmetric (bisector) best-fit lines for all our correlations. The BCES[8] regression considers the measurement errors in both variables and allows for intrinsic scatter in the data. It is a modified form of the ordinary least square (OLS) regression. It calculates the OLS($Y|X$) line by minimizing the scatter in the Y-direction, and the OLS($X|Y$) line by minimizing the scatter in the X-direction. The BCES(Bisector) line symmetrically bisects the OLS($Y|X$) and OLS($X|Y$) lines. We prefer to use the bisector line as it offers equal treatment to the quantities plotted on the X-and Y-axes. Additionally, we also checked the consistency of our correlations by employing the modified-FITEXY (MPFITEXY) regression (Press et al., 1992; Tremaine et al., 2002; Williams et al., 2010; Markwardt, 2012), where we had to bisect the best-fit lines obtained from the forward OLS($Y|X$) and inverse OLS($X|Y$) regressions to obtain the symmetric fit to our data (see Novak et al., 2006, for more details about the MPFITEXY regression).

For our investigation, we adopt a 20% uncertainty for the Sérsic bulge parameter n. Various factors which can contribute to the uncertainty in the measurement of the Sérsic

[7]The physical scale is calculated using the python version of Edward (Ned) L. Wright's cosmological calculator (Wright, 2006), written by James Schombert, assuming the cosmological parameters H_0 = 67.4 (km s^{-1})/Mpc, Ω_m=0.315, and Ω_v=0.685 (Planck Collaboration et al., 2020).

[8]We used the Python module from (Nemmen et al., 2012), which is available at `https://github.com/rsnemmen/BCES`

bulge parameters include: inappropriate sky subtraction; incomplete masking; inaccurate point-spread function (PSF) for the telescope; uncertainties in the identification of components; especially the nuclear (bar/disk/ring/star cluster) or faint components during the multi-component decomposition of the galaxy luminosity. Thus, it is challenging to quantify the uncertainty in the bulge parameters for every galaxy individually.

In past studies, various measures have been taken to quantify realistic errors on the bulge/galaxy Sérsic index. For example, Caon et al. (1993) noted a typical error of $\sim 25\%$ corresponding to a 25% variation in the (observed - fitted) residual, while some studies (e.g. Graham & Driver, 2007a; Savorgnan et al., 2013) adopted a constant uncertainty of $\sim 20\%$, and others employed Monte Carlo simulations (e.g. Beifiori et al. (2012) obtaining up to a $\sim 15\%$ error-bar). Others varied the sky subtraction by $\pm 1\sigma$ to estimate error-bars (Vika et al., 2012), some used mean/median errors based on a broader comparison with published parameters from other studies (Graham & Worley, 2008; Laurikainen et al., 2010) producing up to $\sim 30\%$ uncertainty, whereas Savorgnan (2016) used 20%, 42%, and 52% uncertainties, respectively, for their grade 1, grade 2, and grade 3 galaxies following Savorgnan & Graham (2016b, their Section 4.2). As Savorgnan & Graham (2016b) noted, their generous uncertainties arose when comparing published parameters based upon an array of differing decompositions for the same galaxy. For example, sometimes a single Sérsic component had been fit while other times the image analysis additionally included, as separate components, a disk and sometimes also a bar.

Given that our sky-background intensities are measured carefully (Sahu et al., 2019a, see their Figure 1 and Section 2.2), and that our parameters are obtained from multi-component decompositions, we have ruled out our two major sources of systematic errors (i.e. over/under-estimation of the sky and failing to account for a biasing component), and as such we adopt a 20% uncertainty for n, and a 30% uncertainty for $\mathrm{R_e}$ based on the 1σ scatter in μ_e for our galaxy sample as already described in this section. We do, however, test and confirm that our scaling relations are not significantly dependent upon this. Our results are stable (no change in slope or intercept at the 1σ uncertainty level) upon using an uncertainty up to 30% in n and 40% in $\mathrm{R_e}$. Furthermore, we also performed all the correlations using the major subsample of our total sample for whom the spheroid parameters are derived using $3.6\,\mu$m images (see Table C.1), and the correlations are found to be consistent with the correlations obtained using the total sample within the $\pm 1\sigma$ uncertainty bounds of the slopes and intercepts.

During our linear regressions, we have excluded certain potentially biasing galaxies, which are either stripped galaxies (NGC 4342 and NGC 4486B), a single galaxy with $M_{\mathrm{BH}} < 10^5 M_\odot$ (NGC 404), or more than 2σ outliers (NGC 1300, NGC 3377, NGC 3998, NGC 4945, NGC 5419) in any of the correlations presented here. NGC 4342 and NGC 4486B are stripped of their stellar mass due to the gravitational pull of their massive companion galaxies NGC 4365 (Blom et al., 2014) and NGC 4486 (Batcheldor et al., 2010), respectively. Hence, NGC 4342 and NGC 4486B can bias the black hole scaling relations as they have smaller n or $\mathrm{R_e}$ than they would have had if they weren't stripped of their mass. NGC 404, the only galaxy in our sample with a BH mass below $10^6 M_\odot$, can bias the best-fit lines due to its location at the end of the distribution and thus its elevated torque strength. The galaxies NGC 3377, NGC 3998, NGC 4945, and NGC 5419 in the M_{BH}–n diagram, and NGC 1300 in the M_{BH}–$\mathrm{R_e}$ diagram, are more than $\pm 2\sigma_{\mathrm{rms}}$ outliers from the corresponding best-fit lines and slightly alter their slopes[9]. Hence, these galaxies are better excluded in all our regressions to obtain robust correlations. These eight excluded galaxies are indicated in all the plots. This exclusion leaves us with a reduced sample of 115 galaxies.

4.3 Scaling relations

The stellar masses of our galactic spheroids ($M_{*,\mathrm{sph}}$) are derived from the luminosities measured using the Sérsic model (for the bulge) fit to the equivalent- (or geometric-mean) axis light profile, parameterized by $\mathrm{n}_{\mathrm{sph,eq}}$, $\mathrm{R}_{\mathrm{e,sph,eq}}$, and $\mathrm{I}_{\mathrm{e,sph,eq}}$. Therefore, it is expected to find some correlation between $M_{*,\mathrm{sph}}$ and the Sérsic index, and also between $M_{*,\mathrm{sph}}$ and the effective half-light radius. The issue of parameter coupling potentially explaining the trends between the Sérsic parameters and the luminosity was explored and dismissed using model-independent measures of both luminosity and size (Caon et al., 1993; Trujillo et al., 2001), implying the observed correlation between luminosity versus Sérsic properties (n and $\mathrm{R_e}$) are indeed real. Moreover, the errors in n and $\mathrm{R_e}$ adopted here are not big

[9]Including these galaxies in the regressions changes the slopes by $\sim 1\sigma$ uncertainty level of current slopes.

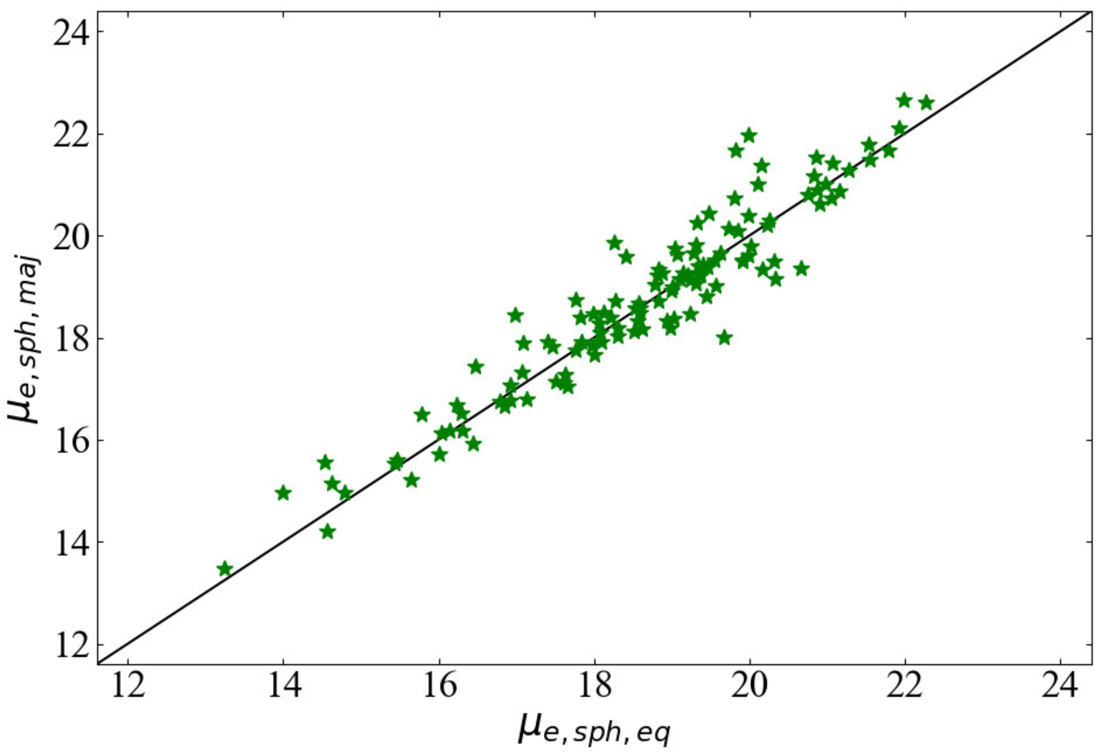

Figure 4.1 The surface brightness at the effective half-light radius from a Sérsic fit to the major-axis light profile ($\mu_{\mathrm{e,sph,maj}}$) plotted against the surface brightness at the effective half-light radius from a Sérsic fit to the the geometric mean-axis light profile ($\mu_{\mathrm{e,sph,eq}}$). This tight distribution of data-points over the one-to-one line quantifies the consistency between the two independent decompositions.

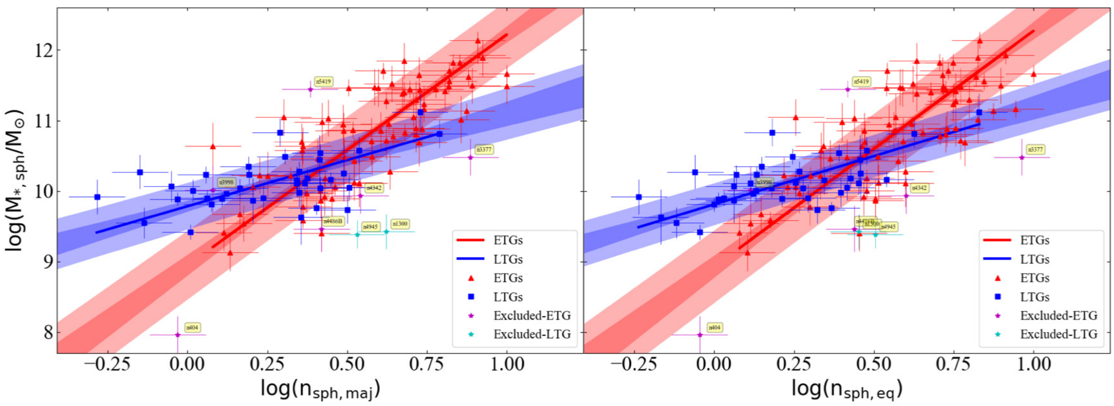

Figure 4.2 Spheroid mass versus major-axis (left panel) and equivalent-axis (right panel) Sérsic index describing the bulge/spheroidal component of the galaxies. In both panels, ETGs and LTGs are represented in red and blue, respectively. The bold red line for ETGs and blue line for LTGs represent the (symmetric) best-fit relations obtained using the BCES(Bisector) regression. The dark shaded region around these lines represents the $\pm 1\sigma$ uncertainty bound on the slopes and intercepts of these lines. The light-shaded region about these lines represent the $\pm 1\sigma$ scatter in the corresponding dataset. Both panels display the different $M_{*,\mathrm{sph}}$–$\mathrm{n}_{\mathrm{sph}}$ relations defined by ETGs and LTGs (see Equations 4.2 and 4.3 for ETGs and LTGs, respectively). Galaxies excluded from our regressions, as discussed in Section 4.2, are marked in magenta and cyan. Additionally, excluding the two extreme right LTGs (blue data-points) still yields consistent relation within 1σ uncertainty bound of the $M_{*,\mathrm{sph}}$–$\mathrm{n}_{\mathrm{sph}}$ relation for LTGs plotted here.

enough for parameter coupling in the fitting process to explain the observed trends.

4.3.1 The $M_{*,\mathrm{sph}} - \mathrm{n}_{\mathrm{sph}}$ diagram

We find two different relations in the $M_{*,\mathrm{sph}}$–$\mathrm{n}_{\mathrm{sph}}$ diagram (Figure 4.2) for the two morphological classes: ETGs and LTGs. Note that the (galaxy absolute magnitude, $\mathfrak{M}_{\mathrm{gal}}$)–n relation for ETGs in Young & Currie (1994), Graham et al. (1996), Jerjen et al. (2000), Graham & Guzmán (2003), and Ferrarese et al. (2006b) pertains to the whole galaxy, not the spheroidal component of the ETG (unless it is an elliptical galaxy). The $\mathfrak{M}_{\mathrm{sph}}$–n relation in Andredakis et al. (1995), Graham (2001), Khosroshahi et al. (2000), and Möllenhoff & Heidt (2001) pertains to the bulge/spheroid component of predominantly spiral galaxies.

The $M_{*,\mathrm{sph}}$–$\mathrm{n}_{\mathrm{sph,maj}}$ relation that we derived for ETGs can be expressed as

$$\log(M_{*,\mathrm{sph}}/M_{\odot}) = (3.27 \pm 0.25)\log(\mathrm{n}_{\mathrm{sph,maj}}/3) + (10.50 \pm 0.06), \tag{4.2}$$

with a total root mean square (rms) scatter of $\Delta_{\mathrm{rms|sph}} = 0.46$ dex in the $\log(M_{*,\mathrm{sph}})$-direction. The intrinsic scatter and correlation coefficients for Equation 4.2 and all other relations presented in this paper are provided in Tables 4.1 and 4.2. As mentioned in Section 4.2, we used the BCES bisector regression that treats the ordinate and abscissa symmetrically. Additionally, using the bisector line from the MPFITEXY regressions, we obtain the slope$= 3.30 \pm 0.18$ and intercept$= 10.50 \pm 0.04$, which is closely consistent with the above relation obtained using the BCES regression. It should be noted that equation 4.2 is for spheroids, and is thus different from the (*Galaxy* mass, $M_{*,\mathrm{gal}}$)–(galaxy Sérsic index) relation for ETG sample containing disk galaxies.

The bulges of LTGs follow a shallower relation which can be expressed as

$$\log(M_{*,\mathrm{sph}}/M_{\odot}) = (1.31 \pm 0.22)\log(\mathrm{n}_{\mathrm{sph,maj}}/3) + (10.41 \pm 0.07), \tag{4.3}$$

with $\Delta_{\mathrm{rms|sph}} = 0.32$ dex. The correlation of $M_{*,\mathrm{sph}}$ with the equivalent axis Sérsic indices ($\mathrm{n}_{\mathrm{sph,eq}}$) for ETGs and LTGs are consistent with the above Equations 4.2 and 4.3, respectively, and are provided in Table 4.2. Equation 4.3 is also consistent with the relation obtained from the bisector MPFITEXY regression which provided the slope$= 1.32 \pm 0.19$ and intercept$= 10.41 \pm 0.06$ for LTGs. Similarly, for other correlations established in this paper, we have checked the best-fit lines using the MPFITEXY regression and these correlations with equivalent-axis bulge parameters are provided in the Appendix C (Table C.2).

Our $M_{*,\mathrm{sph}}$–n relations for ETGs and LTGs support the dual sequences seen in the spheroid luminosity (absolute magnitude)–(Sérsic index) diagram for ETGs and LTGs by Savorgnan (2016, and references therein), which was based on a sub-sample of our current sample. Importantly, our greater sample size has enabled a reduced uncertainty on the slope and intercept of the relations.

We also searched for substructures based on the other morphological information (core-Sérsic vs Sérsic galaxies, galaxies with a disk vs galaxies without a disk, and barred vs non-barred galaxies) and found no statistically significant division, except for a small difference between the best-fit lines for barred and non-barred galaxies (because the majority of our barred galaxies are LTGs)

Each of these relations implies that galaxies with greater spheroid stellar masses have higher spheroid Sérsic indices (Andredakis et al., 1995, their figure 5), i.e., a higher central stellar light concentration. Moreover, the $M_{*,\mathrm{sph}}$–$\mathrm{n_{sph}}$ relations with different slopes for the two morphological types (ETGs and LTGs) imply two different progressions of spheroid mass with the central light concentration. This might be reflecting two different ways the stellar mass evolves in the bulges of ETGs and LTGs. Hence, these distinct relations should be helpful for simulations and semi-analytic models studying the formation and evolution of galaxies with different morphology. We refrain from attempting a classical bulge versus pseudo-bulge classification. We do however note that no extra component for the (peanut shell)-shaped structure associated with a buckled bar (Combes et al., 1990; Athanassoula et al., 2015) is included in the galaxy decomposition because such features are effectively encapsulated by the B6 Fourier harmonic term (Ciambur, 2016; Ciambur & Graham, 2016; Ciambur et al., 2021) and the bar component of the decomposition. Inner discs are modelled as such.

4.3.2 The $M_{\mathrm{BH}} - \mathrm{n_{sph}}$ diagram

Obtaining the Sérsic index of a galactic spheroid is in some ways more straightforward than measuring its mass, or stellar velocity dispersion. This is because the Sérsic index can be obtained from the decomposition of the galaxy light even if the image is not photometrically calibrated. Whereas, measuring the spheroid stellar mass requires decomposition of a flux-calibrated image, which further requires the distance to the galaxy and an appropriate stellar mass-to-light ratio. Similarly, the stellar velocity dispersion measurement requires reducing and analyzing telescope-time-expensive spectra of the central stars of the galaxy.

The correlation between black hole mass and Sérsic index will, obviously, be beneficial for estimating the black hole mass of a galaxy using the Sérsic index of its spheroid (should it have one). Graham et al. (2003) were the first to establish a log-linear M_{BH}–$\mathrm{n_{sph}}$ relation using a sample of 22 galaxies, which yielded $\log \mathrm{M_{BH}} = (6.37 \pm 0.21) + (2.91 \pm 0.38) \log(\mathrm{n_{sph}})$.

It had a comparable rms scatter of $\Delta_{\mathrm{rms|BH}}$=0.33 dex with the contemporary M_{BH}–σ relation ($\Delta_{\mathrm{rms|BH}}$=0.31 dex) of the day. Graham & Driver (2007a) subsequently advocated the log-quadratic relation $\log \mathrm{M_{BH}} = (7.98 \pm 0.09) + (3.70 \pm 0.46) \log(\mathrm{n_{sph}}/3) - (3.10 \pm 0.84)[\log \mathrm{n_{sph}}/3]^2$, based on a sample of 27 galaxies. This resulted in a notably smaller intrinsic scatter (of just 0.18 dex) than that (0.31 dex) about their updated log-linear relation $\log \mathrm{M_{BH}} = (7.81 \pm 0.08) + (2.69 \pm 0.28) \log(\mathrm{n_{sph}}/3)$. In their log-quadratic M_{BH}–$\mathrm{n_{sph}}$ relation, galaxies with smaller Sérsic indices resided on the steeper part of the curve, and galaxies with higher Sérsic indices defined a shallower part of the curve. This might have been an indication of two different relations for low-$\mathrm{n_{sph}}$ and high-$\mathrm{n_{sph}}$ galaxies that they were not able to see because of a small sample.

In consultation with the published literature, Savorgnan et al. (2013) doubled the sample size and derived the M_{BH}–n relations for Sérsic and core-Sérsic galaxies, however, the slopes of the two sub-samples were consistent within their $\pm 1\sigma$ uncertainty bound. Savorgnan (2016) subsequently used their own measurement of spheroid Sérsic index based on multi-component decompositions, to establish a single log-linear $M_{\mathrm{BH}} \propto \mathrm{n_{sph}}^{(3.51 \pm 0.28)}$ relation, which was steeper than the relation reported by Graham & Driver (2007a). This is not surprising, as the slope from a single regression will vary arbitrarily according to the number of low- and high-n spheroids in one's sample. This difference in the M_{BH}–$\mathrm{n_{sph}}$ relation was also because Graham & Driver (2007a) used the forward (Y over X) FITEXY regression routine from Tremaine et al. (2002), which minimized the scatter in the quantity to be predicted, i.e., M_{BH}, yielding a shallower slope for their M_{BH}–$\mathrm{n_{sph}}$ relation. Though Graham & Driver (2007a) did not calculate the bisector/symmetric-fit relation using the FITEXY routine, the BCES bisector regression over their dataset yielded a slope of 2.85 ± 0.40 consistent with Savorgnan (2016)'s relation within the $\pm 1\sigma$ uncertainty bound. Savorgnan (2016) additionally explored the possibility of two different M_{BH}–n relations for ETGs and LTGs, however, due to just 17 LTGs in her sample, she could not find a statistically reliable best-fit line for the LTGs.

Here, we reinvestigate the M_{BH}–$\mathrm{n_{sph}}$ relation, roughly doubling the sample size of 64 from Savorgnan (2016). Upon combining the latest M_{BH}–$M_{*,\mathrm{sph}}$ relations for ETGs and LTGs from Sahu et al. (2019a) and Davis et al. (2019a) with our $M_{*,\mathrm{sph}}$–$\mathrm{n_{sph}}$ relations defined by ETGs and LTGs (Equations 4.2 and 4.3), we expect $M_{\mathrm{BH}} \propto \mathrm{n_{sph}}^{4.15 \pm 0.39}$ and

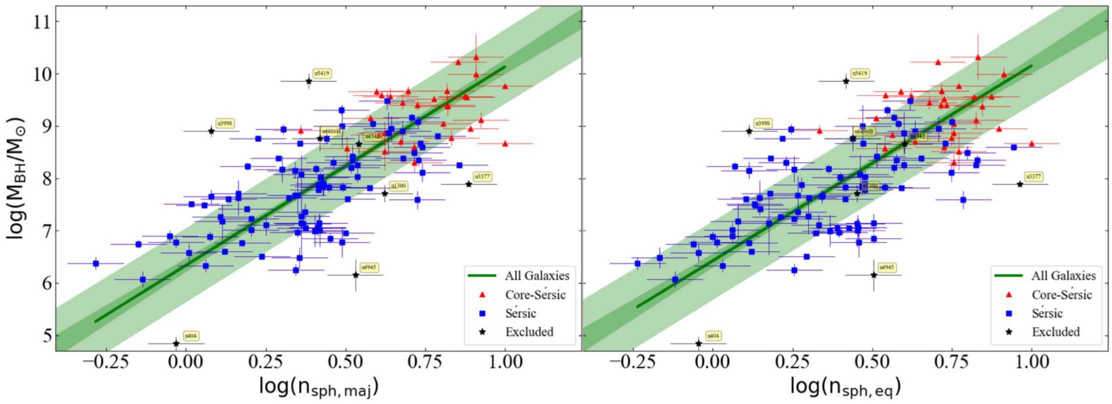

Figure 4.3 Black hole mass versus major-axis (left panel) and equivalent-axis (right panel) bulge/spheroid Sérsic index. Sérsic and core-Sérsic galaxies are shown in red and blue, respectively, and seem to follow the same single-regression M_{BH}–$\mathrm{n_{sph}}$ relation.

$M_{\mathrm{BH}} \propto \mathrm{n_{sph}^{2.83\pm0.63}}$ for ETGs and LTGs, respectively.

We started by performing a single symmetric regression between M_{BH} and $\mathrm{n_{sph}}$ for ETGs and LTGs combined (see Figure 4.3), which gives

$$\log(M_{\mathrm{BH}}/M_{\odot}) = (3.79 \pm 0.23) \log\left(\mathrm{n_{sph,maj}}/3\right) + (8.15 \pm 0.06), \tag{4.4}$$

between M_{BH} and $\mathrm{n_{maj}}$ with a total rms scatter of $\Delta_{\mathrm{rms|BH}} = 0.69$ dex. Similarly, we obtained the single-regression relation between M_{BH} and $\mathrm{n_{sph,eq}}$, presented in Table 3, which is closely consistent with the above M_{BH}–$\mathrm{n_{sph,maj}}$ relation. Notably, this single-regression M_{BH}–$\mathrm{n_{sph,maj}}$ relation is consistent with the Savorgnan (2016) relation within her larger $\pm1\sigma$ error bound of the slope and intercept. The asymmetric BCES($M_{BH}|n$) regression for our total sample yields M_{BH}–$\mathrm{n_{sph,maj}^{(3.15\pm0.22)}}$, which is still consistent with the relation observed in Graham & Driver (2007a), again, within the $\pm1\sigma$ uncertainty limit of slopes. The intercept, however, has changed. This may partly be due to our use of 3.6 μm data while Graham & Driver (2007a) used R-band data.

We further performed separate regressions for the ETGs and LTGs. The symmetric M_{BH}–$\mathrm{n_{sph,maj}}$ relation defined by ETGs can be expressed as

$$\log(M_{\mathrm{BH}}/M_{\odot}) = (3.95 \pm 0.34) \log\left(\mathrm{n_{sph,maj}}/3\right) + (8.15 \pm 0.08), \tag{4.5}$$

with $\Delta_{\rm rms|BH} = 0.65$ dex. The LTGs defined the shallower relation

$$\log(M_{\rm BH}/M_{\odot}) = (2.85 \pm 0.31)\log(\mathrm{n_{sph,maj}}/3) + (7.90 \pm 0.14), \tag{4.6}$$

with $\Delta_{\rm rms|BH} = 0.67$ dex. The $M_{\rm BH}$–$\mathrm{n_{sph,maj}}$ and $M_{\rm BH}$–$\mathrm{n_{sph,eq}}$ relations obtained for ETGs versus LTGs are presented in the left- and right- hand panels of Figure 4.4, respectively. The $M_{\rm BH}$–$\mathrm{n_{sph,eq}}$ relations for ETGs and LTGs are consistent with the above $M_{\rm BH}$–$\mathrm{n_{sph,maj}}$ relations and are presented in Table 4.2. Importantly, the two relations for ETGs and LTGs in the $M_{\rm BH}$–$\mathrm{n_{sph,maj}}$ (and also in $M_{\rm BH}$–$\mathrm{n_{sph,eq}}$) diagram are consistent with the expected relations obtained after combining the $M_{\rm BH}$–$M_{*,sph}$ and $M_{*,sph}$–$\mathrm{n_{sph}}$ relations (as mentioned before) for ETGs and LTGs within the $\pm 1\sigma$ uncertainty bound.

We also performed multiple double regressions by dividing our sample into Sérsic versus core-Sérsic galaxies, galaxies with a disk (ES-, S0-, Sp-Types) versus galaxies without a disk (E-Type), and barred versus non-barred galaxies. In the former two cases, we did not find statistically different relations. Whereas, we see two slightly different $M_{\rm BH}$–$\mathrm{n_{sph}}$ lines for barred and non-barred galaxies because most of our LTGs are barred while most of our ETGs are non-barred. Moreover, the difference between the two relations followed by ETGs and LTGs is more prominent; hence, we conclude that the substructure in the $M_{\rm BH}$–$\mathrm{n_{sph}}$ diagram is due to ETG versus LTG categorization. For a comparison, we provide the $M_{\rm BH}$–$\mathrm{n_{sph,maj}}$ (and $M_{\rm BH}$–$\mathrm{n_{sph,eq}}$) relations obtained for the barred and non-barred galaxies along with the relations for ETGs and LTGs in Tables 4.1 and 4.2.

The $M_{\rm BH}$–Concentration diagram

We also analyzed the relation between black hole mass and the light concentration of spheroids. Trujillo et al. (2001) quantified a central concentration index, for the light profile captured by a Sérsic function, as "a flux ratio" which can be expressed as $\mathrm{C}(\alpha) = \gamma(2\mathrm{n}, \mathrm{b_n}\alpha^{1/\mathrm{n}})/\gamma(2\mathrm{n}, \mathrm{b_n})$. Where, α is equal to $\mathrm{r/R_e}$, and $0 < \alpha < 1$. For a particular α, a higher value of $\mathrm{C}(\alpha)$ represents a spheroid or an elliptical galaxy with a greater central light or mass concentration.

To calculate the concentration index for our spheroids, we use the equivalent axis Sérsic index and the exact value of $\mathrm{b_n}$ obtained using the equation $\Gamma(2n) = 2\gamma(2n, b_n)$. In

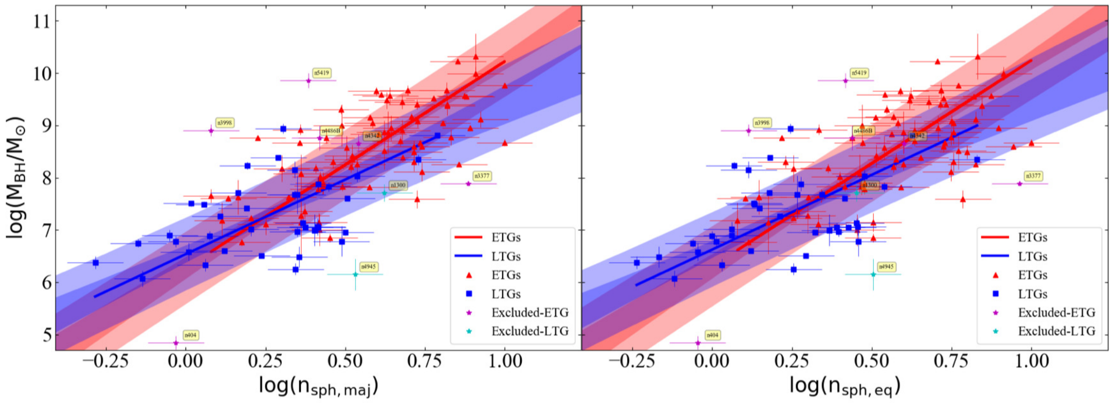

Figure 4.4 Similar to Figure 4.3, but now showing the separate regressions for ETGs and LTGs as expressed in Equations 4.5 and 4.6, resepectively. These relations are consistent with the predicted M_{BH}–n$_{\rm sph}$ relations obtained by combining the latest morphology-dependent M_{BH}–$M_{*,\rm sph}$ relations (Davis et al., 2019a; Sahu et al., 2019a) with the $M_{*,\rm sph}$–n$_{\rm sph}$ relations from Figure 4.2.

Figure 4.5, we have plotted C(α) for our spheroids, for a range of α values, against their equivalent axis Sérsic indices, revealing how both quantities are related monotonically, as already seen in Trujillo et al. (2001).

Graham et al. (2001a) explored a range of values of α and found that $\alpha = 1/3$ produces a minimum scatter in the vertical direction in the $M_{\rm BH}$–C(α) diagram. Moreover, for $\alpha >$ 0.5 the range of concentration index values is so small that it becomes indistinguishable for different profile shapes (i.e., n), which is evident in our Figure 4.5, while low values of $\alpha(< 0.2)$ are not so practical, especially for high redshift galaxies, as they require good spatial resolution Graham et al. (2001b). Therefore, in our investigation of the $M_{\rm BH}$–C(α) relation, we use C(α) at $\alpha = 1/3$ for our spheroids. The uncertainty in C(1/3) is calculated via error propagation based on a 20% uncertainty in the Sérsic index.

The correlation we obtained upon performing a symmetric regression between $M_{\rm BH}$ and C(1/3) for the total (ETGs+LTGs) sample can be expressed as,

$$\log(M_{\rm BH}/M_\odot) = (8.81 \pm 0.53) \log\left[{\rm C}(1/3)/0.4\right] + (8.10 \pm 0.07). \tag{4.7}$$

with $\Delta_{\rm rms|BH} = 0.73$ dex in $M_{\rm BH}$-direction. This is represented in Figure 4.6. This relation is steeper than the relation $M_{\rm BH} \propto {\rm C}(1/3)^{(6.81 \pm 0.95)}$ reported by Graham et al. (2001a)

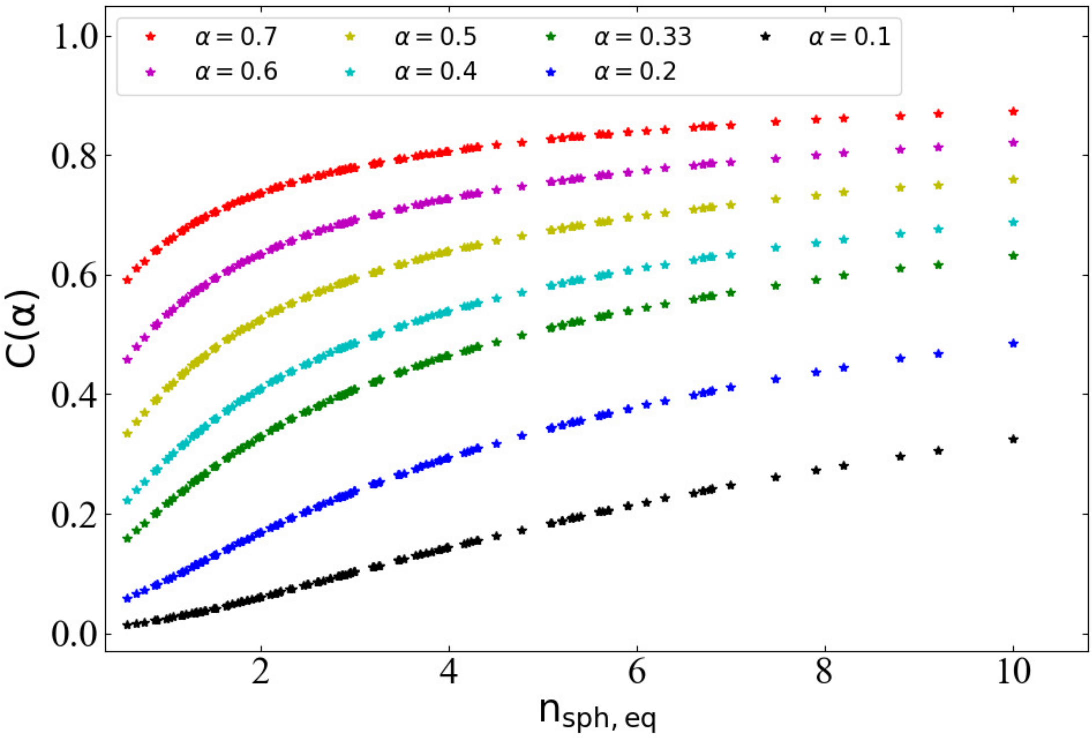

Figure 4.5 Central light concentration index plotted against equivalent axis Sérsic index for a range of α (fraction of effective half-light radius), representing the monotonicity between the concentration index and the Sérsic index. This plot also shows that for a high value of α ($\gtrsim$0.5), the range of C(α) values is very small such that the increment in the C(α) with increasing n becomes minimal for n $\gtrsim$ 2.

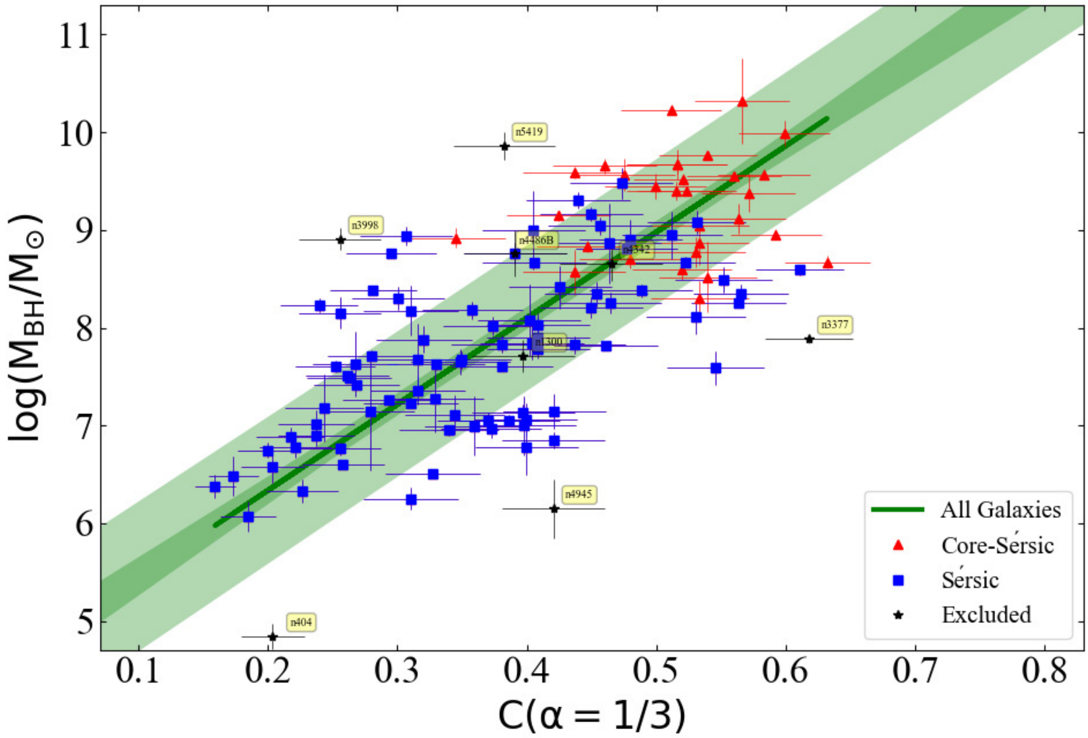

Figure 4.6 Black hole mass versus the spheroid's central concentration index calculated using the equivalent-axis Sérsic index.

which was based on a set of only 21 galaxies.

Here, again, we looked for substructures due to Sérsic versus core-Sérsic galaxies, galaxies with a disk versus galaxies without a disk, barred versus non-barred galaxies, and ETGs versus LTGs. We find two slightly different relations only for the latter two cases, similar to the $M_{\rm BH}$–$n_{\rm sph}$ diagram, which is represented in Figure 4.7. Again, the substructure in the $M_{\rm BH}$–C(α) diagram due to barred and non-barred galaxies is likely due to most of the LTGs being barred, while the dominant substructuring is due to the ETG and LTG sub-morphology. The parameters of the $M_{\rm BH}$–C(1/3) relations defined by ETGs and LTGs are provided in Table 4.2. The best-fit lines obtained for the barred and non-barred galaxies are also provided in Table 4.2 for comparison.

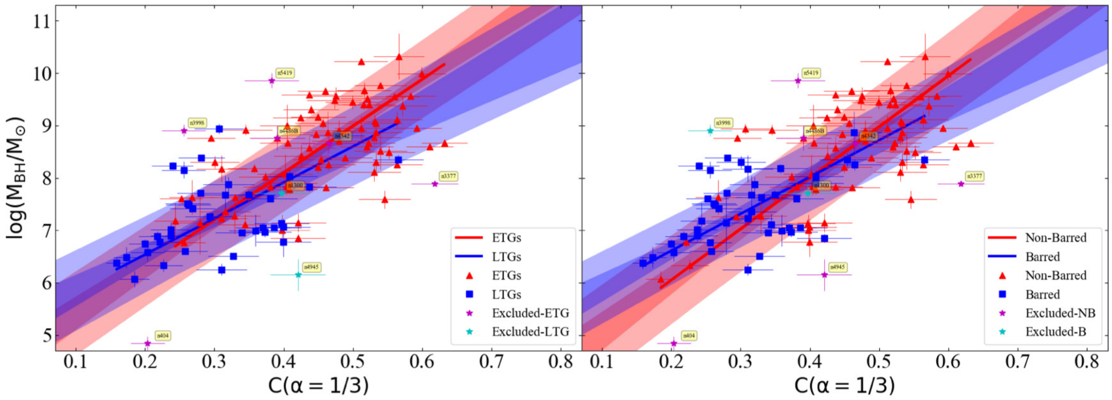

Figure 4.7 Similar to Figure 4.6, but now showing the best-fit lines obtained for ETGs and LTGs (left panel) plus barred and non-barred galaxies (right panel). The different lines obtained for barred and non-barred galaxies (right panel) is a consequence of most of our barred galaxies being LTGs.

4.3.3 The $M_{*,\mathrm{sph}} - \mathrm{R}_{\mathrm{e,sph}}$ diagram

There is a long history of studies which have worked on the galaxy size–luminosity ($\mathrm{L_{gal}}$–$\mathrm{R_{e,gal}}$) relation for ETGs and found it to be curved (see Graham, 2019b, for a review). Here we explore the $M_{*,\mathrm{sph}}$–$\mathrm{R_{e,sph}}$ diagram for the spheroids of ETGs and LTGs in our sample, for whom $\mathrm{R_{e,sph}}$ values were obtained from a careful image analysis.

Upon performing two different regressions for our ETGs and LTGs, we find a tight correlation between $M_{*,\mathrm{sph}}$ and $\mathrm{R_{e,sph}}$ (see Figure 4.8) for both, with remarkably smaller scatter, in the $M_{*,\mathrm{sph}}$-direction, than the $M_{*,\mathrm{sph}}$–n relations[10] (Equations 4.2 and 4.3 with $\Delta_{\mathrm{rms|sph}} = 0.46$ and 0.32 dex). The left- and right-hand panels in Figure 4.8 show the major-axis and equivalent-axis effective half-light radii ($\mathrm{R_{e,sph,maj}}$ and $\mathrm{R_{e,sph,eq}}$), respectively, on the horizontal-axes. The parameters for the $M_{*,\mathrm{sph}}$–$\mathrm{R_{e,sph}}$ relations for both ETGs and LTGs are provided in Tables 4.1 (major-axis) and 4.2 (equivalent-axis).

The best-fit $M_{*,\mathrm{sph}}$–$\mathrm{R_{e,sph}}$ lines for both ETGs and LTGs are log-linear and very close, such that their $\pm 1\sigma$ scatter region (shaded red and blue area in Figure 4.8) almost overlap with each other. Therefore, we further perform a single symmetric regression for our total

[10]The rms scatter in the horizontal direction for Equations 4.2, 4.3, and 4.8 are $\Delta_{\mathrm{rms|n}}$ =0.14 dex, $\Delta_{\mathrm{rms|n}}$ =0.24 dex, and $\Delta_{\mathrm{rms|Re}}$ =0.25 dex, respectively.

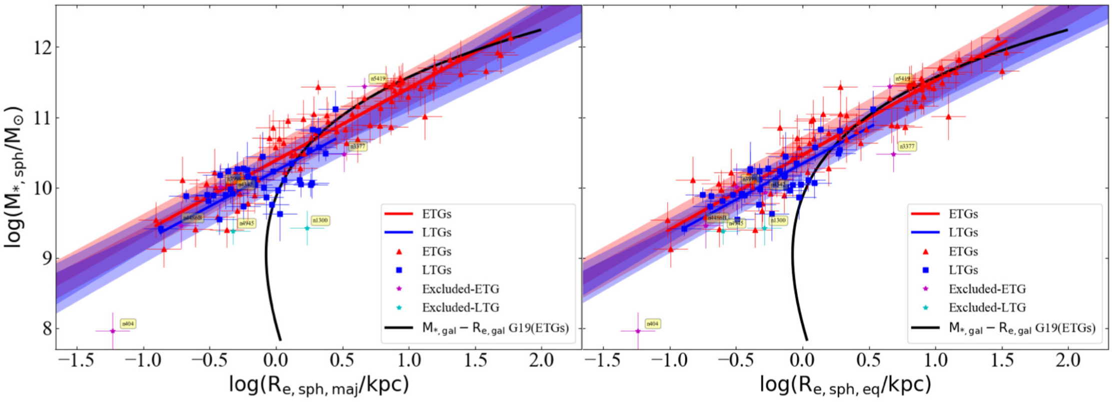

Figure 4.8 Spheroid stellar mass versus major-axis (left panel) and equivalent-axis (right panel) effective half-light radius of the spheroid. Both panels reveal that the spheroids of ETGs and LTGs follow closely consistent relations suggesting that a single $M_{*,\rm sph}$–$R_{\rm e,sph}$ relation (Equation 4.8) for all galaxy types is sufficient for the current data-set. The black curve is the $M_{*,\rm gal}$–$R_{\rm e,gal}$ relation for ETGs taken from Graham (2019b, their Figure 18) abbreviated as "G19".

(ETG+LTG) sample, obtaining

$$\log(M_{*,\rm sph}/M_{\odot}) = (1.08 \pm 0.04) \log\left(R_{\rm e,sph,maj}/\rm kpc\right) + (10.32 \pm 0.03), \tag{4.8}$$

with $\Delta_{\rm rms|sph} = 0.27$ dex. This single-regression is represented in Figure 4.9, where the left-hand and right-hand panels show the $M_{*,\rm sph}$–$R_{\rm e,sph,maj}$ and $M_{*,\rm sph}$–$R_{\rm e,sph,eq}$ relations, respectively. The parameters for the single-regression $M_{*,\rm sph}$–$R_{\rm e,sph,eq}$ relation can be found in Table 4.2, which has consistent slope with the above $M_{*,\rm sph}$–$R_{\rm e,sph,maj}$ relation.

Our total (ETG+LTG) sample also includes some alleged pseudo-bulges, marked in Table-1 of Sahu et al. (2019b) along with their source of identification, suggesting that the above single log-linear $M_{*,\rm sph}$–$R_{\rm e,sph}$ relation applies for both alleged pseudo-bulges and the normal/classical bulges.

For a comparison, we have plotted the $M_{*,\rm gal}$–$R_{\rm e,gal}$ curve for ETGs from Graham (2019b, their Figure 18) in our Figures 4.8 and 4.9. The shallower part of this curve, at the high mass (and size) end, seems to match well with our near-linear $M_{*,\rm sph}$–$R_{\rm e,sph}$ relation for bulges, however, the $R_{\rm e,sph}$ of our spheroids becomes smaller than their $R_{\rm e,gal}$ at $\log(M_{*,\rm sph}) \lesssim 10.5$ dex (or $R_{\rm e} \lesssim 2$ kpc) due to the presence of disks enabling bigger $R_{\rm e,gal}$

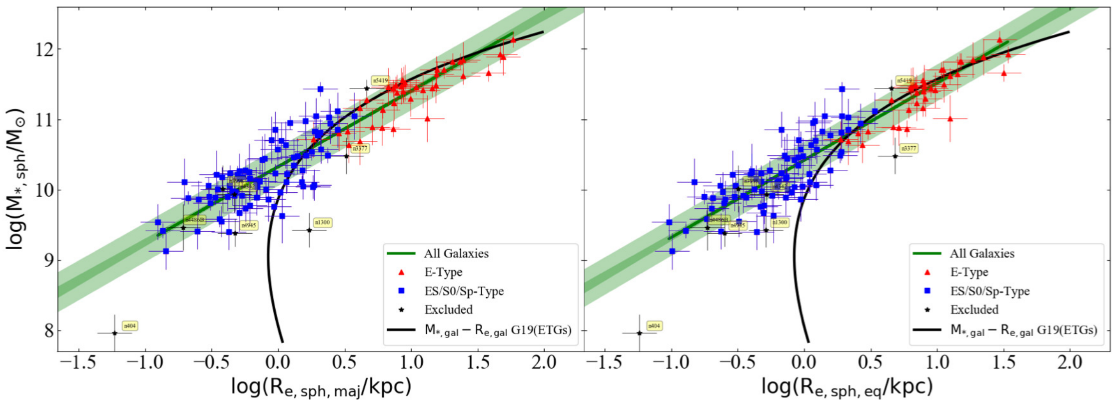

Figure 4.9 Similar to Figure 4.8, but now showing the single-regression $M_{*,\rm sph}$–$\rm R_{e,sph}$ relation defined by the total (ETG+LTG) sample.

for their ETGs[11]. We do not obtain a curved $M_{*,\rm sph}$–$\rm R_{e,sph}$ relation, possibly, because our sample does not include many dwarf/low-mass ETGs or late-type spiral galaxies.

The bend-point of the curved $\rm L_{gal}$–$\rm R_{e,gal}$ relation for ETGs has been of past interest, because many studies have claimed that this bend-point is the point of distinction between dwarf elliptical (dE) and classical spheroids or (normal) elliptical galaxies (Sérsic, 1968b; Kormendy et al., 2009; Fisher & Drory, 2010, 2016). Different physical formation processes have been invoked for these alleged disjoint classes of galaxies (e.g., Tolstoy et al., 2009; Kormendy & Bender, 2012; Somerville & Davé, 2015). Providing a detailed investigation of this curved relation, Graham (2019b, their figure 4) present a (galaxy luminosity)–$\rm R_z$ diagram, where $\rm R_z$ represents the radius of the projected galaxy image enclosing z% of the total light, for z varying from 2% to 97%, including $\rm R_e$ for which z=50%. Graham (2019b) find that all the $\rm L_{B,gal}$–$\rm R_{z_{gal}}$ relations are curved but the location (the absolute magnitude) of the bend-point of each curve changes with z, revealing that the bend-point in the L–$\rm R_{e\,(or\,z=50\%)}$ relation has been used to artificially divide galaxies at a random magnitude based on the random percentage of light used to measure galaxy sizes.

Following Graham (2019b), using their Equation 22, we also calculated the radii containing z = 10% and z = 90% of the spheroid's light, i.e., $\rm R_{10,sph}$ and $\rm R_{90,sph}$, respectively. Figure 4.14 demonstrates how the spheroid stellar mass correlates with the equivalent

[11]This is also partly intuitive because, for a given stellar density, a 2D disk (or a galaxy with a dominant disk) having the same total stellar mass as a 3D spheroidal distribution of stars will extend to a larger radii.

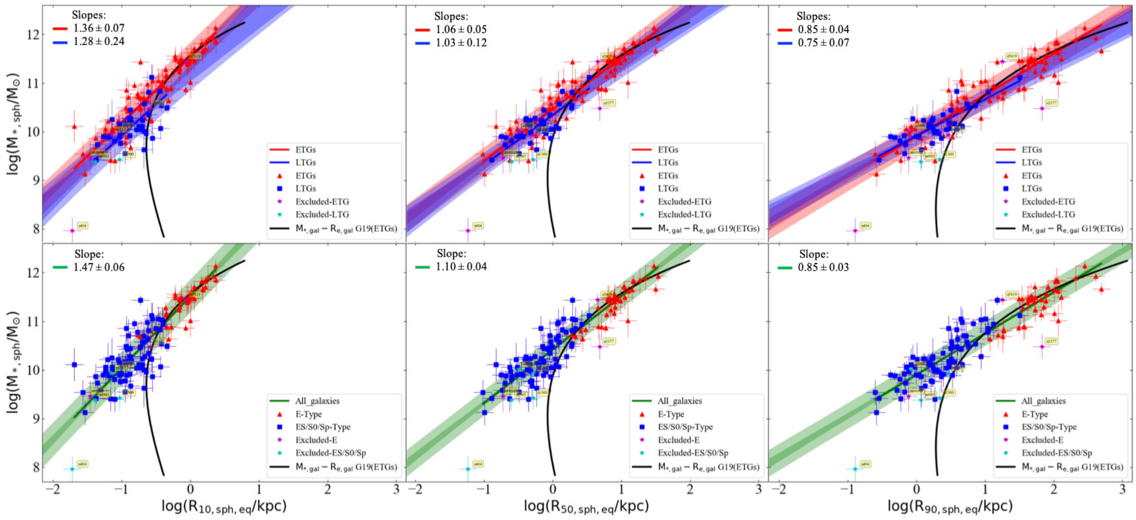

Figure 4.10 Similar to Figure 4.8 and 4.9, but now showing $R_{10,sph,eq}$, $R_{50,sph,eq}$ (or $R_{e,sph,eq}$), and $R_{90,sph,eq}$ on the horizontal axis in the left, middle, and right panels, respectively. Black curves are the $M_{*,gal}$–$R_{z,gal}$ curves from Graham (2019b) for the corresponding percentage ("z%") of enclosed light. The figure demonstrates that in all three cases ETGs and LTGs suggest a single relation between $M_{*,sph}$ and $R_{z,sph}$ for the range of our sample. Importantly, the $M_{*,sph}$–$R_{z,sph}$ relations become shallower with increasing z. All the parameters for the $M_{*,sph}$–$R_{z,sph}$ relations are provided in Table 4.2.

axis radii $R_{10,sph,eq}$, $R_{50,sph,eq}$ (or $R_{e,sph,eq}$), and $R_{90,sph,eq}$, in the left, middle, and right panels, respectively. In all three cases, we find that ETGs and LTGs follow consistent relations suggesting a single $M_{*,sph}$–$R_{z,sph}$ relation in each panel, however, the slope (and intercepts) of the relations change gradually with z. For comparison, we also show the $M_{*,gal}$–$R_{z,gal}$ curves from Graham (2019b), which seem to agree well with the elliptical galaxies at the high mass end of our $M_{*,sph}$–$R_{z,sph}$ relations. Whereas for galaxies with a disk (i.e., ES-, S0-, Sp-types), the radius containing z% of the spheroid's light ($R_{z,sph}$) is smaller than the radius containing z% of whole galaxy's light ($R_{z,gal}$). The parameters for the $M_{*,sph}$–$R_{10,sph,eq}$ and $M_{*,sph}$–$R_{90,sph,eq}$ relations are also provided in Table 4.2. Though for the range of our data-set we observe a (log)-linear relation between $M_{*,sph}$ and $R_{z,sph}$, addition of galaxies at the low-mass and small size end might reveal a curved $M_{*,sph}$–$R_{z,sph}$ relation similar to the $M_{*,gal}$–$R_{z,gal}$ curve for ETGs.

4.3.4 The $M_{\rm BH}$–$\rm R_{e,sph}$ diagram

Combining the $M_{\rm BH}$–$M_{*,\rm sph}$ relations defined by ETGs and LTGs, from Sahu et al. (2019a) and Davis et al. (2019a), with the single-regression $M_{*,\rm sph}$–$\rm R_{e,sph,maj}$ relation (Equation 4.8) followed by our combined sample of ETGs and LTGs, we expect $M_{\rm BH} \propto \rm R_{e,sph,maj}^{1.37\pm0.09}$ and $M_{\rm BH} \propto \rm R_{e,sph,maj}^{2.33\pm0.36}$ for ETGs and LTGs, respectively.

We first used a single regression for the total (ETG+LTG) sample, which yielded a good relation, provided in Tables 4.1 and 4.2 for the major- and equivalent-axis $\rm R_{e,sph}$, respectively, but with a higher scatter than the soon to be revealed separate relations for ETGs and LTGs. Moreover, it is inconsistent with the above prediction of the two relations in the $M_{\rm BH}$–$\rm R_{e,sph}$ diagram.

Upon performing separate regressions for ETGs and LTGs in the $M_{\rm BH}$–$\rm R_{e,sph}$ diagram, we do find two different relations for the two morphological classes. These relations are presented in Figure 4.11 with the left-hand and right-hand panels displaying $\rm R_{e,sph,maj}$ and $\rm R_{e,sph,eq}$, respectively. The relation defined by all ETGs can be expressed as,

$$\log(M_{BH}/M_\odot) = (1.26 \pm 0.08) \log\left(\rm R_{e,sph,maj}/kpc\right) + (8.00 \pm 0.07), \tag{4.9}$$

with $\Delta_{\rm rms|BH} = 0.58$ dex, while LTGs define the relation

$$\log(M_{BH}/M_\odot) = (2.33 \pm 0.31) \log\left(\rm R_{e,sph,maj}/kpc\right) + (7.54 \pm 0.10), \tag{4.10}$$

with $\Delta_{\rm rms|BH} = 0.62$ dex. The slope of the $M_{\rm BH}$–$\rm R_{e,sph,eq}$ relations for ETGs and LTGs are consistent with the corresponding $M_{\rm BH}$–$\rm R_{e,sph,maj}$ relations, and their fit parameters are provided in Table 4.2. These two relations (Equations 4.9 & 4.10) for ETGs and LTGs are in agreement with the expected $M_{\rm BH}$–$\rm R_{e,sph}$ relations mentioned at the beginning of this sub-section. Additionally, we note that our $M_{\rm BH}$–$\rm R_{e,sph,maj}$ relation for ETGs is also consistent with the relation obtained by de Nicola et al. (2019), based on an ETG-dominated sample.

Each of our non-linear, but log-linear, $M_{\rm BH}$–$\rm R_{e,sph}$ relations reveal that galaxies with more massive black holes tend to have a larger (bulge) half-light radii. However, the two different slopes of the $M_{\rm BH}$–$\rm R_{e,sph}$ relations for ETGs and LTGs suggest that the process

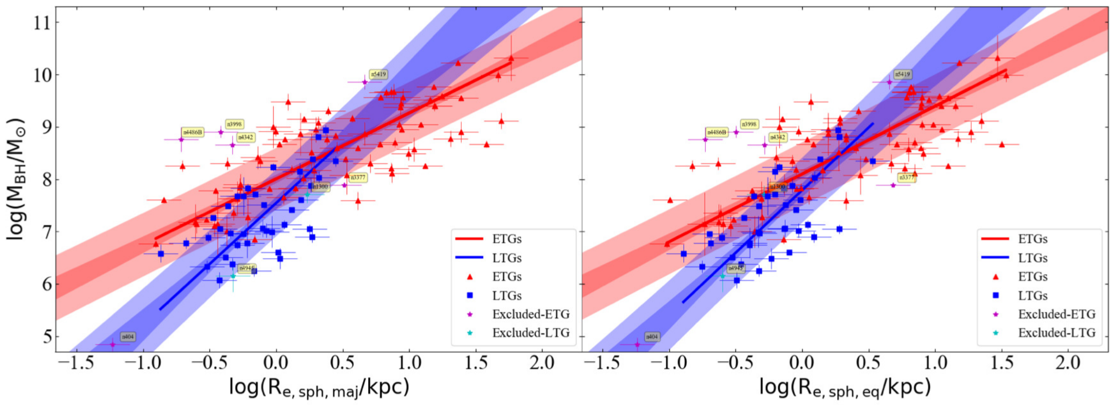

Figure 4.11 Black hole mass versus major-axis (left panel) and equivalent-axis (right panel) effective half-light radius of the spheroid. Both panels reveal that ETGs and LTGs follow two different $M_{\rm BH}$–$R_{e,sph}$ relations (Equations 4.9 and 4.10).

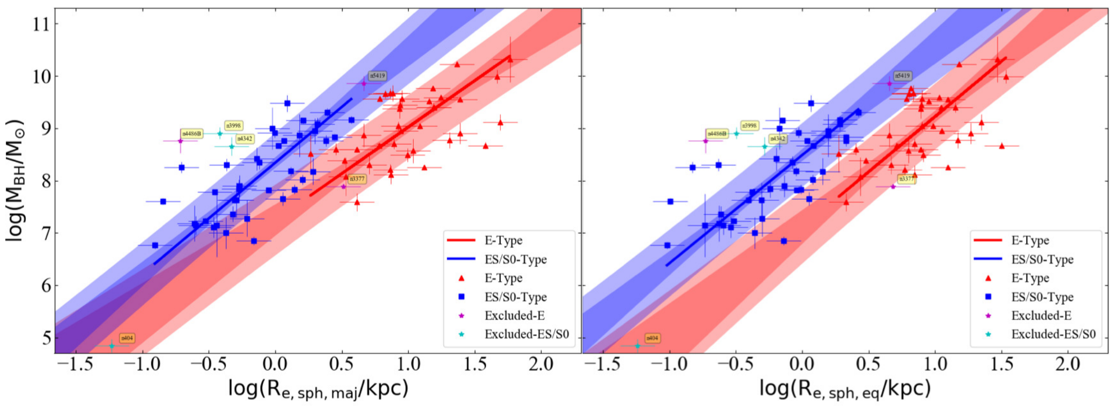

Figure 4.12 Similar to Figure 4.11, but now showing only the ETGs with a disk (ES and S0-types) and ETGs without a disk (E-type), which define two almost parallel $M_{\rm BH}$–$R_{e,sph}$ relations (listed in Tables 4.1 and 4.2) with an offset of $\sim$1 dex in the vertical direction. This explains the related offset in the $M_{\rm BH}$–$M_{*,sph}$ diagram (Sahu et al., 2019a).

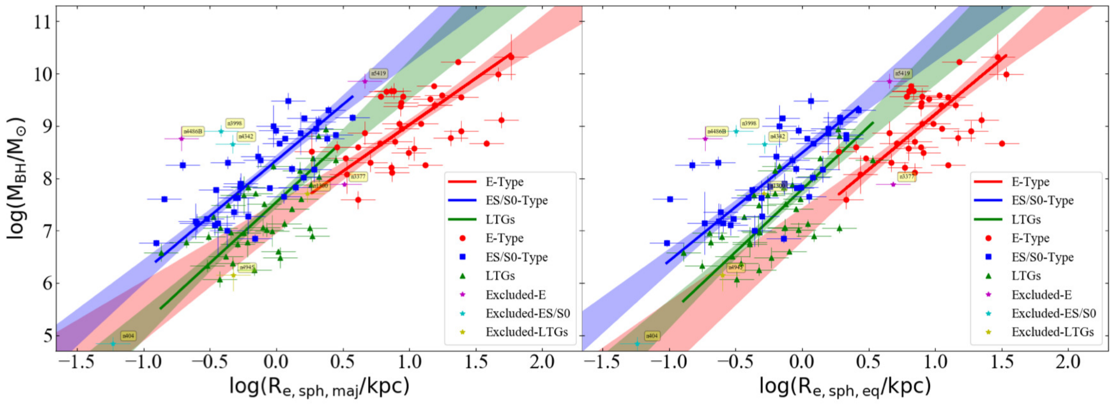

Figure 4.13 Similar to Figure 4.12, but now also showing the $M_{\rm BH}$–$\rm R_{e,sph}$ relation defined by LTGs in the same diagram. Just for clarity, we are not showing the (light-shaded) 1σ scatter regions, which are visible in Figures 4.11 and 4.12.

of evolution between black hole mass and spheroid size ($R_{e,sph}$), which further relates to the spheroid stellar mass, tends to be different for these different morphological types. This also supports our morphology-dependent $M_{\rm BH}$–$M_{*,\rm sph}$, and $M_{\rm BH}$–$M_{*,\rm gal}$ relations (Davis et al., 2018a; Sahu et al., 2019a), where ETGs and LTGs are found to follow two different relations. The total rms scatter about the $M_{\rm BH}$–$\rm R_{e,sph}$ relation is marginally smaller than the total rms scatter about the $M_{\rm BH}$–$M_{*,\rm sph}$ relation for LTGs (cf. $\Delta_{\rm rms|BH}$= 0.64), whereas, for ETGs it is a bit higher about the $M_{\rm BH}$–$\rm R_{e,sph}$ relation (cf. $\Delta_{\rm rms|BH}$= 0.52 about $M_{\rm BH}$–$M_{*,\rm sph}$ relation).

We did not find significantly different relations upon dividing our total sample into Sérsic versus core-Sérsic galaxies, or barred versus non-barred galaxies, in the $M_{\rm BH}$–$R_{e,sph}$ diagram. However, when we perform separate regressions for ETGs with a disk (ES-, and S0-types) and ETGs without a disk (E-type), we find two almost parallel relations which are offset by ~ 1 dex in the $\log(M_{\rm BH})$-direction (see Figure 4.12). ETGs with a disk follow the relation

$$\log(M_{\rm BH}/M_{\odot}) = (2.13 \pm 0.22) \log\left(\rm R_{e,sph,maj}/kpc\right) + (8.34 \pm 0.09), \tag{4.11}$$

with $\Delta_{\rm rms|BH} = 0.55$ dex, and ETGs without a disk define

$$\log(M_{\rm BH}/M_{\odot}) = (1.78 \pm 0.24) \log\left(\rm R_{e,sph,maj}/kpc\right) + (7.24 \pm 0.25), \tag{4.12}$$

with $\Delta_{\mathrm{rms|BH}} = 0.60$ dex. The M_{BH}–$\mathrm{R}_{\mathrm{e,sph,eq}}$ relations for ETGs with disk and ETGs without a disk, which are consistent with above Equations 4.11 and 4.12, respectively, are provided in Table 4.2. The two relations defined by ETGs with and without a disk are steeper than the single-regression M_{BH}–$\mathrm{R}_{\mathrm{e,sph}}$ relation for ETGs (Equation 4.9); however, the vertical scatter is comparable. The M_{BH}–$\mathrm{R}_{\mathrm{e,sph}}$ relation for the LTGs (Equation 4.10) is slightly steeper, but still its slope is consistent with the slope of the relations for ETGs with and without a disk at the 1σ level; however the intercepts are different. The final substructures in the M_{BH}–$\mathrm{R}_{\mathrm{e,sph}}$ diagram, i.e., the relations followed by ETGs with a disk, ETGs without a disk, and LTGs, are presented together in Figure 4.13.

In passing, we note that the M_{BH}–$\mathrm{R}_{\mathrm{e,sph}}$ relation that we obtained for ETGs without a disk—most of which are core-Sérsic galaxies—is also consistent with the relation $M_{\mathrm{BH}} \propto \mathrm{R}_{\mathrm{e}}^{1.86\pm0.26}$ obtained by combining the M_{BH}–(break radius or depleted core radius, R_{b}) and R_{b}–R_{e} relations observed for cored galaxies in Dullo & Graham (2014).

This offset between ETGs with and without a disk in the M_{BH}–$\mathrm{R}_{\mathrm{e,sph}}$ diagram is analogous to the offset found between the parallel relations for ETGs with and without a disk in the M_{BH}–$M_{*,\mathrm{sph}}$ diagram (Sahu et al., 2019a, their figure 8). Also, on combining the M_{BH}–$M_{*,\mathrm{sph}}$ relations defined by ETGs with and without a disk (Sahu et al., 2019a, their Equations 12 and 13), with our $M_{*,\mathrm{sph}}$–$\mathrm{R}_{\mathrm{e,sph}}$ relation (Equation 4.8), we obtain $M_{\mathrm{BH}} \propto \mathrm{R}_{\mathrm{e,sph,maj}}^{2.01\pm0.23}$ and $M_{\mathrm{BH}} \propto \mathrm{R}_{\mathrm{e,sph,maj}}^{2.05\pm0.23}$ ($M_{\mathrm{BH}} \propto \mathrm{R}_{\mathrm{e,sph,eq}}^{2.05\pm0.23}$ and $M_{\mathrm{BH}} \propto \mathrm{R}_{\mathrm{e,sph,eq}}^{2.09\pm0.23}$, for $\mathrm{R}_{\mathrm{e,sph,eq}}$), which are consistent with the observed relations for ETGs with a disk and ETGs without a disk, respectively (Equation 4.11 & 4.12, see Table 4.2 for $M_{\mathrm{BH}} - \mathrm{R}_{\mathrm{e,sph,eq}}$ parameters).

Importantly, as mentioned in Sahu et al. (2019a), this order of magnitude offset has little to do with the black hole masses of these two categories. Qualitatively, this offset can be understood by the different sizes of the spheroid effective half-light radius corresponding to ETGs with a disk (ES and S0) and ETGs without a disk (E). The ellicular (ES) and lenticular (S0) galaxies, which have intermediate/large-scale stellar disks in addition to their spheroids, have a smaller $\mathrm{R}_{\mathrm{e,sph}}$ relative to the elliptical galaxies which are comprised (almost) entirely of spheroids. This difference in $\mathrm{R}_{\mathrm{e,sph}}$ between the two sub-populations of ETGs creates the offset between the M_{BH}–$\mathrm{R}_{\mathrm{e,sph}}$ relations defined by them, and because of the non-zero slope of the M_{BH}–$\mathrm{R}_{\mathrm{e,sph}}$ relations, we see an offset in the vertical direction.

The relation $M_{*,\rm sph} = (M/L) 2\pi R_e^2 \langle I \rangle_e$ (e.g. Equation 8 in Graham, 2019b), where (M/L) represents the stellar mass-to-light ratio and $\langle \rm I \rangle_e$ is the averaged intensity within $\rm R_e$, suggests that $\log(\rm M_{*,sph}) \propto \log(\langle I \rangle_e) + 2\log(R_e)$. This can help us quantitatively understand the origin of the offset (of 1.12 ± 0.20 dex) found in the $\log(M_{\rm BH})$–$\log(M_{*,\rm sph})$ diagram (Sahu et al., 2019a, their section 4.2) between ETGs with and without a stellar disk. Here, we find a vertical offset of 1.41 ± 0.23 dex between the two sub-samples of ETGs in the $\log(M_{\rm BH})$–$2\log(\rm R_{e,sph,eq})$ diagram. Whereas, we do not find separate statistically significant $\log(M_{\rm BH})$–$\log(\langle \rm I \rangle_e)$ relations for these two populations, implying a single $\log(M_{\rm BH})$–$\log(\langle \rm I \rangle_e)$ for ETGs with and with out a disk. This suggests that the offset observed in the $\log(M_{\rm BH})$–$\log(M_{*,\rm sph})$ diagram by Sahu et al. (2019a) originates mainly from the offset in the $\log(M_{\rm BH})$–$\log(\rm R_{e,sph})$ diagram.

Furthermore, in the plot of $M_{\rm BH}$ versus the effective radius of the whole galaxy ($\rm R_{e,gal}$), this offset is expected to disappear, such that all the ETGs will follow a single $M_{\rm BH}$–$\rm R_{e,gal}$ relation, analogous to the combined behaviour of ETGs with and without a disk in the $M_{\rm BH}$–$M_{*,\rm gal}$ diagram (Sahu et al., 2019a, see the right-hand panel of their Figure 8), where the two sub-populations of ETGs follow consistent $M_{\rm BH}$–$M_{*,\rm gal}$ relations.

Similar to the previous subsection, here also we investigate the correlations of black hole mass with radii containing z = 10% and z = 90% of the spheroid's total light, in addition to the 50% ($\rm R_{e,sph}$) radius discussed above. Figure 4.14 presents the correlations we observed between black hole mass and $\rm R_{10,sph,eq}$, $\rm R_{50,sph,eq}$ (or $\rm R_{e,sph,eq}$), and $\rm R_{90,sph,eq}$, respectively in the left, middle, and right panels. The top panels show that ETGs and LTGs define two different $M_{\rm BH}$–$\rm R_{z,sph,eq}$ relations irrespective of z, however, the slopes of the relations become shallower with increasing z. The bottom panels reveal that the offset between the $M_{\rm BH}$–$\rm R_{z,sph,eq}$ relations followed by ETGs with a disk and ETGs without a disk are found in all cases; however, as expected, the amount of the offset varies with z and also the slopes of these relations become shallower with increasing z. The parameters for the $M_{\rm BH}$–$\rm R_{z,sph,eq}$ relations obtained for z = 10% and z = 90% are also presented in Table 4.2.

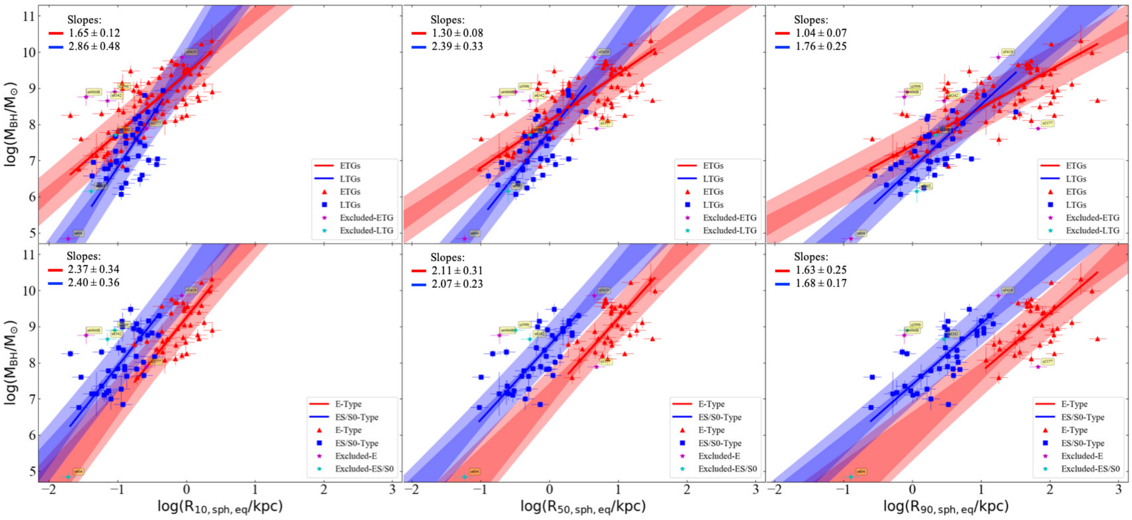

Figure 4.14 Similar to Figure 4.11 and 4.12, but now also showing the correlations of $M_{\rm BH}$ with the radius containing $z = 10\%$ ($R_{10,sph,eq}$) and $z = 90\%$ ($R_{90,sph,eq}$) of the spheroid's light in the left and right panels. Top panels reveal that ETGs and LTGs follow two different relations in all three cases. The bottom panel reveals that the offset between ETGs with and without a disk is obtained in all cases, where the offset varies with z. Additionally, due to the more massive systems having larger Sérsic indices, for all sub-morphologies the slope of the $M_{\rm BH}$–$R_{z,sph,eq}$ relation gradually decreases with increasing z. Intercepts and the scatter about these relations can be found in Table 4.2.

Table 4.1. Correlations of $M_{*,sph}$ and $M_{\rm BH}$ with the bulge/spheroid major-axis properties ($n_{sph,maj}$ and $R_{e,sph,maj}$)

Category (1)	**Number** (2)	α (3)	β dex (4)	ϵ dex (5)	Δ_{rms} dex (6)	r (7)	$\log p$ dex (8)	r_s (9)	$\log p_s$ dex (10)
		$\log(M_{*,sph}/M_\odot) = \alpha \log(n_{sph,maj}/3) + \beta$							
ETGs	77	3.27 ± 0.25	10.50 ± 0.06	0.27	0.46	0.79	-17.14	0.80	-17.32
LTGs	38	1.31 ± 0.22	10.41 ± 0.07	0.23	0.32	0.54	-3.28	0.41	-2.01
		$\log(M_{\rm BH}/M_\odot) = \alpha \log(n_{sph,maj}/3) + \beta$							
All Galaxies	115	3.79 ± 0.23	8.15 ± 0.06	0.60	0.69	0.77	-22.85	0.76	-22.36
ETGs	77	3.95 ± 0.34	8.15 ± 0.08	0.54	0.65	0.71	-12.46	0.69	-11.42
LTGs	38	2.85 ± 0.31	7.90 ± 0.14	0.62	0.67	0.53	-3.20	0.45	-2.36
Non-Barred	71	3.89 ± 0.31	8.15 ± 0.10	0.61	0.70	0.72	-11.80	0.64	-8.61
Barred	44	3.08 ± 0.36	8.00 ± 0.11	0.55	0.61	0.54	-3.76	0.47	-2.95
		$\log(M_{*,sph}/M_\odot) = \alpha \log(R_{e,sph,maj}) + \beta$							
All Galaxies	115	1.08 ± 0.04	10.32 ± 0.03	0.13	0.27	0.92	-47.92	0.90	-42.83
ETGs	77	1.03 ± 0.05	10.39 ± 0.04	0.09	0.25	0.93	-34.73	0.94	-36.98
LTGs	38	1.01 ± 0.15	10.24 ± 0.05	0.16	0.27	0.66	-5.26	0.58	-3.84
		$\log(M_{\rm BH}/M_\odot) = \alpha \log(R_{e,sph,maj}) + \beta$							
ETGs with a disk	39	2.13 ± 0.22	8.34 ± 0.09	0.47	0.55	0.74	-7.21	0.76	-7.81
ETGs without a disk	38	1.78 ± 0.24	7.24 ± 0.25	0.55	0.60	0.55	-3.45	0.52	-3.13
ETGs (All)	77	1.26 ± 0.08	8.00 ± 0.07	0.54	0.58	0.76	-15.10	0.74	-13.95
LTGs	38	2.33 ± 0.31	7.54 ± 0.10	0.54	0.62	0.63	-4.66	0.62	-4.43
All Galaxies	115	1.59 ± 0.09	7.73 ± 0.07	0.63	0.67	0.78	-23.56	0.78	-24.26

Note. — Columns: (1) Subclass of galaxies. (2) Number of galaxies in a subclass. (3) Slope of the line obtained from the BCES(Bisector) regression. (4) Intercept of the line obtained from the BCES(Bisector) regression. (5) Intrinsic scatter in the vertical ($\log M_{*,sph}$ or $\log M_{\rm BH}$)-direction (see Equation 1 from Graham & Driver, 2007a). (6) Total root mean square (rms) scatter in the vertical direction. (7) Pearson correlation coefficient. (8) Pearson correlation probability value. (9) Spearman rank-order correlation coefficient. (10) Spearman rank-order correlation probability value.

Table 4.2. Correlations of $M_{*,\mathrm{sph}}$ and M_{BH} with the bulge/spheroid equivalent-axis properties ($\mathrm{n}_{\mathrm{eq,sph}}, \mathrm{C}(1/3), \mathrm{R}_{\mathrm{e,sph,eq}}, \mathrm{R}_{10,\mathrm{sph,eq}}$, and $\mathrm{R}_{90,\mathrm{sph,eq}}$)

Category (1)	**Number** (2)	α (3)	β dex (4)	ϵ dex (5)	Δ_{rms} dex (6)	r (7)	$\log p$ dex (8)	r_s (9)	$\log p_s$ dex (10)
			$\log(M_{*,\mathrm{sph}}/\mathrm{M}_\odot) = \alpha \log(\mathrm{n}_{\mathrm{sph,eq}}/3) + \beta$						
ETGs	77	3.34 ± 0.24	10.52 ± 0.06	0.32	0.49	0.77	-15.63	0.74	-13.86
LTGs	38	1.37 ± 0.20	10.46 ± 0.07	0.20	0.28	0.63	-4.61	0.55	-3.39
			$\log(M_{\mathrm{BH}}/\mathrm{M}_\odot) = \alpha \log(\mathrm{n}_{\mathrm{sph,eq}}/3) + \beta$						
All Galaxies	115	3.72 ± 0.23	8.20 ± 0.07	0.65	0.73	0.74	-20.14	0.74	-20.22
ETGs	77	3.94 ± 0.37	8.18 ± 0.09	0.63	0.73	0.64	-9.37	0.60	-8.13
LTGs	38	2.86 ± 0.33	7.99 ± 0.16	0.64	0.68	0.49	-2.78	0.50	-2.86
Non-Barred	71	4.20 ± 0.38	8.11 ± 0.10	0.69	0.79	0.64	-8.89	0.54	-5.88
Barred	44	2.91 ± 0.30	8.08 ± 0.13	0.56	0.61	0.52	-3.54	0.45	-2.66
			$\log(M_{\mathrm{BH}}/\mathrm{M}_\odot) = \alpha\, \mathrm{C}(1/3)/0.4 + \beta$						
All Galaxies	115	8.81 ± 0.53	8.10 ± 0.07	0.65	0.73	0.74	-20.16	0.74	-20.17
ETGs	77	8.94 ± 0.86	8.10 ± 0.09	0.63	0.72	0.64	-9.45	0.60	-8.13
LTGs	38	6.88 ± 0.97	7.91 ± 0.16	0.64	0.68	0.47	-2.57	0.50	-2.83
Non-Barred	71	9.75 ± 0.93	8.00 ± 0.11	0.70	0.79	0.64	-8.77	0.54	-5.88
Barred	44	7.03 ± 0.88	8.02 ± 0.13	0.56	0.61	0.51	-3.36	0.45	-2.63
			$\log(M_{*,\mathrm{sph}}/\mathrm{M}_\odot) = \alpha \log(\mathrm{R}_{\mathrm{e,sph,eq}}) + \beta$						
All Galaxies	115	1.10 ± 0.04	10.42 ± 0.03	0.08	0.26	0.93	-50.60	0.92	-46.02
ETGs	77	1.06 ± 0.05	10.46 ± 0.04	0.08	0.26	0.93	-33.85	0.94	-35.31
LTGs	38	1.03 ± 0.12	10.34 ± 0.05	0.00	0.22	0.78	-7.98	0.67	-5.39
			$\log(M_{\mathrm{BH}}/\mathrm{M}_\odot) = \alpha \log(\mathrm{R}_{\mathrm{e,sph,eq}}) + \beta$						
ETGs with a disk	39	2.07 ± 0.23	8.49 ± 0.09	0.52	0.59	0.70	-6.19	0.71	-6.33
ETGs without a disk	38	2.11 ± 0.31	7.11 ± 0.27	0.55	0.61	0.53	-3.27	0.46	-2.43
ETGs	77	1.30 ± 0.08	8.10 ± 0.07	0.56	0.60	0.75	-14.41	0.72	-12.76
LTGs	38	2.39 ± 0.33	7.79 ± 0.13	0.52	0.60	0.66	-5.13	0.66	-5.21
All Galaxies	115	1.62 ± 0.09	7.86 ± 0.06	0.62	0.67	0.78	-23.81	0.78	-24.29
			$\log(M_{*,\mathrm{sph}}/\mathrm{M}_\odot) = \alpha \log(\mathrm{R}_{10,\mathrm{sph,eq}}) + \beta$						
All Galaxies	115	1.47 ± 0.06	11.51 ± 0.04	0.17	0.33	0.88	-38.55	0.86	-34.27
			$\log(M_{\mathrm{BH}}/\mathrm{M}_\odot) = \alpha \log(\mathrm{R}_{10,\mathrm{sph,eq}}) + \beta$						
ETGs with a disk	39	2.39 ± 0.36	10.30 ± 0.32	0.60	0.68	0.61	-4.38	0.63	-4.78
ETGs without a disk	38	2.37 ± 0.34	9.25 ± 0.10	0.53	0.61	0.54	-3.37	0.47	-2.54
ETGs	77	1.65 ± 0.12	9.40 ± 0.09	0.56	0.62	0.73	-13.50	0.71	-12.24
LTGs	38	2.86 ± 0.47	9.67 ± 0.44	0.60	0.69	0.54	-3.30	0.50	-2.83
			$\log(M_{*,\mathrm{sph}}/\mathrm{M}_\odot) = \alpha \log(\mathrm{R}_{90,\mathrm{sph,eq}}) + \beta$						
All Galaxies	115	0.85 ± 0.03	9.90 ± 0.03	0.12	0.26	0.93	-50.53	0.92	-47.05
			$\log(M_{\mathrm{BH}}/\mathrm{M}_\odot) = \alpha \log(\mathrm{R}_{90,\mathrm{sph,eq}}) + \beta$						
ETGs with a disk	39	1.68 ± 0.17	7.40 ± 0.13	0.51	0.56	0.73	-6.89	0.71	-6.35
ETGs without a disk	38	1.63 ± 0.25	6.11 ± 0.42	0.61	0.63	0.47	-2.52	0.41	-1.95
ETGs	77	1.04 ± 0.07	7.41 ± 0.09	0.58	0.60	0.74	-14.09	0.71	-12.17
LTGs	38	1.76 ± 0.25	6.78 ± 0.10	0.54	0.58	0.67	-5.30	0.68	-5.50

Note. — Column names are same as Table 4.1.

4.4 Summary

We have used the largest sample of galaxies to date with directly-measured black hole masses, and carefully measured bulge parameters obtained from multi-component decomposition of their galaxy light in our previous studies (Savorgnan & Graham, 2016b; Davis et al., 2019a; Sahu et al., 2019a). Using this extensive data-set, we have investigated the correlations between black hole mass (M_{BH}) and the bulge Sérsic index ($\mathrm{n_{sph}}$), bulge central light concentration index (C), and the bulge effective half-light radius ($\mathrm{R_{e,sph}}$).

For our sample, we also investigated the correlations between bulge mass ($M_{*,\mathrm{sph}}$) and both the bulge Sérsic index and bulge half-light radius. We then combined these with the latest M_{BH}–$M_{*,sph}$ relations to predict and check upon the observed correlations of M_{BH} with $\mathrm{n_{sph}}$ and $\mathrm{R_{e,sph}}$.

In all of the relations we investigated, we explored the possibility of substructure due to various subcategories of galaxy morphology, i.e., Sérsic versus core-Sérsic galaxies, galaxies with a stellar disk versus galaxies without a stellar disk, barred versus non-barred galaxies, and ETGs versus LTGs.

Parameters for all the correlations presented in this paper are separately listed in Table 4.1 and Table 4.2. The slope of the correlations that we obtained for M_{BH} or $M_{*,\mathrm{sph}}$ with the major-axis bulge parameters ($\mathrm{n_{sph,maj}}$ and $\mathrm{R_{e,sph,maj}}$) are consistent with the slope from the corresponding correlations of M_{BH} or $M_{*,sph}$ with the equivalent-axis bulge parameters ($\mathrm{n_{sph,eq}}$ and $\mathrm{R_{e,sph,eq}}$).

Our prime results can be summarized as follows,

- ETGs and LTGs follow two different $M_{*,\mathrm{sph}}$–$\mathrm{n_{sph}}$ relations (see Figure 4.2), with slopes equal to 3.27±0.25 and 1.31±0.22, and total rms scatter equal to $\Delta_{\mathrm{rms|sph}}$=0.46 dex and 0.32 dex, respectively (Equations 4.2 and 4.3), in the $M_{*,\mathrm{sph}}$–$\mathrm{n_{sph,maj}}$ diagram. As the Sérsic index is a measure of the central concentration of a bulge's light, these different slopes for the $M_{*,\mathrm{sph}}$–$\mathrm{n_{sph}}$ relation suggest distinct mechanisms for the evolution of spheroid mass and central light (or stellar mass) concentration in ETGs and LTGs.

- In the M_{BH}–$\mathrm{n_{sph}}$ diagram, ETGs and LTGs seem to follow two different relations with $M_{\rm BH} \propto {\rm n}_{\rm sph,maj}^{3.95\pm0.34}$ and $M_{\rm BH} \propto {\rm n}_{\rm sph,maj}^{2.85\pm0.31}$ with $\Delta_{\rm rms|BH} = 0.65$ dex and 0.67 dex, respectively (Figure 4.4, Equations 4.5 and 4.6).

- In the diagram showing the black hole mass versus the spheroid central concentration index, C(1/3), we again find two (slightly) different relations due to ETGs and LTGs (Figure 4.7, Table 4.2), analogous to the $M_{\rm BH}$–$\rm n_{sph}$ diagram. The slopes for the $M_{\rm BH}$–C(1/3) relations are 8.94 ± 0.86 and 6.88 ± 0.97 with $\Delta_{\rm rms|BH}$= 0.72 dex and 0.68 dex, respectively, for ETGs and LTGs.

- We find a tight near-linear relation between $M_{*,\rm sph}$ and $\rm R_{e,sph}$ for our range of data (Figures 4.8 and 4.9). Both ETGs and LTGs define the log-linear relation $M_{*,\rm sph} \propto \rm R_{e,sph,maj}^{1.08\pm0.04}$ (Equation 4.8) with $\Delta_{\rm rms|sph}$=0.27 dex. An extended view of the $M_{*,\rm gal}$–$\rm R_{e,gal}$ relation for ETGs is curved (Graham, 2019b), and our $M_{*,\rm sph}$–$\rm R_{e,sph}$ relation, somewhat dominated by massive spheroids, agrees with the quasi-linear part of the curve at high-masses where E-type galaxies dominate.

- ETGs and LTGs define two different relations between black hole mass and bulge $\rm R_e$ (Figure 4.11), such that $M_{\rm BH}$–$\rm R_{e,sph,maj}^{(1.26\pm0.08)}$ and $M_{\rm BH}$–$\rm R_{e,sph,maj}^{(2.33\pm0.31)}$ for ETGs and LTGs, with $\Delta_{\rm rms|BH}$=0.58 dex and 0.62 dex, respectively (Equation 4.9 and 4.10). This is analogous to the substructure in the $M_{\rm BH}$–$M_{*,\rm sph}$ diagram due to ETGs and LTGs (Sahu et al., 2019a).

- In the $M_{\rm BH}$–$\rm R_{e,sph}$ diagram, ETGs with a disk (ES, S0) and ETGs without a disk (E) follow two different, almost parallel, relations with slopes $\sim 2 \pm 0.2$ (Figure 4.12), which are steeper than the above single-regression $M_{\rm BH}$–$\rm R_{e,sph}$ relation for all ETGs (see Tables 4.1 and 4.2 for parameters) and offset by a factor of ~10 in the vertical $M_{\rm BH}$-direction. This is again analogous to the offset observed between the $M_{\rm BH}$–$M_{*,\rm sph}$ relations followed by ETGs with and without a disk (Sahu et al., 2019a). Given $M_{*,\rm sph}$ depends on $\rm R_{e,sph}$ via $M_{*,\rm sph} = (M/L)2\pi R_e^2 \langle I \rangle_e$, we find that the offset in the $M_{\rm BH}$–$M_{*,\rm sph}$ diagram originates from the offset between ETGs with and without a disk in the $M_{\rm BH}$–$\rm R_{e,sph}$ diagram. The reason behind the offset is the smaller spheroid half-light radius of ETGs with a disk relative to that of elliptical (purely spheroidal) galaxies.

- In the $M_{*,\mathrm{sph}}$–$\mathrm{R_{z,sph}}$ and M_{BH}–$\mathrm{R_{z,sph}}$ diagrams for z=10% and 90% (see Figures 4.10 and 4.14), we recover the same substructures as the M_{BH}–$\mathrm{R_{e,sph}}$ and $M_{*,\mathrm{sph}}$–$\mathrm{R_{e,sph}}$ relations mentioned above, with the slopes of correlations gradually decreasing with increasing z (see Table 4.2 for parameters).

The M_{BH}–$\mathrm{n_{sph}}$ and M_{BH}–$\mathrm{R_{e,sph}}$ relations may be useful for predicting the black hole masses of galaxies using their bulge Sérsic index or bulge half-light radius parameters. These parameters can be obtained by performing a multi-component decomposition of the galaxy light profiles obtained from photometrically un-calibrated images. One should be careful while using the M_{BH}–$\mathrm{R_{e,sph}}$ relation, because ETGs with a disk (ES,S0), ETGs without a disk (E), and LTGs (spirals) are found to follow different trends (Figures 4.11 and 4.12). However, when extended ETG or LTG classification is not known, the single regression M_{BH}–$\mathrm{n_{sph}}$ or M_{BH}–$\mathrm{R_{e,sph}}$ relations (provided in Tables 4.1 and 4.2) can still be used to predict M_{BH}, albeit with a higher uncertainty.

Our BH scaling relations, based on local galaxies, form a benchmark for studies investigating the evolution of BH correlations with galaxy properties across cosmic time (Lapi et al., 2014; Park et al., 2015; Sexton et al., 2019; Suh et al., 2020). In addition to enabling one to determine the black hole mass function (e.g. McLure & Dunlop, 2004; Shankar et al., 2004; Graham & Others, 2007; Vika et al., 2009; Davis et al., 2014; Mutlu-Pakdil et al., 2016), these BH scaling relations with bulge Sérsic parameters can also be employed to infer the lifetime of binary black holes (Biava et al., 2019; Li et al., 2020a) and further constrain the BH merger rate. The creation of merger-built spheroids with (initially) higher central stellar densities — which are associated with higher Sérsic indices — should, through dynamical friction (e.g., Chandrasekhar, 1943; Arca-Sedda & Capuzzo-Dolcetta, 2014), experience a quicker inspiral and hardening phase for their binary black holes. The imprint of such a process are the phase-space loss-cones (Begelman et al., 1980) observed as partially-depleted cores in massive spheroids (King & Minkowski, 1966, 1972; Lauer, 1985; Ferrarese et al., 1994; Trujillo et al., 2004; Dullo & Graham, 2014). The eventual coalescence of the black holes results in the emission of gravitational waves (Poincaré, 1906; Einstein, 1916, 1918; Abbott et al., 2016b). Our BH scaling relations will play a key role in constraining the detection of low-frequency gravitational waves generated from BH mergers at high redshifts (Shannon et al., 2015; Lentati et al., 2015; Sesana et al., 2016; Arzoumanian et al., 2018), which also fall in the detection domain of LISA (Amaro-Seoane et al., 2017; Barack et al., 2019).

The different scaling relations for ETGs and LTGs also hold valuable information for simulations, analytical/semi-analytical, and theoretical models of galaxy formation and evolution (e.g. Volonteri & Ciotti, 2013; Heckman & Best, 2014; Conselice, 2014), as they reveal the trends of BH—host bulge/galaxy properties depending on galaxy morphology. These relations can be used for primary size and structure tests in simulations aiming to generate realistic galaxies with supermassive black holes at their center (e.g. Schaye et al., 2015; Hopkins et al., 2018; Mutlu-Pakdil et al., 2018; Davé et al., 2019; Li et al., 2020b). We plan to test our new constraints through a comparison with simulations in our future work. Using our extensive dataset, we will also present the correlation of black hole mass with the internal stellar density of galactic spheroids (Sahu et al. 2020, in preparation). We will also explore the (first morphology aware) fundamental plane in our future work.

4.5 Acknowledgements

We thank the anonymous referee whose comments helped us improve the clarity of this paper. This research was conducted with the Australian Research Council Centre of Excellence for Gravitational Wave Discovery (OzGrav), through project number CE170100004. This project was supported under the Australian Research Council's funding scheme DP17012923.

5

The (Black Hole Mass)-(Spheroid Stellar Density) Relations: M_{BH}–μ (and M_{BH}–Σ) and M_{BH}–ρ

This paper is the fourth in a series presenting (galaxy morphology, and thus galaxy formation)-dependent black hole mass, M_{BH}, scaling relations. We have used a sample of 119 galaxies with directly-measured M_{BH} and host spheroid parameters obtained from multi-component decomposition of, primarily, 3.6 μm Spitzer images. Here, we investigate the correlations between M_{BH} and the projected luminosity density μ, the projected stellar mass density Σ, and the deprojected (internal) stellar mass density ρ, for various spheroid radii. We discover the predicted M_{BH}–$\mu_{0,\mathrm{sph}}$ relation and present the first M_{BH}–$\mu_{\mathrm{e,sph}}$ and M_{BH}–$\rho_{\mathrm{e,int,sph}}$ diagrams displaying slightly different (possibly curved) trends for early- and late-type galaxies (ETGs and LTGs) and an offset between ETGs with (fast-rotators, ES/S0) and without (slow-rotators, E) a disk. The scatter about various M_{BH}–$\langle\Sigma\rangle_{\mathrm{R,sph}}$ (and $\langle\rho\rangle_{\mathrm{r,sph}}$) relations is shown to systematically decrease as the enclosing aperture (and volume) increases, dropping from 0.69 dex when using the spheroid "compactness", $\langle\Sigma\rangle_{\mathrm{1kpc,sph}}$, to 0.59 dex when using $\langle\Sigma\rangle_{\mathrm{5kpc,sph}}$. We also reveal that M_{BH} correlates with the internal density, $\rho_{\mathrm{soi,sph}}$, at the BH's sphere-of-influence radius, such that core-Sérsic (high Sérsic index, n) and (low-n) Sérsic galaxies define different relations with total rms scatters 0.21 dex and 0.77 dex, respectively. The M_{BH}–$\langle\rho\rangle_{\mathrm{soi,sph}}$ relations shall help with direct estimation of tidal disruption event rates, binary BH lifetimes, and together with other BH scaling relations, improve the characteristic strain estimates for

long-wavelength gravitational waves pursued with pulsar timing arrays and space-based interferometers.

5.1 Introduction

The number of galaxies with directly-measured black hole masses, i.e., where observations could resolve the black hole's gravitational sphere-of-influence, has grown to about 145 galaxies (Sahu et al., 2019b). Using state-of-the-art two-dimensional modeling (Ciambur, 2015) and multi-component decompositions (Ciambur, 2016), we have modeled the surface brightness profiles of 123 of these galaxies[1] and their components. We have discovered morphology-dependent correlations between the black hole mass ($M_{\rm BH}$) and various host galaxy properties, such as the galaxy stellar mass ($M_{*,\rm gal}$), the spheroid stellar mass ($M_{*,\rm sph}$), the spheroid central light concentration or Sérsic index ($n_{\rm sph}$), the spheroid effective half-light radius ($R_{\rm e,sph}$), and the central stellar velocity dispersion (Graham, 2012; Graham & Scott, 2013; Scott et al., 2013; Savorgnan et al., 2016; Davis et al., 2018a, 2019a; Sahu et al., 2019a,b, 2020). These have improved as the quality, and the quantity of data has grown. The simple (galaxy morphology)-independent black hole scaling relations[2] (e.g., Dressler & Richstone, 1988; Magorrian et al., 1998; Häring & Rix, 2004; Gültekin et al., 2009a; Kormendy & Ho, 2013; McConnell & Ma, 2013) are, in fact, too simple to accurately trace the coevolution of the different types of galaxies and their black holes. For example, the small and massive bulges of spiral and lenticular galaxies follow $M_{\rm BH}$–$M_{*,\rm sph}$ relations different from that of elliptical galaxies (Sahu et al., 2019a). It is hoped that the advances with morphology-dependent correlations will help identify which correlation is more fundamental, i.e., primary versus secondary. However, one of the potential candidates remains to be explored; it involves stellar density.

Most of the morphology-dependent black hole scaling relations are significantly different to the familiar but now superseded "single relations" obtained when all galaxy types are combined. Crucially, diagrams with differing numbers of different galaxy types can yield "single relations" with different slopes and intercepts. As a result, many of the past

[1]This was the known sample size in 2018 when this projected commenced.

[2]The history of the galaxy/black hole scaling relations is reviewed in Ferrarese & Ford (2005) and Graham (2016).

"single relations" (built by grouping galaxies of different morphological types) are of limited physical meaning because of the way they are representing the ratio of the different galaxy types in that sample[3].

The above realization is fundamental if we are to adequately understand the coevolution of galaxies and their central massive black holes. This is because the black hole mass is, in a sense, aware of the different formation history and physics which went into building its host galaxy. What is important is not simply the amount of mass in stars and perhaps dark matter, but how that mass was assembled (and moves) to create a galaxy's substructure/morphology.

Using a sample of 27 galaxies, Graham & Driver (2007a) observed a strong correlation between M_{BH} and the bulge central concentration, which is quantified by the shape parameter of spheroid's surface brightness profile the Sérsic index (n_{sph}, Trujillo et al., 2001). Graham & Driver (2007a) found a comparable level of (intrinsic) scatter about the M_{BH}–n_{sph} relation as seen in the M_{BH}–(central stellar velocity dispersion: σ) relations observed at that time, which was about 0.3 dex. The observed stellar velocity dispersion traces the underlying mass distribution and radial concentration of light (Graham et al., 2001b). Thus, Graham & Driver (2007a) suggested that a combination of the central stellar density and the central light concentration of a spheroid may be governing the black hole–host spheroid connection.

Some studies (e.g., Graham & Guzmán, 2003; Merritt, 2006) presented a correlation between central concentration and central stellar density, suggesting that one of these quantities can be written in terms of the other; although, it is still not clear which quantity is more fundamental. Graham & Driver (2007a) combined this relation with their linear and curved[4] M_{BH}–n_{sph} relations, to predict both a linear and a curved M_{BH}–(spheroid central surface brightness or central projected density, $\mu_{0,\mathrm{sph}}$) relation (Graham & Driver, 2007a, their equations 9 and 10). Moreover, they suggested that an even better correlation might exist between M_{BH} and the (three-dimensional) deprojected density (ρ, *aka* the

[3]An example can be seen in Sahu et al. (2019a), where a single fit to all early-type galaxies produces a near-linear M_{BH}–$M_{*,\mathrm{sph}}$ relation. However, further investigation suggests that elliptical and lenticular galaxies define different almost quadratic M_{BH}–$M_{*,\mathrm{sph}}$ relations offset from each other by more than 1 dex in the M_{BH}-direction. This offset is reasonable and also addressed in this paper.

[4]Graham & Driver (2007a) also presented an even stronger but curved M_{BH}–n_{sph} relation with an intrinsic scatter of 0.18 dex.

internal or spatial density) at the center of the spheroid. For the first time, here we explore these predicted $M_{\rm BH}$–(projected stellar density) relations and expand this investigation to (deprojected) internal stellar densities.

We present new correlations between $M_{\rm BH}$ and the spheroid surface brightness (projected/column luminosity density), the projected (or column) stellar mass density (Σ), and the deprojected stellar density at various spheroid radii. Our sample of 123 galaxies is described in the following Section 5.2. That section also describes the linear regression applied and the parameter uncertainty used. The calculation of the deprojected density is detailed in the Appendix D.1, where we also compare our numerically calculated internal density with an approximation from the model of Prugniel & Simien (1997).

Section 5.3 presents the correlation between $M_{\rm BH}$ and the spheroid projected (luminosity and stellar mass) density at various radii (center, 1 kpc, 5 kpc, and half-light radius). In Section 5.4, we reveal additional new correlations obtained between $M_{\rm BH}$ and the bulge internal mass density at various (inner and larger) radii, including the sphere-of-influence radius of the black hole. We also provide the projected and deprojected density profiles, $\mu(R)$ and $\rho(r)$, to help explain various trends obtained between $M_{\rm BH}$ and μ, and between $M_{\rm BH}$ and ρ at different spheroid radii.

In all of these diagrams, we also investigate possible dependence on galaxy morphology, e.g., early-type galaxies (ETGs: elliptical E, ellicular ES[5], and lenticular S0) versus late-type galaxies (LTGs: spirals S), centrally-fast (ES, S0, S) versus slow (E) rotators, core-Sérsic[6] versus Sérsic[7] galaxies, and barred versus non-barred galaxies. We compare our findings with the morphology-dependent substructures seen in our recently published correlations (Sahu et al., 2019a,b, 2020). In Section 5.5 we discuss our results and some of the more notable implications. Finally, we summarize the main results of this work in

[5]Ellicular galaxies have an intermediate-scale, rotating stellar disk fully confined within their bulge (Liller, 1966; Savorgnan & Graham, 2016a). The term ellicular is a concatenation made by combining the words "elliptical" and "lenticular" (see Graham, 2019a, for a historical review of galaxy morphology and classification schemes).

[6]The core-Sérsic galaxies are generally the most massive galaxies, likely formed through major gas-poor mergers. The eventual coalescence of their central massive black holes scours out the stars from the central "loss cone" (through the transfer of the binary black hole's orbital angular momenta) and creates a deficit of light at the center, referred to as a "core". The bulge surface brightness profile for a core-Sérsic galaxy is described by a core-Sérsic function (Graham & Others, 2003), which consists of a shallow inner power-law followed by a Sérsic function (Sérsic, 1968a, 1963) at larger radii. Such cores were first noted by King & Minkowski (1966).

[7]Sérsic galaxies do not have a deficit of light at their center.

Section 5.6.

We have used the terms spatial density, and internal density interchangeably for the (3D) deprojected density throughout this paper. All uncertainties are quoted at the $\pm 1\,\sigma$ ($\approx 68\%$) confidence interval.

5.2 Data

We have used the spheroid's structural parameters from Savorgnan & Graham (2016b), Davis et al. (2019a), and Sahu et al. (2019a), which were obtained from multi-component decompositions of 123 galaxies with directly-measured central black hole masses reported in the literature. The direct methods for black hole mass measurement include stellar dynamical modeling, gas dynamical modeling, megamaser kinematics, proper motions (for Sgr A^*), and the latest direct imaging (for M87*). The majority of the galaxy images (81.1%) were in the $3.6\,\mu$m-band taken by the infrared array camera (IRAC, Fazio et al., 2004, resolution $\sim 2''$) onboard the Spitzer Space Telescope. The remaining images came from the archives of the Hubble Space Telescope (HST, 10.7%), the Sloan Digital Sky Survey (SDSS, 2.5%), and the Two Micron All Sky Survey (2MASS, 5.7%). For full details of the image analysis, we refer readers to the aforementioned three studies.

Briefly, we performed 2D modeling of the galaxy images using our in-house[8] software ISOFIT and CMODEL (Ciambur, 2015), which were built into the image reduction and analysis facility (IRAF, Tody, 1986, 1993). ISOFIT fits quasi-elliptical isophotes at each galactic radii. It uses an elliptical coordinate system, thereby improves upon the spherical coordinate system implemented in ELLIPSE (Jedrzejewski, 1987a,b). The angular coordinate known as the "eccentric anomaly" is used for uniform sampling of the quasi-elliptical isophotes, and the code employs Fourier harmonics to capture the isophotal deviations from a pure ellipse (Carter, 1978; Kent, 1984; Michard & Simien, 1988). Thus, ISOFIT generates an (azimuthally-averaged) one-dimensional surface brightness profile along any galaxy axis, together with the radial variations of the isophotal ellipticity (e), position angle, and Fourier coefficients. These parameters are used to create a 2D galaxy model via CMODEL. The model captures all symmetric features about the major-axis (mirror

[8] The software ISOFIT, CMODEL, and PROFILER are publicly available at the GitHub platform (see Ciambur, 2015, 2016, for details).

symmetry) and leaves behind disturbances and star clusters which can be explored in the "residual image".

We disassemble the galaxy model into components with the help of various functions inbuilt in the software PROFILER (Ciambur, 2016). A galaxy can have a bulge, intermediate- or large-scale disk, bar, ansae, rings, depleted core, and nuclear components (e.g., star cluster, nuclear bar, disk, or ring). The presence of disks and bars in our decompositions were verified, whenever possible, through recourse to the literature, including kinematic evidence for disk rotation. We perform this multi-component decomposition using the surface brightness profile along the galaxy's major-axis as well as the so-called "equivalent-axis", which represents a radial-axis equivalent to a circularised form of the galaxy's quasi-elliptical isophotes, such that the total enclosed luminosity remains conserved[9].

The multi-component decomposition process provides us with the surface brightness profiles of individual galaxy components and the detailed galaxy morphology, indicating the presence of a rotating disk, a depleted core, a bar, etc. One of the most noted of all galactic components is the bulge, whose surface brightness distribution is described using the Sérsic (1963) function (Appendix Equation D.1), which is parameterized by the Sérsic index ($n_{\rm sph}$), effective half-light radius ($R_{\rm e,sph}$), and the surface brightness at the half-light radius ($\mu_{\rm e,sph} = -2.5 \log I_{\rm e,sph}$). The equivalent-axis spheroid surface brightness profiles for our 3.6 μm (Spitzer) sample are shown in Figure 5.1.

To obtain the spheroid's internal (deprojected) stellar mass density distribution, $\rho(r)$, we performed an inverse Abel transformation (Abel, 1826) of the (circularly symmetric) equivalent-axis spheroid surface brightness profiles. The numerical calculation of the internal density profiles and a comparison with the Prugniel & Simien (1997) density model (an approximation to the exact deprojection of the Sérsic profile) is presented in the Appendix Section D.1.

The spheroid parameters required to calculate the projected and the internal stellar mass densities, e.g., the bulge surface brightness parameters ($n_{\rm sph}$, $R_{\rm e,sph}$, $\mu_{\rm e,sph}$), along

[9]The equivalent-axis radii, $R_{\rm eq}$, for an isophote is the geometric-mean of the isophote's major- and minor-axis radii ($R_{\rm maj}$ and $R_{\rm min}$, respectively), i.e., $R_{\rm eq} = \sqrt{R_{\rm maj} \times R_{\rm min}}$ or $R_{\rm eq} = R_{\rm maj}\sqrt{1 - e_{\rm maj}}$ (see Ciambur, 2015, 2016, for more details on the isophotal galaxy modeling, multi-component decomposition, and the circularised equivalent-axis).

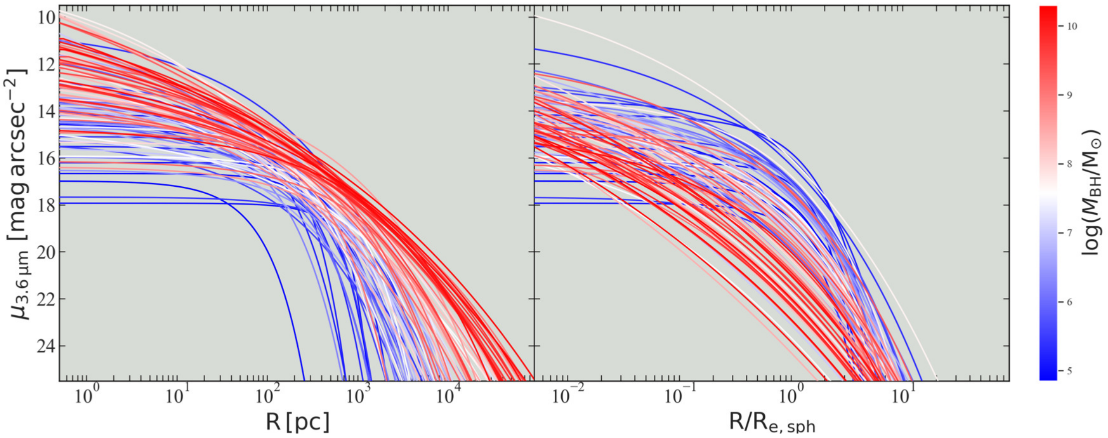

Figure 5.1 Left-hand panel: Spheroid (Sérsic) surface brightness profiles for our 3.6 μm-sample. Right-hand panel: The horizontal axis is normalized at the (projected) half-light radii of each spheroid. The color sequence blue-white-red traces the increasing black hole mass and helps with the understanding of the positive/negative trends observed between $M_{\rm BH}$ and the spheroid surface brightness (and the projected stellar mass density) presented in Section 5.3.

with the galaxy morphology, distances, physical (arcsec-to-kpc) scale[10], stellar mass-to-light ratio, and the image band information for all 123 galaxies are available in Sahu et al. (2020, their Appendix Table A1). Sahu et al. (2020) also tabulates the directly-measured central black hole masses and the bulge stellar masses ($M_{*,\rm sph}$) of these 123 galaxies.

Here, we excluded the galaxies NGC 404, NGC 4342, NGC 4486B, and the Milky Way throughout our investigation, unless expressly stated otherwise. NGC 404 is currently the only galaxy in our sample[11] with a black hole mass below $10^6\,M_\odot$ (Nguyen et al., 2017; Davis et al., 2020) and it may skew/bias the results. Its published black hole mass has a sphere of influence five times smaller than the seeing ($\sim 0.1''$) under which it was measured. NGC 4342 and NGC 4486B have been heavily stripped of their mass due to the gravitational pull of their massive companion galaxies (see Batcheldor et al., 2010; Blom et al., 2014). For the Milky Way, the available surface brightness profile (Kent et al., 1991; Graham & Driver, 2007a) was not flux-calibrated to obtain a calibrated density profile. The exclusion of these galaxies leaves us with a reduced sample of 119 galaxies. All the

[10] The arcsec-to-pc scale was calculated using cosmological parameters from Planck Collaboration et al. (2020).

[11] NGC 4395 (den Brok et al., 2015), NGC 205 , NGC 5102, and NGC 5206 (Nguyen et al., 2018, 2019) are other examples with sub-$10^6\,M_\odot$ black holes that we learned about late but hope to include in future work.

galaxies excluded from the linear regressions (performed to obtain the scaling relations presented here) are shown with a different symbol in the ensuing diagrams.

We use the bivariate correlated errors and intrinsic scatter (BCES) regression (Akritas & Bershady, 1996) to obtain our black hole scaling relations. BCES is a modification of the ordinary least squares regression. It considers measurement errors in both variables (and their possible correlation) and allows for intrinsic scatter in the distribution. We prefer to use the BCES(BISECTOR)[12] line obtained by symmetrically bisecting the BCES($Y|X$) line (which minimizes the error-weighted root mean square, rms, vertical offsets about the fitted line) and the BCES($X|Y$) line (which minimizes the error-weighted rms horizontal offsets about this different fitted line). We do this partly because it is unknown whether the host spheroid density is an independent variable and the central black hole mass is a dependent variable, or vice-versa, or if there is an interplay.

The BCES routine is, however, known to be vulnerable to error if the fitted data range is not large (Tremaine et al., 2002). We have therefore checked our best-fit parameters using a symmetric application (Novak et al., 2006) of the intrinsically non-symmetric modified FITEXY (known as MPFITEXY[13]) regression (Markwardt, 2009; Williams et al., 2010). Both the BCES and MPFITEXY regressions assume Gaussian and homoscedastic (constant variance) distribution of residuals; and thus, in cases where the distribution may have non-Gaussian and heteroscedastic residuals, these linear regression can underestimate the uncertainties of the fitted parameters: slope and intercept. Therefore, we also checked our scaling relations using a symmetric application of LINMIX, a non-symmetric ($Y|X$) regression presented by Kelly (2007) based on a Bayesian method, which allows for heteroscedastic errors. The fit parameters obtained from LINMIX are provided in Appendix D.2.

Uncertainties in $M_{\rm BH}$, and spheroid profile parameters $n_{\rm sph}$ (±0.09 dex), $R_{\rm e,sph}$ (±0.13 dex), and $\mu_{\rm e,sph}$ ($\pm0.58\,{\rm mag\,arcsec^{-2}}$ or ±0.23 dex in $\mu_{\rm e,sph}/2.5$) are taken from Sahu et al. (2020, see their section 2 for more details). The uncertainty in the internal density (ρ_e) at an internal radius equal to the projected half-light radius ($R_{\rm e,sph}$)—obtained by propagating errors in the spheroid parameters through the analytical expression (Equation

[12]The Python module written by (Nemmen et al., 2012) is available at `https://github.com/rsnemmen/BCES`.
[13]Available at `https://github.com/mikepqr/mpfitexy`.

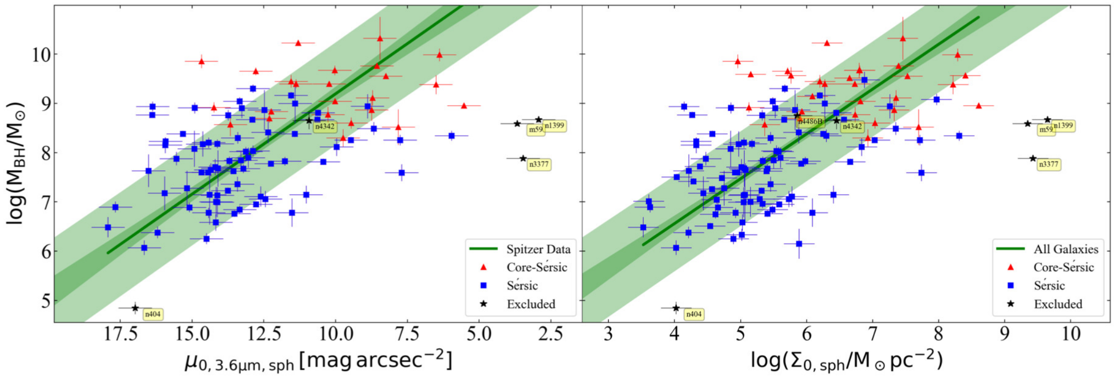

Figure 5.2 Left-hand panel: Black hole mass versus the central surface brightness (in the AB magnitude system) of the spheroids using our 3.6 μm sample. Right-hand panel: Black hole mass versus the projected central stellar mass density, including the 22 non-Spitzer galaxies. The dark green line represents the best-fit obtained from the BCES(BISECTOR) regression. The dark green shaded region around the best-fit line delineates the $\pm 1\sigma$ uncertainty on the slope and intercept, and the light green shaded area outlines the $\pm 1\sigma$ rms scatter in the data. The same description follows for all other correlations presented in this paper. For both Sérsic and core-Sérsic galaxies, $\mu_{0,3.6\mu\mathrm{m,sph}}$ and $\Sigma_{0,\mathrm{sph}}$ have been obtained through the inward extrapolation of the Sérsic portion of their spheroid profiles. Core-Sérsic galaxies have a deficit of light at their core and, hence, their $\mu_{0,3.6\mu\mathrm{m,sph}}$ values depicted here are brighter than the actual value. The galaxies excluded from the regression are marked with a black star.

D.7)—are $\sim \pm 0.30$ dex. For densities at other radii, the error propagation (assuming independent parameters) through the internal density expression (Equation D.6) provides even higher uncertainties due to multiple occurrences of n_{sph} and $R_{\mathrm{e,sph}}$, in addition to ρ_e. Such uncertainties are likely to be overestimated and can affect the best-fit lines. Therefore, we used a constant uncertainty of ± 0.23 dex on the projected mass densities (Σ) and, similarly, a constant uncertainty of ± 0.30 dex on the internal densities for all the correlations, unless stated otherwise. Additionally, we test the stability of our correlations (their slopes and intercepts) using a range of (zero to ± 0.38 dex) uncertainties for the projected and internal densities.

5.3 Black Hole Mass versus Spheroid Projected Density

5.3.1 Central Surface Brightness (μ_0) and Projected Mass Density (Σ_0)

To study the correlation between black hole mass and the host spheroid's central surface brightness ($\mu_{0,\rm sph}$), which is dependent on the image wavelength band, we used our 3.6 μm-sample comprised of 97 galaxies from the reduced sample of 119 galaxies (see Section 5.2). This includes 72 Sérsic galaxies, i.e., galaxies with a Sérsic spheroid surface brightness profile, and 25 core-Sérsic galaxies, i.e., galaxies with a depleted central core whose spheroid profile is described by a shallow central power-law followed by a Sérsic function at larger radii (see Graham & Others, 2003).

Using the (equivalent-axis) surface brightness parameters ($n_{\rm sph}$, $R_{\rm e,sph}$, and $\mu_{\rm e,sph}$) for the spheroids, we calculated $\mu_{0,\rm sph}$ via $\mu_0 = \mu_{\rm e} - 2.5 \log {\rm e}^{\rm b}$ (Equation D.1 at R=0), i.e., an inward extrapolation of the Sérsic fit to the spheroid's surface brightness profile. It is important to note that for our core-Sérsic galaxies, μ_0 has been obtained through the inward extrapolation of the Sérsic part of their spheroid profile (as in the $L_{\rm gal}$–μ_0 diagram of Jerjen et al., 2000). This is because the size of the depleted core is generally much smaller than the $\sim 2''$ spatial resolution of IRAC images (see Dullo & Graham, 2014), and, as such, the (3.6 μm-band) parameters for the central power-law of our core-Sérsic spheroids are not accurate[14]. Thus, the μ_0 used here for the cored galaxies represents their central surface brightness before the damaging effect of binary black holes, which will cause a departure of cored galaxies from an initial $M_{\rm BH}$–μ_0 trend line. This is the case with cored ETGs in the $M_{*,\rm gal}$–μ_0 diagram shown in Graham & Guzmán (2003, their Figure 9), which accounted for the central mass/light deficit in the cored galaxies.

The high-$n_{\rm sph}$ galaxies M 59, NGC 1399 (cored), and NGC 3377 are marked by black stars and have the brightest $\mu_{0,3.6\mu\rm m,sph}$ ($\sim 3\,{\rm mag\,arcsec^{-2}}$) in Figure 5.2. They reside beyond the 2σ scatter of the remaining dataset and have significant leverage on the best-fit line, such that including these three galaxies in the regression changes the slope by 1σ. Therefore, these three galaxies were excluded from the regression (in addition to the four exclusions mentioned in Section 5.2) to obtain the $M_{\rm BH}$–$\mu_{0,3.6\mu\rm m,sph}$ and the $M_{\rm BH}$–$\Sigma_{0,\rm sph}$

[14]The presence of the cores were confirmed through smaller field-of-view high-resolution HST images and the literature when available.

relations reported here.

The $M_{\rm BH}$–$\mu_{0,3.6\mu{\rm m,sph}}$ relation[15] plotted in the left-hand panel of Figure 5.2 was obtained using 94 (Sérsic +core-Sérsic) galaxies with 3.6 μm imaging data, and can be expressed as,

$$\log\left(\frac{\rm M_{BH}}{\rm M_\odot}\right) = (-0.41 \pm 0.04)\left[\mu_{0,3.6\mu{\rm m,sph}} - \frac{13\,{\rm mag}}{{\rm arcsec}^2}\right] + (7.97 \pm 0.10). \tag{5.1}$$

The total (measurement error and intrinsic scatter) rms scatter ($\Delta_{\rm rms|BH}$) is 1.03 dex in the $\log(M_{\rm BH})$-direction. This correlation quantifies how the (Sérsic) spheroids hosting more massive black holes have a brighter central surface brightness, qualitatively consistent with the linear prediction of the $\log(M_{\rm BH})$–$\mu_{0,{\rm sph}}$ relation in Graham & Driver (2007a, their equation 9 based on B-band data). This trend can also be inferred from the spheroid profiles plotted in the left-hand panel of Figure 5.1, where for R tending to zero, μ becomes brighter when moving from low-$M_{\rm BH}$ (blue profiles) to high-$M_{\rm BH}$ (red profiles).

In our $M_{\rm BH}$–$\mu_{0,3.6\mu{\rm m,sph}}$ diagram (Figure 5.2), the core-Sérsic galaxies are represented with the $\mu_{0,3.6\mu{\rm m,sph}}$ value that they presumably would originally have if their cores did not undergo a depletion[16] of light due to coalescing BH binaries in dry major-mergers (Begelman et al., 1980). Hence, one should not use the above relation to estimate $M_{\rm BH}$ using the actual (depleted) central surface brightness ($\mu_{0,{\rm core}}$) for cored galaxies, instead, the μ_0 extrapolated from the Sérsic potion of their spheroid profile can be used. The actual $\mu_{0,{\rm core}}$ for the core-Sérsic galaxies dims with increasing $M_{*,{\rm gal}}$ (Graham & Guzmán, 2003).

To include our remaining (non-Spitzer) sample of 22 galaxies, we mapped the central surface brightness, $\mu_{0,{\rm sph}}$, values to the central surface stellar mass density ($\Sigma_{0,{\rm sph}}$) with the units of solar mass per square parsec ($\rm M_\odot\,pc^{-2}$) using Equation D.5. We obtained a positive log-linear $M_{\rm BH}$–$\Sigma_{0,{\rm sph}}$ relation, which is represented in the right-hand panel of

[15] The uncertainty we assigned to $\mu_{0,3.6\mu{\rm m,sph}}$ is $\pm$0.58mag arcsec^{-2} (the same as assigned to $\mu_{{\rm e},3.6\mu{\rm m,sph}}$); however, consistent relations are obtained upon using up to $\pm$2mag arcsec^{-2} uncertainty.

[16] The deficit of light at the center of core-Sérsic galaxies is generally only a small fraction (5%, average value from Table 5 in Dullo, 2019) of their total spheroid light. This fraction is variable and can be approximately quantified for a given $M_{*,{\rm sph}}$ if we combine the $M_{\rm BH}$–$M_{*,{\rm sph}}$ relation (e.g., from Sahu et al., 2019a) with the $M_{\rm BH}$–$M_{*,{\rm def}}$ relation from the literature (e.g., Graham, 2004; Ferrarese et al., 2006a; Dullo & Graham, 2014; Savorgnan & Graham, 2015).

Figure 5.2. The best-fit relation is provided in Table 5.1 (T1.2), along with the (intrinsic[17] and total) rms scatter, Pearson correlation coefficient, and Spearman rank-order correlation coefficient. The $M_{\rm BH}$–$\mu_{0,3.6\mu{\rm m,sph}}$ and $M_{\rm BH}$–$\Sigma_{0,{\rm sph}}$ relations obtained using only Sérsic galaxies are consistent with the relations obtained when including the core-Sérsic galaxies.

[17]It should be noted that this depends on the adopted parameter uncertainties.

Table 5.1. Correlations between the Black Hole Mass and the Spheroid Projected Density

No. (1)	Category (Eq.#) (2)	Number (3)	$\log(M_{\rm BH}/M_\odot) = (Slope)\,X + (Intercept)$ dex (4)	ϵ dex (5)	$\Delta_{\rm rms\|BH}$ dex (6)	r_p (7)	r_s (8)
			Central Surface Brightness (Figure 5.2, left-hand panel)				
T1.1	3.6 μm sample (Eq. 5.1)	94[a]	$\log(M_{\rm BH}/{\rm M_\odot}) = (-0.41 \pm 0.04)\,[\mu_{0,3.6\mu{\rm m,sph}} - 13\,{\rm mag\,arcsec^{-2}}] + (7.97 \pm 0.10)$	1.00	1.03	-0.52	-0.51
			Central Projected Mass Density (Figure 5.2, right-hand panel)				
T1.2	All types	116[a]	$\log(M_{\rm BH}/{\rm M_\odot}) = (0.91 \pm 0.06)\,\log\left(\Sigma_{\rm 0,sph}/10^6\,{\rm M_\odot\,pc^{-2}}\right) + (8.38 \pm 0.09)$	0.92	0.95	0.57	0.58
			Projected density within 1 kpc (Figure 5.3, left-hand panel)				
T1.3	All types (Eq. 5.2)	119	$\log(M_{\rm BH}/{\rm M_\odot}) = (2.69 \pm 0.18)\,\log\left(\langle\Sigma\rangle_{\rm 1kpc,sph}/10^{3.5}\,{\rm M_\odot\,pc^{-2}}\right) + (7.84 \pm 0.07)$	0.57	0.69	0.78	0.80
			Projected density within 5 kpc (Figure 5.3, right-hand panel)				
T1.4	All types (Eq. 5.3)	119	$\log(M_{\rm BH}/{\rm M_\odot}) = (1.87 \pm 0.10)\,\log\left(\langle\Sigma\rangle_{\rm 5kpc,sph}/10^{2.5}\,{\rm M_\odot\,pc^{-2}}\right) + (8.13 \pm 0.05)$	0.51	0.59	0.83	0.84
			Effective Surface Brightness at $R_{\rm e,sph}$ (Figure 5.5, left-hand panel)				
T1.5	LTGs (3.6 μm sample, Eq. 5.5)	26	$\log(M_{\rm BH}/{\rm M_\odot}) = (0.77 \pm 0.12)\,[\mu_{\rm e,3.6\mu m,sph} - 19\,{\rm mag\,arcsec^{-2}}] + (7.84 \pm 0.17)$	0.75	0.85	0.51	0.54
T1.6	ETGs (3.6 μm sample, Eq. 5.4)	71	$\log(M_{\rm BH}/{\rm M_\odot}) = (0.47 \pm 0.04)\,[\mu_{\rm e,3.6\mu m,sph} - 19\,{\rm mag\,arcsec^{-2}}] + (7.95 \pm 0.11)$	0.78	0.83	0.57	0.57
T1.7	E (3.6 μm sample)	35	$\log(M_{\rm BH}/{\rm M_\odot}) = (0.97 \pm 0.10)\,[\mu_{\rm e,3.6\mu m,sph} - 19\,{\rm mag\,arcsec^{-2}}] + (6.24 \pm 0.34)$	1.03	1.14	0.05	0.08
T1.8	ES/S0 (3.6 μm sample)	36	$\log(M_{\rm BH}/{\rm M_\odot}) = (0.76 \pm 0.10)\,[\mu_{\rm e,3.6\mu m,sph} - 19\,{\rm mag\,arcsec^{-2}}] + (8.41 \pm 0.15)$	0.81	0.92	0.36	0.35
			Projected Density at $R_{\rm e,sph}$ (Figure 5.5, middle panel)				
T1.9	LTGs	39	$\log(M_{\rm BH}/{\rm M_\odot}) = (-1.56 \pm 0.22)\,\log\left(\Sigma_{\rm e,sph}/10^3\,{\rm M_\odot\,pc^{-2}}\right) + (7.75 \pm 0.15)$	0.69	0.77	-0.43	-0.43
T1.10	ETGs	80	$\log(M_{\rm BH}/{\rm M_\odot}) = (-1.11 \pm 0.08)\,\log\left(\Sigma_{\rm e,sph}/10^3\,{\rm M_\odot\,pc^{-2}}\right) + (8.31 \pm 0.09)$	0.76	0.81	-0.55	-0.52
T1.11	E	40	$\log(M_{\rm BH}/{\rm M_\odot}) = (-1.01 \pm 0.39)\,\log\left(\Sigma_{\rm e,sph}/10^3\,{\rm M_\odot\,pc^{-2}}\right) + (8.14 \pm 0.35)$	0.73	0.76	-0.004	-0.01
T1.12	ES/S0	40	$\log(M_{\rm BH}/{\rm M_\odot}) = (-1.60 \pm 0.27)\,\log\left(\Sigma_{\rm e,sph}/10^3\,{\rm M_\odot\,pc^{-2}}\right) + (8.78 \pm 0.18)$	0.76	0.85	-0.35	-0.32
			Projected Density within $R_{\rm e,sph}$ (Figure 5.5, right-hand panel)				
T1.13	LTGs	39	$\log(M_{\rm BH}/{\rm M_\odot}) = (-1.69 \pm 0.28)\,\log\left(\langle\Sigma\rangle_{\rm e,sph}/10^3\,{\rm M_\odot\,pc^{-2}}\right) + (8.45 \pm 0.27)$	0.71	0.80	-0.37	-0.40
T1.14	ETGs	80	$\log(M_{\rm BH}/{\rm M_\odot}) = (-1.24 \pm 0.10)\,\log\left(\langle\Sigma\rangle_{\rm e,sph}/10^3\,{\rm M_\odot\,pc^{-2}}\right) + (8.96 \pm 0.10)$	0.76	0.82	-0.53	-0.50
T1.15	E	40	$\log(M_{\rm BH}/{\rm M_\odot}) = (-1.06 \pm 0.59)\,\log\left(\langle\Sigma\rangle_{\rm e,sph}/10^3\,{\rm M_\odot\,pc^{-2}}\right) + (8.75 \pm 0.18)$	0.71	0.74	-0.02	-0.02
T1.16	ES/S0	40	$\log(M_{\rm BH}/{\rm M_\odot}) = (-1.62 \pm 0.38)\,\log\left(\langle\Sigma\rangle_{\rm e,sph}/10^3\,{\rm M_\odot\,pc^{-2}}\right) + (9.54 \pm 0.37)$	0.78	0.87	-0.27	-0.25

Note. — Columns: (1) Table 1 row number. (2) Galaxy type and equation number in the text (when one exists). (3) Number of galaxies. (4) Scaling relation obtained from the BCES(BISECTOR) regression. (5) Intrinsic scatter in the $\log M_{\rm BH}$-direction (using Equation 1 from Graham & Driver, 2007a). (6) Total root mean square (rms) scatter in the $\log M_{\rm BH}$ direction. (7) Pearson correlation coefficient. (8) Spearman rank-order correlation coefficient.

[a]Regression performed after excluding three outliers, see Section 5.3.1 for more details.

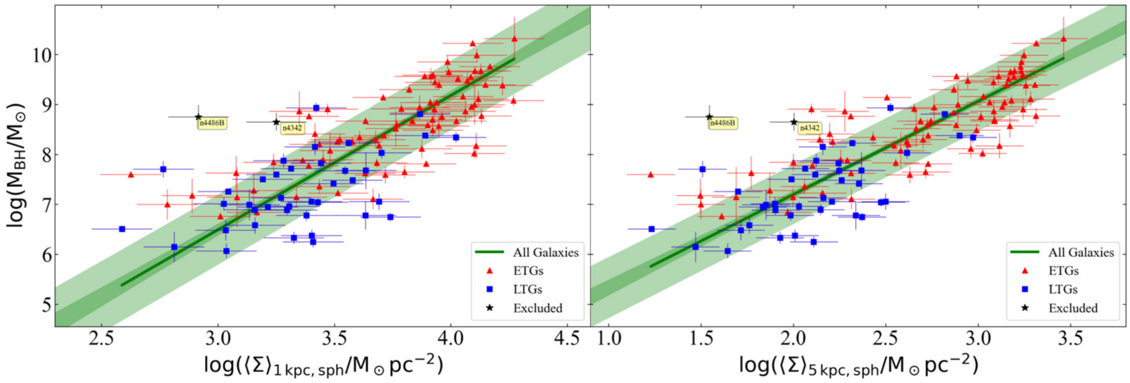

Figure 5.3 Black hole mass plotted against the spheroid's projected stellar mass density within the inner 1 kpc (left-hand panel, Equation 5.2) and the spheroid's projected density within 5 kpc (right-hand panel, Equation 5.3). ETGs and LTGs are marked differently to depict that the two types follow the same relation.

5.3.2 Projected Mass Density within 1 kpc: The Spheroid Compactness $\langle\Sigma\rangle_{\rm 1kpc,sph}$

The projected stellar mass density ($\langle\Sigma\rangle_{\rm 1kpc}$) within the inner 1 kpc of a galaxy has been used as a measure of galaxy "compactness" (Barro et al., 2017; Ni et al., 2020), and to identify compact star forming galaxies (Suess et al., 2021). Interestingly, for star-forming galaxies $\langle\Sigma\rangle_{\rm 1kpc}$ has been found to correlate with the black hole growth[18], and it has been suggested that this correlation is stronger than the connection between the black hole growth and host galaxy stellar mass (see Ni et al., 2020). Additionally, it has been suggested that $\langle\Sigma\rangle_{\rm 1kpc}$ is a better indicator of black hole growth than the projected stellar mass density within the galaxy half-light radius and the projected density within other (smaller or larger) constant (e.g., 0.1 kpc, 10 kpc) radii (Ni et al., 2019, 2020).

Here we investigate a possible correlation between the black hole mass and the average projected stellar mass density ($\langle\Sigma\rangle_{\rm 1kpc,sph}$) within the inner 1 kpc of the host spheroid. Thus, we refer to $\langle\Sigma\rangle_{\rm 1kpc,sph}$ as the spheroid compactness. Most of our sample with directly-measured $M_{\rm BH}$ are quiescent, with $\langle\Sigma\rangle_{\rm 1kpc,sph}$ greater than the critical/threshold

[18]The connection between black hole growth and the host galaxy's stellar mass density is explained by the assumption of a linear correlation between stellar density and gas density for star-forming galaxies (see Lin et al., 2019, and references therein). Thus, a high value of $\langle\Sigma\rangle_{\rm 1kpc}$ for a star-forming galaxy infers a high gas density, and the abundance of gas at the inner galactic regions is known to boost the black hole growth (Dekel et al., 2019; Habouzit et al., 2019).

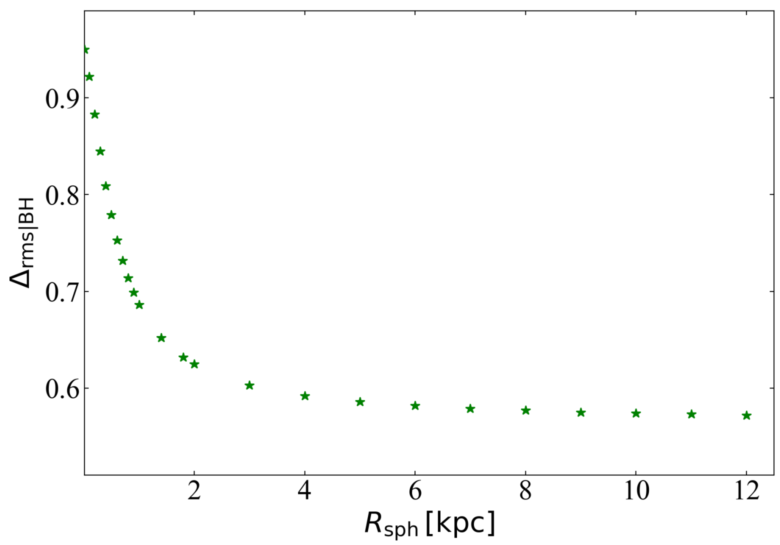

Figure 5.4 The total vertical rms scatter in the M_{BH}–$\langle\Sigma\rangle_{\mathrm{R,sph}}$ relations as a function of R_{sph}.

value ($\langle\Sigma\rangle_{\mathrm{1kpc}} = 3\times10^3\,\mathrm{M_\odot\,pc^{-2}}$, Cheung et al., 2012) used to identify the quiescent galaxies (Hopkins et al., 2021). Additionally, we explored how the correlation between M_{BH} and spheroid compactness compares against the correlation between M_{BH} and the spheroid densities at/within other radii.

We find a tight M_{BH}–$\langle\Sigma\rangle_{\mathrm{1kpc,sph}}$ correlation (left-hand panel in Figure 5.3), where all galaxy types (ETGs+LTGs) seem to follow a single positive relation[19], such that

$$\log\left(\frac{\mathrm{M_{BH}}}{\mathrm{M_\odot}}\right) = (2.69\pm0.18)\log\left(\frac{\langle\Sigma\rangle_{\mathrm{1kpc,sph}}}{10^{3.5}\,\mathrm{M_\odot\,pc^{-2}}}\right) + (7.84\pm0.07), \tag{5.2}$$

with $\Delta_{\mathrm{rms|BH}} = 0.69$ dex (see Table 5.1 for correlation coefficients). Similarly, we also see a positive trend between M_{BH} and the column (stellar mass) density within other projected spheroid radii (e.g., 0.01 kpc, 0.1 kpc, 5 kpc, 10 kpc). This positive trend is evident from the distribution of spheroid profiles in the left-hand panel of Figure 5.1, where, at all fixed radii, the redder profiles with higher M_{BH} are brighter than the bluer profiles with lower

[19]Here, we use a $\pm30\%$ (0.13 dex) uncertainty on the $\langle\Sigma\rangle_{\mathrm{1kpc,sph}}$ (and the later discussed $\langle\Sigma\rangle_{\mathrm{5kpc,sph}}$) values. Consistent relations are obtained when using up to a $\pm40\%$ (0.17 dex) uncertainty.

$M_{\rm BH}$.

The correlation between $M_{\rm BH}$ and densities within fixed physical radii smaller than 1 kpc ($\langle\Sigma\rangle_{\rm 0.01kpc,sph}$ and $\langle\Sigma\rangle_{\rm 0.1kpc,sph}$) are not as tight as the above relation (Equation 5.2). However, we find better $M_{\rm BH}$–$\langle\Sigma\rangle_{\rm R,sph}$ correlations for R > 1 kpc, with a gradually shallower slope and smaller scatter than the $M_{\rm BH}$–$\langle\Sigma\rangle_{\rm 1kpc,sph}$ relation. For example, the relation between $M_{\rm BH}$ and $\langle\Sigma\rangle_{\rm 5kpc,sph}$ shown in the right-hand panel of Figure 5.3. It can be expressed as,

$$\log\left(\frac{\rm M_{BH}}{\rm M_\odot}\right) = (1.87 \pm 0.10)\log\left(\frac{\langle\Sigma\rangle_{\rm 5kpc,sph}}{10^{2.5}\,{\rm M_\odot\,pc^{-2}}}\right) + (8.13 \pm 0.05), \tag{5.3}$$

with the total rms scatter $\Delta_{\rm rms|BH} = 0.59$ dex. A plot of the rms scatter about the $M_{\rm BH}$–$\langle\Sigma\rangle_{\rm R,sph}$ relation as a function of R is shown in Figure 5.4. The scatter asymptotes to $\sim 0.58 \pm 0.01$ dex beyond 5 kpc.

The low (0.69 dex) scatter about the $M_{\rm BH}$–$\langle\Sigma\rangle_{\rm 1kpc,sph}$ relation relative to the 0.95 dex scatter about the $M_{\rm BH}$–$\Sigma_{\rm 0,sph}$ relation (Table 5.1, T1.2) and the (soon to be discussed) $M_{\rm BH}$–$\langle\Sigma\rangle_{\rm e,sph}$ relations suggests that $\langle\Sigma\rangle_{\rm 1kpc,sph}$ is a better predictor of $M_{\rm BH}$ than the latter projected mass densities. However, the $M_{\rm BH}$–$\langle\Sigma\rangle_{\rm R,sph}$ relations for R > 1 kpc is stronger, reflective of the separation of the $\langle\mu\rangle$ (and $\langle\Sigma\rangle$) profiles at large radii.

5.3.3 Surface Brightness and Projected Density at the Half-Light Radius: $\mu_{\rm e,3.6\mu m,sph}$ & $\Sigma_{\rm e,sph}$

Using our 3.6 μm-sample, we see a positive trend between $M_{\rm BH}$ and the surface brightness ($\mu_{\rm e,sph}$) at the projected half-light radius of spheroids (Figure 5.5). A higher magnitude of $\mu_{\rm e,sph}$ corresponds to a lower luminosity density; thus, we find a declining relation between $M_{\rm BH}$ and the effective luminosity density. We observe that ETGs and LTGs in our sample define two different $M_{\rm BH}$–$\mu_{\rm e,3.6\mu m,sph}$ relations, which are represented in the left-hand panel of Figure 5.5. ETGs define the following relation,

$$\log\left(\frac{\rm M_{BH}}{\rm M_\odot}\right) = (0.47 \pm 0.04)\left[\mu_{\rm e,3.6\mu m,sph} - \frac{19\,{\rm mag}}{\rm arcsec^2}\right] + (7.95 \pm 0.11), \tag{5.4}$$

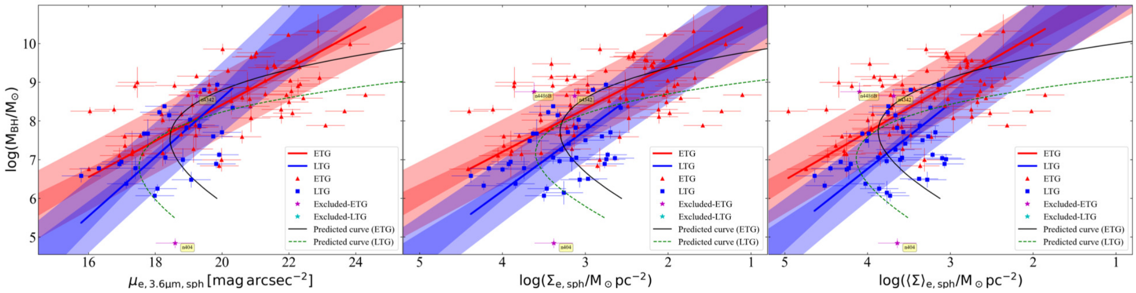

Figure 5.5 Black hole mass versus the bulge surface brightness $\mu_{\mathrm{e,3.6\mu m,sph}}$ at $R_{\mathrm{e,sph}}$ (left-hand panel, Equations 5.4 and 5.5), the projected stellar mass density $\Sigma_{\mathrm{e,sph}}$ at $R_{\mathrm{e,sph}}$ (middle panel, Table 5.1, T1.9 and T1.10), and the average stellar mass density $\langle\Sigma\rangle_{\mathrm{e,sph}}$ within $R_{\mathrm{e,sph}}$ (right-hand panel, Table 5.1, T1.13 and T1.14). ETGs and LTGs seem to define different relations in these diagrams. However, the complete picture of these relations is curved, as shown by the expected black and green curves for ETGs and LTGs, respectively. Note that the horizontal-axes in the middle and right-hand panels are inverted, and in the first panel, the horizontal-axis presents $\mu_{\mathrm{e,3.6\mu m,sph}}$ in a dimming order from left to right.

with $\Delta_{\mathrm{rms|BH}} = 0.83$ dex. Whereas the LTGs follow a steeper relation given by

$$\log\left(\frac{\mathrm{M_{BH}}}{\mathrm{M_\odot}}\right) = (0.77 \pm 0.12)\left[\mu_{\mathrm{e,3.6\mu m,sph}} - \frac{19\,\mathrm{mag}}{\mathrm{arcsec^2}}\right] + (7.84 \pm 0.17), \tag{5.5}$$

with $\Delta_{\mathrm{rms|BH}} = 0.85$ dex.

In order to include our full sample, we mapped $\mu_{\mathrm{e,sph}}$ (mag arcsec^{-2}) to $\Sigma_{\mathrm{e,sph}}$ ($\mathrm{M_\odot pc^{-2}}$) using Equation D.5, and recover two trends defined by ETGs and LTGs in the M_{BH}–$\Sigma_{\mathrm{e,sph}}$ diagram. Similar trends due to ETGs and LTGs are observed in the M_{BH}–($\langle\Sigma\rangle_{\mathrm{e,sph}}$, average projected density within $R_{\mathrm{e,sph}}$) diagram. The M_{BH}–$\Sigma_{\mathrm{e,sph}}$ and M_{BH}–$\langle\Sigma\rangle_{\mathrm{e,sph}}$ relations are depicted, respectively, in the middle and the right-hand panel of Figure 5.5. The fit parameters and the correlation coefficients for these distributions are provided in Table 5.1.

For early-type galaxies, the galaxy luminosity (or mass) has a curved relation with the galaxy surface brightness at/within any scale radius, $R_{\mathrm{z,sph}}$, enclosing (a non-zero) z% of the galaxy's total light (Graham, 2019b). This includes the relation between galaxy luminosity and galaxy surface brightness at/within the half-light (z = 50%) radius, i.e., the $M_{*,\mathrm{gal}}$–$\mu_{\mathrm{e,gal}}$ or $M_{*,\mathrm{gal}}$–$\langle\mu\rangle_{\mathrm{e,gal}}$ relations (see Graham, 2019b, their Figure 3). Simi-

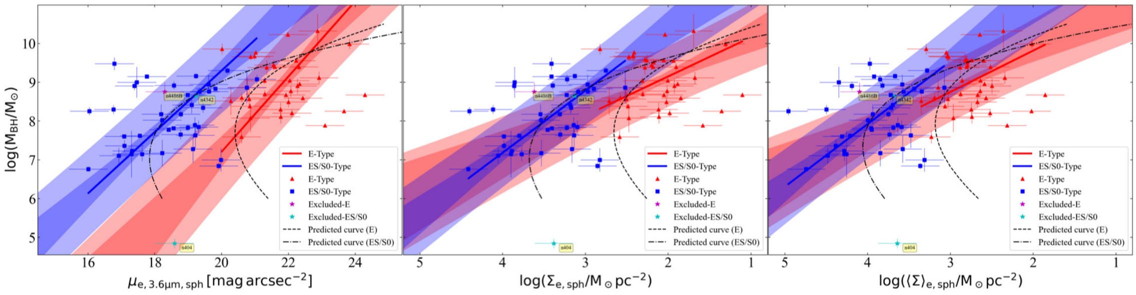

Figure 5.6 Similar to Figure 5.5, but now showing different regressions performed for ETGs with a disk (ES- and S0-types) and ETGs without a disk (E-type). The correlation parameters are provided in Table 5.1 (left panel: T1.7 and T1.8, middle panel: T1.11 and T1.12, right panel: T1.15 and T1.16). The dashed and dot-dashed curves represent the expected relations for E-type and ES/S0-type galaxies, respectively.

larly for spheroids, the $M_{*,\rm sph}$–$\mu_{\rm e,sph}$ and $M_{\rm BH}$–($\mu_{\rm e,sph}$, also $\Sigma_{\rm e,sph}$, and $\langle\Sigma\rangle_{\rm e,sph}$) relations are expected to be curved, as shown in Figure 5.5. These predicted curved $M_{\rm BH}$–$\mu_{\rm e,sph}$ (also $\Sigma_{\rm e,sph}$ and $\langle\Sigma\rangle_{\rm e,sph}$) relations for the spheroidal component of ETGs and LTGs are calculated here using the $M_{\rm BH}$–$n_{\rm sph}$ relations (Sahu et al., 2019a) and $M_{\rm BH}$–$\mu_{0,3.6\mu{\rm m,sph}}$ relations (Equation 5.1), and applying the equation $\mu_{\rm e,sph} = \mu_{0,\rm sph} + 2.5\,{\rm b_n}/\ln(10)$ (or $\Sigma_{\rm e,sph} = \Sigma_{0,\rm sph} - {\rm b_n}/\ln(10)$) for a Sérsic light profile. The densities, $\langle\Sigma\rangle_{\rm e,sph}$, $\langle\mu\rangle_{\rm e,sph}$, and $\mu_{\rm e,sph}$ can be related through Equation 9 in Graham & Driver (2005) and Equation 11 in Graham et al. (2006).

Given the small sample size and limited range of $M_{\rm BH}$ and densities for ETG and LTG subsamples, we refrain from directly fitting a curve to the ETG and LTG distributions in Figure 5.5. However, as the $M_{\rm BH}$–$\mu_{\rm e,sph}$ (also $\Sigma_{\rm e,sph}$ and $\langle\Sigma\rangle_{\rm e,sph}$) relations are expected to be curved, the slopes and intercepts of the fitted lines obtained here depend on the range of $M_{\rm BH}$ and $\mu_{\rm e,sph}$ (also $\Sigma_{\rm e,sph}$ and $\langle\Sigma\rangle_{\rm e,sph}$) values in the current sample. That is, these relations provide a log-linear approximation to the distribution over that range. In the future, using a bigger sample with an extended range of $M_{\rm BH}$ and spheroid density, we shall be able to obtain well fitted $M_{\rm BH}$–$\mu_{\rm e,3.6\mu m,sph}$ (also $\Sigma_{\rm e,sph}$ and $\langle\Sigma\rangle_{\rm e,sph}$) curves which are expected to be different for different galaxy morphology.

Offset between ETGs with and without a disk

Sahu et al. (2019a) observed an offset of 1.12 ± 0.20 dex in the $M_{\rm BH}$-direction, between

ETGs with a disk (ES- and S0-types) and ETGs without a disk (E-type), which defined almost parallel relations in the M_{BH}–$M_{*,\mathrm{sph}}$ diagram. The calculation of $M_{*,\mathrm{sph}}$ is based on the spheroid Sérsic profile, quantified by the parameters n_{sph}, $R_{\mathrm{e,sph}}$, and $\mu_{\mathrm{e},3.6\mu\mathrm{m,sph}}$, and thus the offset between ES/S0- and E-types must have propagated to $M_{*,\mathrm{sph}}$ from these parameters. Further, Sahu et al. (2020) re-observed this offset (1.38 ± 0.28 dex in the M_{BH}-direction) between ETGs with and without a disk in the M_{BH}–$R_{\mathrm{e,sph}}$ diagram, where again these categories defined almost parallel relations. Sahu et al. (2020) did not report any significant offset between ETG subsamples in the M_{BH}–n_{sph} diagram. Here, we next investigated if there is any such offset between ES/S0- and E-types in the M_{BH}–$\mu_{\mathrm{e},3.6\mu\mathrm{m,sph}}$ diagram.

Upon separating the ETGs with and without a disk, we do see the two groups offset from each other in the M_{BH}–$\mu_{\mathrm{e},3.6\mu\mathrm{m,sph}}$, M_{BH}–$\Sigma_{\mathrm{e,sph}}$, and M_{BH}–$\langle\Sigma\rangle_{\mathrm{e,sph}}$ diagrams (Figure 5.6). However, the quality of fit for the two samples is poor (see Table 5.1); thus, it is difficult to quantify the offset accurately. Moreover, as discussed before, the complete M_{BH}–$\mu_{\mathrm{e},3.6\mu\mathrm{m,sph}}$ relations are curved. The expected M_{BH}–$\mu_{\mathrm{e},3.6\mu\mathrm{m,sph}}$ curves for E- and ES/S0-types are shown in Figure 5.6. These curves are also calculated by using the M_{BH}–n_{sph} and M_{BH}–$\mu_{0,\mathrm{sph}}$ lines for the two populations combined with $\mu_{\mathrm{e,sph}} = \mu_{0,\mathrm{sph}} + 2.5\,\mathrm{b_n}/\ln(10)$. Additionally, as these curves are not parallel, the offset between the relations for E-type and ES/S0-type may not be constant throughout.

The declining M_{BH}–(effective surface brightness) relation can also be inferred from the distribution of the spheroid surface brightness profiles for our sample shown in the right-hand panel of Figure 5.1. At the half-light radii ($\mathrm{R/R_e} = 1$) of spheroids, the surface brightness dims when going from low-M_{BH} (blue) to high-M_{BH} (red) profiles. Also, given the radially declining projected density profile, the ES/S0-types with a smaller $R_{\mathrm{e,sph}}$ than the E-types, have a brighter $\mu_{\mathrm{e,sph}}$ (higher $\Sigma_{\mathrm{e,sph}}$ and $\langle\Sigma\rangle_{\mathrm{e,sph}}$) than E-types hosting similar M_{BH}. This is why the direction of the offset between E- and ES/S0-types in these diagrams (Figure 5.6) is opposite to the offset seen in the M_{BH}–$R_{\mathrm{e,sph}}$ and M_{BH}–$M_{*,\mathrm{sph}}$ diagrams, where ES/S0-types have a smaller $R_{\mathrm{e,sph}}$ and $M_{*,\mathrm{sph}}$ than the E-types hosting a similar M_{BH}.

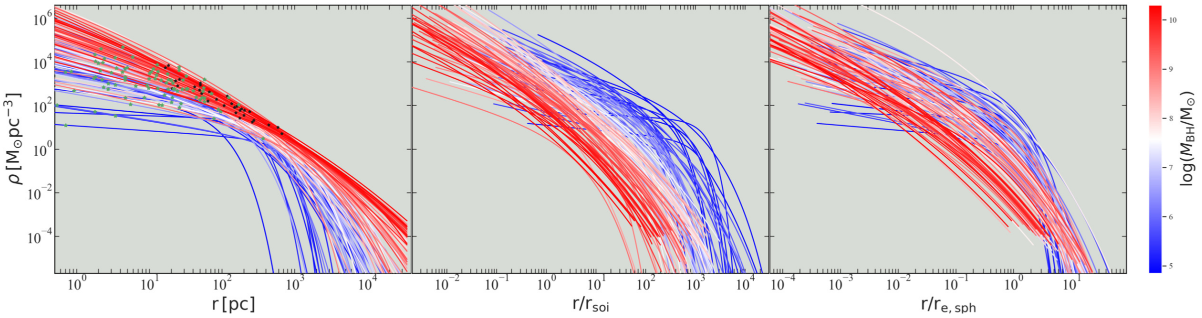

Figure 5.7 Spheroid internal stellar mass density profiles. The sequential color map blue-white-red depicts an increasing order of $M_{\rm BH}$. In the left-hand panel, the black and green colored stars mark the black hole's influence radius for the core-Sérsic and Sérsic galaxies, respectively. The horizontal axes are scaled with respect to the sphere of influence radius (r_{soi}) of black holes and the spheroid's spatial half-light radius r_e for the profiles shown in the middle and right-hand panels, respectively.

5.4 Black Hole Mass versus Spheroid Spatial Density

In an effort to better understand the black hole scaling relations with the host spheroid, and to search for new, potentially improved relations, we have deprojected the (equivalent-axis) Sérsic surface brightness profiles of the spheroids to obtain their spatial (i.e., internal) mass density profiles, as described in the Appendix D.1. These internal density profiles[20] are displayed in Figure 5.7. We used a sequential blue-white-red color map to represent the central black hole masses in increasing order from low-mass (blue) to high-mass (red). The density profiles in the three panels of Figure 5.7 will help one understand the upcoming correlations observed between the black hole mass and the host spheroid's internal density at various radii.

Similar to the projected surface brightness profiles, the (deprojected) internal density profiles, $\rho(r)$, are monotonically declining and can be characterized using the Sérsic surface brightness profile parameters (n, $R_{\rm e}$, $\mu_{\rm e} = -2.5\log {\rm I_e}$, see Equation D.3). Smaller and less massive spheroids, generally quantified by smaller Sérsic parameters (n and $R_{\rm e}$), have a

[20]For our black hole correlations, the internal densities are numerically calculated using the exact integral expressed by Equation D.3. However, the extended internal density profiles in Figure 5.7 are calculated using an approximated model (Prugniel & Simien, 1997). This is because, for some spheroids, the density integral (Equation D.3) did not converge to provide a valid/real density value, especially at larger radii. Moreover, using the approximate model can still explain the qualitative nature of the $M_{\rm BH}$–ρ trends observed here.

shallow inner density profile that descends quickly at outer radii (see the bluer profiles in the left-hand panel of Figure 5.7). On the contrary, more massive spheroids, generally indicated by higher Sérsic parameters (n and $R_{\rm e}$), have a steeper inner density profile with a higher density and a shallower decline at large radii (see the red profiles in the left-hand panel of Figure 5.7).

The horizontal-axes in the middle and the right-hand panels of Figure 5.7 are scaled using the sphere-of-influence radius ($r_{\rm soi}$) of the black holes and the internal (or spatial) half-mass radius ($r_{\rm e,sph}$) of the spheroids, respectively. This accounts for some of the different size scales used and will help with the understanding of the observed ($M_{\rm BH}$)–(spheroid internal density) relations revealed in the following sub-sections.

5.4.1 Spatial Density at the Black Hole's Sphere-of-Influence: $\rho_{\rm soi,sph}$

Based on the exact deprojection of the Sérsic model (Equations D.3) the internal density near the spheroid center, $\rho(r \rightarrow 0)$, tends to infinity[21] for $n > 1$. Hence, as a measure of the central internal density, we chose the internal density at another central radius, where the gravitational potential of the black hole is comparable to that of the host galaxy, known as the sphere-of-influence radius ($r_{\rm soi}$) of the black hole. We denote the spheroid spatial density at $r_{\rm soi}$ by $\rho_{\rm soi,sph}$.

We first calculated $r_{\rm soi}$ using the following standard definition (Peebles, 1972; Frank & Rees, 1976; Merritt, 2004; Ferrarese & Ford, 2005),

$$\mathrm{r_{soi}} = \frac{\mathrm{G\,M_{BH}}}{\sigma^2}, \tag{5.6}$$

where σ is the host galaxy's central (projected) stellar velocity dispersion, which is likely to be dominated by the spheroid component of our galaxies. The stellar velocity dispersions of our galaxies are primarily taken from the HyperLeda (Makarov et al., 2014) database[22], and are listed in Sahu et al. (2019b, their Table 1). The value of $\rho_{\rm soi,sph}$ was numerically calculated using Equation D.3 at $r = r_{\rm soi}$. We also include the core-Sérsic galaxies in the

[21]For $n = 1$, $\rho(r \rightarrow 0)$ tends to a finite value and tends to zero for n < 1 (see Equation D.3). Whereas, based on the Prugniel & Simien (1997) model (Equation D.6) which is an approximation of the exact deprojection, $\rho(r \rightarrow 0)$ tends to infinity for $n \gtrsim 0.6$.

[22]The stellar velocity dispersions available at the HyperLeda database are homogenized to a constant aperture size of $\sim 0.595\,\mathrm{h^{-1}}$ kpc.

$M_{\rm BH}$–$\rho_{\rm soi,sph}$ diagram (Figure 5.8), for whom $\rho_{\rm soi,sph}$ is based on the de-projection of the (inwardly extrapolated) Sérsic component of their core-Sérsic surface brightness profile.

In the $M_{\rm BH}$–$\rho_{\rm soi,sph}$ diagram, seven galaxies (NGC 404, IC 2560, NGC 3079, NGC 4388, NGC 4826, NGC 5055, NGC 6323) are considerably offset (from the main population) towards low $M_{\rm BH}$ and low $\rho_{\rm soi,sph}$. Another (Sérsic) galaxy, NGC 0821, appears somewhat offset towards a high $\rho_{\rm soi,sph}$ value for its black hole mass. We discuss each of these in the following two paragraphs.

NGC 404, which is the only galaxy with an intermediate-mass black hole (IMBH) in our sample, is a genuine outlier from the fitted relation, and it is possible that IMBHs (and/or spheroids with low Sérsic indices) may not follow the log-linear $M_{\rm BH}$–(stellar density) scaling relations defined by the more massive systems. NGC 404 has already been excluded from our correlations (as mentioned in Section 5.2). NGC 5055 has an unusually small central stellar velocity dispersion relative to its black hole mass[23] (see the $M_{\rm BH}$–σ diagram in Sahu et al., 2019b, their Figure 2), resulting in a large $r_{\rm soi}$ and thus a small $\rho_{\rm soi,sph}$.

Galaxies IC 2560, NGC 3079, NGC 4388, NGC 4826, and NGC 6323 have spheroid Sérsic indices between 0.58 and 1.15; thus, they have a shallow inner density profile and a small $\rho_{\rm soi,sph}$. The Sérsic galaxy NGC 0821, on the other hand, has a Sérsic index of 6.1 and hence, a steep inner density profile and a high $\rho_{\rm soi,sph}$. It also contains a faint edge-on intermediate-scale disk (Savorgnan & Graham, 2016b), suggestive of an accretion event.

Including the above eight galaxies significantly biases the best-fit relation defined by most of the sample; hence, we have excluded these galaxies (plus the Milky Way) from our $M_{\rm BH}$–$\rho_{\rm soi,sph}$ relations. Here, we do not exclude the stripped galaxies NGC 4342 and NGC 4486B (described in Section 5.2) because we are dealing with the spheroid spatial density at a central radius, which may not be affected by the outer mass stripping of these galaxies.

Initially, we performed a single regression between $M_{\rm BH}$ and $\rho_{\rm soi,sph}$ using our (Sérsic + core-Sérsic) sample[24], as shown in the top panel of Figure 5.8. We noticed that the

[23] It is also possible that the value of $M_{\rm BH}$ in NGC 5055, measured using gas dynamical modeling, may be an overestimate.

[24] The single regression provides the relation $\log(M_{\rm BH}/{\rm M}_\odot) = (-1.27 \pm 0.07)\log\left(\rho_{\rm soi,sph}/10^{2.5}\,{\rm M}_\odot{\rm pc}^{-3}\right) + (8.55 \pm 0.07)$, with $\Delta_{\rm rms|BH} = 0.77$ dex.

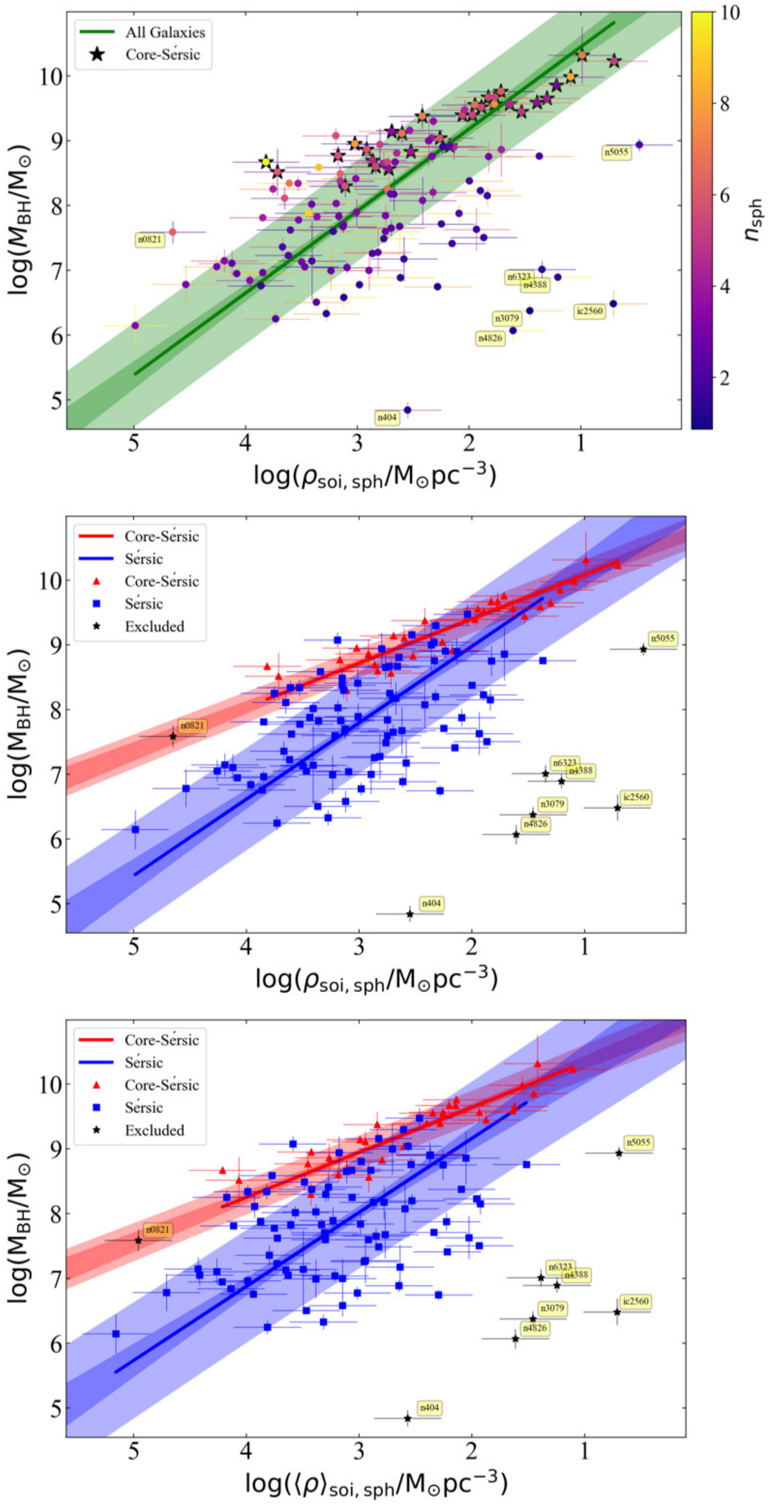

Figure 5.8 Black hole mass versus internal stellar mass density at r_{soi} (top and middle panels) and black hole mass versus (averaged) internal stellar mass density within r_{soi} (bottom panel). The top panel shows a single regression (Footnote 24), where core-Sérsic galaxies (black stars) are distributed in a manner that suggests a different M_{BH}–$\rho_{\mathrm{soi,sph}}$ trend for these high-n_{sph} systems. All the data points in this panel are color-coded according to their Sérsic indices. The middle panel shows the two different M_{BH}–$\rho_{\mathrm{soi,sph}}$ relations defined by Sérsic (blue) and core-Sérsic galaxies (red) galaxies. Similar substructure due to Sérsic (low n_{sph}) and core-Sérsic (high n_{sph}) galaxies are observed in the M_{BH}–$\langle\rho\rangle_{\mathrm{soi,sph}}$ diagram (bottom panel). The excluded galaxies are named. See the text in Section 5.4.1 for details. Note that the horizontal axis is inverted such that the density decreases when going from left to right.

distribution of core-Sérsic galaxies traces a substructure systematically offset from the best-fit line for the ensemble of galaxies, suggesting a different trend for this sub-sample. Therefore, we further performed separate regressions for the core-Sérsic and Sérsic galaxies, presented in the middle panel of Figure 5.8. We observed a tight, shallower relation for the core-Sérsic galaxies, given by

$$\log\left(\frac{\rm M_{BH}}{\rm M_{\odot}}\right) = (-0.68 \pm 0.06)\log\left(\frac{\rho_{\rm soi,sph}}{10^{2.5}\,{\rm M_{\odot}pc^{-3}}}\right) + (9.06 \pm 0.05), \tag{5.7}$$

with $\Delta_{\rm rms|BH} = 0.21$ dex. Curiously, this relation has the lowest total rms scatter of all the black hole scaling relations[25]. For Sérsic galaxies (with n $\gtrsim$ 1), we found a relatively steeper relation,

$$\log\left(\frac{\rm M_{BH}}{\rm M_{\odot}}\right) = (-1.18 \pm 0.10)\log\left(\frac{\rho_{\rm soi,sph}}{10^{2.5}\,{\rm M_{\odot}pc^{-3}}}\right) + (8.39 \pm 0.10), \tag{5.8}$$

with $\Delta_{\rm rms|BH} = 0.77$ dex. The correlation coefficients for the above two relations are presented in Table 5.2. Here, we needed to know $M_{\rm BH}$ to measure $r_{\rm soi}$ and thus $\rho_{\rm soi,sph}$, voiding Equations 5.7 and 5.8 as black hole mass predictor tools for individual galaxies but leaving them as constraints for simulations. They may offer a means to predict $\rho_{\rm soi,sph}$ for a given $M_{\rm BH}$ when the host spheroid surface brightness parameters are not known (as done in Biava et al., 2019, using other black hole scaling relations).

The scatter in the above relations is smaller than that about the $M_{\rm BH}$–$\mu_{0,\rm sph}$ (and $M_{\rm BH}$–$\Sigma_{0,\rm sph}$) relations, perhaps indicating that $M_{\rm BH}$ has a better relation with $\rho_{\rm soi,sph}$, supporting the prediction in Graham & Driver (2007a). On their own, the core-Sérsic galaxies appear to have no correlation in the $M_{\rm BH}$–$\mu_{0,\rm sph}$ diagram (Figure 5.2). However, the overlapping nature of (the spheroid component of) their density profiles seen in the

[25] It is noted that $r_{\rm soi}$ is derived from $M_{\rm BH}$ (Equation 5.6). For a roughly similar value of σ among core-Sérsic galaxies, those with bigger $M_{\rm BH}$ have a larger $r_{\rm soi}$ (see the left-hand panel of Figure 5.7). The slope in Equation 5.7 tracks the average slope across 20-1000 pc of the high-n (red) profiles in Figure 5.7. The low scatter observed for the core-Sérsic spheroids is not solely because $\rho_{\rm soi,sph}$ was derived using $M_{\rm BH}$; if it was as simple as that, then the Sérsic galaxies would also display a tight relation. The low scatter is also because of the over-lapping density profiles of core-Sérsic spheroids, from $\sim$20 pc to $\sim$1 kpc, as seen in the left hand panel of Figure 5.7.

left-hand panel of Figure 5.7 (also see Dullo & Graham, 2012, their Figure 18), coupled with Equation 5.6, supports the tight trend for core-Sérsic galaxies seen in Figure 5.8. The smaller scatter observed for the core-Sérsic relation can be understood from the tight distribution of black points marking $r_{\rm soi}$ and $\rho_{\rm soi,sph}$ on the density profiles of the core-Sérsic spheroids in the left-hand panel of Figure 5.7. The green points, marking $r_{\rm soi}$ and $\rho_{\rm soi,sph}$ on the density profiles of the Sérsic spheroids, are more scattered, explaining the higher rms scatter about the $M_{\rm BH}$–$\rho_{\rm soi,sph}$ relation in Equation 5.8 for the Sérsic spheroids.

Figure 5.7 (left-hand panel) also explains why there will be a strong correlation between black hole mass and the isophotal or isodensity radius measured at faint/low densities. It is easy to see that the use of ever-lower densities will result in an ever greater separation of the curves. A result due to the different Sérsic indices (n) and the trend between $M_{\rm BH}$ and n (e.g., Graham & Driver, 2007a; Sahu et al., 2020).

As with the $M_{\rm BH}$–$\rho_{\rm soi,sph}$, a similar apparent separation between core-Sérsic and Sérsic galaxies is recovered in the $M_{\rm BH}$–$\langle\rho\rangle_{\rm soi,sph}$ diagram involving the average spatial density within $r_{\rm soi}$, as shown in the bottom panel of Figure 5.8 (see Table 5.2 rows T2.3 and T2.4 for fit parameters). However, the scatter is a bit higher than about the $M_{\rm BH}$–$\rho_{\rm soi,sph}$ relations. Again,the circular reasoning noted in Footnote 25 applies, and it should be noted that the values of $\langle\rho\rangle_{\rm soi,sph}$ (and $\rho_{\rm soi,sph}$) for the core-Sérsic spheroids are higher than the actual values because these are based on the de-projection of the (inwardly extrapolated) Sérsic portion of their surface brightness profiles, which intentionally do not account for the deficit of light (see footnote 16) in the core, $r \lesssim R_{\rm b}$.

For the core-Sérsic galaxies, the $M_{\rm BH} \propto$ (stellar mass deficit: $M_{*,def}^{0.27}$) relation (Dullo & Graham, 2014, their equation 18) suggests that galaxies with high $M_{\rm BH}$ have a higher mass deficit. Upon accounting for the mass deficit to obtain the actual $\rho_{\rm soi,sph,core}$ (and $\langle\rho\rangle_{\rm soi,sph,core}$), all the core-Sérsic galaxies will move towards a lower $\rho_{\rm soi,sph}$ (and $\langle\rho\rangle_{\rm soi,sph}$), i.e., towards right in Figure 5.8 (where the horizontal axes are inverted). However, galaxies with higher $M_{\rm BH}$ shall shift more than the galaxies with lower $M_{\rm BH}$, generating a slightly shallower (negative/declining) slope than the slope of the relation presented here (Equation 5.7), but still preserving the apparent core-Sérsic versus Sérsic substructuring.

The negative correlations between $M_{\rm BH}$ and $\rho_{\rm soi,sph}$ (and $\langle\rho\rangle_{\rm soi,sph}$) can be visualized from the vertical ordering of blue-to-red shades (i.e., low-to-high $M_{\rm BH}$) of the spheroid density profiles, shown in the middle panel of Figure 5.7, with the radial-axis normalized at $r_{\rm soi}$. Broadly speaking, at the influence radius (and any fixed multiple of this radius substantially beyond $r/r_{\rm soi} = 1$), the stellar density increases while going from the high-$M_{\rm BH}$ (reddish profiles) to low-$M_{\rm BH}$ (bluer profiles). The general (negative) $M_{\rm BH}$–$\rho_{\rm soi,sph}$ trend for our sample arises from massive black holes having larger spheres-of-influence, relative to low-mass black holes, combined with the spheroid's radially-declining density profiles. However, the resultant relations for the core-Sérsic and Sérsic galaxies are dependent on the sample selection and, thus, the range of Sérsic profiles included in each subsample, as discussed in the following subsection.

Investigating the core-Sérsic versus Sérsic substructure

One may wonder if the substructures in the $M_{\rm BH}$–$\rho_{\rm soi,sph}$ (and $M_{\rm BH}$–$\langle\rho\rangle_{\rm soi,sph}$) diagrams seen between core-Sérsic and Sérsic galaxies may be related to a similar division observed in the L–σ and $M_{\rm BH}$–σ diagrams (see Davies et al., 1983; Held & Mould, 1994; Matković & Guzmán, 2005; Bogdán et al., 2018; Sahu et al., 2019b). This may be because some of the division seen in the $M_{\rm BH}$–$\rho_{\rm soi,sph}$ and $M_{\rm BH}$–$\langle\rho\rangle_{\rm soi,sph}$ diagram may be influenced by the use of the central stellar velocity dispersion while calculating $r_{\rm soi}$. Or conversely, the substructures observed in the $M_{\rm BH}$–σ diagram may partly be a reflection of the $M_{\rm BH}$–$\rho_{\rm soi,sph}$ (or $\langle\rho\rangle_{\rm soi,sph}$) relations, if $\rho_{\rm soi,sph}$ influences σ.

To test this connection, we tried an alternative estimation of the black hole's influence radius denoted by $r_{\rm soi,2BH}$. The radius $r_{\rm soi,2BH}$ marks the sphere within which the stellar mass is equivalent to twice the central black hole's mass (Merritt, 2004). Upon using the internal density ($\rho_{\rm soi,2BH,sph}$) calculated at $r_{\rm soi,2BH}$, we recover the substructure between core-Sérsic and Sérsic galaxies in the $M_{\rm BH}$–$\rho_{\rm soi,2BH,sph}$ diagram[26] (not shown), albeit with an increased scatter. This test demonstrated that the substructuring seen in Figure 5.8 is not due to the propagation of σ via Equation 5.6.

To investigate another scenario underlying the apparent substructures in the $M_{\rm BH}$–$\rho_{\rm soi,sph}$ (and $M_{\rm BH}$–$\langle\rho\rangle_{\rm soi,sph}$) diagrams, we color-coded the data points in the top panel of

[26]The core-Sérsic galaxies follow the relation $\log(M_{\rm BH}/{\rm M_\odot}) = (-0.65 \pm 0.07)\log\left(\rho_{\rm soi,2BH,sph}/10^{2.5}\,{\rm M_\odot pc^{-3}}\right) + (8.73 \pm 0.09)$, and Sérsic galaxies follow $\log(M_{\rm BH}/{\rm M_\odot}) = (-0.98 \pm 0.07)\log\left(\rho_{\rm soi,2BH,sph}/10^{2.5}\,{\rm M_\odot pc^{-3}}\right) + (7.76 \pm 0.10)$, with $\Delta_{\rm rms|BH} = 0.29$ dex and 0.87 dex, respectively.

Figure 5.8 according to their Sérsic indices. This Sérsic index color map divides the data in the $M_{\rm BH}$–$\rho_{\rm soi,sph}$ diagram in different diagonal zones, in a sequential order of $n_{\rm sph}$, such that one can obtain a set of $M_{\rm BH}$–$\rho_{\rm soi,sph}$ relations applicable for different ranges of $n_{\rm sph}$. For example, roughly, we can point out three zones in the top panel of Figure 5.8: the excluded data points near the bottom right of the plot with the smallest Sérsic indices ($n_{\rm sph} \lesssim 1.5$); the blue-purple-magenta points with $1.5 \lesssim n_{\rm sph} \lesssim 5$ in the middle, and the red-orange-yellow points with $n_{\rm sph} \gtrsim 5$ in the upper-left part of the diagram. Most of our core-Sérsic galaxies fall in the third zone, which is why we observe them defining a different $M_{\rm BH}$–$\rho_{\rm soi,sph}$ relation than the majority of the Sérsic galaxies which fall in the second zone.

The distribution of data-points in the top panel of Figure 5.8 can be better represented on an $M_{\rm BH}$–$\rho_{\rm soi,sph}$–$n_{\rm sph}$ plane. This plane will be investigated in our future exploration of a black hole fundamental plane. We note that our calculation of $\rho_{\rm soi,sph}$ depends on $n_{\rm sph}$ and $M_{\rm BH}$, and thus these terms are not independently measured quantities. As noted, a high $M_{\rm BH}$, associated with a large $n_{\rm sph}$ (see Sahu et al., 2020, for the $M_{\rm BH}$–$n_{\rm sph}$ relation), will generate a large $r_{\rm soi}$ and thus lower $\rho_{\rm soi,sph}$.

5.4.2 Spatial Mass Density within 1 kpc: The Spheroid Spatial Compactness $\langle\rho\rangle_{\rm 1kpc,sph}$

The internal mass density is a better measure of the inner density than the projected column density. Hence, we introduce $\langle\rho\rangle_{\rm 1kpc,sph}$, the spatial version of the projected spheroid compactness $\langle\Sigma\rangle_{\rm 1kpc,sph}$ (Section 5.3.2), defined as the mean internal stellar mass density within the inner 1 kpc of the spheroids.

We find a positive correlation between the black hole mass and the spheroid spatial compactness without any detectable substructuring due to the morphological classes of galaxies. The single-regression $M_{\rm BH}$–$\langle\rho\rangle_{\rm 1kpc,sph}$ relation[27], shown in the left-hand panel of

[27] Similar to the $M_{\rm BH}$–$\langle\Sigma\rangle_{\rm 1kpc,sph}$ diagram (Section 5.3.2), we use a ±30% (0.13 dex) uncertainty on $\langle\rho\rangle_{\rm 1kpc,sph}$ (and $\langle\rho\rangle_{\rm 5kpc,sph}$). We obtain consistent relations upon using up to ±40% (0.17 dex) uncertainty.

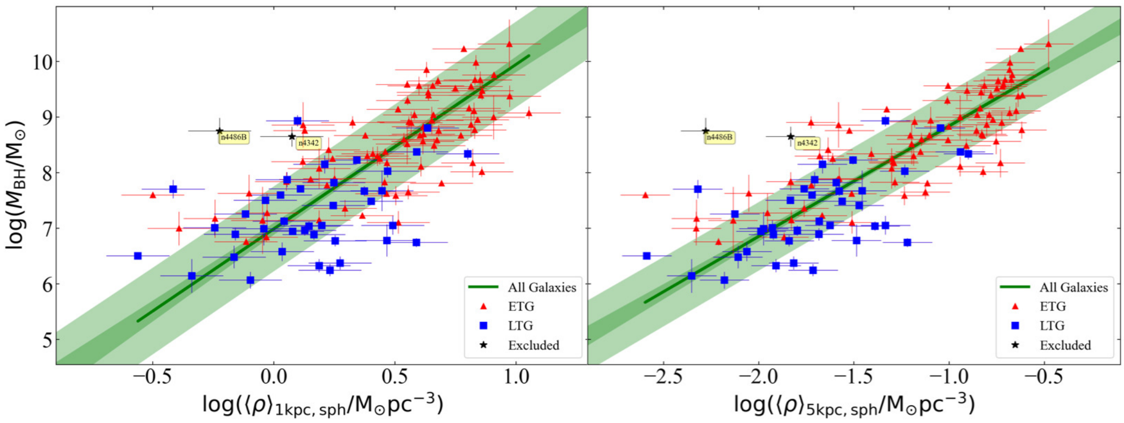

Figure 5.9 Black hole mass plotted against the internal stellar mass density within the internal spheroid radius of 1 kpc (left-hand panel, Equation 5.9) and the internal density within the internal spheroid radius of 5 kpc (right-hand panel, Equation 5.10). Similar to Figure 5.3, all galaxy types follow a single relation in these diagrams.

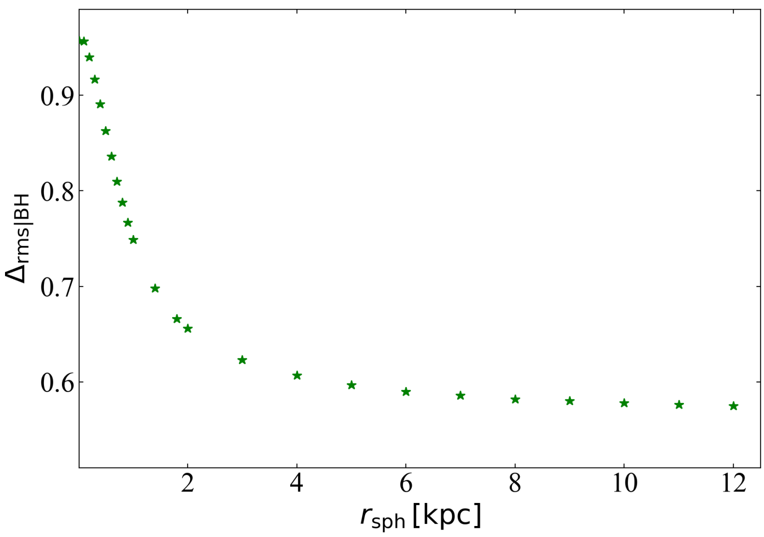

Figure 5.10 $\Delta_{rms|BH}$ versus r_{sph} for the M_{BH}–$\langle\rho\rangle_{r,sph}$ relations.

Figure 5.9, can be expressed as

$$\log\left(\frac{\mathrm{M_{BH}}}{\mathrm{M_\odot}}\right) = (2.96 \pm 0.21)\log\left(\frac{\langle\rho\rangle_{\mathrm{1kpc,sph}}}{10^{0.5}\,\mathrm{M_\odot\,pc^{-3}}}\right) + (8.47 \pm 0.07), \tag{5.9}$$

and has $\Delta_{\mathrm{rms|BH}} = 0.75$ dex. The M_{BH}–$\langle\rho\rangle_{\mathrm{1kpc,sph}}$ relation is marginally steeper than the M_{BH}–$\langle\Sigma\rangle_{\mathrm{1kpc,sph}}$ relation (Equation 5.2), and has a slightly higher vertical scatter. However, the orthogonal (perpendicular to the best-fit line) scatter in both the diagrams is comparable ($\sim$0.24 dex).

We find positive trends between M_{BH} and the internal spheroid density within other constant radii (e.g., 0.1 kpc, 5 kpc, 10 kpc) as well. The left-hand panel in Figure 5.7 shows that, in general, the high-M_{BH} profiles reside above the low-M_{BH} profiles at all radii; thus, the galactic spheroids with higher M_{BH} are relatively denser than the spheroids with lower M_{BH}, when compared at a fixed physical radius. This partly explains the positive trends obtained for the correlations of black hole mass with the spatial compactness, $\langle\rho\rangle_{\mathrm{1kpc,sph}}$, and the internal density at/within any fixed spatial radii. However, there is a varying scatter in the relations that decreases with larger radii.

A plot of the vertical $\Delta_{\mathrm{rms|BH}}$ versus r_{sph} for the M_{BH}–$\langle\rho\rangle_{\mathrm{r,sph}}$ relations is shown in Figure 5.10. For $\mathrm{r_{sph}} < 1$ kpc, the M_{BH}–$\langle\rho\rangle_{\mathrm{r,sph}}$ relations have a higher scatter than Equation 5.9, whereas, for $\mathrm{r_{sph}} > 1$ kpc the M_{BH}–$\langle\rho\rangle_{\mathrm{r,sph}}$ relations are relatively stronger and have a gradually decreasing scatter with increasing r_{sph}, analogous to the M_{BH}–$\Sigma_{\mathrm{R,sph}}$ relations (Section 5.3.2). This can be readily understood by again looking at the left-hand panel of Figure 5.7, even though it shows the density profiles, ρ, rather than the somewhat similar mean density profiles, $\langle\rho\rangle$. There, one can see a cleaner separation of profiles of different M_{BH} (and Sérsic index, n) when moving to larger radii, which is due to the increasingly longer tails of the high-n light profiles.

For a comparison, the M_{BH}–$\langle\rho\rangle_{\mathrm{5kpc,sph}}$ relation (see the right-hand panel of Figure 5.9), which has $\Delta_{\mathrm{rms|BH}} = 0.61$ dex, can be expressed as,

$$\log\left(\frac{\mathrm{M_{BH}}}{\mathrm{M_\odot}}\right) = (1.99 \pm 0.11)\log\left(\frac{\langle\rho\rangle_{\mathrm{5kpc,sph}}}{10^{-1.5}\,\mathrm{M_\odot\,pc^{-3}}}\right) + (7.85 \pm 0.06). \tag{5.10}$$

The smaller scatter in the above relation when compared to the $M_{\rm BH}$–$\langle\rho\rangle_{\rm 1kpc,sph}$ relation, and the quasi-saturation of $\Delta_{\rm rms|BH}$ for $\rm r_{sph} \gtrsim 5\,kpc$ (Figure 5.10), suggests that $\langle\rho\rangle_{\rm 5kpc,sph}$ can be preferred over $\langle\rho\rangle_{\rm 1kpc,sph}$ to predict $M_{\rm BH}$.

Overall, the $M_{\rm BH}$–$\langle\rho\rangle_{\rm r,sph}$ relations are steeper than the $M_{\rm BH}$–$\langle\Sigma\rangle_{\rm R,sph}$ relations for any fixed spheroid radius ($r = R$), with a marginally higher vertical scatter and similar orthogonal scatter. Hence, potentially both properties ($\langle\rho\rangle_{\rm r,sph}$ and $\langle\Sigma\rangle_{\rm R,sph}$) of a spheroid are equally good predictors of the central black hole's mass.

5.4.3 Internal Density at and within the Spheroid Spatial Half-Light Radius: $\rho_{\rm e,int,sph}$ & $\langle\rho\rangle_{\rm e,int,sph}$

Using the spheroid internal density profiles, we calculated the spheroid spatial half-mass radius, $r_{\rm e,sph}$, which represents a sphere enclosing 50% of the total spheroid mass (or luminosity, for a constant mass-to-light ratio). The ratio $r_{\rm e,sph}/R_{\rm e,sph}$ is approximately 1.33 (Ciotti, 1991).

We find that ETGs and LTGs define different (negative) trends between $M_{\rm BH}$ and the internal stellar mass density ($\rho_{\rm e,int,sph}$) at $r = r_{\rm e,sph}$, as shown in panel-a of Figure 5.11. The $M_{\rm BH}$–$\rho_{\rm e,int,sph}$ relation followed by ETGs can be expressed as

$$\log\left(\frac{\rm M_{BH}}{\rm M_\odot}\right) = (-0.64 \pm 0.04)\log\left(\frac{\rho_{\rm e,int,sph}}{\rm M_\odot pc^{-3}}\right) + (7.81 \pm 0.10), \tag{5.11}$$

with $\Delta_{\rm rms|BH} = 0.73$ dex. The steeper relation followed by LTGs, with $\Delta_{\rm rms|BH} = 0.69$ dex, is given by

$$\log\left(\frac{\rm M_{BH}}{\rm M_\odot}\right) = (-1.02 \pm 0.13)\log\left(\frac{\rho_{\rm e,int,sph}}{\rm M_\odot pc^{-3}}\right) + (7.20 \pm 0.11). \tag{5.12}$$

These two relations have a smaller scatter than the $M_{\rm BH}$–$\Sigma_{\rm e,sph}$ relations for ETGs and LTGs (cf., 0.81 dex and 0.77 dex, respectively). The relatively smaller scatter and smaller uncertainties on the fit parameters suggests that $\rho_{\rm e,int,sph}$ can be a better predictor of $M_{\rm BH}$ than $\Sigma_{\rm e,sph}$ (see Table 5.1 rows T1.9 and T1.10).

As we have repeatedly found, the shallower slope for the ETGs is of limited physical value. Its value reflects the sample selection and thus the relative number of ETGs with and without a disk. Further analysis of the $M_{\rm BH}$–$\rho_{\rm e,int,sph}$ diagram reveals an offset between the ETGs with a rotating stellar disk[28] (ES, S0) and ETGs without a rotating stellar disk (E), as shown in panel-c of Figure 5.11. The parameters for the $M_{\rm BH}$–$\rho_{\rm e,int,sph}$ relations obtained for the two ETGs sub-populations are presented in Table 5.2 (T2.9 and T2.10). Notably, these two sub-categories of ETGs follow steeper $M_{\rm BH}$–$\rho_{\rm e,int,sph}$ relations than Equation 5.11, almost parallel to each other but offset from each other by more than an order of magnitude in the $M_{\rm BH}$-direction. This offset is analogous to the offset found in the $M_{\rm BH}$–$M_{*,\rm sph}$ (Sahu et al., 2019a), $M_{\rm BH}$–$R_{\rm e,sph}$ (Sahu et al., 2020), and $M_{\rm BH}$–$\langle\Sigma\rangle_{\rm e,sph}$ diagrams (Section 5.3.3). This offset originates from the smaller effective sizes ($R_{\rm e,sph}$) and higher $\langle\Sigma\rangle_{\rm e,sph}$ of the ES/S0-type galaxies relative to that of E-type galaxies possibly built from major mergers.

Similar trends and morphological substructures are found between $M_{\rm BH}$ and the average internal density, $\langle\rho\rangle_{\rm e,int,sph}$, within $r_{\rm e,sph}$ (see panels b and d of Figure 5.11). The parameters for the $M_{\rm BH}$–$\langle\rho\rangle_{\rm e,int,sph}$ relations are provided in Table 5.2 (T2.11, T2.12, T2.13, T2.14). The right-hand panel in Figure 5.7 presents the spheroid spatial density profiles for our sample with the radial-axis normalized at $r_{\rm e,sph}$. At the spatial half-light radius, where $\log(r/r_{\rm e,sph}) = 0$, the increasing spatial density when going from high-$M_{\rm BH}$ to low-$M_{\rm BH}$ profiles is quite clear. This explains the negative $M_{\rm BH}$–$\rho_{\rm e,int,sph}$ (and $\langle\rho\rangle_{\rm e,int,sph}$) correlations.

Table 5.2 also provides the morphology-dependent relations obtained between $M_{\rm BH}$ and the spatial density $\langle\rho\rangle_{\rm e,sph}$ within the projected half-light radius ($r = R_{\rm e,sph}$), which are analogous to the substructures in the $M_{\rm BH}$–$\rho_{\rm e,int,sph}$ diagram. The $M_{\rm BH}$–$\langle\rho\rangle_{\rm e,sph}$ relation defined by our ETGs (Table 5.2 row T2.16) is consistent with that of Saglia et al. (2016). However, they do not report any of the vital substructures in this diagram due to ETGs (E, ES/S0) and LTGs. Without this awareness of the host galaxy morphology, the physical meaning to the slope and intercept of one's fitted $M_{\rm BH}$–$\langle\rho\rangle_{\rm e,sph}$ relation is hampered due to the bias associated with the randomness of one's sample selection. Indeed, this is why

[28]While disks obviously require rotation for stability, our multicomponent decompositions (Sahu et al., 2019a) were checked against the literature's "kinematic" data for confirmation of rotation.

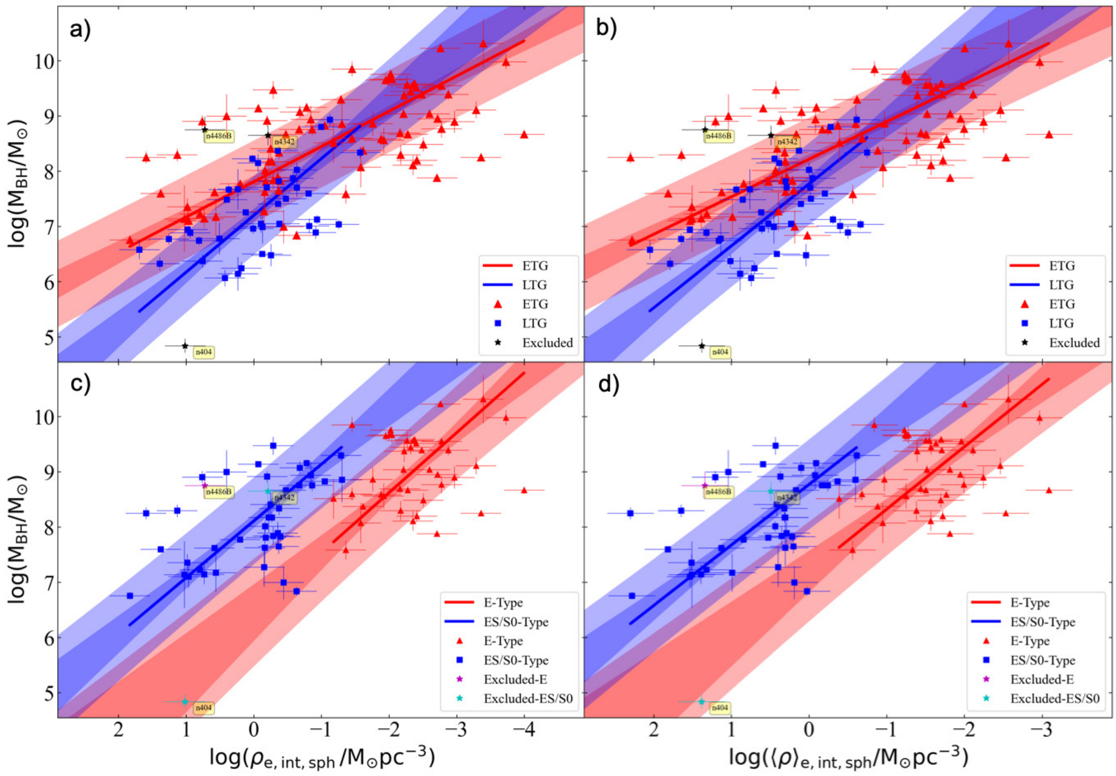

Figure 5.11 Black hole mass versus internal stellar mass density at $r = r_{\rm e,sph}$ (left-hand panels) and within $r_{\rm e,sph}$ (right-hand panels). Top panels show that ETGs and LTGs follow two different $M_{\rm BH}$–$\rho_{\rm e,int,sph}$ relations (panel a, Equations 5.11 and 5.12) and $M_{\rm BH}$–$\langle\rho\rangle_{\rm e,int,sph}$ relations (panel b, Table 5.2, T2.11 and T2.12). The bottom panels present only ETGs, where ETGs with a disk (ES- and S0-types) and ETGs without a disk (E-type) are found to follow almost parallel $M_{\rm BH}$–$\rho_{\rm e,int,sph}$ (panel c, Table 5.2, T2.9 and T2.10) and $M_{\rm BH}$–$\langle\rho\rangle_{\rm e,int,sph}$ (panel d, Table 5.2, T2.13 and T2.14) relations, offset in the vertical direction by more than an order of magnitude (see Table 5.2 for best-fit parameters). Note that the horizontal axes of all the panels are inverted, such that the internal density decreases when going from left to right.

our ETGs relation has a slope of -0.68 rather than roughly ~ -1.1, as followed by the E-type galaxies, the ES/S0-type galaxies, and the spiral galaxies (see Table 5.2 rows T2.16, T2.17, and T2.18).

Finally, we again note here that similar to the $M_{\rm BH}$–$\Sigma_{\rm e,sph}$ (and $\langle\Sigma\rangle_{\rm e,sph}$) relations (see Figures 5.5 and 5.6 in Section 5.3.3), the complete picture of the $M_{\rm BH}$–$\rho_{\rm e,int,sph}$ (and $\langle\rho\rangle_{\rm e,int,sph}$) distributions are curved, which may be revealed in future using a larger sample. The slopes of the linear relations presented here are dependent on the mass range of our sample.

Table 5.2. Correlations between the Black Hole Mass and the Spheroid Internal Density

No. (1)	Category (Eq.#) (2)	Number (3)	$\log(M_{\rm BH}/M_\odot) = (Slope)\, X + Intercept$ dex (4)	ϵ dex (5)	$\Delta_{\rm rms\|BH}$ dex (6)	r_p (7)	r_s (8)
			Internal Density at $r_{\rm soi}$ (Figure 5.8, middle panel)				
T2.1	Core-Sérsic (Eq. 5.7)	31	$\log(M_{\rm BH}/{\rm M_\odot}) = (-0.68 \pm 0.06) \log\left(\rho_{\rm soi,sph}/10^{2.5}\,{\rm M_\odot\,pc^{-3}}\right) + (9.06 \pm 0.05)$	0.00	0.21	-0.92	-0.93
T2.2	Sérsic (Eq. 5.8)	83[a]	$\log(M_{\rm BH}/{\rm M_\odot}) = (-1.18 \pm 0.10) \log\left(\rho_{\rm soi,sph}/10^{2.5}\,{\rm M_\odot\,pc^{-3}}\right) + (8.39 \pm 0.10)$	0.68	0.77	-0.54	-0.50
			Internal Density within $r_{\rm soi}$ (Figure 5.8, bottom panel)				
T2.3	Core-Sérsic	31	$\log(M_{\rm BH}/{\rm M_\odot}) = (-0.69 \pm 0.07) \log\left(\langle\rho\rangle_{\rm soi,sph}/10^{2.5}\,{\rm M_\odot\,pc^{-3}}\right) + (9.29 \pm 0.04)$	0.07	0.25	-0.89	-0.92
T2.4	Sérsic	83[a]	$\log(M_{\rm BH}/{\rm M_\odot}) = (-1.14 \pm 0.09) \log\left(\langle\rho\rangle_{\rm soi,sph}/10^{2.5}{\rm M_\odot\,pc^{-3}}\right) + (8.59 \pm 0.12)$	0.78	0.85	-0.43	-0.40
			Internal Density within 1 kpc of Spheroid (Figure 5.9, left-hand panel)				
T2.5	All Galaxies (Eq. 5.9)	119	$\log(M_{\rm BH}/{\rm M_\odot}) = (2.96 \pm 0.21) \log\left(\langle\rho\rangle_{\rm 1kpc,sph}/10^{0.5}\,{\rm M_\odot\,pc^{-3}}\right) + (8.47 \pm 0.07)$	0.63	0.75	0.73	0.75
			Internal Density within 5 kpc of Spheroid (Figure 5.9, right-hand panel)				
T2.6	All Galaxies (Eq. 5.10)	119	$\log(M_{\rm BH}/{\rm M_\odot}) = (1.99 \pm 0.11) \log\left(\langle\rho\rangle_{\rm 5kpc,sph}/10^{-1.5}\,{\rm M_\odot\,pc^{-3}}\right) + (7.85 \pm 0.06)$	0.53	0.61	0.82	0.84
			Internal Density at $r_{\rm e,sph}$ (Figure 5.11, left-hand panels)				
T2.7	LTGs (Eq. 5.12)	39	$\log(M_{\rm BH}/{\rm M_\odot}) = (-1.02 \pm 0.13) \log\left(\rho_{\rm e,int,sph}/{\rm M_\odot\,pc^{-3}}\right) + (7.20 \pm 0.11)$	0.63	0.69	-0.56	-0.58
T2.8	ETGs (Eq. 5.11)	80	$\log(M_{\rm BH}/{\rm M_\odot}) = (-0.64 \pm 0.04) \log\left(\rho_{\rm e,int,sph}/{\rm M_\odot\,pc^{-3}}\right) + (7.81 \pm 0.10)$	0.70	0.73	-0.64	-0.61
T2.9	E	40	$\log(M_{\rm BH}/{\rm M_\odot}) = (-1.09 \pm 0.11) \log\left(\rho_{\rm e,int,sph}/{\rm M_\odot\,pc^{-3}}\right) + (6.45 \pm 0.26)$	0.76	0.82	-0.26	-0.21
T2.10	ES/S0	40	$\log(M_{\rm BH}/{\rm M_\odot}) = (-1.03 \pm 0.10) \log\left(\rho_{\rm e,int,sph}/{\rm M_\odot\,pc^{-3}}\right) + (8.11 \pm 0.12)$	0.70	0.77	-0.52	-0.50
			Internal Density within $r_{\rm e,sph}$ (Figure 5.11, right-hand panels)				
T2.11	LTGs	39	$\log(M_{\rm BH}/{\rm M_\odot}) = (-1.12 \pm 0.15) \log\left(\langle\rho\rangle_{\rm e,int,sph}/{\rm M_\odot\,pc^{-3}}\right) + (7.78 \pm 0.13)$	0.64	0.72	-0.53	-0.56
T2.12	ETGs	80	$\log(M_{\rm BH}/{\rm M_\odot}) = (-0.68 \pm 0.05) \log\left(\langle\rho\rangle_{\rm e,int,sph}/{\rm M_\odot\,pc^{-3}}\right) + (8.22 \pm 0.09)$	0.70	0.74	-0.63	-0.59
T2.13	E	40	$\log(M_{\rm BH}/{\rm M_\odot}) = (-1.13 \pm 0.13) \log\left(\langle\rho\rangle_{\rm e,int,sph}/{\rm M_\odot\,pc^{-3}}\right) + (7.20 \pm 0.21)$	0.75	0.81	-0.26	-0.17
T2.14	ES/S0	40	$\log(M_{\rm BH}/{\rm M_\odot}) = (-1.09 \pm 0.12) \log\left(\langle\rho\rangle_{\rm e,int,sph}/{\rm M_\odot\,pc^{-3}}\right) + (8.77 \pm 0.12)$	0.71	0.79	-0.49	-0.44
			Internal Density within $R_{\rm e,sph}$				
T2.15	LTGs	39	$\log(M_{\rm BH}/{\rm M_\odot}) = (-1.16 \pm 0.16) \log\left(\langle\rho\rangle_{\rm e,sph}/{\rm M_\odot\,pc^{-3}}\right) + (8.04 \pm 0.16)$	0.65	0.73	-0.52	-0.54
T2.16	ETGs	80	$\log(M_{\rm BH}/{\rm M_\odot}) = (-0.68 \pm 0.05) \log\left(\langle\rho\rangle_{\rm e,sph}/{\rm M_\odot\,pc^{-3}}\right) + (8.40 \pm 0.08)$	0.70	0.74	-0.63	-0.59
T2.17	E	40	$\log(M_{\rm BH}/{\rm M_\odot}) = (-1.13 \pm 0.13) \log\left(\langle\rho\rangle_{\rm e,sph}/{\rm M_\odot\,pc^{-3}}\right) + (7.50 \pm 0.19)$	0.75	0.81	-0.26	-0.17
T2.18	ES/S0	40	$\log(M_{\rm BH}/{\rm M_\odot}) = (-1.11 \pm 0.12) \log\left(\langle\rho\rangle_{\rm e,sph}/{\rm M_\odot\,pc^{-3}}\right) + (9.06 \pm 0.13)$	0.71	0.79	-0.49	-0.44

Note. — Column names are same as in Table 5.1.

[a] After excluding eight significant outliers, marked in Figure 5.8, which can significantly affect the best-fit line for the ensemble of Sérsic galaxies.

5.5 Implications and Discussion

5.5.1 Prediction of $M_{\rm BH}$

We have shown how and explained why the BH mass correlates with a range of projected and internal stellar densities of the host spheroid. Plotting the density profiles of the (123 − Milky Way=) 122 spheroids together in the same figure reveals that the spheroids with larger BH masses reside in profiles with larger half-light radii, higher Sérsic indices, and longer tails to the light profile (Figures 5.1 and 5.7). At larger radii, the separation of spheroids with low-$M_{\rm BH}$ and low-n profiles from those with high-$M_{\rm BH}$ and high-n profiles becomes cleaner. Consequently, and counter-intuitively, the use of densities calculated at larger radii yields less scatter in the $M_{\rm BH}$–density diagram (Section 5.3.2 and 5.4.2).

The $M_{\rm BH}$–$\langle\Sigma\rangle_{\rm 5kpc,sph}$ relation (Equation 5.3) and the $M_{\rm BH}$–$\langle\rho\rangle_{\rm 5kpc,sph}$ relation (Equation 5.10) have similar rms scatters (0.59 dex and 0.61 dex), and are applicable to all galaxy types. The scatter in these diagrams is comparable to the morphology-dependent $M_{\rm BH}$–$M_{*,\rm sph}$ relations (cf., 0.50 dex, 0.57 dex, and 0.64 dex for E-, ES/S0-, and S-types, respectively) and the $M_{\rm BH}$–$R_{\rm e,sph}$ relations (cf., 0.59 dex, 0.61 dex, and 0.60 dex for E-, ES/S0-, and S-types, respectively), and smaller than the morphology-dependent $M_{\rm BH}$–$n_{\rm sph}$ relation (cf., 0.73 dex and 0.68 dex for ETGs and LTGs, respectively). Thus, $\langle\Sigma\rangle_{\rm 5kpc,sph}$ and $\langle\rho\rangle_{\rm 5kpc,sph}$ can predict $M_{\rm BH}$ as good as predicted using $M_{*,\rm sph}$ and $R_{\rm e,sph}$, and better than $M_{\rm BH}$ predicted using $n_{\rm sph}$. However, the density at 5 kpc may be very low for spheroids with $R_{\rm e}$ less than half a kpc, and these relations become more of a reflection of the $M_{\rm BH}$–n relations, and to a lesser degree the $M_{\rm BH}$–$R_{\rm e}$ relations (Sahu et al., 2020).

The 3.6 μm $M_{\rm BH}$–$\mu_{0,\rm sph}$ (Equation 5.1) and the $M_{\rm BH}$–$\mu_{\rm e,sph}$ relations (see Table 5.1) offer an alternative way to predict $M_{\rm BH}$ using $\mu_{0,\rm sph}$ or $\mu_{\rm e,sph}$, just from a calibrated (3.6 μm) spheroid surface brightness profile, without requiring either galaxy distance (for local galaxies where the cosmological corrections are very small) or a stellar mass-to-light ratio which can be complicated to choose. However, due to a higher scatter about these relations, the error bars on the predicted $M_{\rm BH}$ will be higher than obtained using the $M_{\rm BH}$–$n_{\rm sph}$ and $M_{\rm BH}$–$R_{\rm e,sph}$ relations (see Sahu et al., 2020). The values of $n_{\rm sph}$ and $R_{\rm e,sph}$ can also be obtained from an uncalibrated surface brightness profile. Plausibly, the high scatter in the $M_{\rm BH}$–$\mu_{\rm 0,sph}$ diagram is due to the use of a *column* density, and the high scatter in the $M_{\rm BH}$–$\mu_{\rm e,sph}$ diagram arises from a curved distribution of points.

For comparison, the $M_{\rm BH}$–ϕ relation for spiral galaxies (Seigar et al., 2008; Berrier et al., 2013) also has a small scatter of 0.43 dex (Davis et al., 2017), where ϕ is the pitch angle, i.e., the winding angle of the spiral arms. This relation can provide good estimates of $M_{\rm BH}$ for spiral galaxies. Including all galaxy types, the $M_{\rm BH}$–σ relation has a scatter of 0.53 dex; however, the $M_{\rm BH}$–σ diagram has different relations for core-Sérsic (cf., 0.46 dex) and Sérsic (cf., 0.55 dex) galaxies, which can provide a better estimate of $M_{\rm BH}$ than the single relation, if the core-Sérsic or Sérsic morphology is known. Another, preferred relation to predict $M_{\rm BH}$ may be the morphology-dependent $M_{\rm BH}$–$M_{*,\rm gal}$ relation (cf., 0.58 dex and 0.79 dex for ETGs and LTGs, respectively Sahu et al., 2019a), where, one does not need to go through the multi-component decomposition process to obtain the galaxy stellar mass, $M_{*,\rm gal}$.

The tight $M_{\rm BH}$–$\rho_{\rm soi,sph}$ relation for the core-Sérsic galaxies has the least total scatter (0.21 dex, see Table 5.2) among all the black hole scaling relations; whereas the $M_{\rm BH}$–$\rho_{\rm soi,sph}$ relation obtained for the Sérsic galaxies has a higher scatter (0.77 dex). The relation for core-Sérsic galaxies only captures the upper envelope of high-$n_{\rm sph}$ spheroids in the $M_{\rm BH}$–$\rho_{\rm soi,sph}$ diagram, while the relation for Sérsic galaxies describes the average relation for spheroids with a medium value of n (between ~ 1.5 to ~ 5). Overall, the $M_{\rm BH}$–$\rho_{\rm soi,sph}$ diagram suggests that the inclusion of $n_{\rm sph}$ as a third parameter will lead to a black hole plane with a considerably reduced scatter. However, if it was to turn out that the mass of the black hole is better connected to the stellar density within its sphere of influence and the stellar concentration (quantified by n), it is not useful for predicting $M_{\rm BH}$, because $\rho_{\rm soi,sph}$ requires knowledge of $r_{\rm soi}$ and thus $M_{\rm BH}$.

5.5.2 Dependence of the Black Hole Scaling Relations on the Galaxy Morphology

Sahu et al. (2020) did not report on the offset between the ETG subpopulations (E vs ES/S0-types) in the $M_{\rm BH}$–$\mu_{\rm e,sph}$ (or $\langle\mu\rangle_{\rm e,sph}$, or $\Sigma_{\rm e,sph}$, or $\langle\Sigma\rangle_{\rm e,sph}$) diagrams, that we reinvestigated here. Our investigation here has revealed an offset between the E- and ES/S0-type galaxy samples (Figure 5.6). However, the $M_{\rm BH}$–$\mu_{\rm e,sph}$ correlations obtained for the E- and ES/S0-types are weak, and their slopes and the offset are not established. This is plausibly because they follow a curved relation with varying slopes, and we have sampled the bend points of the curves (see Figure 5.6). Consequently, there is not a strong correlation between $M_{\rm BH}$ and the various effective densities for our sample (Section 5.3.3).

Morphology-dependent divisions in the $M_{\rm BH}$–$n_{\rm sph}$ (ETG vs LTG), $M_{\rm BH}$–$R_{\rm e,sph}$ (E vs ES/S0 vs LTG), and, as seen here, the $M_{\rm BH}$–$\mu_{\rm e,sph}$ (E vs ES/S0 vs LTG) diagrams, propagate into the $M_{\rm BH}$–$M_{*,\rm sph}$ (E vs ES/S0 vs LTG, Sahu et al., 2019a) diagrams. Similarly, these morphological substructures are also propagated to the $M_{\rm BH}$–$\rho_{\rm e,int,sph}$ (and $\langle\rho\rangle_{\rm e,int,sph}$) diagrams presented here (Figure 5.11). Although the ETGs and LTGs seem to define distinct tight relations, there is an order of magnitude offset[29] in the $M_{\rm BH}$-direction between ETGs without a disk (E-type or slow-rotators) and ETGs with a disk (ES/S0-types or fast-rotators). The offset between E- and ES/S0-type galaxies is a combined effect of a smaller bulge size ($R_{\rm e,sph}$) and brighter $\mu_{\rm e,sph}$ (higher $\Sigma_{\rm e,sph}$ and $\langle\Sigma\rangle_{\rm e,sph}$) of the ES/S0-type galaxies compared to that of E-type galaxies hosting a similar black hole mass (Section 5.3.3).

As discussed in Section 5.4.1, the Sérsic versus core-Sérsic division in the $M_{\rm BH}$–$\rho_{\rm soi,sph}$ diagram (Figure 5.8) remains independent of whether or not $r_{\rm soi}$ is calculated using the central stellar velocity dispersion. Hence, the Sérsic versus core-Sérsic substructures observed in the $M_{\rm BH}$–σ diagram (Sahu et al., 2019b) and the $M_{\rm BH}$–$\rho_{\rm soi,sph}$ (or $\langle\rho\rangle_{\rm soi,sph}$) diagrams are not directly related. Nonetheless, the $M_{\rm BH}$–σ and $M_{\rm BH}$–$\rho_{\rm soi,sph}$ relations are respectively aware of the galaxy morphology, and thus the galaxies' evolutionary tracks and their central light/mass concentration, i.e., Sérsic index (see the top panel in Figure 5.8 and the description in Section 5.4.1).

5.5.3 Fundamental Black Hole Scaling Relation

Many studies have suggested that the $M_{\rm BH}$–σ relation may be the most fundamental/universal relation (e.g., Ferrarese & Merritt, 2000; Gebhardt et al., 2000; Ferrarese & Ford, 2005) between a black hole and the host galaxy due to its obvious link with the galaxy's gravitational potential and the appearance of $M_{\rm BH} \propto \sigma^{4-5}$ relations in theories

[29]This offset between ETG with and without a disk is minimized in the $M_{\rm BH}$–$M_{*,\rm gal}$ diagram, where Sahu et al. (2019a) revealed only two distinct relations due to (all) ETGs and LTGs.

trying to explain black hole feedback (Silk & Rees, 1998; Fabian, 1999). These claims are based on past observations which reported a single $M_{\rm BH}$–σ relation for all galaxy types (including bulge-less galaxies), and a smaller scatter seen in the $M_{\rm BH}$–σ diagram relative to the $M_{\rm BH}$–$M_{*,\rm sph}$ relation.

Several studies have explored if a third parameter, such as the half-light radius, may reduce the scatter about the $M_{\rm BH}$–σ relation (e.g., Marconi & Hunt, 2003; Feoli & Mele, 2005; de Francesco et al., 2006; Hopkins et al., 2007; Feoli & Mancini, 2011; Soker & Meiron, 2011). Gains have been marginal at best. In recent years, Saglia et al. (2016) investigated the $M_{\rm BH}$-$\langle\rho\rangle_{\rm e}$-$\sigma$ relation and van den Bosch (2016) advocated for an $M_{\rm BH}$-$R_{\rm e}$-L relation, while de Nicola et al. (2019) and Marsden et al. (2020) confirmed their findings of limited gains over the $M_{\rm BH}$–σ relation. However, over the years, increments in the scatter about the $M_{\rm BH}$–σ relation to ~ 0.5 dex with growing sample size (see the introduction in Sahu et al., 2019b), plus the revelation of a Sérsic ($M_{\rm BH} \propto \sigma^{\sim 5}$) versus core-Sérsic ($M_{\rm BH} \propto \sigma^{\sim 8}$) division in the $M_{\rm BH}$–σ diagram (e.g., Bogdán et al., 2018; Sahu et al., 2019b; Dullo et al., 2020b), undermine the perceived superiority of σ.

Importantly, if the relation with the least scatter should be the primary criteria for deciding the fundamental black hole scaling relation, recent studies further confound the situation. For example: the $M_{\rm BH}$–$\rho_{\rm soi,sph}$ relation (Equation 5.7) for core-Sérsic galaxies has a total rms scatter of 0.21 dex; the $M_{\rm BH}$–($R_{\rm b}$: break radius) relation for core-Sérsic galaxies has $\Delta_{\rm rms|BH} = 0.29$ dex (Dullo et al., 2020b); the $M_{\rm BH}$–(pitch angle) relation for spiral galaxies has $\Delta_{\rm rms|BH} = 0.43$ dex (Davis et al., 2017); and the $M_{\rm BH}$–$M_{*,\rm sph}$ relation for ETGs has $\Delta_{\rm rms|BH} = 0.52$ dex (Sahu et al., 2019a). Moreover, the substructure in the $M_{\rm BH}$–$\rho_{\rm soi,sph}$ diagram (Figure 5.8) due to different ranges of $n_{\rm sph}$ values suggest the existence of a possibly stronger $M_{\rm BH}$–$\rho_{\rm soi,sph}$–$n_{\rm sph}$ relation, which shall be investigated in future work. Of course, $\rho_{\rm soi,sph}$ is calculated using $M_{\rm BH}$, so some care will be required in such an exploration.

5.5.4 Super Massive Black Hole Binary Merger Timescale

The stellar density around a super massive black hole binary (SMBHB) plays an essential role in accelerating the merger of the black holes through dynamical friction (Chandrasekhar, 1943; Begelman et al., 1980; Arca-Sedda & Capuzzo-Dolcetta, 2014). During a galaxy merger, dynamical friction pushes the black holes towards the core of the galaxy merger remnant, forming a binary at parsec scales. The SMBHB goes through a hydrodynamical interaction with the surrounding stars (and dust/gas), entering a hardening phase, i.e. when the binding energy of the binary exceeds the average kinetic energy of stars around it (Holley-Bockelmann, 2016). The binary then transitions from the hardening to the gravitational wave (GW) emission phase, which eventually drives the binary to merge (Celoria et al., 2018). The major part of a binary lifetime is spent in this transition phase/separation (Sesana & Khan, 2015), the orbital frequency at this transition separation is known as the transition frequency. This time period ($\approx$ binary lifetime) can be estimated using the average stellar density ($\langle\rho\rangle_{\rm soi}$), and stellar velocity dispersion ($\sigma_{\rm soi}$) at the sphere-of-influence of the binary and the binary's orbital eccentricity (e.g., Sesana & Khan, 2015, their equation 7). The transition frequency, which is a part of GW strain model (discussed next), is also estimated using $\langle\rho\rangle_{\rm soi}$, $\sigma_{\rm soi}$, and eccentricity (Chen et al., 2017, their equation 21).

Recently, Biava et al. (2019) estimated the SMBHB lifetime, as discussed above, using Sérsic parameters of a remnant-bulge hosting a given (binary) black hole mass. They used the $M_{\rm BH}$–$M_{*,\rm sph}$ relation (Savorgnan et al., 2016), the $M_{*,\rm sph}$–$\rm R_{e,sph}$ relation (Dabringhausen et al., 2008), and the $M_{\rm BH}$–$n_{\rm sph}$ relation (Davis et al., 2019a) to obtain the Sérsic parameters of bulges hosting $10^5 - 10^8\,M_{\odot}$ binary black holes, with the assumption that the merger remnants follow these relations. Using these bulge parameters, they applied the Prugniel & Simien (1997) density model to obtain $\langle\rho\rangle_{\rm soi}$ to estimate the binary lifetime using the model from Sesana & Khan (2015, their equation 7).

Now, using our $M_{\rm BH}$–$\langle\rho\rangle_{\rm soi}$ relations obtained here and the $M_{\rm BH}$–σ relations (e.g., Sahu et al., 2019b), one can directly obtain the $\langle\rho\rangle_{\rm soi}$ values and the central σ, respectively, for a given $M_{\rm BH}$, and using the central σ as a proxy for $\sigma_{\rm soi}$, one can estimate the typical binary lifetime more directly. One can also apply the expression of mean aperture correction for stellar velocity dispersion (from e.g., Jorgensen et al., 1995; Cappellari et al., 2006) to drive $\sigma_{\rm soi}$ using the central σ (normalized at aperture size of 0.595 kpc) obtained from our $M_{\rm BH}$–σ relation and $r_{\rm soi}$. Similarly, using the $\langle\rho\rangle_{\rm soi}$ and σ values for a given $M_{\rm BH}$ (and some binary eccentricity), the estimation of the transition frequency can be more straightforward (see Chen et al., 2017, their equation 21). This way, one would not need to go through various black hole scaling relations for the bulge parameters to obtain $\langle\rho\rangle_{\mathrm{soi}}$, using an approximation for σ, and choosing an approximate density model, e.g., as suggested in Sesana & Khan (2015) and followed in Biava et al. (2019).

However, one should note that for galaxies with either a nuclear disk or nuclear star cluster, the $\langle\rho\rangle_{\mathrm{soi}}$ will be higher than estimated using the M_{BH}–$\langle\rho\rangle_{\mathrm{soi}}$ relations for just spheroids. Whereas, for core-Sérsic galaxies, the $\langle\rho\rangle_{\mathrm{soi}}$ will be lower than estimated using the M_{BH}–$\langle\rho\rangle_{\mathrm{soi}}$ relation.

5.5.5 Predicting the Gravitational Wave Strain

The long-wavelength gravitational waves (GWs: mHz - nHz), emitted during the SMBHB merger, fall in the detection band of pulsar timing arrays (PTAs: µHz - nHz), laser interferometer space antenna (LISA: 0.1 Hz to 0.1 mHz, Amaro-Seoane et al., 2017), and other planned space interferometers, such as TianQuin (Luo et al., 2016). These detectors aim to detect the stochastic GW background (GWB) and individual GWs, which are challenging to predict (Sesana et al., 2009; Mingarelli et al., 2017). The detectable amplitude (per unit logarithmic frequency) of perturbations due to the GWB is quantified by the characteristic strain (h_c), a typical estimate of which is required for different detectors sensitive to different wavelength ranges of GWs (e.g., see the sensitivity curves for various detectors in Moore et al., 2015).

The GWB characteristic strain can be modeled by integrating the SMBHB merger rate across redshift for a range of chirp-mass[30] (see the model described in Chen et al., 2019). The estimation of SMBHB merger rate is dependent on the observed galaxy mass function, galaxy pair fraction, SMBHB merger time scale (galaxy merger time scale + binary lifetime), and the (black hole)–galaxy scaling relations (Sesana, 2013). The (black hole)–galaxy scaling relations convert the galaxy mass function and the galaxy pair fraction into the black hole mass function (BHMF) and the black hole pair fraction (BHPF).

Often, a constant $M_{*,\mathrm{sph}}/M_{*,\mathrm{gal}}$ ratio has been combined with the old linear M_{BH}–$M_{*,\mathrm{sph}}$ relation to obtain an $M_{\mathrm{BH}}/M_{*,\mathrm{gal}}$ ratio, which is used to convert the galaxy mass function into the BHMF (e.g., Shannon et al., 2015; Chen et al., 2019). This causes

[30] Chirp mass of a binary comprising of objects with masses M_1 and M_2 is given by $\mathcal{M} = (M_1 M_2)^{3/5}/(M_1 + M_2)^{1/5}$ (e.g., see Cutler & Flanagan, 1994). It influences the orbital evolution of the binary, e.g., the orbital frequency which governs the emitted GW frequency.

a bias in the estimated GWB characteristic strain (e.g., Mapelli & Others, 2012, show that a quadratic $M_{\rm BH}$–$M_{*,\rm sph}$ relation, instead of a linear relation, changes the predicted extreme mass-ratio inspiral event rate by an order of magnitude). The use of our new morphology-dependent $M_{\rm BH}$–$M_{*,\rm gal}$ relations (Sahu et al., 2019a) will provide a direct way to obtain a better BHMF and BHPF. Coupled with these, the better estimates of the binary lifetime (Section 5.5.4) will improve the SMBHB merger rate, which will ultimately improve the predictions for the detectable GWB strain for PTAs and GW space missions.

5.5.6 Tidal Disruption Event Rate

The $M_{\rm BH}$–$\langle\rho\rangle_{\rm soi}$ relation may also help model the rate of tidal disruption events (TDEs, Hills, 1975). This is important because, apart from probing the black hole population and their environments (especially for BHs in inactive galaxies), TDEs are used to estimate the black hole mass (Mockler et al., 2019; Zhou et al., 2021), and they form the electromagnetic counterparts of the extreme mass-ratio inspirals (EMRIs).

TDEs are expected to occur more frequently in galaxies with an elevated central stellar density or a nuclear star cluster (Frank & Rees, 1976). The TDEs also require $M_{\rm BH} \lesssim 10^8\,{\rm M_\odot}$ because the weaker tidal forces at, and beyond, the Schwarzchild-Droste radii (Schwarzschild, 1916; Droste, 1917) of more massive black holes are insufficient to tear open stars and produce a TDE (Rees, 1988; Komossa, 2015). TDE rate ($\Gamma_{\rm TDE}$) versus $\langle\rho\rangle_{\rm soi}$ relation in Pfister et al. (2020, their equation 8) provides a lower limit of $\Gamma_{\rm TDE}$ for a given $\langle\rho\rangle_{\rm soi}$. Combining their $\Gamma_{\rm TDE}$–$\langle\rho\rangle_{\rm soi}$ relation with our $M_{\rm BH}$–$\langle\rho\rangle_{\rm soi}$ relation for Sérsic galaxies, we can obtain a relation between $M_{\rm BH}$ and TDE rate as

$$\Gamma_{\rm TDE}/{\rm year}^{-1} = 0.16 \times ({\rm M_{BH}/M_\odot})^{-0.6}, \tag{5.13}$$

which can be used to obtain a typical estimate of the TDE rate for a given $M_{\rm BH}$. This can be refined further through the use of a set of $M_{\rm BH}$–$\langle\rho\rangle_{\rm soi}$ relations, applicable for different ranges of Sérsic index and $M_{\rm BH} \lesssim 10^8\,M_\odot$, or the creation of an $M_{\rm BH}$–$\langle\rho\rangle_{\rm soi}$–$n_{\rm sph}$ plane. We shall leave this for future work. It is worth noting that exact estimates of $\Gamma_{\rm TDE}$ are expected to vary depending on the presence of a nuclear star cluster.

5.6 Conclusion

We used the largest-to-date sample of galaxies which have a careful multi-component decomposition of their projected surface brightness profile (Savorgnan & Graham, 2016b; Davis et al., 2019a; Sahu et al., 2019a) and a directly-measured central black hole mass present in the literature (Section 5.2). We build upon our recent (published) work, where we revealed morphology-dependent M_{BH}–($M_{*,\mathrm{sph}}$ and $M_{*,\mathrm{gal}}$) relations (Davis et al., 2018a, 2019a; Sahu et al., 2019a), M_{BH}–σ relations (Sahu et al., 2019b), and M_{BH}–(n_{sph} and $\mathrm{R}_{\mathrm{e,sph}}$) relations (Sahu et al., 2020).

Here, we investigated the connection between the black hole mass and the host spheroid's projected and internal stellar mass densities (Sections 5.3 and 5.4, respectively). More specifically, we presented the scaling relations of M_{BH} with the spheroid projected luminosity density (μ, $\mathrm{mag\,arcsec^{-2}}$) and projected stellar mass density (Σ and $\langle\Sigma\rangle$, $\mathrm{M_{\odot}\,pc^{-2}}$) at and within various spheroid radii (e.g., $\mathrm{R} = 0, 1\,\mathrm{kpc}, 5\,\mathrm{kpc}$, and $R_{\mathrm{e,sph}}$).

Importantly, we explored the correlation of M_{BH} with the internal stellar mass density ρ ($\mathrm{M_{\odot}\,pc^{-3}}$), which is a better measure of density than the projected column density. We deprojected the (Sérsic) surface brightness profiles of our galactic spheroids using the inverse Abel transformation (Appendix D.1) and numerically calculated the internal densities at various internal radii, including the black hole's sphere-of-influence radius (r_{soi}), fixed physical internal radii (e.g., 1 kpc, 5 kpc), and the spatial half-mass radius $r_{\mathrm{e,sph}}$. We investigated possible correlations between M_{BH} and the internal stellar mass density at and within these spheroid radii. We also presented the density profiles (Figure 5.7), which help in understanding the various observed M_{BH}–ρ correlations (Table 5.2).

In all these cases, we explored the dependence of the black hole scaling relations on the host galaxy morphology, i.e., possible division/substructure in the scaling diagrams due to ETGs versus LTGs, Sérsic versus core-Sérsic spheroids, barred versus non-barred galaxies, and galaxies with and without a stellar disk. The slopes and intercepts of the scaling relations depicted in the figures of this paper— obtained using the BCES(BISECTOR) routine (Table 5.1 and 5.2)—are consistent with the parameters obtained using the symmetric application of the Bayesian linear regression routine LINMIX (Table D.1). Sometimes LINMIX gives slightly smaller uncertainties on the slope and intercept, and other times slightly larger uncertainties than reported by the BCES(BISECTOR) routine. The only exception of note is that for the E and ES/S0 sample, LINMIX gives roughly twice as large uncertainties on the slope and intercept. The uncertainties obtained using the LINMIX routine for these diagrams seem more realistic as the distribution of our sample in these diagrams may have non-Gaussian and herteroscedastic residuals, in which case the BCES (and MFITEXY) regressions can provide underestimated errors. Despite this, the correlation coefficients and total rms scatters, used in this paper to compare different relations, are similar.

The main results are summarized below.

- Spheroids with higher $M_{\rm BH}$ have a brighter central surface brightness $\mu_{0,\rm sph}$ (Equation 5.1) or higher central projected stellar mass density $\Sigma_{0,\rm sph}$ (Figure 5.2). This is true for Sérsic spheroids without depleted cores. This is qualitatively consistent with the linear $M_{\rm BH}$–$\mu_{0,\rm sph}$ relation predicted in Graham & Driver (2007a). However, the total rms scatter in the $M_{\rm BH}$–$\mu_{0,\rm sph}$ (and $\Sigma_{0,\rm sph}$) diagrams are notably high (~ 1 dex, see the fit parameters in Table 5.1).

- $M_{\rm BH}$ defines a positive correlation with the average projected density, $\langle\Sigma\rangle_{\rm 1kpc,sph}$, within the inner 1 kpc of the host spheroid (*aka* the spheroid compactness). The relation has $\Delta_{\rm rms|BH} = 0.69$ dex (Equation 5.2), and is followed by all galaxy types (see the left-hand panel of Figure 5.3, and Section 5.3.2).

- $M_{\rm BH}$ has a stronger correlation with $\langle\Sigma\rangle_{\rm R,sph}$ for $\rm R > 1\,kpc$, than with the spheroid compactness $\langle\Sigma\rangle_{\rm 1kpc,sph}$, such that the slope of the relation and the scatter decreases with increasing R. The total scatter starts saturating at ~ 0.59 dex beyond $\sim 5\,$kpc (see Figure 5.4).

- In the $M_{\rm BH}$–$\mu_{\rm e,sph}$ and $M_{\rm BH}$–$\Sigma_{\rm e,sph}$ (and $\langle\Sigma\rangle_{\rm e,sph}$) diagrams, ETGs and LTGs (S-types) follow different negative relations (Figure 5.5, Table 5.1). The negative trend is because spheroids with higher $M_{\rm BH}$ have a larger half-light radius with a lower density at/within these radii relative to that of spheroids with lower $M_{\rm BH}$. Further investigation reveals an offset between the E- and ES/S0-type galaxies in these diagrams, with suggestively similar slopes as that of LTGs (see Figure 5.6). However, the correlation coefficients are very poor, and the high scatter across these relations makes it difficult to quantify this offset correctly. Moreover, the actual distributions for the E-, ES/S0-, and S-types are expected to be curved; the predicted curves are also presented in Figures 5.5 and 5.6 (Section 5.3.3).

- $M_{\rm BH}$ correlates with the internal density at and within the corresponding sphere-of-influence radius ($\rho_{\rm soi,sph}$ and $\langle\rho\rangle_{\rm soi,sph}$, Figure 5.8). The Sérsic and core-Sérsic galaxies seem to define two different relations with a negative slope. The core-Sérsic galaxies define a shallower $M_{\rm BH}$–$\rho_{\rm soi,sph}$ relation with $\Delta_{\rm rms|BH} = 0.21$ dex, whereas, the Sérsic galaxies with n $\gtrsim 1$ follow a steeper relation with $\Delta_{\rm rms|BH} = 0.77$ dex (see Table 5.2). This substructuring is primarily due to the range of high Sérsic index profiles for the core-Sérsic spheroids (see the top panel of Figure 5.8 and Section 5.4.1). The data suggests an $M_{\rm BH}$–$\rho_{\rm soi,sph}$–$n_{\rm sph}$ plane, which will be the subject of future work.

- Analogous to the (projected) spheroid compactness $\langle\Sigma\rangle_{\rm 1kpc,sph}$, we introduced the spheroid spatial compactness, $\langle\rho\rangle_{\rm 1kpc,sph}$, which is a measure of density within a sphere of 1 kpc radius. The quantity $\langle\rho\rangle_{\rm 1kpc,sph}$ defines a positive correlation with the $M_{\rm BH}$, which has $\Delta_{\rm rms|BH} = 0.75$ dex (see Equation 5.9 and the left-hand panel in Figure 5.9). As with $\langle\Sigma\rangle_{\rm 1kpc,sph}$, we do not find a morphological dependence in the $M_{\rm BH}$–$\langle\rho\rangle_{\rm 1kpc,sph}$ diagram.

- Analogous to the $M_{\rm BH}$–$\langle\Sigma\rangle_{\rm R,sph}$ diagram, we find stronger correlations between $M_{\rm BH}$ and $\langle\rho\rangle_{\rm r,sph}$ for r > 1 kpc. The slope of the $M_{\rm BH}$–$\langle\rho\rangle_{\rm r,sph}$ relation and the total scatter decreases with increasing internal radius r, where $\Delta_{\rm rms|BH}$ asymptotes at ~ 0.6 dex for r $\gtrsim$ 5kpc (Figure 5.10). The $M_{\rm BH}$–$\langle\rho\rangle_{\rm 5kpc,sph}$ relation (Equation 5.10) is shown in Figure 5.9. Given the comparable scatter in the $M_{\rm BH}$–$\langle\Sigma\rangle_{\rm R,sph}$ and $M_{\rm BH}$–$\langle\rho\rangle_{\rm r,sph}$ diagrams, both the relations seem equally good predictors of $M_{\rm BH}$, where the density within 5 kpc can be preferred over the density within 1 kpc (Section 5.4.2).

- In the $M_{\rm BH}$–$\rho_{\rm e,int,sph}$ and $M_{\rm BH}$–$\langle\rho\rangle_{\rm e,int,sph}$ diagrams, ETGs and LTGs appear to define two different relations with a negative slope (top panels in Figure 5.11). Further analysis reveals that ETGs with a disk (E) and ETGs without a disk (ES/S0) appear to follow two different almost parallel relations, offset by more than an order of magnitude in the $M_{\rm BH}$-direction (bottom panels in Figure 5.11). They roughly have the same slope (~ -1) as the relation for LTGs (Table 5.2). However, the relation may be curved, in which case the observed slope is a function of our sample's range of black hole mass. This morphology-dependent pattern has also been seen in the $M_{\rm BH}$–$M_{*,\rm sph}$ (Sahu et al., 2019a), $M_{\rm BH}$–$R_{\rm e,sph}$ (Sahu et al., 2019b), and $M_{\rm BH}$–$\Sigma_{\rm e,sph}$ diagrams (Figures 5.5 and 5.6).

The revelation of morphology-dependent substructure in diagrams of black hole mass with various host spheroid/galaxy properties makes it more complex to conclude which relation may be the best to predict $M_{\rm BH}$ or the most fundamental relation. It also rewrites the notion of the coevolution of galaxies and their black holes. The black holes appear to be aware of the galaxy morphology and thus the formation physics of the galaxy.

The central densities ($\mu_{0,\rm sph}$, $\Sigma_{0,\rm sph}$, $\langle\rho\rangle_{\rm soi,sph}$, and $\rho_{\rm soi,sph}$) are based on the inward extrapolation of the Sérsic component of the spheroid's surface brightness model; however, additional nuclear star clusters or partially depleted cores will modify these densities. In future work, we hope to use high-resolution HST images to measure the depleted cores of the core-Sérsic galaxies and extract the nuclear star clusters from the host galaxy profile. This will enable us to revisit the $M_{\rm BH}$–central density relations.

The $M_{\rm BH}$–density relations revealed in this paper have a wide range of applications (Section 5.5). For example: an alternative way to estimate the black hole mass in other galaxies; forming tests for realistic simulated galaxies with a central black hole; estimating the SMBH binary merger time scales; constraining the orbital frequency of the SMBHB during the transition from binary hardening to the GW emission phase; modeling the tidal disruption event rates (e.g., Equation 5.13); estimating/modeling the SMBH binary merger rate; and modifying the characteristic strains for the detection of long-wavelength gravitational waves for pulsar timing arrays and space interferometers.

5.7 Acknowledgements

This research was conducted with the Australian Research Council Centre of Excellence for Gravitational Wave Discovery (OzGrav), through project number CE170100004. This project was supported under the Australian Research Council's funding scheme

DP17012923. This material is based upon work supported by Tamkeen under the NYU Abu Dhabi Research Institute grant CAP[3]. I (NS) thank the astrophysics group at the University of Queensland for hosting me and providing an office space for one year during the covid-19 pandemic. I additionally thank my thesis examiners Prof. Richard McDermid and Dr. Dieu Nyugen for providing helpful comments for this paper.

6
Conclusion

The central massive black hole (BH) feeds on the gas, dust, and stellar content of the immediately surrounding part of the host galaxy, which is often dominated by the galactic bulge, except for rare bulge-less (disk-dominant) galaxies (e.g., Davis et al., 2018a). The dynamical friction between materials inspiraling into the BH releases a tremendous amount of energy and illuminates the hot accretion disk around the BH. Additionally, the BHs accreting at high rates can cause powerful bipolar gas outflows originating from the accretion disk, which forms a feedback accredited to regulate the host galaxy's gas content and, thus, growth (Silk, 2005; King, 2010; Ginat et al., 2016). Black hole feedback is not entirely understood; however, the interplay between the host galaxy and its BH suggests a co-evolution, which can be understood through the correlations observed between them. As recapped in the **Introduction**, this motivated numerous studies for establishing a correlation between the black hole mass (M_{BH}) and stellar spheroid mass ($M_{*,\mathrm{sph}}$) and the M_{BH} versus central stellar velocity dispersion (σ) of a galaxy.

The initial studies found a linear M_{BH}–$M_{*,\mathrm{sph}}$ relation. However, later investigation with an increased sample size revealed a dependence on the galaxy morphology[1] (Graham & Scott, 2013; Savorgnan et al., 2016), where the galaxy morphology is tied with the galaxy formation and evolution physics. The first studies on the M_{BH}–σ relation reported a minimal (consistent with zero) intrinsic scatter, suggesting it to be the most fundamental black hole relation. However, there was a discrepancy in slope, and the later studies showed

[1] A review of studies on scaling relations until 2016 can be found in Graham (2016).

increased intrinsic scatter (e.g., 0.38 dex, 0.41 dex, 0.49 dex, respectively, reported in McConnell & Ma, 2013; Saglia et al., 2016; van den Bosch, 2016) and possible substructures and upturn linked with galaxy morphology (Hu, 2008; Graham, 2013; Woo et al., 2013a; Bogdán et al., 2018).

Doubling the sample size in Savorgnan & Graham (2016b) to 127 local ($z \sim 0$) galaxies with reliable directly-measured BH masses and spheroid properties measured through meticulous multi-component decomposition, this thesis answered many questions which remained and built upon the previous efforts reviewed in **Chapter 1**. In addition to the BH scaling relations with the $M_{*,\rm sph}$ and σ, this work expanded the search for a primary BH relation with the total galaxy stellar mass ($M_{*,\rm gal}$) and spheroid structural properties, e.g., size ($R_{\rm e,sph}$), central light concentration ($n_{\rm sph}$), projected ($\mu_{\rm sph}$) and the internal ($\rho_{\rm sph}$) stellar mass density. Importantly, this study emphasised investigating the possibility of a substructure (a division, an offset, or a curve) in these BH scaling diagrams dependent on the host galaxy morphology.

6.1 Summary

Using an example multi-component galaxy NGC 4762, **Chapter 2** describes our image reduction and the two essential techniques: extracting the two-dimensional galaxy model (with Isofit and Cmodel, Ciambur, 2015) and multi-component decomposition of galaxy light (with Profiler, Ciambur, 2016). Galaxy modelling using software Isofit and Cmodel was crucial in capturing all the photometric and structural galaxy properties, e.g., surface brightness profile (μ), ellipticity profile (e), position angle profile, and the structural irregularities quantified by higher-order Fourier coefficients. Further, while disassembling total galaxy light into its components, the additional hints from high-resolution HST images, kinematic databases, and literature references, if available, were used to identify nuclear components, stellar disks, and bars, respectively. This process provided a detailed galaxy morphology, a precise measure of the bulge luminosity and its structural properties captured using the Sérsic function, luminosity and orientation of the disk (and all other components) extracted using special functions inbuilt in Profiler, and the total galaxy luminosity. The decomposition profiles for 44 ETGs that I worked on are provided in Appendix A , and profiles for the remaining 40 ETGs and 43 LTGs are available in Savorgnan & Graham (2016b) and Davis et al. (2019a), respectively. **Chapter 2** also elaborates on the crucial choice of the mass-to-light ratio (e.g., Meidt et al., 2014, for 3.6 μm-band) used to obtain the stellar mass from the corrected luminosity, and the error analysis to estimate realistic errors associated with the spheroid and total galaxy stellar masses.

In **Chapter 2**, we revealed a mass discrepancy, upon comparison between our 3.6 μm-based masses with the stellar masses based on K-band (2MASS), i-band (SDSS), and r-band (SDSS) luminosities taken from the NASA/IPAC Extragalaxtic Database (NED), and mass-to-light ratios for the corresponding bands from Bell & de Jong (2001), Taylor et al. (2011), and Roediger & Courteau (2015), respectively, all based on the Chabrier (2003) initial mass function of stars. This led us to introduce a mass correction coefficient (υ, Davis et al., 2019a) in our BH scaling relations to account for the mass discrepancy (i.e., to bring them into an agreement with our masses) while estimating BH mass using a (bulge or galaxy) stellar mass based on a different colour and mass-to-light ratio prescription. This test study was small and incomplete; however, it alarms us to be mindful of mass discrepancy when using mass estimates from different studies. In future, one can update and expand the comparison performed in **Chapter 2** to multiple wavelengths and mass-to-light ratio prescriptions to produce an extended correction coefficient (υ) table.

Importantly, **Chapter 2** presents the investigation of $M_{\rm BH}$–$M_{*,\rm sph}$ diagram, focussing on determining whether there is a break in this relation on dividing our sample into core-Sérsic versus Sérsic galaxies, galaxies with and without a bar, galaxies with and without a disk (i.e., fast versus slow rotating galaxies), and ETGs versus LTGs. Starting with ETGs, we find that there is a tight but non-linear (to be specific a super-linear[2]) $M_{\rm BH}$–$M_{*,\rm sph}$ relation. However, this single regression relation for ETGs is superficial, because further investigation reveals a substructure due to ETGs with a disk (ES, S0) and ETGs without a disk (E), such that the two categories follow almost parallel $M_{\rm BH}$–$M_{*,\rm sph}$ relations, but offset by more than an order of magnitude (1.12 dex) in the $M_{\rm BH}$-direction. This offset is due to smaller spheroids of ES/S0-type galaxies relative to that of almost pure spheroidal E-type galaxies, hosting a similar $M_{\rm BH}$. A detailed investigation to understand this offset

[2]Here, super-linear relation refers to a power-law slope between one and two.

is performed in **Chapters 4** and **5**, and its origin is now well understood. Interestingly, this offset has also been seen in a recent simulation by Marshall et al. (2020).

Adding the LTGs (spiral galaxies) from Davis et al. (2019a) to the $M_{\rm BH}$–$M_{*,\rm sph}$ diagram revealed that LTGs define a super-quadratic[3] relation with a slope slightly steeper but essentially consistent within $\pm 1\sigma$ error-bars of the slope followed by ES/S0-type and E-type galaxies. Thus, overall, there are three substructures in the $M_{\rm BH}$–$M_{*,\rm sph}$ diagram due to ETGs without a disk (E), ETGs with a disk (ES/S0), and spiral galaxies (S), which define almost parallel relations with different intercepts. Another important revelation of **Chapter 2** is the existence of a tight $M_{\rm BH}$–$M_{*,\rm gal}$ relation, dependent on galaxy morphology such that LTGs and (all) ETGs define distinct trends. In this diagram, the offset between the ETG sub-populations is minimized, because the addition of remaining galaxy mass to $M_{*,\rm sph}$ of ES/S0-type galaxies (horizontally) shifts them closer to the E-type galaxies (for whom $M_{*,\rm gal} \approx M_{*,\rm sph}$), suggesting a single $M_{\rm BH}$–$M_{*,\rm gal}$ relation for all ETGs.

By 2019, the sample of galaxies with directly-measured $M_{\rm BH}$ using primary methods, mentioned in the **Introduction**, reached 145. The $M_{\rm BH}$–central stellar velocity dispersion (σ) presented in **Chapter 3** was investigated using 143 galaxies for whom σ values were available in literature. We discovered a clear upturn in the $M_{\rm BH}$–σ relation at the high-$M_{\rm BH}$ end, such that the (massive) core-Sérsic galaxies (with a deficit of light at centres) defined a tight and much steeper $M_{\rm BH}$–σ relation than the Sérsic galaxies. We suspected that these different $M_{\rm BH}$–σ trends for core-Sérsic and Sérsic galaxies are because of the evolutionary tracks they followed (e.g., some scenarios mentioned in Ciotti & van Albada, 2001; Burkert & Silk, 2001). The core-Sérsic galaxies evolve through gas-poor (dissipationless) major-mergers, during which their central black holes add up without significantly raising the stellar velocity dispersions, ultimately resulting in a steeper $M_{\rm BH}$–σ relation, as seen here. Whereas, the Sérsic galaxies, which generally evolve through the gas-rich process, e.g., gas-abundant accretion or gas-rich minor mergers, increase their central velocity dispersions considerably along with the increase in their $M_{\rm BH}$, resulting in a shallower $M_{\rm BH}$–σ relation than that of core-Sérsic galaxies. This upturn, which promotes the presence of ultra massive black holes ($M_{\rm BH} > 10^{10}\, M_{\odot}$), has been attested in a recent

[3] A power-law slope between two and three.

study by Dullo et al. (2020a). It is worthy of note that an upturn in the $M_{\rm BH}$–σ diagram for most massive spheroids was also anticipated in some theoretical studies and simulations (e.g., King, 2010; Volonteri & Ciotti, 2013) and it was also observed by Bogdán et al. (2018) for brightest cluster galaxies, most of which are cored galaxies built through dry major-mergers.

Chapter 3 also demonstrates our analysis for other possible morphological dependencies, e.g., ETGs versus LTGs, fast versus slow rotators, AGN hosts (mainly Seyferts, identified using the catalogue of Véron-Cetty & Véron, 2010) versus non-AGNs, and barred versus non-barred galaxies, where, barred galaxies are speculated to have an elevated σ (e.g., Graham & Scott, 2013; Hartmann et al., 2014). We did not find any significant substructure in the $M_{\rm BH}$–σ diagram due to these morphological classes. Further investigation suggested that Graham & Scott (2013) observed an offset between barred and non-barred galaxies because of the wrong bar-classification of eight galaxies, as their opted morphological classifications failed to identify the bar component in these galaxies.

Importantly, we revealed a bent (galaxy luminosity: $L_{3.6\mu m}$)–σ relation for ETG using our primary 3.6 μm sample, and also updated the bent V-band $\mathrm{Ł}_{\rm V}$–σ relation using the modified data-set of Lauer et al. (2007). Here, the bend is also because of core-Sérsic and Sérsic galaxies, which define the steeper and shallower arm of the L–σ relation, respectively. The bent L–σ relation is consistent with the previous bent/curved relations based on B- and R-band luminosities (e.g., Matković & Guzmán, 2005; de Rijcke et al., 2005; Graham & Soria, 2018). However, with our ($M_{\rm BH} > 10^{\sim 6}\, M_{\odot}$) limited sample, we could not see the nature of these relations at lower masses. In addition to ETGs, we also showed the behaviour of spiral galaxies in the L–σ diagram. These $M_{*,\rm gal}$–σ (and also $M_{*,\rm sph}$–σ) relations were further mated with the M_{BH}–σ relations to test the consistency with previously revealed M_{BH}–$M_{*,gal}$ (and also M_{BH}–$M_{*,\rm sph}$) relations.

With our bent σ–$M_{*,\rm gal}$ relation, we partially addressed a selection bias claimed in Shankar et al. (2016), based on an offset observed between ETGs with dynamically measured $M_{\rm BH}$ and a sample of ETGs without dynamically measured $M_{\rm BH}$ (from SDSS) in the σ–$M_{*,\rm gal}$ diagram. Shankar et al. (2016) suggested that a selection bias arises in the BH relations due to current limitations to resolve the gravitational sphere-of-influence of the BHs in other distant galaxies. While it is reasonable that the resolution limit can cause a sample selection bias in the observed BH correlations, we found that our bent σ–$M_{*,\mathrm{gal}}$ relation matched well with their σ–M_{star} curve traced by the SDSS ETG sample they used and reduced the offset significantly. Additionally, we estimated a $\sim 10\%$ contamination of LTGs in their ETG-sample, which may have caused the higher offset/gap at lower $M_{*,\mathrm{gal}}$ ($\sim 10^{10} M_{\odot}$).

Continuing our endeavour to discover the most fundamental relation, in **Chapters 4** and **5**, we extended our study of M_{BH}-spheroid connections to spheroid structural properties and mass distribution. **Chapter 4** revealed that ETGs and LTGs define two slightly different trends between M_{BH} and the central light concentration, i.e., n_{sph} (and the concentration index). This is consistent with the predicted relations on combining our M_{BH}–$M_{*,\mathrm{sph}}$ relations with the $M_{*,\mathrm{sph}}$–n_{sph} relations for ETGs and LTGs. In the M_{BH}–$R_{\mathrm{e,sph}}$ diagram as well, ETGs and LTGs define two different relations, where further an offset is seen between ETGs with a disk (ES/S0) and ETGs without a disk (E), analogous to the substructures in the M_{BH}–$M_{*,\mathrm{sph}}$ diagram. These relations as well are consistent with the predicted relations on combining the M_{BH}–$M_{*,\mathrm{sph}}$ relations with the tight $M_{*,\mathrm{sph}}$–$R_{\mathrm{e,sph}}$ relation observed here. Graham (2019b) showed that the extended galaxy mass-effective size relation is curved. We could not observe a curve in the $M_{*,\mathrm{sph}}$–$R_{\mathrm{e,sph}}$ relation, as our sample does not include low-mass or dwarf galaxies; however, the high-mass end of our $M_{*,\mathrm{sph}}$–$R_{\mathrm{e,sph}}$ relation, occupied by mainly elliptical galaxies, agrees well with the high-mass (shallow, almost linear) part of the (galaxy mass)-(galaxy size) curve for ETGs in Graham (2019b).

Chapter 5 presented our investigation on the correlation between M_{BH} and the spheroid projected luminosity density using the Spitzer sample and the internal stellar mass density using the total sample. Where the internal density, being the true measure of spheroid density at/within any radius rather than the projected density, is speculated to have a better correlation with M_{BH} than the projected density Graham & Driver (2007a). Additionally, all the M_{BH}–μ_{sph} correlations based on the 3.6 μm luminosity are mapped to the M_{BH}–(projected stellar mass density, Σ) diagram to include our remaining non-Spitzer sample as well.

The spheroid projected luminosity density profile is the Sérsic surface brightness model used to extract the bulge luminosity during the galaxy light decomposition process. The spheroid internal (or spatial) densities for galactic bulges were determined using an inverse Abel transformation of their (projected) bulge surface brightness profiles, described in **Appendix D**. This chapter revealed a correlation between $M_{\rm BH}$ and the central projected density[4], $\mu_{0,\rm sph}$, suggesting a brighter centre for bulges with more massive BHs consistent with the prediction in Graham & Driver (2007a). In the correlation between $M_{\rm BH}$ and the projected density μ_e at $\rm R_{e,sph}$ (and $M_{\rm BH}$–$\langle\mu\rangle_{\rm e,sph}$) we recover the three morphology-dependent substructures due to E-type, ES/S0-type, and LTGs, analogous to the $M_{\rm BH}$–$M_{*,\rm sph}$ and $M_{\rm BH}$–$\rm R_{e,sph}$ diagrams. However, due to a high scatter in the $M_{\rm BH}$–$\mu_{\rm e,sph}$ (and $\langle\mu\rangle_{\rm e,sph}$) diagram, we could not obtain a well-constrained measure of the offset.

As the $M_{*,\rm sph}$ is calculated using the Sérsic profile parametrized by $\rm n_{sph}$, $\rm R_{e,sph}$, and μ_e, the morphological substructures originated in the $M_{\rm BH}$–$n_{\rm sph}$ (ETG, LTG), $M_{\rm BH}$–$\rm R_{e,sph}$ (E, ES/S0, LTG), and $M_{\rm BH}$–$\mu_{\rm e,sph}$ (E, ES/S0, LTG) diagrams collectively propagate to the $M_{\rm BH}$–$M_{*,\rm sph}$ diagram. Particularly, the offset between ETG subsamples originates from the $M_{\rm BH}$–$R_{\rm e,sph}$ and $M_{\rm BH}$–$\mu_{\rm e,sph}$ diagrams, where $R_{\rm e,sph}$ and $\mu_{\rm e,sph}$ are obviously coupled. Essentially, this offset is because of smaller bulges of ES/S0-type galaxies relative to that of E-type galaxies, and it is reflected in the (vertical) $M_{\rm BH}$-direction due to non-zero slopes of these relations. Similarly, as the estimation of the internal stellar mass density, $\rho_{\rm e,sph}$, at $R_{\rm e,sph}$ is also dependent on the above three Sérsic parameters, we re-discover the substructures due to E-types, ES/S0-type, and LTGs in the $M_{\rm BH}$–ρ_e diagram as well. Where, the $M_{\rm BH}$–ρ_e relations are tighter than the $M_{\rm BH}$–$\mu_{\rm e,sph}$ relations, as expected.

Additionally, we reveal a strong correlation between $M_{\rm BH}$ and spheroid compactness parameter ($\langle\Sigma\rangle_{\rm 1kpc}$, the projected density within the inner one kpc radius of a spheroid) tighter than the $M_{\rm BH}$–(Σ_0 and $\Sigma_{\rm e}$) correlations, as suggested in (Ni et al., 2019, 2020; Hopkins et al., 2021). However, we also find that the $M_{\rm BH}$–$\langle\Sigma\rangle_{\rm R}$ relation becomes tighter with increasing R[5], saturating at about 5 kpc. This investigation is extended to the $M_{\rm BH}$–$\langle\rho\rangle_{\rm r}$ diagram, which revealed an analogous behaviour. Thus, instead of $\langle\Sigma\rangle_{\rm 1kpc}$ (or $\langle\rho\rangle_{\rm 1kpc}$), $\langle\Sigma\rangle_{\rm 5kpc}$ (or $\langle\rho\rangle_{\rm 5kpc}$) can provide an even better prediction of the $M_{\rm BH}$.

[4]The spheroid central projected density was obtained through inward extrapolation of the Sérsic surface brightness profile for both Sérsic and core-Sérsic galaxies. Thus, for core-Sérsic galaxies, the value of $\mu_{0,\rm sph}$ used here represents their surface brightness before core-scouring by the binary BHs.

[5]It is also noted that the fixed projected radius, R (or spatial radius, r), represent different physical scales for different sizes of spheroids. Thus, the quantities $\langle\Sigma\rangle_{\rm R}$ or $\langle\rho\rangle_{\rm r}$ may not hold any particular physical significance.

Importantly, **Chapter 5** revealed the correlation between $M_{\rm BH}$ and the internal density at/within the sphere-of-influence (soi) of BHs ($\rho_{\rm soi}$ and $\langle\rho\rangle_{\rm soi}$). Here the core-Sérsic galaxies and Sérsic galaxies seem to follow different $M_{\rm BH}$–$\rho_{\rm soi}$ (and $\langle\rho\rangle_{\rm soi}$) trends, such that the relation for cored galaxies has the least total scatter (~ 0.2 dex) among all other BH scaling relations. These $M_{\rm BH}$–$\rho_{\rm soi}$ relations can be of direct assistance in estimating the tidal disruption event rates, binary black hole merger time scale, the orbital frequency of gravitational wave emission phase, and the characteristic strain of the long-wavelength gravitational waves generated by massive black hole mergers. Additionally, our further investigation suggests that the apparent substructure in the $M_{\rm BH}$–$\rho_{\rm soi}$ diagram due to core-Sérsic and Sérsic categories may be a reflection of their high and intermediate spheroid Sérsic indices. Thus, our current picture of the $M_{\rm BH}$–$\rho_{\rm soi}$ relation is not complete; this relation may be a part of a black hole plane with the Sérsic index, n, as the third parameter.

To conclude, the major outcomes of this thesis are as follows:

- **Two-dimensional modelling and multicomponent decomposition** of 44 early-type galaxies. This process provided precise estimates of the structural properties and mass of the galactic components, including the bulge and for the whole galaxy.

- Raises the issue of **mass discrepancy**, even on using mass-to-light ratios based on the same initial mass function of stars. This mass discrepancy, and further, inaccurate black hole mass estimation, can be avoided using a **mass correction coefficient** υ.

- **The black hole mass versus spheroid stellar mass relation** is non-linear (on a log-log scale) and dependent on galaxy morphology. Here, ETGs without a disk (E), ETGs with a disk (ES/S0), and spiral galaxies (S, LTGs) define different trends, with almost similar power-law slopes (~ 2) but different intercepts.

- There exists a correlation between **black hole mass and the total galaxy stellar mass**, as tight as the black hole mass versus spheroid stellar mass relation. The black hole mass–galaxy stellar mass relations are also non-linear and dependent on galaxy morphology, where the LTGs follow a much steeper relation with a power-law slope twice that of ETGs.

- There is a **division in the black hole mass versus host stellar velocity dispersion** relation, such that the (massive, dry-merger driven) core-Sérsic galaxies and (relatively low-mass, gas-rich accretion/merger driven) Sérsic galaxies define the steep and shallow part of the $M_{\rm BH}$–σ relation, at the high- and relatively low-mass ends, respectively.

- A **break in the luminosity versus stellar velocity dispersion** relation for ETGs, famously known as the Faber-Jackson relation, is recovered using near infrared (3.6μm) luminosity for the first time. Here again, the break is due to core-Sérsic (all of which are ETGs) and Sérsic ETGs galaxies following a steep and shallow power-law, respectively. Additionally, the LTGs follow an even shallower trend in the L–σ diagram.

- Our bent velocity dispersion-galaxy stellar mass relation **reduces the bias** observed by Shankar et al. (2016) in the σ–$M_{*,\rm gal}$ diagram for ETGs. We find hints that the remaining (reduced) offset may potentially be because of 10% contamination of LTGs in the ETG sample of Shankar et al. (2016). A conclusive investigation will be presented in future work.

- There is a **correlation between black hole mass and the spheroid structural parameters** $n_{\rm sph}$, $R_{\rm e,sph}$, and $\mu_{\rm e,sph}$. All three diagrams have morphology-dependent substructures. The $M_{\rm BH}$–n diagram has different relations for ETGs and LTGs; the $M_{\rm BH}$–$R_{\rm e,sph}$ and $M_{\rm BH}$–$\mu_{\rm e,sph}$ diagrams have three substructures due to ETGs without a disk, ETGs with a disk, and spiral galaxies.

- There is a positive relation between **black hole mass and the spheroid central projected density** qualitatively consistent with the prediction in Graham & Driver (2007a).

- **Black hole mass correlates with the spheroid internal density at the sphere-of-influence of the black hole** ($\rho_{\rm soi}$), such that there are substructures dependent on the spheroid shape parameter (n), which may be the third parameter of the $M_{\rm BH}$–$\rho_{\rm soi}$–n plane. This black hole plane will be investigated in future work.

- **Black hole mass versus spheroid internal density at/within the half-light radius**, i.e., $M_{\rm BH}$–$\rho_{\rm e}$ (and $\langle\rho\rangle_{\rm e}$) diagrams also have morphology-dependent substructures due to ETGs without a disk, ETGs with a disk, and spiral galaxies, analogous to the $M_{\rm BH}$–$M_{*,\rm sph}$ diagram.

The prevalence of (consistent) morphology-dependent substructures in the correlation between $M_{\rm BH}$ and various host galaxy properties suggests that these relations hold the information about a galaxy's formation and evolution, which shapes its apparent morphology. This link between $M_{\rm BH}$ and host morphology indicates that there is a co-evolution between a black hole and the host galaxy, aware of their evolutionary track. The discovery of morphology-dependent substructures in the BH scaling diagrams is a significant development in understanding the black hole–host galaxy correlations. However, these divisions also complicate the search for a single fundamental relation based on the least intrinsic (or total rms) scatter in a relation (see **Chapter 5**). This is because we observed that different galaxy types have minimal scatter in different diagrams. In the future, extended galaxy samples with directly measured black hole masses and high-resolution galaxy images (and consequently, reduced measurement errors in the host galaxy properties) can help clarify if there is indeed a single fundamental line or perhaps a plane.

6.2 Applications and future scope

Our black hole scaling relations provide various alternatives to predict $M_{\rm BH}$ in other galaxies using various host galaxy/spheroid properties. The morphology-dependent $M_{\rm BH}$–$M_{*,\rm sph}$ or $M_{\rm BH}$–σ relations can provide a precise prediction of $M_{\rm BH}$, if $M_{*,\rm sph}$ or σ of the host galaxy is known along with the detailed morphology. However, the $M_{\rm BH}$–$n_{\rm sph}$, $M_{\rm BH}$–$R_{\rm e,sph}$, and $M_{\rm BH}$–$\mu_{\rm e,sph}$ (or $\mu_{0,\rm sph}$) relations are easier to apply, because obtaining $n_{\rm sph}$, $R_{\rm e,sph}$, or $\mu_{\rm e,sph}$ of a galactic spheroid is more straightforward than measuring its mass, or stellar velocity dispersion. Parameters n and $\rm R_e$ can be measured even from the bulge profile obtained after the decomposition of a photometrically un-calibrated galaxy image. Whereas measuring the $M_{*,\rm sph}$ requires decomposition of a flux-calibrated image, distance to the galaxy, luminosity corrections, and an appropriate mass-to-light ratio. Similarly, σ requires reducing and analyzing the telescope-time-expensive stellar spectra of the galaxy.

The $M_{\rm BH}$–Σ ($\Sigma_{\rm 1kpc}$ or $\Sigma_{\rm 5kpc}$) and $M_{\rm BH}$–ρ (e.g., $\rho_{\rm soi}$, $\rho_{\rm 1kpc}$, $\rho_{\rm 5kpc}$, $\rho_{\rm e}$) relations are also substitute scaling relations for directly predicting $M_{\rm BH}$, if the host projected or internal density is known. Importantly, our $M_{\rm BH}$–$M_{*,\rm gal}$ relations provide a straightforward way to estimate $M_{\rm BH}$ in other galaxies without going through the rigorous multi-component decomposition process to extract bulge properties.

The morphology-dependent scaling relations revealed in this thesis offer ramifications for the virial factor required in the reverberation mapping method, morphology-dependent black hole mass functions, and better constraints for detecting gravitational waves from massive black hole mergers, as proposed below.

Morphology-aware virial factor for reverberation mapping

The limited spatial resolution of current telescopes restricts the direct dynamical measurements of black hole mass in distant galaxies as their black hole influence regions can not be resolved. In such a situation, reverberation mapping (RM) is a rising indirect $M_{\rm BH}$ measurement method for distant/low-mass AGNs with broad-line regions (BLRs), which utilizes the time resolution instead of spatial resolution. With angular sizes of micro-arcseconds, the BLR regions can be easily constrained using the currently achievable temporal resolution (Bentz & Katz, 2015). RM uses the time difference between the continuum emission from AGN and the reverberated emission from the gas cloud in the BLR region surrounding the AGN to measure the corresponding radial distance (r) of the BLR cloud, given the constant speed of light. As the motion of BLR clouds is under the influence of the BH's gravitational potential, it can be used to constrain the central BH mass assuming a virialized system such that $M_{\rm BH} = f(\Delta \rm v^2 r/G)$. Wherein, the quantity $(\Delta \rm v^2 r/G)$ is known as the virial product (VP), and the line velocity width (Δv) is calculated from the Doppler broadening of the BLR emission line.

Here the virial factor, f, accounts for the geometry/orientation of the BLR region and converts the observed velocity broadening into the Keplerian velocity of the BLR cloud (Peterson & Wandel, 2000). The exact value of the virial factor is difficult to measure. However, this factor can be estimated by calibrating a data-set of AGNs with known VP and a host galaxy property (stellar mass or stellar velocity dispersion) with the directly observed black hole-galaxy correlations. Several different values of this factor have been used in literature, which are mainly dependent on different versions of the M_{BH}–σ relation as it evolved over the last two decades (e.g., see Graham & Others, 2011; Park et al., 2012; Woo et al., 2013a).

Given that the virial factor depends on the geometry/orientation of the BLR region, it is reasonable that it may be connected with galaxy morphology, and its value should be morphology-aware. These morphology-aware virial factors can be estimated using our latest morphology-dependent scaling relations established based on, hitherto, the largest sample of galaxies with directly-measured black hole masses. For example: using the M_{BH}–$M_{*,\mathrm{gal}}$ relation for ETGs and LTGs, we can obtain separate virial factors for ETGs and LTGs; the M_{BH}–σ relation can provide separate virial factors for massive quiescent core-Sérsic and relatively active Sérsic galaxies; or to add more details, the M_{BH}–$M_{*,\mathrm{sph}}$ (or M_{BH}–$R_{\mathrm{e,sph}}$) relations can be used to calculate virial factors for pure spheroidal E-type galaxies, ES/S0-type galaxies, and spiral S-type galaxies.

Pursuit of gravitational waves

Merging supermassive black holes are the prominent source of long-wavelength (mHz to nHz) gravitational waves being searched for by pulsar timing arrays (PTAs, μHz - nHz) and also fall in the detection domain of the upcoming Laser Interferometer Space Antenna (LISA, 0.1 Hz to 0.1 mHz, Amaro-Seoane et al., 2017). The stochastic gravitational-wave background (GWB) or even deterministic low-frequency GWs are not detected yet given the challenge to disentangle this signal from other noises in PTA data (Goncharov et al., 2021). Using our modified morphology-dependent black hole scaling relations, we can improve the GWB strain model to look for these long-wavelength GWs in the PTA and LISA data. An example can be seen in Mapelli & Others (2012), where the use of the quadratic relation instead of a linear M_{BH}–$M_{*,\mathrm{sph}}$ relation changes the predicted event rates by an order of magnitude. The GWB strain is modelled by integrating the individual characteristic strains over the SMBH Binary (SMBHB) population. Here, the characteristic strain (h_c) is the amplitude of the perturbation in space-time caused by the GW per unit logarithmic frequency interval. To pinpoint the modifications, let us consider the GWB strain model from Chen et al. (2017):

$$h_c^2(f) = \int dz \int d\mathcal{M} \, \frac{d^2n}{dzd\mathcal{M}} \, h_{c,r}^2 \left(f \frac{f_{p,0}}{f_{p,t}} \right) \left(\frac{f_{p,t}}{f_{p,0}} \right)^{-4/3} \left(\frac{\mathcal{M}}{\mathcal{M}_0} \right)^{5/3} \left(\frac{1+z}{1+z_0} \right)^{-1/3} \tag{6.1}$$

where, $\frac{d^2n}{dzd\mathcal{M}}$ is the SMBH binary merger rate which infers the co-moving differential number density of merging SMBHBs (i.e., the number of merging SMBHBs per Mpc^3) per unit red-shift (z) and unit chirp mass $\mathcal{M}$ $(= (m_1 m_2)^{3/5}/(m_1+m_2)^{1/5})$. Further, $h_{c,r}$ is the characteristic strain of a reference binary with chirp mass $\mathcal{M}_0$, red-shift z_0, eccentricity e_0, and the peak frequency of the spectrum $f_{p,0}$. During a galaxy merger, the dynamic friction pushes their SMBHs towards the core of the remnant galaxy, forming a binary at parsec scales, which interacts with the surrounding stars and enters a binary hardening phase, when their binding energy becomes higher than the average kinetic energy of the surrounding stars. The SMBHB further transitions from the hardening phase to the GW emission phase, which drives the merger. The orbital frequency of this transition, known as the transition frequency (f_t), is given by,

$$f_t = 0.356\mathrm{nHz} \left(\frac{1}{\mathrm{F(e)}} \frac{\rho_{\mathrm{i},100}}{\sigma_{200}} \zeta_0 \right)^{3/10} \left(\frac{\mathcal{M}}{10^9 \mathrm{M}_\odot} \right)^{-2/5} \tag{6.2}$$

where, F(e) is a univariate function of eccentricity, $\sigma_{200} = \sigma/(200\,\mathrm{km\,s^{-1}})$ is the central stellar velocity dispersion of the galaxy, $\rho_{\mathrm{i},100} = \rho_{\mathrm{i}}/(100\,\mathrm{M_\odot\,pc^{-3}})$ is the internal stellar density at the radius of sphere-of-influence of the BH, and the correction factor ζ_0 accounts for the possible systematic uncertainties in ρ_i and σ.

The SMBHB merger rate ($\frac{d^2n}{dzd\mathcal{M}}$) is the main ingredient of the GWB strain model (Equation 6.1). This merger rate further depends on the galaxy stellar mass function (GSMF), galaxy pair fraction (GPF), SMBH merger time-scale, and the scaling relation between the black hole mass and host galaxy properties (Sesana, 2013). The black hole-galaxy relations convert the GSMF into a BH mass function (BHMF) and the GPF into BH pair fraction. The results of this thesis can provide the following modifications in the SMBH binary merger rate model.

Morphology-aware black hole mass function: Until now, many studies aiming to estimate the GW strain (e.g., Siemens et al., 2013; Shannon et al., 2015) have been using the single linear M_{BH}–$M_{*,\mathrm{sph}}$ relation along with the assumption of a constant bulge-to-total galaxy mass ($M_{*,\mathrm{sph}}/M_{*,\mathrm{gal}}$) ratio to convert the GSMF into a BHMF. Here, neither the M_{BH}–$M_{*,\mathrm{sph}}$ relation is simply linear, nor the $M_{*,\mathrm{sph}}/M_{*,\mathrm{gal}}$ ratio is constant, and these assumptions may be causing a significant systematic error in the merger rate model. Our direct M_{BH}–$M_{*,\mathrm{gal}}$ correlations can solve this problem; however, we need to take into account that ETGs and LTGs define two different M_{BH}–$M_{*,\mathrm{gal}}$ relations. Now, one can obtain the morphology-aware BHMF either by directly applying the M_{BH}–$M_{*,\mathrm{gal}}$ relations to the already available morphology-dependent GSMF (e.g., Vulcani et al., 2011; Hashemizadeh et al., 2021) or generate a new GSMF for ETGs and LTGs using an appropriate galaxy sample with known morphology (e.g., Casura et al., 2019).

SMBH merger time-scale: To keep the merger rate estimation simple, often the galaxy merger time-scale is used to approximate the SMBH merger time-scale (e.g., Chen et al., 2019). However, the SMBH merger time-scale is further delayed during the transition from the hardening to the GW emission phase, where most of SMBHB lifetime is spent at the transition phase (Sesana & Khan, 2015). If the density at the black hole influence radius and the stellar velocity dispersion are known, one can estimate this time-scale following the model in Sesana & Khan (2015) for a given binary eccentricity. For example, Biava et al. (2019) presented a model for the SMBHB merger time-scale, where they used the M_{BH}–$M_{*,\mathrm{sph}}$, $M_{*,\mathrm{sph}}$–$R_{\mathrm{e,sph}}$, and M_{BH}–n_{sph} relations from different studies to estimate Sérsic parameters of a remnant bulge hosting a SMBHB (assuming the SMBHB and the remnant bulge follows these relations), and applied the Prugniel & Simien (1997) density model to obtain the internal density at black hole influence radius ρ_i (or ρ_{soi}). However, given that we now have a direct M_{BH}–ρ_{soi} and M_{BH}–σ relation, one can directly obtain the ρ_{soi} and σ for a given SMBHB mass, and further have an estimate of the SMBH merger time-scale for a given eccentricity, following Sesana & Khan (2015, their equation 7).

Incorporate possible offset: Sesana et al. (2016) suggested a significant impact of the selection-biased black hole scaling relations, flagged in Shankar et al. (2016), on the predicted amplitude of GWs. As summarised in the previous section, we have partially addressed this bias in **Chapter 3**, where we found that our morphology-dependent BH scaling relations reduce the offset in the σ–$M_{*,\mathrm{gal}}$ diagram observed by Shankar et al. (2016). In a forthcoming paper, we will compare our black hole sample with some other samples (without dynamical BH mass measurements) to check upon this bias and further incorporate the results in the final strain model.

Each of the above steps has many potential applications for related extragalactic and cosmological studies. Collectively, all these factors will provide a significantly improved GWB strain model to put constraints on detectable GW amplitude and event rates for ground-based detection by PTAs and space-based detection by LISA and other future interferometers.

Future of black hole scaling relations

The latest morphology-dependent black hole-galaxy correlations along with the $M_{*,\mathrm{sph}}$-$R_{\mathrm{e,sph}}$, $M_{*,\mathrm{sph}}$–Sérsic index, and $M_{*,\mathrm{gal}}$–σ relations, can offer various tests for current simulations (e.g., Schaye et al., 2015; Mutlu-Pakdil et al., 2018; Hopkins et al., 2018; Davé et al., 2019; Li et al., 2020b) trying to generate realistic galaxies with a central BH and the theoretical studies investigating the inter-dependence of BH and spheroid (or galaxy) properties and BH feedback models (e.g., Ding et al., 2020).

BH scaling relations based on local galaxies (z $\sim$ 0) work as the local benchmark for studying the evolution of these relations to high redshifts. Some studies (e.g., Park et al., 2015; Sexton et al., 2019; Li et al., 2021) based on a sample active galaxies suggest that the M_{BH}–σ and M_{BH}–$M_{*,\mathrm{sph}}$ relations, up to at least z $\sim$ 0.6, are consistent with local BH scaling relation and, suggesting no evolution of these BH relations. However, they do not explore the morphology-dependence in BH scaling relations, which should be considered in future studies. Extending this study to even higher redshifts can further improve the models for the BH mass function, BH merger rates, and ultimately the gravitational wave strain models described above, which currently assume that the local scaling relation applies at high redshifts as well. A well-constrained virial factor to be used in the reverberation mapping of high-redshift AGNs will complement this study.

As also hinted in **Chapter 5** of this thesis, the possibility of a black hole fundamental plane should also be explored, as it may provide a better understanding and insight into the co-evolution of galaxies and their massive black holes. Moreover, possibly reduced scatter about a plane than a line will enable more accurate predictions of BH masses in other galaxies. Using a subset of the current sample of galaxies with directly measured BH masses, a few studies have already commenced exploring the black hole plane (e.g., Saglia et al., 2016; van den Bosch, 2016; de Nicola et al., 2019). Excluding the alleged pseudo-bulges Saglia et al. (2016) found a few BH planes (e.g., $M_{\rm BH}$–σ–ρ_e and $M_{\rm BH}$–σ–r_e planes) with scatter comparable to their $M_{\rm BH}$–σ relation. However, later two studies did not find a BH plane stronger than the $M_{\rm BH}$–σ relation of the time. The study of BH planes aiming to uncover a fundamental BH plane needs to be expanded considering various galaxy properties in the investigation and, importantly, the dependence on galaxy morphology as strongly suggested by this thesis.

The black hole scaling diagrams, additionally, need to incorporate low-mass or dwarf galaxies and be complemented with new diagrams involving nuclear star clusters and globular clusters, which potentially host IMBHs ($M_{\rm BH} < 10^5 M_{\odot}$). These goals shall be achievable in coming years through high-resolution observations with upcoming telescopes such as the James Webb Space Telescope (JWST, Gardner et al., 2006; Kalirai, 2018), Multi-conjugate adaptive optics Assisted Visible Imager and Spectrograph (MAVIS, Ellis et al., 2020), Advanced Telescope for High-ENergy Astrophysics (ATHENA, Barcons et al., 2017), the next generation Very Large Array (ngVLA, Di Francesco et al., 2019), Extremely Large Telescope (ELT, Batcheldor & Koekemoer, 2009), and the Square Kilometre Array (SKA, Cembranos et al., 2020).

Bibliography

Abazajian, K. N., Adelman-McCarthy, J. K., Agüeros, M. A., et al. 2009, ApJS, 182, 543

Abbott, B. P., Abbott, R., Abbott, T. D., et al. 2016a, ApJ, 818, L22

Abbott, B. P., Abbott, R., Abbott, T. D., et al. 2016b, Phys. Rev. Lett., 116, 061102

Abbott, R., Abbott, T. D., Abraham, S., et al. 2020, Phys. Rev. Lett., 125, 101102

Abel, N. H. 1826, Journal für die reine und angewandte Mathematik, 1, 153

Adelman-McCarthy, J. K., Agüeros, M. A., Allam, S. S., et al. 2008, The Astrophysical Journal Supplement Series, 175, 297

Aihara, H., Allende Prieto, C., An, D., et al. 2011, The Astrophysical Journal Supplement Series, 193, 29

Aitken, R. G. 1906, PASP, 18, 111

Akritas, M. G., & Bershady, M. A. 1996, ApJ, 470, 706

Almoznino, E., Loinger, F., & Brosch, N. 1993, MNRAS, 265, 641

Amaro-Seoane, P., Audley, H., Babak, S., et al. 2017, arXiv e-prints, arXiv:1702.00786

Anderson, W. 1929, Zeitschrift fur Physik, 56, 851

Anderssen, R. S., & de Hoog, F. R. 1990, in Numerical Solution of Integral Equations, ed. M. A. Golberg (Boston, MA: Springer US), 373–410

Andredakis, Y. C., Peletier, R. F., & Balcells, M. 1995, MNRAS, 275, 874

Anglés-Alcázar, D., Faucher-Giguère, C.-A., Quataert, E., et al. 2017, MNRAS, 472, L109

Arca-Sedda, M., & Capuzzo-Dolcetta, R. 2014, ApJ, 785, 51

Arzoumanian, Z., Baker, P. T., Brazier, A., et al. 2018, ApJ, 859, 47

Athanassoula, E. 2002, ApJ, 569, L83

Athanassoula, E. 2005, MNRAS, 358, 1477

Athanassoula, E., Laurikainen, E., Salo, H., & Bosma, A. 2015, MNRAS, 454, 3843

Baade, W., & Minkowski, R. 1954, ApJ, 119, 206

Baade, W., & Zwicky, F. 1934, Proceedings of the National Academy of Science, 20, 259

Baes, M., Buyle, P., Hau, G. K. T., & Dejonghe, H. 2003, MNRAS, 341, L44

Baker, J., Barke, S. F., Bender, P. L., et al. 2019, arXiv e-prints, arXiv:1907.11305

Baldassare, V. F., Reines, A. E., Gallo, E., & Greene, J. E. 2015, ApJ, 809, L14

Barack, L., Cardoso, V., Nissanke, S., et al. 2019, Classical and Quantum Gravity, 36, 143001

Barcons, X., Barret, D., Decourchelle, A., et al. 2017, Astronomische Nachrichten, 338, 153

Bardeen, J. M., & Wagoner, R. V. 1969, ApJ, 158, L65

Barro, G., Faber, S. M., Koo, D. C., et al. 2017, ApJ, 840, 47

Batcheldor, D. 2010, ApJ, 711, L108

Batcheldor, D., Axon, D., Valluri, M., Mandalou, J., & Merritt, D. 2013, AJ, 146, 67

Batcheldor, D., & Koekemoer, A. M. 2009, PASP, 121, 1245

Batcheldor, D., Robinson, A., Axon, D. J., Perlman, E. S., & Merritt, D. 2010, ApJ, 717, L6

Bateman, H., & Erdélyi, A. 1953, Higher transcendental functions, Calif. Inst. Technol. Bateman Manuscr. Project (New York, NY: McGraw-Hill)

Baumgardt, H. 2017, MNRAS, 464, 2174

Baumgardt, H., & Makino, J. 2004, Progress of Theoretical Physics Supplement, 155, 313

Baumgardt, H., Sollima, A., & Hilker, M. 2020, in Star Clusters: From the Milky Way to the Early Universe, ed. A. Bragaglia, M. Davies, A. Sills, & E. Vesperini, Vol. 351, 400–403

Baumgardt, H., He, C., Sweet, S. M., et al. 2019, MNRAS, 488, 5340

Bedregal, A. G., Aragón-Salamanca, A., & Merrifield, M. R. 2006, MNRAS, 373, 1125

Begelman, M. C. 1984, in IAU Symposium, Vol. 110, VLBI and Compact Radio Sources, ed. R. Fanti, K. I. Kellermann, & G. Setti, 227

Begelman, M. C., Blandford, R. D., & Rees, M. J. 1980, Nature, 287, 307

Begelman, M. C., & Nath, B. B. 2005, MNRAS, 361, 1387

Beifiori, A., Courteau, S., Corsini, E. M., & Zhu, Y. 2012, MNRAS, 419, 2497

Belczynski, K., Bulik, T., Fryer, C. L., et al. 2010, ApJ, 714, 1217

Bell, E. F., & de Jong, R. S. 2001, ApJ, 550, 212

Bellstedt, S., Graham, A. W., Forbes, D. A., et al. 2017, MNRAS, 470, 1321

Bennert, V. N., Auger, M. W., Treu, T., Woo, J.-H., & Malkan, M. A. 2011, ApJ, 742, 107

Bennert, V. N., Treu, T., Auger, M. W., et al. 2015, ApJ, 809, 20

Bentz, M. C., & Katz, S. 2015, PASP, 127, 67

Bentz, M. C., & Manne-Nicholas, E. 2018, ApJ, 864, 146

Berrier, J. C., Davis, B. L., Kennefick, D., et al. 2013, ApJ, 769, 132

Berrier, J. C., Davis, B. L., Kennefick, D., et al. 2013, ApJ, 769, 132

Bertin, E., & Arnouts, S. 1996, Astronomy and Astrophysics Supplement Series, 117, 393

Biava, N., Colpi, M., Capelo, P. R., et al. 2019, MNRAS, 487, 4985

Binney, J. 1982, ARA&A, 20, 399

Binney, J., & Tremaine, S. 1987, Galactic dynamics

Blandford, R. D. 1999, in Astronomical Society of the Pacific Conference Series, Vol. 182, Galaxy Dynamics - A Rutgers Symposium, ed. D. R. Merritt, M. Valluri, & J. A. Sellwood, 87

Blanton, M. R., Schlegel, D. J., Strauss, M. A., et al. 2005, AJ, 129, 2562

Blom, C., Forbes, D. A., Foster, C., Romanowsky, A. J., & Brodie, J. P. 2014, MNRAS, 439, 2420

Boehle, A., Ghez, A. M., Schödel, R., et al. 2016, ApJ, 830, 17

Boekholt, T. C. N., & Others. 2018, MNRAS, 476, 366

Bogdán, Á., Lovisari, L., Volonteri, M., & Dubois, Y. 2018, ApJ, 852, 131

Boizelle, B. D., Barth, A. J., Walsh, J. L., et al. 2019, ApJ, 881, 10

Bolton, J. G., Stanley, G. J., & Slee, O. B. 1949, Nature, 164, 101

Bonfini, P., González-Martín, O., Fritz, J., et al. 2018, MNRAS, 478, 1161

Bonoli, S., Mayer, L., & Callegari, S. 2014, MNRAS, 437, 1576

Brown, J. S., Valluri, M., Shen, J., & Debattista, V. P. 2013, ApJ, 778, 151

Burbidge, G. R., Burbidge, E. M., & Sandage, A. R. 1963, Reviews of Modern Physics, 35, 947

Burkert, A., & Silk, J. 2001, ApJ, 554, L151

Busarello, G., Longo, G., & Feoli, A. 1992, A&A, 262, 52

Buson, L. M., Bertola, F., Bressan, A., Burstein, D., & Cappellari, M. 2004, A&A, 423, 965

Buta, R. J., Sheth, K., Regan, M., et al. 2010, ApJS, 190, 147

Calvi, R., Vulcani, B., Poggianti, B. M., et al. 2018, MNRAS, 481, 3456

Caon, N., Capaccioli, M., & D'Onofrio, M. 1993, MNRAS, 265, 1013

Capaccioli, M. 1989, in World of Galaxies (Le Monde des Galaxies), ed. J. Corwin Harold G. & L. Bottinelli, 208–227

Capak, P. L., Teplitz, H. I., Brooke, T. Y., Laher, R., & Science Center, S. 2013, in American Astronomical Society Meeting Abstracts, Vol. 221, American Astronomical Society Meeting Abstracts #221, 340.06

Capetti, A., Marconi, A., Macchetto, D., & Axon, D. 2005, A&A, 431, 465

Cappellari, M. 2008, MNRAS, 390, 71

Cappellari, M., Bacon, R., Bureau, M., et al. 2006, MNRAS, 366, 1126

Cappellari, M., Emsellem, E., Krajnović, D., et al. 2011, MNRAS, 416, 1680

Carter, D. 1978, MNRAS, 182, 797

Carter, D., Bridges, T. J., & Hau, G. K. T. 1999, MNRAS, 307, 131

Carter, D., & Jenkins, C. R. 1993, MNRAS, 263, 1049

Casura, S., Liske, J., Robotham, A. S. G., Taranu, D. S., & Laine, J. 2019, in The Art of Measuring Galaxy Physical Properties, 26

Celoria, M., Oliveri, R., Sesana, A., & Mapelli, M. 2018, arXiv e-prints, arXiv:1807.11489

Celotti, A., Miller, J. C., & Sciama, D. W. 1999, CQG, 16, A3

Cembranos, J. A. R., de la Cruz-Dombriz, Á., Gammaldi, V., & Méndez-Isla, M. 2020, Physics of the Dark Universe, 27, 100448

Chabrier, G. 2003, PASA, 115, 763

Chandrasekhar, S. 1931, ApJ, 74, 81

Chandrasekhar, S. 1932, ZAp, 5, 321

Chandrasekhar, S. 1935, MNRAS, 95, 207

Chandrasekhar, S. 1943, ApJ, 97, 255

Chen, S., Sesana, A., & Conselice, C. J. 2019, MNRAS, 488, 401

Chen, S., Sesana, A., & Del Pozzo, W. 2017, MNRAS, 470, 1738

Cheung, E., Faber, S. M., Koo, D. C., et al. 2012, ApJ, 760, 131

Chilingarian, I. V., Katkov, I. Y., Zolotukhin, I. Y., et al. 2018, ApJ, 863, 1

Choi, E., Somerville, R. S., Ostriker, J. P., Naab, T., & Hirschmann, M. 2018, ApJ, 866, 91

Ciambur, B. C. 2015, ApJ, 810, 120

Ciambur, B. C. 2016, PASA, 33, e062

Ciambur, B. C., Fragkoudi, F., Khoperskov, S., Di Matteo, P., & Combes, F. 2021, MNRAS, 503, 2203

Ciambur, B. C., & Graham, A. W. 2016, MNRAS, 459, 1276

Ciambur, B. C., Graham, A. W., & Bland-Hawthorn, J. 2017, MNRAS, 471, 3988

Ciotti, L. 1991, A&A, 249, 99

Ciotti, L., & Ostriker, J. P. 2001, ApJ, 551, 131

Ciotti, L., & van Albada, T. S. 2001, ApJ, 552, L13

Cirasuolo, M., Shankar, F., Granato, G. L., De Zotti, G., & Danese, L. 2005, ApJ, 629, 816

Clark, B. G., & Kellermann, K. I. 1968, The Astronomical Journal Supplement, 73, 170

Clausius, R. 1870, Annalen der Physik, 217, 124

Colbert, E. J. M., & Mushotzky, R. F. 1999, ApJ, 519, 89

Cole, S., Lacey, C. G., Baugh, C. M., & Frenk, C. S. 2000, MNRAS, 319, 168

Combes, F., Debbasch, F., Friedli, D., & Pfenniger, D. 1990, A&A, 233, 82

Combes, F., & Elmegreen, B. G. 1993, A&A, 271, 391

Combes, F., & Sanders, R. H. 1981, A&A, 96, 164

Combes, F., García-Burillo, S., Audibert, A., et al. 2019, A&A, 623, A79

Conroy, C., Gunn, J. E., & White, M. 2009, ApJ, 699, 486

Conselice, C. J. 2014, ARA&A, 52, 291

Courteau, S., Cappellari, M., de Jong, R. S., et al. 2014, Reviews of Modern Physics, 86, 47

Coziol, R., Andernach, H., Caretta, C. A., Alamo- Martínez, K. A., & Tago, E. 2009, AJ, 137, 4795

Cretton, N., de Zeeuw, P. T., van der Marel, R. P., & Rix, H.-W. 1999, ApJS, 124, 383

Cretton, N., & van den Bosch, F. C. 1999, ApJ, 514, 704

Croton, D. J., Springel, V., White, S. D. M., et al. 2006, MNRAS, 365, 11

Curtis, H. D. 1913, Lick Observatory Bulletin, 248, 43

Curtis, H. D. 1917, PASP, 29, 206

Curtis, H. D. 1918, Publications of Lick Observatory, 13, 9

Cutler, C., & Flanagan, É. E. 1994, Phys. Rev. D, 49, 2658

Dabringhausen, J., Hilker, M., & Kroupa, P. 2008, MNRAS, 386, 864

Dalla Bontà, E., Ferrarese, L., Corsini, E. M., et al. 2009, ApJ, 690, 537

Danzmann, K. 2017, in Society of Photo-Optical Instrumentation Engineers (SPIE) Conference Series, Vol. 10566, Proc. SPIE, 1056610

Davé, R., Anglés-Alcázar, D., Narayanan, D., et al. 2019, MNRAS, 486, 2827

Davies, R. L., Efstathiou, G., Fall, S. M., Illingworth, G., & Schechter, P. L. 1983, ApJ, 266, 41

Davis, B. L., & Graham, A. W. 2021, PASA, 38, e030

Davis, B. L., Graham, A. W., & Cameron, E. 2018a, ApJ, 869, 113

Davis, B. L., Graham, A. W., & Cameron, E. 2019a, arXiv e-prints, arXiv:1810.04887

Davis, B. L., Graham, A. W., & Combes, F. 2019b, ApJ, 877, 64

Davis, B. L., Graham, A. W., & Seigar, M. S. 2017, MNRAS, 471, 2187

Davis, B. L., Berrier, J. C., Johns, L., et al. 2014, ApJ, 789, 124

Davis, T. A., Bureau, M., Onishi, K., et al. 2018b, MNRAS, 473, 3818

Davis, T. A., Nguyen, D. D., Seth, A. C., et al. 2020, MNRAS, 496, 4061

de Francesco, G., Capetti, A., & Marconi, A. 2006, A&A, 460, 439

de Nicola, S., Marconi, A., & Longo, G. 2019, MNRAS, 490, 2130

de Rijcke, S., Michielsen, D., Dejonghe, H., Zeilinger, W. W., & Hau, G. K. T. 2005, A&A, 438, 491

de Vaucouleurs, G. 1959a, Handbuch der Physik, 53, 275

de Vaucouleurs, G. 1959b, Handbuch der Physik, 53, 311

de Vaucouleurs, G. 1969, Astrophysical Letters, 4, 17

de Vaucouleurs, G., de Vaucouleurs, A., Corwin Herold G., J., et al. 1991, Third Reference Catalogue of Bright Galaxies

Dekel, A., Lapiner, S., & Dubois, Y. 2019, arXiv e-prints, arXiv:1904.08431

den Brok, M., Seth, A. C., Barth, A. J., et al. 2015, ApJ, 809, 101

Di Francesco, J., Chalmers, D., Denman, N., et al. 2019, in Canadian Long Range Plan for Astronomy and Astrophysics White Papers, Vol. 2020, 32

Di Matteo, T., Colberg, J., Springel, V., Hernquist, L., & Sijacki, D. 2008, ApJ, 676, 33

Di Matteo, T., Springel, V., & Hernquist, L. 2005, Nature, 433, 604

Diamond-Stanic, A. M., & Rieke, G. H. 2012, ApJ, 746, 168

Ding, X., Treu, T., Silverman, J. D., et al. 2020, ApJ, 896, 159

Dolag, K. 2015, in IAU General Assembly, Vol. 29, 2250156

D'Onofrio, M., Zaggia, S. R., Longo, G., Caon, N., & Capaccioli, M. 1995, A&A, 296, 319

Dressler, A. 1989, in Active Galactic Nuclei, Vol. 134, 217

Dressler, A., & Richstone, D. O. 1988, ApJ, 324, 701

Driver, S. 2006, in The Fabulous Destiny of Galaxies: Bridging Past and Present, 409

Driver, S. P., Liske, J., & Graham, A. W. 2007, in Astronomical Society of the Pacific Conference Series, Vol. 374, From Stars to Galaxies: Building the Pieces to Build Up the Universe, ed. A. Vallenari, R. Tantalo, L. Portinari, & A. Moretti, 481

Driver, S. P., Norberg, P., Baldry, I. K., et al. 2009, Astronomy and Geophysics, 50, 5.12

Droste, J. 1917, Koninklijke Nederlandse Akademie van Wetenschappen Proceedings Series B Physical Sciences, 19, 197

Drouart, G., De Breuck, C., Vernet, J., et al. 2014, A&A, 566, A53

Dubois, Y., Devriendt, J., Slyz, A., & Teyssier, R. 2012, MNRAS, 420, 2662

Dullo, B. T. 2014, in Astronomical Society of the Pacific Conference Series, Vol. 480, Structure and Dynamics of Disk Galaxies, ed. M. S. Seigar & P. Treuthardt, 75

Dullo, B. T. 2019, ApJ, 886, 80

Dullo, B. T., Bouquin, A. Y. K., Gil De Paz, A., Knapen, J. H., & Gorgas, J. 2020a, arXiv e-prints, arXiv:2006.10128

Dullo, B. T., Gil de Paz, A., & Knapen, J. H. 2020b, arXiv e-prints, arXiv:2012.04471

Dullo, B. T., & Graham, A. W. 2012, ApJ, 755, 163

Dullo, B. T., & Graham, A. W. 2013, ApJ, 768, 36

Dullo, B. T., & Graham, A. W. 2014, MNRAS, 444, 2700

Eddington, A. S. 1924, Nature, 113, 192

Einstein, A. 1916, Sitzungsberichte der Königlich Preußischen Akademie der Wissenschaften (Berlin, 688

—. 1918, Sitzungsberichte der Königlich Preußischen Akademie der Wissenschaften (Berlin, 154

Elbert, O. D., Bullock, J. S., & Kaplinghat, M. 2018, MNRAS, 473, 1186

Ellis, S., McDermid, R., Cresci, G., et al. 2020, in Society of Photo-Optical Instrumentation Engineers (SPIE) Conference Series, Vol. 11447, Society of Photo-Optical Instrumentation Engineers (SPIE) Conference Series, 11447A0

Emsellem, E., & van de Ven, G. 2008, ApJ, 674, 653

Erwin, P., Thomas, J., Saglia, R. P., et al. 2018, MNRAS, 473, 2251

Erwin, P., Saglia, R. P., Fabricius, M., et al. 2015, MNRAS, 446, 4039

Escudero, C. G., Faifer, F. R., Bassino, L. P., Calderón, J. P., & Caso, J. P. 2015, MNRAS, 449, 612

Eskridge, P. B., Frogel, J. A., Pogge, R. W., et al. 2000, AJ, 119, 536

Event Horizon Telescope Collaboration, Akiyama, K., Alberdi, A., et al. 2019, ApJ, 875, L6

Faber, S. M., & Jackson, R. E. 1976, ApJ, 204, 668

Fabian, A. C. 1999, MNRAS, 308, L39

Fabian, A. C., & Canizares, C. R. 1988, Nature, 333, 829

Falcón-Barroso, J., Peletier, R. F., Emsellem, E., et al. 2004, MNRAS, 350, 35

Farouki, R. T., Shapiro, S. L., & Duncan, M. J. 1983, ApJ, 265, 597

Farrell, S. A., Webb, N. A., Barret, D., Godet, O., & Rodrigues, J. M. 2009, Nature, 460, 73

Fath, E. A. 1909, Popular Astronomy, 17, 504

Fazio, G. G., Hora, J. L., Allen, L. E., et al. 2004, ApJS, 154, 10

Fedorova, E., Vasylenko, A., Hnatyk, B. I., & Zhdanov, V. I. 2016, Astronomische Nachrichten, 337, 96

Feigelson, E. D., & Babu, G. J. 1992, ApJ, 397, 55

Feoli, A., & Mancini, L. 2011, International Journal of Modern Physics D, 20, 2305

Feoli, A., & Mele, D. 2005, International Journal of Modern Physics D, 14, 1861

Ferrarese, L. 2002, ApJ, 578, 90

Ferrarese, L., Cote, P., Blakeslee, J. P., et al. 2006a, arXiv e-prints, astro

Ferrarese, L., & Ford, H. 2005, Space Sci. Rev., 116, 523

Ferrarese, L., & Merritt, D. 2000, ApJ, 539, L9

Ferrarese, L., van den Bosch, F. C., Ford, H. C., Jaffe, W., & O'Connell, R. W. 1994, AJ, 108, 1598

Ferrarese, L., Côté, P., Jordán, A., et al. 2006b, ApJS, 164, 334

Ferrers, N. M. 1877, Quart. J. Pure Appl. Math., 14, 1

Finkelstein, D. 1958, Physical Review, 110, 965

Fisher, D. B., & Drory, N. 2010, ApJ, 716, 942

Fisher, D. B., & Drory, N. 2016, in Astrophysics and Space Science Library, Vol. 418, Galactic Bulges, ed. E. Laurikainen, R. Peletier, & D. Gadotti, 41

Fontanot, F., Monaco, P., Cristiani, S., & Tozzi, P. 2006, MNRAS, 373, 1173

Frank, J., & Rees, M. J. 1976, MNRAS, 176, 633

Frenkel, J. 1928, Zeitschrift fur Physik, 50, 234

Fukugita, M., & Peebles, P. J. E. 2004, ApJ, 616, 643

Gadotti, D. A., Seidel, M. K., Sánchez- Blázquez, P., et al. 2015, A&A, 584, A90

Gadotti, D. A. D. A., & Kauffmann, G. 2009, MNRAS, 399, 621

Gardner, J. P., Mather, J. C., Clampin, M., et al. 2006, Space Sci. Rev., 123, 485

Gebhardt, K., Bender, R., Bower, G., et al. 2000, ApJ, 539, L13

Gebhardt, K., Richstone, D., Tremaine, S., et al. 2003, ApJ, 583, 92

Genzel, R. 2021, arXiv e-prints, arXiv:2102.13000

Ginat, Y. B., Meiron, Y., & Soker, N. 2016, MNRAS, 461, 3533

Goncharov, B., Reardon, D. J., Shannon, R. M., et al. 2021, MNRAS, 502, 478

Gordon, J. P., Zeiger, H. J., & Townes, C. H. 1955, Physical Review, 99, 1264

Gould, A. 2013, ArXiv e-prints, arXiv:1303.0834

Graham, A. 2007a, in Bulletin of the American Astronomical Society, Vol. 39, American Astronomical Society Meeting Abstracts, 759

Graham, A., & Colless, M. 1997, MNRAS, 287, 221

Graham, A., Lauer, T. R., Colless, M., & Postman, M. 1996, ApJ, 465, 534

Graham, A. W. 2001, AJ, 121, 820

Graham, A. W. 2002, ApJ, 568, L13

Graham, A. W. 2004, ApJ, 613, L33

Graham, A. W. 2007b, MNRAS, 379, 711

Graham, A. W. 2008a, ApJ, 680, 143

Graham, A. W. 2008b, PASA, 25, 167

Graham, A. W. 2012, ApJ, 746, 113

Graham, A. W. 2013, in Planets, Stars and Stellar Systems Vol. 6, by Oswalt, Terry D.; Keel, William C., ISBN 978-94-007-5608-3. Springer Science+Business Media Dordrecht, 2013, p. 91, ed. T. D. Oswalt & W. C. Keel, Vol. 6 (Dordrecht: Springer Netherlands), 91

Graham, A. W. 2014, in Astronomical Society of the Pacific Conference Series, Vol. 480, Structure and Dynamics of Disk Galaxies, ed. M. S. Seigar & P. Treuthardt, 185

Graham, A. W. 2016, in Astrophysics and Space Science Library, Vol. 418, Galactic Bulges, ed. E. Laurikainen, R. Peletier, & D. Gadotti, 263

Graham, A. W. 2019a, MNRAS, 1547

Graham, A. W. 2019b, PASA, 36, e035

Graham, A. W., Ciambur, B. C., & Savorgnan, G. A. D. 2016a, ApJ, 831, 132

Graham, A. W., & Driver, S. P. 2005, Publications of the Astronomical Society of Australia, 22, 118

Graham, A. W., & Driver, S. P. 2007a, ApJ, 655, 77

Graham, A. W., & Driver, S. P. 2007b, MNRAS, 380, L15

Graham, A. W., Dullo, B. T., & Savorgnan, G. A. D. 2015, ApJ, 804, 32

Graham, A. W., Durré, M., Savorgnan, G. A. D., et al. 2016b, ApJ, 819, 43

Graham, A. W., Erwin, P., Caon, N., & Trujillo, I. 2001a, ApJ, 563, L11

Graham, A. W., Erwin, P., Caon, N., & Trujillo, I. 2003, in Revista Mexicana de Astronomia y Astrofisica Conference Series, Vol. 17, Revista Mexicana de Astronomia y Astrofisica Conference Series, ed. V. Avila-Reese, C. Firmani, C. S. Frenk, & C. Allen, 196–197

Graham, A. W., & Guzmán, R. 2003, AJ, 125, 2936

Graham, A. W., & Li, I.-h. 2009, ApJ, 698, 812

Graham, A. W., Merritt, D., Moore, B., Diemand, J., & Terzić, B. 2006, AJ, 132, 2711

Graham, A. W., & Others. 2003, AJ, 125, 2951

Graham, A. W., & Others. 2007, MNRAS, 378, 198

Graham, A. W., & Others. 2011, MNRAS, 412, 2211

Graham, A. W., & Scott, N. 2013, ApJ, 764, 151

Graham, A. W., & Scott, N. 2015, ApJ, 798, 54

Graham, A. W., & Soria, R. 2018, arXiv e-prints, arXiv:1812.01231

Graham, A. W., Soria, R., & Davis, B. L. 2018, ArXiv e-prints, arXiv:1811.03232

Graham, A. W., Trujillo, I., & Caon, N. 2001b, AJ, 122, 1707

Graham, A. W., & Worley, C. C. 2008, MNRAS, 388, 1708

Greene, J. E., & Ho, L. C. 2006, ApJ, 641, L21

Greene, J. E., Strader, J., & Ho, L. C. 2020, ARA&A, 58, 257

Greene, J. E., Peng, C. Y., Kim, M., et al. 2010, ApJ, 721, 26

Greene, J. E., Seth, A., Kim, M., et al. 2016, ApJ, 826, L32

Greenstein, J. L., & Matthews, T. A. 1963, AJ, 68, 279

Gültekin, K., Gebhardt, K., Kormendy, J., et al. 2014, ApJ, 781, 112

Gültekin, K., Richstone, D. O., Gebhardt, K., et al. 2009a, ApJ, 695, 1577

Gültekin, K., Richstone, D. O., Gebhardt, K., et al. 2009b, ApJ, 698, 198

Habouzit, M., Genel, S., Somerville, R. S., et al. 2019, MNRAS, 484, 4413

Hailey, C. J., & Others. 2018, Nature, 556, 70

Halliday, C. 1998, PhD thesis, -

Häring, N., & Rix, H.-W. 2004, ApJ, 604, L89

Hartmann, M. 2011, PhD thesis, University of Central Lancashire

Hartmann, M., Debattista, V. P., Cole, D. R., et al. 2014, MNRAS, 441, 1243

Hashemizadeh, A., Driver, S. P., Davies, L. J. M., et al. 2021, MNRAS, 505, 136

Hawking, S. W., & Penrose, R. 1970, Proceedings of the Royal Society of London Series A, 314, 529

Hazard, C., Mackey, M. B., & Shimmins, A. J. 1963, Nature, 197, 1037

Heckman, T. M., & Best, P. N. 2014, ARA&A, 52, 589

Held, E. V., de Zeeuw, T., Mould, J., & Picard, A. 1992, AJ, 103, 851

Held, E. V., & Mould, J. R. 1994, AJ, 107, 1307

Herschel, J. F. W. 1864, Philosophical Transactions of the Royal Society of London Series I, 154, 1

Herschel, W. 1786, Philosophical Transactions of the Royal Society of London Series I, 76, 457

Herschel, W. 1789, Philosophical Transactions of the Royal Society of London Series I, 79, 212

Herschel, W. 1802, Philosophical Transactions of the Royal Society of London Series I, 92, 477

Hewish, A., Bell, S. J., Pilkington, J. D. H., Scott, P. F., & Collins, R. A. 1968, Nature, 217, 709

Hills, J. G. 1975, Nature, 254, 295

Hilz, M., Naab, T., & Ostriker, J. P. 2013, MNRAS, 429, 2924

Hiner, K. D. 2012, PhD thesis, University of California, Riverside

Hirano, S., & Others. 2017, Science, 357, 1375

Ho, L. 1999, in Astrophysics and Space Science Library, Vol. 234, Observational Evidence for the Black Holes in the Universe, ed. S. K. Chakrabarti, 157

Hobbs, G., & Dai, S. 2017, arXiv e-prints, arXiv:1707.01615

Hohl, F. 1971, ApJ, 168, 343

Holley-Bockelmann, K. 2016, in AAS/High Energy Astrophysics Division, Vol. 15, AAS/High Energy Astrophysics Division #15, 301.04

Hopkins, P. F., Hernquist, L., Cox, T. J., et al. 2006, The Astrophysical Journal Supplement Series, 163, 1

Hopkins, P. F., Hernquist, L., Cox, T. J., Robertson, B., & Krause, E. 2007, ApJ, 669, 67

Hopkins, P. F., & Quataert, E. 2010, MNRAS, 407, 1529

Hopkins, P. F., Wellons, S., Angles-Alcazar, D., Faucher-Giguere, C.-A., & Grudic, M. Y. 2021, arXiv e-prints, arXiv:2103.10444

Hopkins, P. F., Wetzel, A., Kereš, D., et al. 2018, MNRAS, 480, 800

Hoyle, F., & Fowler, W. A. 1963, MNRAS, 125, 169

Hu, J. 2008, MNRAS, 386, 2242

Hubble, E. P. 1926, ApJ, 64, 321

Hubble, E. P. 1929, ApJ, 69, 103

Hubble, E. P. 1936, Realm of the Nebulae

Humason, M. L. 1932, PASP, 44, 267

Huré, J. M., Hersant, F., Surville, C., Nakai, N., & Jacq, T. 2011, A&A, 530, A145

Inayoshi, K., & Haiman, Z. 2016, ApJ, 828, 110

Israelian, G. 1997, BAAS, 29, 1466

Ivanenko, D. D., & Kurdgelaidze, D. F. 1965, Astrophysics, 1, 251

Jarrett, T. H., Chester, T., Cutri, R., Schneider, S. E., & Huchra, J. P. 2003, AJ, 125, 525

Jeans, J. H. 1902, Philosophical Transactions of the Royal Society of London Series A, 199, 1

Jeans, J. H. 1919a, Problems of cosmogony and stellar dynamics

—. 1919b, JRASC, 13, 215

—. 1928, Astronomy and cosmogony

Jedrzejewski, R. I. 1987a, MNRAS, 226, 747

Jedrzejewski, R. I. 1987b, in Structure and Dynamics of Elliptical Galaxies, ed. P. T. de Zeeuw, Vol. 127, 37–46

Jennison, R. C. 1958, MNRAS, 118, 276

Jerjen, H., Binggeli, B., & Freeman, K. C. 2000, AJ, 119, 593

Jiang, F., van Dokkum, P., Bezanson, R., & Franx, M. 2012, ApJ, 749, L10

Jiang, Y.-F., & Others. 2011, ApJ, 742, 68

Jonas, J. 2007, in From Planets to Dark Energy: the Modern Radio Universe, 7

Jorgensen, I., Franx, M., & Kjaergaard, P. 1995, MNRAS, 276, 1341

Kalirai, J. 2018, Contemporary Physics, 59, 251

Kannappan, S. J., & Gawiser, E. 2007, ApJ, 657, L5

Kawasaki, M., Kusenko, A., & Yanagida, T. T. 2012, Physics Letters B, 711, 1

Kelly, B. C. 2007, ApJ, 665, 1489

Kelly, B. C., & Merloni, A. 2012, Advances in Astronomy, 2012, 970858

Kent, S. M. 1984, ApJS, 56, 105

Kent, S. M., Dame, T. M., & Fazio, G. 1991, ApJ, 378, 131

Kerr, R. P. 1963, Phys. Rev. Lett., 11, 237

Khandai, N., Feng, Y., DeGraf, C., Di Matteo, T., & Croft, R. A. C. 2012, MNRAS, 423, 2397

Khosroshahi, H. G., Wadadekar, Y., & Kembhavi, A. 2000, ApJ, 533, 162

King, A. 2019, Saas-Fee Advanced Course, 48, 95

King, A., & Nealon, R. 2019, MNRAS, 487, 4827

King, A. R. 2010, MNRAS, 402, 1516

King, I. R., & Minkowski, R. 1966, ApJ, 143, 1002

King, I. R., & Minkowski, R. 1972, in IAU Symposium, Vol. 44, External Galaxies and Quasi-Stellar Objects, ed. D. S. Evans, D. Wills, & B. J. Wills, 87

Kippenhahn, R., & Weigert, A. 1990, Stellar Structure and Evolution

Kızıltan, B., Baumgardt, H., & Loeb, A. 2017, Nature, 542, 203

Klypin, A. A., Trujillo-Gomez, S., & Primack, J. 2011, ApJ, 740, 102

Knapen, J. H. 2005, Astronomy and Geophysics, 46, 6.28

Knapen, J. H. 2010, in Galaxies and their Masks, ed. D. L. Block, K. C. Freeman, & I. Puerari, 201

Knapen, J. H., & Beckman, J. E. 1994, in Mass-Transfer Induced Activity in Galaxies, ed. I. Shlosman, 100

Knox-Shaw, H. 1915, Helwan Institute of Astronomy and Geophysics Bulletins, 15, 129

Komossa, S. 2015, Journal of High Energy Astrophysics, 7, 148

Kormendy, J. 2000, Elliptical Galaxies With Nuclear Disks of Stars: Black Hole Search and Stellar Populations, HST Proposal

Kormendy, J., & Bender, R. 2012, The Astrophysical Journal Supplement Series, 198, 2

Kormendy, J., & Bender, R. 2013, ApJ, 769, L5

Kormendy, J., Bender, R., & Cornell, M. E. 2011, Nature, 469, 374

Kormendy, J., Fisher, D. B., Cornell, M. E., & Bender, R. 2009, ApJS, 182, 216

Kormendy, J., & Ho, L. C. 2013, Annual Review of Astronomy and Astrophysics, 51, 511

Kormendy, J., & Kennicutt Robert C., J. 2004, ARA&A, 42, 603

Kormendy, J., & Richstone, D. 1995, ARA&A, 33, 581

Kormendy, J., Bender, R., Magorrian, J., et al. 1996, in American Astronomical Society Meeting Abstracts, Vol. 189, 111.01

Kourkchi, E., Khosroshahi, H. G., Carter, D., et al. 2012, MNRAS, 420, 2819

Krajnović, D., McDermid, R. M., Cappellari, M., & Davies, R. L. 2009, MNRAS, 399, 1839

Krajnović, D., Cappellari, M., McDermid, R. M., et al. 2018, MNRAS, 477, 3030

Kruskal, M. D. 1960, Physical Review, 119, 1743

Kuo, C. Y., Braatz, J. A., Condon, J. J., et al. 2011, ApJ, 727, 20

Laine, S., van der Marel, R. P., Lauer, T. R., et al. 2003, AJ, 125, 478

LaMassa, S. M., & Others. 2013, ApJ, 765, L33

Landau, L. D. 1932, Phys. Zs. Sowjet, 1, 285

Lange, R., Driver, S. P., Robotham, A. S. G., et al. 2015, MNRAS, 447, 2603

Laor, A. 1998, ApJ, 505, L83

Laor, A. 2001, ApJ, 553, 677

Lapi, A., Raimundo, S., Aversa, R., et al. 2014, ApJ, 782, 69

Laplace, P. S. 1796, The system of the world by P.S. Laplace; translated from the French by J. Pond in 1809 (Printed for R. Phillips)

Läsker, R., Ferrarese, L., van de Ven, G., & Shankar, F. 2014, ApJ, 780, 70

Lauer, T. R. 1985, ApJ, 292, 104

Lauer, T. R., Ajhar, E. A., Byun, Y. I., et al. 1995, AJ, 110, 2622

Lauer, T. R., Faber, S. M., Richstone, D., et al. 2007, ApJ, 662, 808

Laurikainen, E., Salo, H., & Buta, R. 2005, MNRAS, 362, 1319

Laurikainen, E., Salo, H., Buta, R., & Knapen, J. H. 2007, MNRAS, 381, 401

Laurikainen, E., Salo, H., Buta, R., & Knapen, J. H. 2009, ApJ, 692, L34

Laurikainen, E., Salo, H., Buta, R., & Knapen, J. H. 2011, MNRAS, 418, 1452

Laurikainen, E., Salo, H., Buta, R., Knapen, J. H., & Comerón, S. 2010, MNRAS, 405, 1089

Lemaître, G. 1933, Annales de la Société Scientifique de Bruxelles, 53, 51

Lentati, L., Taylor, S. R., Mingarelli, C. M. F., et al. 2015, MNRAS, 453, 2576

Levine, D., Wu, X., Good, J., et al. 2009, in Astronomical Data Analysis Software and Systems XVIII, ed. D. A. Bohlender, D. Durand, & P. Dowler, Vol. 411, 29

Li, J. I. H., Shen, Y., Ho, L. C., et al. 2021, ApJ, 906, 103

Li, K., Bogdanovic, T., & Ballantyne, D. R. 2020a, arXiv e-prints, arXiv:2007.02051

Li, Y., Habouzit, M., Genel, S., et al. 2020b, ApJ, 895, 102

Licquia, T. C., & Newman, J. A. 2015, ApJ, 806, 96

Liller, M. H. 1966, ApJ, 146, 28

Lima Neto, G. B., Gerbal, D., & Márquez, I. 1999, MNRAS, 309, 481

Lin, L., Pan, H.-A., Ellison, S. L., et al. 2019, ApJ, 884, L33

Lo, K. Y. 2005, ARA&A, 43, 625

Longo, G., Zaggia, S. R., Busarello, G., & Richter, G. 1994, Astronomy and Astrophysics Supplement Series, 105, 433

Lundmark, K. 1925, MNRAS, 85, 865

Luo, J., Chen, L.-S., Duan, H.-Z., et al. 2016, Classical and Quantum Gravity, 33, 35010

Lynden-Bell, D. 1969, Nature, 223, 690

Lynden-Bell, D., Faber, S. M., Burstein, D., et al. 1988, ApJ, 326, 19

Lynden-Bell, D., & Rees, M. J. 1971, MNRAS, 152, 461

Maccarone, T. J., Kundu, A., Zepf, S. E., & Rhode, K. L. 2007, Nature, 445, 183

Magorrian, J., Tremaine, S., Richstone, D., et al. 1998, AJ, 115, 2285

Makarov, D., Prugniel, P., Terekhova, N., Courtois, H., & Vauglin, I. 2014, A&A, 570, A13

Malumuth, E. M., & Kirshner, R. P. 1981, ApJ, 251, 508

Mapelli, M. 2016, MNRAS, 459, 3432

Mapelli, M., & Others. 2012, A&A, 542, A102

Marconi, A., Axon, D. J., Maiolino, R., et al. 2008, ApJ, 678, 693

Marconi, A., & Hunt, L. K. 2003, ApJ, 589, L21

Marconi, A., Risaliti, G., Gilli, R., et al. 2004, MNRAS, 351, 169

Markwardt, C. 2012, MPFIT: Robust non-linear least squares curve fitting

Markwardt, C. B. 2009, in Astronomical Society of the Pacific Conference Series, Vol. 411, Astronomical Data Analysis Software and Systems XVIII, ed. D. A. Bohlender, D. Durand, & P. Dowler, 251

Márquez, I., Lima Neto, G. B., Capelato, H., Durret, F., & Gerbal, D. 2000, A&A, 353, 873

Marsden, C., Shankar, F., Ginolfi, M., & Zubovas, K. 2020, Frontiers in Physics, 8, 61

Marshall, M. A., Mutch, S. J., Qin, Y., Poole, G. B., & Wyithe, J. S. B. 2020, MNRAS, 494, 2747

Martín-Navarro, I., Burchett, J. N., & Mezcua, M. 2020, MNRAS, 491, 1311

Martín-Navarro, I., La Barbera, F., Vazdekis, A., et al. 2015, MNRAS, 451, 1081

Martinez-Valpuesta, I., Knapen, J. H., & Buta, R. 2007, AJ, 134, 1863

Matković, A., & Guzmán, R. 2005, MNRAS, 362, 289

Mayall, N. U. 1934, Publications of the Astronomical Society of the Pacific, 46, 134

Mayall, N. U. 1939, PASP, 51, 282

Mayer, L., & Others. 2007, Science, 316, 1874

Mazure, A., & Capelato, H. V. 2002, A&A, 383, 384

Mazzalay, X., Thomas, J., Saglia, R. P., et al. 2016, MNRAS, 462, 2847

McConnell, N. J., & Ma, C.-P. 2013, ApJ, 764, 184

McConnell, N. J., Ma, C.-P., Graham, J. R., et al. 2011, ApJ, 728, 100

McLure, R. J., & Dunlop, J. S. 2004, MNRAS, 352, 1390

Meert, A., Vikram, V., & Bernardi, M. 2015, MNRAS, 446, 3943

Mehrgan, K., Thomas, J., Saglia, R., et al. 2019, arXiv e-prints, arXiv:1907.10608

Meidt, S. E., Schinnerer, E., van de Ven, G., et al. 2014, ApJ, 788, 144

Meijer, C. S. 1936, Nieuw Arch. Wiskd., II. Ser., 18, 10

Merritt, D. 2004, in Coevolution of Black Holes and Galaxies, ed. L. C. Ho, 263

Merritt, D. 2006, Memorie della Societa Astronomica Italiana, 77, 750

Merritt, D., & Ferrarese, L. 2001, ApJ, 547, 140

Merritt, D., & Milosavljević, M. 2005, Living Reviews in Relativity, 8, 8

Messier, C. 1781, Catalogue des Nébuleuses et des Amas d'Étoiles (Catalog of Nebulae and Star Clusters), Connoissance des Temps ou des Mouvements Célestes

Mezcua, M. 2017, International Journal of Modern Physics D, 26, 1730021

Michard, R., & Simien, F. 1988, A&AS, 74, 25

Michell, J. 1784, Philosophical Transactions of the Royal Society of London Series I, 74, 35

Miller, M. C. 2003, in American Institute of Physics Conference Series, Vol. 686, The Astrophysics of Gravitational Wave Sources, ed. J. M. Centrella, 125–134

Miller, M. C., & Colbert, E. J. M. 2004, International Journal of Modern Physics D, 13, 1

Miller, M. C., & Hamilton, D. P. 2002, MNRAS, 330, 232

Mingarelli, C. M. F., Lazio, T. J. W., Sesana, A., et al. 2017, Nature Astronomy, 1, 886

Minkowski, R. 1962, in IAU Symposium, Vol. 15, Problems of Extra-Galactic Research, ed. G. C. McVittie, 112

Mitchell, P. D., Lacey, C. G., Baugh, C. M., & Cole, S. 2013, MNRAS, 435, 87

Mockler, B., Guillochon, J., & Ramirez-Ruiz, E. 2019, ApJ, 872, 151

Moffat, A. F. J. 1969, A&A, 3, 455

Molaeinezhad, A., Zhu, L., Falcón-Barroso, J., et al. 2019, MNRAS, 488, 1012

Möllenhoff, C., & Heidt, J. 2001, A&A, 368, 16

Moore, C. J., Cole, R. H., & Berry, C. P. L. 2015, Classical and Quantum Gravity, 32, 15014

Morganti, R. 2017, Ap&SS, 4, 42

Muñoz-Mateos, J. C., Sheth, K., Gil de Paz, A., et al. 2013, ApJ, 771, 59

Muñoz-Mateos, J. C., Sheth, K., Gil de Paz, A., et al. 2016, ApJ, 818, 101

Mutlu-Pakdil, B., Seigar, M. S., & Davis, B. L. 2016, ApJ, 830, 117

Mutlu-Pakdil, B., Seigar, M. S., Hewitt, I. B., et al. 2018, MNRAS, 474, 2594

Natarajan, P., & Treister, E. 2009, MNRAS, 393, 838

Natarajan, P., & Volonteri, M. 2012, MNRAS, 422, 2051

Neistein, E., & Netzer, H. 2014, MNRAS, 437, 3373

Nemmen, R. S., Georganopoulos, M., Guiriec, S., et al. 2012, Science, 338, 1445

Newman, E., & Adamo, T. 2014, Scholarpedia, 9, 31791

Newman, E. T., & Janis, A. I. 1965, Journal of Mathematical Physics, 6, 915

Nguyen, D. D., Seth, A. C., den Brok, M., et al. 2017, ApJ, 836, 237

Nguyen, D. D., Seth, A. C., Neumayer, N., et al. 2018, ApJ, 858, 118

Nguyen, D. D., Seth, A. C., Neumayer, N., et al. 2019, ApJ, 872, 104

Nguyen, D. D., den Brok, M., Seth, A. C., et al. 2020, ApJ, 892, 68

Ni, Q., Yang, G., Brandt, W. N., et al. 2019, MNRAS, 490, 1135

Ni, Q., Brandt, W. N., Yang, G., et al. 2020, MNRAS

Novak, G. S., Faber, S. M., & Dekel, A. 2006, ApJ, 637, 96

Nowak, N., Saglia, R. P., Thomas, J., et al. 2007, MNRAS, 379, 909

Oesch, P. A., Brammer, G., van Dokkum, P. G., et al. 2016, ApJ, 819, 129

Oh, S.-H., de Blok, W. J. G., Walter, F., Brinks, E., & Kennicutt Robert C., J. 2008, AJ, 136, 2761

Oke, J. B. 1963, Nature, 197, 1040

Onishi, K., Iguchi, S., Davis, T. A., et al. 2017, MNRAS, 468, 4663

Onken, C. A., Ferrarese, L., Merritt, D., et al. 2004, ApJ, 615, 645

Opik, E. 1922, ApJ, 55, 406

Oppenheimer, J. R., & Snyder, H. 1939, Physical Review, 56, 455

Oppenheimer, J. R., & Volkoff, G. M. 1939, Physical Review, 55, 374

Oser, L., Naab, T., Ostriker, J. P., & Johansson, P. H. 2012, ApJ, 744, 63

Park, D., Kelly, B. C., Woo, J.-H., & Treu, T. 2012, ApJS, 203, 6

Park, D., Woo, J.-H., Bennert, V. N., et al. 2015, ApJ, 799, 164

Pasham, D. R., Cenko, S. B., Zoghbi, A., et al. 2015, ApJ, 811, L11

Paturel, G., Petit, C., Prugniel, P., et al. 2003, A&A, 412, 45

Peebles, P. J. E. 1972, ApJ, 178, 371

Penrose, R. 1965, Phys. Rev. Lett., 14, 57

Penrose, R. 1969, Nuovo Cimento Rivista Serie, 1, 252

Peterson, B. M. 2014, Space Sci. Rev., 183, 253

Peterson, B. M., & Wandel, A. 2000, ApJ, 540, L13

Pfister, H., Volonteri, M., Dai, J. L., & Colpi, M. 2020, MNRAS, 497, 2276

Pignatelli, E., Salucci, P., & Danese, L. 2001, MNRAS, 320, 124

Pillepich, A., Springel, V., Nelson, D., et al. 2018, MNRAS, 473, 4077

Planck Collaboration, Aghanim, N., Akrami, Y., et al. 2020, A&A, 641, A6

Poincaré, H. 1906, Academie des Sciences Paris Comptes Rendus, 150, 1504

Press, W. H., Teukolsky, S. A., Vetterling, W. T., & Flannery, B. P. 1992, Numerical recipes in FORTRAN. The art of scientific computing

Prugniel, P., & Simien, F. 1997, 122, 111

Querejeta, M., Meidt, S. E., Schinnerer, E., et al. 2015, The Astrophysical Journal Supplement Series, 219, 5

Quillen, A. C., Bower, G. A., & Stritzinger, M. 2000, The Astrophysical Journal Supplement Series, 128, 85

Rees, M. J. 1984, ARA&A, 22, 471

Rees, M. J. 1988, Proceedings of the Indian National Science Academy Part A, 54, 216

Reines, A. E., Sivakoff, G. R., Johnson, K. E., & Brogan, C. L. 2011, Nature, 470, 66

Reynolds, J. H. 1920, MNRAS, 80, 746

Reynolds, J. H. 1925, MNRAS, 85, 1014

Richings, A. J., Uttley, P., & Körding, E. 2011, MNRAS, 415, 2158

Rindler, W. 1956, MNRAS, 116, 662

Roediger, J. C., & Courteau, S. 2015, MNRAS, 452, 3209

Rosse, T. E. O. 1850, Philosophical Transactions of the Royal Society of London Series I, 140, 499

Rubin, V. 1995, Spectroscopy of the Rapidly Rotating Nuclear Disk in the Virgo s0 NGC4526, HST Proposal

Rusli, S. P., Erwin, P., Saglia, R. P., et al. 2013a, AJ, 146, 160

Rusli, S. P., Thomas, J., Saglia, R. P., et al. 2013b, AJ, 146, 45

Ruszkowski, M., Nagai, D., Zhuravleva, I., et al. 2019, BAAS, 51, 326

Sabra, B. M., Saliba, C., Abi Akl, M., & Chahine, G. 2015, ApJ, 803, 5

Safronov, V. S. 1960, Annales d'Astrophysique, 23, 979

Saglia, R. P., Opitsch, M., Erwin, P., et al. 2016, ApJ, 818, 47

Saha, K., Graham, A. W., & Rodríguez-Herranz, I. 2018, ApJ, 852, 133

Sahu, N., Graham, A. W., & Davis, B. L. 2019a, ApJ, 876, 155

Sahu, N., Graham, A. W., & Davis, B. L. 2019b, ApJ, 887, 10

Sahu, N., Graham, A. W., & Davis, B. L. 2020, ApJ, 903, 97

Salo, H., Laurikainen, E., Laine, J., et al. 2015, The Astrophysical Journal Supplement Series, 219, 4

Salpeter, E. E. 1964, ApJ, 140, 796

Salucci, P., & Others. 2000, MNRAS, 317, 488

Salviander, S., Shields, G. A., Gebhardt, K., & Bonning, E. W. 2007, ApJ, 662, 131

Sandage, A. 1961, The Hubble Atlas of Galaxies

Sandage, A. 1965, ApJ, 141, 1560

Sandage, A. 2004, Episodes in the Development of the Hubble Galaxy Classification, ed. D. L. Block, I. Puerari, K. C. Freeman, R. Groess, & E. K. Block, Vol. 319, 39

Sani, E., & Others. 2011, MNRAS, 413, 1479

Sarzi, M., Rix, H.-W., Shields, J. C., et al. 2001, ApJ, 550, 65

Satyapal, S., Secrest, N. J., McAlpine, W., et al. 2014, ApJ, 784, 113

Savorgnan, G., Graham, A. W., Marconi, A., et al. 2013, MNRAS, 434, 387

Savorgnan, G. A. D. 2016, ApJ, 821, 88

Savorgnan, G. A. D., & Graham, A. W. 2015, MNRAS, 446, 2330

Savorgnan, G. A. D., & Graham, A. W. 2016a, MNRAS, 457, 320

Savorgnan, G. A. D., & Graham, A. W. 2016b, ApJS, 222, 10

Savorgnan, G. A. D., Graham, A. W., Marconi, A., & Sani, E. 2016, ApJ, 817, 21

Schaffer, S. 1979, Journal for the History of Astronomy, 10, 42

Scharwächter, J., McGregor, P. J., Dopita, M. A., & Beck, T. L. 2013, MNRAS, 429, 2315

Schaye, J., Crain, R. A., Bower, R. G., et al. 2015, MNRAS, 446, 521

Schechter, P. L. 1980, AJ, 85, 801

Schmidt, M. 1963, Nature, 197, 1040

Schmidt, M. 1965, in Quasi-Stellar Sources and Gravitational Collapse, ed. I. Robinson, A. Schild, & E. L. Schucking, 455

Schombert, J., & Smith, A. K. 2012, Publications of the Astronomical Society of Australia, 29, 174

Schramm, M., Silverman, J. D., Greene, J. E., et al. 2013, ApJ, 773, 150

Schulze, A., & Gebhardt, K. 2011, ApJ, 729, 21

Schwarzschild, K. 1916, Abh. Konigl. Preuss. Akad. Wissenschaften Jahre 1906,92, Berlin,1907, 1916, 189

Schwarzschild, M. 1979, ApJ, 232, 236

Scott, N., Graham, A. W., & Schombert, J. 2013, ApJ, 768, 76

Secrest, N. J., Satyapal, S., Gliozzi, M., et al. 2012, ApJ, 753, 38

Secrest, N. J., Satyapal, S., Moran, S. M., et al. 2013, ApJ, 777, 139

Seigar, M. S., Graham, A. W., & Jerjen, H. 2007, MNRAS, 378, 1575

Seigar, M. S., Kennefick, D., Kennefick, J., & Lacy, C. H. S. 2008, ApJ, 678, L93

Seigar, M. S., Kennefick, D., Kennefick, J., & Lacy, C. H. S. 2008, ApJ, 678, L93

Sellwood, J. A. 2014, Reviews of Modern Physics, 86, 1

Sérsic, J. L. 1963, BAAA, 6, 41

Sérsic, J. L. 1968a, Atlas de Galaxias Australes - English Translation of the chapter "Photometric Analysis", Tech. rep.

Sérsic, J. L. 1968b, Bulletin of the Astronomical Institutes of Czechoslovakia, 19, 105

Sesana, A. 2013, MNRAS, 433, L1

Sesana, A., & Khan, F. M. 2015, MNRAS, 454, L66

Sesana, A., Shankar, F., Bernardi, M., & Sheth, R. K. 2016, MNRAS, 463, L6

Sesana, A., Vecchio, A., & Volonteri, M. 2009, MNRAS, 394, 2255

Seth, A. C., Cappellari, M., Neumayer, N., et al. 2010, ApJ, 714, 713

Sexton, R. O., Canalizo, G., Hiner, K. D., et al. 2019, ApJ, 878, 101

Seyfert, C. K. 1943, ApJ, 97, 28

Seymour, N., Altieri, B., De Breuck, C., et al. 2012, ApJ, 755, 146

Shankar, F., Marulli, F., Bernardi, M., et al. 2013, MNRAS, 428, 109

Shankar, F., Salucci, P., Granato, G. L., De Zotti, G., & Danese, L. 2004, MNRAS, 354, 1020

Shankar, F., Weinberg, D. H., & Miralda-Escudé, J. 2009, ApJ, 690, 20

Shankar, F., Bernardi, M., Sheth, R. K., et al. 2016, MNRAS, 460, 3119

Shankar, F., Bernardi, M., Richardson, K., et al. 2019, MNRAS, 485, 1278

Shannon, R. M., Ravi, V., Lentati, L. T., et al. 2015, Science, 349, 1522

Shapley, H., & Paraskevopoulos, J. S. 1940, Proceedings of the National Academy of Science, 26, 31

Shen, J., & Gebhardt, K. 2010, ApJ, 711, 484

Sheth, K., Regan, M., Hinz, J. L., et al. 2010, Publications of the Astronomical Society of the Pacific, 122, 1397

Shields, G. A. 1999, PASP, 111, 661

Siemens, X. 2019, in American Astronomical Society Meeting Abstracts, Vol. 233, American Astronomical Society Meeting Abstracts #233, 149.24

Siemens, X., Ellis, J., Jenet, F., & Romano, J. D. 2013, Classical and Quantum Gravity, 30, 224015

Silk, J. 2005, MNRAS, 364, 1337

Silk, J., & Rees, M. J. 1998, A&A, 331, L1

Simmons, B. D., Lintott, C., Schawinski, K., et al. 2013, MNRAS, 429, 2199

Slipher, V. M. 1913, Lowell Observatory Bulletin, 1, 56

—. 1917, Lowell Observatory Bulletin, 3, 59

Soker, N., & Meiron, Y. 2011, MNRAS, 411, 1803

Somerville, R. S., & Davé, R. 2015, ARA&A, 53, 51

Soria, R., Hau, G. K. T., Graham, A. W., et al. 2010, MNRAS, 405, 870

Springel, V., White, S. D. M., Jenkins, A., et al. 2005, Nature, 435, 629

Stappers, B., & Kramer, M. 2011, in American Astronomical Society Meeting Abstracts, Vol. 217, American Astronomical Society Meeting Abstracts #217, 124.04

Stoner, E. 1930, The London, 9, 944

Stoner, E. C. 1929, The London, Edinburgh, and Dublin Philosophical Magazine and Journal of Science, 7, 63

Suess, K. A., Kriek, M., Price, S. H., & Barro, G. 2021, arXiv e-prints, arXiv:2101.05820

Suh, H., Civano, F., Trakhtenbrot, B., et al. 2020, ApJ, 889, 32

Taylor, E. N., Hopkins, A. M., Baldry, I. K., et al. 2011, MNRAS, 418, 1587

Terrazas, B. A., Bell, E. F., Henriques, B. M. B., et al. 2016, ApJ, 830, L12

Terrazas, B. A., Bell, E. F., Pillepich, A., et al. 2020, MNRAS, 493, 1888

Terzić, B., & Graham, A. W. 2005, MNRAS, 362, 197

Thater, S., Krajnović, D., Cappellari, M., et al. 2019, A&A, 625, A62

Thomas, J., Ma, C.-P., McConnell, N. J., et al. 2016, Nature, 532, 340

Thomas, J., Saglia, R. P., Bender, R., et al. 2004, MNRAS, 353, 391

Thorne, K. S. 1974, ApJ, 191, 507

Tody, D. 1986, in Society of Photo-Optical Instrumentation Engineers (SPIE) Conference Series, Vol. 627, Instrumentation in astronomy VI, ed. D. L. Crawford, 733

Tody, D. 1993, in Astronomical Society of the Pacific Conference Series, Vol. 52, Astronomical Data Analysis Software and Systems II, ed. R. J. Hanisch, R. J. V. Brissenden, & J. Barnes, 173

Tolman, R. C. 1930, Proceedings of the National Academy of Science, 16, 511

Tolstoy, E., Hill, V., & Tosi, M. 2009, ARA&A, 47, 371

Tonry, J. L. 1981, ApJ, 251, L1

Toomre, A. 1964, ApJ, 139, 1217

Tremaine, S., Gebhardt, K., Bender, R., et al. 2002, ApJ, 574, 740

Trujillo, I., Erwin, P., Asensio Ramos, A., & Graham, A. W. 2004, AJ, 127, 1917

Trujillo, I., Graham, A. W., & Caon, N. 2001, MNRAS, 326, 869

Valencia-S, M., Eckart, A., Zuther, J., et al. 2012, in Journal of Physics Conference Series, Vol. 372, Journal of Physics Conference Series, 012048

van den Bergh, S. 1976, ApJ, 206, 883

van den Bosch, R. C. E. 2016, ApJ, 831, 134

van der Marel, R. P. 2004, in Coevolution of Black Holes and Galaxies, ed. L. C. Ho, 37

van der Marel, R. P., Cretton, N., de Zeeuw, P. T., & Rix, H.-W. 1998, ApJ, 493, 613

van der Marel, R. P., & van den Bosch, F. C. 1998, AJ, 116, 2220

Véron-Cetty, M. P., & Véron, P. 2010, A&A, 518, A10

Vika, M., Driver, S. P., Cameron, E., Kelvin, L., & Robotham, A. 2012, MNRAS, 419, 2264

Vika, M., Driver, S. P., Graham, A. W., & Liske, J. 2009, MNRAS, 400, 1451

Vishveshwara, C. V. 1970, Nature, 227, 936

Vitral, E., & Mamon, G. A. 2020, A&A, 635, A20

Vogelsberger, M., Genel, S., Springel, V., et al. 2014, MNRAS, 444, 1518

Volonteri, M., & Ciotti, L. 2013, ApJ, 768, 29

Volonteri, M., Lodato, G., & Natarajan, P. 2008, MNRAS, 383, 1079

Volonteri, M., Natarajan, P., & Gültekin, K. 2011, ApJ, 737, 50

Volonteri, M., Pfister, H., Beckman, R. S., et al. 2020, arXiv e-prints, arXiv:2005.04902

Vulcani, B., Poggianti, B. M., Aragón-Salamanca, A., et al. 2011, MNRAS, 412, 246

Walsh, J. L., Barth, A. J., Ho, L. C., & Sarzi, M. 2013, ApJ, 770, 86

Walsh, J. L., van den Bosch, R. C. E., Gebhardt, K., et al. 2015, ApJ, 808, 183

Walsh, J. L., van den Bosch, R. C. E., Gebhardt, K., et al. 2017, ApJ, 835, 208

Wandel, A. 1999, ApJ, 519, L39

Webb, N. A., Guérou, A., Ciambur, B., et al. 2017, A&A, 602, A103

Wheeler, J. A. 1968, American Scientist, 56, 1

Williams, M. J., Bureau, M., & Cappellari, M. 2010, MNRAS, 409, 1330

Wolfe, A. M., & Burbidge, G. R. 1970, ApJ, 161, 419

Woo, J.-H., Schulze, A., Park, D., et al. 2013a, ApJ, 772, 49

—. 2013b, ApJ, 772, 49

Woo, J.-H., Treu, T., Malkan, M. A., & Bland ford, R. D. 2006, ApJ, 645, 900

Wright, E. L. 2006, PASP, 118, 1711

Wu, X., Roby, T., & Ly, L. 2010, in Astronomical Data Analysis Software and Systems XIX, ed. Y. Mizumoto, K. I. Morita, & M. Ohishi, Vol. 434, 14

Wyithe, J. S. B., & Loeb, A. 2003, ApJ, 595, 614

Yang, X., Yang, J., Paragi, Z., et al. 2017, MNRAS, 464, L70

Yee, H. K. C. 1992, in Astronomical Society of the Pacific Conference Series, Vol. 31, Relationships Between Active Galactic Nuclei and Starburst Galaxies, ed. A. V. Filippenko, 417

Yepes, G., Martínez-Vaquero, L. A., Gottlöber, S., & Hoffman, Y. 2009, in American Institute of Physics Conference Series, Vol. 1178, 5th International Workshop on the Dark Side of the Universe, ed. C. Balazs & F. Wang, 64–75

Yıldırım, A., van den Bosch, R. C. E., van de Ven, G., et al. 2015, MNRAS, 452, 1792

York, D. G., Adelman, J., Anderson John E., J., et al. 2000, AJ, 120, 1579

Young, C. K., & Currie, M. J. 1994, MNRAS, 268, L11

Yu, L.-M., Bian, W.-H., Wang, C., Zhao, B.-X., & Ge, X. 2019, MNRAS, 488, 1519

Zel'dovich, Y. B. 1964, Soviet Physics Doklady, 9, 195

Zhou, Z. Q., Liu, F. K., Komossa, S., et al. 2021, ApJ, 907, 77

Zwicky, F. 1933, Helvetica Physica Acta, 6, 110

A

Appendix

A.1 Surface Brightness Profiles for Early-type Galaxies

Here we provide the major-axis and equivalent-axis (i.e. geometric mean axis = $\sqrt{R_{maj}R_{min}}$) surface brightness profiles (AB magnitude system) for the 41 ETGs that we modeled (apart from NGC 4762, Figure 2.3) . Magnitudes and stellar masses of these galaxies, and their spheroids are presented in Table 2.4 in the main paper. The current paper does not directly use the parameters from our decomposition of these light profiles; however, we intend to use them in our upcoming work, where we will tabulate them there.

A.1.1 Light profiles from Spitzer 3.6μm images

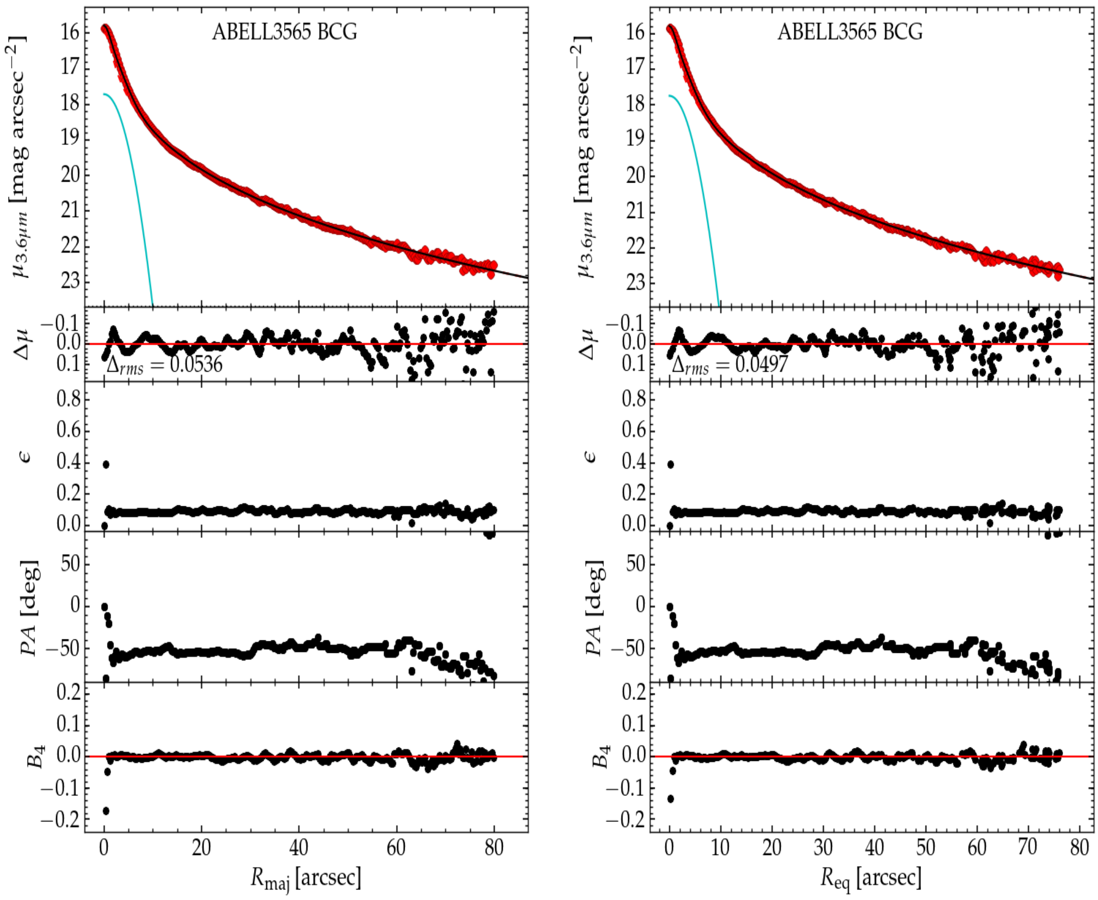

Figure A.1 ABELL 3565 BCG (IC 4296): elliptical galaxy with an extended spheroid fit using a Sérsic function (—) plus a Gaussian (—) accounting for extra light from a central source. IC 4296 has a very high velocity dispersion suggesting it may be a core-Sérsic galaxy, but we do not have evidence for a deficit of light at its core in the Spitzer data.

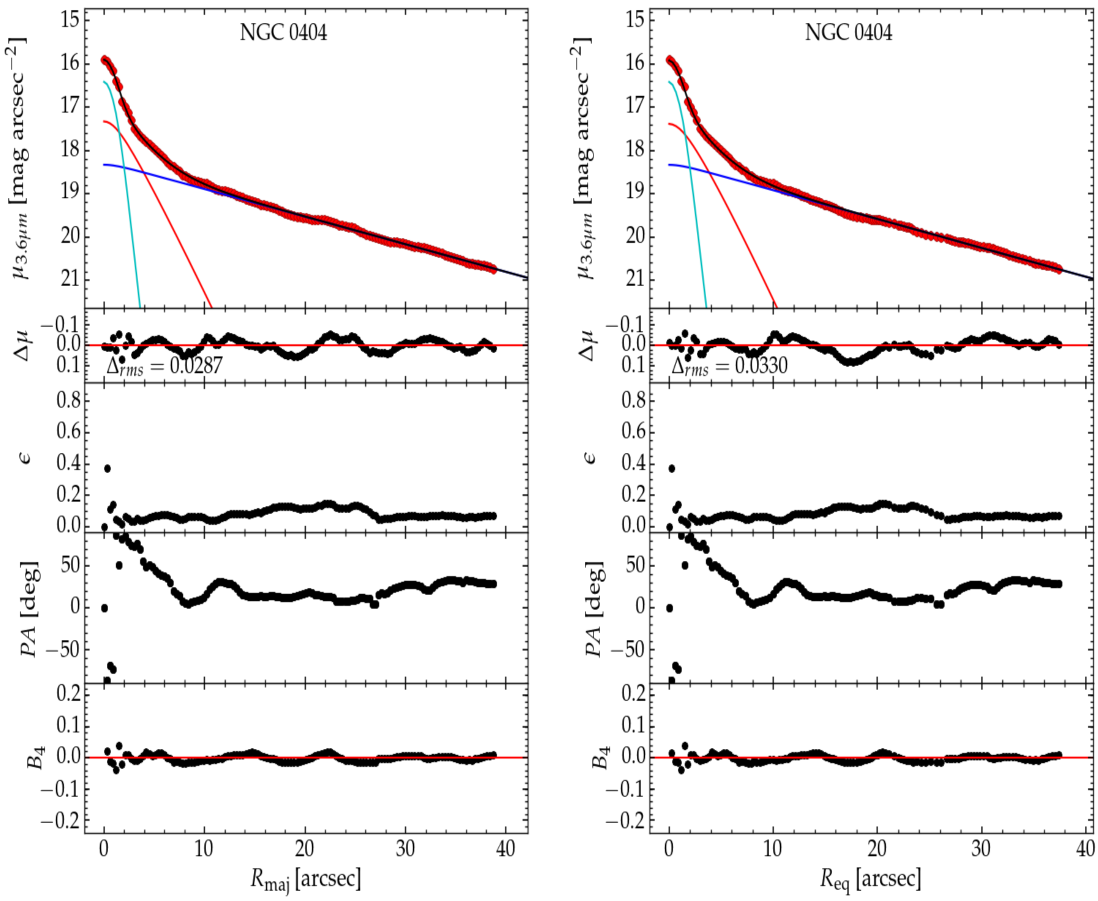

Figure A.2 NGC 404: a dwarf lenticular galaxy hosting an AGN at its center and a nuclear star cluster (Nguyen et al., 2017). We fit a Sérsic function (—) for its bulge, an exponential for the disk (—), and a Gaussian (—) for the central AGN.

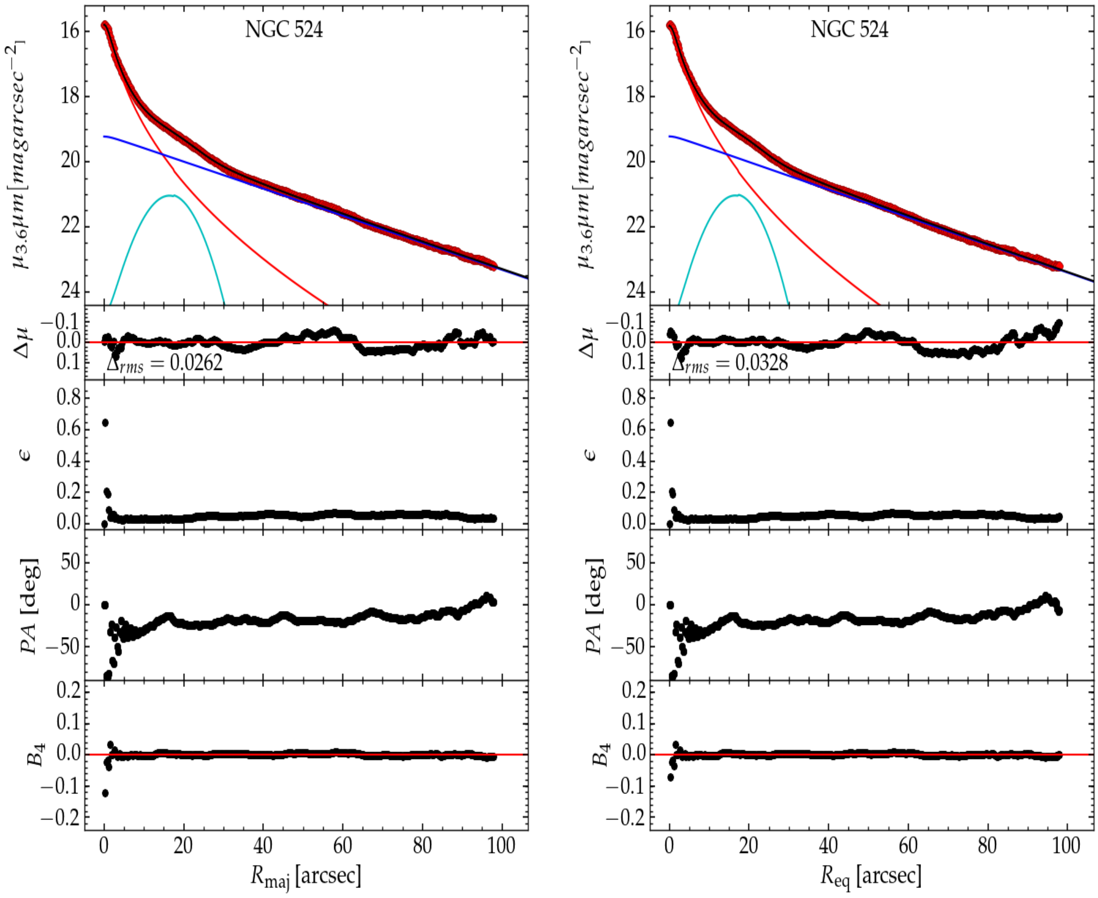

Figure A.3 NGC 524: a face-on lenticular galaxy with a core-Sérsic (—) bulge (Richings et al., 2011). The galaxy has a faint ring at about $R_{maj} = 20''$ which we fit using a Gaussian (—), and there is an extended exponential disk (—).

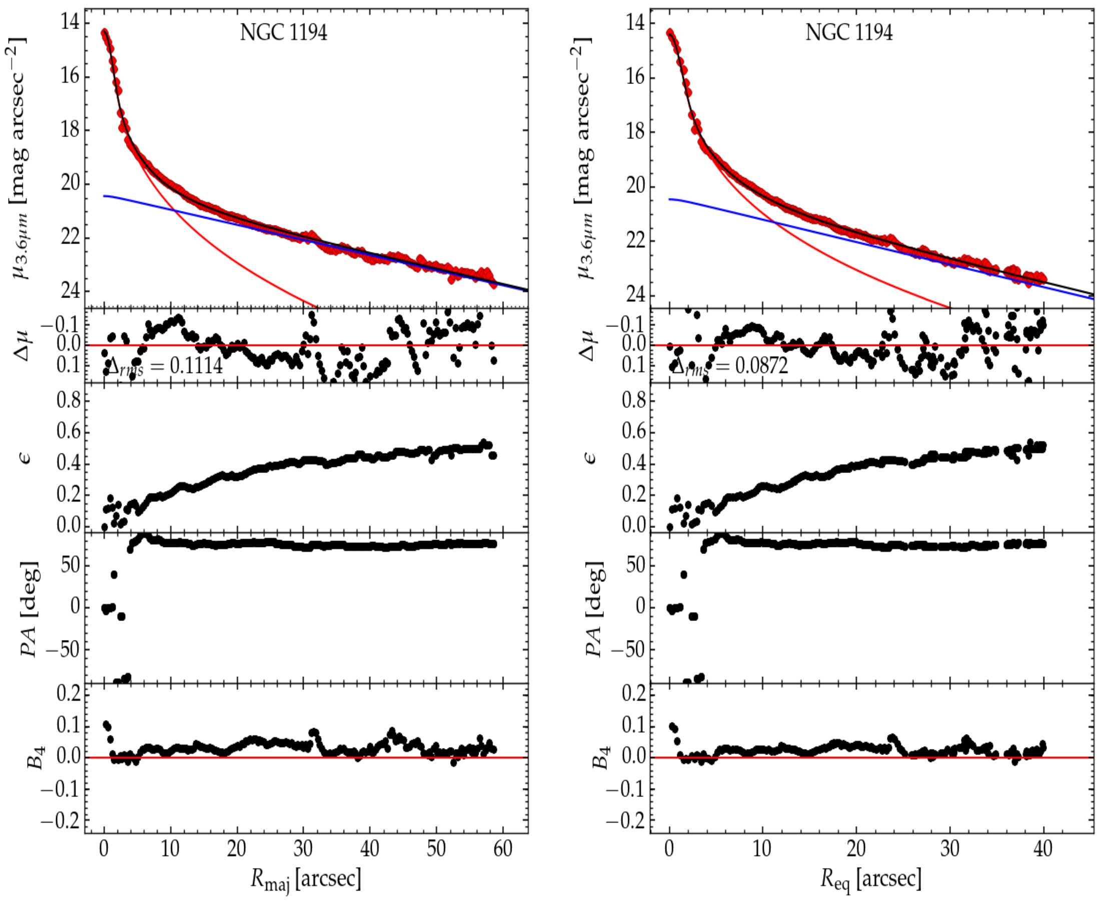

Figure A.4 NGC 1194: a lenticular, warped disk (Fedorova et al., 2016) galaxy, fit with a Sérsic bulge (—) and an extended exponential disk (—). It also has a faint debris tail, suggesting it may have undergone a merger, and Fedorova et al. (2016) also hypothesize that NGC 1194 may harbor two black holes.

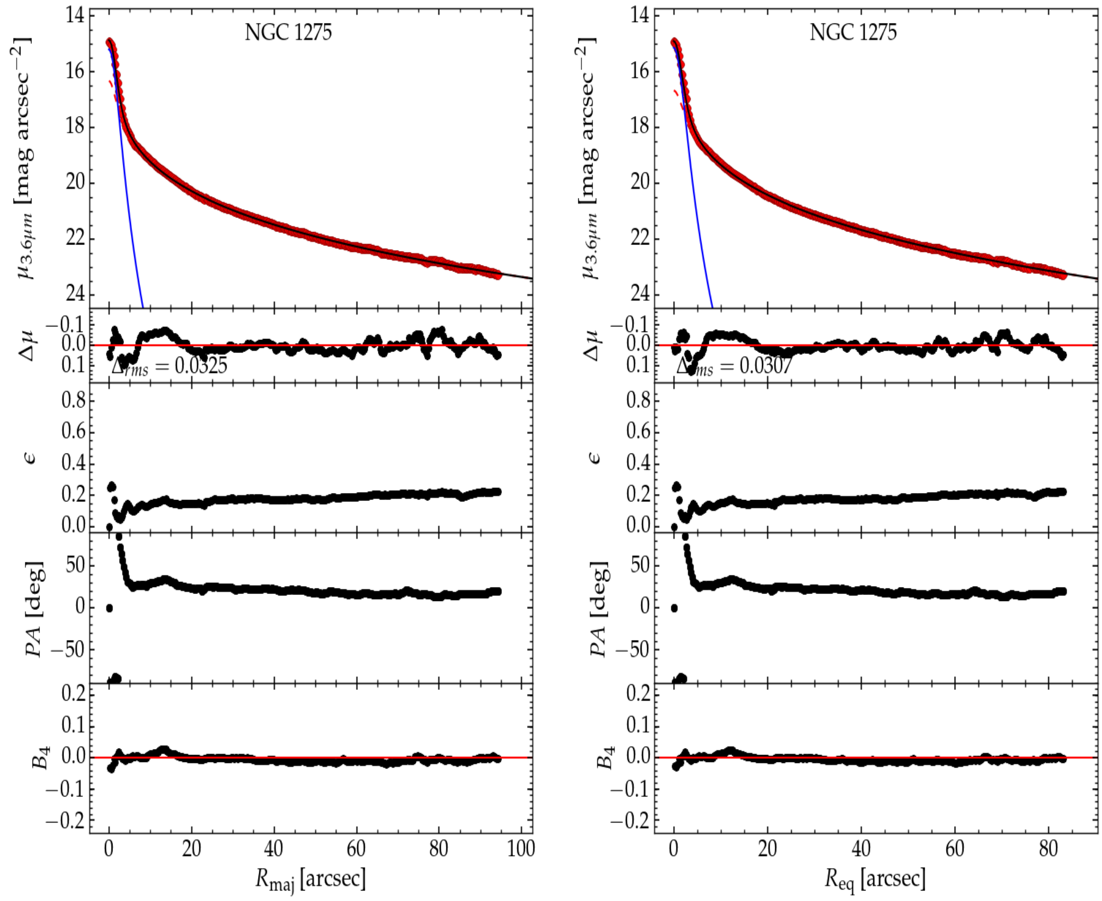

Figure A.5 NGC 1275: a peculiar elliptical galaxy with an extended bright object at the center (resolved in HST images), fit using an inclined disk (—) along with the extended Sérsic spheroid (—). The sharp bump in the ellipticity and position profile also hints at the presence of a central disky object.

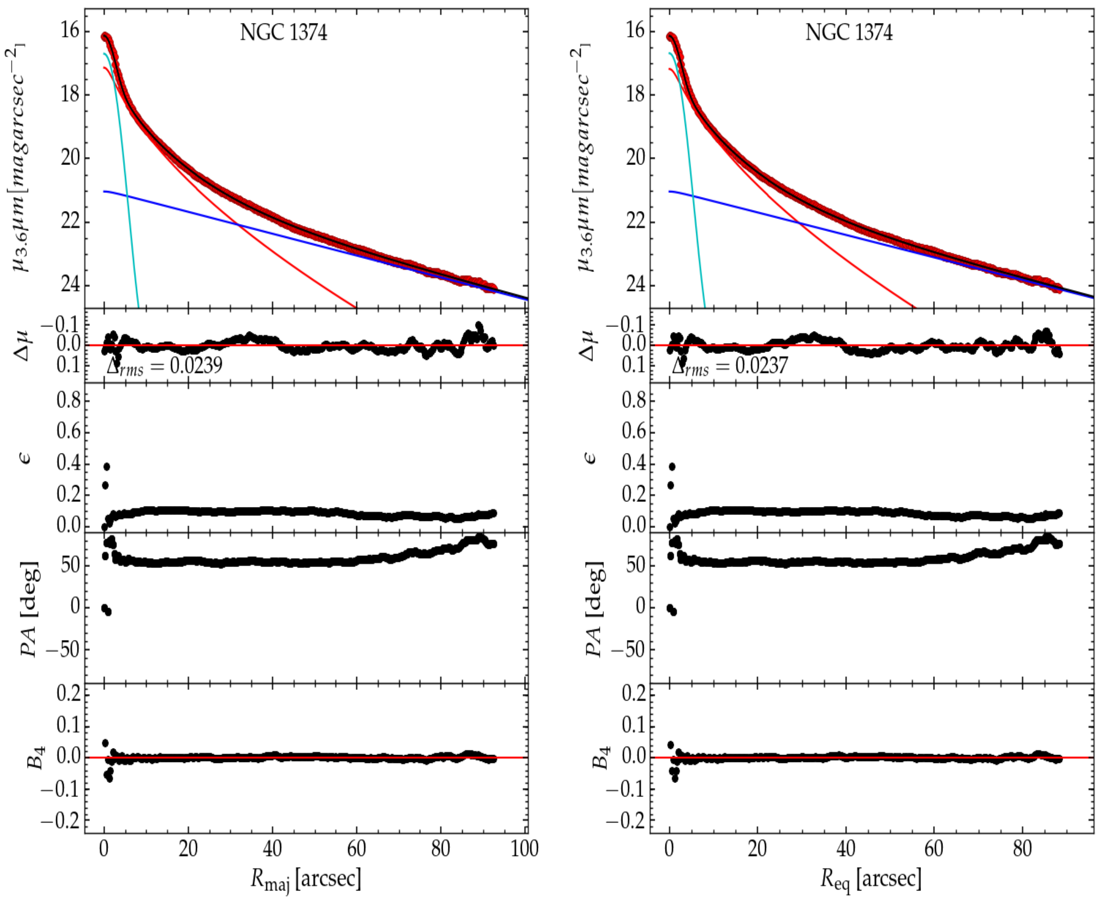

Figure A.6 NGC 1374: a face-on lenticular galaxy (Longo et al., 1994; D'Onofrio et al., 1995) suspected to have a depleted stellar core (Rusli et al., 2013a). Due to the lack of evidence for a depleted core we fit a Sérsic function (—) to its bulge plus a Gaussian (—) for a nuclear source possibly related to a peak at $\sim 5''$ from the center of the rotation curve presented by Longo et al. (1994). We also fit an exponential disk (—) component, based on the kinematic profile from D'Onofrio et al. (1995).

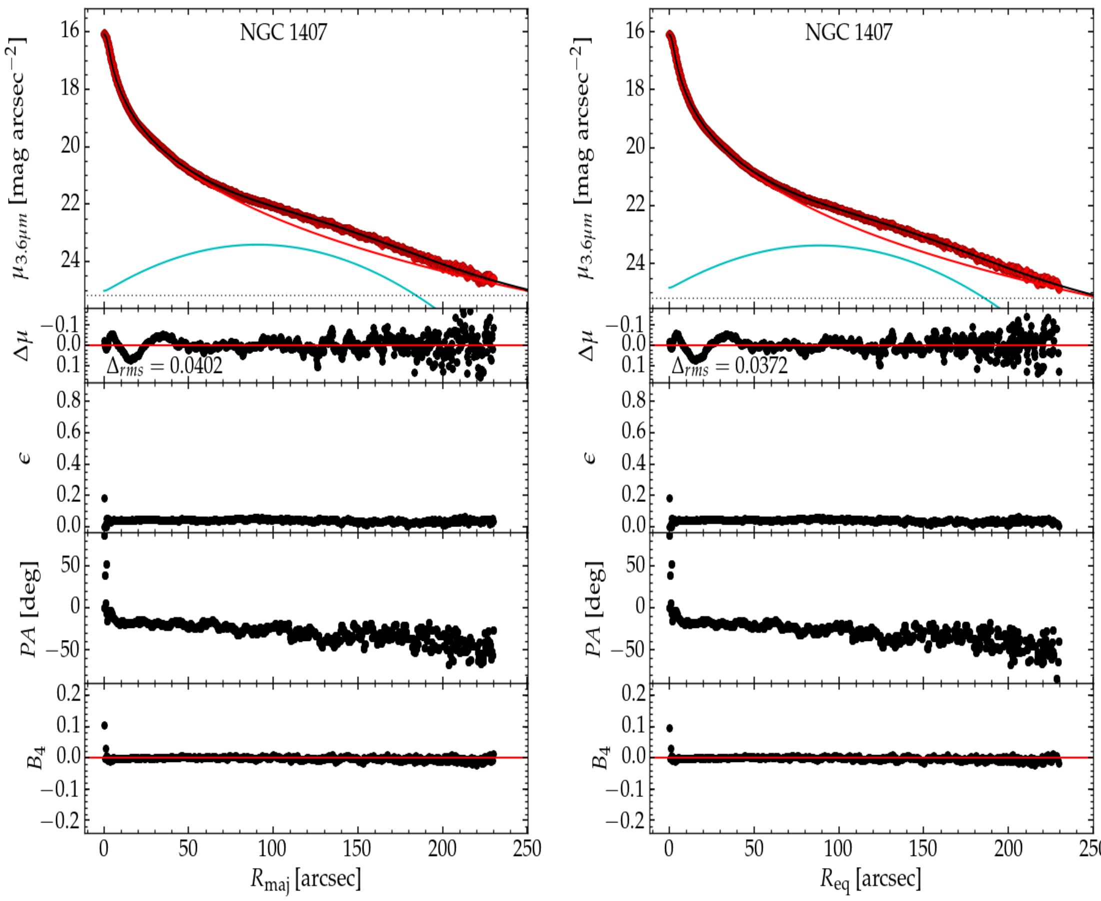

Figure A.7 NGC 1407: a massive elliptical galaxy with a deficit of light at it core. Its surface brightness profile is fit using a core-Sérsic function (—) and a broad Gaussian (—) which accounts well for the bump in the light profile, possibly due to a semi-digested galaxy.

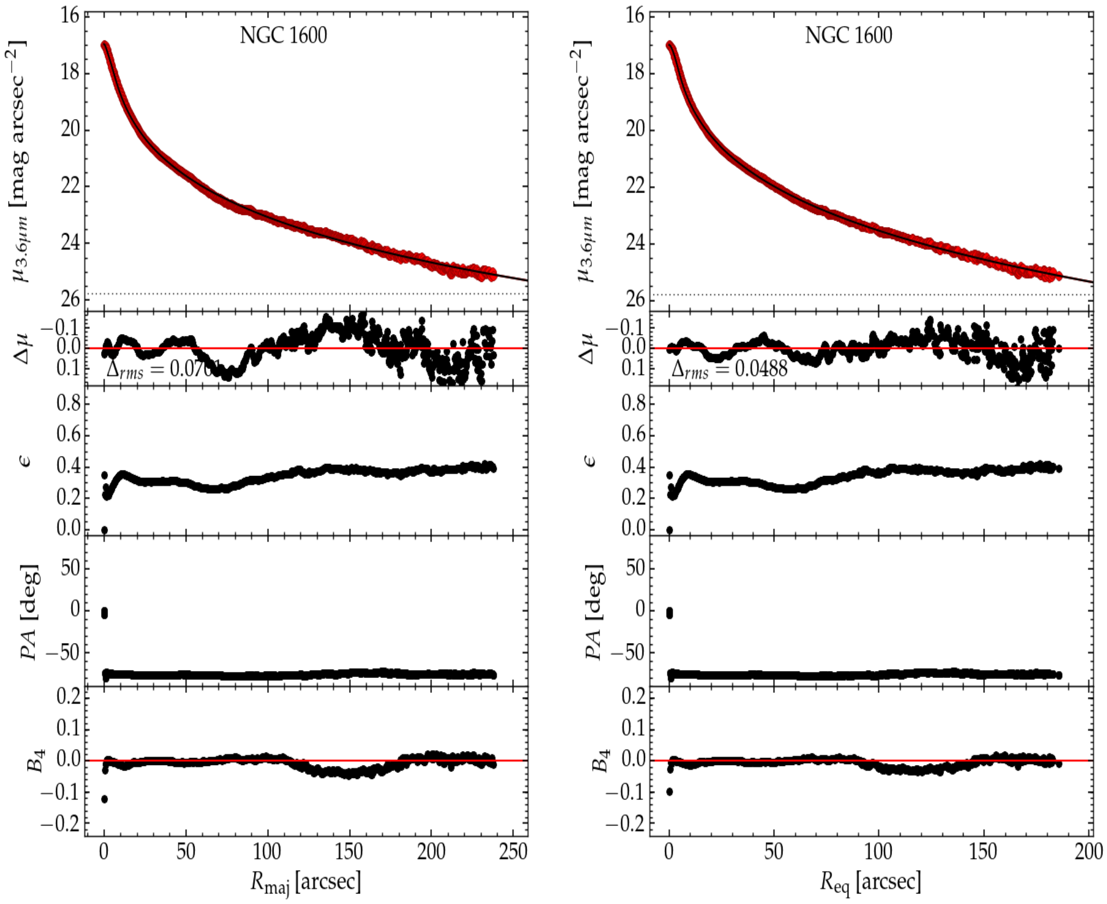

Figure A.8 NGC 1600: an elliptical galaxy with a depleted core. Its spheroid is fit using a core-Sérsic function (—). The shallow dip in the B_4 profile is associated with the presence of a tidal debris tail at $\sim 150''$ along the semi-major axis, which makes the galaxy look boxy (negative B_4) at those radii.

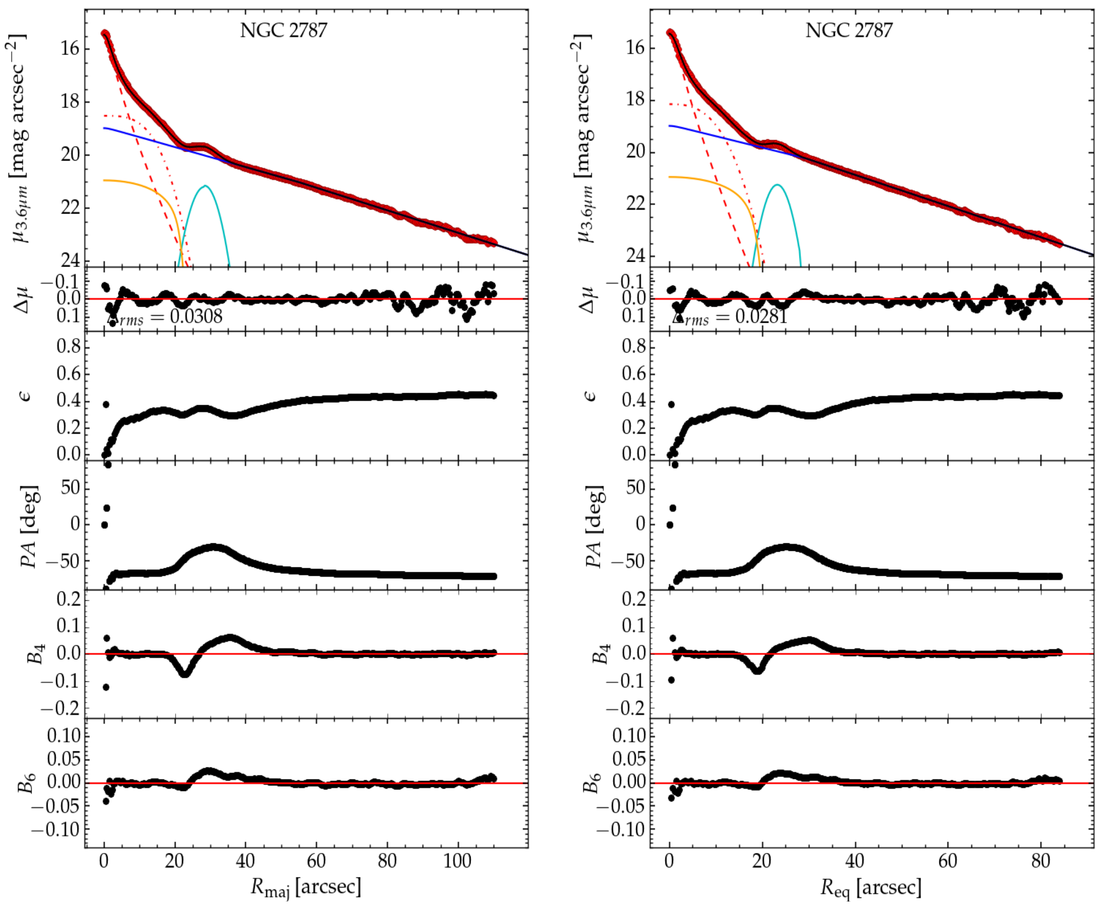

Figure A.9 NGC 2787: it is a barred lenticular galaxy with its multi-component fit comprised of a Sérsic function for the bulge (- - -), a low index Sérsic function for the prominent bar-lens/pseudobulge (-·-·-), a Ferrers function for the bar (—), a Gaussian for the ansae (—), and a slightly truncated exponential model for the extended disk (—). The dip in the ellipticity, B_4, and B_6 profiles at $R_{maj} \approx 22''$, and the bump in the ellipticity, position angle, B_4 and B_6 profiles at $\sim 30''$, corresponds to the perturbation of the isophotes due to the bar/barlens and ansae, respectively.

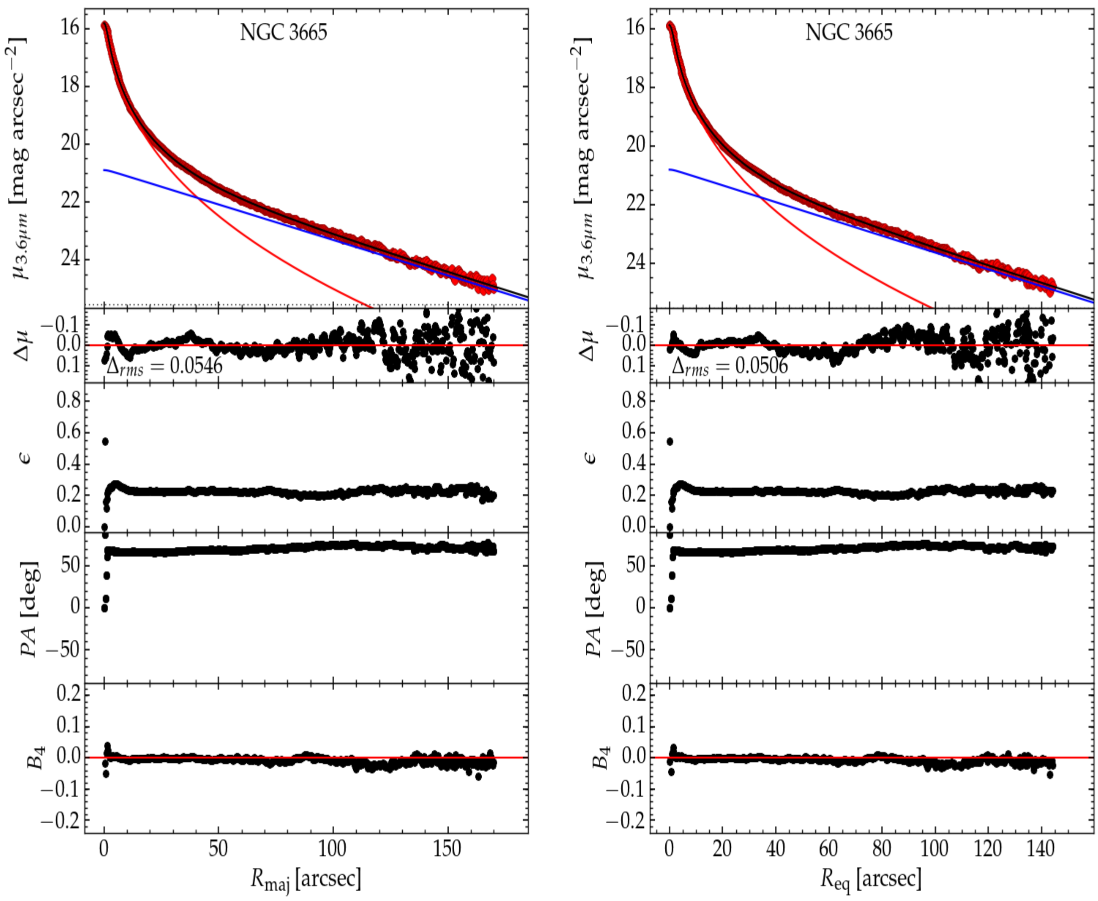

Figure A.10 NGC 3665: a lenticular galaxy with a Sérsic bulge (—) and an extended exponential disk (—).

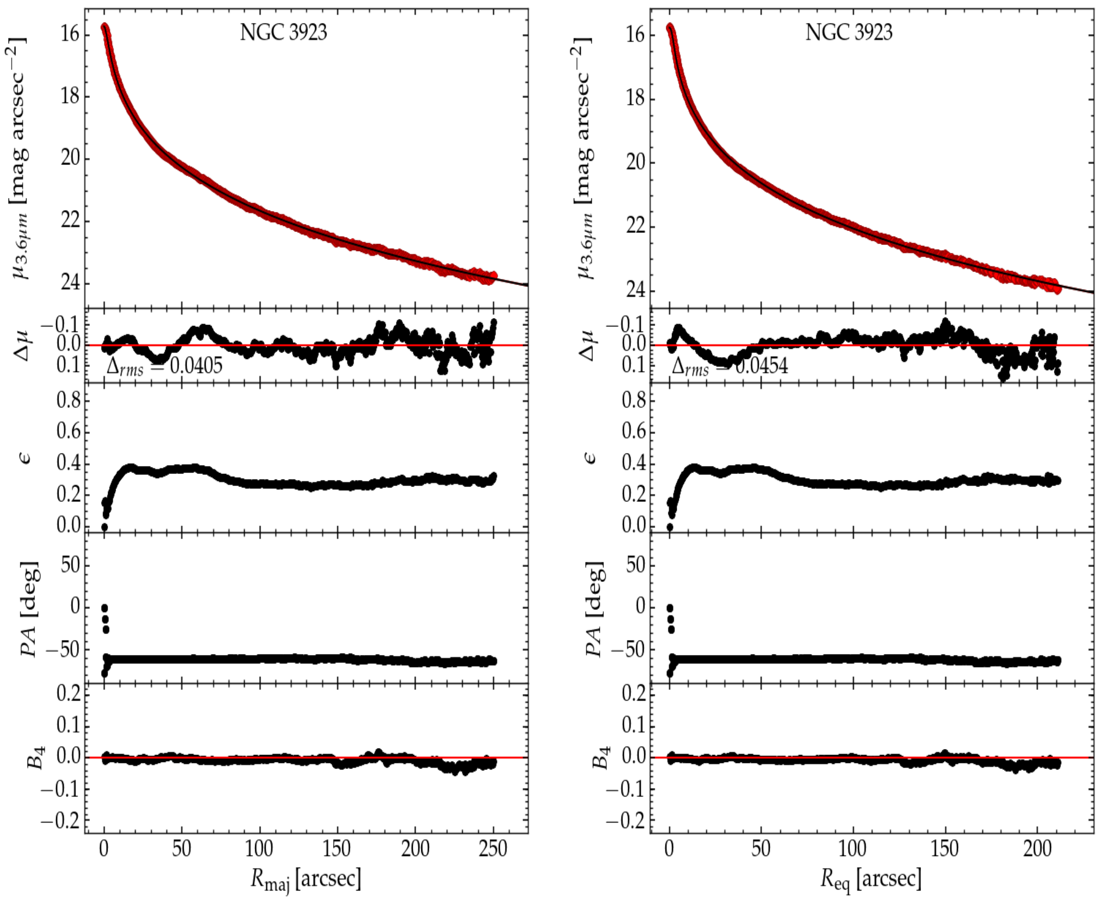

Figure A.11 NGC 3923: a massive elliptical with a deficit of light in its core, fit using a core-Sérsic function (—).

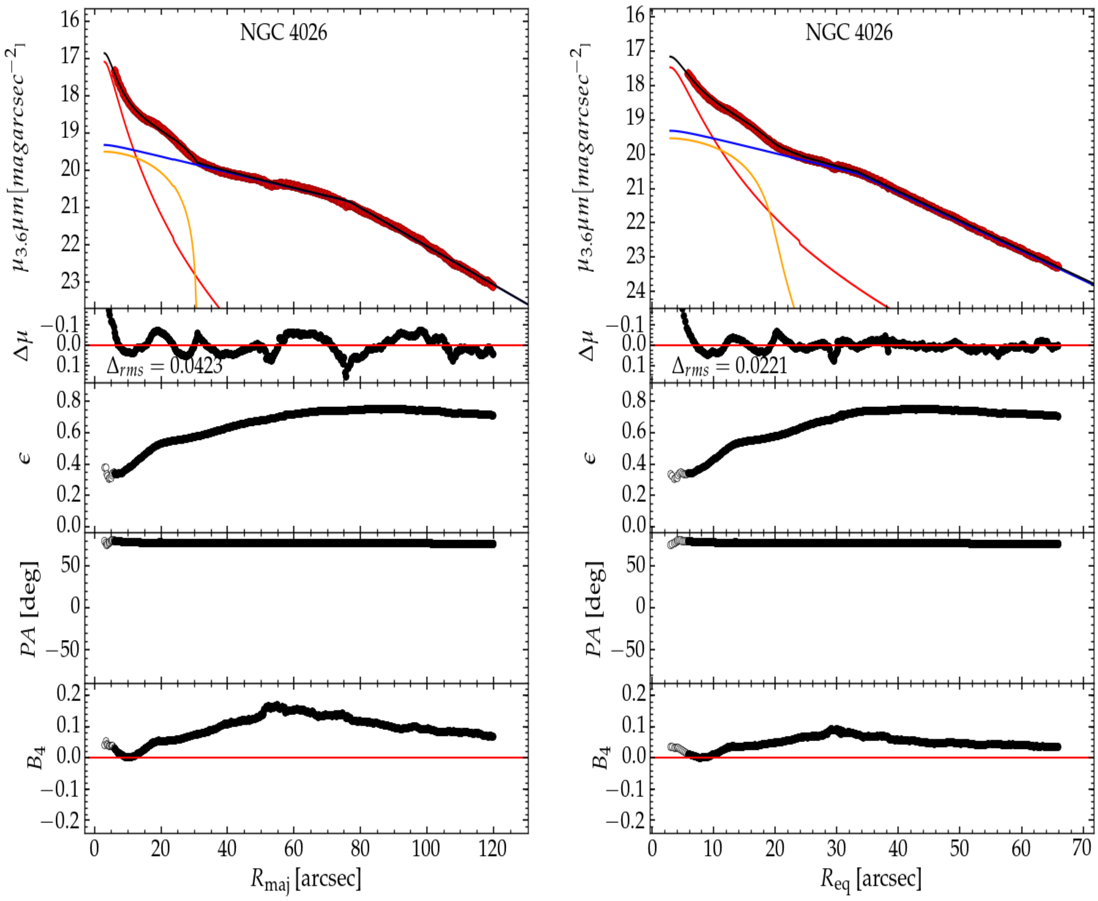

Figure A.12 NGC 4026: an edge-on lenticular galaxy with a Sérsic bulge (—), a faint bar ending at about $R_{maj} = 30''$ and fit using Ferrers (—) function, plus a truncated exponential disk (—).

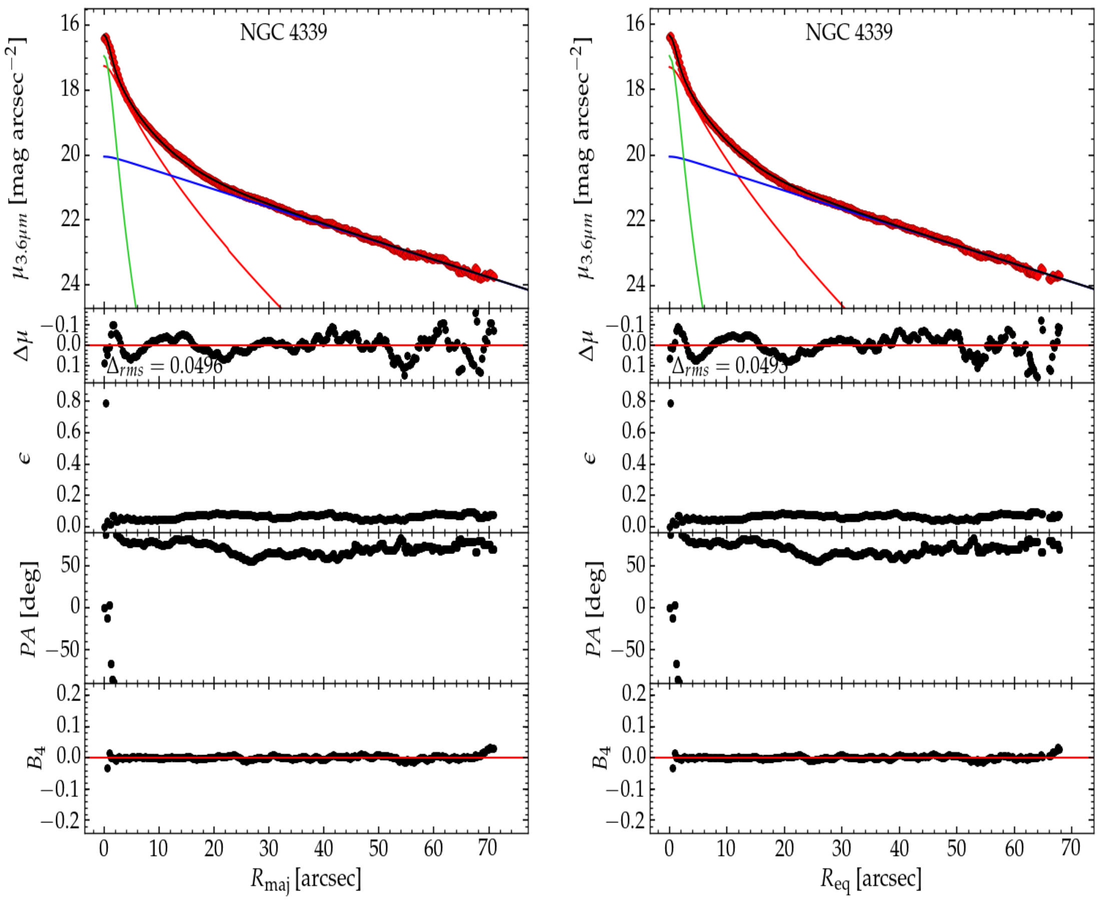

Figure A.13 NGC 4339: a face-on lenticular galaxy (Halliday, 1998) with a central point source, a Sérsic bulge (—), and an exponential disk (—).

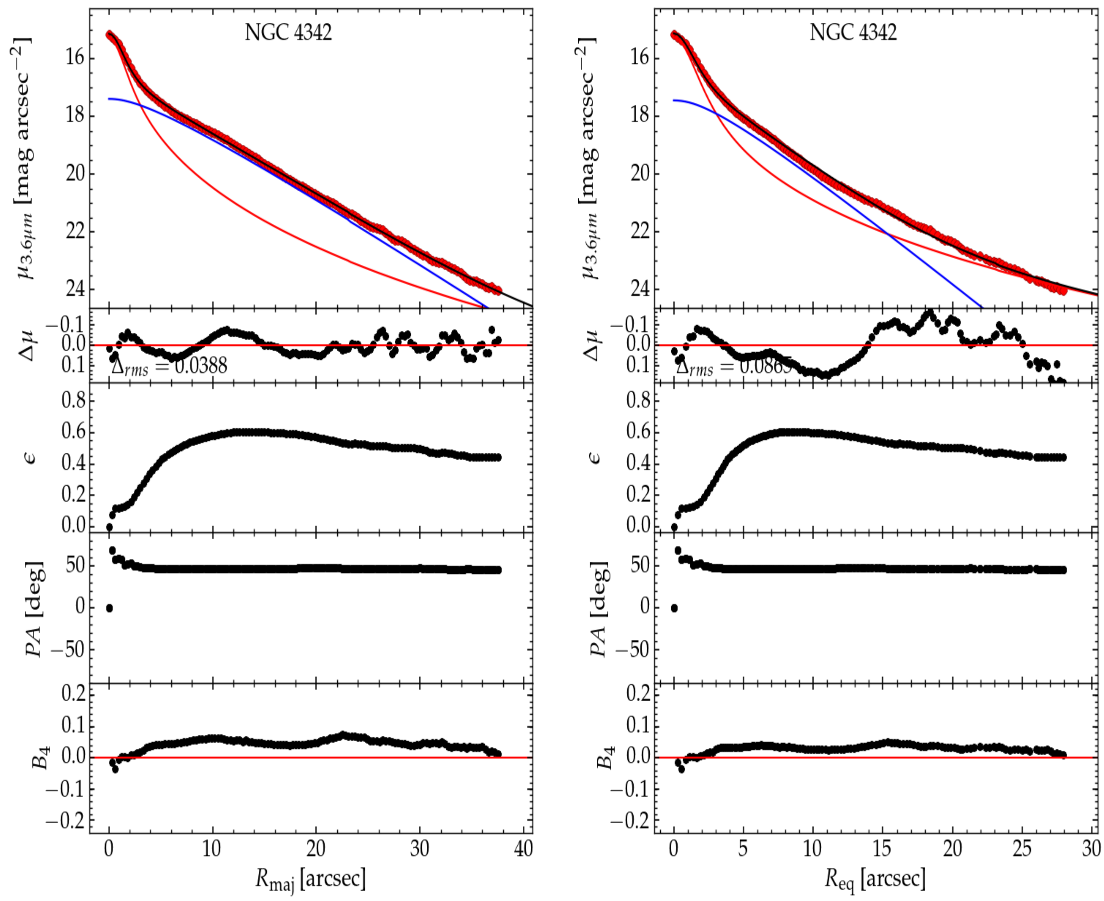

Figure A.14 NGC 4342: a dwarf ellicular galaxy, with most of its mass tidally stripped by the massive companion galaxy NGC 4365 (Blom et al., 2014). Its light profile has been fit using an extended Sérsic bulge (—) and an intermediate-scale inclined disk (—), evident from the bump in the ellipticity profile at intermediate radii.

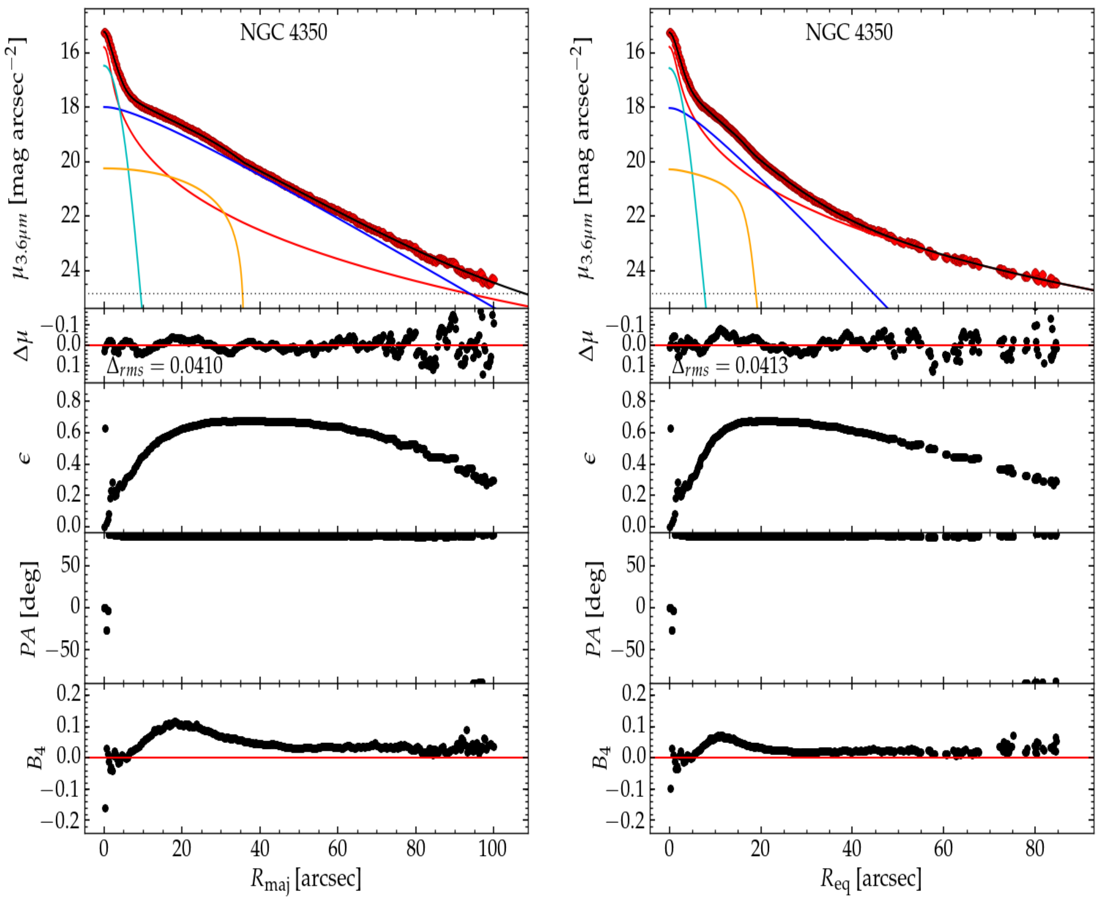

Figure A.15 NGC 4350: an ellicular (ES) galaxy with a faint bar (Pignatelli et al., 2001). The bump in the B_4 profile at $R_{maj} \approx 20''$ reflects the combined effect of bar and high inclination of the galaxy. As apparent from the ellipticity profile, the spheroid of NGC 4350, fit using a Sérsic function (—), takes over the intermediate-scale disk (—), fit using an inclined exponential, at larger radii. The bar component is fit using a Ferrers (—) function and the central Gaussian (—) accounts for extra light at the galaxy center (Pignatelli et al., 2001).

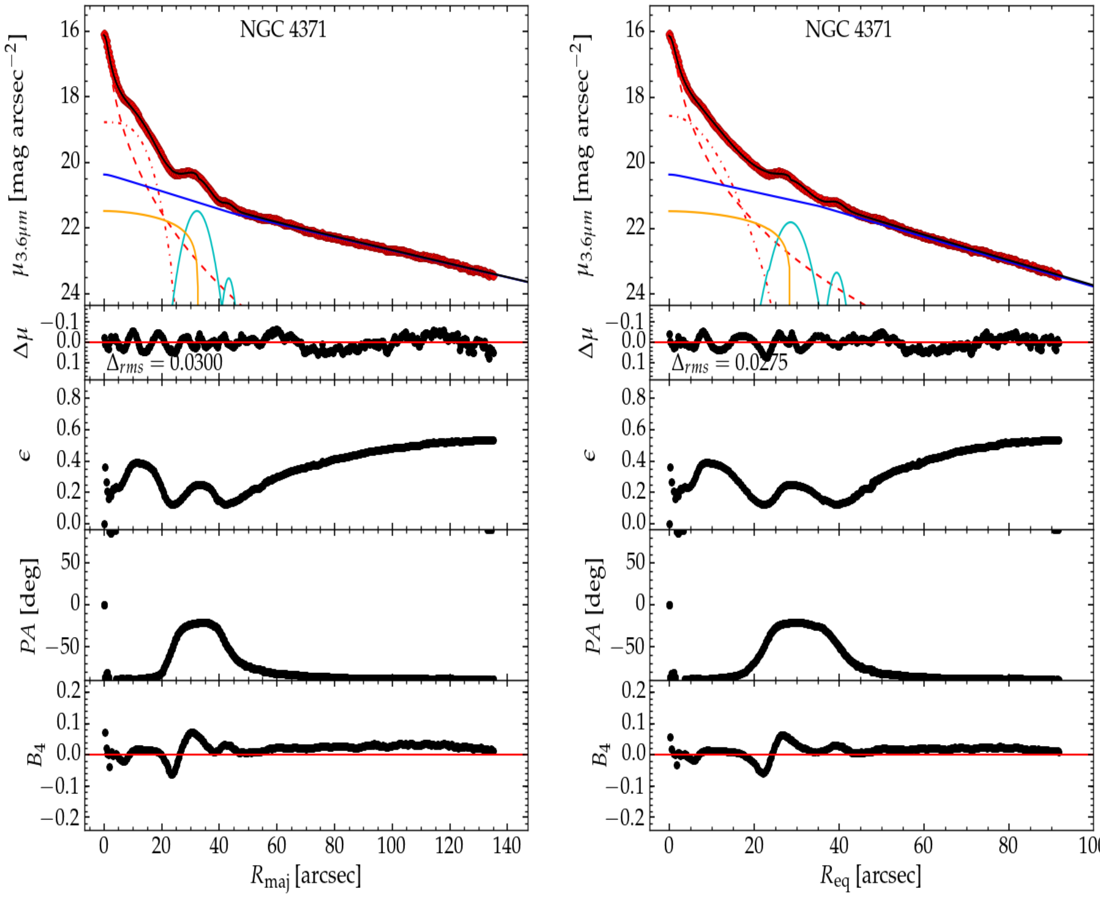

Figure A.16 NGC 4371: a barred lenticular, SB(r)0, galaxy with a pseudobulge (Erwin et al., 2015) fit here with a Sérsic function (- - -) for the bulge, a bar-lens (or pseudobulge) fit using a low Sérsic index function (-·-·-), a bar fit using Ferrers function (—), an ansae at the end of the bar fit using a Gaussian (—), an outer faint ring fit using a low width Gaussian (—), and an extended disk (—) truncated at $R_{maj} \approx 44''$. Gadotti et al. (2015) call the two parts of the truncated disk as inner disk and (outer) disk. Erwin et al. (2015) treat the bulge and the (oval-shaped) barlens as a single entity naming it a "composite bulge".

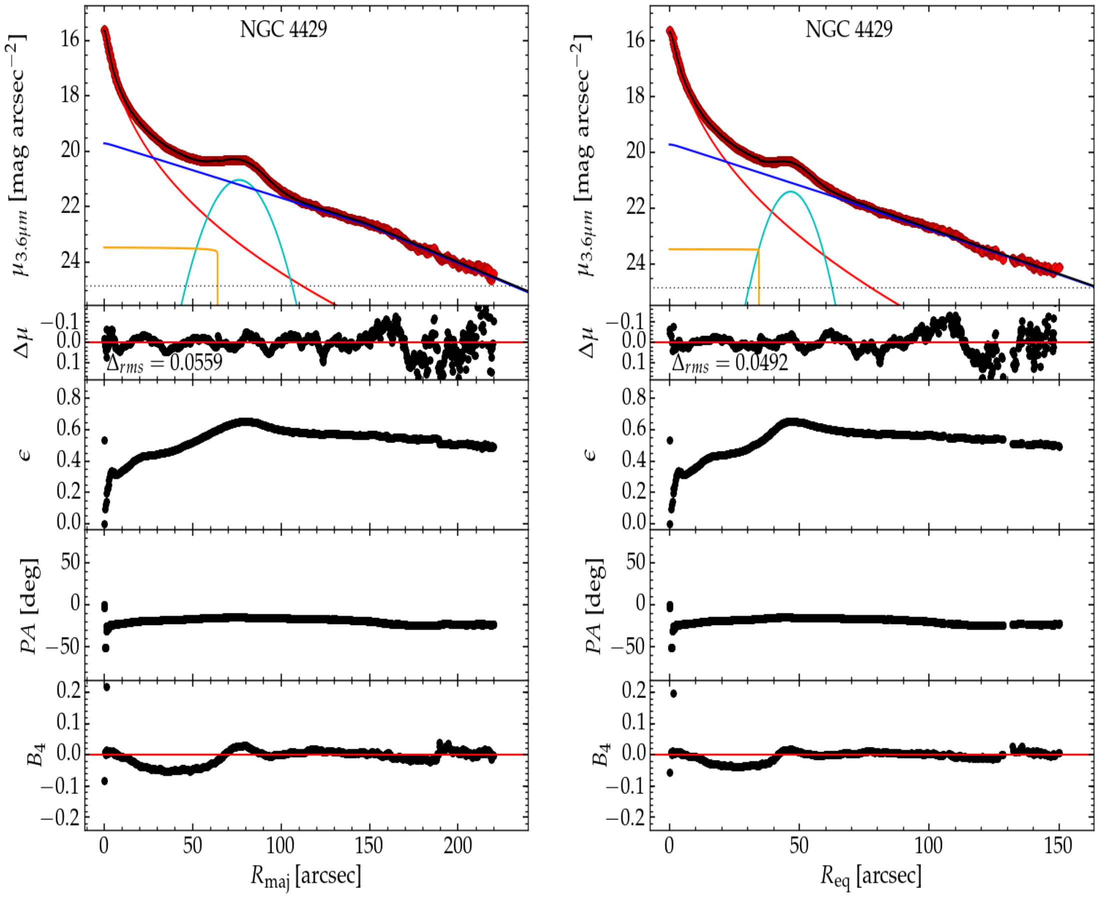

Figure A.17 NGC 4429: a lenticular galaxy with a boxy (peanut shell)-shaped bulge and a bar (Davis et al., 2018b) fit using a Sérsic and a Ferrers (—) function, respectively. The galaxy has a prominent outer ring at around $R_{maj} \approx 80''$, fit here using a Gaussian (—), plus a truncated (at around $150''$ along R_{maj}) exponential disk (—).

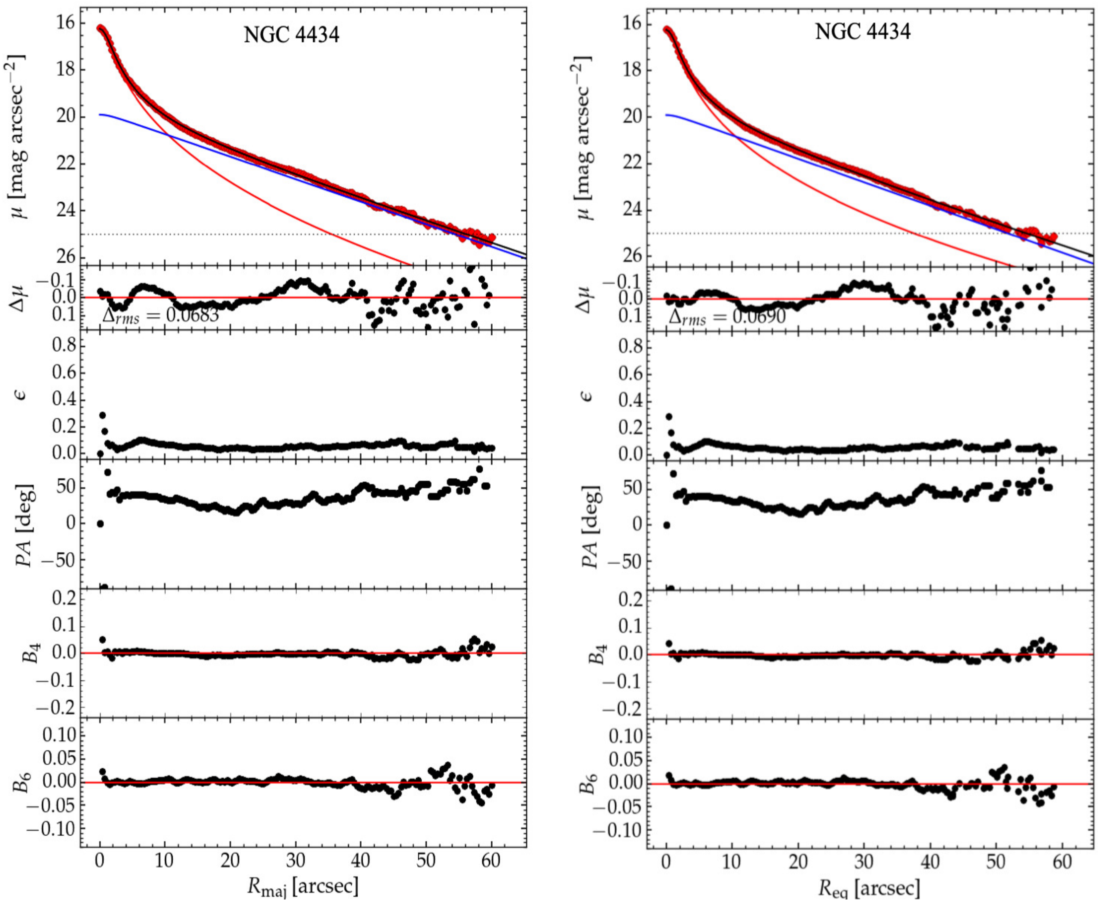

Figure A.18 NGC 4434: a lenticular galaxy with a Sérsic bulge (—) and an exponential disk (—).

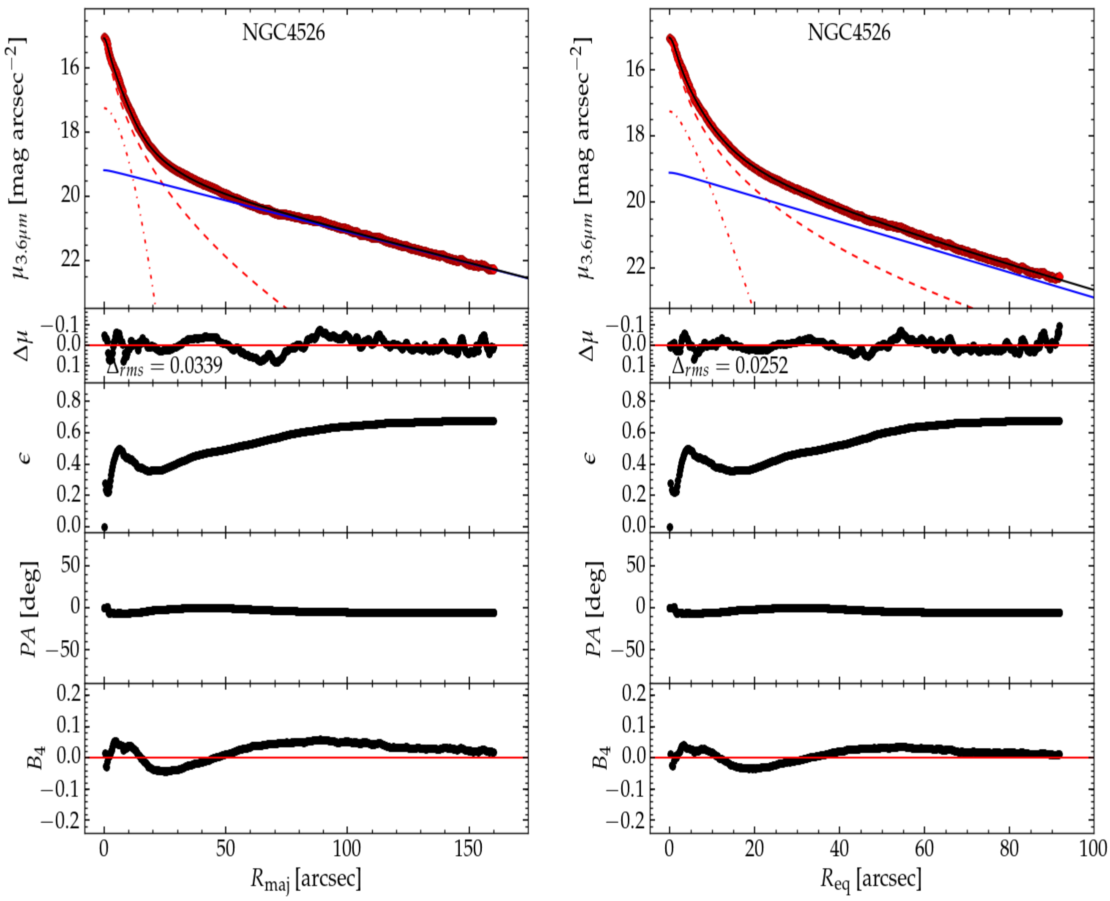

Figure A.19 NGC 4526: a lenticular galaxy with a Sérsic bulge (- - -), an extended exponential disk (—), plus a fast rotating nuclear disk (Rubin, 1995) extending up to $\sim 20''$ and causing the bump in the ellipticity and B_4 profile. The nuclear disk is fit using a low Sérsic index function (-·-·-). A faint bar, as claimed by de Vaucouleurs et al. (1991), could not be clearly seen in the Spitzer image of the galaxy. However, the addition of a weak bar ending at $R_{maj} \approx 40 - 50''$, coupled with a broken exponential disk with a bend at $R_{maj} \approx 90''$, might be plausible but would not greatly impact on our bulge parameters.

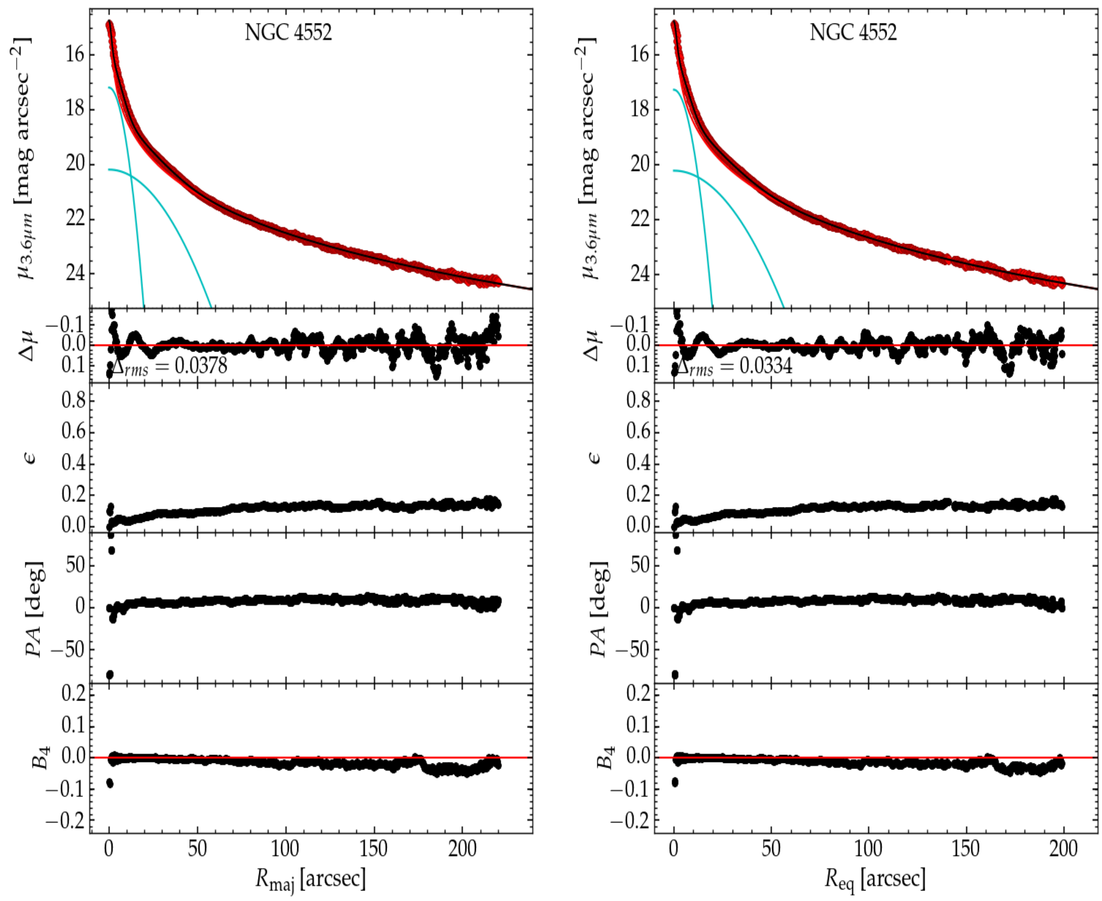

Figure A.20 NGC 4552: a massive elliptical galaxy with a dust ring at its core (Bonfini et al., 2018) which blocks light in the optical filter and can mimic the depleted core of a core-Sérsic galaxy, while in near-infrared filters it can mimic a central point source. Hence, we fit a central Gaussian (—) for extra light, a Sérsic function (—) for the extended spheroid, and another Gaussian (—) at the bump in the light profile at $R_{maj} \approx 35''$ which could be due to light from an undigested galaxy.

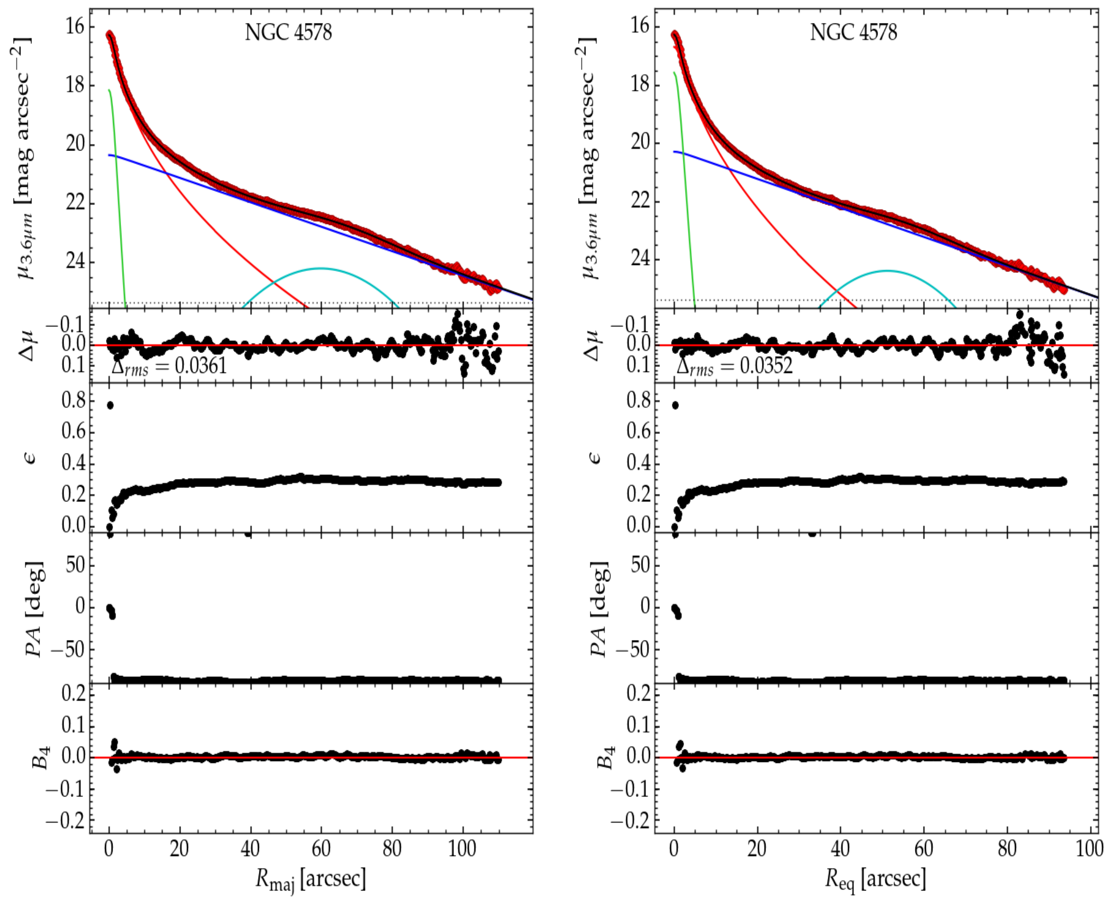

Figure A.21 NGC 4578: a lenticular galaxy with a central point source (—), a Sérsic bulge (—), an exponential disk (—) and a faint ring (de Vaucouleurs et al., 1991) bumping up the light profile at ($R_{maj} \approx 67''$).

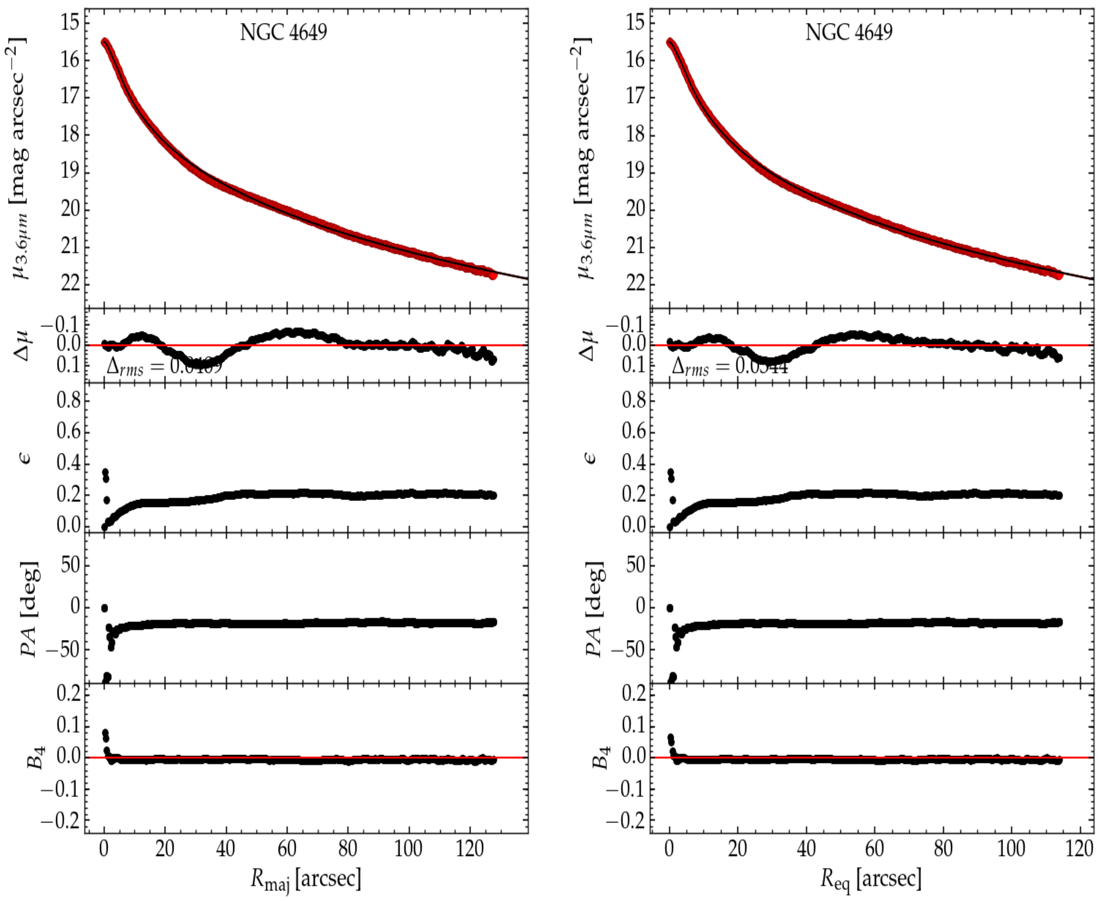

Figure A.22 NGC 4649: a massive elliptical galaxy with a deficit of light at its core, fit using a core-Sérsic function (—).

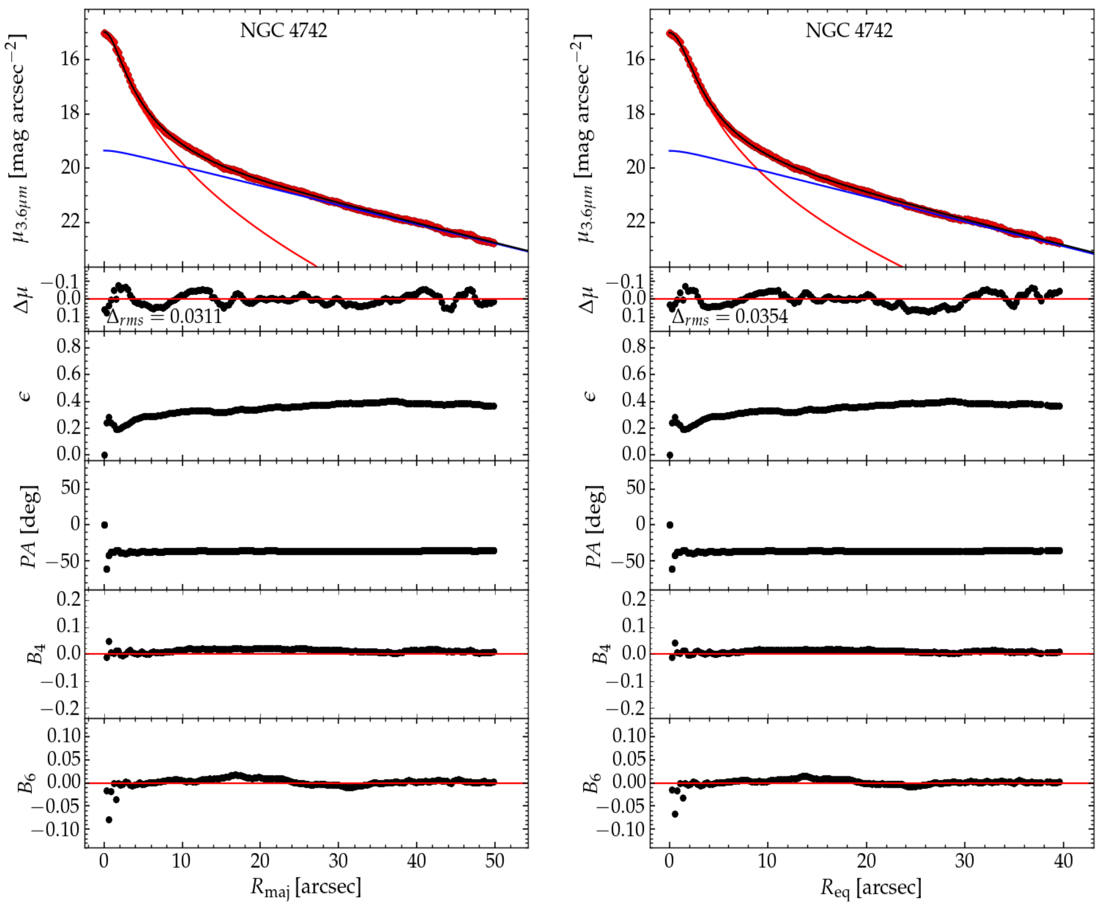

Figure A.23 NGC 4742: a lenticular galaxy with a Sérsic bulge (—) and an exponential disk (—).

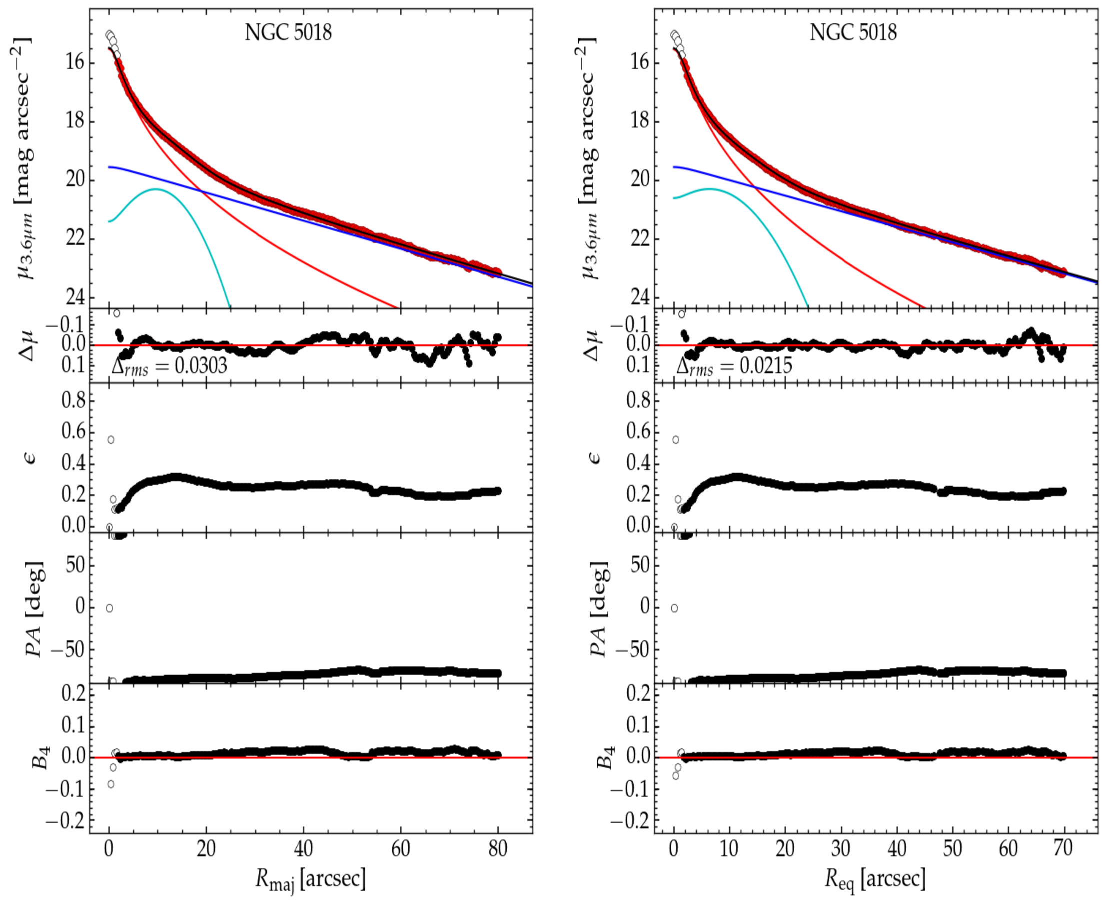

Figure A.24 NGC 5018: a post-merger remnant (Buson et al., 2004), lenticular galaxy with an elongated debris tail revealing the previous merger. We have added a Gaussian (—) for the bump in the profile at $R_{maj} \approx 14''$ — accounting for the undigested merged galaxy — along with a Sérsic bulge (—), plus an exponential disk (—). We excluded the inner data (up to $2''$) during the fitting.

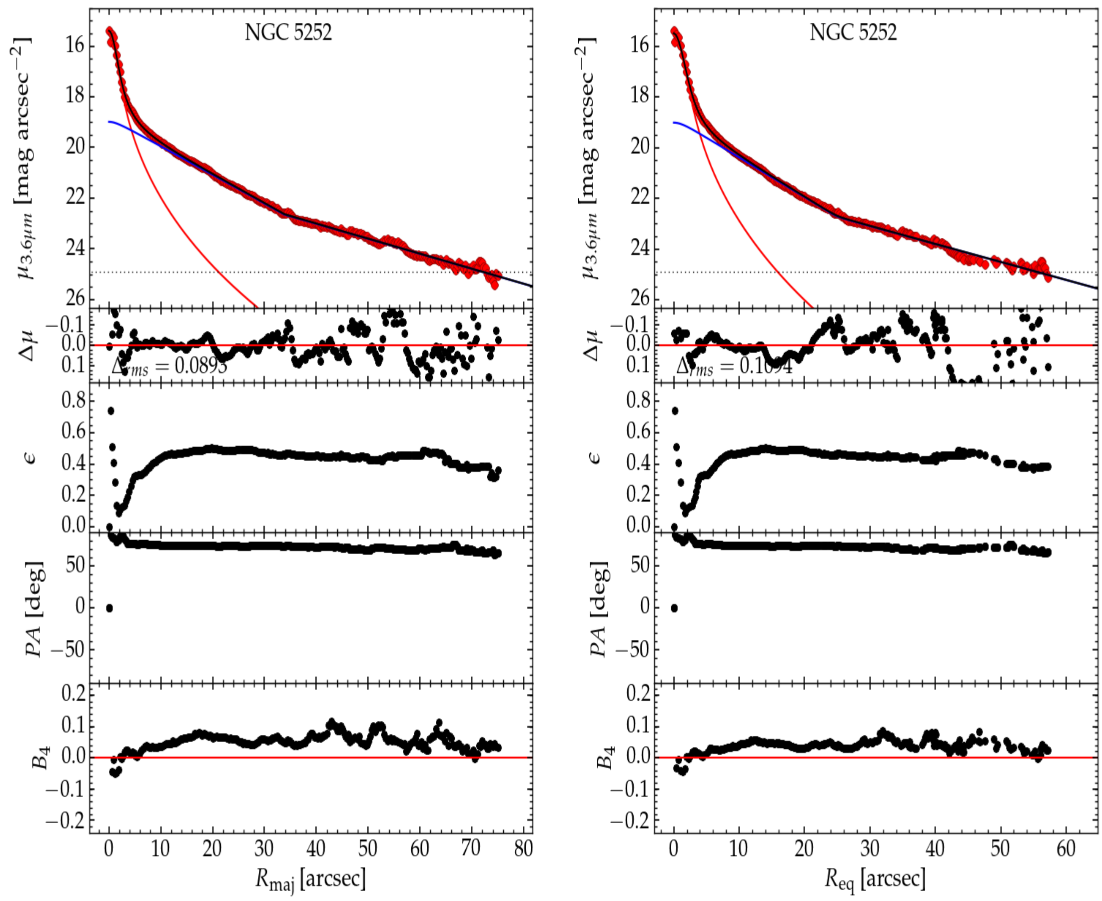

Figure A.25 NGC 5252: a lenticular galaxy with a with Sérsic bulge (—) and a warped truncated disk (—). NGC 5252 hosts a pair of AGNs, one is the central SMBH while the other (at 10 kpc distance from center) is an intermediate mass black hole (Yang et al., 2017). With $R_{e,sph} = 0.672$ kpc, $M_{*,sph} = 7.1 \times 10^{10} M_{\odot}$,and $M_{*,gal} = 2.4 \times 10^{11} M_{\odot}$, NGC 5252 is a "compact massive spheroid".

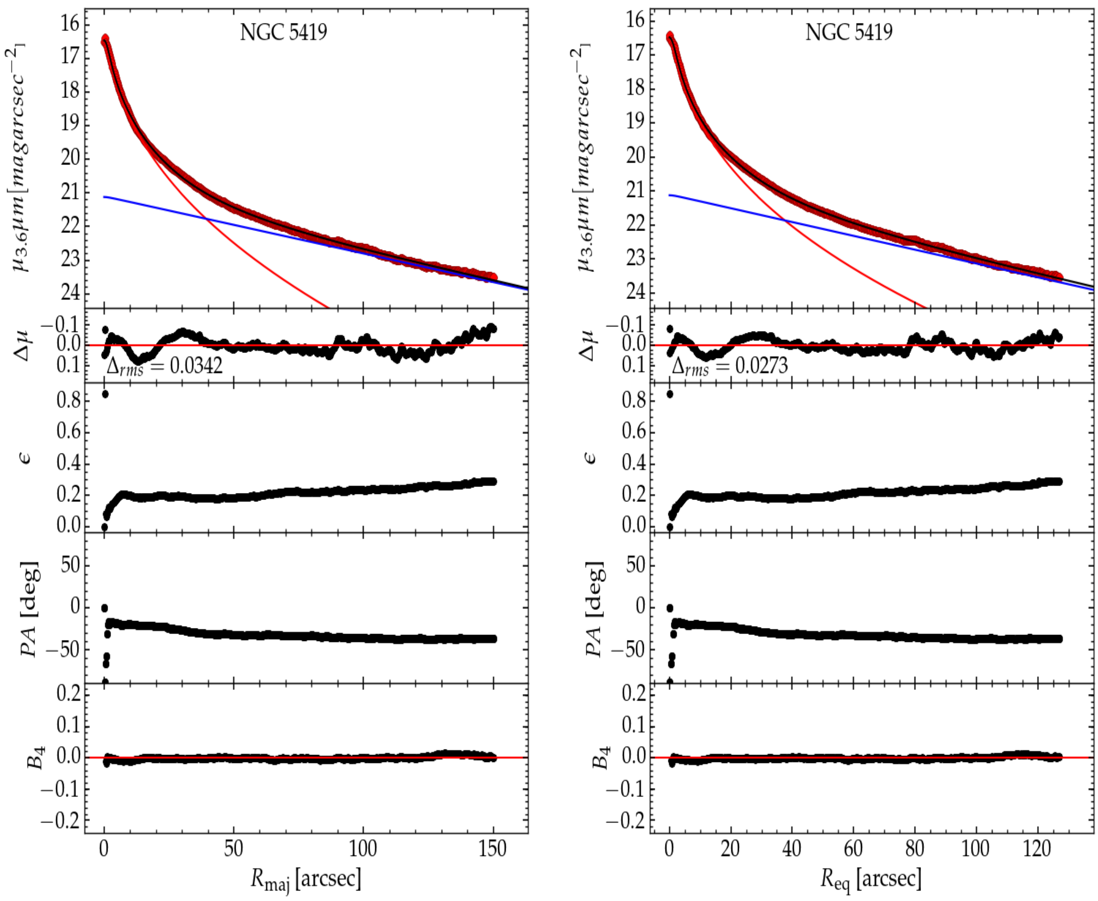

Figure A.26 NGC 5419: a "BCG (Coziol et al., 2009)" massive elliptical galaxy with a depleted core (Mazzalay et al., 2016) and an extended stellar halo. Its spheroid is fit using a core-Sérsic function (—) and for its halo we use an exponential (—) function (de Vaucouleurs, 1969; Seigar et al., 2007). We do not include the (cluster's) halo light as a part of the galaxy's total light.

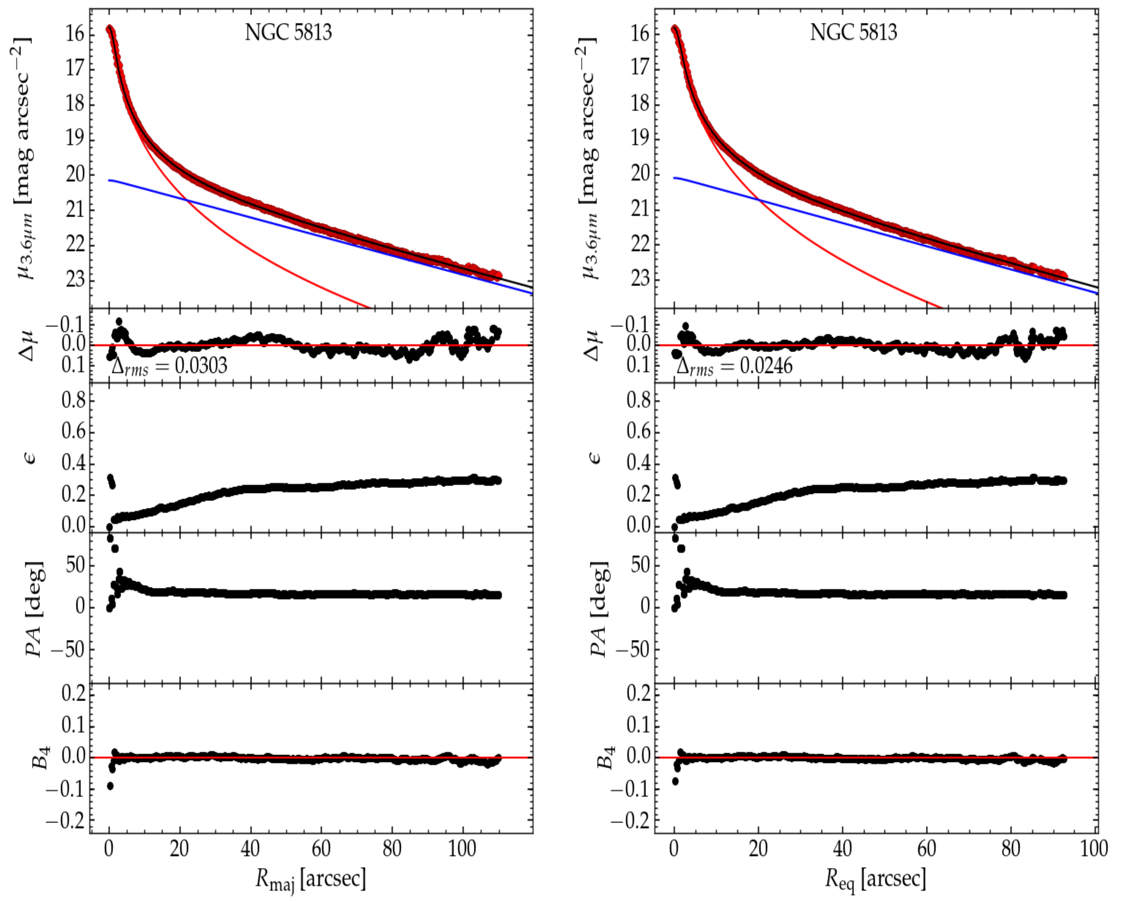

Figure A.27 NGC 5813: a core-Sérsic (—) galaxy (Dullo & Graham, 2014) with an outer exponential (—) disk (Trujillo et al., 2004). It also has a counter-rotating core (Carter & Jenkins, 1993) which could not be resolved.

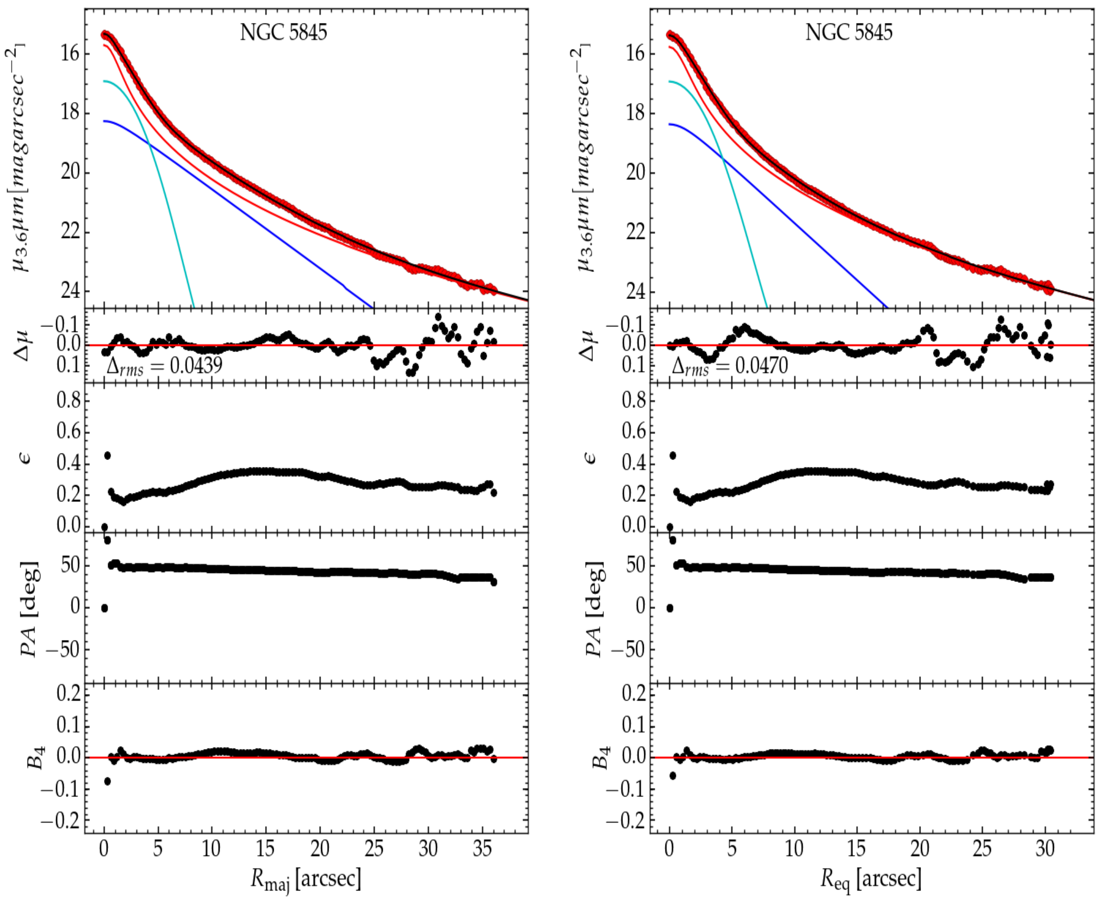

Figure A.28 NGC 5845: an ellicular galaxy with an extended Sérsic spheroid (—) and an intermediate-scale disk (—) suggested by the elevation in the ellipticity profile around $R_{maj} \approx 14''$. Kormendy (2000) call it a "Rosetta stone" object which contains a dust disk and a stellar disk. The double peak rotation curve in Jiang et al. (2012) suggests that there is another inner disk, which we fit with a Gaussian (—).

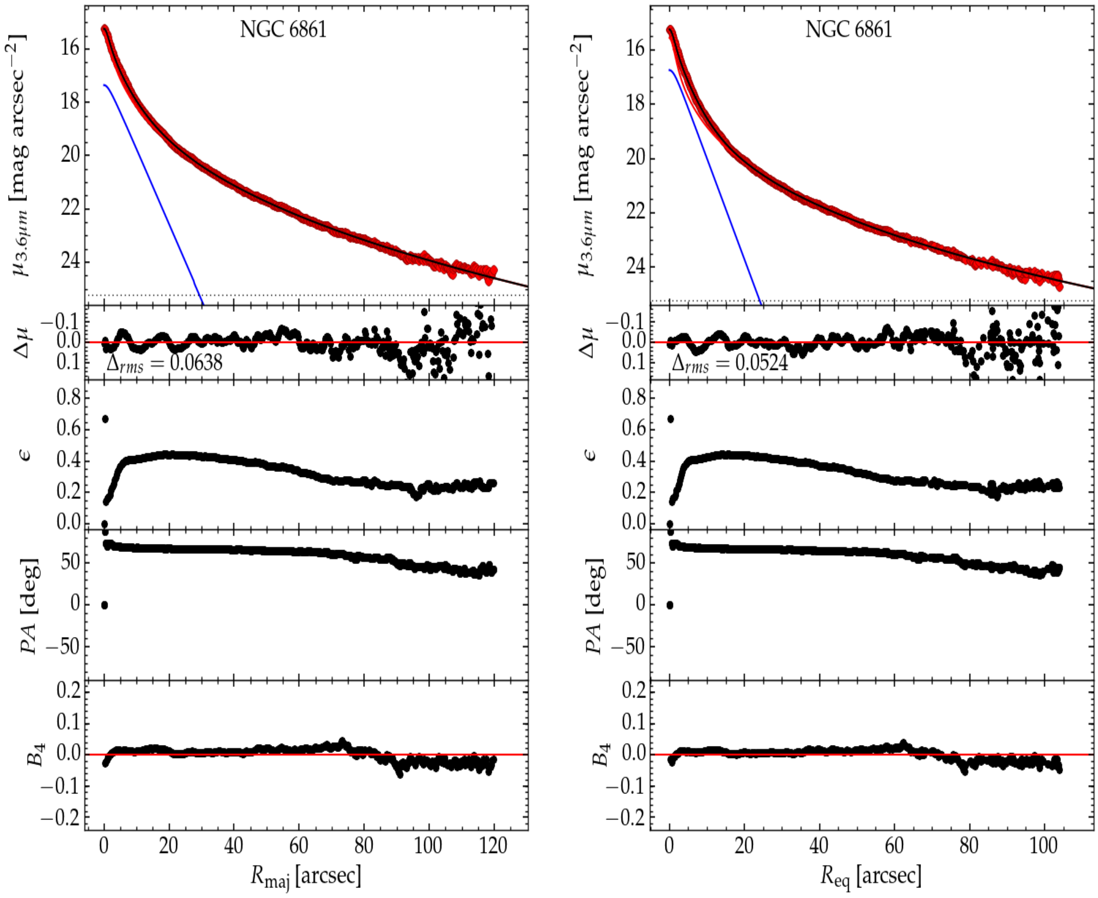

Figure A.29 NGC 6861: an ellicular (ES) galaxy with an extended Sérsic bulge (—) plus an intermediate-scale disk (Rusli et al., 2013b; Escudero et al., 2015) fit here using an exponential function (—).

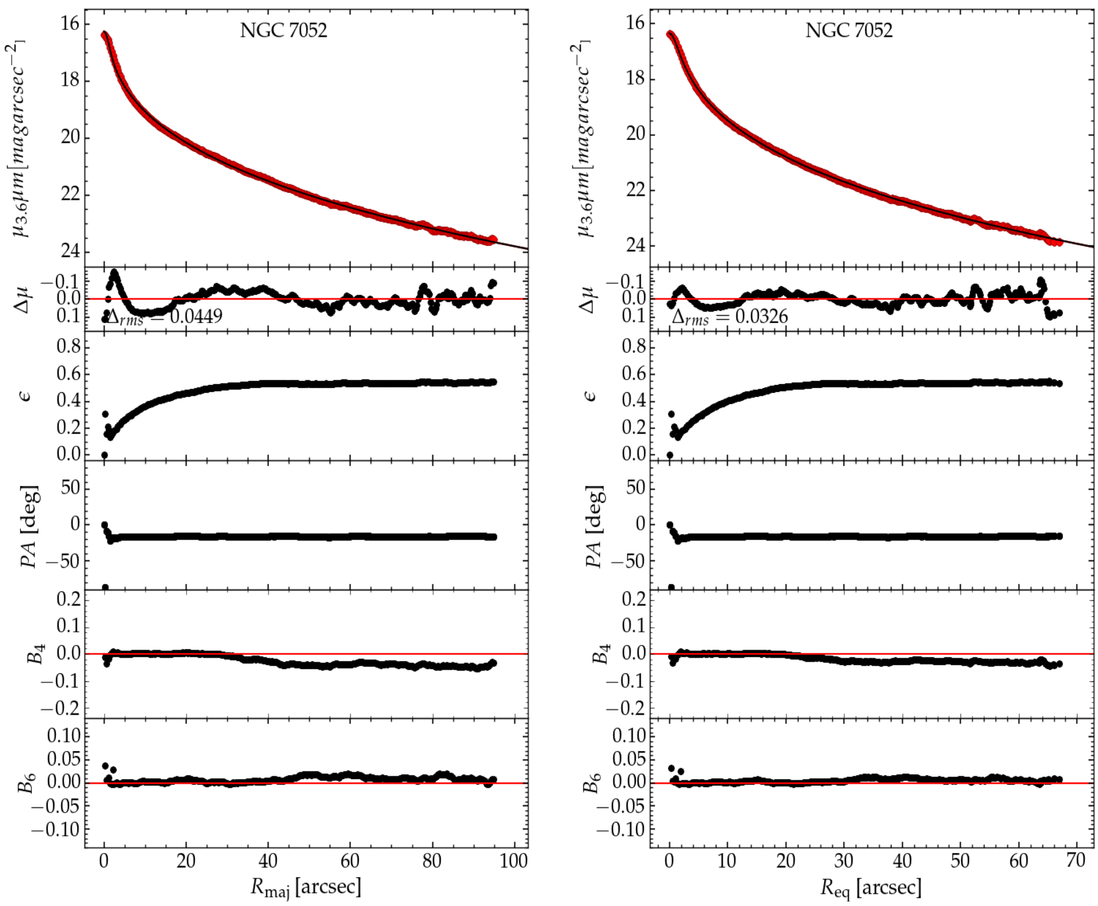

Figure A.30 NGC 7052: a massive elliptical core-Sérsic (—) galaxy (Quillen et al., 2000).

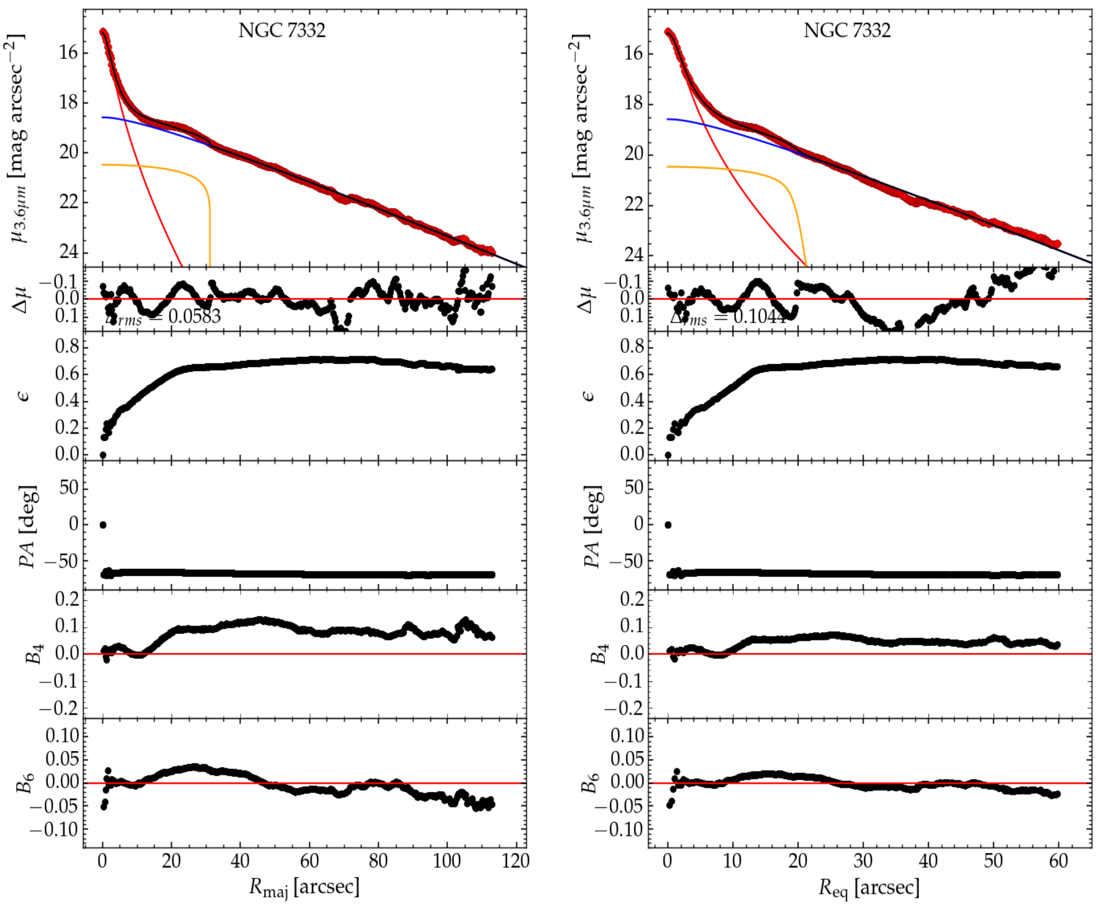

Figure A.31 NGC 7332: a peculiar (edge-on) lenticular galaxy. It has a Sérsic bulge (—), a weak bar (Falcón-Barroso et al., 2004) fit using a Ferrers (—) function, and an outer exponential truncated disk (—). According to Falcón-Barroso et al. (2004), NGC 7332 also has an inner disk but it could not be seen in the Spitzer image.

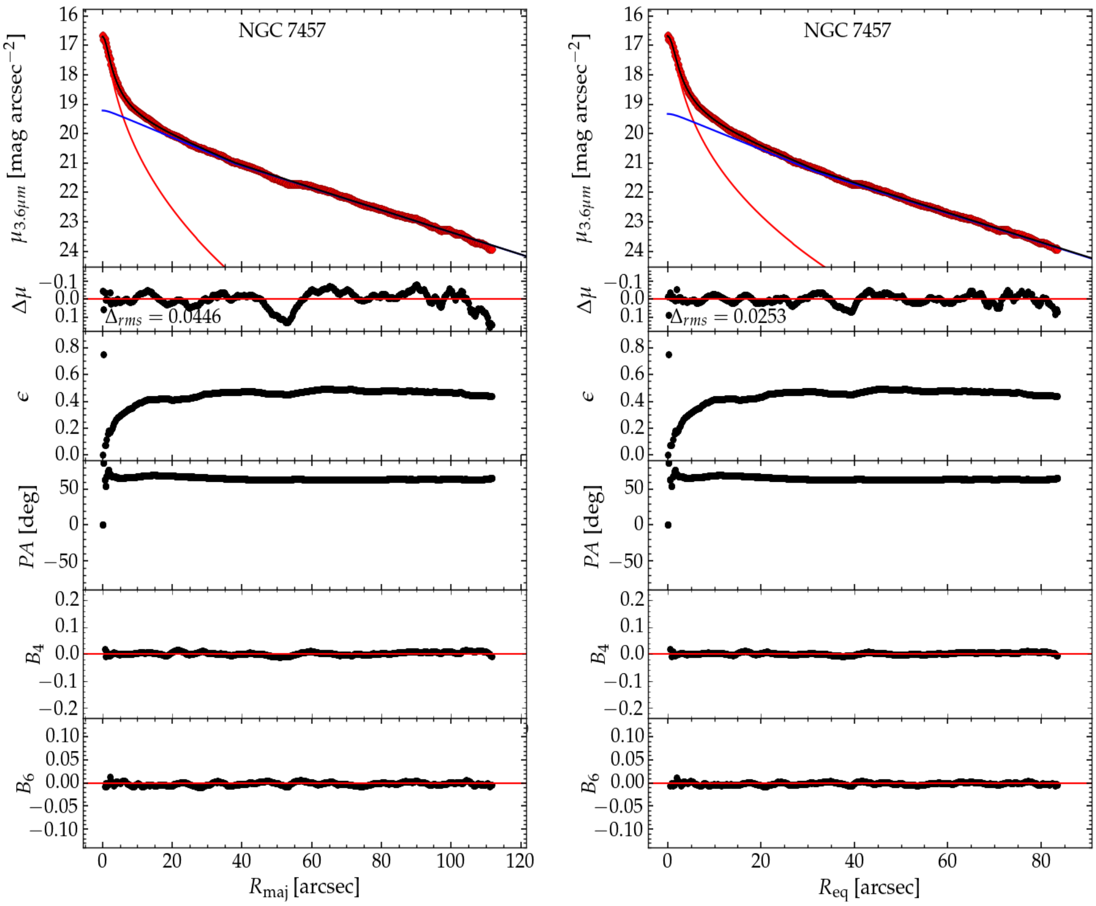

Figure A.32 NGC 7457: a lenticular galaxy with a Sérsic bulge (—) and truncated exponential disk (—).

A.1.2 Light profile from K_s-band images (AB mag)

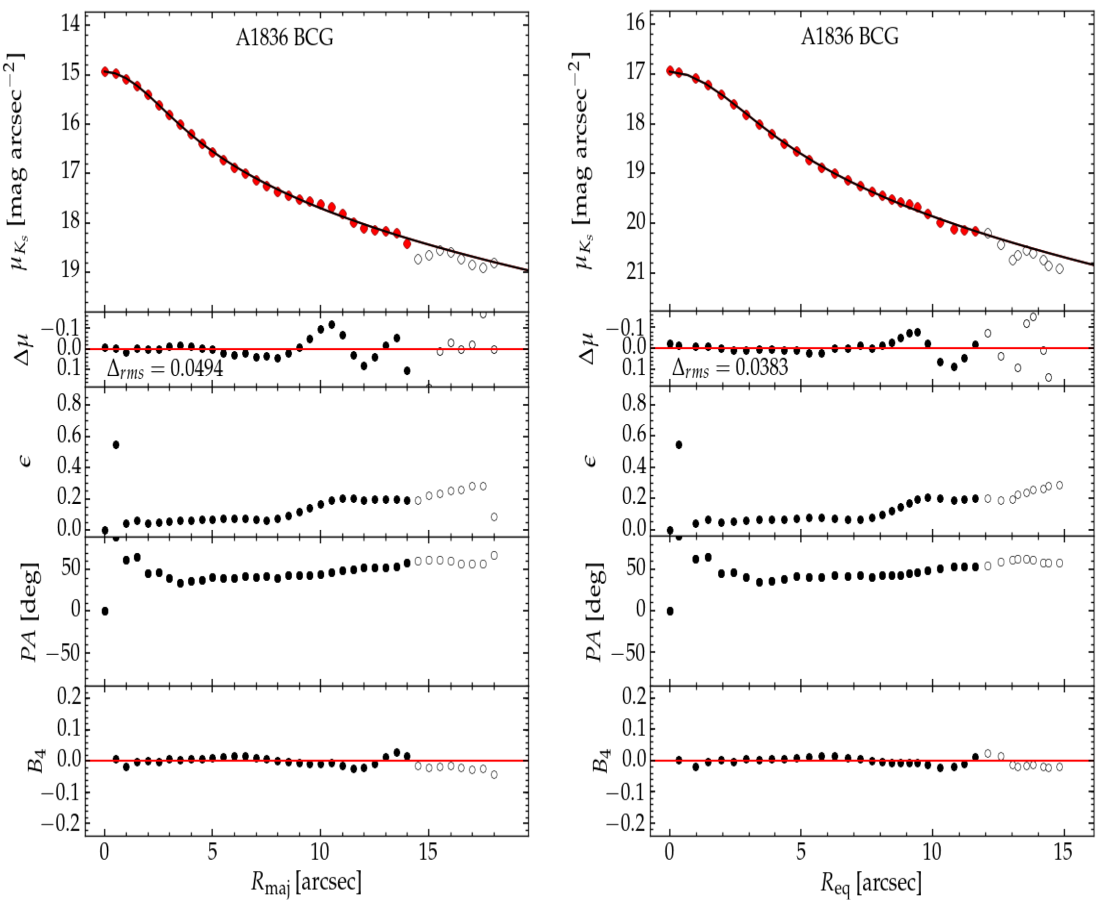

Figure A.33 A1836 BCG: a massive elliptical Brightest Cluster Galaxy (BCG). Its light profile and very high velocity dispersion suggests that it may have a depleted core, hence we fit its light profile using a core-Sérsic function (—).

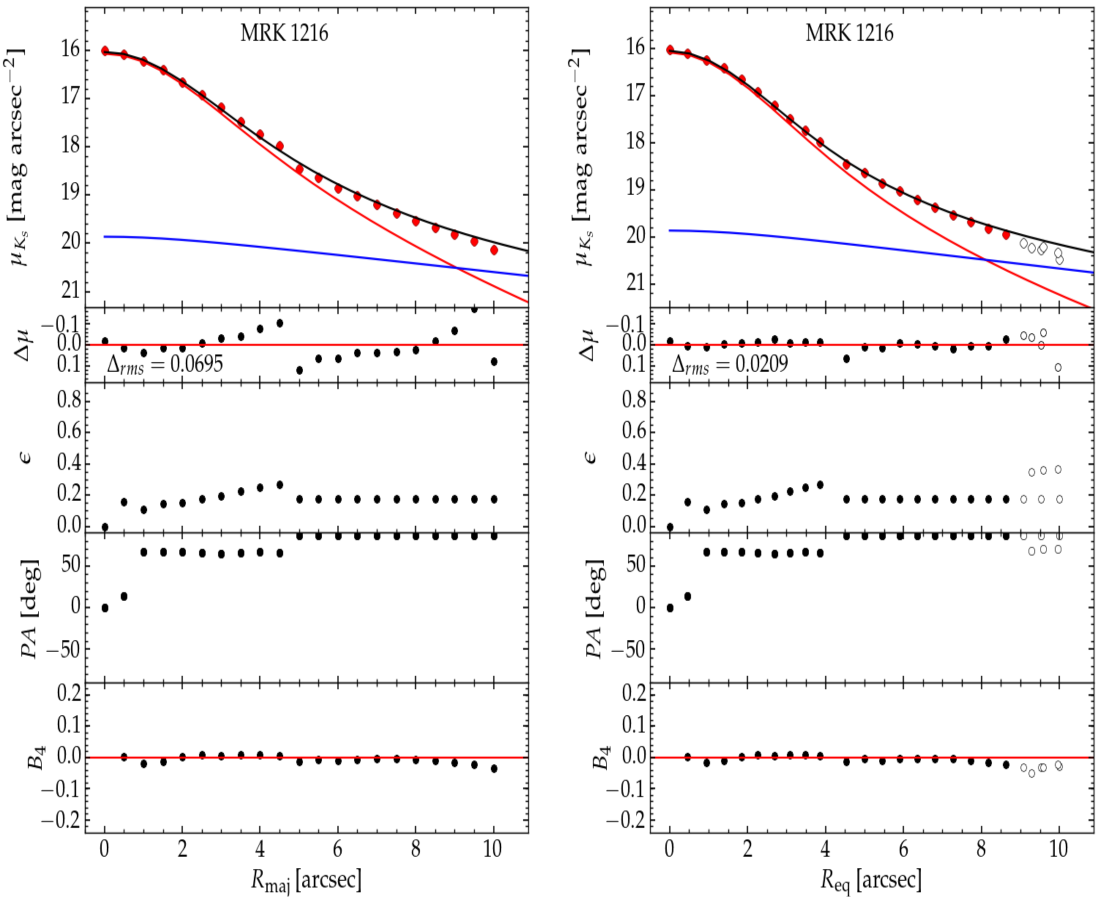

Figure A.34 MRK 1216: an ellicular galaxy with a Sérsic bulge (—) and with a flat exponential model (—) fit here to the stellar halo (Yıldırım et al., 2015). With limited radial extent, and mediocre spatial resolution, our surface brightness profile does not enable a detailed decomposition. Comparison with Savorgnan & Graham (2016a) suggests that we may be in error with this galaxy. However it does not stand out as unusual in our diagrams involving $M_{*,sph}$.

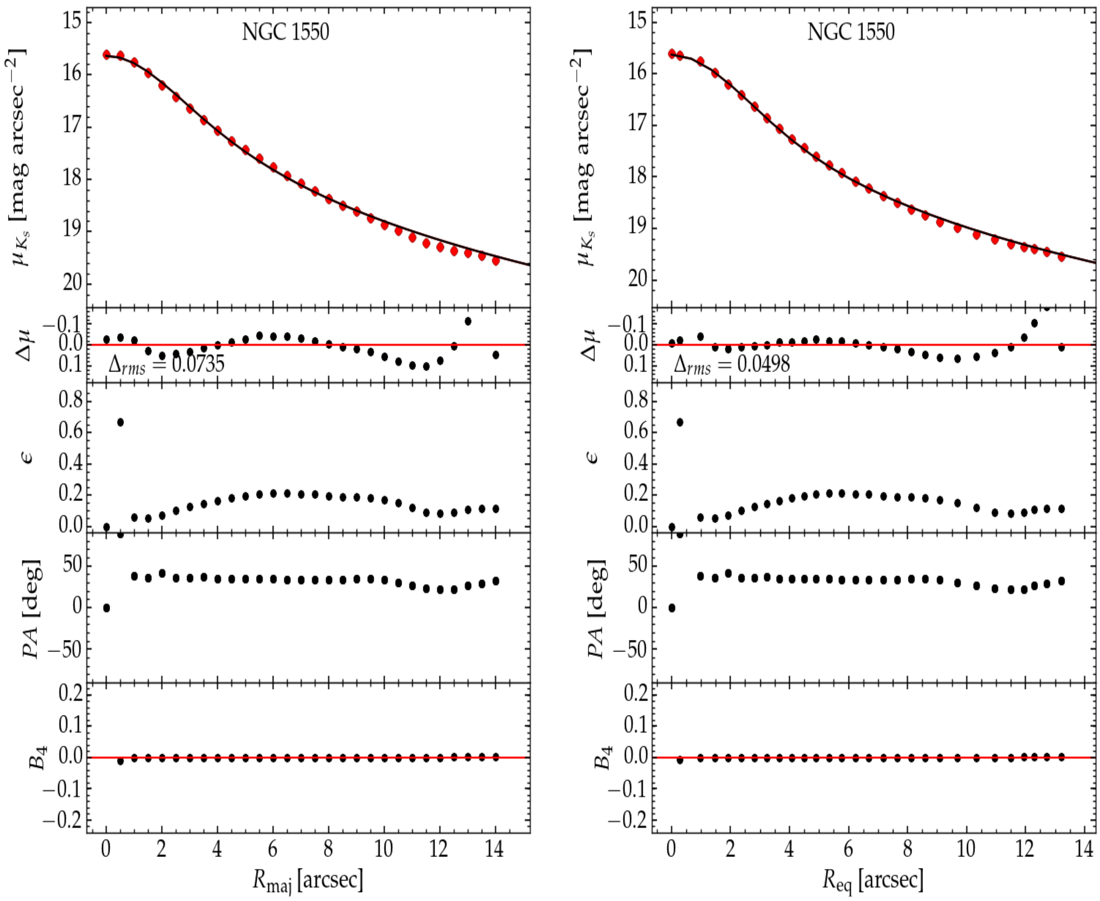

Figure A.35 NGC 1550: an elliptical galaxy with a depleted core (Rusli et al., 2013a), fit using a core-Sérsic function (—).

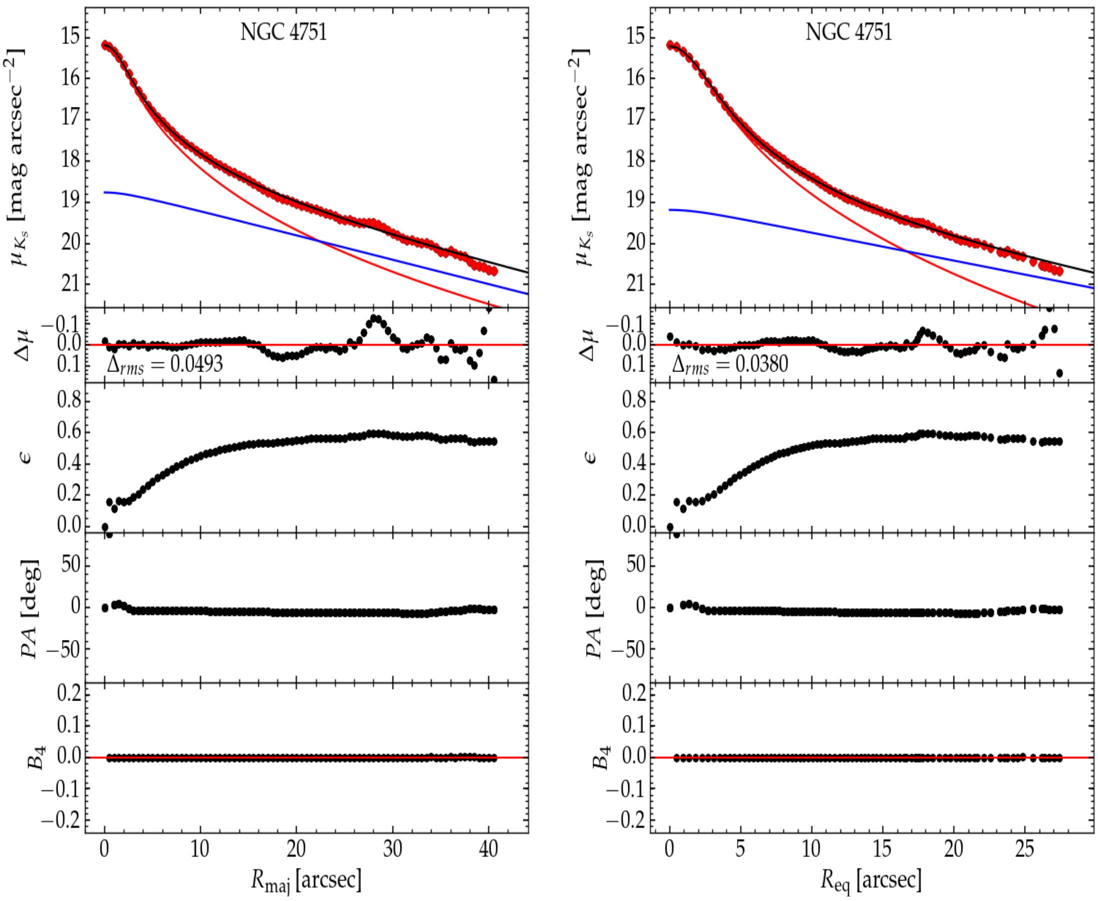

Figure A.36 NGC 4751: a lenticular galaxy with a very high velocity dispersion and M_{BH} which suggest it may have a depleted core. Hence, we fit a core-Sérsic function (—) to its spheroid, plus an extended exponential disk (—).

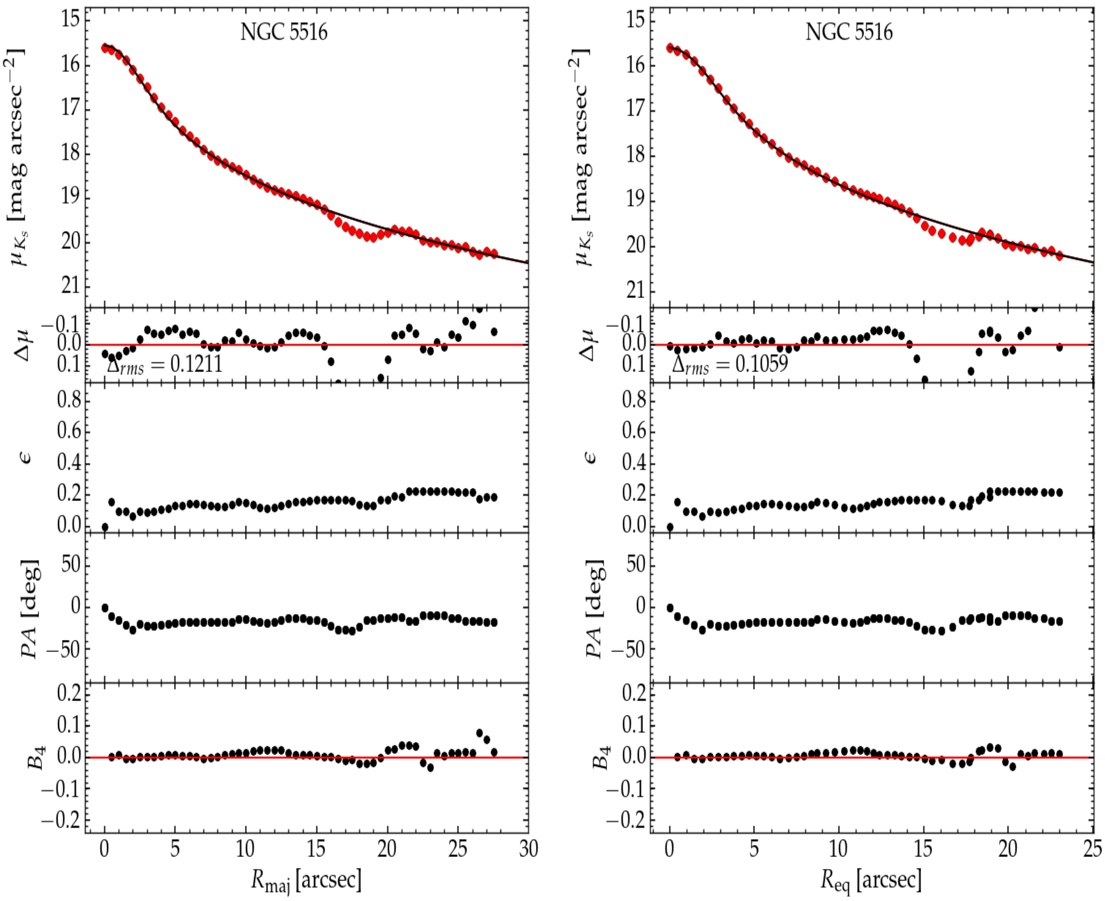

Figure A.37 NGC 5516: an elliptical galaxy (Rusli et al., 2013a) fit using a core-Sérsic function (—).

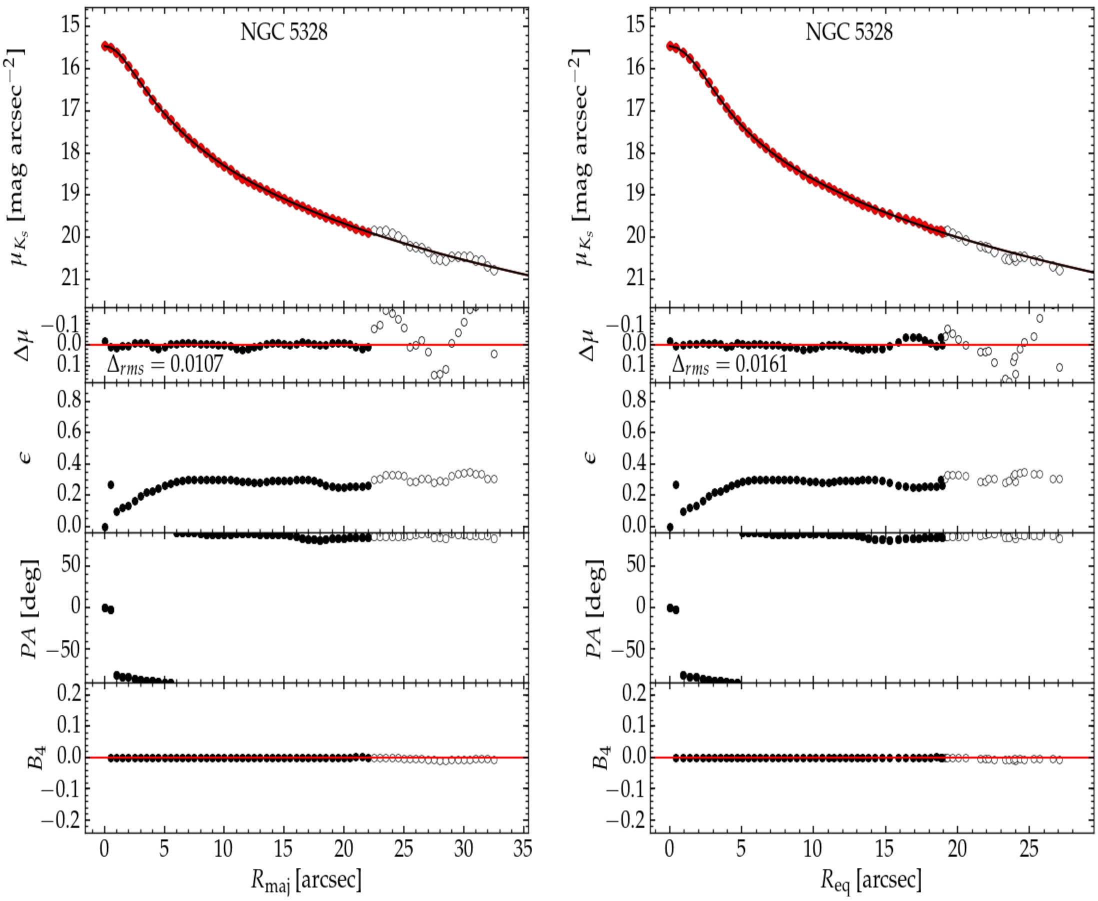

Figure A.38 NGC 5328: a massive elliptical core-Sérsic (—) galaxy (Rusli et al., 2013a).

A.1.3 Light profile from SDSS r'-band images (AB mag)

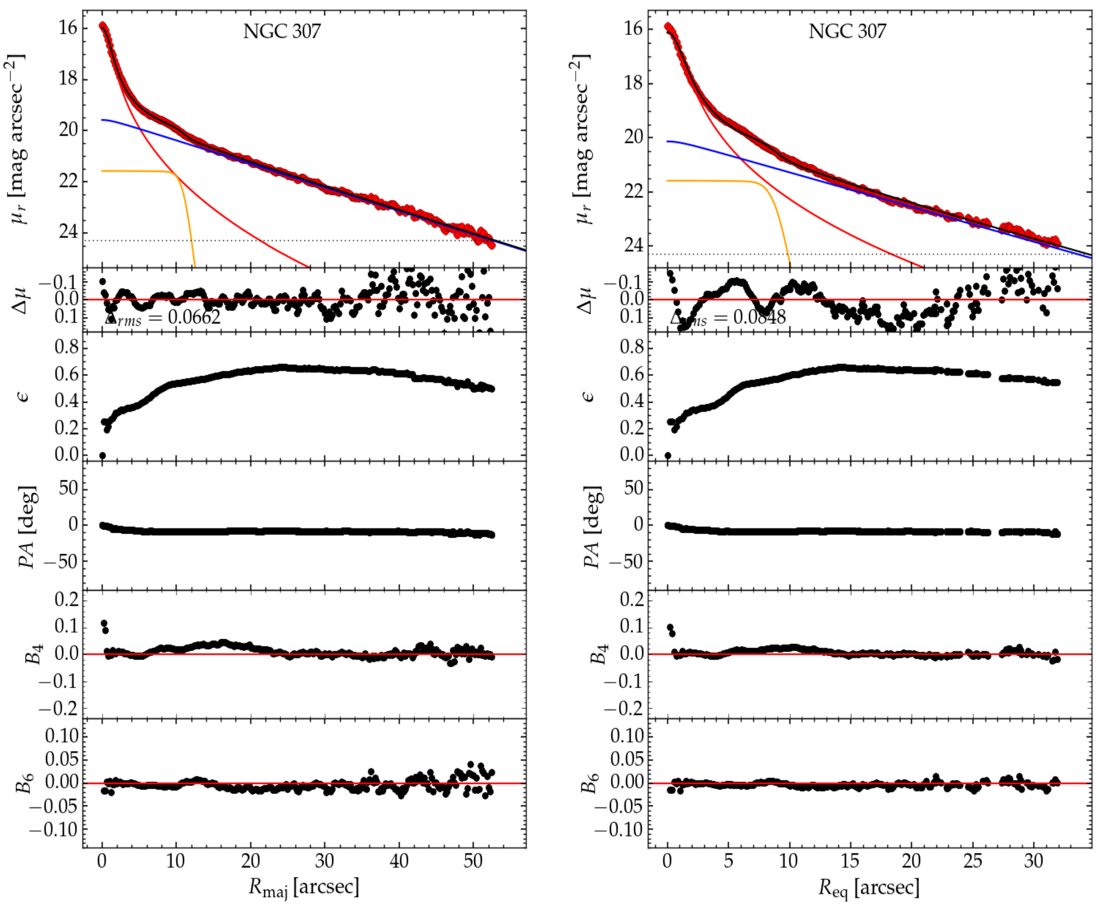

Figure A.39 NGC 307: a lenticular galaxy with a weak bar (Erwin et al., 2018) fit using a Ferrers (—) function, along with a Sérsic bulge (—), and an exponential disk (—).

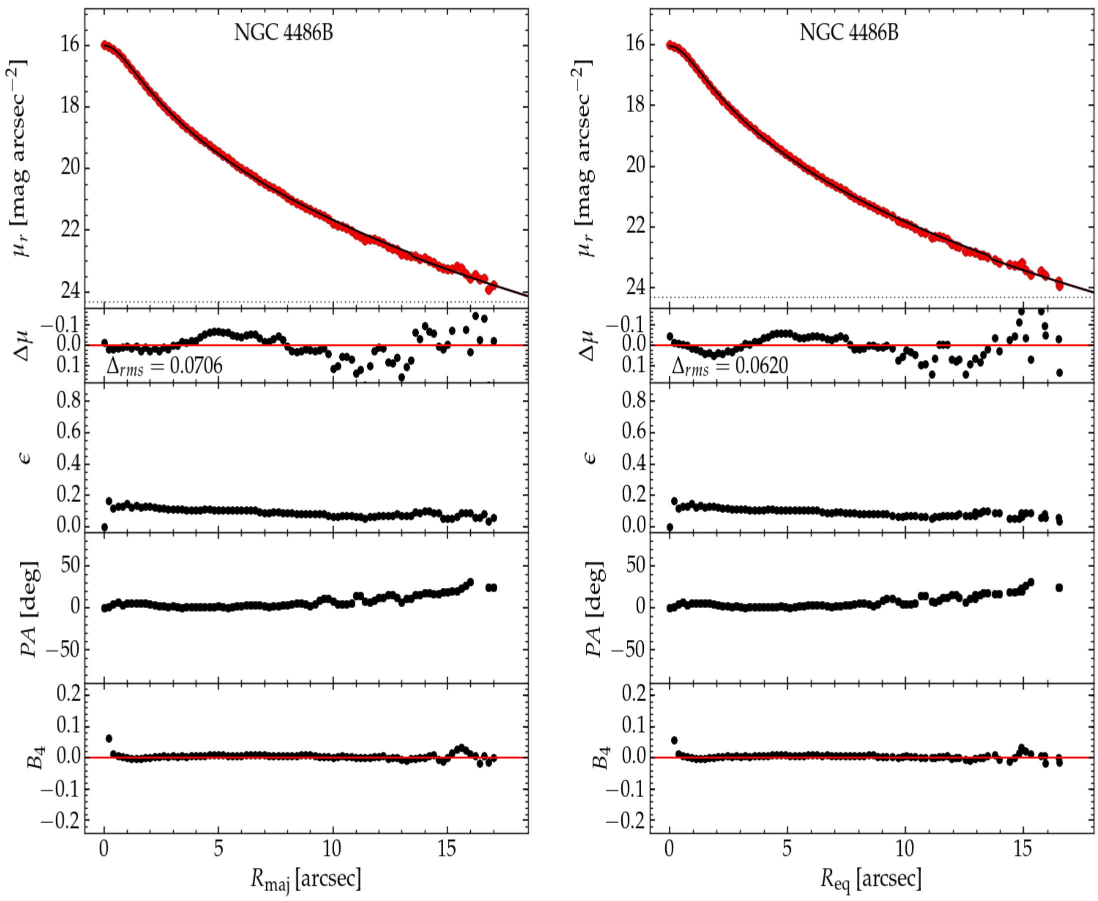

Figure A.40 NGC 4486B: a “compact elliptical” galaxy fit with a Sérsic bulge (—). Most of its mass is stripped off due to the gravitational interaction with the massive companion galaxy NGC 4486.

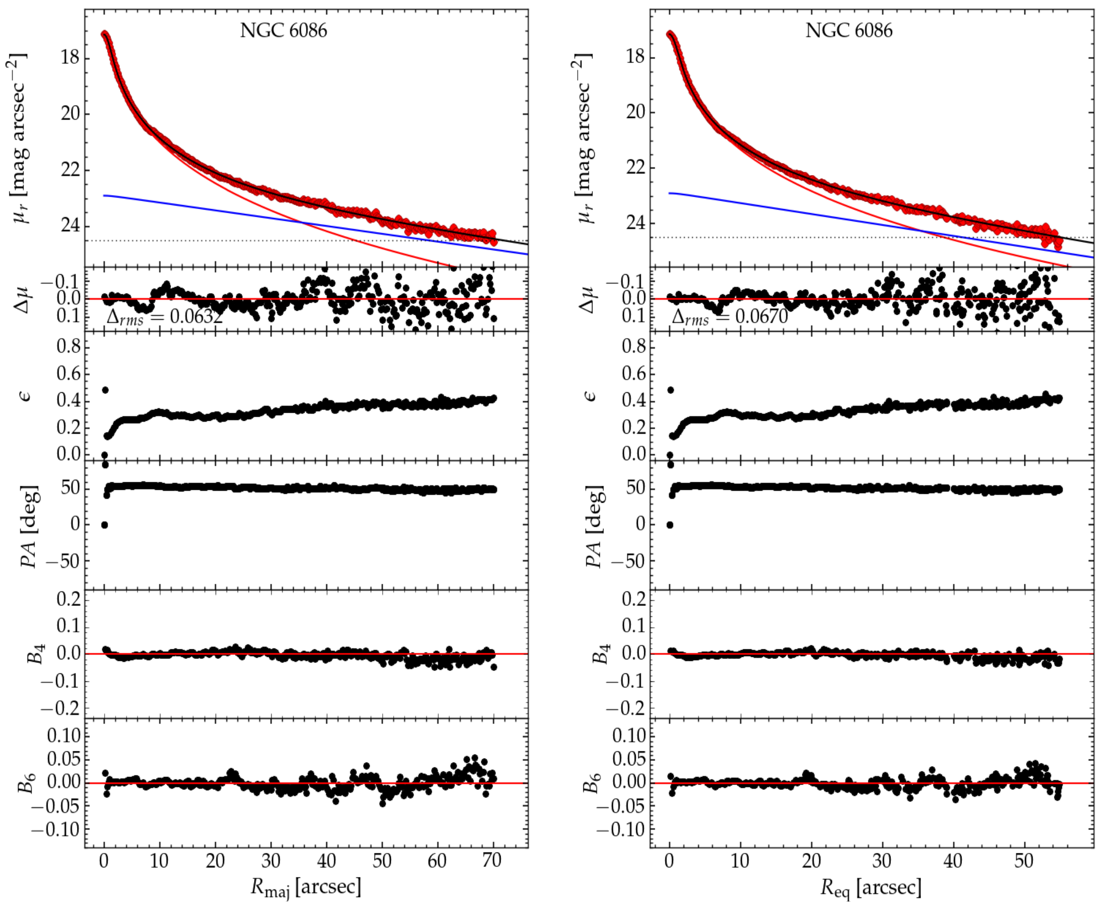

Figure A.41 NGC 6086: a massive elliptical BCG, with a depleted core (Laine et al., 2003) fit using a core-Sérsic function (—) plus an extended halo fit using an exponential (—) function (de Vaucouleurs, 1969; Seigar et al., 2007). According to Carter et al. (1999), NGC 6086 has a counter-rotating core but a rather slow rotation at the outer radii. The total galaxy light does not include the light from the (cluster) halo.

B

Appendix

Table B.1. Black Hole Mass versus Velocity Dispersion [$\log(M_{\rm BH}/{\rm M}_\odot) = \alpha \log(\sigma/200) + \beta$]

Regression (1)	**Minimization** (2)	α (3)	β (dex) (4)	ϵ (dex) (5)	$\Delta_{rms\|BH}$ (dex) (6)	r (7)	r_s (8)
			Early-Type and Late-Type Galaxies				
			91 Early-Type Galaxies				
BCES(*Bisector*)	*Symmetric*	5.71 ± 0.33	8.32 ± 0.05	0.32	0.44		
BCES($M_{\rm BH}\|\sigma$)	$M_{\rm BH}$	5.22 ± 0.36	8.34 ± 0.05	0.32	0.43	0.86	0.85
BCES($\sigma\|M_{\rm BH}$)	σ	6.29 ± 0.35	8.29 ± 0.06	0.34	0.47		
			46 Late-Type Galaxies				
BCES(*Bisector*)	*Symmetric*	5.82 ± 0.75	8.17 ± 0.14	0.57	0.63		
BCES($M_{\rm BH}\|\sigma$)	$M_{\rm BH}$	4.07 ± 0.90	7.90 ± 0.17	0.54	0.58	0.59	0.49
BCES($\sigma\|M_{\rm BH}$)	σ	10.06 ± 1.74	8.83 ± 0.30	0.85	0.96		
			Single Regression on (137) Early and Late-Type Galaxies				
BCES(*Bisector*)	*Symmetric*	6.10 ± 0.28	8.27 ± 0.04	0.43	0.53		
BCES($M_{\rm BH}\|\sigma$)	$M_{\rm BH}$	5.50 ± 0.29	8.26 ± 0.04	0.42	0.51	0.86	0.87
BCES($\sigma\|M_{\rm BH}$)	σ	6.82 ± 0.32	8.29 ± 0.05	0.46	0.58		
			Sérsic and Core-Sérsic Galaxies				
			102 Sérsic Galaxies				
BCES(*Bisector*)	*Symmetric*	5.75 ± 0.34	8.24 ± 0.05	0.46	0.55		
BCES($M_{\rm BH}\|\sigma$)	$M_{\rm BH}$	4.86 ± 0.34	8.16 ± 0.05	0.45	0.52	0.78	0.78
BCES($\sigma\|M_{\rm BH}$)	σ	7.02 ± 0.52	8.34 ± 0.07	0.54	0.64		
			35 Core-Sérsic Galaxies				
BCES(*Bisector*)	*Symmetric*	8.64 ± 1.10	7.91 ± 0.20	0.25	0.46		
BCES($M_{\rm BH}\|\sigma$)	$M_{\rm BH}$	7.74 ± 1.15	8.04 ± 0.18	0.25	0.43	0.73	0.65
BCES($\sigma\|M_{\rm BH}$)	σ	9.77 ± 1.70	7.74 ± 0.31	0.27	0.52		
			Galaxies with and without a disk				
			93 ES, S0, Sp-Type Galaxies				
BCES(*Bisector*)	*Symmetric*	5.72 ± 0.34	8.22 ± 0.06	0.47	0.56		
BCES($M_{\rm BH}\|sigma$)	$M_{\rm BH}$	4.86 ± 0.35	8.15 ± 0.05	0.45	0.53	0.79	0.78
BCES($\sigma\|M_{\rm BH}$)	σ	6.94 ± 0.51	8.32 ± 0.07	0.54	0.64		
			44 E-Type Galaxies				

Table B.1 (cont'd)

Regression (1)	Minimization (2)	α (3)	β (dex) (4)	ϵ (dex) (5)	$\Delta_{rms\|BH}$ (dex) (6)	r (7)	r_s (8)
BCES($Bisector$)	*Symmetric*	6.69 ± 0.59	8.25 ± 0.10	0.30	0.43		
BCES($M_{\rm BH}\|\sigma$)	$M_{\rm BH}$	6.05 ± 0.67	8.32 ± 0.10	0.29	0.41	0.82	0.80
BCES($\sigma\|M_{\rm BH}$)	σ	7.47 ± 0.69	8.16 ± 0.12	0.32	0.47		
Galaxies with and without a bar							
50 Barred Galaxies							
BCES($Bisector$)	*Symmetric*	5.30 ± 0.54	8.14 ± 0.10	0.45	0.53		
BCES($M_{\rm BH}\|\sigma$)	$M_{\rm BH}$	3.97 ± 0.59	7.97 ± 0.10	0.43	0.49	0.65	0.61
BCES($\sigma\|M_{\rm BH}$)	σ	7.86 ± 1.30	8.48 ± 0.19	0.61	0.71		
87 Non-Barred Galaxies							
BCES($Bisector$)	*Symmetric*	6.16 ± 0.42	8.28 ± 0.06	0.40	0.51		
BCES($M_{\rm BH}\|\sigma$)	$M_{\rm BH}$	5.57 ± 0.43	8.30 ± 0.06	0.40	0.49	0.86	0.86
BCES($\sigma\|M_{\rm BH}$)	σ	6.88 ± 0.45	8.25 ± 0.07	0.44	0.55		
Galaxies with and without an AGN							
41 AGN host Galaxies							
BCES($Bisector$)	*Symmetric*	6.26 ± 0.49	8.21 ± 0.09	0.55	0.63		
BCES($M_{\rm BH}\|\sigma$)	$M_{\rm BH}$	5.37 ± 0.51	8.16 ± 0.09	0.53	0.60	0.83	0.79
BCES($\sigma\|M_{\rm BH}$)	σ	7.48 ± 0.66	8.28 ± 0.10	0.63	0.72		
96 Galaxies without AGN							
BCES($Bisector$)	*Symmetric*	5.92 ± 0.31	8.30 ± 0.05	0.37	0.48		
BCES($M_{\rm BH}\|\sigma$)	$M_{\rm BH}$	5.43 ± 0.33	8.29 ± 0.05	0.37	0.46	0.87	0.88
BCES($\sigma\|M_{\rm BH}$)	σ	6.51 ± 0.33	8.30 ± 0.05	0.39	0.51		

Note. — Columns: (1) Type of regression performed. (2) The coordinate direction in which the offsets from the regression line is minimized. (3) Slope of the regression line. (4) Intercept of the regression line. (5) Intrinsic scatter in the log($M_{\rm BH}$)-direction (using Equation 1 from Graham & Driver, 2007a). (6) Total root mean square (rms) scatter in the log($M_{\rm BH}$)-direction. (7) Pearson correlation coefficient. (8) Spearman rank-order correlation coefficient.

Table B.2. Regression Lines Including All 143 Galaxies With Velocity Dispersions [$\log(M_{\rm BH}/{\rm M}_{\odot}) = \alpha \log(\sigma/200) + \beta$]

Category (1)	Number (2)	α (3)	β (dex) (4)	ϵ (dex) (5)	$\Delta_{rms\|BH}$ (dex) (6)	r (7)	r_s (8)
Early-Type Galaxies	95	5.05 ± 0.26	8.37 ± 0.04	0.33	0.44	0.90	0.87
Late-Type Galaxies	48	4.47 ± 0.80	8.04 ± 0.15	0.67	0.70	0.56	0.46
All Galaxies	143	5.29 ± 0.32	8.30 ± 0.04	0.50	0.58	0.86	0.86
Sérsic Galaxies	108	4.83 ± 0.35	8.22 ± 0.06	0.52	0.59	0.80	0.77
Core-Sérsic Galaxies	35	8.50 ± 1.10	7.91 ± 0.20	0.25	0.46	0.73	0.65
Galaxies with a disk (ES, S0, Sp-types)	98	4.90 ± 0.38	8.21 ± 0.06	0.54	0.60	0.79	0.76
Galaxies without a disk (E-type)	45	5.41 ± 0.66	8.40 ± 0.10	0.31	0.42	0.88	0.82
Barred Galaxies	52	4.05 ± 0.54	8.01 ± 0.10	0.45	0.51	0.74	0.66
Non-Barred Galaxies	91	5.46 ± 0.34	8.36 ± 0.06	0.48	0.55	0.86	0.86
AGN host Galaxies	42	5.23 ± 0.75	8.20 ± 0.08	0.62	0.67	0.82	0.81
Galaxies without AGN	101	5.26 ± 0.28	8.34 ± 0.05	0.44	0.52	0.87	0.87

Note. — Columns: (1) Subclass of galaxies. (2) Number of galaxies in a subclass. (3) Slope of the line obtained from the BCES(Bisector) regression. (4) Intercept of the line obtained from the BCES(Bisector) regression. (5) Intrinsic scatter in the $\log(M_{\rm BH})$-direction (using Equation 1 from Graham & Driver, 2007a). (6) Total root mean square (rms) scatter in the $\log(M_{\rm BH})$ direction. (7) Pearson correlation coefficient. (8) Spearman rank-order correlation coefficient.

Table B.3. Galaxy Luminosity versus Velocity Dispersion [$\log(L) = \alpha \log(\sigma/200) + \beta$]

Regression (1)	Minimization (2)	α (3)	β (dex) (4)	ϵ (dex) (5)	$\Delta_{rms\|L}$ (dex) (6)	r (7)	r_s (8)
V-band							
97 Core-Sérsic ETGs							
BCES(*Bisector*)	*Symmetric*	4.86 ± 0.54	8.52 ± 0.07	0.30	0.37	0.52	0.53
BCES($L\|\sigma$)	L	3.38 ± 0.48	8.70 ± 0.06	0.28	0.32		
BCES($\sigma\|L$)	σ	8.55 ± 1.53	8.08 ± 0.19	0.44	0.58		
80 Sérsic ETGs							
BCES(*Bisector*)	*Symmetric*	2.44 ± 0.18	8.41 ± 0.04	0.28	0.31	0.73	0.69
BCES($L\|\sigma$)	L	1.93 ± 0.18	8.35 ± 0.04	0.27	0.29		
BCES($\sigma\|L$)	σ	3.30 ± 0.36	8.51 ± 0.05	0.35	0.38		
3.6 μm							
24 Core-Sérsic ETGs							
BCES(*Bisector*)	*Symmetric*	5.16 ± 0.53	8.56 ± 0.08	0.00	0.19	0.86	0.76
BCES($L\|\sigma$)	L	5.48 ± 0.70	8.51 ± 0.11	0.00	0.20		
BCES($\sigma\|L$)	σ	4.86 ± 0.47	8.60 ± 0.07	0.00	0.18		
42 Sérsic ETGs							
BCES(*Bisector*)	*Symmetric*	2.97 ± 0.43	8.72 ± 0.07	0.33	0.36	0.61	0.61
BCES($L\|\sigma$)	L	2.10 ± 0.40	8.68 ± 0.06	0.32	0.33		
BCES($\sigma\|L$)	σ	5.04 ± 0.92	8.81 ± 0.09	0.49	0.53		
24 LTGs (All Sérsic)							
BCES(*Bisector*)	*Symmetric*	2.10 ± 0.41	8.90 ± 0.09	0.17	0.20	0.70	0.68
BCES($L\|\sigma$)	L	1.64 ± 0.44	8.83 ± 0.10	0.16	0.18		
BCES($\sigma\|L$)	σ	2.89 ± 0.42	9.03 ± 0.08	0.21	0.25		

Note. — Columns: (1) Type of regression performed. (2) The coordinate direction in which the offsets from the regression line is minimized. (3) Slope of the regression line. (4) Intercept of the regression line. (5) Intrinsic scatter in the $\log(L)$-direction (using Equation 1 from Graham & Driver, 2007a). (6) Total root mean square (rms) scatter in the $\log(L)$-direction. (7) Pearson correlation coefficient. (8) Spearman rank-order correlation coefficient.

C

Appendix

C.1 Data Set for Chapter 4

In Table C.1, first 83 galaxies are ETGs, and the remaining are LTGs, where the galaxies with a depleted core are marked with superscript "a" on their names in the first column. The spheroid Sérsic model parameters $(\mathrm{n}, \mathrm{Re}, \mu)$, morphology, and spheroid stellar masses are taken from our previous studies Savorgnan & Graham (2016b), Sahu et al. (2019a), and Davis et al. (2019a). For NGC 1271 and NGC 1277 these parameters are borrowed from Graham et al. (2016a) and Graham et al. (2016b), respectively. Spheroid parameters for the Milky Way are taken from Graham & Driver (2007a) who used the uncalibrated bulge surface brightness profile of Milky Way from Kent et al. (1991). The spheroid mass of Milky Way is taken from Licquia & Newman (2015).

Table C.1. Galaxy Sample

No.	Galaxy	Band	Υ_λ & $\mathfrak{M}_{\odot,\lambda}$	Type	n_{maj}	$R_{e,maj}$	$\mu_{e,maj}$	$\log\left(\frac{I_{e,maj}}{M_\odot/pc^2}\right)$	n_{eq}	$R_{e,eq}$	$\mu_{e,eq}$	$\log\left(\frac{I_{e,eq}}{M_\odot/pc^2}\right)$	C	scale	$\log\left(\frac{M_{*,\mathrm{sph}}}{M_\odot}\right)$	Distance	$\log\left(\frac{M_{\mathrm{BH}}}{M_\odot}\right)$	Ref.
			$\left(\frac{M_\odot}{L_\odot}\right)$ & mag			arcsec	$\frac{\mathrm{mag}}{\mathrm{arcsec}^2}$	dex		arcsec	$\frac{\mathrm{mag}}{\mathrm{arcsec}^2}$	dex		$\frac{\mathrm{kpc}}{\mathrm{arcsec}}$	dex	Mpc	dex	
	(1)	(2)	(3)	(4)	(5)	(6)	(7)	(8)	(9)	(10)	(11)	(12)	(13)	(14)	(15)	(16)	(17)	(18)
1	IC 1459[a]	3.6 μm	(0.6, 3.26)	E	6.60	63.10	18.49	2.32	7.00	57.30	18.59	2.28	0.60	0.1366	11.55 ± 0.12	28.4	9.38 ± 0.20	SG16
2	NGC 0821	3.6 μm	(0.6, 3.26)	E	5.30	36.50	18.40	2.36	6.10	18.90	17.83	2.58	0.62	0.1127	10.69 ± 0.33	23.4	7.59 ± 0.17	SG16
3	NGC 1023	3.6 μm	(0.6, 3.26)	SB0	2.10	9.20	14.96	3.73	2.00	7.40	14.79	3.80	0.32	0.0536	10.21 ± 0.12	11.1	7.62 ± 0.05	SG16
4	NGC 1316	3.6 μm	(0.6, 3.26)	SAB0*	2.00	21.50	15.55	3.50	1.80	15.90	15.43	3.54	0.30	0.0897	11.05 ± 0.26	18.6	8.18 ± 0.26	SG16
5	NGC 1332	3.6 μm	(0.6, 3.26)	ES	5.10	34.70	17.44	2.74	3.70	18.00	16.47	3.13	0.35	0.1074	11.05 ± 0.33	22.3	9.16±0.07	SG16
6	NGC 1399[a]	3.6 μm	(0.6, 3.26)	E	10.00	405.10	21.80	1.00	10.00	338.10	21.53	1.10	0.63	0.0935	11.66 ± 0.12	19.4	8.67±0.06	SG16
7	NGC 2549	3.6 μm	(0.6, 3.26)	SB0	2.30	6.10	15.57	3.49	1.50	3.10	14.54	3.90	0.24	0.0594	9.59 ± 0.12	12.3	7.15±0.6	SG16
8	NGC 2778	3.6 μm	(0.6, 3.26)	SAB0	1.30	2.30	15.61	3.47	1.20	2.20	15.46	3.53	0.24	0.1074	9.41 ± 0.26	22.3	7.18±0.34	SG16
9	NGC 3091[a]	3.6 μm	(0.6, 3.26)	E	7.60	100.50	20.43	1.55	6.60	51.20	19.47	1.94	0.49	0.2447	11.61 ± 0.12	51.2	9.56±0.04	SG16
10	NGC 3115	3.6 μm	(0.6, 3.26)	S0	4.40	43.60	16.67	3.04	5.10	34.40	16.85	2.97	0.58	0.0455	10.77 ± 0.12	9.4	8.94±0.25	SG16
11	NGC 3245	3.6 μm	(0.6, 3.26)	SAB0	2.90	4.40	14.96	3.73	1.70	2.40	14.00	4.12	0.24	0.0979	10.06 ± 0.12	20.3	8.30 ±0.12	SG16
12	NGC 3377	3.6 μm	(0.6, 3.26)	E	7.70	61.80	19.16	2.05	9.20	91.70	20.33	1.58	0.73	0.0527	10.48 ± 0.26	10.9	7.89 ±0.04	SG16
13	NGC 3379[a]	3.6 μm	(0.6, 3.26)	E	5.20	57.20	17.93	2.54	5.30	50.90	17.84	2.58	0.53	0.0498	10.8 ± 0.26	10.3	8.60 ±0.12	SG16
14	NGC 3384	3.6 μm	(0.6, 3.26)	SAB0	1.60	5.50	14.21	4.03	1.80	5.60	14.56	3.89	0.32	0.0546	10.06 ± 0.12	11.3	7.23 ±0.05	SG16
15	NGC 3414	3.6 μm	(0.6, 3.26)	E	4.80	28.00	18.10	2.48	4.50	25.50	18.08	2.48	0.46	0.118	10.83 ± 0.12	24.5	8.38 ±0.06	SG16
16	NGC 3489	3.6 μm	(0.6, 3.26)	SB0	1.50	2.20	13.47	4.33	1.30	1.70	13.25	4.41	0.25	0.0565	9.54 ± 0.26	11.7	6.76 ±0.07	SG16
17	NGC 3585	3.6 μm	(0.6, 3.26)	E	5.20	105.00	19.13	2.06	6.30	86.30	19.24	2.02	0.65	0.094	11.3 ± 0.26	19.5	8.49 ±0.13	SG16
18	NGC 3607	3.6 μm	(0.6, 3.26)	E	5.50	69.30	19.00	2.12	5.60	65.50	19.01	2.11	0.54	0.107	11.23 ± 0.26	22.2	8.11 ±0.18	SG16
19	NGC 3608[a]	3.6 μm	(0.6, 3.26)	E	5.20	47.50	18.93	2.14	5.70	43.40	19.00	2.12	0.58	0.1074	10.89 ± 0.26	22.3	8.30 ±0.18	SG16
20	NGC 3842[a]	3.6 μm	(0.6, 3.26)	E	8.10	100.70	21.43	1.16	8.20	73.60	21.07	1.31	0.61	0.4643	11.92 ± 0.12	98.4	9.99 ± 0.13	SG16
21	NGC 3998	3.6 μm	(0.6, 3.26)	SAB0	1.20	5.80	15.15	3.65	1.30	4.80	14.63	3.86	0.26	0.0662	10.02 ± 0.33	13.7	8.91 ±0.11	SG16
22	NGC 4261[a]	3.6 μm	(0.6, 3.26)	E	4.70	52.60	18.58	2.29	4.30	47.30	18.53	2.31	0.45	0.1481	11.38 ± 0.26	30.8	8.70± 0.09	SG16
23	NGC 4291[a]	3.6 μm	(0.6, 3.26)	E	4.20	15.00	17.14	2.86	5.90	15.40	17.51	2.71	0.70	0.1228	10.71 ± 0.26	25.5	8.52± 0.36	SG16
24	NGC 4374[a]	3.6 μm	(0.6, 3.26)	E	7.80	101.60	19.01	2.11	7.90	129.8	19.57	1.89	0.60	0.0864	11.49 ± 0.26	17.9	8.95± 0.05	SG16
25	NGC 4459	3.6 μm	(0.6, 3.26)	S0	3.10	18.40	16.69	3.04	2.60	13.00	16.23	3.22	0.34	0.0758	10.48 ± 0.26	15.7	7.83± 0.09	SG16
26	NGC 4472[a]	3.6 μm	(0.6, 3.26)	E	6.60	190.20	19.33	1.98	5.40	135.30	18.83	2.18	0.44	0.0825	11.7 ± 0.12	17.1	9.40± 0.05	SG16
27	NGC 4473	3.6 μm	(0.6, 3.26)	E	2.30	45.90	17.93	2.54	2.90	36.90	18.10	2.47	0.46	0.0739	10.64 ± 0.26	15.3	8.08± 0.36	SG16
28	NGC 4486[a]	3.6 μm	(0.6, 3.26)	E	10.00	203.00	19.87	1.77	5.90	87.10	18.26	2.41	0.33	0.0753	11.49 ± 0.26	16.8	9.81± 0.05	SG16
29	NGC 4564	3.6 μm	(0.6, 3.26)	S0	2.60	5.00	15.23	3.62	3.00	6.00	15.65	3.45	0.45	0.0705	10.01 ± 0.12	14.6	7.78± 0.06	SG16
30	NGC 4596	3.6 μm	(0.6, 3.26)	SB0	2.70	6.60	15.93	3.34	3.00	9.00	16.44	3.14	0.44	0.082	10.18 ± 0.12	17.0	7.90± 0.20	SG16
31	NGC 4621	3.6 μm	(0.6, 3.26)	E	5.50	48.00	18.02	2.51	8.80	90.90	19.67	1.85	0.87	0.0859	11.16 ± 0.12	17.8	8.59± 0.05	SG16
32	NGC 4697	3.6 μm	(0.6, 3.26)	E	7.20	239.30	20.62	1.47	6.70	226.40	20.90	1.35	0.53	0.0551	11.01 ± 0.33	11.4	8.26± 0.05	SG16
33	NGC 4889[a]	3.6 μm	(0.6, 3.26)	E	8.10	119.70	21.01	1.33	6.80	60.80	20.11	1.69	0.48	0.4863	12.14 ± 0.12	103.2	10.32± 0.44	SG16
34	NGC 5077[a]	3.6 μm	(0.6, 3.26)	E	4.20	23.50	17.67	2.65	5.70	23.00	18.01	2.52	0.68	0.1975	11.28 ± 0.12	41.2	8.87± 0.22	SG16
35	NGC 5128	3.6 μm	(0.6, 3.26)	S0*	1.20	61.30	15.73	3.42	2.20	60.80	16.01	3.30	0.42	0.0185	10.64 ± 0.33	3.8	7.65± 0.13	SG16
36	NGC 5576	3.6 μm	(0.6, 3.26)	E	3.30	61.50	19.41	1.95	3.70	49.30	19.34	1.98	0.49	0.1194	10.87± 0.12	24.8	8.20± 0.10	SG16
37	NGC 5846[a]	3.6 μm	(0.6, 3.26)	E	6.40	105.10	19.67	1.85	5.70	83.40	19.28	2.01	0.48	0.1165	11.42 ± 0.26	24.2	9.04± 0.05	SG16
38	NGC 6251[a]	3.6 μm	(0.6, 3.26)	E	6.80	41.70	19.82	1.81	5.60	30.10	19.31	2.01	0.44	0.4927	11.82 ± 0.12	104.6	8.77± 0.16	SG16
39	NGC 7619[a]	3.6 μm	(0.6, 3.26)	E	5.30	63.20	19.53	1.91	5.20	58.00	19.55	1.90	0.51	0.2461	11.64 ± 0.26	51.5	9.40± 0.09	SG16
40	NGC 7768[a]	3.6 μm	(0.6, 3.26)	E	8.40	92.90	21.37	1.19	6.70	42.10	20.15	1.68	0.45	0.5301	11.89 ± 0.26	112.8	9.11± 0.15	SG16
41	NGC 1271	H (HST)	(1.4, 3.33)	ES	4.26	3.25	16.75	3.43	4.16	3.07	16.79	3.41	0.46	0.3794	10.95± 0.1	80.0	9.48± 0.16	GCS16a
42	NGC 1277	V (HST)	(11.65, 4.82)	ES	5.34	6.00	20.73	3.35	5.63	5.60	21.05	3.22	0.56	0.3445	11.43 ± 0.1	72.5	9.08± 0.12	GDS16b

Table C.1 (cont'd)

No.	Galaxy	Band	Υ_λ & $\mathfrak{M}_{\odot,\lambda}$	Type	n_{maj}	$R_{e,maj}$	$\mu_{e,maj}$	$\log(\frac{I_{e,maj}}{M_\odot/pc^2})$	n_{eq}	$R_{e,eq}$	$\mu_{e,eq}$	$\log(\frac{I_{e,eq}}{M_\odot/pc^2})$	C	scale	$\log(\frac{M_{*,\rm sph}}{M_\odot})$	Distance	$\log(\frac{M_{\rm BH}}{M_\odot})$	Ref.
			$(\frac{M_\odot}{L_\odot})$ & mag			arcsec	$\frac{\rm mag}{\rm arcsec^2}$	dex		arcsec	$\frac{\rm mag}{\rm arcsec^2}$	dex		$\frac{\rm kpc}{\rm arcsec}$	dex	Mpc	dex	
	(1)	(2)	(3)	(4)	(5)	(6)	(7)	(8)	(9)	(10)	(11)	(12)	(13)	(14)	(15)	(16)	(17)	(18)
43	A1836 BCG[a]	K_s	(0.7, 5.08)	E	4.10	23.99	19.36	2.80	3.47	14.75	20.66	2.28	0.39	0.7335	11.70 ± 0.12	158	9.59± 0.06	SGD19a
44	A3565 BCG	3.6 μm	(0.6, 6.02)	E	3.85	43.21	21.29	2.31	3.82	41.10	21.28	2.31	0.45	0.1951	11.47± 0.26	40.7	9.04± 0.09	SGD19a
45	NGC 0307	r′ (SDSS)	(2.8, 4.65)	SAB0	3.33	3.00	18.82	3.42	3.76	3.33	19.44	3.17	0.49	0.2523	10.43 ± 0.33	52.8	8.34± 0.13	SGD19a
46	NGC 0404	3.6 μm	(0.6, 6.02)	S0	0.93	3.99	18.58	3.39	0.90	3.89	18.59	3.38	0.20	0.0148	7.96± 0.27	3.1	4.85± 0.13	SGD19a
47	NGC 0524[a]	3.6 μm	(0.6, 6.02)	SA0(rs)	2.29	8.79	18.67	3.35	2.16	8.35	18.57	3.39	0.34	0.1122	10.57± 0.26	23.3	8.92± 0.10	SGD19a
48	NGC 1194[a]	3.6 μm	(0.6, 6.02)	S0*	3.76	3.52	18.34	3.49	3.91	3.56	18.56	3.40	0.47	0.2542	10.71± 0.33	53.2	7.81± 0.04	SGD19a
49	NGC 1275	3.6 μm	(0.6, 6.02)	E	4.78	70.69	22.62	1.78	4.31	53.6	22.27	1.92	0.44	0.3464	11.84 ± 0.26	72.9	8.90± 0.20	SGD19a
50	NGC 1374	3.6 μm	(0.6, 6.02)	S0	1.68	12.56	19.65	2.96	1.65	11.74	19.62	2.97	0.29	0.0926	10.22 ± 0.26	19.2	8.76± 0.05	SGD19a
51	NGC 1407[a]	3.6 μm	(0.6, 6.02)	E	3.95	49.67	20.89	2.46	3.89	47.29	20.87	2.47	0.45	0.1349	11.46 ± 0.27	28	9.65± 0.08	SGD19a
52	NGC 1550[a]	K_s	(0.7, 5.08)	E	7.50	24.80	20.87	2.17	7.48	24.8	21.16	2.05	0.58	0.2465	11.13 ± 0.12	51.6	9.57± 0.06	SGD19a
53	NGC 1600[a]	3.6 μm	(0.6, 6.02)	E	7.14	76.57	22.66	1.77	5.08	49.58	21.98	2.04	0.38	0.3048	11.82 ± 0.12	64	10.23± 0.05	SGD19a
54	NGC 2787	3.6 μm	(0.6, 6.02)	SB0(r)	1.36	4.06	17.32	3.89	1.27	2.88	17.08	3.99	0.25	0.0353	9.13 ± 0.26	7.3	7.60± 0.06	SGD19a
55	NGC 3665	3.6 μm	(0.6, 6.02)	S0	2.76	14.44	19.28	3.11	2.74	12.78	19.34	3.09	0.39	0.1666	11.03 ± 0.26	34.7	8.76± 0.10	SGD19a
56	NGC 3923[a]	3.6 μm	(0.6, 6.02)	E	4.78	85.97	21.50	2.22	4.77	78.78	21.55	2.20	0.5	0.1006	11.4 ± 0.15	20.9	9.45± 0.13	SGD19a
57	NGC 4026	3.6 μm	(0.6, 6.02)	SB0	3.45	3.10	16.14	4.36	3.98	2.35	16.04	4.40	0.51	0.0638	10.11 ± 0.33	13.2	8.26± 0.11	SGD19a
58	NGC 4339	3.6 μm	(0.6, 6.02)	S0	1.46	6.64	19.22	3.13	1.40	6.42	19.21	3.14	0.27	0.0772	9.67 ± 0.26	16.0	7.63± 0.33	SGD19a
59	NGC 4342	3.6 μm	(0.6, 6.02)	ES	3.48	4.22	18.48	3.43	3.99	4.69	19.23	3.13	0.51	0.1108	9.94 ± 0.25	23.0	8.65± 0.18	SGD19a
60	NGC 4350	3.6 μm	(0.6, 6.02)	EBS	4.30	18.84	20.8	2.50	3.97	19.45	20.75	2.52	0.44	0.0811	10.28 ± 0.26	16.8	8.86± 0.41	SGD19a
61	NGC 4371	3.6 μm	(0.6, 6.02)	SB(r)0	2.83	8.46	19.49	3.02	3.19	8.90	19.91	2.85	0.45	0.0816	9.89 ± 0.26	16.9	6.85± 0.08	SGD19a
62	NGC 4429	3.6 μm	(0.6, 6.02)	SB(r)0	2.56	16.42	19.05	3.20	2.31	11.29	18.78	3.31	0.34	0.0796	10.46± 0.26	16.5	8.18± 0.09	SGD19a
63	NGC 4434	3.6 μm	(0.6, 6.02)	S0	2.68	4.94	19.06	3.20	2.93	5.31	19.31	3.10	0.43	0.1079	9.91 ± 0.26	22.4	7.85± 0.17	SGD19a
64	NGC 4486B	r′ (SDSS)	(2.8, 4.65)	E	2.63	2.60	18.20	3.66	2.74	2.53	18.30	3.62	0.4	0.0739	9.47 ± 0.33	15.3	8.76± 0.24	SGD19a
65	NGC 4526	3.6 μm	(0.6, 6.02)	S0	2.28	13.01	18.19	3.54	2.96	14.88	18.98	3.23	0.47	0.0816	10.7 ± 0.26	16.9	8.67± 0.05	SGD19a
66	NGC 4552	3.6 μm	(0.6, 6.02)	E	5.42	83.62	22.12	1.97	5.36	71.5	21.92	2.05	0.52	0.0719	10.88 ± 0.25	14.9	8.67± 0.05	SGD19a
67	NGC 4578	3.6 μm	(0.6, 6.02)	S0(r)	2.30	7.82	19.26	3.11	1.99	6.32	19.14	3.16	0.31	0.0787	9.77 ± 0.26	16.3	7.28± 0.35	SGD19a
58	NGC 4649[a]	3.6 μm	(0.6, 6.02)	E	4.96	93.03	21.01	2.42	5.21	80.59	20.98	2.43	0.54	0.0791	11.44 ± 0.12	16.4	9.67± 0.10	SGD19a
69	NGC 4742	3.6 μm	(0.6, 6.02)	S0	2.62	3.37	17.13	3.97	3.20	3.41	17.62	3.77	0.48	0.0748	9.87 ± 0.26	15.5	7.15± 0.18	SGD19a
70	NGC 4751[a]	K_s	(0.7, 5.08)	S0	3.79	12.47	18.74	3.02	3.25	5.48	17.76	3.41	0.38	0.1295	10.49 ± 0.26	26.9	9.15± 0.05	SGD19a
71	NGC 4762	3.6 μm	(0.6, 6.02)	SB0	2.36	4.39	17.89	3.66	1.85	2.24	17.09	3.98	0.29	0.1089	9.97 ± 0.28	22.6	7.36± 0.15	SGD19a
72	NGC 5018	3.6 μm	(0.6, 6.02)	S0*	2.64	8.29	18.4	3.46	2.51	6.20	18.22	3.54	0.36	0.1944	10.98 ± 0.27	40.6	8.02± 0.09	SGD19a
73	NGC 5252	3.6 μm	(0.6, 6.02)	S0	3.08	2.07	17.82	3.71	2.95	1.47	17.46	3.85	0.39	0.4569	10.85 ± 0.26	96.8	9.00± 0.40	SGD19a
74	NGC 5328[a]	K_s	(0.7, 5.08)	E	6.58	25.11	20.29	2.40	5.21	22.46	20.26	2.42	0.42	0.3053	11.49 ± 0.12	64.1	9.67± 0.15	SGD19a
75	NGC 5419[a]	3.6 μm	(0.6, 6.02)	E	2.42	17.24	19.80	2.91	2.62	16.83	20.01	2.82	0.40	0.2683	11.45 ± 0.12	56.2	9.86± 0.14	SGD19a
76	NGC 5516[a]	K_s	(0.7, 5.08)	E	5.99	51.27	21.54	1.90	5.32	32.30	20.86	2.18	0.47	0.2788	11.44 ± 0.12	58.4	9.52± 0.06	SGD19a
77	NGC 5813[a]	3.6 μm	(0.6, 6.02)	S0	4.02	18.54	20.74	2.53	3.65	14.16	19.81	2.90	0.42	0.1504	10.86 ± 0.26	31.3	8.83± 0.06	SGD19a
78	NGC 5845	3.6 μm	(0.6, 6.02)	ES	3.33	6.02	19.16	3.16	3.27	5.29	19.10	3.18	0.42	0.1213	10.12 ± 0.26	25.2	8.41± 0.22	SGD19a
79	NGC 6086[a]	r′ (SDSS)	(2.8, 4.65)	E	4.37	13.89	21.68	2.30	4.20	12.41	21.78	2.26	0.46	0.6441	11.52 ± 0.26	138	9.57± 0.17	SGD19a
80	NGC 6861	3.6 μm	(0.6, 6.02)	ES	3.07	18.69	19.35	3.08	3.52	20.13	20.17	2.75	0.48	0.1314	10.94± 0.29	27.3	9.30± 0.08	SGD19a
81	NGC 7052[a]	3.6 μm	(0.6, 6.02)	E	3.20	34.42	21.84	2.36	3.46	20.04	20.82	2.50	0.46	0.3161	11.46 ± 0.12	66.4	8.57± 0.23	SGD19a
82	NGC 7332	3.6 μm	(0.6, 6.02)	EB0	1.78	2.87	16.78	4.11	2.15	2.43	16.92	4.05	0.37	0.1198	10.22 ± 0.34	24.9	7.11± 0.20	SGD19a
83	NGC 7457	3.6 μm	(0.6, 6.02)	S0	2.63	6.31	19.62	2.97	2.84	6.51	19.98	2.83	0.42	0.0676	9.40 ± 0.26	14	7.00± 0.30	SGD19a
84	Circinus	3.6 μm	(0.45, 6.02)	SABb	2.21	33.26	18.29	3.37	1.80	23.13	18.06	3.47	0.29	0.0204	10.12 ± 0.2	4.2	6.25± 0.11	DGC19a

Table C.1 (cont'd)

No.	Galaxy	Band	Υ_λ & $\mathfrak{M}_{\odot,\lambda}$	Type	n_{maj}	$R_{e,maj}$	$\mu_{e,maj}$	$\log(\frac{I_{e,maj}}{M_\odot/pc^2})$	n_{eq}	$R_{e,eq}$	$\mu_{e,eq}$	$\log(\frac{I_{e,eq}}{M_\odot/pc^2})$	C	scale	$\log(\frac{M_{*,\mathrm{sph}}}{M_\odot})$	Distance	$\log(\frac{M_{\mathrm{BH}}}{M_\odot})$	Ref.
			$(\frac{M_\odot}{L_\odot})$ & mag			arcsec	$\frac{\mathrm{mag}}{\mathrm{arcsec}^2}$	dex		arcsec	$\frac{\mathrm{mag}}{\mathrm{arcsec}^2}$	dex		$\frac{\mathrm{kpc}}{\mathrm{arcsec}}$	dex	Mpc	dex	
	(1)	(2)	(3)	(4)	(5)	(6)	(7)	(8)	(9)	(10)	(11)	(12)	(13)	(14)	(15)	(16)	(17)	(18)
85	ESO558-G009	I (HST)	(1.88, 4.52)	Sbc	1.28	0.62	18.17	3.47	1.63	0.68	18.62	3.29	0.31	0.542	9.89 ± 0.11	115.4	7.26± 0.04	DGC19a
86	IC 2560	3.6 µm	(0.45, 6.02)	SBb	2.27	7.15	19.64	2.84	0.68	3.92	19.07	3.07	0.15	0.149	9.63 ± 0.39	31.0	6.49± 0.20	DGC19a
87	J0437+2456	I (HST)	(1.88, 4.52)	SB	1.73	1.22	19.42	2.96	1.97	0.87	19.40	2.97	0.35	0.343	9.90 ± 0.2	72.8	6.51± 0.05	DGC19a
88	Milky Way	2.4 µm	...	SBbc	1.32	7.49°	...	...	1.32	5.85°	...	...	...	0.38E-4	9.96 ± 0.05	7.86E-3	6.6± 0.02	GD07
89	Mrk 1029	I (HST)	(1.88, 4.52)	S	1.15	0.47	16.53	4.13	1.07	0.28	16.29	4.23	0.23	0.6392	9.90 ± 0.11	136.9	6.33± 0.12	DGC19a
90	NGC 0224	3.6 µm	(0.45, 6.02)	SBb	2.20	418.6	19.58	2.87	1.30	173.6	18.41	3.33	0.22	0.0036	10.11 ± 0.09	0.8	8.15± 0.16	DGC19a
91	NGC 0253	3.6 µm	(0.45, 6.02)	SABc	2.53	55.55	19.22	3.00	2.33	27.89	18.82	3.16	0.34	0.0168	9.76 ± 0.09	3.5	7.00± 0.30	DGC19a
92	NGC 1068	K_s	(0.62, 5.08)	SBb	0.71	10.52	16.17	3.99	0.87	8.29	16.14	4.00	0.20	0.0488	10.27 ± 0.24	10.1	6.75± 0.08	DGC19a
93	NGC 1097	3.6 µm	(0.45, 6.02)	SBb	1.95	15.72	18.71	3.21	1.52	11.39	18.27	3.39	0.26	0.1199	10.83 ± 0.2	24.9	8.38± 0.04	DGC19a
94	NGC 1300	3.6 µm	(0.45, 6.02)	SBbc	4.20	24.37	21.97	1.91	2.83	7.39	19.99	2.70	0.31	0.07	9.42 ± 0.25	14.5	7.71± 0.16	DGC19a
95	NGC 1320	3.6 µm	(0.45, 6.02)	Sa	3.08	3.35	17.93	3.53	2.87	2.23	17.40	3.74	0.38	0.1809	10.25 ± 0.4	37.7	6.78± 0.29	DGC19a
96	NGC 1398	3.6 µm	(0.45, 6.02)	SBab	3.44	17.53	19.75	2.80	3.00	10.38	19.04	3.08	0.38	0.1194	10.57 ± 0.2	24.8	8.03± 0.11	DGC19a
97	NGC 2273	I (HST)	(1.88, 4.52)	SBa	2.24	2.99	18.13	3.47	2.49	3.15	18.52	3.31	0.39	0.1519	9.98 ± 0.2	31.6	6.97± 0.09	DGC19a
98	NGC 2960	3.6 µm	(0.45, 6.02)	Sa*	2.59	2.35	18.04	3.49	2.86	2.19	18.30	3.39	0.42	0.338	10.44 ± 0.36	71.1	7.06± 0.17	DGC19a
99	NGC 2974	3.6 µm	(0.45, 6.02)	SB	1.56	9.21	18.49	3.30	1.17	6.53	18.12	3.45	0.23	0.1036	10.23 ± 0.13	21.5	8.23± 0.07	DGC19a
100	NGC 3031[b]	3.6 µm	(0.45, 6.02)	Sab	2.81	36.19	18.34	3.35	3.46	42.98	18.93	3.12	0.50	0.0169	10.16 ± 0.11	3.5	7.83± 0.09	DGC19a
101	NGC 3079	3.6 µm	(0.45, 6.02)	SBcd	0.52	5.91	16.79	3.98	0.58	4.35	17.13	3.84	0.16	0.0796	9.92 ± 0.25	16.5	6.38± 0.12	DGC19a
102	NGC 3227	3.6 µm	(0.45, 6.02)	SABa	2.60	17.91	20.26	2.59	1.90	8.34	19.32	2.97	0.28	0.1017	10.04 ± 0.17	21.1	7.88± 0.14	DGC19a
103	NGC 3368	3.6 µm	(0.45, 6.02)	SABa	1.19	5.98	17.07	3.86	1.00	4.83	16.92	3.92	0.21	0.0517	9.81 ± 0.1	10.7	6.89± 0.09	DGC19a
104	NGC 3393	I (HST)	(1.88, 4.52)	SBa	1.14	1.64	17.27	3.82	1.36	1.77	17.63	3.68	0.27	0.2664	10.23 ± 0.12	55.8	7.49± 0.05	DGC19a
105	NGC 3627	3.6 µm	(0.45, 6.02)	SBb	3.17	11.07	18.44	3.32	2.10	3.92	16.98	3.90	0.28	0.0512	9.74 ± 0.2	10.6	6.95± 0.05	DGC19a
106	NGC 4151	3.6 µm	(0.45, 6.02)	SABa	2.24	6.23	17.75	3.59	1.85	6.00	17.77	3.59	0.29	0.0916	10.27 ± 0.15	19.0	7.68± 0.37	DGC19a
107	NGC 4258	3.6 µm	(0.45, 6.02)	SABb	3.21	41.8	20.14	2.64	2.60	26.4	19.73	2.80	0.34	0.0368	10.05 ± 0.18	7.6	7.60± 0.01	DGC19a
108	NGC 4303	3.6 µm	(0.45, 6.02)	SBbc	1.02	2.28	16.51	4.09	0.90	2.16	15.78	4.38	0.20	0.0594	9.42 ± 0.1	12.3	6.58± 0.17	DGC19a
109	NGC 4388	3.6 µm	(0.45, 6.02)	SBcd	0.89	21.68	21.68	2.02	1.15	14.3	19.82	2.77	0.24	0.0859	10.07 ± 0.22	17.8	6.90± 0.11	DGC19a
110	NGC 4501	3.6 µm	(0.45, 6.02)	Sb	2.33	21.22	19.53	2.88	2.83	20.35	19.91	2.73	0.44	0.0541	10.11 ± 0.16	11.2	7.13± 0.08	DGC19a
111	NGC 4594	3.6 µm	(0.45, 6.02)	Sa	6.14	44.94	19.38	2.94	4.24	41.36	19.46	2.91	0.35	0.0462	10.81 ± 0.2	9.6	8.81± 0.03	DGC19a
112	NGC 4699	3.6 µm	(0.45, 6.02)	SABb	5.35	24.44	19.51	2.89	6.77	29.75	20.31	2.57	0.69	0.1141	11.12 ± 0.26	23.7	8.34± 0.10	DGC19a
113	NGC 4736[b]	3.6 µm	(0.45, 6.02)	Sab	0.93	9.79	16.17	4.22	1.03	9.65	16.31	4.17	0.22	0.0214	9.89 ± 0.09	4.4	6.78± 0.10	DGC19a
114	NGC 4826	3.6 µm	(0.45, 6.02)	Sab	0.73	13.89	17.86	3.55	0.76	11.93	17.98	3.50	0.18	0.0269	9.55 ± 0.22	5.6	6.07± 0.15	DGC19a
115	NGC 4945[b]	K_s	(0.62, 5.08)	Sc	3.40	26.33	18.48	3.06	3.19	13.93	17.99	3.26	0.40	0.018	9.39 ± 0.19	3.7	6.15± 0.30	DGC19a
116	NGC 5055	3.6 µm	(0.45, 6.02)	Sbc	2.02	55.12	20.09	2.66	1.76	43.52	19.85	2.75	0.29	0.0429	10.49 ± 0.11	8.9	8.94± 0.10	DGC19a
117	NGC 5495	I (HST)	(1.88, 4.52)	SBc	2.60	3.75	20.21	2.65	2.46	3.99	20.23	2.64	0.36	0.4767	10.54 ± 0.12	101.1	7.04± 0.08	DGC19a
118	NGC 5765b	I (HST)	(1.88, 4.52)	SABb	1.46	1.11	18.72	3.25	1.51	1.00	18.83	3.21	0.28	0.6257	10.04 ± 0.13	133.9	7.72± 0.05	DGC19a
119	NGC 6264	I (HST)	(1.88, 4.52)	SBb	1.04	1.13	19.23	3.06	1.35	1.05	19.37	3.00	0.27	0.7152	10.01 ± 0.15	153.9	7.51± 0.06	DGC19a
120	NGC 6323	I (HST)	(1.88, 4.52)	SBab	1.60	1.53	20.39	2.58	1.15	1.71	19.98	2.75	0.22	0.5488	9.86 ± 0.31	116.9	7.02± 0.14	DGC19a
121	NGC 7582	3.6 µm	(0.45, 6.02)	SBab	2.20	5.33	17.04	3.88	2.21	4.55	17.66	3.63	0.35	0.0959	10.15 ± 0.2	19.9	7.67± 0.09	DGC19a
122	UGC 3789	I (HST)	(1.88, 4.52)	SABa	2.37	1.60	18.38	3.37	2.67	3.11	19.03	3.11	0.41	0.2372	10.18 ± 0.14	49.6	7.06± 0.05	DGC19a
123	UGC 6093	I (HST)	(1.88, 4.52)	SBbc	1.55	1.84	19.27	3.04	1.41	1.27	18.87	3.20	0.26	0.7103	10.35 ± 0.14	152.8	7.41± 0.03	DGC19a

Note. — Column: (1) Galaxy name. (2) Wavelength-band (λ) of the image used in parent studies (Column 18). Images for the first 41 galaxies were calibrated to Vega magnitude system and the images of the remaining galaxies (except the Milky Way) were calibrated to AB magnitude system. (3) The stellar mass-to-light ratio (Υ_λ) and the absolute magnitude of the Sun ($\mathfrak{M}_{\odot,\lambda}$) used to obtain the bulge stellar mass. Davis et al. (2019a) used a reduced (by 25%) stellar mass-to-light ratio for their LTGs observed at 3.6 µm-band following Querejeta et al. (2015) who reported on the dust glow at 3.6 µm in LTGs. (4) Galaxy morphology based on the multi-component decomposition of the galaxy light performed in studies listed in Column 18. Galaxy mergers are highlighted with an $*$. (5) Bulge major-axis Sérsic index parameter. (6) Bulge major-axis effective half-light radius. (7) Bulge surface brightness at the corresponding major-axis half-light radius listed in column 6. (8) Logarithm of the bulge intensity at the major-axis half-light radius in the units of $M_\odot/pc^2$, calculated using $[(\mu_e - \mathrm{Dist.Mod.} - \mathfrak{M}_{\odot,\lambda} - 2.5\log(1/\mathrm{scale}^2) - 2.5\log(\Upsilon_\lambda))/(-2.5)]$ (Graham et al., 2006, their Equation 10). (9)-(12) Similar to columns (5)-(8), but obtained from an independent multi-component decomposition of the galaxy light profile along the equivalent-axis ($R_{eq} = \sqrt{R_{maj} * R_{min}}$). (13) Concentration index (C) calculated using the equivalent-axis bulge Sérsic index and Equation 6 from Trujillo et al. (2001) using $\alpha = 1/3$. (14) Physical scale in kpc arcsec^{-1}, assuming cosmological parameters from Planck Collaboration et al. (2020). (15) Logarithm of the spheroid stellar mass in units of solar mass. (16) Galaxy distance in megaparsec. (17) Logarithm of the directly-measured black hole mass in units of solar mass. (18) Parent studies which performed multi-component decompositions to obtain the bulge parameters. Where SG16=Savorgnan & Graham (2016b), SGD19a=Sahu et al. (2019a), DGC19a=Davis et al. (2019a), GCS16a=Graham et al. (2016a) , GDS16b=Graham et al. (2016b), and GD07=Graham & Driver (2007a). Original sources for black hole mass and distances can be found in Savorgnan et al. (2016), and Sahu et al. (2019a) for ETGs and Davis et al. (2019a) for LTGs.

Table C.2. Correlations of $M_{*,\rm sph}$ and $M_{\rm BH}$ with the bulge equivalent-axis properties ($\rm n_{eq,sph}, C(1/3), and\, R_{e,sph,eq}$) calculated using a symmetric application of the MPFITEXY regression (see Section 4.2)

Category (1)	**Number** (2)	$\boldsymbol{\alpha}$ (3)	$\boldsymbol{\beta}$ **dex** (4)	$\boldsymbol{\epsilon}$ **dex** (5)	$\boldsymbol{\Delta_{\rm rms}}$ **dex** (6)
$\log(M_{*,\rm sph}/\rm M_\odot) = \alpha \log(n_{sph,eq}/3) + \beta$					
ETGs	77	3.36 ± 0.20	10.52 ± 0.04	0.30	0.48
LTGs	38	1.47 ± 0.19	10.48 ± 0.06	0.20	0.29
$\log(M_{\rm BH}/\rm M_\odot) = \alpha \log(n_{sph,eq}/3) + \beta$					
ETGs	77	3.94 ± 0.36	8.18 ± 0.07	0.62	0.73
LTGs	38	2.90 ± 0.55	8.00 ± 0.18	0.63	0.69
$\log(M_{\rm BH}/\rm M_\odot) = \alpha\, C(1/3)/0.4 + \beta$					
ETGs	77	8.85 ± 0.81	8.10 ± 0.08	0.62	0.72
LTGs	38	7.03 ± 1.50	7.94 ± 0.18	0.64	0.68
$\log(M_{*,\rm sph}/\rm M_\odot) = \alpha \log(R_{e,sph,eq}) + \beta$					
All Galaxies	115	1.12 ± 0.03	10.42 ± 0.02	0.07	0.25
$\log(M_{\rm BH}/\rm M_\odot) = \alpha \log(R_{e,sph,eq}) + \beta$					
ETGs with a disk	39	2.08 ± 0.23	8.49 ± 0.09	0.51	0.60
ETGs without a disk	38	2.09 ± 0.35	7.12 ± 0.36	0.53	0.61
ETGs	77	1.30 ± 0.09	8.10 ± 0.06	0.56	0.60
LTGs	38	2.41 ± 0.29	7.79 ± 0.10	0.51	0.60

Note. — Columns: (1) Subclass of galaxy. (2) Number of galaxies in subclass. (3) Slope of the line obtained from the MPFITEXY(Bisector) regression. (4) Intercept of the line obtained from the MPFITEXY(Bisector) regression. (5) Intrinsic scatter in the vertical ($\log M_{*,\rm sph}$ or $\log M_{\rm BH}$)-direction. (6) Total root mean square (rms) scatter in the vertical direction.

D
Appendix

D.1 Calculation of The Bulge Internal Density

The surface brightness (projected/column luminosity density) profile of a galactic spheroid or an elliptical galaxy is very well described using the (Sérsic, 1963, 1968a) function, which can be expressed as

$$\mathrm{I(R)} = \mathrm{I_e} \exp\left[-\mathrm{b}\left\{\left(\frac{\mathrm{R}}{\mathrm{R_e}}\right)^{1/\mathrm{n}} - 1\right\}\right]. \tag{D.1}$$

It is parametrized by the Sérsic index (n), the scale radius ($\mathrm{R_e}$), and the intensity ($\mathrm{I_e}$) at $\mathrm{R_e}$. The term b is a function of n, defined such that the scale radius $\mathrm{R_e}$ encloses 50% of the total spheroid light; therefore, $\mathrm{R_e}$ is known as the (projected) effective half-light radius[1]. As noted by Ciotti (1991), the exact value of b can be obtained using $\Gamma(2\mathrm{n}) = 2\gamma(2\mathrm{n}, \mathrm{b})$ or it can be approximated as $\mathrm{b} = 1.9992\,\mathrm{n} - 0.327$ for the value of n between 0.5 to 10 (Capaccioli, 1989). The parameter n is the profile *shape parameter* and quantifies the central light concentration of the spheroid (Trujillo et al., 2001). The intensity, $\mathrm{I_e}$, is related to the surface brightness (μ in mag/arcsec^2) at $\mathrm{R_e}$, via $\mu_\mathrm{e} \equiv -2.5\log(\mathrm{I_e})$.

As mentioned in Section 5.2, the bulge Sérsic profile parameters used here are taken from Sahu et al. (2020, their Table A1). Sahu et al. (2020) provide both major-axis bulge surface brightness parameters ($\mathrm{n_{maj}}, \mathrm{R_{e,maj}}, \mu_\mathrm{e,maj}$) and the equivalent-axis bulge

[1]See Graham (2019b) for a detailed review of popular galactic radii and Graham & Driver (2005) for an overview of the Sérsic model.

surface brightness parameters ($n_{eq}, R_{e,eq}, \mu_{e,eq}$) obtained by independent multi-component decompositions of galaxy surface brightness profiles along the major-axis and geometric mean-axis (equivalent to a circularised axis), respectively, (see Sahu et al., 2019a, for more details on the decomposition process). As described below, we used the equivalent-axis bulge parameters to utilize their circular symmetry while calculating the (deprojected) internal bulge density profile.

Using the inverse Abel (integral) transformation (Abel, 1826; Anderssen & de Hoog, 1990), the spatial luminosity density, $j(r)$, for a spherical system can be expressed in terms of derivative ($\mathrm{d\,I(R)/d\,R}$) of the projected luminosity density profile (see Binney & Tremaine, 1987) as,

$$\mathrm{j(r)} = -\frac{1}{\pi}\int_{\mathrm{r}}^{\infty}\frac{\mathrm{dI(R)}}{\mathrm{dR}}\frac{\mathrm{dR}}{\sqrt{\mathrm{R^2 - r^2}}}, \tag{D.2}$$

where R represents a projected radius and r represents a 3D spatial (or internal) radius. Using the Sérsic profile (Equation D.1) for I(R) and a stellar mass-to-light ratio, Υ_λ (suitable for the corresponding image wavelength λ), to convert the luminosity into stellar mass, the spatial mass density profile, $\rho(r) \equiv \Upsilon_\lambda\, j(r)$, can be expressed in a simplified integral form (Ciotti, 1991; Graham & Colless, 1997) as,

$$\rho(\mathrm{r}) = \Upsilon_\lambda \frac{\mathrm{I_e b e^b}}{\pi \mathrm{r}}\left(\frac{\mathrm{r}}{\mathrm{R_e}}\right)^{1/\mathrm{n}}\int_0^1 \frac{\mathrm{e}^{(-\mathrm{b(r/R_e)^{1/n}/t})}}{\mathrm{t^2}\sqrt{\mathrm{t^{-2n} - 1}}}\mathrm{dt}. \tag{D.3}$$

The above transformation (Equation D.2) is applicable for a spherical system, and we can use the equivalent-axis bulge Sérsic parameters (n_{eq}, $R_{e,eq}$, and $I_{e,eq}$) to obtain ρ(r).

Using R_e in parsec (pc), I_e in solar luminosity per unit area ($L_\odot/pc^2$), and Υ_λ in the units of solar mass per solar luminosity ($M_\odot/L_\odot$), we obtain ρ(r) in the units of $M_\odot/pc^3$ from the above integral (Equation D.3). The surface brightness μ_e (in mag/arcsec^2) at the half-light radius can be mapped into I_e ($L_\odot/pc^2$) using the following equation taken from Graham et al. (2006),

$$-2.5\log(\mathrm{I_e\,[L_\odot pc^{-2}]}) = \mu_\mathrm{e} - \mathrm{DM} - \mathfrak{M}_{\odot,\lambda} - 2.5\log(1/\mathrm{s}^2), \tag{D.4}$$

where $\mathrm{DM} = 25 + 5\log[\mathrm{Distance\,(Mpc)}]$ is the distance modulus, $\mathfrak{M}_{\odot,\lambda}$ is the absolute magnitude of the Sun in the corresponding wavelength-band λ, and s is the physical size scale for a galaxy in pc arcsec^{-1}. The projected stellar mass density $\Sigma\,(\mathrm{M_\odot\,pc^{-2}})$ at any projected radius R can be calculated using μ_R via,

$$-2.5\log(\Sigma_\mathrm{R}\,[\mathrm{M_\odot pc^{-2}}]) = \mu_\mathrm{R} - \mathrm{DM} - \mathfrak{M}_{\odot,\lambda} - 2.5\log(1/\mathrm{s}^2) - 2.5\log(\Upsilon_\lambda). \quad (\mathrm{D.5})$$

The solution of the above integral (Equation D.3) can be expressed with the Meijer-G function[2] (Meijer, 1936; Bateman & Erdélyi, 1953; Mazure & Capelato, 2002), which we numerically calculated using a *Mathematica* script to obtain the internal densities at various spheroid radii, used in Section 5.4.

Prugniel & Simien (1997, PS hereafter) provides a remarkably simple, and one of the closest, approximation to the deprojected Sérsic profile (Equation D.3), which can be expressed as,

$$\rho(\mathrm{r}) = \rho_\mathrm{e}\left(\frac{\mathrm{r}}{\mathrm{R_e}}\right)^{-\mathrm{p}} \exp\left\{-\mathrm{b}\left[\left(\frac{\mathrm{r}}{\mathrm{R_e}}\right)^{1/\mathrm{n}} - 1\right]\right\}. \quad (\mathrm{D.6})$$

Here, ρ_e is the spatial mass density at $\mathrm{r} = \mathrm{R_e}$, and p is a function of n, obtained by maximizing the agreement between this approximated $\rho(r)$ profile (Equation D.6) and the exactly deprojected (Sérsic) density profile (Equation D.3). The value of p is given by $p = 1.0 - 0.6097/n + 0.05563/n^2$ for a radial range of $10^{-2} \lesssim r/R_e \lesssim 10^3$ and index range of $0.6 \lesssim n \lesssim 10$ (Lima Neto et al., 1999; Márquez et al., 2000). On equating the total mass obtained from the projected Sérsic profile (Equation D.1) with the total mass calculated using the PS spatial density profile (Equation D.6), considering a constant mass-to-light ratio, one has

$$\rho_\mathrm{e} = \Upsilon\left(\frac{\mathrm{I_e}}{2\mathrm{R_e}\mathrm{b}^{\mathrm{n(p-1)}}}\right)\left[\frac{\Gamma(2\mathrm{n})}{\Gamma(\mathrm{n}(3-\mathrm{p}))}\right]. \quad (\mathrm{D.7})$$

Owing to its simple analytical form and the model parameters common to the Sérsic luminosity profile, the PS model makes it easy to estimate the internal density profile of elliptical galaxies and the spheroids of multi-component (i.e., ES-, S0-, and Spiral-type)

[2] For some cases, it turns out as a sum of generalized hypergeometric function residues. See `http://functions.wolfram.com/HypergeometricFunctions/MeijerG/26/01/02/` for how Meijer-G function and Hypergeometric functions are linked.

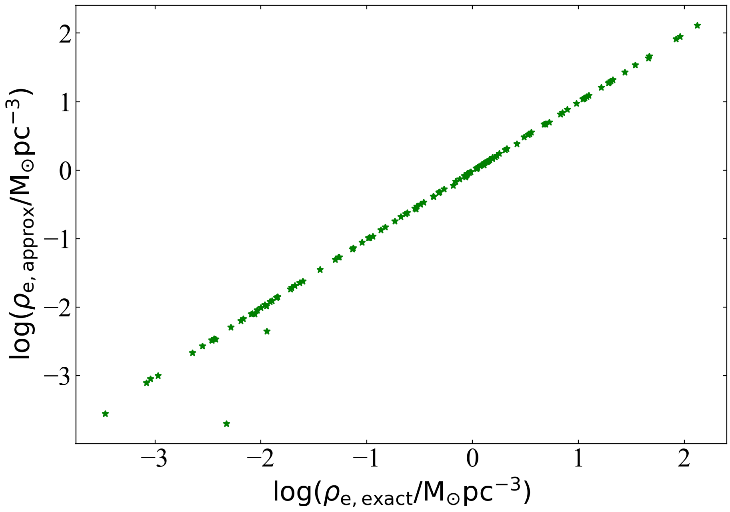

Figure D.1 The spatial density at R_e calculated using the PS model ($\rho_{\rm e,approx}$) plotted against the numerically calculated (Equation D.3) spatial density ($\rho_{\rm e,exact}$).

galaxies. Thus, Equations D.3 and D.6, both, are applicable for a galaxy/component whose surface brightness profile can be described using a Sérsic function; however, Equation D.3 can provide the most accurate value.

For core-Sérsic galaxies, i.e., galaxies with power-law + Sérsic spheroid surface brightness profiles, Terzić & Graham (2005, their equation 5) modified the PS model and presented an expression for the deprojected core-Sérsic spheroid density profile. However, as we do not have precise parameters for the power-law core of our core-Sérsic galaxies, we use the Sérsic part of their surface brightness profile and deproject its inward extrapolation to obtain the central/inner ρ for core-Sérsic galaxies.

The approximation of the deprojected density profiles can be imprecise ($<10\%$ diferrence at $0.01 < \mathrm{R/R_e} < 100\,\mathrm{R_e}$ for $\mathrm{n} > 2$) to emulate the actual density profiles at the central radii, especially for low Sérsic index spheroids. See the comparisons in Terzić & Graham (2005, their figure 4), Emsellem & van de Ven (2008), and Vitral & Mamon (2020). Therefore, for our black hole–internal density correlations, we prefer to use the numerically calculated internal densities from Equation D.3.

In Figure D.1, we have compared $\rho_{\rm e,approx}$ at $r = R_e$ calculated using the PS model (Equation D.7) against $\rho_{\rm e,exact}$, numerically calculated using Equation D.3. Here, we see an almost one-to-one match between the two values, except for galaxies M 59, NGC 1399, and NGC 3377, the three offset galaxies in Figure 5.2 with $n_{\rm sph,eq} \gtrsim 8.8$. The two offset points shown in Figure D.1 are M 59 and NGC 1399, whereas, for NGC 3377, the exact integral (Equation D.3) did not converge to provide an appropriate value of $\rho_{\rm e,exact}$.

Given the agreement between the exact and approximate internal densities at $\rm r = R_e$ for the majority of the sample, for NGC 3377, we have used $\rho_{\rm e}$ obtained from the PS model. Similarly, for some instances, where the exact $\rho(r)$ integral (Equation D.3) did not converge or provide a valid density value, we used the internal densities obtained using the PS model (Equation D.7). This does not have a significant effect on the best-fit relations presented here. The extended density profiles in Figure 5.7 are obtained using the PS model, as it can still explain the qualitative nature of the trends observed in the $M_{\rm BH}$–ρ diagrams.

D.2 Fit parameters obtained using linmix

Table D.1. Correlations between the Black Hole Mass and the Spheroid Density obtained using LINMIX routine

No. (1)	Category (2)	Number (3)	$\log(M_{\rm BH}/M_\odot) = (Slope)\,X + Intercept$ dex (4)	$\Delta_{\rm rms\|BH}$ dex (5)	r_p (6)
			Central Surface Brightness (Figure 5.2, left-hand panel)		
T3.1	3.6 μm sample	94	$\log(M_{\rm BH}/{\rm M_\odot}) = (-0.41 \pm 0.05)\,[\mu_{0,3.6\mu{\rm m,sph}} - 13\,{\rm mag\,arcsec^{-2}}] + (7.98 \pm 0.09)$	1.03	-0.53
			Central Projected Mass Density (Figure 5.2, right-hand panel)		
T3.2	All types	116	$\log(M_{\rm BH}/{\rm M_\odot}) = (0.91 \pm 0.08)\,\log\left(\Sigma_{0,\rm sph}/10^{6}\,{\rm M_\odot\,pc^{-2}}\right) + (8.38 \pm 0.08)$	0.95	0.58
			Projected density within 1 kpc (Figure 5.3, left-hand panel)		
T3.3	All types	119	$\log(M_{\rm BH}/{\rm M_\odot}) = (2.70 \pm 0.15)\,\log\left(\langle\Sigma\rangle_{\rm 1kpc,sph}/10^{3.5}\,{\rm M_\odot\,pc^{-2}}\right) + (7.83 \pm 0.05)$	0.69	0.83
			Projected density within 5 kpc (Figure 5.3, right-hand panel)		
T3.4	All types	119	$\log(M_{\rm BH}/{\rm M_\odot}) = (1.87 \pm 0.08)\,\log\left(\langle\Sigma\rangle_{\rm 5kpc,sph}/10^{2.5}\,{\rm M_\odot\,pc^{-2}}\right) + (8.13 \pm 0.06)$	0.59	0.86
			Effective Surface Brightness at $R_{\rm e,sph}$ (Figure 5.5, left-hand panel)		
T3.5	LTGs (3.6 μm sample, Eq. 5.5)	26	$\log(M_{\rm BH}/{\rm M_\odot}) = (0.77 \pm 0.18)\,[\mu_{\rm e,3.6\mu m,sph} - 19\,{\rm mag\,arcsec^{-2}}] + (7.84 \pm 0.18)$	0.85	0.57
T3.6	ETGs (3.6 μm sample)	71	$\log(M_{\rm BH}/{\rm M_\odot}) = (0.47 \pm 0.06)\,[\mu_{\rm e,3.6\mu m,sph} - 19\,{\rm mag\,arcsec^{-2}}] + (7.96 \pm 0.10)$	0.82	0.60
T3.7	E (3.6 μm sample)	35	$\log(M_{\rm BH}/{\rm M_\odot}) = (1.00 \pm 0.35)\,[\mu_{\rm e,3.6\mu m,sph} - 19\,{\rm mag\,arcsec^{-2}}] + (6.20 \pm 0.8)$	1.17	0.02
T3.8	ES/S0 (3.6 μm sample)	36	$\log(M_{\rm BH}/{\rm M_\odot}) = (0.75 \pm 0.19)\,[\mu_{\rm e,3.6\mu m,sph} - 19\,{\rm mag\,arcsec^{-2}}] + (8.42 \pm 0.17)$	0.92	0.43
			Internal Density at $r_{\rm soi}$ (Figure 5.8, middle panel)		
T3.9	Core-Sérsic	31	$\log(M_{\rm BH}/{\rm M_\odot}) = (-0.65 \pm 0.05)\,\log\left(\rho_{\rm soi,sph}/10^{2.5}\,{\rm M_\odot\,pc^{-3}}\right) + (9.07 \pm 0.10)$	0.21	-0.97
T3.10	Sérsic	83	$\log(M_{\rm BH}/{\rm M_\odot}) = (-1.19 \pm 0.14)\,\log\left(\rho_{\rm soi,sph}/10^{2.5}\,{\rm M_\odot\,pc^{-3}}\right) + (8.40 \pm 0.09)$	0.78	-0.60
			Internal Density within 1 kpc of Spheroid (Figure 5.9, left-hand panel)		
T3.11	All Galaxies	119	$\log(M_{\rm BH}/{\rm M_\odot}) = (2.97 \pm 0.19)\,\log\left(\langle\rho\rangle_{\rm 1kpc,sph}/10^{0.5}\,{\rm M_\odot\,pc^{-3}}\right) + (8.47 \pm 0.06)$	0.76	0.79
			Internal Density within 5 kpc of Spheroid (Figure 5.9, right-hand panel)		
T3.12	All Galaxies	119	$\log(M_{\rm BH}/{\rm M_\odot}) = (2.00 \pm 0.09)\,\log\left(\langle\rho\rangle_{\rm 5kpc,sph}/10^{-1.5}\,{\rm M_\odot\,pc^{-3}}\right) + (7.84 \pm 0.04)$	0.61	0.85
			Internal Density at $r_{\rm e,sph}$ (Figure 5.11, left-hand panels)		
T3.13	LTGs	39	$\log(M_{\rm BH}/{\rm M_\odot}) = (-1.02 \pm 0.17)\,\log\left(\rho_{\rm e,int,sph}/{\rm M_\odot\,pc^{-3}}\right) + (7.21 \pm 0.14)$	0.69	-0.61
T3.14	ETGs	80	$\log(M_{\rm BH}/{\rm M_\odot}) = (-0.64 \pm 0.06)\,\log\left(\rho_{\rm e,int,sph}/{\rm M_\odot\,pc^{-3}}\right) + (7.82 \pm 0.09)$	0.73	-0.66
T3.15	E	40	$\log(M_{\rm BH}/{\rm M_\odot}) = (-1.07 \pm 0.29)\,\log\left(\rho_{\rm e,int,sph}/{\rm M_\odot\,pc^{-3}}\right) + (6.50 \pm 0.60)$	0.81	-0.25
T3.16	ES/S0	40	$\log(M_{\rm BH}/{\rm M_\odot}) = (-1.01 \pm 0.18)\,\log\left(\rho_{\rm e,int,sph}/{\rm M_\odot\,pc^{-3}}\right) + (8.13 \pm 0.11)$	0.76	-0.55

Note. — Columns: (1) Table 3 row number. (2) Galaxy type. (3) Number of galaxies in a category. (4) Correlation obtained using the Bayesian regression routine LINMIX from Kelly (2007). We used the python script for this routine taken from `https://github.com/jmeyers314/linmix`. (5) Total rms scatter (measurement err plus intrinsic scatter) in the $\log M_{\rm BH}$-direction. (6) Pearson linear correlation coefficient.

E

Authorship Indication Forms

SWINBURNE UNIVERSITY OF TECHNOLOGY

Swinburne Research

Authorship Indication Form

For HDR students

NOTE

This Authorship Indication form is a statement detailing the percentage of the contribution of each author in each submitted/published 'paper'. This form must be signed by each co-author and the Principal Supervisor. This form must be added to the publication of your final thesis as an appendix. Please fill out a separate form for each published paper to be included in your thesis.

DECLARATION

We hereby declare our contribution to the publication of the 'paper' entitled:

Black Hole Mass Scaling Relations for Early-type Galaxies. I. MBH–M*,sph and MBH–M*,gal

First Author

Name: Nandini Sahu Signature: Nandini Sahu

Percentage of contribution: 80 % Date: 30 / 07 / 2021

Brief description of contribution to the 'paper' and your central responsibilities/role on project:

Second Author

Name: Alister W. Graham Signature: ______

Percentage of contribution: 15 % Date: __ / __ / ____

Brief description of your contribution to the 'paper':

Third Author

Name: Benjamin L. Davis Signature: Ben Davis

Percentage of contribution: 5 % Date: 19 / 08 / 2021

Brief description of your contribution to the 'paper':

Fourth Author

Name:____Signature:____________________

Percentage of contribution: ____% Date: _ _ / _ _ / _ _ _ _

Brief description of your contribution to the 'paper':

Principal Supervisor:

Name: Alister W. Graham Signature: alister graham

Date: 30 / 07 / 2021

In the case of more than four authors please attach another sheet with the names, signatures and contribution of the authors.

SWIN BUR NE
SWINBURNE UNIVERSITY OF TECHNOLOGY

Swinburne Research

Authorship Indication Form

For HDR students

NOTE

This Authorship Indication form is a statement detailing the percentage of the contribution of each author in each submitted/published 'paper'. This form must be signed by each co-author and the Principal Supervisor. This form must be added to the publication of your final thesis as an appendix. Please fill out a separate form for each published paper to be included in your thesis.

DECLARATION

We hereby declare our contribution to the publication of the 'paper' entitled:

Revealing Hidden Substructures in the MBH–σ Diagram, and Refining the Bend in the L–σ Relation

First Author

Name: Nandini Sahu Signature: Nandini Sahu

Percentage of contribution: 80 % Date: 30 / 07 / 2021

Brief description of contribution to the 'paper' and your central responsibilities/role on project:

Second Author

Name: Alister W. Graham Signature:

Percentage of contribution: 15 % Date: __ / __ / ____

Brief description of your contribution to the 'paper':

Third Author

Name: Benjamin L. Davis Signature: Ben Davis

Percentage of contribution: 5 % Date: 19 / 08 / 2021

Brief description of your contribution to the 'paper':

Fourth Author

Name:____Signature:______________________

Percentage of contribution: ____%   Date: _ _ / _ _ / _ _ _ _

Brief description of your contribution to the 'paper':

Principal Supervisor:

Name: Alister W. Graham   Signature: alister graham

Date: 30 / 07 / 2021

In the case of more than four authors please attach another sheet with the names, signatures and contribution of the authors.

Swinburne Research

Authorship Indication Form

For HDR students

NOTE

This Authorship Indication form is a statement detailing the percentage of the contribution of each author in each submitted/published 'paper'. This form must be signed by each co-author and the Principal Supervisor. This form must be added to the publication of your final thesis as an appendix. Please fill out a separate form for each published paper to be included in your thesis.

DECLARATION

We hereby declare our contribution to the publication of the 'paper' entitled:
Defining the (Black Hole)–Spheroid Connection with the Discovery of Morphology-dependent Substructure in the MBH–n_sph and MBH–Re,sph Diagrams: New Tests for Advanced Theories and Realistic Simulations

First Author

Name: Nandini Sahu Signature: Nandini Sahu

Percentage of contribution: 80 % Date: 30/ 07/ 2021

Brief description of contribution to the 'paper' and your central responsibilities/role on project:

Second Author

Name: Alister W. Graham Signature:

Percentage of contribution: 15 % Date: __ / __ / ____

Brief description of your contribution to the 'paper':

Third Author

Name: Benjamin L. Davis Signature: Ben Davis

Percentage of contribution: 5 % Date: 19 / 08 / 2021

Brief description of your contribution to the 'paper':

Fourth Author

Name:____Signature:____________________

Percentage of contribution: ____%   Date: _ _ / _ _ / _ _ _ _

Brief description of your contribution to the 'paper':

Principal Supervisor:

Name: Alister W. Graham   Signature: alister graham

Date: 30 / 07 / 2021

In the case of more than four authors please attach another sheet with the names, signatures and contribution of the authors.

Swinburne Research

Authorship Indication Form

For HDR students

NOTE

This Authorship Indication form is a statement detailing the percentage of the contribution of each author in each submitted/published 'paper'. This form must be signed by each co-author and the Principal Supervisor. This form must be added to the publication of your final thesis as an appendix. Please fill out a separate form for each published paper to be included in your thesis.

DECLARATION

We hereby declare our contribution to the publication of the 'paper' entitled:

The (Black Hole Mass)--(Spheroid Stellar Density) Relations: MBH--\mu (MBH--\Sigma) and MBH --\rho

First Author

Name: Nandini Sahu Signature: Nandini Sahu

Percentage of contribution: 80 % Date: 16/ 12 / 2021

Brief description of contribution to the 'paper' and your central responsibilities/role on project:

Second Author

Name: Alister W. Graham Signature: Alister Graham

Percentage of contribution: 15 % Date: 19/ 12 / 2021

Brief description of your contribution to the 'paper':

Third Author

Name: Benjamin L. Davis Signature: Ben Davis

Percentage of contribution: 5 % Date: 16 / 12 / 2021

Brief description of your contribution to the 'paper':

Fourth Author

Name:____Signature:____________________

Percentage of contribution: ____%   Date: _ _ / _ _ / _ _ _ _

Brief description of your contribution to the ‘paper’:

Principal Supervisor:

Name: Alister W. Graham   Signature:________________________

Date: _ _ / _ _ / _ _ _ _

In the case of more than four authors please attach another sheet with the names, signatures and contribution of the authors.